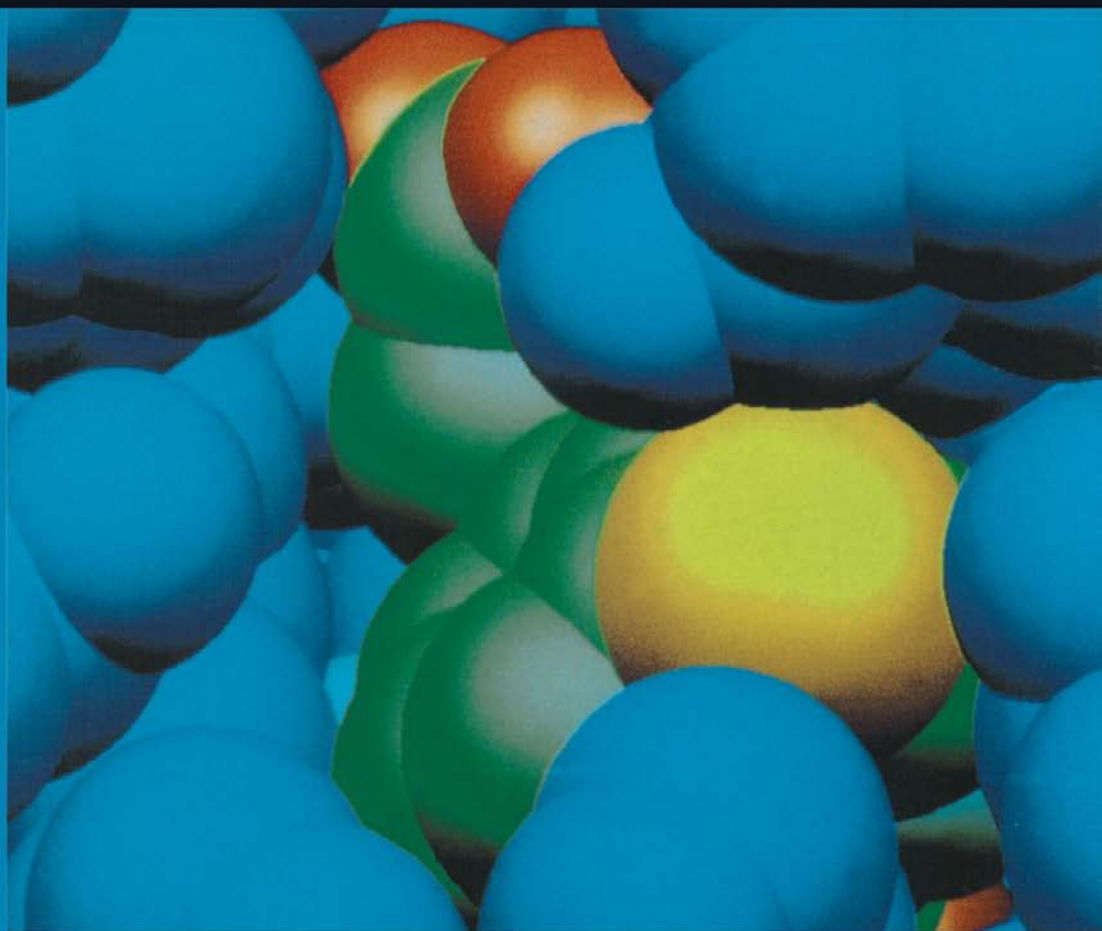


THEORETICAL AND COMPUTATIONAL CHEMISTRY 12



Energetic Materials

Part 1. Decomposition, Crystal and Molecular Properties

Peter Politzer
Jane S. Murray
editors

Energetic Materials

Part 1. Decomposition, Crystal and Molecular Properties

THEORETICAL AND COMPUTATIONAL CHEMISTRY

SERIES EDITORS

Professor P. Politzer

Department of Chemistry
University of New Orleans
New Orleans, LA 70148, U.S.A.

Professor Z.B. Maksić

Rudjer Bošković Institute
P.O. Box 1016,
10001 Zagreb, Croatia

VOLUME 1

**Quantitative Treatments of Solute/Solvent
Interactions**

P. Politzer and J.S. Murray (Editors)

VOLUME 2

**Modern Density Functional Theory: A Tool for
Chemistry**

J.M. Seminario and P. Politzer (Editors)

VOLUME 3

**Molecular Electrostatic Potentials: Concepts and
Applications**

J.S. Murray and K. Sen (Editors)

VOLUME 4

**Recent Developments and Applications of Modern
Density Functional Theory**

J.M. Seminario (Editor)

VOLUME 5

Theoretical Organic Chemistry

C. Párkányi (Editor)

VOLUME 6

**Pauling's Legacy: Modern Modelling of the Chemical
Bond**

Z.B. Maksić and W.J. Orville-Thomas (Editors)

VOLUME 7

**Molecular Dynamics: From Classical to Quantum
Methods**

P.B. Balbuena and J.M. Seminario (Editors)

VOLUME 8

Computational Molecular Biology

J. Leszczynski (Editor)

VOLUME 9

**Theoretical Biochemistry: Processes and Properties
of Biological Systems**

L.A. Eriksson (Editor)

VOLUME 10

Valence Bond Theory

D.L. Cooper (Editor)

VOLUME 11

**Relativistic Electronic Structure Theory, Part 1.
Fundamentals**

P. Schwerdtfeger (Editor)

VOLUME 12

**Energetic Materials, Part 1. Decomposition, Crystal
and Molecular Properties**

P. Politzer and J.S. Murray (Editors)

VOLUME 13

Energetic Materials, Part 2. Detonation, Combustion

P. Politzer and J.S. Murray (Editors)

Energetic Materials

Part 1. Decomposition, Crystal and Molecular Properties

Edited by

Peter Politzer

Jane S. Murray

Department of Chemistry
University of New Orleans
New Orleans, LA 70148, USA



ELSEVIER

2003

Amsterdam – Boston – Heidelberg – London – New York – Oxford – Paris
San Diego – San Francisco – Singapore – Sydney – Tokyo

ELSEVIER B.V.
Sara Burgerhartstraat 25
P.O. Box 211, 1000 AE Amsterdam, The Netherlands

© 2003 Elsevier B.V. All rights reserved.

This work is protected under copyright by Elsevier, and the following terms and conditions apply to its use:

Photocopying

Single photocopies of single chapters may be made for personal use as allowed by national copyright laws. Permission of the Publisher and payment of a fee is required for all other photocopying, including multiple or systematic copying, copying for advertising or promotional purposes, resale, and all forms of document delivery. Special rates are available for educational institutions that wish to make photocopies for non-profit educational classroom use.

Permissions may be sought directly from Elsevier's Science & Technology Rights Department in Oxford, UK: phone: (+44) 1865 843830, fax: (+44) 1865 853333, e-mail: permissions@elsevier.com. You may also complete your request on-line via the Elsevier homepage (<http://www.elsevier.com>), by selecting 'Customer Support' and then 'Obtaining Permissions'.

In the USA, users may clear permissions and make payments through the Copyright Clearance Center, Inc., 222 Rosewood Drive, Danvers, MA 01923, USA; phone: (+1) (978) 7508400, fax: (+1) (978) 7504744, and in the UK through the Copyright Licensing Agency Rapid Clearance Service (CLARCS), 90 Tottenham Court Road, London W1P 0LP, UK; phone: (+44) 207 631 5555; fax: (+44) 207 631 5500. Other countries may have a local reprographic rights agency for payments.

Derivative Works

Tables of contents may be reproduced for internal circulation, but permission of Elsevier is required for external resale or distribution of such material. Permission of the Publisher is required for all other derivative works, including compilations and translations.

Electronic Storage or Usage

Permission of the Publisher is required to store or use electronically any material contained in this work, including any chapter or part of a chapter.

Except as outlined above, no part of this work may be reproduced, stored in a retrieval system or transmitted in any form or by any means, electronic, mechanical, photocopying, recording or otherwise, without prior written permission of the Publisher.

Address permissions requests to: Elsevier's Science & Technology Rights Department, at the phone, fax and e-mail addresses noted above.

Notice

No responsibility is assumed by the Publisher for any injury and/or damage to persons or property as a matter of products liability, negligence or otherwise, or from any use or operation of any methods, products, instructions or ideas contained in the material herein. Because of rapid advances in the medical sciences, in particular, independent verification of diagnoses and drug dosages should be made.

First edition 2003

Library of Congress Cataloging in Publication Data

A catalog record from the Library of Congress has been applied for.

British Library Cataloguing in Publication Data

A catalogue record from the British Library has been applied for.

ISBN: 0 444 51518 6

ISSN: 1380 - 7323 (Series)

Ⓢ The paper used in this publication meets the requirements of ANSI/NISO Z39.48-1992 (Permanence of Paper).
Printed in Hungary.

PREFACE

Our own involvement in the area of energetic materials stems from the second half of a New Orleans Saints football game in 1979, which one of us (P.P.) was attending together with Rod Bartlett (a contributor to these volumes). The Saints were losing by a large score, and with interest in the game waning, Rod spent much of the second half expounding, to a very receptive listener, the opportunities in energetic materials research. Whether this area has since been advanced or set back as a result of the Saints' ineptness that afternoon is for others to decide. What is certain, however, is that during these years we have been extremely fortunate in having the assistance, encouragement and support of a very fine group of project officers:

Dick Miller and Judah Goldwasser, ONR;
David Squire, Ron Husk and Bob Shaw, ARO;
Larry Davis, AFOSR;
Jack Alster and Frank Owens, ARDEC;
Bob McKenney, Norm Klausutis and Paul Bolduc, AFATL;
Horst Adolph, NSWC;
and Leonard Caveny, BMDO.

We are grateful to all of them.

In putting together these two volumes, we have greatly appreciated the enthusiastic encouragement and suggestions that we received from Betsy Rice and her willingness to prepare the overview that begins each volume, in addition to her other contribution. Finally, we want to thank Mick Coleman and Bob Murray for their much-needed help with various aspects, often tedious, of the editing process.

Peter Politzer and Jane S. Murray

This Page Intentionally Left Blank

TABLE OF CONTENTS

Part 1

Overview of Research in Energetic Materials	
<i>B. M. Rice</i>	1
Chapter 1. A Survey of the Thermal Stability of Energetic Materials	5
<i>J. C. Oxley</i>	
1. Introduction.....	5
2. Nitrate Esters.....	7
3. Nitroarenes.....	11
4. Nitroalkanes.....	14
5. Nitramines.....	16
6. New Energetic Materials.....	19
6.1 New Nitrogen Heterocycles.....	20
6.2 NF ₂ Compounds.....	26
7. Energetic Salts.....	27
8. Summary of Thermal Stability and our Approach.....	30
Chapter 2. Characterisation of Explosive Materials Using Molecular Dynamics Simulations	49
<i>P. Capkova, M. Pospisil, P. Vavra and S. Zeman</i>	
1. Introduction.....	49
2. Strategy of Molecular Dynamics Simulations.....	50
3. Results and Discussion.....	53
3.1 Decomposition of RDX and β -HMX.....	54
3.2 Decomposition of DADNE and NQ.....	56
3.3 Parameters characterizing the decomposition process.....	57
4. Conclusions.....	59
Chapter 3. Nitro\leftrightarrow<i>aci</i>-nitro Tautomerism in High-Energetic Nitro Compounds	61
<i>P.V. Bharatam and K. Lammertsma</i>	
1. Nitro \leftrightarrow <i>aci</i> -nitro tautomerism.....	61
2. Nitromethane \leftrightarrow <i>aci</i> -nitromethane tautomerism.....	63
3. Tautomerism in Substituted Nitroethylenes.....	69

4. Tautomerism in Nitroaromatic Compounds.....	72
5. Tautomerism in NTO, HMX, RDX and 5-Nitro-1H-Tetrazole.....	77

Chapter 4. Decomposition Mechanism of 1,1-Diamino-Dinitroethylene (FOX-7): An Overview of the Quantum Chemical Calculation.....91

A. Gindulyte, L. Massa, L. Huang and J. Karle

1. Introduction.....	92
2. Nitroethylene Computational Details.....	95
3. Nitroethylene Results.....	96
4. DADNE Computational Details.....	97
5. DADNE Results and Discussion.....	98
5.1 Initial Step of DADNE Decomposition.....	99
5.2 Isonitrite, 3	101
5.3 Hydrogen Atom Migration from NH ₂ to NO ₂	102
5.4 HONO Elimination.....	102
5.5 CO Elimination.....	103
5.6 NH ₂ Radical Elimination.....	103
5.7 Final Stages of DADNE Decomposition.....	103
6. Additional Check on the Accuracy of DFT Calculations.....	104
7. Concluding Remarks.....	104

Chapter 5. Quantum-chemical Dynamics with the Slater-Roothaan Method.....111

B.I. Dunlap

1. Introduction.....	111
2. Robust and Variational Fitting.....	114
3. The Slater-Roothaan Method.....	116
4. Symmetry and Balanced DFT Dynamics.....	119
5. 2-D Chemical Dynamics.....	121
6. Conclusion.....	122

Chapter 6. Molecular Dynamics Simulations of Energetic Materials.....125

D. C. Sorescu, B. M. Rice, and D. L. Thompson

1. Introduction.....	125
2. The General Method of Molecular Dynamics Simulations.....	128
3. Molecular Dynamics Studies of Energetic Materials.....	131
3.1 Gas-Phase Reactions of Energetic Materials.....	131
3.1.1 RDX: Initial Decomposition Reactions.....	132
3.1.2 HMX: Initial Decomposition Reactions.....	139
3.1.3 DMNA: A Prototypical Nitramine.....	140

3.1.4 Nitromethane Decomposition.....	142
3.1.5 Methylene Nitramine Decomposition.....	144
3.2 Non-reactive Models.....	146
3.2.1 Non-reactive Models.....	146
3.2.2 Reactive Models.....	166
3.2.3 First Principles Simulations Models.....	173

Chapter 7. Structure and Density Predictions for Energetic Materials.....185

J. R. Holden, Z. Du and H. L. Ammon

1. The Development of MOLPAK (MOLEcular PAcKing).....	188
2. Examples of Coordination Sphere Building Procedures.....	196
3. MOLPAK Overview and Structure Prediction.....	197
4. Summary and Challenges.....	211

Chapter 8. X-ray Crystallography - Beyond Structure in Energetic Materials.....215

A. A. Pinkerton, E. A. Zhurova and Y.-S. Chen

1. Introduction.....	215
2. Experimental Protocol.....	216
3. Data Reduction.....	218
4. Data Analysis.....	220
4.1 Structure Model - Spherical Atom.....	220
4.2 Structure Model - Atom Centered Multipole Model.....	221
5. Refinements.....	224
6. Electron Density Distributions.....	225
6.1 Residuals.....	225
6.2 Deformation Densities.....	225
6.3 Laplacian of the Electron Density.....	228
7. Topological Analysis.....	228
7.1 Atomic Charges.....	232
7.2 Bond Critical Point Properties.....	232
8. Properties.....	235
8.1 Electrostatic Potential.....	235
8.2 Energy Density Distribution.....	236
8.3 Energy Density Critical Points.....	237
8.4 Hydrogen Bonding.....	240
9. Conclusion.....	241

Chapter 9. Computational Approaches to Heats of Formation.....247

P. Politzer, P. Lane and M. C. Concha

1. Introduction.....	247
----------------------	-----

2. Specific Approaches to ΔH_f	248
3. Computational Methodologies.....	252
3.1 <i>Ab Initio</i>	252
3.2 Density Functional.....	253
3.3 <i>Ab Initio</i> /Empirical and Density Functional/ Empirical Combinations.....	256
4. Liquid and Solid Phase Heats of Formation.....	258
5. Applications and Discussion.....	259
5.1 Boron and Aluminum Combustion Products.....	259
5.2 H/C/N/O/F Energetic Compounds.....	260
6. Summary and Conclusions.....	271

Chapter 10. Thermodynamics and Mechanical Properties of HMX from Atomistic Simulations.....279

D. Bedrov, G. D. Smith, and T. D. Sewell

1. Introduction.....	279
2. Force Field.....	281
2.1 General Philosophy.....	281
2.2 Quantum Chemistry.....	282
2.3 Force Field Parametrization and Validation.....	288
3. Simulations of Liquid HMX.....	292
3.1 Viscosity and Self-diffusion Coefficient.....	292
3.2 Thermal Conductivity.....	298
4. Crystalline HMX.....	302
4.1 Structural Properties.....	302
4.2 Enthalpy of Sublimation.....	306
4.3 Hydrostatic Compression.....	307
4.4 Anisotropic Elasticity.....	316
5. Conclusions.....	320

Chapter 11. Optical absorption in PETN and RDX.....327

W. F. Perger

1. Background.....	327
2. The Approach.....	328
2.1 Optical Absorption and the Use of Crystal Program.....	328
2.2 Computational Procedure.....	331
3. Results for PETN and RDX.....	332
3.1 PETN.....	333
3.2 RDX.....	333
4. Conclusions and Future Work.....	338

Chapter 12. Interactions of Model Organic Species and Explosives with Clay Minerals.....	341
<i>A. Michalkova, L. Gorb and J. Leszczynski</i>	
1. Introduction.....	341
1.1 Interactions of Energetic Materials with Soils.....	343
2. Computational Methods.....	346
3. Interactions of Clay Minerals with Water Molecules.....	348
3.1 Experimental Study.....	349
3.2 Theoretical Study.....	351
3.3 Summary.....	355
4. Interactions of Clay Minerals with Small Organic Molecules.....	356
4.1 Experimental Study.....	356
4.1.1 D-FA and D-MFA Systems.....	357
4.1.2 K-DMSO System.....	357
4.2 Theoretical Study.....	358
4.2.1 D-FA and D-MFA Systems.....	359
4.2.2 K-DMSO System.....	363
4.3 Summary.....	365
5. Interactions of Clay Minerals with Energetic Materials.....	366
5.1 Experimental Study.....	366
5.1.1 Summary.....	371
5.2 Theoretical Study.....	372
5.2.1 Interaction of 1,3,5-Trinitrobenzene with Nonhydrated Surface of Clay Minerals.....	372
5.2.2 Interaction of 1,3,5-Trinitrobenzene with Hydrated Surface of Clay Minerals.....	377
5.2.3 Summary.....	380
6. General Conclusions and Future Research Area.....	381
Chapter 13. Chemistry and Applications of Dinitramides.....	389
<i>P. Sjöberg</i>	
1. History.....	389
2. Synthetic Methods.....	390
3. Chemistry and Properties.....	392
3.1 Reactivity.....	392
3.2 Physical Properties.....	393
3.3 Chemical Stability and Compatibility.....	393
3.4 Sensitivity.....	396
4. Applications.....	398
4.1 Propulsion.....	398
4.2 Explosive Compositions.....	399

4.2.1	Phase-stabilizer in Ammonium Nitrate (AN)...	400
4.2.2	Liquid Monopropellant.....	400
4.2.3	Automotive Safety.....	401
5.	Improvement of ADN.....	401
5.1	Stabilization of ADN.....	401
5.2	Handling Properties.....	402
 Chapter 14. Polynitrogens as Promising High-Energy Density		
Materials: Computational Design.....		405
<i>O. Kwon and M. L. McKee</i>		
1.	Introduction.....	405
2.	Known Computational Facts of Polynitrogens.....	407
2.1	Computational Methodology.....	408
2.2	N ₄	409
2.3	N ₅	410
2.4	N ₆	411
2.5	N ₇	411
2.6	N ₈	412
2.7	N ₉ , N ₁₀ , N ₁₁ and N ₁₂	412
2.8	Larger polynitrogens.....	413
3.	Nitrogen-rich Compounds, EN _n	414
4.	Conclusions.....	416
 Chapter 15. Electronic Structure Calculations as a Tool		
in the Quest for Experimental		
Verification of N₄.....		421
<i>T. Brinck, M. Bittererova and H. Ostmark</i>		
1.	Introduction.....	421
2.	Energetics.....	422
2.1	N ₄ Singlet Potential Energy Surface.....	422
2.2	N ₄ Triplet Potential Energy Surface.....	425
3.	Synthesis.....	429
3.1	Excited State N ₂ Reactions.....	429
3.2	Nitrogen Atom Reactions.....	430
4.	Detection.....	433
4.1	IR and Raman Spectroscopy.....	433
4.2	LIF Spectroscopy.....	435
5.	Summary.....	437
 Chapter 16. Changing the Properties of N₅⁺ and N₅⁻ by		
Substitution.....		441
<i>S. Fau and R. J. Bartlett</i>		
1.	Introduction.....	441

2. Computational Methods.....	443
3. Results.....	444
3.1 CHN_4^+	444
3.2 N_4P^+ and N_3P_2^+	445
3.3 CN_3O^+	448
3.4 Derivatives of N_5^-	450
4. Summary and Conclusions.....	451
Index for Parts 1 and 2.....	457

Part 2

Overview of Research in Energetic Materials

<i>B. M. Rice</i>	1
-------------------------	---

Chapter 1. Sensitivity Correlations.....5

P. Politzer and J. S. Murray

1. Introduction.....	5
2. Background.....	7
3. Sensitivity Correlations.....	8
4. TATB: A Case Study.....	10
5. Electrostatic Potential.....	12
6. Summary.....	18

Chapter 2. A Study of Chemical Micro-Mechanisms of Initiation of Organic Polynitro Compounds.....25

S. Zeman

1. Introduction.....	25
2. Data Sources.....	27
2.1 Impact Sensitivity Data.....	27
2.2 Electric Spark Sensitivity Data.....	27
2.3 Detonation Velocity.....	27
2.4 NMR Chemical Shifts.....	27
3. Basic Mechanisms of Thermal Decomposition of Organic Polynitro and Polynitroso Compounds.....	35
4. Initiation of Polynitro Compounds.....	36
4.1 Chemical Micro-Mechanism of Initiation by Impact.....	36
4.2 Chemical Micro-Mechanism of Initiation of Detonation.....	40
4.3 Chemical Micro-Mechanism of Initiation by Electric Shock.....	43

4.4 Chemical Micro-Mechanism of Fission of Polynitro Compounds by Action of Heat and its Relation to Detonation.....	45
5. Conclusions.....	46
Chapter 3. Dynamics of Energy Disposal in Unimolecular Reactions.....	53
<i>C. Stopera and M. Page</i>	
1. Chemical Issues in the Initiation of Detonations.....	54
2. The Key Role of Unimolecular Reactions.....	54
3. Quantum Chemistry Provides Potential Energy Surface.....	56
4. Computing the Reaction Path.....	57
5. The Reaction Hamiltonian.....	61
6. Methylene Nitramine Decomposition.....	64
7. Concluding Remarks.....	68
Chapter 4. Initiation and Decomposition Mechanisms of Energetic Materials.....	71
<i>M.R. Manaa</i>	
1. Introduction.....	71
2. Initiation Models.....	72
3. Nonradiative Energy Transfer in Nitromethane.....	73
4. Effects of Pressure and Vacancies.....	75
4.1.1 Uniform Compression.....	75
4.1.2 Uniaxial Compression.....	77
4.1.3 C-H High Stretch Under Uniaxial Compression.....	79
4.2 Effect of Molecular Vacancies.....	81
4.2.1 Uniform Compression.....	83
4.2.2 Uniaxial Compression.....	85
4.3 Summary.....	86
5. Decomposition of HMX.....	87
5.1 Computational Model.....	90
5.2 Kinetics of HMX Decomposition.....	91
5.3 Summary.....	96
Chapter 5. Initiation due to Plastic Deformation from Shock or Impact.....	101
<i>C. S. Coffey</i>	
1. Introduction.....	101
2. AFM and STM Observations of the Microscopic Processes of Plastic Deformation.....	103
2.1 Micro-Indentations.....	104

2.2	Shock Response of Heavily Confined Crystals.....	105
2.3	Impact Observations.....	106
2.4	Extreme Plastic Flow.....	106
2.5	Comparison with Gold.....	107
2.6	Summary of Experimental Observations.....	107
3.	Theoretical Developments.....	108
3.1	The Deformed Lattice Potential.....	108
3.2	Plastic Flow and Energy Dissipation.....	109
3.3	Dislocation Tunneling, Particle Size Effects and Shear Band Formation.....	111
3.4	Summary of Theoretical Results.....	112
4.	Calculations.....	113
4.1	Anomalous Plastic Deformation in Impacted RDX.....	113
4.2	Estimation of Shear Band Temperatures.....	114
4.3	Yield Stress and Particle Size.....	115
4.4	Approximate Energy Dissipation Rate and $P^2 \Delta t$ Initiation Threshold.....	116
4.5	Initiation by Non-Planar Shock Waves.....	118
4.6	Initiation of Detonation.....	119
5.	Conclusions.....	120

Chapter 6. Fast Molecular Processes in Energetic Materials.....

125

D. D. Dlott

1.	Introduction.....	125
2.	The Phenomenology of Energetic Materials.....	126
2.1	Types of Energetic Materials.....	127
2.2	Shock Waves.....	127
2.2.1	Shock Waves in Continuous Elastic Media.....	128
2.2.2	Shock Fronts in Real Materials.....	132
2.3	Detonations.....	135
2.4	Low Velocity Initiation.....	137
2.5	Shock Initiation.....	139
2.6	Sensitivity.....	141
3.	Molecular Level Structure of Energetic Materials.....	143
3.1	How Chemical Bonds are Broken.....	143
3.2	Band Structure of Molecular Solids.....	144
3.3	Molecular Crystals under Dynamic Shock Compression.....	147
3.3.1	Shock-induced Electronic Excitations.....	147
3.3.2	Shock-induced Mechanical Excitations.....	148
3.3.3	Dynamic Picture of Shock Excitation.....	150
3.4	Shock Compression of Nanometric Energetic	

Materials.....	151
4. Up-pumping, Sensitivity and Ignition.....	153
4.1 Nitromethane Shock Initiation and the Induction Time.....	154
4.2 Doorway Vibrations in Up-pumping.....	156
4.3 Up-pumping Calculations, Simulations and Sensitivity.....	160
4.4 Up-pumping and Anharmonic Defects.....	163
4.5 Up-pumping and Thermal Conductivity.....	163
4.6 Coherent Pumping of Vibrations.....	165
5. Hot Spot Formation in Porous Materials.....	168
6. Molecular Response in Detonation.....	172
7. Fast Processes in Nanometric Energetic Materials.....	175
8. Concluding Remarks.....	179

Chapter 7. The Equation of State and Chemistry of Detonation Products.....193

L. E. Fried, W. M. Howard, and J. M. Zaug

1. Introduction.....	193
2. Computational Method.....	198
3. Fluid Equations of State.....	200
4. Condensed Equations of State.....	207
5. Application to Detonation.....	209
6. Experimental.....	210
7. Results and Discussion.....	213
8. Conclusions.....	221

Chapter 8. Combustion Mechanisms and Simplified-Kinetics Modeling of Homogeneous Energetic Solids.....225

M.Q. Brewster

1. Introduction.....	226
2. Mathematical Model of Macroscopically Steady Combustion...	227
2.1 Condensed Phase Model.....	228
2.1.1 Governing Equations.....	228
2.1.2 Solution of Condensed Phase Equations.....	231
2.2 Gas Phase Model.....	234
2.2.1 Governing Equations.....	234
2.2.2 Solution of Gas Phase Equations.....	239
2.3 Complete Model--Gas and Condensed Phases.....	243
2.3.1 High Gas Activation Energy Solution (Intermediate Pressures).....	244
2.3.2 Low Gas Activation Energy Solution	

(Intermediate Pressures).....	244
2.3.3 High and Low Pressure Regimes (Condensed Phase Controlled Burning).....	244
2.3.4 Sensitivity Parameters.....	245
3. Results for Macroscopically Steady Combustion.....	249
3.1 Parametric (Non-Dimensional) Results for Benchmark Case.....	249
3.1.1 Burning Rate or Mass Flux.....	250
3.1.2 Surface Temperature, Heat Feedback, and Flame Standoff Distance.....	252
3.1.3 Sensitivity Parameters.....	255
3.2 Results for Common Materials.....	258
3.2.1 NC/NG Double Base Propellant.....	259
3.2.2 HMX.....	268
3.3 Summary of Steady-State Results.....	273
4. Quasi-Steady Theory of Unsteady Condition.....	273
4.1 Non-Linear Formulation.....	274
4.2 Linear Formulation.....	276
5. Results for Quasi-Steady, Oscillatory Combustion.....	278
5.1 Parametric (Non-Dimensional) Results for Benchmark Case.....	278
5.2 Results for Common Materials.....	285
5.2.1 NC/NG Double Base Propellant.....	286
5.2.2 HMX.....	286
6. Intrinsic Stability.....	288
7. Concluding Remarks.....	290

Chapter 9. Modeling of Nitramine Propellant Combustion and Ignition.....295

E. S. Kim, R. Yang and V. Yang

1. Introduction.....	297
1.1 Modeling Development of Steady-State Combustion of Nitramine Propellants.....	298
1.2. Modeling Development of Ignition of Nitramine Propellants.....	299
1.3 Modeling Development of Combustion of Nitramine/GAP Pseudo-Propellants.....	300
2. Theoretical Formulation.....	302
2.1 Steady-State Combustion of RDX Monopropellant.....	302
2.2 Laser-Induced Ignition of RDX Monopropellant.....	303
2.3 Steady-State Combustion of Nitramine/GAP Pseudo-Propellants.....	305
2.4 Conservation Equations.....	306

2.4.1	Gas-Phase Processes.....	306
2.4.2	Gas-Phase Chemical Kinetics.....	307
2.4.3	Subsurface Two-Phase Processes.....	308
2.4.4	Subsurface Chemical Kinetics and Phase Transition.....	309
2.4.5	Solid-Phase Processes.....	311
2.4.6	Radiative Heat Transfer.....	311
2.4.7	Boundary Conditions.....	313
3.	Numerical Method.....	314
4.	Discussion of Model Results.....	315
4.1	Steady-State Combustion of Nitramine Propellants.....	316
4.2	Laser-Induced Ignition of RDX Monopropellant.....	322
4.3	Steady-State Combustion of HMX/GAP and RDX/GAP Pseudo-Propellants.....	332
4.3.1	HMX/GAP Pseudo-Propellant.....	332
4.3.2	RDX/GAP Pseudo-Propellant.....	340
5.	Concluding Remarks.....	346

Chapter 10. Use of Kinetic Models for Solid State

	Reactions in Combustion Simulations.....	351
	<i>J. Wang and C.A. Wight</i>	
1.	Introduction.....	351
1.1	Steady Combustion Models vs. Unsteady Combustion Models.....	352
1.2	Surface Reaction Kinetics.....	353
2.	Model.....	356
3.	Results and Discussion.....	360
3.1	Validation of the Steady State Combustion with WSB Model.....	360
3.2	Ignition Time.....	361
3.3	Pressure Sensitivity and Surface Temperature.....	362
3.4	Temperature Sensitivity.....	364
3.5	Effect of Kinetic Models.....	365
3.5.1	First-order Reaction Model.....	365
3.5.2	Second-order Reaction Model.....	367
4.	Conclusion.....	369

Chapter 11. Towards Reliable Prediction of Kinetics and Mechanisms for Elementary Processes: Key Combustion Initiation Reactions of Ammonium Perchlorate.....

	<i>R.S. Zhu and M.C. Lin</i>	
1.	Introduction.....	374

2. Computational Methods.....	375
2.1 Ab Initio Calculations.....	375
2.2 Rate Constant Calculations.....	377
3. Results and Discussion.....	379
3.1 Unimolecular Decomposition of HClO_4 and HClO_3	379
3.2 Reactions of H and HO with HClO_4	382
3.2.1 $\text{H} + \text{ClO}_4$ Reaction.....	382
3.2.2 $\text{HO} + \text{HClO}_4$ Reaction.....	386
3.3 Unimolecular Decomposition of ClO_x ($x = 2 - 4$).....	390
3.3.1 ClOO and OClO	390
3.3.2 $s\text{-ClO}_3$	393
3.3.3 ClO_4	394
3.4 Bimolecular Reactions of ClO_x ($x = 1\text{-}3$).....	395
3.4.1 $\text{HO} + \text{ClO}$	395
3.4.2 $\text{HO} + \text{OClO}$ Reaction.....	400
3.4.3 $\text{HO} + \text{ClO}_3$	404
3.4.4 $\text{HO}_2 + \text{ClO}$	406
3.4.5 $\text{HO}_2 + \text{OClO}$	411
3.4.6 $\text{O} + \text{ClO}$ and its Reverse Reaction, $\text{Cl} + \text{O}_2$	413
3.4.7 $\text{ClO} + \text{ClO}$	415
3.4.8 $\text{ClO} + \text{OClO}$	423
4. Concluding Remarks.....	436
Index for Parts 1 and 2.....	445

This Page Intentionally Left Blank

Overview of Research in Energetic Materials

Betsy M. Rice

U. S. Army Research Laboratory, Aberdeen Proving Ground, MD
21005-5069

Energetic materials encompass different classes of chemical compositions of fuel and oxidant that react rapidly upon initiation and release large quantities of force (through the generation of high-velocity product species) or energy (in the form of heat and light). Energetic materials are typically classified as explosives, propellants, pyrotechnics or incendiaries, and distinctions among the classes are usually in terms of the types of products generated and rates of reactions. These particular features have been advantageously employed in a wide variety of industrial and military applications, but often these utilizations have not been fully optimized, mainly due to the inability to identify and understand the individual fundamental chemical and physical steps that control the conversion of the material to its final products.

The conversion of the material is usually not the result of a single-step reaction, or even a set of a few simple consecutive chemical reactions. Rather, it is an extremely complex process in which numerous chemical and physical events occur in a concerted and synergistic fashion, and whose reaction mechanisms are strongly dependent on a wide variety of factors. For instance, the performance of a material is a strong function of the temperature and pressure of its environment and of its mechanical properties. The rate of energy release can be modified by additives or by varying the concentrations of fuel and oxidizer. The response of the material can be affected by the manner in which it was processed. The properties and behavior of the material can change over time. The rate of the conversion of the material is strongly dependent on the conditions of the initiation. For example, an explosive can be ignited to burn, a process that can be thought of as a reaction wave that proceeds through the material at subsonic speeds. Or it could be shock-initiated to detonation, where detonation can be described as a reaction wave that proceeds through the material at supersonic speeds. For these cases, the product concentrations and species are not the

same. Also, these processes often occur under extreme conditions of temperature and pressures, making experimental measurement difficult. These are but a few of the complexities associated with studies of reactions of energetic materials that make resolving the individual details so difficult. They are also the reason that research in the field of energetic materials is so exciting! These difficulties have required the development of a variety of innovative theoretical methods, models and experiments designed to probe details of the various phenomena associated with the conversion of energetic materials to products.

Probably the majority of experimental and theoretical efforts in energetic materials research to date have been directed toward assessing performance. The focus is often on quantifying the amount of energy that is released, identifying key reaction mechanisms, or investigating ways in which the energy release can be manipulated and controlled. However, increased environmental and safety concerns are placing new emphases on understanding other aspects of energetic materials, such as toxicity, processing emissions, combustion emissions, wear and erosion on combustion fixtures from reaction products, contamination of ground water or soil, environmentally-friendly synthesis and processing, destruction or disposal, life-span (chemical stability), storage, handling, or vulnerability to a variety of external stimuli. Naturally, models are emerging that can be used to investigate these aspects of energetic materials.

The high time and pecuniary costs associated with the synthesis or formulation, testing and fielding of a new energetic material has called for the inclusion of modeling and simulation into the energetic materials design process. This has resulted in growing demands for accurate models to predict properties and behavior of notional energetic materials before committing resources for their development. For example, in earlier times, extensive testing and modification of proposed candidate materials for military applications could take decades before the material was actually fielded, in order to assure the quality and consistent performance of the material in the desired application. Predictive models that will allow for the screening and elimination of poor candidates before the expenditure of time and resources on synthesis and testing of advanced materials promise significant economic benefit in the development of a new material.

The growing demands for predictive models of energetic materials have not eliminated the need for experimentation on energetic materials; rather, they call for increasingly detailed experimental studies to allow critical assessment, correction and enhancement of the models. This is a particularly challenging requirement, since the time and length scales of

most experiments are often many orders of magnitude larger than those of some of the models (i.e. atomistic). Nonetheless, advances are being made in designing experiments to probe behavior of energetic materials at ever-decreasing time and spatial scales; some of these are described in these volumes.

The contributions to these volumes will highlight challenges faced by researchers in the energetic materials community, as well as describe research activities directed toward fundamental characterization of properties and behavior of these interesting materials. An assortment of theoretical studies of energetic materials processes at different time and length scales and under different conditions is presented. Accompanying these are discussions of the complexity, assumptions and levels of empiricism of the models used in these studies. Also included, in order to provide perspective, are surveys of experiments designed to investigate the complex and unique chemical and physical processes occurring in energetic materials. It is hoped that the works presented in these volumes will stimulate further investigations and advances in the area of energetic materials research.

This Page Intentionally Left Blank

Chapter 1

A survey of the thermal stability of energetic materials

Jimmie C. Oxley

Chemistry Dept; University of Rhode Island; Kingston, RI 02881

1. INTRODUCTION

It is reported that the Chinese discovered black powder as early as 200 AD, but the earliest surviving record is in a Chinese military manual "Wu Jing Zong Yao" dated 1044 A.D. The Chinese used this new found powder for warfare, attaching bamboo tubes of gun powder to arrows to make "rocket arrows" and sometimes bundling many rocket arrows onto launchers which were hauled into battle on wheelbarrows, also a Chinese invention. The Chinese formula reached Europe in the 13th century, and the Europeans were firing bombards by 1327 A.D. Sir Francis Bacon, who published the formula in the West, was so impressed by its awesome power that he speculated man would give up making war when he saw the terror of black powder [1].

Black Powder	Chinese 200 AD	Bacon 1242 AD	present day
salt peter KNO_3	72.5%	37.5%	74%
charcoal	19.0%	31.25%	15.6%
sulfur	8.4%	31.25%	10.4%

Man did not give up war, nor did he find a peaceful use for black powder until the 1600's. Then, for the first time in Hungary, black powder was used for mining. Tenny L. Davis credits black powder as one of the three inventions responsible for ending the Middle Ages [1]. (The other two were the printing press and the discovery of the New World.) The first

commercial production in the United States was by DuPont (1802)[2]. World War I saw the maximum use of black powder.

To function as good explosives, formulations must maximize expansion volume (i.e. density and gas formation) and heat release. For a substance to function as an explosive, its molecules must (a) be broken down to smaller molecules without high energy costs (weak linkages) so that the net decomposition reaction is exothermic; (b) contain sufficient oxygen to quickly oxidize most of the molecule to gas--carbon and hydrogen to CO, CO₂ and H₂O; (c) undergo oxidative breakdown rapidly enough that the energy release supports the shock wave. It was nearly four hundred years after the Western world had adopted black powder before explosives using these principles, the first "high explosives," appeared. By the mid- to late nineteenth century, Lavoisier had "fathered" modern chemistry and died in the French revolution; Bertholet had published his famous treatise on chemistry; and nitration reactions had been discovered: alcohols with mixed acid (sulfuric and nitric) made highly flammable, if not explosive, species [3].

Most military explosives satisfy requirements (a) and (b) by containing only carbon (C), hydrogen (H), oxygen (O), and nitrogen (N). The oxygen is found usually in nitro groups since it is relatively easy to break the X-NO₂ bond, and the nitrogen can convert to nitrogen gas, while the oxygen aids the gasification of carbon and hydrogen. Chronologically, nitrate esters (O-NO₂ e.g. nitrocellulose, nitroglycerin) were the first high explosives discovered in the mid-nineteenth century. Nitroarenes (C-NO₂, e.g. picric acid, TNT) came into use at the end of the nineteenth century. Nitramines (N-NO₂, e.g. RDX), though discovered about the same time as TNT, did not come into their own until World War II and later. In modern explosive design requirements (a) and (b) still dictate that compounds be designed to be dense and have positive heats of formation. High oxygen content is less important in high nitrogen /low carbon containing materials.

In the United States about five billion pounds of explosives are used annually. Most are used for commercial purposes and are ammonium-nitrate based formulations [2,4]. There are less than a dozen chemical explosives that are manufactured in bulk quantities. These were "discovered" in the fifty-year period between 1850 and 1900 [5,6,7,8,9,10]. New explosives have been synthesized, yet optimization of synthesis, study of stability and

sensitivity, and optimizing the formulations takes decades. This problem is not new; the development of nitrocellulose and nitroglycerin as useful explosives also took decades. Thermal stability must be evaluated and quantified, not only under the intended parameters of manufacture or storage, but outside these limits where a catastrophic upset might occur. Often, as in the case of nitrocellulose, the intrinsic thermal stability is low or easily deteriorated by contamination so that a stability enhancement agent is necessary. To find a stabilizing agent, the mechanism of decomposition must be thoroughly understood. Thus, thermal stability must be evaluated over a wide range of temperatures and the decomposition mechanism(s) determined before stabilizing agents can be chosen rationally.

2. NITRATE ESTERS

Nitrocellulose or "gun cotton" was discovered by Braconnot (France, 1833) and patented by Schonbein (1846) (Fig. 1). It is speculated that in order to determine whether the action of nitric acid was a reaction or merely a sorption into fibrous material, Sobrero (1846) treated glycerin, a liquid, with nitric acid and found a true reaction took place. Hence, nitrocellulose and nitroglycerin were discovered within a decade of each other, but neither found widespread use until the 1860's when methods of stabilizing them were devised. Between 1865 and 1868, Abel patented improved preparations of nitrocellulose. He found that pulping allowed impurities, such as residual acid, to be more easily washed out by "poaching" and resulted in improved stability. The Abel stability test is named after him[5].

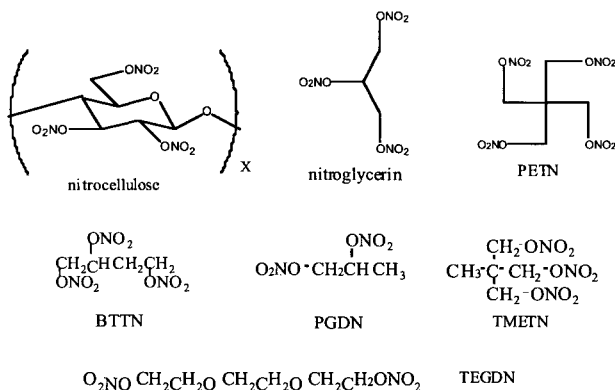
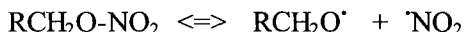


Fig. 1 Nitrate Esters

While complex nitrate esters, such as nitrocellulose and nitroglycerin, were the first to find application as explosives, understanding the mechanisms of nitrate ester decomposition was accomplished through the study of simpler compounds [11-16]. Ethanol nitrate was examined by numerous researchers, and they concluded the first, and rate-determining, step was reversible loss of NO_2 .



Griffiths, Gilligan, and Gray studied 2-propanol nitrate pyrolysis and found it exhibited more β -cleavage than primary nitrate esters [17]. It yielded nearly equal amounts of 2-propanol nitrite and acetaldehyde, as well as small amounts of acetone, nitromethane, and methyl nitrite. Homolytic cleavage of the RO-NO_2 bond formed the 2-propoxy radical, which subsequently reacted with nitric oxide to produce 2-propanol nitrite, or it could eliminate methyl radical to form acetaldehyde and methyl-derived products; or it could be converted to acetone by oxidization or loss of a hydrogen atom. Dinitrates of butanediol were investigated by Powling and Smith [18]. They found that 1,4-butanediol dinitrate, following cleavage of one NO_2 moiety, decomposed to formaldehyde, nitrogen dioxide, and ethylene, whereas 2,3-butanediol dinitrate gave acetaldehyde in place of formaldehyde and ethylene. A similar intramolecular decomposition to gaseous products has been proposed for nitroglycerin [19]. Ng, Field, and Hauser used time-of-flight mass spectrometry to identify the decomposition products of pentaerythritol tetranitrate (PETN); based on their results they postulated the decomposition involved the formation of the tertiary tris-(nitroxymethyl)methyl radical [20].

A comprehensive study examined the thermal stability and decomposition mechanism of a large number of primary, secondary, and tertiary mononitrates: n-pentanol, 3-buten-1-ol, ethanol, neopentanol, 2-phenylethanol, 2-propanol, cyclohexanol, 2-methyl-2-propanol, and 2-methyl-2-butanol nitrates. Hydrogen-donating solvents, capable of capping radical intermediates, were employed to stabilize intermediates for identification and to divert the oxides of nitrogen from further complicating the course of degradation. The reversibility of NO_2 homolysis was demonstrated by solvent cage effects and isotopic labeling experiments. To shed light on the timing of the loss of NO_2 and CH_2O from primary alkanol nitrates, certain nitrate esters leading to stabilized alkyl radicals were designed to favor concerted fragmentation. The effect of β -substitution was studied by using nitrate esters

of varying degrees of substitution. Nitrate esters with multiple nitrate ester moieties were also examined: 1,4-butanediol dinitrate; 1,5-pentanediol dinitrate; 2,2-dimethyl-1,3-propanediol dinitrate; 1,1,1-tris(hydroxymethyl)- ethane trinitrate; and PETN. These thermal decomposition studies illustrated three general principles [21].

a) The rate-determining step in nitrate ester thermolysis is usually homolytic cleavage of the RO-NO₂ bond but tertiary nitrates can undergo E1 elimination.

b) The presence of radical-stabilizing substituents on the β-carbon determines the rate and extent of β-scission and elimination of formaldehyde.

c) In compounds containing more than one nitrate ester, the structural orientation has a marked effect on the reaction products. The thermolysis of compounds of this sort can result in ring closure or sequential elimination of NO₂ and CH₂O if the nitrate esters are in close proximity (Fig. 2).

Most nitrate esters are in the same physical state at ambient temperature as their parent alcohol. With few exceptions (e.g. highly symmetric PETN and the polymeric nitrocellulose), most are liquids. Many nitrate esters find use in propellants. Present-day studies on nitrocellulose primarily focus on its reactions during combustions [22,23]. The Navy uses a variety of liquid nitrate esters as plasticizers and propellants [trimethylolethane trinitrate (TMETN), triethylene glycol dinitrate (TEGDN), 1,2-propylene glycol dinitrate (PGDN), 1,2,4 butanetriol trinitrate (BTTN)]. Brill et al have examined the thermal decomposition of some of these nitrate esters using T-jump (heating at 2000°/sec) FT-IR. They reported the relationship between the nitrate ester and its pyrolysis products was straightforward. The amounts of NO₂ and CH₂O produced were proportional to the number of -NO₂ and -CH₂O- groups in the starting material [24]. Less conventional uses of nitrate esters include the use of ethyl hexyl nitrate ester as a cetane modifier in diesel fuel [25] and isopropyl nitrate ester as the principle ingredient in a number of Russian enhanced-blasted explosive devices, such as the RPO-A [26].

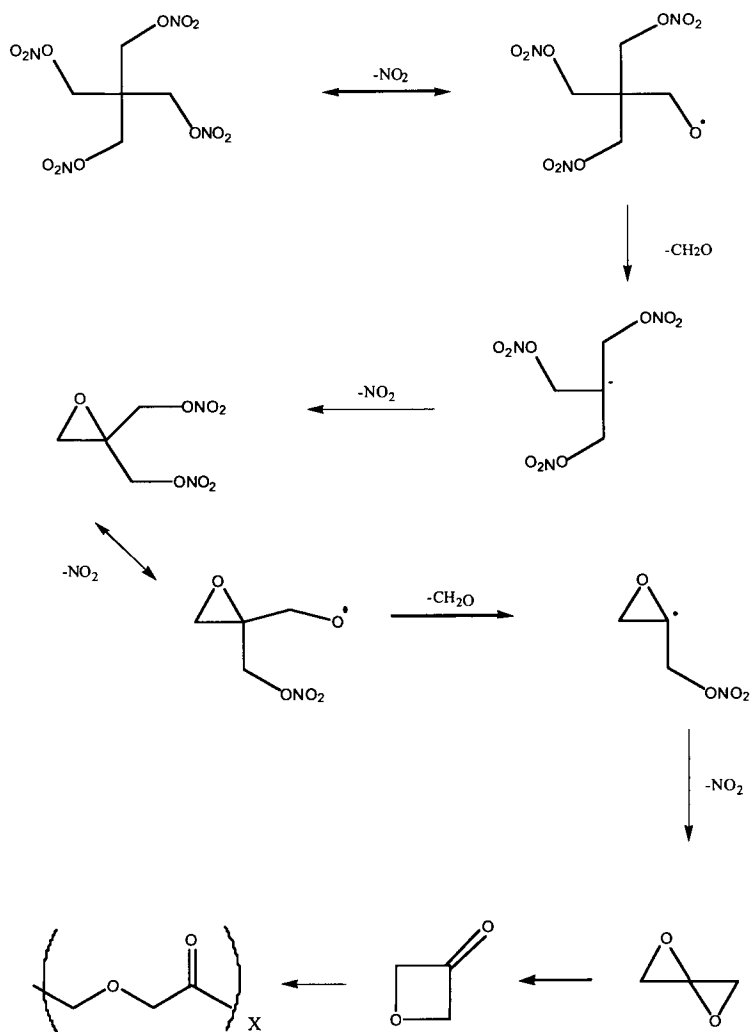
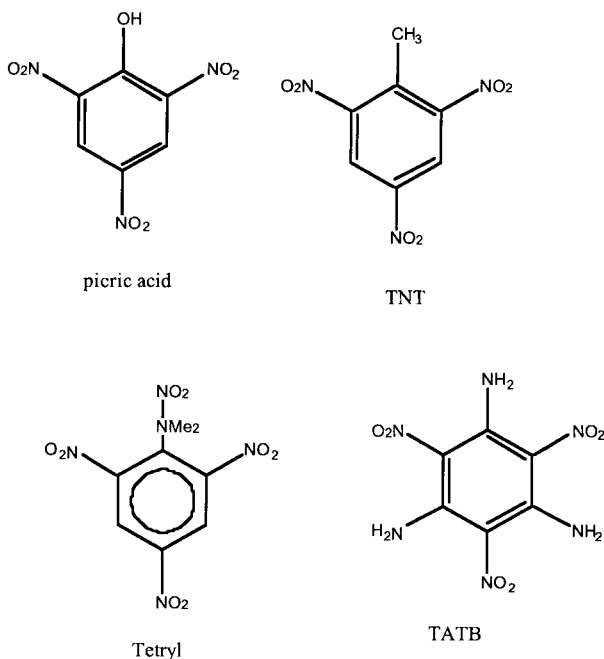


Fig. 2 Proposed Decomposition Pathway of PETN (Ref. 21)

3. NITROARENES

The nitroarenes, picric acid and TNT, have been used as explosives since the late 1800's (Fig. 3). At temperatures over which the thermal stability

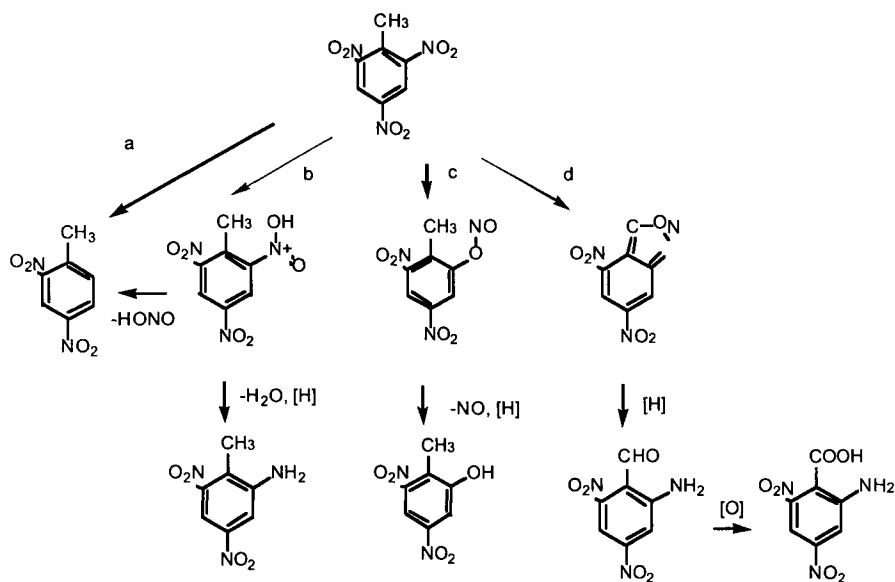


of

Figure 3 Nitroarenes Used as Explosives

nitroarenes is normally studied, three modes of decomposition are postulated: a) homolysis of the C-NO₂ bond; b) inter- or intra-molecular hydrogen transfer to the nitro group, resulting in HONO loss; and c) nitro/nitrite isomerization. The relative dominance of these decomposition pathways changes with temperature [27]. Homolysis is a high energy event (294 kJ/mol, 70 kcal/mol) observed mainly at high temperatures. Hydrogen transfer requires about half the energy of the homolysis. The necessary hydrogen may come from another nitroarene (intermolecular) or from another group on the same arene ring (intramolecular). Typical activation parameters are shown in Table 1. Following the initial step, several possible decomposition pathways are available (Fig. 4). While the thermal

decomposition mechanisms of nitrotoluenes have received much attention [27-37], the thermal decomposition studies of nitroanilines, e.g. TATB (triaminotrinitrobenzene), have been relatively neglected [27, 38-40]. There have been several attempts to understand the special stability of TATB. It has been suggested that the key to TATB insensitivity is the thermoneutral formation of benzofurazan and benzofuroxan rings as the first decomposition step (Fig. 5) [40].



a homolysis of NO_2 b intermolecular H transfer; c nitro/nitrite rearrangement; d intramolecular H transfer

Figure 4 Schematic of Possible Decomposition Routes for TNT.

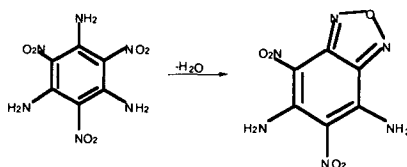


Figure 5 Transformation of TATB

Table 1: Summary of Arrhenius Parameters

Table 1. Summary of Arrhenius Parameters							
Bond	Reaction	Ea (kcal/mol)		Ea kJ/mol	Log A s ⁻¹	Ref.	
		range	average				
C-ONO			40	168		50	
N-NO ₂	Homolysis	43	49	44	184	12-18	63
		38	53	44	184	13-20	63
		37	47	45	188	13-17	149
				46	192	16	150
				47	196		137
				53	222	20	54
				50	210		27
				47	197		50
C-NO ₂ arene Arene	Homolysis	61	72	66	276		27
				70	294		27
	Isomerization -HONO from CH or			56	234	13	29
				48	201		27
C-NO ₂	Homolysis	39	61	50	209		48
				62	259	17.5	51
				60	252		27
	HONO loss	41	46	45	188	11.5	56
		39	50	44	184		48
C-NO ₂	Homolysis	39	43	41	171		110
				51	213	18.0	54
				49	205	17.5	51
				45	188		137
	HONO loss	39	47	43	180	11.5	51
C-NF ₂	Homolysis			60	251	17.5	51
	HF loss	24	29	27	113		137
				42	176	13.5	51
C-NF ₂	Homolysis	40	54	47	196	16.0	112
				45	188		111

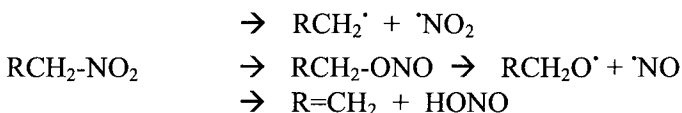
Range of activation energies (Ea) are given for reports of multiple compounds.

To shed light on the apparent special stability of TATB, a parametric study was performed on $C_6H_{5-a}Y(NO_2)_a$ and $C_6H_{6-(a+b)}Y_b(NO_2)_a$, where $a = 1$ to 3 and $b = 1$ to 3 [41]. It was found that both in solution and in the condensed-phase, the thermal stability of the nitroarenes decreased as the number of nitro groups was increased from one to three. In the solution studies, increasing the number of hydroxy, methyl, or amino groups on trinitrobenzene also decreased the thermal stability. Destabilization was due to the fact that a group ortho to the nitro group could transfer a proton to NO_2 , thus, lowering the energy necessary to break the C-N bond. In some cases, the thermal stability of the homologous series of the neat compounds followed the solution trend of decreased stability with increased substitution; but some series did not. The trend was maintained in the hydroxy-trinitrobenzene series and in the amino-trinitrotoluene series. However, in the studies of the neat compounds $(CH_3)_n$ -TNB, $(NH_2)_n$ -TNB or Br_n -TNB ($n = 1, 2$, or 3 and TNB = s-trinitrobenzyl), the thermal stability increased with substitution in the series. This increased stability was attributed to an increase in the crystal lattice integrity, as molecular weight and symmetry increased, rather than to a change in the elementary chemistry. In the thermolyses of the neat compounds, high melting species, such as TATB, exhibited the highest thermal stability in their homologous series. It was reasoned that since decomposition is slower in the solid state than in the liquid, the high melting species may appear more thermally stable than low melting ones, even though the intrinsic molecular stability of the high melting species is lower. Such a balance between thermal stability of the molecular structure and the crystal lattice led to homologous series which showed stability trends parallel and sometimes opposite to those in solution. These observations indicated that the thermal stability of TATB might be a function of its crystal lattice stability rather than an intrinsic property of the molecule [41].

4. NITROALKANES

Few nitroalkanes have found use as explosives. Nitromethane (CH_3NO_2) is a notable exception, and there have been numerous studies of its decomposition pathway [42,43,44]. It has been reported that nitromethane is sensitized to detonation by acidic and basic media. This sensitizing effect is approximately linear with the pK_a [45]. The best explanation of the effect is that nitromethane undergoes autocatalytic decomposition by an ionic mechanism under acidic or basic conditions [46,47]. Among other mononitroalkanes, nitroethane, the nitropropanes, and chloropicrin $Cl_3C(NO_2)$, have been the most extensively studied. The decomposition

triggers proposed are the same as those for nitroarenes: a) homolysis of the C-NO₂ bond; b) inter- or intra-molecular hydrogen transfer to the nitro group, resulting in HONO loss; and c) nitro/nitrite isomerization. The relative dominance of these pathways depends on temperature; since homolysis requires the most energy, it is favored at high temperatures (Table 1) [29,48-50].



Shaw calculated the isokinetic point between homolysis and elimination as 770K for mononitro- and vicinal dinitro-alkanes and as 370K for gem-dinitro species [51]. In gem-polynitro species the C-NO₂ bond is weaker than in mononitro compounds due to inductive effects [52]; thus, homolysis is thought to be the principal decomposition pathway in 2,2 dinitropropane and hexanitroethane [48]. Octanitrocubane has recently been synthesized (Fig. 6). Its crystal density was lower (1.979 g/cm³) than the predicted 2.1 [53]. Like hexanitrobenzene, octanitrocubane has a perfect oxygen balance, but at this point it appears unlikely that further development of this compound will be undertaken.

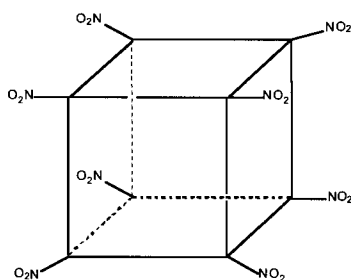


Figure 6 Octanitrocubane

5. NITRAMINES

The nitramines, which have found practical application as explosives are multi-functional nitramines, usually cyclic (Fig. 7). Nitramines have been studied by many groups and multiple decomposition pathways

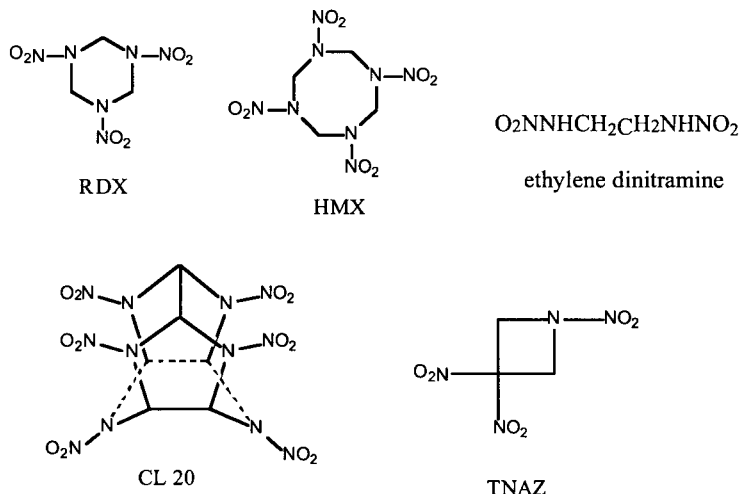
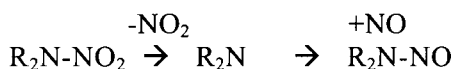


Fig. 7 Nitramines Commonly Used as Explosives

have been postulated [54-63]. Behrens postulate four decomposition pathways for the decomposition of liquid hexahydro-1,3,5-trinitro-s-triazine (RDX) (Fig. 8) [61]. These are not inconsistent with the major decomposition pathways Brill postulated for octahydro-1,3,5,7-tetranitro-1,3,5,7-tetrazocine (HMX) (Fig. 9) [62]. A long time controversy was the mode and importance of nitrosamine production. Formation of the nitrosamine was generally believed to proceed through N-NO_2 homolysis, subsequent reduction of NO_2 to NO , followed by recombination of NO with the amine nitrogen [54,55,56,57,58,61,63]. Indeed, the observed activation energy for decomposition of secondary nitramines falls in a range comparable to the N-NO_2 bond energy (Table 1) [63]. Isotopic labeling studies both supported and denied this mechanism [61,63].



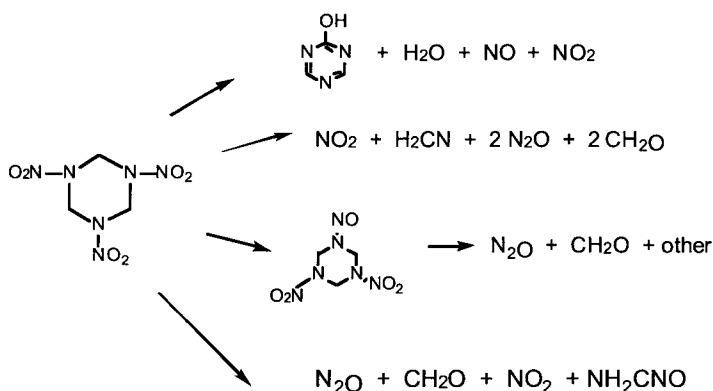


Fig. 8 Behren's Proposed Routes of RDX Decomposition (Ref. 61)

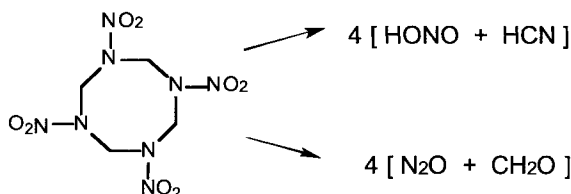


Fig. 9 Brill's Proposed Routes of HMX Decomposition (Ref. 62)

We examined the thermal decomposition of a number of nitramines in dilute solution and in the melt phase. The nitramines included acyclic dialkyl mononitramines, where the dialkyls were methyl, ethyl, propyl and isopropyl; cyclic mononitramines (N-nitro-piperidine and N-nitropyrrolidine); and cyclic multi functional nitramines (N-dinitropiperazine; 1,3-dinitro-1,3-diazacyclopentane; 1,3-dinitro-1,3-diazacyclohexane; RDX; and HMX). For all nitramines, the predominant condensed-phase product was the nitrosamine though the amount formed depending on the nitramine and the phase of the thermolysis. The common trigger in the decompositions was N-NO₂ homolysis, but the fate of the resultant amine radical depended on the phase. In solution the radical was stabilized sufficiently so that it resisted further decomposition and, instead, reacted with NO to form nitrosamine. In vapor or condensed phase, the amine radical underwent further reaction; therefore,

little nitrosamine was formed. In the case of multi-functional RDX and HMX, the loss of only one NO₂ group triggered the breakdown of the entire heterocycle. In monofunctional nitramines, N-N scission meant the most likely fate of each nitrogen atom was formation of nitrogen gas. In RDX and HMX, once the first N-N bond is broken, the rest of the heterocycle can unravel, the extra nitramine functionalities forming nitrous oxide rather than nitrogen gas (Fig. 10). In solution, the decomposition gases were predominately N₂, and more nitrosamine was observed than in the vapor or condensed phase because the amine radical remaining after initial NO₂ loss was stabilized by the solvent, preventing further unraveling of the ring. This explains the reason previous labeling experiments with neat HMX and RDX showed no scrambling of ¹⁵N label in the N₂O [61], while this study showed label scrambling in all the nitrogen-containing decomposition gases of dimethylnitramine [63]. In dimethylnitramine decomposition, nitrous oxide was a minor product. In the decomposition of RDX or HMX, formation of N₂O and CH₂O was an important decomposition pathway; however, the production of nitrous oxide in these species was by an entirely different route than it was in dimethylnitramine. It arose from the decomposition of the partially decomposed ring (H₂C=N-NO₂)₂. It has been suggested that RDX exhibits a somewhat lower activation energy than other cyclic nitramines, e.g. HMX, because an alternate decomposition pathway, loss of three HNO₂ species, is stabilized by the formation of an aromatic ring [60].

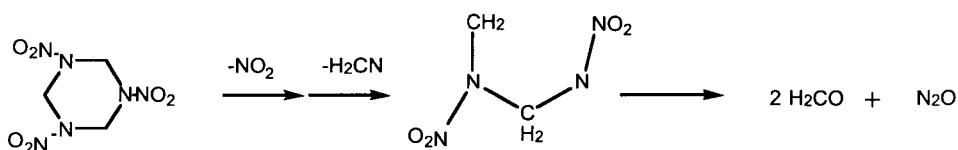


Figure 10 Oxley's Proposed Decomposition Route for RDX (Ref. 63)

In general, compounds containing N-NO₂ have more positive heats of formation than those containing C-NO₂, and multi-cyclic compounds achieve higher density than mono-cyclic. For these reasons, the synthesis of caged nitramines is pursued, and in 1987 Nielsen patented the synthesis of 2,4,6,8,10,12-hexanitro-2,4,6,8,10,12-hexaazaisowurtzitane (HNIW or CL-20) [64,65]. Like HMX, CL-20 exists in several solid polymorphs, four of which can be isolated at ambient conditions [66, 67]. CL-20 can be

purchased as the epsilon or beta polymorph. The epsilon is the preferable and most common formulation for most applications since it has the highest density and greatest thermal stability (by DSC) [68]. Initial studies of the stability of CL-20 used electron paramagnetic resonance (EPR). Not unexpectedly it produced NO₂ radicals in greater abundance than RDX and HMX [69]. Its gas-phase dissociation also yielded high concentrations of NO₂, but, unlike RDX and HMX, few ring fragments with nitro groups still attached. The ring fragments were primarily [C_xH_yN_z]⁺, in contrast to RDX and HMX which gave predominately oxygen-containing ions. Doyle attributed this to a number of structural differences between the cyclic nitramines and the caged nitramine--notably the C-C bond found in CL-20 and not the cyclic nitramines [70]. Brill also noted the difference in decomposition of the two cyclic nitramines and CL-20. Autocatalysis did not appear to play a major role. In the first 50% of decomposition, the predominate reaction was N-NO₂ homolysis. In the case of the cyclic nitramines, N-NO₂ homolysis lowered the barrier to C-N fission to the extent that the rings unraveled, being alternating CN(NO₂) fragments, whereas in CL-20 radical recombination could stabilize the structure [71]. High-pressure studies identified a ξ CL-20 polymorph; its decomposition yields little NO₂ [72, 73]. CL-20 has been formulated in a number of binders, e.g. 94% CL-20 with Estane, ethyl vinyl acetate, HTPB (hydroxy-terminated polybutadiene), and BAMO/AMMO [bis(azidomethyl)oxetane/ azidomethyl-methyloxetane]. Since 1997, Thiokol has sold about 8000 pounds of CL-20 for experimental use [74]. While CL-20 has a higher detonation velocity than HMX and performs 14% better than HMX in cylinder expansion, it is also more sensitive to initiation, as judged by wedge tests [66].

6. NEW ENERGETIC MATERIALS

In the last several decades, the major advances in energetic materials have been the development of energetic polymers and a number of monomolecular energetic compounds which do not fit neatly into the above categories [64]. These are in various stages of development, and it is difficult to predict which will become useful explosives or propellants. One unusual mixed functionality species is 1,1-diamino-2,2-dinitroethylene (FOX-7 or DADNE) (Fig. 11). It was synthesized in 1998, and several

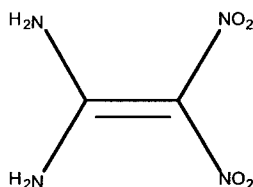


Fig. 11 FOX-7

military agencies are examining its potential as an insensitive explosive or burn-rate modifier [75,76]. Its insensitivity is thought to arise from a nearly planar structure that which is a result of a strong 2-dimensional network of hydrogen bonds [77]. Its detonation velocity is only slightly lower than RDX, yet it is far less sensitive to drop weight impact and friction (Table 2). However, its ignition temperature is slightly lower than RDX (215 °C versus 220°C).

6.1 New Nitrogen-Heterocycles

1,3,3-Trinitroazetidine (TNAZ), synthesized by Archibald in 1983, is the first new energetic material in decades to be stable above its melting temperature (101°C) [78,79]. Studies are ongoing to make it practical as an explosive [79-83]. Examining the decomposition of four- (TNAZ), six-, and eight-membered, gem-dinitroalkyl cyclic nitramines, Brill speculated that because the C-(NO₂)₂ linkage was weaker than that of N-NO₂, homolysis of C-NO₂ should be the first step in decomposition [84,85]. This was the case for the six- and eight-membered rings, but results were less clear for thermolysis of TNAZ [84,86]. In a theoretical study of TNAZ, Politzer predicted an energy difference in products of N-NO₂ scission (44.6 kcal/mol) versus C-NO₂ scission (46.6 kcal/mol) of only 2 kcal/mol [87]. Experimental work showed both N-NO₂ bond homolysis and C-NO₂ cleavage were important decomposition pathways (Fig. 12) [86]. Under the conditions of the experiments (neat thermolyses, 160° to 280°C), N-NO₂ homolysis was favored, although its dominance was not huge (66% of the initial 10% decomposition). NO was observed (by ¹⁵N-labeling experiments) to come from the nitro group on the azetidine nitrogen. The activation energy for TNAZ decomposition [E_a = 195 kJ/mol (46.6 kcal/mol); A = 3.55 E+17 sec⁻¹] was similar to that of pure nitramines. Ring strain, as expected, made TNAZ thermally unstable

compared to HMX. A small DKIE (1.4) was observed as well as a sensitivity to ammonia; these may result from the C-NO₂ cleavage pathway in which hydrogen transfer to the nitro group may assist in bond breakage [86].

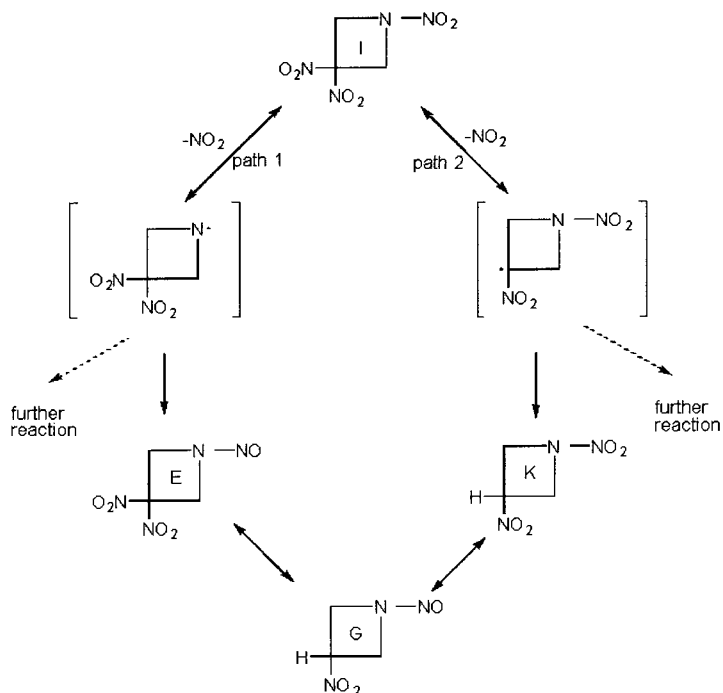


Figure 12 Proposed TNAZ Decomposition Routes

The potential of using 5-nitro-2,4-dihydro-3H-1,2,4-triazol-3-one (NTO) as an insensitive high explosive was examined in the late 1980's [88-97]. The thermolysis of NTO yields a brown insoluble residue and the nitrogen-containing gases, dinitrogen, nitrous oxide, nitric oxide and hydrogen cyanide. ¹⁵N labeling studies showed that more than 50% of N₂ came from the nitrogen atoms in the 1 and 2 positions of NTO. About

Table 2: Properties of Various Explosives

Explosive & Propellant Properties	MW (g)	m.p. (°C)	dens ity g/cc	state/color	%OB CO ₂	vapor pres mm @ 20°C	T _{exp} (°C)	Det Velo. m/s	Dcr mm	Drop Wt. cm	% TNT by Trauzel	Pb block cm ³ /10g or % TNT
NITRATE ESTERS												
Methyl nitrate	77	bp 65	1.22	L none	-10			6300	18		203%	610
NG, nitroglycerin	227	13	1.48	L cream	4	1.5E-03	270	7700	2		207%	620
EGDN, ethylene glycol dinitrate	152	-23	1.48	L cream	0	0.048	237	7300			200%	600
DEGN, diethylene glycol dinitrate	196	2	1.38	L none	-41	3.6E-03		6600			137%	410
NC, nitrocellulose (14.4%N)	325		1.67	S cream	-29		160		20	50	123%	370
PETN, pentaerythritol tetranitrate	316	143	1.76	S white	-10	8E-5*	210	8400	6	12	174%	523
NITROALKANES												
NM, nitromethane, CH ₃ NO ₂	61	-29	1.14	L none	-39	37	315	6200	3	100	110%	110%
DMNB, 2,3-dimethyl-2,3-dinitrobutane	176	210		L none	-127	2.1E-03		taggant				
NITROARENES												
1,3-DNB, dinitrobenzene	168	89	1.50	S cream	-95		>360	6100	1	>200	81%	242
TNB, 1,3,5 trinitrobenzene	213	121	1.76	S gm-ylw	-56		520	7300		123	108%	325
Ammonium Picrate	246	280	1.72	S yellow	-52			7150			93%	280
Picric acid	229	122	1.77	S yellow	-45	1.0E-09	300	7350	4	79	105%	315
Styphnic Acid, trinitroresorcinol	245	176	1.83	S yllw-red	-36				14		95%	284
Tetryl, trinitrophenylmethyl nitramine	267	129	1.73	S yellow	-47	3.5E-5*	187	7850	6	49	137%	410
TATB, traminotrinitrobenzene	258	350d	1.93	S yellow	-56	1E-4**	347	7619	4	>320	58%	175
TACOT	388	378d	1.84	S lt-orange	-74		337	7250	5	102	96%	
2,4-DNT, dinitrotoluene	182	69	1.52	S lt yellow	-114	9E-07	270		1	>200	80%	240
TNT, 2,4,6-trinitrotoluene	227	81	1.65	S cream	-74	0.1*	288	6950	5	212	100%	300
Trinitroaniline (picramide)	228	188	1.76	S org-red	-56			7300	3.5		103%	310
Trinitroanisol	243	68	1.61	S lt yellow	-63			6800	12		98%	295
Trinitrobenzoic acid	257	228d		S yellow	-47				2		94%	283
Trinitrochlorobenzene	240	83	1.80	S lt yellow	-45			7200			105%	315
Trinitrocresol	243	107	1.68	S yellow	-63			6850			95%	285
HNS, 2,4,6,2',4',6'-hexanitrostilbene	450	318d	1.74	S cream	-68	1E-9*	320			54	100%	301
Hexanitrodiphenylamine	439	240	1.64	S yellow	-53			7200	5		108%	325
NITRAMINES												
RDX	222	204d	1.82	S white	-22	4E-5*	217	8600	8	22	160%	480
HMX	296	280d	1.96	S white	-22	3E-9*	253	9100	8	26	160%	480
CL20, hexanitrohexaazaisowurtzitane	438	210d	2.04	S white				10030			176%	

Ethylene Diamine Dinitrate	186	188	1.58	S	white	-26		6800	2		117%	350
EDNA, ethylene dinitramine	150	176	1.71	S	white	-32		7570			137%	410
Urea Nitrate	123	140	1.59	S	white	-7					90%	270
TAGN, triaminoguanidine nitrate	167	216	1.50	S	white	-34		5300			117%	350
NQ, nitroguanidine	104	245d	1.65	S	white	-31	230	7570	13	>320	102%	305
Guanidine Nitrate NHC(NH ₂) ₂ HNO ₃	122	217		S	white	-26			2.5		80%	240
MISCELLANEOUS												
TATP, triacetone triperoxide	222	96	1.20	S	white	-151	sublimes	14C	5300	10	83%	250
HMTD hexamethylenetriperoxidediamine	208		1.57	S	white	-92.2		4500				
2,2, dimethylhydrazine	60			L								
FOX-7 (NH ₂) ₂ C=C(NO ₂) ₂			1.88	S	yellow			205	8870	0.9		>350
NTO, nitrotriazole	130	270d		S	white			270			86	
FEFO, C ₅ H ₆ N ₄ O ₁₀ F ₂	320	14		L			2E-04	~195		37		
AN, NH ₄ NO ₃	80	169	1.72	S	white	20		246	3500	3-15	149	60% 180
ADN, NH ₄ N(NO ₂) ₂	124	92	1.80	S	white							
HAN, HONH ₃ NO ₃	95	48		S/L	white							
AP, NH ₄ ClO ₄	118	450d	1.95	S	white	34	4.4e-9*	—		47	65%	195
PRIMARY EXPLOSIVES												
Pb(N ₃) ₂	291	—	4.80	S	white	-6		—	~5000		37%	110
Pb Styphnate	468		3.00	S	lt-orange	-22		5200			43%	130
Tetrazene	188		1.70	S	wht-ylw	-60					52%	155
DDNP, diazodinitrophenol	210		1.63	S		-61		6600			109%	326
* = at 100C ** = at 150C												
FORMULATIONS												
Pentolite (TNT/PETN) (50/50)												PBX-9404 (HMX/NC/trichloroethylphosphate/DPA) (94/2/4/1)
Baratol (Ba(NO ₃) ₂ /TNT) (76/24)												PBX 9011 (HMX/Estane) (90/7)
Comp B (RDX/TNT/wax) (50/50-60/40)												PBX 9501 (HMX/Estane/BDNPA-F) (95/2.5/2.5)
Octol (HMX/TNT) (70/30-75/25)												PBX-9407 (RDX/polyvinyl chloride) (94/6)
Comp A-3 (RDX/wax) (90/10-92/8)												LX-07 (HMX/Viton A) (90/10)
Cyclotol (RDX/TNT) (75/25-68/32) + 1% wax or .3-6% calcium silicate												LX-10 (HMX/Viton A) (95/5)
C-4 (RDX/ polyisobutylene, dioctyl adipate or sebacate, pet oil) (92/2/5/1)												LX-14 (HMX/Estane) (95.5/4.5)
DETASHEET (PETN, acetyl tributyl citrate, NC) DuPont brand												
PBX-9010 [RDX/polystyrene (KelF800)] (89/11 -91/9)												

25% of nitrogen atoms in N_2 came from the 4 and 6 positions. Most (~76%) of the nitrous oxide resulted from the interactions between nitrogens at the 1 or 2 position of NTO and the 6 position (NO_2). A mechanism involving homolysis of the nitro group was postulated. Over the temperature range 220° to 280°C, neat NTO exhibited a global activation energy of 78.6 kcal/mole with frequency factor of $2.5 \times 10^{29} s^{-1}$. Below 255°C the kinetics of NTO, neat and in solution, could be analyzed as first order, but above 255°C autocatalytic decomposition of neat NTO was evident, although only in sealed containers. While this could easily be attributed to catalysis by NO_2 lost from the 5 position of NTO, the same autocatalysis was observed in 2,4-dihydro-3H-1,2,4-triazol-3-one (TO) which lacks the nitro group [91]. One study examined the thermal stability of NTO and ten other triazoles. It was found that those with a carbonyl or an amino group substituent at C3 experienced enhanced decomposition rates in the presence of exogenous NO_2 . Therefore, it was concluded that NO_2 attacked at the carbonyl position (C3). Triazoles with a nitro group or amino substituent at what would be the 5 position of NTO exhibited intermolecular deuterium kinetic isotope effects. This was interpreted as evidence that at low temperature the loss of the nitro group was as $HONO$, while at higher temperatures the loss was by simple $C-NO_2$ homolysis. Although both mechanisms involve loss of the nitro group from the 5 position of NTO, only slight quantities of TO and 1,2,4-triazole were observed. The main condensed-phase product was an insoluble residue representing about 31% of the mass of the original NTO. Brill et al. have reported azines, melamine and melon as NTO decomposition products [97]. Based on the decomposition kinetics and the observed decomposition gases and the assumed polymer precursor (CN_2), several decomposition routes were proposed (Fig. 13) [91].

It is likely over the next decade a number of nitrogen heterocycles and their salts will be explored for use in energetic formulations. Both tetrazoles and triazoles have been considered as the main ingredient in air-bag formulations [98]. Characterization studies of two such tetrazoles appeared in the same journal issue [99,100]. The decompositions of 5-aminotetrazole (5-AT) and several other amino tetrazoles were characterized using thermal analysis (DSC, DTA and gas evolution); products were identified using FTIR and GC/MS. Two routes of decomposition were suggested: one involving the elimination of nitrogen

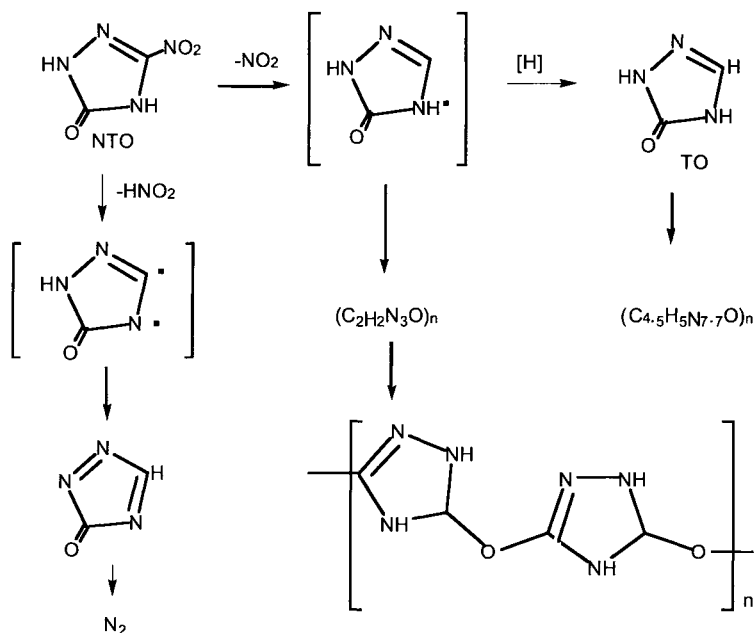


Fig. 13 Proposed Decomposition Route for NTO (Ref. 91)

and the other the loss of hydrozoic acid (HN_3). Condensed phase products include melamine (from 5-AT), and from the other tetrazoles such products as trimethylmelamine, 1,2,4-triazole, and various polymeric species, speculated to be melam, melem or melon. These have also been postulated in the decomposition of NTO and nitroguanidine, suggesting a common intermediate such as cyanide or cyanamide. The nitrocyanamide anion, NCNNO_2^- was identified by x-ray crystallography as a thermolysis product of the di-anionic 5-nitraminotetrazole [99]. That study also showed the di-anions were more stable than the mono-anions which were more stable than the 5-nitraminotetrazole. Minier et al. has examined the thermal stability of 2,4-dinitroimidazole [101]. Oxley et al. studied a number of novel 3,6-disubstituted-1,2,4,5-tetrazines prepared by Hiskey, whose aim was to produce tetrazines capable of easy substitution for synthetic intermediates (Fig. 14) [102, 103]. As in the photodissociation of 3,6-substituted-1,2,4,5-tetrazines, the thermal decomposition resulted in formation of N_2 and substituted nitriles. The rate-determining step in the thermal decomposition pathway was postulated to be loss of one of the

substituents [103]. Efforts to prepare high-nitrogen energetic rings continue and include a number of multi-cyclic compounds [104].

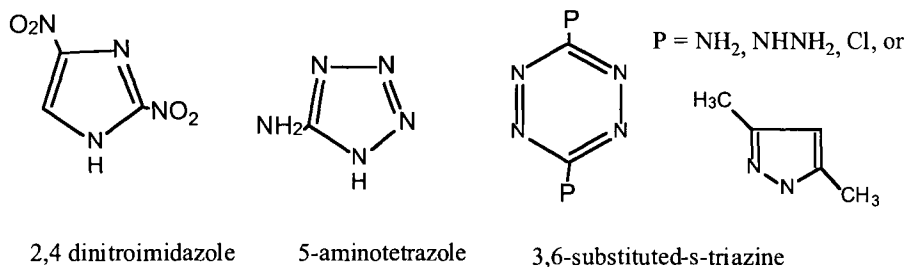
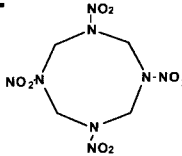
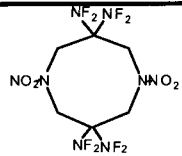
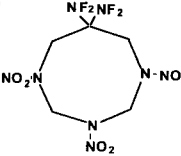
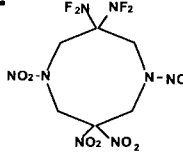


Figure 14 Some Energetic Nitrogen Heterocycles

6.2 NF₂ Compounds

Bis(difluoramino)-substituted heterocyclic nitramines are sought due to their potential for high density and high energy (Table 3) [106, 107]. Recently Chapman et al have reported the synthesis of 3,3,7,7-tetrakis-(difluoramino)octahydro-1,5-dinitro-1,5-diazocine (HNFX) and 3,3-bis(difluoramino)octahydro-1,5,7,7-tetranitro-1,5-diazocine (TNFX). While these materials are still awaiting thorough characterization, it is likely that they will prove slightly more stable than the nitro analog. Politzer has calculated that the N-NF₂ bond is 3 to 6 kcal/mol stronger than the N-NO₂ bond and that the replacement has little effect on the dissociation energy of other N-NO₂ or C-NO₂ bonds in the molecule [108]. Despite the paucity of difluoramino compounds, there have been a handful of decomposition studies [109-115]. Because the bond energies of N-NO₂, C-(NO₂)₂, and C-(NF₂)₂ are close in magnitude (Table 1), decomposition kinetics alone did not allow determination of the initial site of decomposition. Electron impact mass spectrometry studies suggest the difluoramino linkage is the first to cleave, but a thermal decomposition study of seven nitro- and difluoramino-substituted six-membered rings (nitrocyclohexane; 1,1-dinitro-cyclohexane; 1,1,4,4-tetranitrocyclohexane; 1,1,4,4-tetrakis-(difluoramino)cyclohexane; 1,4-dinitropiperazine; 1,4,4-trinitro-piperidine; and 4,4-bis(difluoramino)-1-nitropiperidine) suggested the following order for susceptibility to decomposition [115]: N-NO₂ > C-(NO₂)₂ > C-(NF₂)₂. The difference in

Table 3: Comparing NO₂ to NF₂ Performance*

				
	HMX	HNFX		TNFX
density (g/cm ³)	1.90	1.99	1.90	1.87
pressure (Kbar)	374	474	386	374
ISP (sec)	272	285	271	273

* data from reference 26

bond energies among the compounds is small. Geminal bis(difluoramino) compounds appeared to be somewhat more stable than the corresponding gem-dinitro compounds. Where a nitramine functionality was present, the nitroso analog was observed as a major decomposition product. The decomposition of gem-bis(difluoramino) and gem-dinitro compounds exhibited similarities. Both experienced loss of one geminal NX₂ group followed by the rearrangement of the remaining NX₂. Where X was oxygen, loss of the initial nitro by homolysis was favored; rearrangement of the remaining nitro followed by homolysis of NO resulted in a C=O bond. Where X was fluorine, the initial difluoramino could be lost as HNF₂. The remaining difluoramino reacted by losing fluorine, leaving C=NF or by losing HNF, resulting in =C-F; the latter was mainly observed [115].

7. ENERGETIC SALTS

Sprengelexplosives, which are intimate mixtures of oxidizers and fuels, were first used in the late 1800's, (e.g. chlorate and nitrobenzene for blasting Hell's Gate harbor, NY) [116]. Though chlorates and nitrates were the usual oxidizers, other oxidizers were occasionally used. Fuels ranged from nitrobenzene to coal dust. Ammonium nitrate (AN, NH₄NO₃) was probably the first energetic salt to find use as an explosive. It was patented in 1867 by two Swedish chemists for use as an explosive alone or mixed with charcoal, sawdust, naphthalene, etc. Nobel purchased the invention and used AN in dynamites. During World War I, AN was mixed with TNT in various proportions to make Amatol. The greatest industrial disaster in the U.S. came from an attempt to re-cycle World War II AN by shipping unused military stores to Europe for use as fertilizer. Two ships loaded with

wax-coated AN detonated killing about 600 people (Texas City, April 1947). A second such accident a few months later (Brest, France) caused international limitations to be placed on the carbon-content of AN. A decade later, AN became the principle ingredient in most commercial explosive formulations, replacing the more hazardous dynamite almost entirely [11,117]. As of this writing, there is only one commercial dynamite factory in the U.S., and AN-based explosives are used in the U.S. at the rate of over 5 billion pounds a year. There have been various attempts to use AN in military formulations. They have been unsuccessful because of the inability to control phase changes with accompanying density changes and because the relatively slow energy release of AN make it unsuitable for applications requiring metal penetration/ fragmentation. However, AN is a viable option where high gas volume is required; thus it may be the energetic of choice for the next generation of air-bag propellants.

No other energetic salts approach the same magnitude of usage as AN. Chlorates are used in pyrotechnic formulations but are generally considered too hazardous for large-scale use. The less hazardous perchlorate is used as the ammonium salt in rocket propellants (AP, NH_4ClO_4), and voluminous literature exists [118-130]. Hydroxylammonium nitrate [HAN, HONH_2NO_3], though not a new compound, received a great deal of military attention in the 1980's and 1990's as a carbon-free liquid propellant [131]. Unfortunately, the poor thermal stability of HAN has never been overcome completely. Accidents occurred at HAN manufacturing sites and even at two facilities manufacturing hydroxylamine (Concept Science, Allentown, PA; Feb. 1999 and Nissin Chemical, Japan, June 2000).

Ammonium dinitramide [ADN, $\text{NH}_4(\text{NO}_2)_2$] was first synthesized in Russia in 1972 (Luk'yanov) and in the U.S. in 1989 (Bottaro, SRI) [132]. ADN has been considered as a propellant ingredient due to its calculated performance and lack of chlorine, but its poor density somewhat offsets these advantages (Table 4). A considerable effort has been undertaken to solve its physical problems (poor morphology, high hygroscopicity, low thermal stability) and improve its synthesis [133-138]. In 1991, the first-bench scale synthesis produced material at \$4000/lb. By 1997 Bofors had patented a aqueous solution preparation which afforded ADN at \$525/lb. ADN is much less thermally stable than AN, probably due to a substantially lower melting point (94°C) and light sensitivity. However, like AN, addition

of urea increases its thermal stability. A Cab-o-sil coating and a prilling process are being considered to increase ease of handling [139].

Table 4: Properties of Propellant Ingredients*

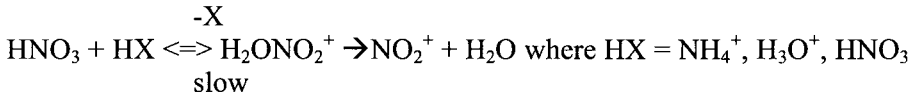
	ADN	AP
melting point (°C)	93	>200
DSC decomposition (°C)	150	>250
heat of formation (kcal/mol)	-35.8	-70.7
density (g/cm ³)	1.8	1.95

* data from reference 139

Each of the ammonium salts, and even hydroxylammonium nitrate, initiate decomposition in the same fashion—loss of amine. Indeed, ammonium nitrate, perchlorate, and dinitramide all sublime.



The next step depends on the temperature regime. In the case of ammonium nitrate, at low temperatures (less than 290°C) the predominant pathway is protonation of nitric acid and subsequent formation of nitronium [140].



Ammonium perchlorate and ammonium dinitramide can decompose by similar routes, but perchlorate, in particular, has several other decomposition pathways available. One decomposition route of ADN produces ammonium nitrate and N₂O [138].

The energetic salts discussed above are energetic due to the oxidizing ability of the anion. Energetic salts are also derived from energetic nitrogen-containing, heterocyclic rings: anions and cations of triazoles (NTO) and tetrazoles; cations of azeditine (TNAZ), tetrazines, and imidazole. In 1999 a new inorganic cation was synthesized—pentanitrogen N₅⁺. Its synthesis is so recent that it is impossible to judge whether it will become a useful energetic or remain a synthetic novelty [141]. Precedent suggests that should it become a useful energetic, it will be after decades of studies compounding it with the best anion, formulating it with the optimum binder, and studying its hazards and performance properties.

8. SUMMARY OF THERMAL STABILITY AND OUR APPROACH

Politzer calculated that shock sensitivity of nitramines or aliphatic nitro compounds was directly related to bond strength of N-NO₂ or C-NO₂ [59]. In general, nitramines are more thermally stable than nitroarenes, and nitroarenes are more thermally stable than nitrate esters. All three classes of energetic materials share one common mechanism by which they can decompose--homolysis of the X-NO₂ bond. The relative bond energies for this bond are estimated as O-NO₂, 40 kcal/mol, N-NO₂ 47 kcal/mol, and C-NO₂ 70 kcal/mol for nitroarenes [50]. If homolytic cleavage of NO₂ were the only decomposition route, then nitroarenes would be significantly more thermally stable than nitramines, in line with their bond energies (Table 5). However, nitroarenes are extremely sensitive to acids for protons attack the NO₂ group, lowering the energy necessary to dissociate it from the ring, allowing it to leave as HNO₂. Some nitroarenes are also sensitive to bases for they can react with the acidic protons on nitrotoluenes to form Meisenheimer complexes [142]. There are several decomposition pathways available to each type of energetic material. The dominant reaction path is dependent upon the temperature of the study.

Table 5: Comparative Thermal Stabilities of Classes of Explosive Compounds*

functional group	compound	isothermal rate constants (sec-1)		DSC exotherm max °C at 20°/min
		at 200°C	at 240°C	
O-NO ₂	PETN	2.70E-02	too fast	210
N-NO ₂	RDX	5.90E-04	2.00E-02	257
C-NO ₂	TNT	4.40E-06	9.10E-05	330
salt	AN	8.60E-06	1.10E-04	320

* data from reference 151

In our laboratory thermal stability is roughly assessed by differential scanning calorimetry (DSC). DSC has several advantages. (1) DSC requires little (0.2 to 1 mg) of what is often precious compound. (2) DSC gives a quick determination of the general temperature range more detailed studies should target. (3) The general features of the DSC curve may indicate the complexity of the decomposition pathway. (4) DSC gives a rough idea of the energetics of the compound; this is necessary for preliminary safety and performance estimations. We used sealed quartz capillary tubes for most DSC runs to avoid potential reaction with the metal

pans and to retain decomposition gases. This technique was developed at DOW Chemical, and we adapted it for use with energetic materials [143,144].

Following preliminary DSC studies, isothermal decompositions of small quantities (1-3 mg) of compound are performed at temperatures generally below the observed DSC exothermic maximum. Samples are usually thermolyzed in sealed Pyrex tubes. Use of Pyrex usually precludes reaction with the container that often occurs with metal reaction vessels. Sealed vessels also prevent corrosive decomposition products, e.g. NO₂ or HF, from damaging laboratory instrumentation. Sealed reaction vessels confine the decomposition products where they can easily be identified and quantified. It is obvious that highly reactive decomposition products such as formaldehyde are not observed by this technique, but they would not be expected to survive over the time of these decomposition experiments (seconds to hours, depending on the temperature). Seal vessel thermolyses mimic real storage scenarios where the sample is self-confined. However, autocatalysis may occur in sealed vessels that would not be observed in open ones. On the other hand, in unsealed tubes sublimation of the sample may become competitive with decomposition.

Decomposition rate constants are measured over as wide a temperature range as possible. Only the first one third to one half of the decomposition can be analyzed before it becomes severely autocatalytic. With the rate constants, an Arrhenius plot can be constructed and activation parameters calculated. Activation energies and pre-exponential factors correlate the decomposition rates with temperature. In addition, the magnitude of the activation energy may shed light on the key step in the decomposition process, and Arrhenius parameters are necessary in many explosive code calculations. Our procedure is to input the activation parameters into the Frank-Kamentskii equation [145] and use it to predict critical temperature of a reasonable size (e.g. 1 kilogram) of the energetic material:

$$E/T_c = R \ln (r^2 \rho Q A E) / (T_c^2 \theta s R)$$

[where r is radius (cm), s is shape factor (0.88 infinite slab, 2.00 infinite cylinder, 3.32 sphere), R is gas constant, (1.99 cal/mol deg), ρ is density (g/cm³), θ is thermal conductivity (cal/deg cm sec), Q is heat of decomposition (cal/g), E is activation energy (cal/mol), A is pre-exponential

factor (sec^{-1}), and T_c is critical temperature (Kelvin)]. The prediction assumes only convective dissipation of heat, but this is usually the case in accident scenarios. The predicted critical temperature can be tested at an appropriately equipped facility. If runaway self-heating ensues at a temperature near that predicted by laboratory kinetics, the kinetics obtained from micro-samples are validated. Another advantage of the large-scale tests is that they allow observation of a sample at much lower temperatures than can be observed in the laboratory (because such low temperatures do not result in detectable decomposition with small samples over any reasonable length of time).

After the decomposition kinetics of the neat compound have been determined in the condensed phase, study of the gas-phase decomposition can be revealing. Adjustment of the reaction parameters (size of sample and thermolysis temperature) assure that most of the sample is in the gas phase. Addition of other reactive species to the thermolysis can also shed light on decomposition pathways. For example, the decompositions of both TNT [31] and ammonium nitrate [117, 140] were accelerated by both acids and bases, while the decomposition of the nitramines RDX, HMX, and TNAZ were not affected by either [63,86]. These observations were used in determining the decomposition pathways of each compound. Thermolysis of compounds in solution may show decomposition rates significantly different from the neat compound. The solvent prevents intermolecular interactions and facilitates trapping of intermediates. In the case of nitramines, the kinetics were not greatly different in solution as opposed to neat; however, the products obtained for some of the nitramines, e.g. RDX and HMX, were dramatically different. Both of these observations were useful in elucidating the decomposition mechanism [63]. The decomposition of 5-nitro-2,4-dihydro-3H-1,2,4-triazol-3-one (NTO) was dramatically different depending on whether it was decomposed neat, in acetone, or in methanol [91]. Neat, the decomposition product, nitrogen dioxide, catalyzed decomposition. In acetone, this auto-catalysis was quenched. In methanol, decomposition was accelerated by proton transfer to NTO.

Probing for proton transfer in the rate-determining step can be accomplished using deuterated compounds or solvents [63,86,91,138,140]. If the deuterated explosive is available, it can be examined neat and in solution. If no deuterium kinetic isotope effect (DKIE) is exhibited by the neat deuterated explosive, then hydrogen transfer can be ruled out in the

rate-determining step. However, if a DKIE is observed with the neat compound, further experimentation is necessary to determine if the effect is inter- or intra-molecular. Performing the thermolysis in an inert solvent is the definitive experiment. If the hydrogen transfer is intramolecular, then the DKIE is observed even when the explosive molecules are separated from each other by solvent. Explosives like TNT and NTO exhibit both inter- and intra-molecular DKIE [91]. However, deuterated explosive can be hard to obtain; therefore, the experiment often is limited to comparing the rate of the explosive decomposition in proteo- versus deuterio-solvents, such as benzene. When benzene acts as a proton source, the production of biphenyl is also observed. In a few cases, such as the thermal decomposition of nitrate esters, solvent viscosity affects the decomposition rate. In that case O-NO₂ homolysis was reversible; trapping the nitrogen dioxide near the alkoxy radical enhanced the back reaction [21].

While decomposition kinetics can shed light on the principle decomposition step, identification and quantification of equilibrium decomposition products have more potential to elucidate the decomposition pathway and assess real-world stability problems. Clues to the decomposition pathway can be found by examining differences in kinetics of a compound decomposed neat, in condensed phase, neat in gas phase, dissolved in a solvent, or in the presence of additives. Mass spectrometers (MS) coupled to gas or liquid chromatographs are advantageous for identification and quantification of decomposition products. Tentative identifications are based on MS fragmentation patterns. Where possible MS assignments are confirmed by comparison with authentic samples. Isotope labeling studies are very helpful in product identification, and in a number of specific studies we have synthesized and thermolyzed the necessary isotopomers (NTO [91, 146], TNAZ [86,147], ADN [138], hexamethylene triperoxide diamine (HMTD) [148]). However, in the case of brand-new compounds, preparation of isotopomers may not be possible since initial synthetic pathways may not be developed to the point where isotopically labeled starting materials would be available. In such cases we rely on the MS fragmentation patterns and logical trends and precedents.

The value of studying a family of compounds should not be underestimated. For example, studying the thermal decomposition of NTO was difficult because the range of temperatures over which it could be examined was limited (activation energy was 79 kcal/mol), it reacted with

most solvents it dissolved in, and its major decomposition product was an intractable tar. However, scientists at Los Alamos National Laboratory had prepared a number of triazole rings. By comparing the reactivity of ten of these, some general reactivities were identified. It was found that only rings with either NH_2 or O attached to carbon exhibited accelerated decomposition in the presence of NO_2 and that a DKIE was only seen with rings having NO_2 or NH_2 groups. Certain trends in product formation were also noted. These observations helped to pinpoint the reactive sites within NTO [91].

Different research groups have different approaches to elucidating decomposition pathways. Thus, a wide variety of activation parameters have been published (Table 1). This is a result of examining the decomposition on different timescales or temperatures. Often if the rate constants are calculated for a common temperature, they will be similar in magnitude [97]. It is rare that the first paper published about a compound tells the entire story. For example, the papers on nitramine decomposition, cited herein, span thirty-five years. Each reveals a different piece of the story or supports previous postulates. Consider the mechanisms illustrated by Figs. 8-10. These are the results of several researchers approaching the problem from different perspectives; yet, they make similar conclusions. As new ways of probing reaction chemistry become available, they should be implemented. At the same time the reaction chemistry should be examined by the more conventional techniques, and an effort should be made to correlate the results.

REFERENCES

- [1] T.L. Davis, "The Chemistry of Powder and Explosives," Angriff Press. (reprint of two volumes 1941, 1943)
- [2] R. Hopler (ed), ISEE Blasters' Handbook 17th ed., International Society of Explosive Engineers, Cleveland, OH, (1998).
- [3] M. Berthelot, Explosives and Their Power (translated from French by C. N. Hake, W. Macnab), John Murray, London, (1892).
- [4] Institute of Makers of Explosives 75th Anniversary Book, (from U.S.Bureau of Mines) (1988)
- [5] S.M. Kaye, Encyclopedia of Explosives and Related Items; U.S. Army Armament Research & Development Com.; PATR-2700, Dover; (1960) 78.
- [6] T.R. Gibbs, A. Popolato, LASL Explosive Property Data, U Calif. Press, Berkeley, (1980)

- [7] B.M. Dobratz LLNL Explosives Handbook Properties of Chemical Explosives and Explosive Simulants, Lawrence Livermore Laboratory UCRL-52997; March (1981). Military Explosives Army Technical Manual TM9-1200-214, Sept. (1984).
- [8] R. Meyer Explosives, 3rd ed. VCH, Essen, Germany (1987).
- [9] T. Urbanski "Chemistry and Technology of Explosives"; Vols. 1,2,3,4; Pergamon Press, New York; 1964, 1965, 1967, 1984.
- [10] M.A. Cook "The Science of High Explosives" J. Am. Chem. Soc. Monograph, R.E. Krieger Pub. Florida, facsimile (1958).
- [11] J.C. Oxley, B. Walters and J. Zukas (eds.) "The Chemistry of Explosives" Chpt 5 and "Safe Handling of Explosives" Chpt 11, "Explosives Effects and Applications," Springer, New York, (1998).
- [12] L. Phillips "The Thermal Decomposition of Organic Nitrates," Nature, 160, (1947) 753; *ibid*, 165 (1950) 564.
- [13] F.H. Pollard, R.M.H. Wyatt, H.S.B. Marshall "Retarding (Inhibiting) and Sensitizing Effects of Nitrogen Dioxide in Alkyl Nitrate Decompositions," Nature 165 (1950) 564-565.
- F.H. Pollard; H.S.B. Marshall; A.E. Pedler "The Thermal Decomposition of Ethyl Nitrate," Trans. Faraday Soc., 52 (1956) 59-67.
- [14] J. B. Levy "The Thermal Decomposition of Nitrate Esters. I. Ethyl Nitrate," J. Am. Chem. Soc., 76 (1954) 3254-3257. J.B. Levy "The Thermal Decomposition of Nitrate Esters. II. The Effect of Additives on Thermal Decomposition of Ethyl Nitrate," J. Am. Chem. Soc., 76 (1954) 3790-3793.
- [15] G.K. Adams, C.E.H. Bawn "Homogeneous Decomposition of Ethyl Nitrate," Trans. Faraday Soc. 45 (1949) 494-499.
- [16] R. Boschan, R.T. Merrow, R.W. VanDolah "The Chemistry of Nitrate Esters" Chem. Rev., (1955) 485-510.
- [17] J.F. Griffiths, M.F. Gilligan, P. Gray "Pyrolysis of Isopropyl Nitrate .I. Decomposition at Low Temperatures and Pressures," Combust. Flame, 24 (1975) 11-19. J.F. Griffiths, M.F. Gilligan, P. Gray "Pyrolysis of Isopropyl Nitrate .II. Decomposition at High Temperatures And Pressures," Combust. Flame, 26 (1976) 385-393.
- [18] J. Powling, W.A. Smith "The Combustion of 2,3- and 1,4- Butanediol Dinitrates and Some Aldehyde-Nitrogen Dioxide Mixtures," Combust. Flame 2 (1958) 157-170.
- [19] C.E. Waring, G. Krastins "The Kinetics and Mechanism of Thermal Decomposition of Nitroglycerine," J. Phys. Chem., 74 (1970) 999-1006.

- [20] W.L. Ng, J.E. Field, H.M. Hauser "Study of Thermal Decomposition of Pentaerythritol Tetranitrate," J. Chem. Soc., Perkin Trans., 6 (1976) 637-639.
- [21] M.A. Hiskey, K.R. Brower, J.C. Oxley "Thermal Decomposition of Nitrate Esters," J. Phys. Chem., 95 (1991) 3955-3960.
- [22] M.A. Schroeder, R.A. Fifer, M.S. Miller, R.A. Pesce-Rodriguez, C.J.S. McNesby, G. Singh "Condensed-phase Processes During Combustion of Solid Gun Propellants. I. Nitrate Ester Propellants," Combust. Flame, 126 (2001) 1569-1576 & II. 1577-1598.
- [23] R.A. Fifer, "Chemistry of Nitrate Esters and Nitramine Propellants" Chp 4, Fundamentals of Solid- Propellant Combustion; K.K. Kuo, M. Summerfield (eds.); Progress in Astronautics and Aeronautics, 90 AIAA Inc.: New York (1984), pp 177-237.
- [24] B.D. Roos, T.B. Brill, "Thermal Decomposition of Energetic Materials 82. Correlations of Gaseous Products with the Composition of Aliphatic Nitrate Esters," Combust. Flame, 128(1-2) (2002) 181-190. Y. Oyumi, T.B. Brill, "Thermal Decomposition of Energetic Materials 14. Selective Product Distributions Evidenced in Rapid, Real-Time Thermolysis of Nitrate Esters at Various Pressures," Combust. Flame, 66 (1986) 9-16.
- [25] J.C. Oxley, J.L. Smith, E. Rogers, W. Ye, A. Aradi, T. Henley, "Heat-Release Behavior of Fuel Combustion Additives," Energy and Fuel, 5 (2001) 1194-1199. J.C. Oxley, J.L. Smith, E. Rogers, W. Ye, A. Aradi, T. Henley, "Fuel Combustion Additives: A Study of their Thermal Stabilities and Decomposition Pathways," Energy and Fuel, 14(6) (2000) 1252-1264.
- [26] NRC committee on Advanced Energetic Materials and Manufacturing Technology, 2003.
- [27] T.B. Brill, K.J. James, "Kinetics and Mechanisms of Thermal Decomposition of Nitroaromatic Explosives," J. Phys. Chem., 93 (1993) 2667-2692. *ibid* "Thermal Decomposition of Energetic Materials. 61 Perfidy in the Amino-2,4,6-Trinitrobenzene Series of Explosives," J. Phys. Chem. 97(34) (1993) 8752-8758. *ibid*. "Thermal Decomposition of Energetic Materials. 62 Reconciliation of the Kinetics and Mechanisms of TNT on the Time Scale from Microseconds to Hours," J. Phys. Chem., 97(34) (1993) 8759-8763.
- [28] L. Minier, K. Brower, J.C. Oxley "The Role of Intermolecular Reactions in Thermolysis of Aromatic Nitro Compounds in Supercritical Aromatic Solvents," J.Org.Chem., 56 (1991) 3306-3314.

- [29] W. Tsang, D. Robaugh, W.G. Mallard, "Single-Pulse Shock-Tube Studies on C-NO₂ Bond Cleavage During Decomposition of Some Nitroaromatic Compounds," *J. Phys. Chem.*, 90 (1986) 5968-5973.
- [30] K.E. Lewis, D.F. McMillen, D.M. Golden, "Laser Powered Homogeneous Pyrolysis of Aromatic Nitro Compounds," *J. Phys. Chem.*, 84 (1980) 226.
- A.C. Gonzalez, C.W. Larson, D.F. McMillen, D.M. Golden, "Mechanism of Decomposition of Nitroaromatics. Laser-Powered Homogeneous Pyrolysis of Substituted Nitrobenzenes," *J. Phys. Chem.*, 89 (1985) 4809.
- [31] J.C. Oxley, J.L. Smith, W. Wang, "Compatibility of Ammonium Nitrate with Monomolecular Explosives, Part I," *J. Phys. Chem.*, 98 (1994) 3893-3900. J.C. Oxley, J.L. Smith, W. Wang, "Compatibility of Ammonium Nitrate with Monomolecular Explosives, Part II: Nitroarenes," *J. Phys. Chem.*, 98 (1994) 3901-3907.
- [32] T.M. McKinney, L.F. Warren, I.B. Goldberg, J.T. Swanson, "EPR Observations of Nitroxide Free Radicals During Thermal Decomposition of 2,4,6-Trinitrotoluene and Related Compounds," *J. Phys. Chem.*, 90 (1986) 1008.
- [33] J.C. Dacons, H.G. Adolph, M.J. Kamlet, "Some Novel Observations Concerning the Thermal Decomposition of 2,4,6-Trinitrotoluene," *J. Phys. Chem.*, 74 (1970) 3035.
- [34] K. Suryanarayanan, C. Capellos, "Flash Photolysis of 2,4,6-Trinitrotoluene Solutions," *Int. J. Chem. Kinet.*, 6(1) (1974) 89.
- [35] S.A. Shackelford, J.W. Beckmann, J.S. Wilkes, "Deuterium Isotope Effects In Thermal Decomposition of Liquid 2,4,6-Trinitrotoluene: Application to Mechanistic Studies Using Isothermal Differential Scanning Calorimetry Analysis," *J. Org. Chem.*, 42 (1977) 4201.
- [36] R.N. Rogers, "Thermochemistry of Explosives," *Thermochim. Acta*, 11 (1975) 131.
- [37] S. Zeman, "Thermal Stabilities of Polynitroaromatic Compounds and their Derivatives," *Thermochim. Acta*, 31 (1979) 269.
- [38] M. Farber, R.D. Srivastava, "Thermal Decomposition of 1,3,5-Triamino-trinitrobenzene," *Combust. Flame*, 42 (1981) 165.
- [39] J. Sharma, W.L. Garrett, F.J. Owens, "X-Ray Photoelectron Study of Electronic Structure and UV, and Isothermal Decomposition of 1,3,5-Triamino-2,4,6-Trinitrobenzene," *J. Phys. Chem.*, 86 (1982) 1657.
- J. Sharma, J.C. Hoffsommer, D.J. Glover, C.S. Coffey, F. Santiago, A. Stolovy, S. Yasuda, J.R. Asay and R.A. Graham and G.K. Straub, (eds.) V.L. Vogel, "Comparative Study of Molecular Fragmentation in Sub-Initiated TATB

- Caused by Impact, UV, Heat and Electron Beams," in *Shock Waves in Condensed Matter*, Elsevier: NY, (1984) 543-546.
- [40] E. Catalano, C.E. Rolon, "On The Solid State Products of Thermal Decomposition of Confined and Unconfined Triaminotrinitrobenzene," *Thermochim. Acta*, 61 (1983) 37 and 53.
- [41] J.C. Oxley, J.L. Smith, H. Ye, R.L. McKenney, P.R. Bolduc, "Thermal Stability Studies on Homologous Series of Nitroarenes," *J. Phys. Chem.*, 99(24) (1995) 9593-9602.
- [42] M.J.S. Dewar, J.P. Ritchie, J. Alster, "Ground States of Molecules. 65. Thermolysis of Molecules Containing NO₂ Groups," *J. Org. Chem.*, 50 (1985) 1031-1036.
- [43] A.M. Wodtke, E.J. Hints, Y.T. Lee, "Infrared Multiphoton Dissociation of Three Nitroalkanes," *J. Phys. Chem.*, 90 (1986) 3549-3558.
- [44] D.B. Moss, K.A. Trentelman, P.L. Houston, "The 193-NM Photodissociation Dynamics of Nitromethane," *J. Chem. Phys.*, 96 (1992) 237-247.
- [45] B.M. Rice, D.L. Thompson, "Classical Dynamics Studies of the Unimolecular Decomposition of Nitromethane," *J. Chem. Phys.*, 93 (1990) 7986-8000.
- [46] R. Shaw, Sixth Symposium (International) on Detonation, ACR-221, Office of Naval Research, (1976) 98.
- [47] N.C. Blais, R. Engelke, S.A. Sheffield, "Mass Spectroscopic Study of the Chemical Reaction Zone in Detonating Liquid Nitromethane," *J. Phys. Chem. A*, 101 (1997) 8285-8295.
- [48] G.M. Nazin, G.B. Manelis, F.I. Dubovitskii, "Thermal Decomposition of Aliphatic Nitro Compounds," *Russian Chem. Rev.*, 37(8) (1968) 603-612.
- [49] G.F. Adams, R.W. Shaw Jr., "Chemical Reactions in Energetic Materials," *Annu. Rev. Phys. Chem.*, 43 (1992) 311-340.
- [50] C.F. Melius, "Rate and Equilibrium Studies in Jackson-Meisenheimer," *Proceedings, 25th JANNAF Combust. Meet.*, Huntsville, L (1988).
- [51] R. Shaw, "Chemical Reactions in Energetic Materials," *Int. J. Chem. Kinet.*, V (1973) 261-269.
- [52] J.C. Ruhl, D.H. Evans, P. Hapiot, P. Neta, "Fast Cleavage Reactions following Electron Transfer. Reduction of 1,1-Dinitrocyclohexane," *J. Am. Chem. Soc.*, 113 (1991) 5188-5194.
- [53] D.A. Hrovat, W.T. Borden, P.E. Eaton, B. Kahr, "A Computational Study of the Interactions among the Nitro Groups in Octanitrocubane," *J. Am. Chem. Soc.*, 123 (2000) 1289-1293.

- M.X. Zhang, P.E. Eaton, R. Gilardi, "Hepta- and Octanitrocubanes" *Angew. Chem. Int. Ed.*, 39(2) (2000) 401-404.
- [54] J.M. Flournoy, "Thermal Decomposition of Gaseous Dimethyl Nitramine," *J. Phys. Chem.*, 36 (1962) 1106-1107; *ibid*, 1107-1108.
- [55] F.C. Rauch, A.J. Fanelli, "The Thermal Decomposition Kinetics of Hexahydro-1,3,5-Triazine," *J. Phys. Chem.*, 73 (1969) 1604-1608.
- [56] J.D. Cosgrove, A.J. Owen, "The Thermal Decomposition of 1,3,5-Trinitro-1,3,5-Triazine (RDX)-Part II: The Effects of The Products," *Combust. Flame*, 22 (1974) 19-22.
- [57] T.L. Boggs, "The Thermal Behavior of Cyclotrimethylenetrinitramine (RDX) and Cycloctetramethylenetetranitramine (HMX)" Chp 3 in *Fundamentals of Solid-Propellant Combustion*; K.K. Kuo, M. Summerfield, (eds.); Prog. Astronautics Aeronautics; AIAA: NY, 90 (1984) 121-173.
- [58] J.C. Hoffsommer, D.J. Glover, "Thermal Decomposition of 1,3,5-Trinitro-1,3,5-Triazine (RDX): Kinetics of Nitroso Intermediates Formation," *Combust. Flame*, 59 (1985) 303.
- [59] P. Politzer, J.S. Murray, P. Lane, P. Sjöberg, H.G. Adolph, "Shock-sensitivity Relationships for Nitramines and Nitroaliphatics," *Chem. Phys. Lett.*, 181(1) (1991) 78-82.
- [60] D. Naud, R. Brower, "Pressure Effects on The Thermal Decomposition of Nitramines, Nitrosamines, and Nitrate Esters," *J. Org. Chem.*, 57 (1992) 3303-3308. J. Wang, K.R. Brower, D.L. Naud, "Evidence of an Elimination Mechanism in Thermal Decomposition of Hexahydro-1,3,5-Trinitro-1,3,5-Triazine and Related Compounds Under High Pressure," *J. Org. Chem.*, 62 (1997) 9055-9060.
- [61] R. Behrens, S. Bulusu, *J. Phys. Chem.*, 95 (1991) 5838-5845.
ibid "Thermal Decomposition of Energetic Materials. 3. Temporal Behaviors of the Rates of Formation of the Gaseous Pyrolysis Products from Condensed Phase Decomposition of 1,3,5-Trinitrohexahydro-s-Triazine," *J. Phys. Chem.*, 96 (1992) 8877-8891 and 8891-8897.
- B. Suryanarayana, R.J. Graybush, J.R. Autera, *Chem. Ind.*, 1967, 2177.
- [62] T. Brill, "Connecting the Chemical Composition of a Material to Its Combustion Characteristics," *Prog. Energ. Combust. Sci.*, 18 (1992) 91-116.
- [63] J.C. Oxley, M.A. Hiskey, D. Naud, R. Szekeres, "Thermal Decomposition of Nitramines: Dimethylnitramine, Diisopropyl-nitramine, and N-Nitropiperidine," *J. Phys. Chem.*, 96 (1992) 2505-2509. J.C. Oxley, A. Kooh, R. Szekeres, W. Zheng, "Mechanisms of Nitramines Thermolysis," *J. Phys. Chem.*, 98 (1994) 7004-7008.

- [64] R.S. Miller "Research on New Energetic Materials" in MRS Decomposition, Combustion, & Detonation Chemistry of Energetic Materials, Brill, Russell, Tao, Wardle (eds.), 1996.
- [65] A.T. Nielsen, A.P. Chafin, S.L. Christian, D.W. Moore, M.P. Nadler, R.A. Nissan, D.J. Vanderah, R.D. Gilardi, C.F. George, J.L. Flippen-Anderson, "Synthesis of Polyazapolycyclic Caged Polynitramines," *Tetrahedron*, 54 (1998), 11793-11812.
- [66] R.L. Simpson, P.A. Urtiew, D.L. Ornellas, G.L. Moody, K.J. Scribner, D.M. Hoffman, "CL-20 Performance Exceeds that of HMX and its Sensitivity is Moderate," *Propellants, Explosives, Pyrotechnics*, 22 (1997) 249-255.
- C.M. Tarver, R.L. Simpson, P.A. Urtiew, "Shock Initiation of an ϵ -CL-20-Estane Formulation," *Am. Physical Soc., Proceed. Am. Inst. Physics*, Seattle, (1996) 891-894.
- [67] STANAG 4566 Ed 1, 7th draft, "Explosives Specification for ϵ CL-20..." NATO Military Agency for Standardization Standardization Agreement.
- [68] M. Foltz, C.L. Coon, F. Garcia, A.L. Nichols III, "The Thermal Stability of the Polymorphs of Hexanitrohexaazaisowurtzitane," *Propellants, Explosives, Pyrotechnics*, 19 (1994) Part I 19-25 & Part II 133-144.
- [69] M.D. Pace, "Free Radical Mechanisms in High Density Nitro-Compounds: Hexanitroisowurtzitane, a New High-Energy Nitramine," *Mole. Cryst. & Liquid Cryst.*, 219 (1992) 139-148.
- [70] R.J. Doyle, Jr., *Org. Mass Spectrom.*, 26 (1991) 723-726.
- [71] D.G. Patil, T.B. Brill, "Thermal Decomposition of Energetic Materials 53. Kinetics and Mechanism of Thermolysis of Hexanitroazaisowurtzitane," *Combust. Flame.*, 87 (1991) 145-151.
- [72] T.P. Russell, P.J. Miller, G.J. Piermarini, S. Block, "High-Pressure Phase Transition in γ -Heanitrohexaazaisowurtzitane," *J. Phys. Chem.*, 96 (1992) 5509-5512.
- [73] D.C. Sorescu, B.M. Rice, D.L. Thompson, "Molecular Packing and NPT-Molecular Dynamics Investigation of the Transferability of the RDX Intermolecular Potential to 2,4,6,8,10,12-Hexanitrohexaazaisowurtzitane," *J. Phys Chem B*, 102 (1998) 948-952. *ibid*; "A Transferable Intermolecular Potential for Nitramine Crystals" *J. Phys Chem A*, 102 (1998) 8386-8392. *ibid*; "Theoretical Studies of the Hydrostatic Compression of RDX, HMX, HNIW, and PETN Crystals," *J. Phys Chem B*, 103 (1999) 6783-6790.
- [74] L.F. Cannizzo, "CL-20 Status Report" to NRC Committee on Advanced Energetic Materials & Manufacturing Technologies, Oct. 2001.

- [75] N.V. Latypov, J. Bergman, A. Langlet, U. Wellmar, U. Bemm, "Synthesis and Reactions of 1,1,-Diamino-2,2-dinitroethylene" *Tetrahedron*, 54, (1998), 11525-11536.
- [76] H. Ostmark, A. Langlet, H. Bergman, N. Wingborg, U. Wellmar, U. Bemm, FOA presentation.
- [77] C. Wight, "The Use of FOX-7 as a Propellant Additive" report to NRC Committee on Advanced Energetic Materials & Manufacturing Technologies, April 2002.
- [78] T.G. Archibald, R. Gilardi, K. Baum, C. George, "Synthesis and X-Ray Structure of 1,3,3-Trinitroazetidine," *J. Org. Chem.*, 55(1990) 2920-2924.
- [79] M. Hiskey, M. D. Coburn, M. A. Mitchell, B.C. Benicewicz, "Synthesis of 3,3-Dinitroazetidine from 1-Tert-Butyl-3,3-Dinitroazetidine," *J. Heterocycl. Chem.*, 2 (1992) 1855. M. D. Coburn, M.A. Hiskey, T. G. Archibald, "Scale-Up and Waste-minimization of the Los Alamos Process for 1,3,3-trinitroazetidine (TNAZ)" *Waste Management*, 17(1997) 143-146.
- [80] N. L. Garland, H. D. Ladouceur, A.P. Baronavski, H.H. Nelson, "Laser-Induced Decomposition of Energetic Materials" *JANNAF 35th Combustion Subcom & 17th Propulsion Syst. Hazards Sub.*; Tucson, AZ, 1998 pp 161-166.
- [81] C.L. Yu, Y. X. Zhang, S.H. Bauer, "Estimation of the Equilibrium Distribution of Products Generated During High Temperature Pyrolyses of 1,3,3-Trinitroazetidine; Thermochemical Parameters" *J. Mole. Struct. (Theory)*, 432 (1998) 63-68.
- [82] B. Persson, H. Ostmark, , H. Bergman "An HPLC Method for Analysis of HNIW and TNAZ in an Explosive Mixture," *Propellants, Explosives, Pyrotechnics*, 22 (1997) 238-239.
- [83] S. Lyster; Y. S. Eng; M. Joyce.; R. Perez.; J. Alster; D. Stec *Proceeding of ADPA Manufacture Compatibility of Plastics and other Materials with Explosives, Propellants, Pyrotechnics and Processing of Explosives, Propellants, and Ingredients*, San Diego, CA, 80, April 1991.
- [84] Y. Oyumi, T. B. Brill, "Thermal Decomposition of Energetic Materials. 4. High-Rate, In Situ, Thermolysis of the Four, Six, and Eight Membered, Oxygen-Rich, Gem-Dinitroalkyl Cyclic Nitramines, TNAZ, DNNC, and HNDZ," *Combust. Flame*, 62 (1985) 225-231.
- [85] L. Batt, *The Chemistry of Functional Groups*, Suppl. F, Part 1 (S. Patai, ed.), Wiley, NY 1982, 417.
- [86] J.C. Oxley, J.L. Smith, W. Zheng, E. Rogers, M.D. Coburn, "Thermal Decomposition Pathways of 1,3,3-Trinitroazetidine (TNAZ), Related 3,3-Dinitroazetidinium Salts, and 15N, 13C, and 2H Isotopomers" *J. Phys. Chem*

- A ,101(1997) 4375-4483. W. Zheng, E. Roger; M. Coburn, J. Oxley, J. Smith, "Mass Spectral Fragmentation Pathways in 1,3,3-Trinitroazetidine" J. Mass Spec., 32 (1997)525-532.
- [87] P. Politzer; J. M. Seminario, "Energy Changes Associated With Some Decomposition Steps of 1,3,3-Trinitroazetidine. A Non-Local Density Functional Study," Chem. Phys. Letts, 207 (1993) 27-30.
- [88] K.Y. Lee, M.D. Coburn, "3-Nitro-1,2,4-Triazol-5-One, a Less Sensitive Explosive," U.S. Patent 4, 733 (1988) 610. K.Y. Lee, L.B. Chapman, M.D. Coburn, "3-Nitro-1,2,4-Triazol-5-One, A Less Sensitive Explosive," J. Energ. Materials, 5 (1987) 27.
- [89] B.C. Beard; J. Sharma, "The Radiation Sensitivity of NTO," J. Energ. Materials, 7(1989) 181. B.C. Beard; J. Sharma , "Early Decomposition Chemistry of NTO (3-Nitro-1,2,4-triazol-5-one)," J. Energ. Mat., 11(1993) 325-343
- [90] H. Ostmark; H. Bergman; G. Aqvist, "The Chemistry of 3-Nitro-1,2,4-triazol-5-one (NTO): Thermal Decomposition," Thermochim. Acta, 213 (1993) 165-175.
- [91] J.C. Oxley, J.L. Smith; E. Rogers; X.X. Dong "NTO Decomposition Products Tracked with N-15 Labels" J. Phys. Chem., 101(1997) 3531-3536.
- J.C. Oxley; J.L. Smith; K.E. Yeager; E. Rogers; X.X. Dong "NTO Decomposition Studies" in MRS Decomposition, Combustion, & Detonation Chemistry of Energetic Materials, Brill, Russell, Tao, Wardle (eds.), 1996.
- J.C.Oxley, J.L. Smith, Z. Zhou, R.L. McKenney, "Thermal Decomposition Studies on NTO and NTO/TNT" J. Phys. Chem, 99 (1995) 10383-10391.
- [92] T.R. Bochter, D.J. Beardall, C.A. Wight, L. Fan, T.J. Burkley, "Thermal Decomposition Mechanism of NTO," J. Phys. Chem., 100,(1996), 8802-8806. G.T. Long, B.A. Brems, C.A. Wight, "Thermal Activation of the High Explosive NTO: Sublimation, Decomposition, and Autocatalysis," J. Phys. Chem. B, 106 (2002) 4022-4026.
- [93] N.L. Garland, H.D. Ladoucer, H.H. Nelson, "Laser-Induced Decomposition of NTO," J. Phys. Chem. A, ,101(1997) 8508-8512.
- [94] D.F. McMillen, D. C.Erlich, C. He, C.H. Becker, D.A. Shockey "Fracture-induced and Thermal Decomposition of NTO Using Laser Ionization Mass Spectrometry," Combust. Flame, 111 (1997) 133-160.
- [95] C. Meredith, T.P.Russell, R.C. Mowrey, J.R. McDonald "Decomposition of 5-Nitro-2,4-dihydro-3H-1,2,4-triazol-3-one (NTO): Energetics Associated with Several Proposed Initiation Routes," J. Phys. Chem. A, 102(1998) 471-477.

- [96] W.L. Yim, Z.F.Liu, "Applications of Ab Initio Molecular Dynamics for a Priori Elucidation of the Mechanism in Unimolecular Decomposition: The Case of 5-Nitro-2,4-dihydro-3H-1,2,4-triazol-3-one(NTO)," J. Am. Chem. Soc., 123(2001) 2243-2250.
- [97] G.K. Williams, S.F. Palopoli, T.B. Brill, "Thermal Decomposition of Energetic Materials 65. Conversion of Insensitive Explosives (NTO, ANTA) and Related Compounds to Polymeric Melon-like Cyclic Azine Burn-rate Suppressants," Combust. Flame, 98 (1994) 197-204.
- G.K. Williams, P.E. Gongwer, T.B. Brill, "Thermal Decomposition of Energetic Materials 66. Kinetic Compensation Effects in HMX, RDX, and NTO" J. Phys. Chem., 98(1994) 12242-12247.
- G.K. Williams, T.B. Brill, "Thermal Decomposition of Energetic Materials 68. Decomposition and Sublimation Kinetics of NTO and Evaluation of Prior Kinetic Data," J. Phys. Chem., 99 (1995) 12536-12539.
- [98] U.S. air bag patents: Canterbury, Schlueter, Adams, Walsh, 6,071,364 (2000); Canterbury, 5,765,866 (1998); Highsmith, Lund, Blau, Hinshaw, Doll, 5,516,377 (1994); Khandhadia, 5,514,230 (1996); Taylor, Deppert, Burnes, 5,467,715 (1995); Lyon, 5,460,668 (1995); Poole, Kwong, 5,386,775 (1995); Lund, Stevens, Edwards, Shaw, 5,197,758 (1993); G.K. Lund, M.R. Stevens, 5,160,386 (1992); Poole, 5,139,588 (1992); Poole, 5,084,118 (1992); Poole, 5,035,757 (1991); Poole, 4,948,439 (1990); Wardle, Hinshaw, Hajik, 4,931,112 (1990); Poole, Wilson, 4,909,549 (1990); G. Lundstrom, G.C. Shaw, 4,370,181 (1983); G.C.Shaw, 4,369,079 (1983).
- [99] B.C. Tappan, C.D. Incarvito, A.L. Rheingold, T.B. Brill, "Thermal Decomposition of Energetic Materials 79 Thermal, Vibrational, and X-ray Structural Characterization of Metal Salts of Mono- and Di-Anionic 5-Nitraminotetrazole" Thermochim. Acta, 384(2002) 113-120.
- [100] A.I. Lesnikovich, O.A. Ivashkevich, S.V. Levchik, A.I. Balabanovich, P.N. Gaponik, A.A. Kulak, "Thermal Decomposition of Aminotetrazoles" Thermochim. Acta, 384(2002) 233-251.
- [101] L. Minier, R. Behrens, Jr., S. Bulusu, "Solid-phase Thermal Decomposition of 2,4-Dinitroimidazole," Decomposition, Combustion, and Detonation Chemistry of Energetic Materials, M.R.S. Proceedings," T.B. Brill, T.P. Russell, W.C. Tao, R.B. Wardle (eds.) 418 (1996) 111-117.
- [102] D. E. Chavez; M. A. Hiskey, "Synthesis of the Bi-Heterocyclic Parenting System 1,2,4-Triazolo[4,3-b][1,2,4,5] Tetrazine and Some 3,6-Disubstituted Derivatives," J. Heterocycl. Chem. 35(1998) 1329-1332.

- D. E. Chavez, M. A. Hiskey, "1,2,4,5-Tetrazine-Based Energetic Materials," *J. Energ. Mat.*, 17(1999) 357-377. D. E. Chavez, M. A. Hiskey, R.D. Gilardi, "3,3'-Azobis(6-Amino-1,2,4,5-Tetrazine): A Novel High-Nitrogen Energetic Material," *Angew. Chem. Int. Ed.*, 39 (2000) 1791-1793.
- [103] J.C. Oxley; J.L. Smith; J. Zhang "Decomposition of 3,6-Substituted s-Tetrazines;" *J. Phys. Chem. A.*, 104(2000) 6764- 6777.
- [104] W. Koppes, report to NRC Committee on Advanced Energetic Materials & Manufacturing Technologies, April 2002.
- [105] R.D. Chapman; M. F. Welker; C.B. Kreutzberger, "Difluoroamination of Heterocyclic Ketones: Control of Microbasicity," *J. Org. Chem.*, 63, (1998) 1566-1570.
- [106] Theodore Axenrod; Xiao-Pei Guan Sun, Jianguang Qi; Lida, Robert Chapman, Richard D.Gilardi; "Synthesis of 3,3-Bis(difluoramino)octahydro-1,5,7,7-1,5-diazocine(TNFX), a Diversified Energetic Heterocycle," *Tetrahedron Letters*, 42(2001) 2621-2623.
- [107] A.V. Fokin, Yu. N. Studnev, L. D. Kuznetsova, "Syntheses Based on (N,N-Difluoroamino)Dinitro Acetonitrile," *Russ. Chem. Bull.*, 45(1996) 1952-1954. A.V. Fokin, Yu Studnev, A.I. Rapkin, L.D. Kuznetsova "Geminal(difluoroamino) Nitro Compounds" *Russ. Chem. Bull.* , 45(1996) 2547-2550.
- [108] P. Politzer, P. Lane, M. E. Grice, M. C. Concha, P. C. Redfern, "Comparative Computational Analysis of Some Nitramine and Difluoramine Structures, Dissociation Energies and Heats of Formation," *J. Mole. Struct. (Theory)*, 338 (1995) 249-256.
- [109] V. N. Grebennikov, G. M. Nazin, G. B. Manells, "Thermal Decomposition of a-(Difluoroamino) Polynitroalkanes," *Russ. Chem. Bull.*, 44 (1995) 628-630.
- [110] V. N. Grebennikov, G. B. Manells, A. V. Fokin, "Structure and Thermal Stability of Difluoroamino Compounds in Liquid State," *Russ. Chem. Bull.*, 43(1994) 315-319.
- [111] D.S. Ross, R. Shaw "The Kinetics of the Unimolecular Dehydrofluorination of Methyl difluoramine," *J. Phys. Chem.*, 75 (1971) 1170-1172. R. Shaw "Dehydrofluorination of Chemically Activated 1,2-Bisdifluoramino propane" *Int. J. Chem. Kinet.*, IX(1977) 689-691. D.S. Ross, T. Mill, M.B. Hill, "Unimolecular Decomposition of Bis(difluoroamino)-propane, *J. Am. Chem. Soc.*, 94 (1972) 8776-8778.
- [112] J.M. Sullivan, A.E. Axworthy, T.J. Houser, "Kinetics of The Gas-Phase Pyrolysis of Poly(Difluoroamino)Fluoromethanes," *J. Phys. Chem.*, 74 (1970), 2611-2620.

- [113] V. I. Pepekin "Thermochemistry of Difluoroamino Nitro Compounds," Chem. Phys. Rep., 13 (1994) 67-80.
- [114] B. L. Korsunskii, A. G. Korepin, "Kinetics of The Thermal Decomposition of Bis (2,2-dinitropropyl)-N-fluoroamine," Russ. Chem. Bull., 44 (1995) 847-850.
- [115] J.C. Oxley, J.L. Smith, J. Zhang, C Bedford, "A Comparison of the Thermal Decomposition of Nitramines and Difluoroamines" J. Phys. Chem. A, 105 (2001) 579-590. J. Zhang, J. Oxley, J. Smith, C. Bedford, R. Chapman "Mass Spectral Fragmentation Pathways in Cyclic Difluoroamino and Nitro Compounds" J. Mass Spectrometry, 35 (2000), 841-852.
- [116] R. Hopler, , personal communication.
- [117] J.C. Oxley, S.M. Kaushik, N.S. Gilson "Thermal Decomposition of Ammonium Nitrate-Based Composites", Thermochem. Acta, 153 (1989) 269-286. J.C. Oxley, S.M. Kaushik, N.S. Gilson, "Ammonium Nitrate Explosives--Thermal Stability and Compatibility on Small and Large Scale" Thermochem. Acta , 212 (1992) 77-85.
- [118] J.C. Oxley; J.L. Smith; B. Valenzuela "Ammonium Perchlorate Decomposition: Neat and Solution" J. Energ. Mat., 13 (1995) 57-91.
- [119] P.W.M. Jacobs, H.M. Whitehead, "Decomposition and Combustion of Ammonium Perchlorate," Chem. Rev. (1969) 551-590.
- [120] L.L. Bircumshaw, B.H. Newman "The Thermal Decomposition of Ammonium Perchlorate I. Introduction, Experimental, Analysis of Gaseous Products and Thermal Decomposition Experiments," Proc. Roy. Soc. (London) A227 (1954) 115-132; *ibid*, "The Thermal Decomposition of Ammonium Perchlorate II. The Kinetics of the Decomposition, the Effect of Particle Size, and Discussion of Results" A227 (1955) 228-241. L.L.Bircumshaw, T.R. Phillips, "The Kinetics of the Thermal Decomposition of Ammonium Perchlorate" J. Chem. Soc. 122 (1957) 4741-4747.
- [121] J.V. Davies, P.W.M. Jacobs, A. Russell-Jones "Thermal Decomposition of Ammonium Perchlorate" Trans. Faraday Soc. 63 (1967), 1737-1748.
- P.W.M. Jacobs, A. Russell-Jones, "The Thermal Decomposition and Ignition of Mixtures of Ammonium Perchlorate and Copper Chromite," 11th Symp. Combustion (1967), 457-462.
- [122] D.S.F. Solymosi Structure and Stability of Salts of Halogen Oxyacids in the Solid Phase, Wiley; London; 1977, pp 195-265.
- [123] T.L. Boggs, "Response of Amonium Perchlorate to Thermal and Mechanical Shock Stimuli" Naval Weapons Center TP 7053, 1990.

- [124] K.J. Kraeutle, "The Decomposition of Crystalline and Granular Ammonium Perchlorate" CPIA Pub., I(12) (1967) 535-543.
- [125] J.C. Petricciani, S.E. Wiberley, W.H. Bauer, T.W. Clapper, "The Effects of a Chlorate Impurity on the Thermal Stability of Ammonium Perchlorate" J. Phys. Chem. 64 (1960) 1309-1311.
- [126] W.A. Rosser, S.H. Inami, H. Wise, "Thermal Decomposition of Ammonium Perchlorate," Combust. Flame, 12 (1968) 427-435.
W.A. Rosser, S.H. Inami, H. Wise, "Dissociation Pressure of Ammonium Perchlorate" J. Phys. Chem. (1963) 1077-1079. *ibid* (1966) 723-729.
- [127] V.V. Boldyrev, V.V. Alexandrov, A.V. Boldyreva, V.I. Gritsan, Yu. Ya Karpenko, O.P. Korobeinitchev, V.N. Panfilov, E.F. Khairtdinov, "On the Mechanism of the Thermal Decomposition of Ammonium Perchlorate," Combust. Flame, 15(1970) 71-78.
- [128] M. D. Pace, "Nitrogen Radical from Thermal and Photochemical Decomposition of Ammonium Perchlorate, Ammonium Dinitramide, and Cyclic Nitramines," M. R. S. Proceed, 296 (1993) 53-60.
- [129] Encyclopedia of Explosives and Related Items, Vol 2.; eds. B.T. Fedoroff; O.E. Sheffield, U.S. Army Armament Research & Development Command; Dover, NJ, 1962, pp C184-C185.
- [130] J.A. Conkling, Chemistry of Pyrotechnics, Marcel Dekker, NY, 1985, pp 58-61.
- [131] J.S. Gardner, J.C. Oxley, J.L. Smith, "Thermal Stability of a HAN-Based Liquid Gun Propellant" J. Thermal Analysis, 49 (1997) 1315-1319.
J.S. Gardner, J.C. Oxley; J.L. Smith; E. Roger; K Yeager; W. Zheng "Microcalorimetry Studies on HAN-Based Liquid Propellant," Proceed. JANNAF Propulsion Systems Hazards Subcommittee, Huntsville, AL 1997.
J.C. Oxley; J.L. Smith; J. A. Askins, N. S. Gilson, H. Feng, M. Banks, J.S. Gardner, "Thermal Stability Analysis of HAN-Based Liquid Gun Propellants," Proceed. JANNAF Propulsion Systems Hazards Subcommittee, Fort Lewis, WA, May 1993.
J.C. Oxley, K.R. Brower, "Thermal Decomposition of Hydroxylamine Nitrate" SPIE , 872 (1988) 63-69.
- [132] M.J. Rossi, J.C. Bottaro, D.F. McMillen, Int. J. Chem.Kinet., 25 (1993) 549. M.J. Rossi, D.F. McMillen, D. M. Golden, "Low Pressure Thermal Decomposition Studies Selected Nitramine and Dinitramine Energetic Materials" ONR Final Report AD-A247 972 March 1992.
- [133] T.B. Brill, P.J. Brush, D.G. Patil "Sensitivity and Performance Characterization of Ammonium Dinitramide," Combust. Flame, 92(1993), 178.

- [134] T.P. Russell, A.G.Stern, W.M.Koppes, C.D. Bedford, "Thermal Decomposition and Stabilization of Ammonium Dinitramide" CPIA 29th JANNAF Combustion Sub. Mtg.; Hampton, VA; Oct. 1992; Vol II, 339. T.P. Russell, G.J. Piermarini, S. Block, P.J. Miller, J. Phys. Chem., 100 (1996) 3248.
- [135] S. Vyazovkin, C.A. Wight; "Thermal Decomposition of Ammonium Dinitramide at Moderate and High Temperatures," J. Phys. Chem., 101 (1996) 7217-7221.
- [136] M. D. Pace, "Spin Trapping of Nitrogen Dioxide from Photolysis of Sodium Nitrite, Ammonium Nitrate, Ammonium Dinitramide, and Cyclic Nitramines," J Phys Chem, 98 (1994) 6251-6257.
- [137] P. Politzer, J.M. Seminario, M.C. Concha, P. Redfern, J. Mole. Struct.(Theory), 287 (1993) 235. P. Politzer, J.M.Seminario, "Computational Study of the Structure of Dinitraminic acid, $\text{HN}(\text{NO}_2)_2$, and the Energetics of Some Possible Decomposition Steps," Chem. Phys. Let. 216 (1993) 348.
- [138] J.C. Oxley, J.L. Smith, W. Zheng, E. Rogers, M.D. Coburn, "Thermal Decomposition Studies on Ammonium Dinitramide (ADN) and ^{15}N and ^2H Isotopomers" J. Phys. Chem, 101 (1997) 5646-5652.
- [139] R.Wardle, "The ADN Saga" report to NRC Committee on Advanced Energetic Materials & Manufacturing Technologies, Oct. 2001.
- [140] K.R. Brower, J.C. Oxley, M.P Tewari, "Homolytic Decomposition of Ammonium Nitrate at High Temperature" J.Phy. Chem. 93(1989) 4029-4033
- [141] K.O. Christe, W.W. Wilson, J.A. Sheehy, J.A. Boatz, "A Novel Homoleptic Poytnitrogen Ion as a High Energy Density Material" Angew Chem. Int. Ed, 38 (1999) 2004.
- [142] F. Terrier, "Rate and Equilibrium Studies in Jackson Meisenheimer Complexes," Chem. Rev., 82 (1982) 77.
- [143] J.C. Oxley, "Cook-off: Small-Scale Thermal Hazards Analysis" 1992 JANNAF Propulsion Systems Hazards Subcom. Mtg. Cookoff Workshop; Silver Springs, MD, May, 1992.
- [144]. L.F. Whiting, M.S. LaBean, S.S. Eadie, "Evolution of A Capillary Tube Sample Container for Differential Scanning Calorimetry," Thermochem. Acta, 136 (1988) 231.
- [145] F. Frank-Kamenetskii, Diffusion and Heat Transfer in Chemical Kinetics; Plenum Press, NY 1969.

- [146] J.C. Oxley, J.L. Smith, K.E. Yeager, M.D. Coburn, D.G. Ott, "Synthesis of ^{15}N -Labeled Isomers of 5-Nitro-2,4-dihydro-3H-1,2,4-triazol-3-one (NTO)" *J. Energ. Mat.*, 13 (1995), 93-105.
- [147] M.D. Coburn, M.A. Hiskey, J.C. Oxley, J.L. Smith, W. Zheng, E. Rogers, "Synthesis and Spectra of Some ^2H , ^{13}C , and ^{15}N Isomers of 1,3,3-Trinitroazetidine and 3,3-Dinitroazetidinium Nitrate" *J. Energ. Mat.*, 16 (1998) 73-99.
- [148] J.C. Oxley, J.L. Smith, H. Chen, E. Cioffi, "Decomposition of Multi-Peroxidic Compounds: Part II: Hexamethylene Triperoxide Diamine (HMTD)" *Thermochim. Acta*, 388 (2002) 215-225.
- [149] F. I. Dubovitskii, B. L. Korsunskii, "Kinetics of the Thermal Decomposition of N-Nitro-compounds" *Russ Chem. Rev.*, 50 (1981) 958-978.
- [150] R. Shaw, F. E. Walker, "Estimated Kinetics and Thermochemistry of Some Initial Unimolecular Reactions in the Thermal Decomposition of 1,3,5,7-Tetranitro-1,3,5,7-tetraazacyclooctane in the Gas Phase" *J. Phys. Chem.* 81 (1977) 2572-2576.
- [151] J.C. Oxley, J.L. Smith, E. Rogers, X. Dong, "Gas Production from Thermal Decomposition of Explosives: Assessing the Thermal Stabilities of Energetic Materials from Gas Production Data" *J. Energ. Mat.*, 18 (2000), 97-121.

Chapter 2

Characterisation of explosive materials using molecular dynamics simulations

P. Čapková^a, M. Pospíšil^a, P. Vávra^b and S. Zeman^b

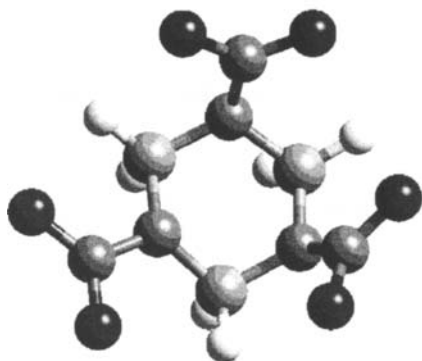
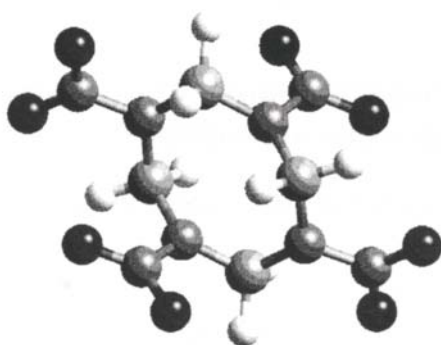
^aDepartment of Chemical Physics and Optics, Faculty of Mathematics and Physics, Charles University Prague, Ke Karlovu 3, 12116 Prague 2, Czech Republic.

^bDepartment of Theory and Technology of Explosives, University of Pardubice, 53210 Pardubice, Czech Republic.

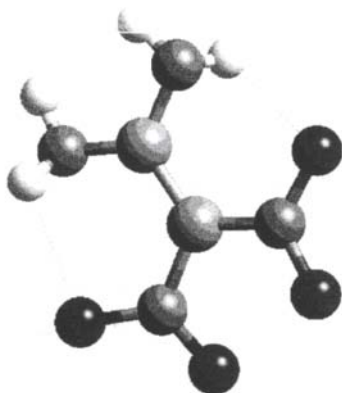
1. INTRODUCTION

Classical molecular dynamics simulations of the unimolecular decomposition have been performed for selected molecules exhibiting different impact sensitivity and different detonation energy: (1) $(\text{CH}_2\text{NNO}_2)_3$, more commonly known as RDX, (2) $(\text{CH}_2\text{NNO}_2)_4$, known as HMX, (3) $(\text{NH}_2)_2\text{CC}(\text{NO}_2)_2$, known as DADNE and (4) $(\text{NH}_2)_2\text{CNNO}_2$, known as NQ. A potential energy was described using empirical force field. The analysis of dynamic trajectories enabled us to reveal step by step the mechanism of decomposition and to determine the parameters characterizing the impact sensitivity and explosives performance (detonation energy) of these energetic materials. This work is a continuation of previous studies focused to unraveling of molecular decomposition process in explosive materials, see Ref.1-10. We use the classical molecular dynamics in *Cerius² (Materials Studio)* modeling environment, Ref. 11, for the simulation of molecular decomposition. The aim of the present work is to reveal step by step the mechanism of explosion and to find the way of reliable characterization of explosive materials using classical molecular dynamics simulations of the uni-molecular decomposition process. The structure of four molecules selected for dynamic simulations are reported in Ref. 12-15, for RDX, β -HMX, DADNE and NQ. Molecular structures are shown in the Fig. 1a-d.

a) RDX

b) β -HMX

c) DADNE



d) NQ

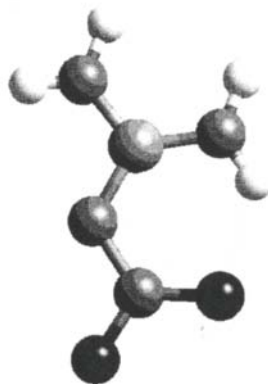


Fig. 1. Initial models of molecules for dynamic simulations:

- a) RDX - cyclotrimethylene-trinitramine, $(\text{CH}_2\text{NNO}_2)_3$;
- b) β -HMX - β -cyclotetramethylene-tetranitramine, $(\text{CH}_2\text{NNO}_2)_4$;
- c) DADNE - 1,1-diamino-2,2-dinitroethylene, $(\text{NH}_2)_2\text{CC}(\text{NO}_2)_2$;
- d) NQ - nitroguanidine, $(\text{NH}_2)_2\text{CNNO}_2$.

Impact sensitivities were studied using drop weight apparatus and were reported together with calculated detonation energy in Ref. 16. Comparing the molecular structures of a chosen molecules and their impact sensitivities characterized by the height h , i.e. the critical value of the fall height of the drop weight (see Table 1), we can divide these molecules into two groups:

1. I. group: molecules RDX and β -HMX with high sensitivity, i.e. with low h value ~ 24 cm and ~ 26 cm, see Table 1;
2. II. group: molecules DADNE and NQ with low impact sensitivity, i.e. $h \sim 100$ cm and ~ 177 cm., see Table 1.

Similarity in behavior of molecules belonging to the same group and the differences between groups I and II led us to investigate the decomposition process just for these four types of molecules using classical molecular dynamics simulations. Analyzing the molecular dynamics trajectories we will focus our attention to the following goals:

- To reveal the mechanism and kinetics of the decomposition process at the molecular scale;
- To derive the parameters characterizing the impact sensitivity;
- To derive the parameters characterizing the detonation energy.

Special attention will be paid to the investigation of two decomposition pathways for molecules RDX, which have been reported in previous studies Ref. 3,7,10 as R1 and R2



In the reaction R1 the rupture of the first C-N bond is followed by the rupture of the first N-NO₂ bond (release of the nitrogroup), as one can see in the Fig. 2a. Then the rest of the molecule is gradually totally decomposed. Reaction R2 starts with the rupture of three C-N bonds and subsequent break up of the molecule into three CH₂NNO₂ fragments (see Fig. 2b). Afterwards the NO₂ groups are released from these fragments. Dynamics trajectory enables the animation of molecular motion with the time resolution 1 fs and the visualization of the molecular decomposition process in real time.

2. STRATEGY OF MOLECULAR DYNAMICS SIMULATIONS

A natural starting point for a theoretical study is to investigate the chemical decomposition at the molecular scale. Classical molecular dynamics simulations in *Cerius²* (*Materials Studio*) modeling environment were carried out to calculate dynamics trajectory for one isolated molecule. Searching for the

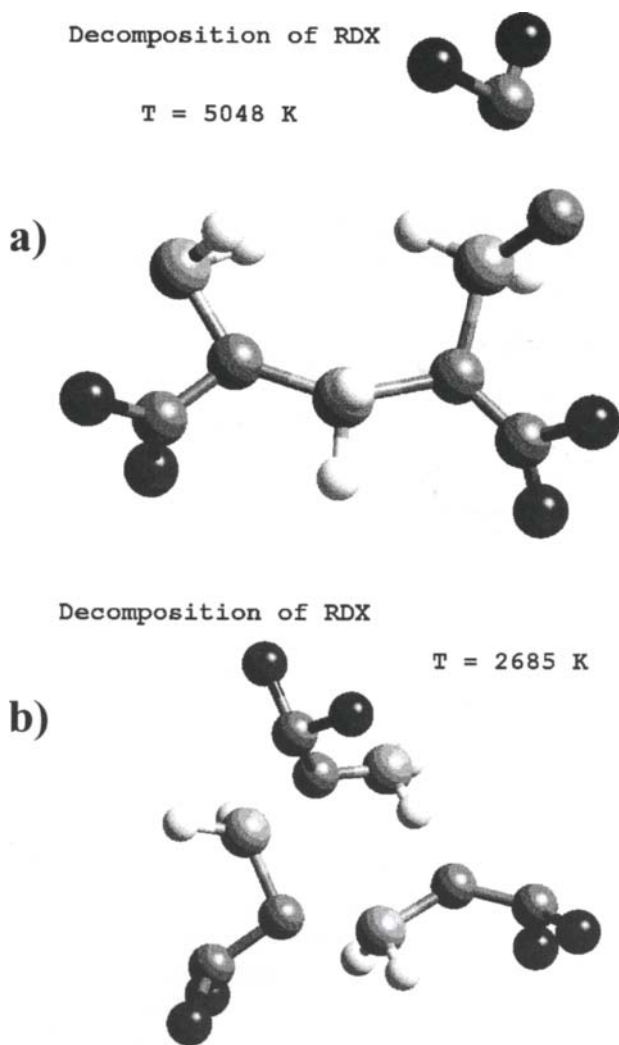


Fig. 2. Decomposition of RDX, snapshots extracted from dynamics trajectories:

- a) Reaction R1 at temperature 5048 K;
- b) Reaction R2 at temperature 2685 K.

optimum strategy we have found the following conditions for dynamics simulations:

- We used the "*Impulse dynamics*", that means at the beginning the system get the initial impulse, corresponding approximately to double of the chosen temperature to assign the initial velocities to the atoms using Maxwell-Boltzmann equation.
- The calculations were performed in *microcanonical ensemble* (NVE). Newtons equations of motion were integrated by using Verlet integrator. Although the temperature is not controlled during NVE dynamics, *Cerius²* allows us to hold the temperature within specified tolerances by periodic rescaling of the velocities.
- Dynamics trajectories were calculated under following conditions: force field *cvff_950*, see Ref. 17, has been used with dynamics time step 0.001ps. The length of the dynamic trajectory in *ps*, the initial temperature and consequently the initial energy impulse were dependent on the sensitivity of a given molecule and have estimated as a result of dynamic simulations experiments. Atomic charges in *Cerius²* are calculated using the charge equilibration method (Ref.18).
- Building the initial models we used the crystallographic conformation as a starting geometry for dynamic simulations.

As a result of dynamic simulations we obtained the dynamic trajectory file including the time dependence of the temperature, kinetic, potential and total energy and development of the decomposition process. The animation of the molecular motion during dynamic simulations enables us to visualize the time dependence of the uni-molecular decomposition process, starting from the first bond scission to the release of the nitro-groups NO₂. The course of dynamic trajectories, i.e. the time dependence of temperature, kinetic, potential and total energy allows us to estimate the parameters characterizing the explosives as to the sensitivity and performance.

3. RESULTS AND DISCUSSION

Analysis of dynamic trajectories revealed the mechanism of the molecular decomposition for selected molecules: RDX, β -HMX, DADNE and NQ. The time dependence of the kinetic energy for these molecules is in the Fig. 3-7. The course of dynamic trajectories showed the similar character of the decomposition process for molecules of the I.group i.e. RDX, and β -HMX. Molecules of the II.group - DADNE and NQ also exhibit similar features during decomposition process, however the character of the dynamic trajectories and

decomposition for DADNE and NQ is different from the I.group (RDX and β -HMX), as one can see comparing the Fig. 3-7. Analyzing dynamic trajectories we paid attention to the time, temperature and kinetic energy corresponding to the rupture of the first bond in the molecule and to the release of the first NO_2 group from the molecule. The initial temperature impulse assigned to the system in present dynamic simulations was set up as the temperature necessary for the start of decomposition process in time interval 0 – 100 ps. In general the use of lower temperature leads to a later start of decomposition, anyway the character of dynamic trajectories remains the same for a given molecule. The time corresponding to the start of decomposition (i.e. the moment when the first bond is definitely ruptured) is for given molecule affected by the temperature of the thermal bath. However the role of statistics should be taken into account. Therefore all the characteristic parameters derived from dynamic trajectories at certain temperature were averaged over 20 independent impulse dynamic trajectories.

3.1 Decomposition of RDX and β -HMX

Two decomposition processes suggested on the base of experiment by B.M. Rice et al. Ref. 7 and Shalashilin & Thompson Ref. 3, were confirmed by the analysis of dynamic trajectories for both molecules RDX and β -HMX. However our results of molecular dynamics simulations did not confirm the conclusion of Rice, see Ref. 7, that the reaction R1 ($\text{RDX} \rightarrow \text{C}_3\text{H}_6\text{N}_5\text{O}_4 + \text{NO}_2$) occurs at low temperatures and the reaction R2 ($\text{RDX} \rightarrow 3\text{CH}_2\text{NNO}_2$) is more probable at high temperatures. Analysis of 40 dynamic trajectories for RDX and β -HMX showed that both reactions occur at low and high temperatures with the same probability. Dynamic simulations show that most probable decomposition process is the combination of reaction R1 and R2. In such a case the first NO_2 group is released neither after first C-N bond rupture (R1), nor after all C-N bond rupture (R2), but after the second (in case of β -HMX second or third) C-N bond rupture according to the scheme: $\text{C-N} \rightarrow \text{C-N} \rightarrow \text{C-N} \rightarrow \text{N-NO}_2 \rightarrow \text{C-N}$.

Two examples of the dynamic trajectories (the time dependence of the kinetic energy) for the molecule RDX are presented in the Fig. 3 and 4, where the Fig. 3 illustrates the reaction pathway R1 and the Fig. 4 shows the trajectory for the reaction R2. Arrows mark the points on the dynamic trajectory corresponding to the rupture of C-N and N- NO_2 bonds. Fig. 5 shows the example of trajectory for β -HMX, where the decomposition process is the combination of R1 and R2 reactions. Anyway the character of dynamic trajectories and consequently the character of molecular decomposition is very similar for RDX and β -HMX.

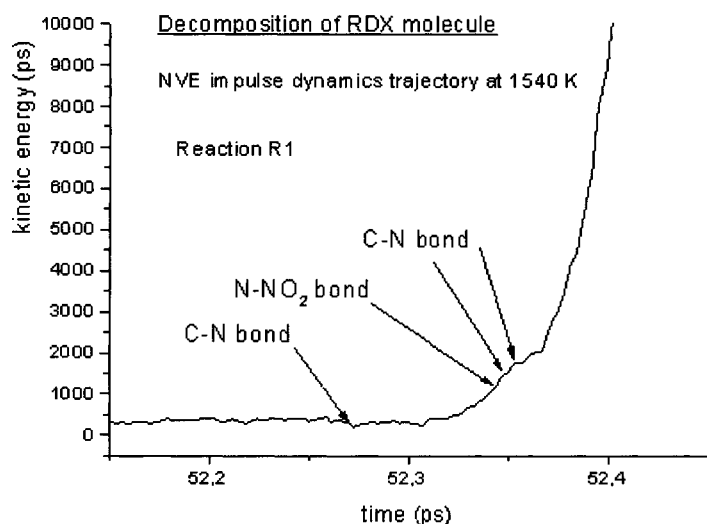


Fig.3. Impulse dynamics trajectory for RDX , reaction R1.

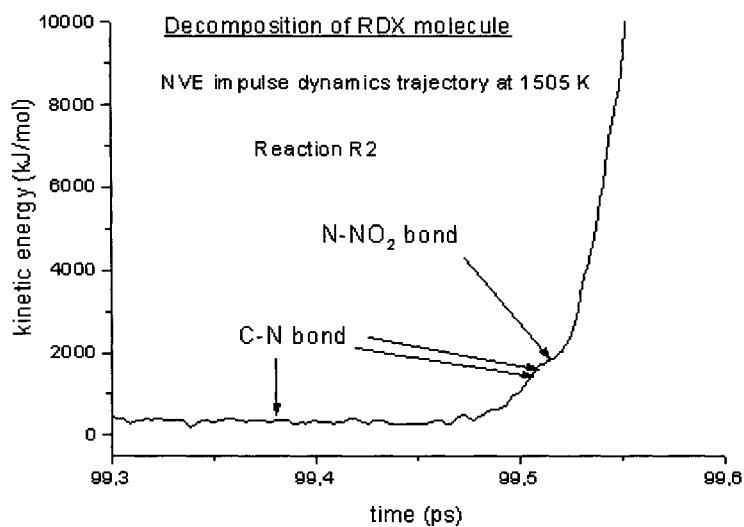


Fig. 4. Impulse dynamics trajectory for RDX, reaction R2

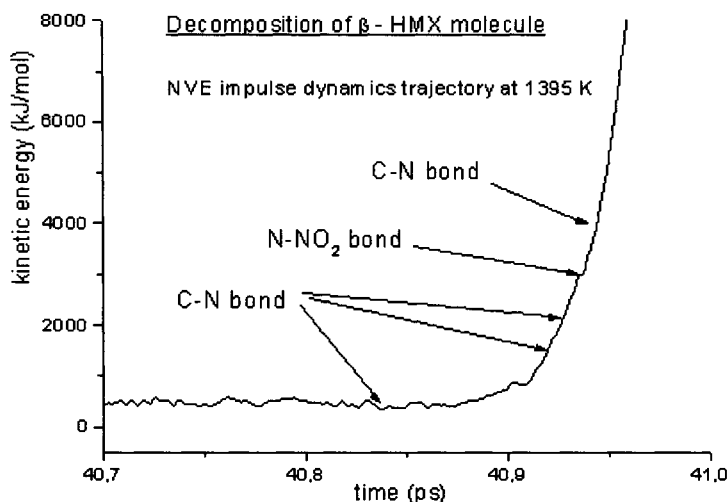


Fig. 5. Impulse dynamics trajectory for β -HMX.

3.2 Decomposition of DADNE and NQ

The course of dynamic trajectory for DADNE and NQ is very different from that for RDX and β -HMX, as one can see from the comparison of Fig. 3 – 7. The difference is in the time dependence of kinetic energy after the start of decomposition process. In case of RDX and β -HMX the kinetic energy starts to increase dramatically during the decomposition, anyway the increase is monotonous. Decomposition of DADNE and NQ starts with the rupture of N-H bond followed by the rupture of C-N bond. However in this case the decomposition is accompanied with the large fluctuations of kinetic energy, as one can see in the Fig. 6 and 7.

3.3 Parameters characterizing the decomposition process

Analysis of dynamic trajectories enabled us to determine two parameters, characterizing the decomposition process:

- $\langle E_k(NO_2) \rangle$ - as the average value of kinetic energy corresponding to the rupture of C (or N)- NO_2 bond and release of the first NO_2 group (averaging over set of dynamic trajectories)
- $\langle \Delta E_{k50} \rangle$ - as the average increment of the kinetic energy in 50 fs after the end of decomposition, which was defined as the moment when molecules is split

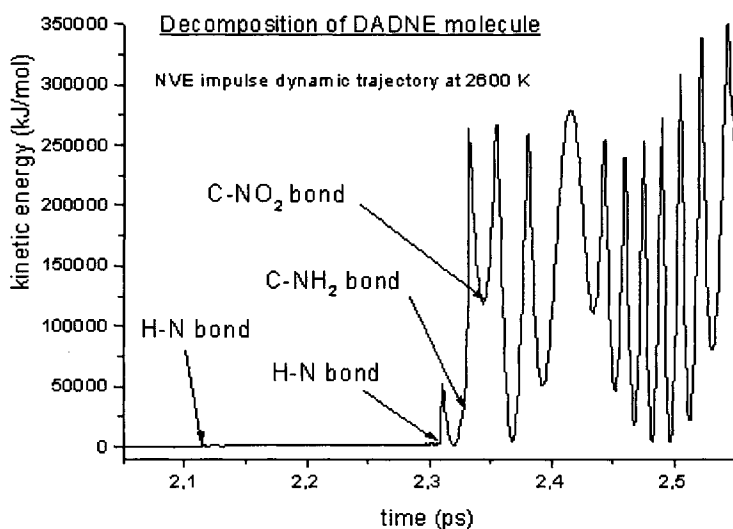


Fig. 6. Impulse dynamics trajectory for DADNE

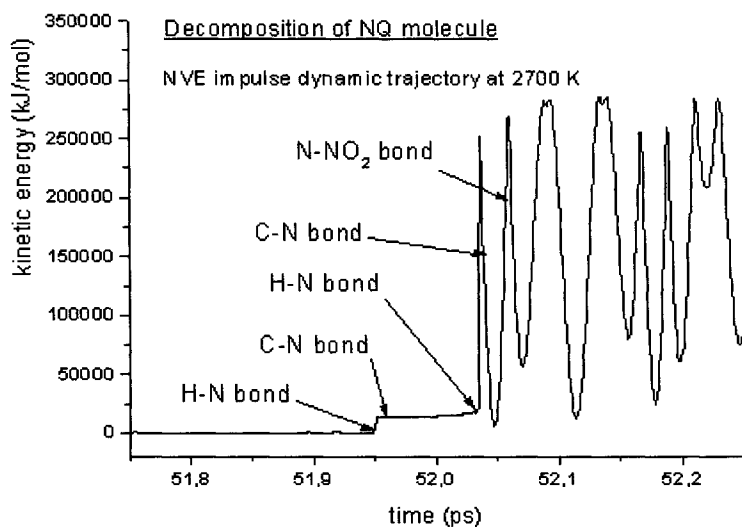


Fig. 7. Impulse dynamics trajectory for NQ.

into fragments containing 2-3 atoms. The time $t(\text{N-NO}_2)$, when the first nitro-group is released is not convenient starting point for the estimation of $\langle \Delta E_{k50} \rangle$, as it depends strongly on the reaction pathway (R1 or R2), as one can see in the Fig. 3-5.

In case of RDX and β -HMX the value of $\langle \Delta E_{k50} \rangle$ characterizes reliably the slope of the monotonous $E_k \sim \text{time}$ dependence immediately after the decomposition. In case of DADNE and NQ the vibrating $E_k \sim \text{time}$ dependence during and after the decomposition requires a strong smoothing to catch the trend of the energy curve. Thus in this case the parameter $\langle \Delta E_{k50} \rangle$ provide us only with a qualitative very rough characteristics. Calculated parameters $\langle E_k(\text{NO}_2) \rangle$ and $\langle \Delta E_{k50} \rangle$ are summarized in Table 1 together with the experimentally determined characteristic h (the critical value of the fall height of the drop weight) and calculated E_D (detonation energy) overtaken from the Ref.5.

To compare the reaction pathways R1 and R2 we analyzed dynamic trajectories for RDX corresponding to the process R1 and R2 in the Fig. 3 and 4. The parameters estimated from these two trajectories are:

- $E_k(\text{NO}_2)$ – instantaneous value of kinetic energy corresponding to the release of the first nitro-group in the dynamics trajectory,
- $E_k(d)$ – instantaneous kinetic energy corresponding to the decomposition of the molecule (splitting into fragments) at the time t_d
- ΔE_{k50} – increment of kinetic energy per 50 fs after the t_d (time of the molecule decomposition).

These parameters are summarized in the Table 2. As one can see in Table 2, the release of the first nitro-group and the gradual rupture of C-N bonds may differ in various reaction pathways R1, R2 or in mixed R1/2 pathway. It is evident, that the instantaneous value of $E_k(\text{NO}_2)$ obtained from one dynamic trajectory only, can not be the reliable characteristics of decomposition process. On the other hand the parameters $E_k(d)$ and ΔE_{k50} do not change significantly for various trajectories corresponding the same molecule and can serve as characteristics of decomposition process for a given molecule.

The comparison of calculated and experimental characteristics for all investigated molecules is in the Table 1. As one can see the $\langle E_k(\text{NO}_2) \rangle$ parameters exhibit the same trend as the h values in dependence on the molecule type. On the other hand, the course of $\langle \Delta E_{k50} \rangle$ values agrees with the course of the detonation energy E_D in dependence on the molecule type. Both calculated parameters $\langle E_k(\text{NO}_2) \rangle$ and $\langle \Delta E_{k50} \rangle$ obtained from the classical molecular dynamics simulations agree with the experimental characteristic h and calculated values of E_D in Ref. 5,16.

Table 1.

Comparison of experimental (h) and calculated value of E_D with characteristics of the explosive materials $\langle E_k(NO_2) \rangle$, $\langle \Delta E_{k50} \rangle$ obtained from dynamics trajectories; h - the impact sensitivity, E_D - detonation energy, $\langle E_k(NO_2) \rangle$ – average kinetic energy corresponding to the release of the first nitro-group in the dynamics trajectory, $\langle \Delta E_{k50} \rangle$ – average kinetic energy increment per 50 fs after the molecule decomposition.

Molecule:	h (cm)	$\langle E_k(NO_2) \rangle$ (kJ/mol)	E_D (kJ/cm ³)	$\langle \Delta E_{k50} \rangle$ (kJ/mol)
RDX	24	1500	8.321	24600
β -HMX	26	1700	8.858	29900
DADNE	100	119500	7.889	15000
NQ	177	190200	6.650	8200

Table 2.

Decomposition of RDX, comparison of trajectory parameters for reactions R1 and R2. Comparison of dynamic characteristics for decomposition of RDX molecule by reaction R1 and R2: $E_k(NO_2)$ - kinetic energy corresponding to the release of the first nitro-group in the dynamics trajectory, $E_k(d)$ – energy corresponding to the decomposition of the molecule (splitting into fragments), ΔE_{k50} – increment of kinetic energy per 50 fs after the molecule decomposition. Values in this table are not averaged and represent instantaneous values determined from two different trajectories illustrated in the Fig. 3 and 4.

	$E_k(NO_2)$ (kJ/mol)	$E_k(d)$ (kJ/mol)	ΔE_{k50} (kJ/mol)
Reaction R1	1200	1711	24900
Reaction R2	1760	1760	24300

4. CONCLUSIONS

Classical molecular dynamics simulations revealed in details the mechanism of the molecular decomposition for four selected molecules: RDX, β -HMX, DADNE and NQ. Parameters obtained from dynamic trajectories agree with the experimental characteristics h , describing the impact sensitivity and with calculated values of detonation energy for all investigated molecules. The parameters obtained from dynamics simulations could be used for fast effective testing of explosive materials. Anyway the method of testing based on dynamic simulations still needs to be worked out more preciously. That means:

- to extend the tests to large sets of dynamic trajectories
- to include the dynamic simulations of decomposition in crystal structure, what is very time-consuming

- to extend the tests to a larger group of explosive materials to confirm the validity of present conclusions.

Anyway, present results offered us a good chance to characterize the explosive materials by a reliable way using classical molecular dynamics simulations.

ACKNOWLEDGEMENTS:

The authors express their gratitude to the Ministry of Industry and Commerce of the Czech Republic for supporting the work within the framework of research project No. FC-M2/05 and to Grant Agency of the Czech Republic for support of an access to the crystallography database in Cambridge (within the framework of the project No. 203/02/0436).

REFERENCES:

- [1] P. Politzer, J.S. Murray, J.M. Seminario, P. Lane, M.E. Grice and M.C. Concha, *J. Mol. Struct. (Theochem)*, 573 (2001) 1.
- [2] M.M. Kuklja, *J. Phys. Chem. B*, 105 (2001) 10159.
- [3] D.V. Shalashilin and D.L. Thompson, *J. Phys. Chem. A*, 101 (1997) 961.
- [4] Y. Kohno, K. Ueda and A. Imamura, *J. Phys. Chem.*, 100 (1996) 4701.
- [5] P. Vávra, Proc. 4th Seminar "New Trends in Research of Energetic Materials" Univ. of Pardubice, Pardubice, Czech Republic, April 2001, pp. 345-351.
- [6] S. Zeman, R. Huczala and Z. Friedl, *J. Energet. Mater.*, 20 (2002) 53.
- [7] B.M. Rice, G.F. Adams, M. Page and D.L. Thompson, *J. Phys. Chem.*, 99 (1995) 5016.
- [8] C.J. Wu and L.E. Fried, Proc. 11th International Symposium on Detonation, Colorado, 1998, pp. 490-497.
- [9] H. Dorsett, Computational Studies of FOX-7, a New Insensitive Explosive, DSTO Aeronautical and Maritime Research Laboratory, Salisbury South Australia, 2000, pp. 1-19.
- [10] C.J. Wu and L.E. Fried, *J. Phys. Chem. A*, 101 (1997) 8675.
- [11] *Cerius²* documentation, Molecular Simulations Inc, San Diego, 2000.
- [12] C.S. Choi and E. Prince, *Acta Cryst. B*, 28 (1972) 2857.
- [13] C.S. Choi and H. P. Boutin, *Acta Cryst. B*, 26 (1970) 1235.
- [14] U. Bemm and H. Östmark, *Acta Cryst. C*, 54 (1998) 1997.
- [15] A.J. Bracuti, *J. Chem. Crystallography*, 29 (1999) 671.
- [16] P. Vávra, Proc. 3rd Seminar "New Trends in Research of Energetic Materials" Univ. of Pardubice, Pardubice, Czech Republic, April 2000, pp. 223-232.
- [17] A.T. Hagler, E. Huler and S. Lifson, *J. Am. Chem. Soc.*, 96 (1974) 5319.
- [18] A.K. Rappé and W.A. Goddard III, *J. Phys. Chem.*, 95 (1991) 3358.

Chapter 3

Nitro \rightleftharpoons *aci*-nitro Tautomerism in High-Energetic Nitro Compounds.

P.V. Bharatam^a and K. Lammertsma

^aDepartment of Chemistry, Guru Nanak Dev University, Amritsar – 143 005, Punjab, India.

^bDepartment of Chemistry, Vrije Universiteit, 1081 HV Amsterdam, The Netherlands

One of the important processes occurring during detonation of high-energetic nitro compounds is tautomerism, which involves the transfer of a hydrogen either by an unimolecular 1,3- or 1,5-shift or by a bimolecular process where the transfer occurs intermolecularly [1-9]. This hydrogen shift leads to the formation of *aci*-nitro compounds, which dissociate by release of energy to give smaller fragments. Tautomerism is competitive to many other processes that occur during detonation. In this chapter, we describe the nitro \rightleftharpoons *aci*-nitro tautomerism and provide details from experimental and theoretical studies.

1. Nitro \rightleftharpoons *aci*-nitro tautomerism

Hydrogen transfer reactions involving a 1,3-H shift are very common in organic and biological systems. Investigations into tautomerism have lead to greater understanding of such concepts as acid-base relationships, structure-reactivity correlations, hydrogen bonding, etc. and have provided valuable insights into the nature of chemical processes. More prevalent tautomeric processes are keto-enol

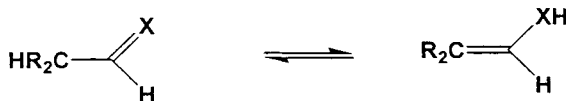


Table 1

Parent tautomeric processes and energetic data.^a

Tautomeric process	Compounds	ΔE	PA	Ref.
Keto \rightleftharpoons enol	$\text{CH}_3\text{-CH=O} \rightleftharpoons \text{CH}_2\text{=CH-OH}$	10.8	365.9	11b
Imine \rightleftharpoons enamine	$\text{CH}_3\text{-CH=NH} \rightleftharpoons \text{CH}_2\text{-CH-NH}_2$	3.9	377.1	13
Amide \rightleftharpoons imidic	$\text{NH}_2\text{-CH=O} \rightleftharpoons \text{NH=CH-OH}$	11.5	359.5	18
Oxime \rightleftharpoons nitroso	$\text{CH}_2\text{=N-OH} \rightleftharpoons \text{CH}_3\text{-NO}$	12.0	362.5	16
Nitro \rightleftharpoons <i>aci</i> -nitro	$\text{CH}_3\text{-NO}_2 \rightleftharpoons \text{CH}_2\text{=NO-OH}$	14.1	355.9	3
Nitramide \rightleftharpoons <i>aci</i> -nitramide	$\text{NH}_2\text{-NO}_2 \rightleftharpoons \text{NH=NO-OH}$	8.8	339.7	28

^a All energies are obtained at G2 level with ZPE corrections at MP2/6-31G*. ΔE is the tautomeric energy difference. PA is the proton affinity of the most stable anion.

[10-12], imine-enamine [13-15], nitroso-oxime [16], thiol-thione [17], amide-iminol [18], nitro-*aci*-nitro [3], hydrazo-azo [19], phenol-keto [20] etc. Keto-enol tautomerism is the most commonly observed and most widely studied process, and is very important in many chemical, biochemical and medicinal chemistry applications. Theoretical studies provide much insight into the details of the tautomeric processes including electronic and energetic aspects. Key indicators, such as the energy difference between the tautomers, the energy requirement for ionization of the two tautomers, the energy barrier for the 1,3-H shift, structural features of the various conformers of the tautomers, atomic and group charges of the tautomers, etc., can be obtained with high-accuracy *ab initio* theoretical methods. Table 1 gives a list of important tautomeric processes with selected energy data. Cooperativity between two or more tautomeric processes is also known to occur and they can influence one another significantly [21].

Nitro \rightleftharpoons *aci*-nitro tautomerism occupies a special role as it has been speculated to occur under conditions where high energy explosives detonate. It has been proposed as one of the important initial steps responsible for the cascade of reactions leading to the high energy release during detonation [1]. Nitro \rightleftharpoons *aci*-nitro tautomerism in nitro compounds $\text{R}_2\text{CH-NO}_2$ leads to nitronic acids, $\text{R}_2\text{C=N(O)OH}$. Kinetic studies show similar pK_a values for nitronic acids and their carbon counterparts, the carboxylic acids [1]. Nitroalkane \rightleftharpoons nitronic acid tautomerism has been assumed not to be an acid-catalyzed process because of the poor basicity of NO_2 group [4]. However, recent work by Erden et al. showed that this tautomerism can, in fact, be achieved under acid catalyzed



conditions [7]. Table 1 shows that the parent nitronic acid is thermodynamically unstable by about 14 kcal/mol, yet nitronic acids play an important role as reactive intermediates in many redox, photochemical, and pyrolytic processes, and in syntheses such as the Nef and Victor Meyer reactions [4]. Nitronic acids become more stable on aromatic substitution of the α -carbon as in diphenylmethane nitronic acid [6a] and by inter- [6a] and intramolecular hydrogen bonding [6b]. Nitronic esters are derived from *aci*-nitro compounds and have been applied in asymmetric synthesis [6b]. The *aci*-nitro anion is the key intermediate in the nitro = *aci*-nitro tautomeric process. It is also the common intermediate in many chemical reactions that involve nitro compounds and can be isolated as the sodium nitronate salt $\text{R}_2\text{C}=\text{NO}_2^-\text{Na}^+$ [1]. Appropriately substituted aromatic nitro derivatives may yield nitronic acids as is the case for o-nitrotoluene [8,22]. Nitro = *aci*-nitro tautomerism has been found to play an important role in catalysis [23,24] as well as under biological conditions [25-27]. In this chapter, the discussion has been limited to nitro = *aci*-nitro tautomerism that occurs in high energetic nitro compounds with examples taken from both experimental and theoretical studies. The discussion will deal with nitro = *aci*-nitro tautomerism in progressively complex systems starting with the most simple of all, nitromethane, followed by substituted nitroethylenes, then advancing to nitro aromatic systems, and finally to the larger nitro compounds like NTO, RDX and HMX.

2. Nitromethane \rightleftharpoons *aci*-nitromethane tautomerism

Tautomerism in nitromethane is the simplest example of nitro = *aci*-nitro tautomerism. *Aci*-nitromethane has been generated and characterized by Schwarz and co-workers using neutralization-reionization mass spectrometry [29, 30]. Formation of stable *aci*-nitromethane ions has been shown to occur via the elimination of ethylene from the molecular ion of 1-nitropropene [31]. Formation of *aci*-nitromethane by a concerted acid-catalyzed ring opening of nitrocyclopropanes has been shown to occur by Cao et al. [7c]. The unsaturated character of *aci*-nitromethane has been used for trapping various free radical species like NO_2^\cdot and NO^\cdot [32,33]. Bilski et al. have shown that *aci*-nitromethane can be oxidized with singlet oxygen, which makes it a useful

method for spin trapping of this reagent [34]. The electronic structure of the excited states of *aci*-nitromethane have been studied experimentally by Beijersbergen, et al. using charge-transfer collisions with cesium and sodium atoms [35]. Nitromethane has been considered to be a very weak acid, because as a liquid it is in equilibrium with *aci*-nitromethane and the *aci*-anion [1, 36]. The pK_a of nitromethane has been determined at 10.21, which is close to that of phenol, 9.99 [37]. Chemisorption of nitromethane on MgO(100) has been shown to give *aci*-nitromethane and the *aci*-anion [38]. In strongly basic solutions, nitromethane is transformed into its tautomeric form [39-42].

On thermal decomposition of nitromethane formation of nitric oxide, nitrous oxide, carbon monoxide, carbon dioxide, methane, ethane, ethylene, water, hydrogen cyanide, and formaldehyde has been observed [43-58]. A simple C-N bond breaking process cannot explain the formation of these products. Hence, hydrogen and/or oxygen transfer processes are viable alternatives. Whereas ample evidence has been generated for the nitro-nitrite rearrangement of nitromethane under photochemical and thermal conditions, [43, 44, 54-58] experimental evidence showing the presence of unimolecular hydrogen transfer in nitromethane remains scarce [38-42]. However, recent studies on the decomposition of liquid nitromethane have provided evidence for the participation of *aci*-nitromethane and the *aci*-anion [59-61]. Very recent studies on the electronic structure of solid nitromethane [62] suggest that its C-H bond stretching is strongly dependent on the pressure anisotropy prior to detonation and thereby give further support for the abstraction of a proton during detonation [63]. These studies indicate that nitro \rightleftharpoons *aci*-nitro tautomerism even plays an important role in the detonation of nitromethane. In the next section structural and electronic features of nitromethane, *aci*-nitromethane, and the nitromethide anion are described followed by an evaluation of the energetics of the tautomeric process.

Nitromethane, CH₃-NO₂: The equilibrium structure of singlet nitromethane has been studied at several levels of theory [3,60,64-71]. Two conformations are possible for nitromethane, staggered (**1s**) and eclipsed (**1e**), but the eclipsed form has been characterized as a transition structure at MP2/6-31G* with an imaginary frequency of 30 cm⁻¹ [3]. Rotation around the H₃C-NO₂ bond occurs essentially without barrier; the estimated value is only 0.01 kcal/mol. This is in accordance with a microwave study, which reports a C-N rotation barrier of only 6 cal/mol [72,73]. The C-N bond length of nitromethane has been estimated with X-ray single crystal diffraction [74], neutron diffraction [46,75], microwave spectroscopy [72,73], MP2/6-31G* [3], and B3LYP/6-31+G* [71] at respectively 1.449, 1.486, 1.489, 1.485, and 1.491 Å, showing that the theoretical estimates compare very well with those determined by experimental methods. The experimentally reported vibrational frequencies of nitromethane

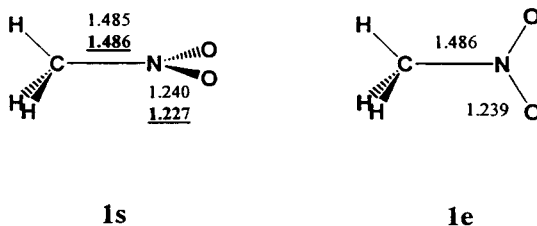


Fig. 1 The two conformations of nitromethane with MP2/6-31G* and neutron diffraction (underlined) bond distances in Å.

[49] show a similarly good agreement with those obtained by theoretical methods [3,71]. The G2 estimated atomization energy for nitromethane of -570.69 kcal/mol compares well with the -573.13 kcal/mol that is based on the JANAF Tables [3, 76].

Aci-nitromethane, $H_2C=NO_2H$: Two conformations can be considered for *aci*-nitromethane, *cis* (**2c**) and *trans* (**2t**), which differ in the orientation of the OH group relative to the NO unit. The *trans* conformer has the larger dipole moment ($\mu = 5.05$ D versus $\mu = 2.16$ D for the *cis*) and is a transition structure for N-OH bond rotation. The calculated N-OH bond rotational barrier is 6.8 kcal/mol at G1 [3]. It was initially postulated, that the *cis* isomer is more stable due to the presence of an intramolecular hydrogen bond [64]. However, an electron density analysis did not indicate the presence of any hydrogen bonding between the *aci*-nitro hydrogen and the NO unit, although the H...O distance of 2.13 Å is rather short [3]. The repulsive electrostatic interaction between the two lone pairs of *trans aci*-nitromethane makes this conformation less stable. The calculated atomization energy for *cis aci*-nitromethane is -566.6 kcal/mol. Curiously, Hu et al. [77] reported for *cis aci*-nitromethane (**2c**) two minima, **2c-i** and **2c-ii**, at 6-311++G** (Scheme I). They also located a transition structure with a barrier of 6.7 kcal/mol for converting **2c-i** into its resonance form **2c-ii**

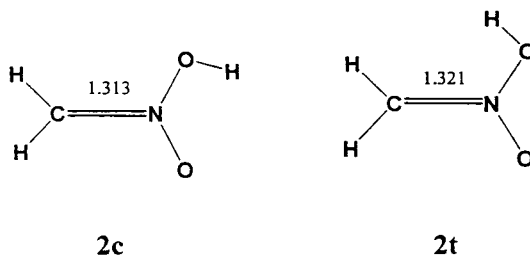
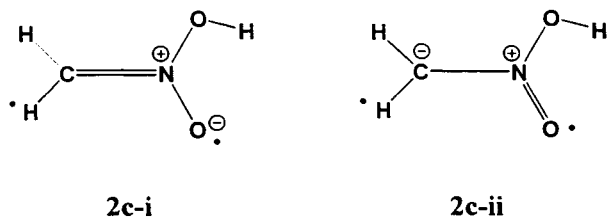


Fig. 2 *Cis* and *trans aci*-nitromethane. MP2/6-31G* bond lengths are in Å.

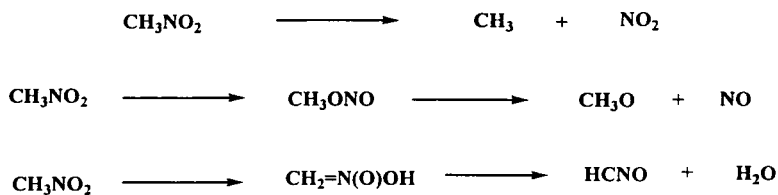
**Scheme I**

with a reverse barrier of only 0.2 kcal/mol. Clearly, this work requires closer scrutiny.

Nitromethide Anion, $CH_2=NO_2^-$: The presence of the nitromethide anion (3) in the nitromethane detonation process has been proposed in many studies. Such an anion plays an important role in unimolecular as well as in bimolecular transfer of hydrogen. The unimolecular 1,3-hydrogen shift is thermally a symmetry forbidden process and has been shown to have a very high energy barrier (64.0 kcal/mol at G2MP2//B3LYP/6-311++G**) [77]. Hence, tautomerization involving the nitromethide anion is important. The nitromethide anion with potential Y-aromatic properties has a C_{2v} symmetric structure at MP2/6-31G*. Using more flexible basis sets, a slight pyramidalization of the methylene group results with a small energy barrier for inversion at carbon (32 cal/mol at MP2/6-31++G*) [3]. Bader's electron density analysis shows that the negative charge of the nitromethide anion is mostly located on the oxygens, making these very receptive for protonation to give *aci*-nitromethane (2).

Tautomerism: The energy difference between tautomers **1s** and **2c** is sensitive to the theoretical method employed. The ΔE between the tautomers has been estimated at 22.9, 19.1, 12.7, 14.7, 14.1 and 14.1 kcal/mol using respectively MP2/6-31G*, MP4/6-311++G** (+ZPE), B3LYP/6-311+G**, G2MP2//B3LYP/6-311++G**, and the G1 and G2 levels of theory [3, 64,77]. The calculated equilibrium constant for the tautomeric process under gas-phase conditions is about 4.5×10^{11} [3]. These data clearly illustrate that *aci*-nitromethane is less stable than nitromethane and that the equilibrium should prefer nitromethane under normal circumstances, but they also illustrate that the *aci*-form can play a significant role under slightly higher energy conditions, which is the case during detonation. As noted, the unimolecular 1,3 hydrogen shift of nitromethane (**1s**) to give *aci*-nitromethane (**2c**) is a symmetry forbidden high energy process.

Scheme II



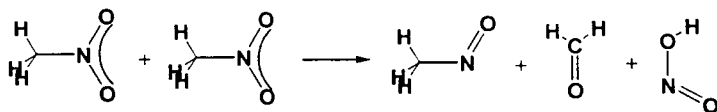
Nitromethane and aci-nitromethane dissociations: The unimolecular decomposition of nitromethane has been studied extensively both by experimental and theoretical methods [43-64,77-83]. Three paths (Scheme II) appear to be competitive: (i) simple C-N bond dissociation, requiring 62 kcal/mol, (ii) nitro-nitrate isomerization (64.6 kcal/mol) followed by N-O dissociation (45 kcal/mol), and (iii) decomposition of *aci*-nitromethane. Hu et al. explored the potential energy (PE) surface of nitromethane and identified isomerizations and dissociations of *aci*-nitromethane at G2MP2//B3LYP/6-311++G** [77]. They reported that breaking of the C=N bond in *aci*-nitromethane requires a hefty 84.6 kcal/mol. This can be expected because of the presence of double bond character in the C=N bond and because a CH₂ carbene would be formed. The concerted elimination of water from *aci*-nitromethane, to give HCNO + H₂O, was found to be the most favored path, requiring an activation energy of only 48.2 kcal/mol. Elimination of water has been observed for protonated *aci*-nitromethane during the reaction of nitromethane with aluminium phenolates [84]. Other reactions involving 1,2 shifts of OH, NO, and O and their subsequent decompositions were found to have higher energy barriers ranging from 60-104 kcal/mol. These are not considered here. Hu et al. concluded that the preferred path is breaking the H₃C-NO₂ bond because it required 2.7 kcal/mol less than the nitro-nitrite rearrangement and 2.1 kcal/mol less than the *aci*-nitromethane formation [77]. However, given that the 1,3-H shift is not an allowed process, the formation of *aci*-nitromethane might not follow a unimolecular but instead a bimolecular path after which water can be eliminated.

Bimolecular nitromethane ⇌ aci-nitromethane tautomerism: Several studies on the decomposition of liquid and solid nitromethane point to the involvement of *aci*-nitromethane or the nitromethide anion [59-62] and indicate that bimolecular paths are important for the tautomeric process. Winey and Gupta interpreted their Raman data to reflect strong intermolecular associations and bimolecular reactions [59b]. They observed a progressive broadening of the CH₃ peak, which implies strengthening of the intermolecular interactions, which occur through hydrogen bonding. Cook et al. proposed a head-to-tail mechanism for

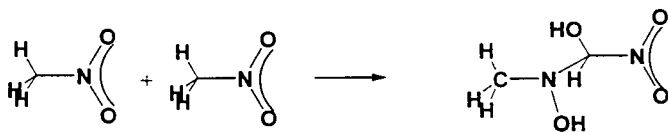
the bimolecular process to give nitrosomethane, formaldehyde, and HONO (Scheme III) [85]. The estimated activation energy of 119 kcal/mol for this process is much higher than the unimolecular processes considered earlier. Further studies employing better theoretical methods and complete optimizations are required before discarding this route. The bimolecular path proposed by Bardo [86,87] involves an association leading to a rearranged dimer (Scheme IV) in which oxygen and hydrogen atoms are exchanged between two nitromethane molecules. Bardo proposed a modification by considering the formation of nitromethanol [88] with subsequent dissociation of NO₂ (Scheme V). Winey and Gupta explained their experimental results on the basis of this mechanism, because it accounts for the observed CH₃ peak broadening in their Raman experiments [59b].

Bernasconi et al. [89] reported the hydrogen shifts from nitromethane to nitromethide anion and from protonated nitromethane to *aci*-nitromethane to

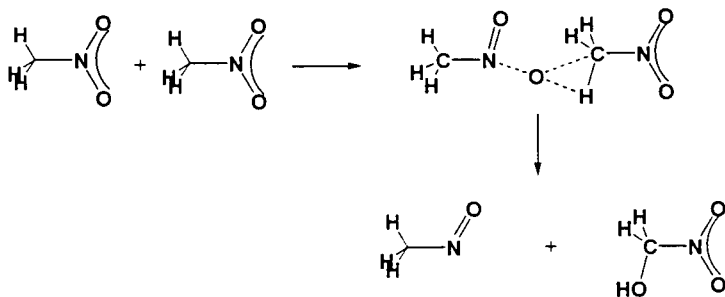
Scheme III



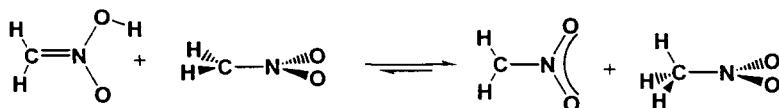
Scheme IV



Scheme V



Scheme VI

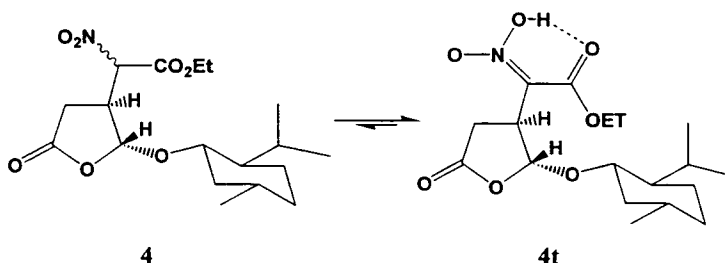


occur via carbon-to-carbon proton transfers. Based on MP2/6-311+G** calculations they concluded that the transition state for these hydrogen transfers is highly imbalanced, mainly due to the π acceptor nature of the NO_2 group. Odier et al. [90] performed theoretical studies on a cluster of three nitromethane molecules to explain the properties of solid nitromethane. They suggested that the C-N bond of the central nitromethane is strengthened by the presence of the two additional molecules. Beksic et al. [91] studied by *ab initio* methods the deprotonation of nitromethane under basic conditions using $(\text{OH})\cdot\text{nH}_2\text{O}$ clusters. They reported that considerable delocalization of negative charge from the hydroxide anion to the nitromethide anion accompanies the nitromethane deprotonation and that this accounts for the observed 'nitromethane anomaly'. Politzer et al. [82] studied the amine sensitization of nitromethane, which enhances its detonation properties [39,42]. Using B3LYP/6-31+G* they obtained an energy barrier of 33 kcal/mol for the reaction that involves the nitromethide anion, which is much less than the C- NO_2 bond breaking process (55 kcal/mol).

All these studies on bimolecular processes indirectly indicate the involvement of *aci*-nitromethane, but more detailed studies will be required to estimate the energy requirements for its formation. Our own preliminary analysis for the bimolecular transfer of hydrogen between carbon and oxygen shows this process to be spontaneous for the transfer from *aci*-nitromethane to the nitromethide anion, whereas that from nitromethane is ~ 10 kcal/mol endothermic (Scheme VI). Thus, under gas phase conditions H-transfer from *aci*-nitromethane to the nitromethide anion should occur exclusively, but the reverse process may well occur in liquid and solid phases as the endothermicity is only modest. This is further supported by the 12 kcal/mol stabilization that results on the spontaneous carbon to oxygen transfer of hydrogen from protonated nitromethane to nitromethane [28].

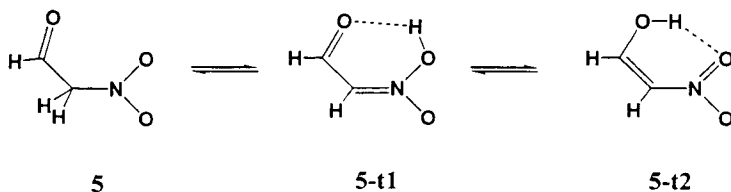
3. Tautomerism in Substituted Nitroethylenes.

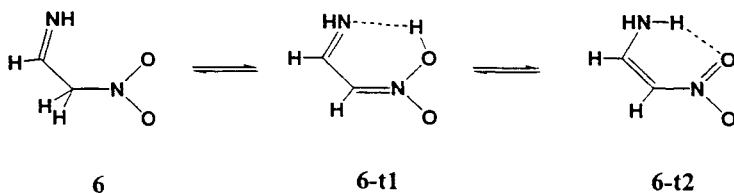
Nitronic acids are stabilized by inter- and intramolecular hydrogen bonding. Kang et al. [6b] showed that nitro compound **4** is slowly, but spontaneously converted to nitronic acid tautomer **4t** due to the stabilization that results from



the intramolecular hydrogen bond in the nitronic acid derivative. This indicates that intramolecular forces also strongly influence the nitro \rightleftharpoons *aci*-nitro tautomerism. The ONOH group adopts an *anti* arrangement in **4t**. Such an *anti* conformation represents, however, an *aci*-nitromethane transition structure (**2t**) for the rotation of the N-OH group to a *syn* conformation. Virtually all nitronic acids, including the *aci* tautomers of *o*-substituted nitroaromatics (see later), prefer a *syn* ONOH arrangement. This suggests that the intramolecular H-interaction in **4t** is not only strong enough to stabilize the nitronic acid over the nitro tautomer, but that it is also responsible for stabilizing its *anti* conformation. It has been reported that ortho substitution in nitroaromatics enhances the formation of the *aci*-nitro tautomer because of intramolecular H-bonding [8].

When a compound can be subject to more than one tautomeric process, it is expected that they influence each other. To investigate such effects in conjunction with the influence of H-bonding we reported on the interrelationship of the keto-enol, imine-enamine and nitro \rightleftharpoons *aci*-nitro tautomerism for substituted nitroethylenes [21]. These three systems are subject to tautomerism via 1,3-H-shifts, but can also undergo thermally allowed 1,5-H-shifts. A brief account is given using G2(MP2) energies. We start with nitroacetaldehyde. The keto substituent reduces the energy for its nitro \rightleftharpoons *aci*-nitro tautomerism from 14.6 kcal/mol for nitromethane to only 4.7 kcal/mol (**5** \rightarrow **5-t1**). *Aci*-tautomer **5-t1** is stabilized by an intramolecular H-bond whose strength is estimated at 12.8 kcal/mol. *Cis*-nitrovinylalcohol **5-t2**, which is even marginally more stable than





5 and related via a 1,3-H shift (keto-enol) and to 5-t1 via a symmetry allowed 1,5-H shift, is also stabilized by an intramolecular H-bond with a strength of 7 kcal/mol. The barrier for the 1,5-H shift amounts to only 5.1 kcal/mol and illustrates that *aci*-nitro derivatives are easily accessible in systems enabling intramolecular H-bonding.

Likewise, the -C(H)=NH group (6) reduces the nitro \rightleftharpoons *aci*-nitro tautomerization energy by 9.2 kcal/mol, again due to intramolecular H-bonding (6-t1). The strength of this bond in β -iminonitronic acid is estimated at 14.3 kcal/mol whereas it amounts to only 4.3 kcal/mol in the *cis*-2-nitrovinylamine (6-t2) tautomer. The 1,5-hydrogen shift of this tautomer has a barrier of 11.2 kcal/mol. Due to the presence of the strong H-bonds in both β -ketonitronic acid (5-t1) and β -iminonitronic acid (6-t1), these structures favor an *anti*-ONOH arrangement for the nitronic acid group over a *cis*-ONOH conformation by 8.8 and 6.0 kcal/mol, respectively.

In the absence of a stabilizing H-bond, nitro \rightleftharpoons *aci*-nitro tautomerism remains a higher energy process, although conjugative effects are important as the 11.0 kcal/mol needed for the 1,3-H shift of 3-nitropropene (7 \rightarrow 7-t1) illustrates. The 1,5-H shift of 1-nitropropene (7-t2) requires a sizeable 39.6 kcal/mol, which, however, is well accessible as demonstrated by the pyrolysis of nitroalkanes [92]. Table 2 summarizes the influence of the tautomeric processes on each other. It also shows that the nitro group reduces the energy difference for the acetaldehyde and vinyl alcohol tautomers by 11.5 kcal/mol to slightly

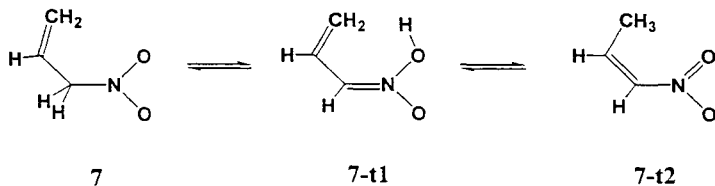


Table 2

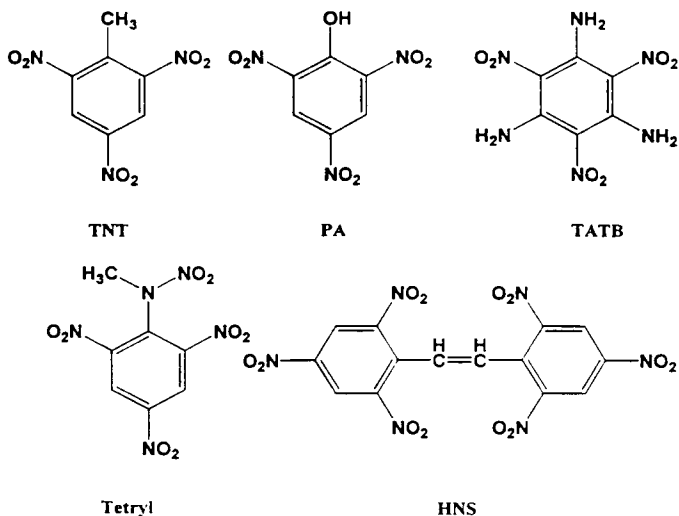
Energy differences between tautomers and the influence of the NO₂, CHO, CHNH and vinyl substituent (in kcal/mol) at G2MP2 level.

	-H	-NO ₂	-C(H)=O	-C(H)=NH	-C(H)=CH ₂
Keto \rightleftharpoons enol	11.1	-0.4			
Imine \rightleftharpoons enamine	4.0	-7.3			
Nitro \rightleftharpoons <i>aci</i> -nitro	14.6		4.7	5.4	11.0
<i>Substituent effect</i>					
Keto \rightleftharpoons enol		11.5			
Imine \rightleftharpoons enamine		11.3			
Nitro \rightleftharpoons <i>aci</i> -nitro			9.9	9.2	3.6

favor the alcohol. Likewise it reverses the imine-enamine tautomers by 11.7 kcal/mol to strongly favor the enamine.

4. Tautomerism in nitroaromatic compounds

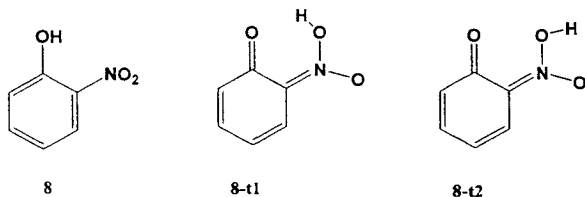
Trinitrotoluene (TNT), Picric Acid (PA), Triaminotrinitrobenzene (TATB), hexanitrostilbene (HNS), 2,4,6-(trinitrophenyl)methynitramine (Tetryl), 1,3,7,9-6H-benzotriazolo[2,1-a]benzotriazol-5-ium (TACOT) and their higher order nitro derivatives, are important nitroaromatic explosives. One of the competing initial steps in the detonation of these nitroaromatics has been shown to involve



hydrogen migration to the nitro group followed by degradation of the HONO group [8]. This is a particularly favorable process when the nitro group is ortho to a substituent with an acidic hydrogen.

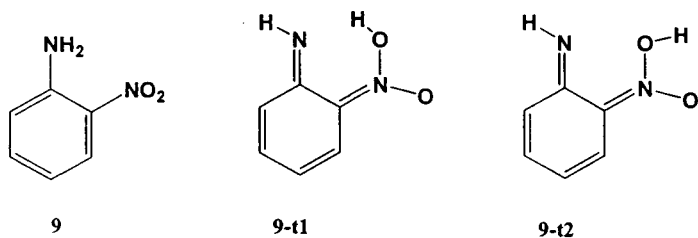
The relatively high thermal decomposition rate of 2-nitrotoluene in comparison to that of 3- and 4-nitrotoluenes (at 200°C; 400 : 0.8 : 2) is a clear example of the ortho substituent effect. The ortho CH₃, NH₂ and OH groups have been shown to play a very significant role in the pyrolysis of aromatic nitro compounds [8]. Formation of anthranil in both laser-assisted homogeneous pyrolysis and shock tube pyrolysis appeared to be a competitive process to the C-NO₂ bond scission for o-nitrotoluene [22a,93-95]. Similarly, the formation of furazan and furaxan derivatives has been reported to result from the pyrolysis of 2,4,6-trinitroaniline [96-97]. These reactions have been discussed to involve nitro \rightleftharpoons *aci*-nitro tautomerism to give short-lived *aci*-nitro tautomers [98-100]. Whereas shock and impact sensitivities may differ much from one nitroaromatic compound to another, the initial chemical steps are believed to be similar. For example, the impact sensitivity of PA is much higher than that of TNT, which is again higher than that of TATB. These differences have been attributed to subtle changes in the nitro \rightleftharpoons *aci*-nitro tautomeric equilibria for these systems.

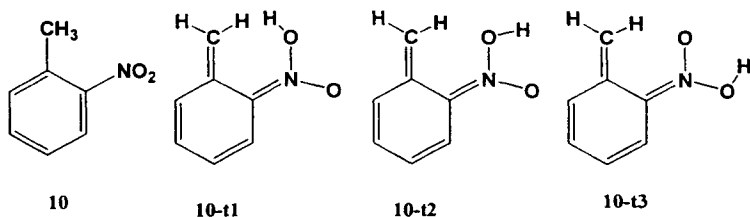
For nitrophenols, experimental data suggest their decomposition to be initiated by the transfer of the phenolic hydrogen to the NO₂ group [101-102]. This view has been supported by both an AM1 study by Fan et al. [103] and an HF/6-31G* study by Chen et al. [104]. Politzer and co-workers [9], using HF/3-21G, showed o-nitrophenol (**8**) to be able to undergo a 1,5-hydrogen shift to give the 1.5 kcal/mol less stable *aci*-nitro tautomer (**8-t1**) but also that such tautomerism does not occur for o-nitroaniline (**9**). They argued that this different behavior could be responsible for the smaller impact sensitivity of TATB as compared to that of PA. Brill and James [8] attributed the formation of quinone derivatives to the small energy difference between the nitrophenol tautomers. Chen and co-workers [104] reported on the molecular structures of mono-nitrophenols and their thermal decomposition tautomers. At HF/6-31G* they found five o-nitrophenol tautomers/conformers with three having an *aci*-nitro group. The *aci*-nitro tautomer with an *anti*-ONOH unit (**8-t1**) appeared not



to be a minimum in contrast to *cis*-ONOH conformer **8-t2**, which is the most stable tautomer of o-nitrophenol with an energy difference of 17.4 kcal/mol. We estimated that the 1,5-H shift of o-nitrophenol to give **8-t2** requires 27.6 kcal/mol at B3LYP/6-311+G**//B3LYP/6-31+G* with a barrier of 32.4 kcal/mol [28]. The barrier for the tautomerization of **8** is much higher than expected for a simple 1,5-H shift because the transition state also reflects a N-OH bond rotation. On the reaction path connecting the two tautomers, there is only a shoulder (but not a minimum) corresponding to **8-t1**.

Nitro derivatives of aniline are less sensitive than those of phenol and toluene [105]. Experimental observations suggest that the impact sensitivity reduces with an increase in the number of amino groups. For example, triamino-trinitro-benzene (TATB) is less sensitive than diamino-trinitro-benzene (DATB) with mono-amino-trinitro-benzene (Picramide, PAm) being the least sensitive of the three. Charge delocalization by means of resonance and push-pull effects have been attributed to this phenomenon. Intramolecular hydrogen bonding has also been noted to lower the impact sensitivities of aminobenzenes. Brill and James [8] could not identify a single parameter to explain the observed trend in sensitivities and argued that a combination of factors is more plausible. Experimental results indicate that N-H and N-OH scissions and intramolecular H-transfers are likely processes to influence the sensitivities of nitroanilines [106-112]. Xiao et al. [111] calculated C-NO₂ bond orders for a series of nitro anilines and proposed these to be a guide for the relative C-N bond strengths. Our B3LYP/6-311+G**//B3LYP/6-31+G* study [28] indicates intramolecular H-bonding in aromatic nitro compounds to be important, but that this effect is much weaker in o-nitroaniline (**9**) (0.1 kcal/mol) than in o-nitrophenol (6 kcal/mol). Conversion of o-nitroaniline to *ac*initro tautomer **9-t2**, having a syn-ONOH group, is 38.2 kcal/mol endothermic with a barrier of 42.4 kcal/mol; this 1,5-H shift shows only a weak shoulder that can be related to structure **9-t1**. The larger endothermicity for forming **9-t2** as compared to the corresponding oxygen derivative is mainly due to loss of aromaticity rather than to loss of H-bonding; the reduced H-bonding can be associated with the non-planarity of **9-t2**. Apparently and may be not unexpectedly, nitrophenols display a higher





tendency for formation of quinone-like structures than the nitroanilines.

The chemistry of *o*-nitrotoluene (**10**) has been studied extensively as a model for aromatic nitro compounds [8,93-95,113-115]. The *aci*-nitro tautomer of *o*-nitrotoluene can be generated photochemically, but its kinetic stability is very small so that it rearranges back to **10** [98]. *Ac*i-nitro tautomers of 2,4-dinitrotoluene, 2,4,6-trinitrotoluene, and related compounds have also been generated by photochromic methods [98,116-117]. Il'ichev and Wirz [113] carried out a survey of the B3LYP/6-311+G** potential energy surface for **10** and its isomers and showed that the 1,5-H shift from the methyl to the nitro group, which results in *aci*-nitro tautomer **10-t1**, is a 41 kcal/mol endothermic process. This estimate is only slightly larger than ours of 38 kcal/mol for the 1,5-H shift in 1-nitropropene, using the same method. Il'ichev and Wirz also reported that the *aci*-nitro tautomer of **10** might exist in three different forms, i.e., *anti* (**10-t1**), *cis* (**10-t2**), and *trans* (**10-t3**). However, the barrier for converting **10-t1** into the more stable **10-t2** is only 0.02 kcal/mol. Rearranging this structure into the 4 kcal/mol more stable **10-t3** by means of a 1,3-H shift requires 20.3 kcal/mol, which is much less than is typical for most other related 1,3-H shifts. The kinetic stability of *aci*-nitro tautomer **10-t2** is modest as the barrier for conversion back to *o*-nitrotoluene amounts to only 10 kcal/mol, which explains why photochemically generated **10-t2** isomerizes to *o*-nitrotoluene. Other processes such as the 34 kcal/mol exothermic OH-transfer from the *aci*-nitro group to the CH₂ group of **10-t3** are believed not to be competitive with the re-isomerization, because of the high barrier involved (70.5 kcal/mol) [28].

The noted studies show the 1,5-hydrogen shift in *o*-nitrophenol, *o*-nitroaniline, and *o*-nitrotoluene to be a feasible process like that for the *cis* substituted nitroethylenes. Strong hydrogen bonding in *o*-nitrophenol eases the 1,5-H shift with its subsequent N-OH bond rotation to an overall barrier of 32.4 kcal/mol. The much smaller degree of hydrogen bonding renders a higher barrier (42.4 kcal/mol) for the corresponding process of *o*-nitroaniline. Figure 3 shows the kinetic stability for the hydrocarbon *aci*-nitro tautomer **10-t2** to be much higher than for both **9-t2** and **8-t2**. One contributor is the difference in

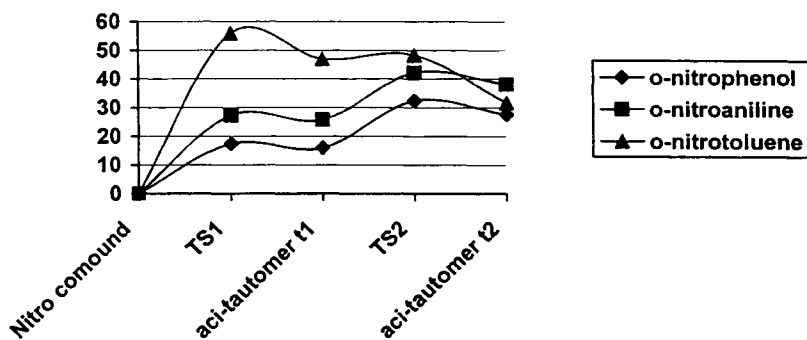


Fig. 3. Potential energy surface of o-nitrophenol, o-nitroaniline and o-nitrotoluene.

their reverse 1,5-H shift barriers of respectively 13.1, 4.0 and 4.8 kcal/mol [28], but foremost the lack of stabilizing H-bonding in o-nitrotoluene gives a high activation barrier for the tautomerization process. Nevertheless, the estimated energy requirement for tautomerization in each of these systems is much less than the C-NO₂ bond dissociation energy (ca. 60 kcal/mol). Hence formation of *aci*-nitro derivatives via nitro = *aci*-nitro tautomerism is a plausible chemical process at the time of detonation of these and related nitroaromatic compounds.

The influence of ortho substituents on the C-NO₂ rotation barrier was addressed recently by several groups [112-114,119]. They showed that intermolecular hydrogen bonds and steric factors play both an important role on the strength of the C-NO₂ π -interaction. For example, Chen and Chen reported C-NO₂ bond rotation barriers for nitrobenzene, nitrotoluene, nitrophenol, and nitroaniline of respectively 5.9, 2.4, 12.2, and 9.5 kcal/mol at B3LYP/6-31+G* [114]. As a result of the differences in the nature of the ortho interactions, the 1,5-hydrogen shift in PA is much easier than it is in TNT, which that in 2,4,6-trinitroaniline (Picramid, PAm) being more difficult still. This order in the ability to undergo a 1,5-H shift is similar to the impact sensitivity of the compounds, i.e. PA > TNT > PAm. Hence, it is suggestive that the impact sensitivities and hence the decomposition processes in these aromatic nitro compounds are greatly influenced by nitro = *aci*-nitro tautomerism, which in turn are influenced strongly by the type of ortho substituent.

The 1,5-H shift for 2,6-dinitrophenol (2,6-DNP), 2,6-dinitroaniline (2,6-DNA), 2,6-dinitrotoluene (2,6-DNT), 2,4,6-trinitrophenol (Picric Acid, PA),

Table 3

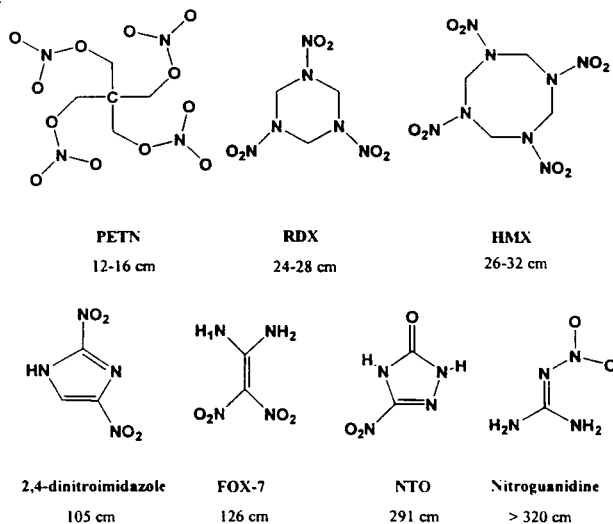
Nitro = <i>aci</i> -nitro tautomerisation energies of nitroaromatic compounds (in kcal/mol) at B3LYP/6-31G*.			
	2-nitro	2,6-dinitro	2,4,6-trinitro
Phenol	28.1	26.3 (2,6-DNP)	25.5 (PA)
Aniline	39.4	42.6 (2,6-DNA)	42.7 (PAm)
Toluene	37.2	35.7 (2,6-DNT)	33.0 (TNT)

2,4,6-trinitroaniline (Picramide, PAm), and 2,4,6-trinitrotoluene (TNT) [28] follow the trends observed for the mononitro compounds with only slight, but important differences. Only selected items will be reviewed briefly (Table 3). Introducing a second nitro group ortho to the OH/NH₂/CH₃ substituent lowers the energy slightly for tautomerization (i.e., the 1,5-H shift) for both 2,6-DNP and 2,6-DNT by 1.8 and 1.5 kcal/mol, respectively, while it increases for 2,6-DNA by 3.2 kcal/mol. Introducing a third para-nitro group as in PA, PAm and TNT magnifies these effects even further as is evident from the respective tautomerization energies of 25.5, 42.7, and 33.0 kcal/mol. Evidently, additional nitro substitution increases the tautomerization energy for 2-nitroaniline but decreases that for both 2-nitrophenol and 2-nitrotoluene. This phenomenon is due to the extra stabilization that the NH₂ group provides to the nitro tautomer through a second hydrogen bond to the other ortho nitro group. The tautomerization energy for the corresponding OH/CH₃-carrying systems reduces instead due the electrostatic repulsion between the OH/CH₃ and the second ortho nitro group. Interestingly, this calculated trend in tautomerization energies is in accord with the reported impact sensitivities, noting that a system with higher tautomerization energy is expected to show less impact sensitivity. This correlation further supports the notion that nitro = *aci*-nitro tautomerization plays an important role in the detonation of nitroaromatic compounds.

5. Tautomerism in NTO, HMX, RDX and 5-Nitro-1H-Tetrazole

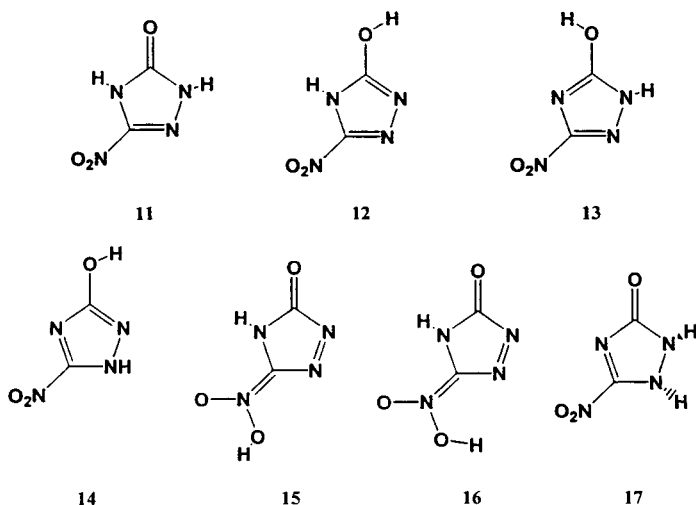
Non-aromatic compounds carrying nitro groups are also known to display explosive characteristics, some of which are shown in Scheme VII together with their impact sensitivities ($h_{50\%}$ in cm) [105, 121-123]. Amongst the explosives shown tetranitrate pentaerythritol (PETN) is the most sensitive one ($h_{50\%}$ = 13 cm), slightly more than RDX and HMX, which have $h_{50\%}$ values of 28 and 32 cm, respectively. Nitroguanidine is the least sensitive ($h_{50\%}$ > 320 cm), closely followed by NTO ($h_{50\%}$ = 291 cm) and 1,1-diamino-2,2-dinitro-ethylene (FOX-7, $h_{50\%}$ = 126 cm). Experimental and theoretical studies have shown that tautomerism and positional isomerism play an important role in the initiation stage of the detonation of some of these compounds [124-129]. However, we restrict this review to the more thoroughly studied NTO, RDX, HMX and 5-

Scheme VII



nitro-1H-tetrazole for which nitro = *aci*-nitro tautomerism was discussed specifically.

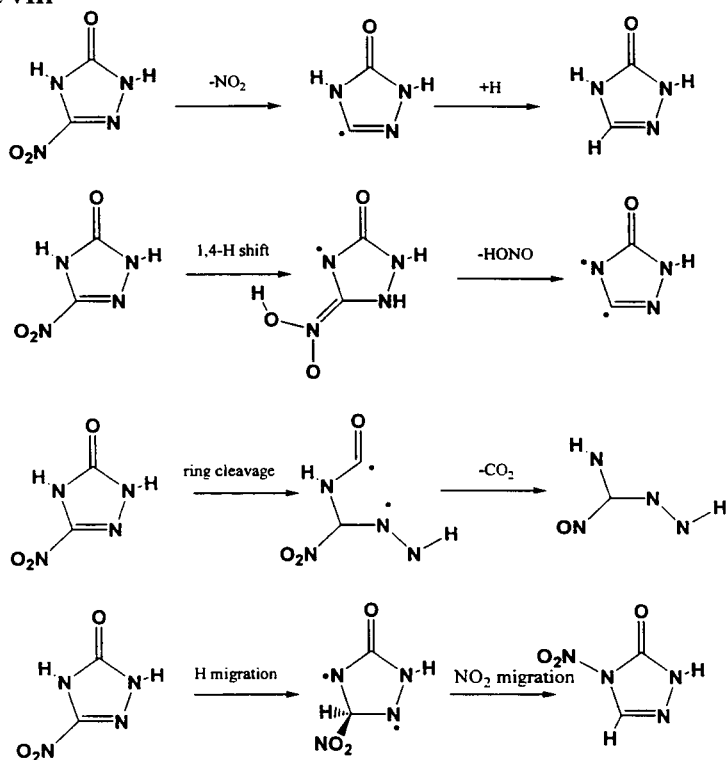
a. Tautomerism in NTO: 5-Nitro-2,4-dihydro-3H-1,2,4-triazol-3-one (NTO) has desirable explosive properties such as high energy release on decomposition, high detonation velocities, good thermal stability, a low chemical sensitivity to radiation damage, and it is relatively insensitive to impact and shock [129]. Decomposition of NTO has been shown to give a large number of products that include NO, CO₂, N₂O, HCN, HNCO, and CO [130-141]. Analyses of the products suggested that dissociation of the C-NO₂ bond may not initiate the controlled thermal decomposition of NTO [134]. However, while several mechanistic paths have been proposed, there is still no consensus on the most probable reaction channel. Based on photochemical and thermal studies, Menapace et al. [136] proposed that early loss of HONO is involved in the NTO decomposition. GC/MS analysis by Ostmark et al. [135] showed features that are consistent with the primary loss of NO₂ and/or HONO, which is also supported by the high-temperature (220-280°C) experiments by Oxley et al. [138]. Primary and secondary deuterium kinetic isotope effect (DKIE) studies clearly indicate that hydrogen transfer is involved in the rate determining step at low temperatures [136,138]. On the other hand, Williams et al. [131,137] detected neither NO₂ nor HONO by IR spectroscopy in the initial stage of the dissociation. Also a pulsed IR laser pyrolysis study of thin films did not detect NO₂ and HONO as products at the onset of decomposition [142]. Botcher et al.



have suggested that intramolecular oxidation of the keto carbon by the nitro group with concurrent rupturing of the ring structure occurs [142]. Instead, the nitro-nitrite rearrangement is the preferred path according to a laser ionization study by McMillen et al. [139]. A kinetic study by Wight and co-workers indicated an initial bimolecular step [142]. This study together with the results reported by Menapace et al. [136] and by Garland et al. [140] suggests that intermolecular hydrogen abstraction is the predominant step in the NTO decomposition. Detailed studies by Oxley indicated two distinct mechanistic paths, one involving CO_2 and N_2 evolution and the other involving migration of the nitro group from carbon to the adjacent nitrogen ring atom [141].

Several groups have performed theoretical studies to identify the mechanism by which NTO dissociates [142-151]. We reported on the energetics of tautomerization, ionization, and bond dissociations of NTO and six of its tautomeric forms, **11-17** [71]. At B3LYP/6-311+G** nitronic acids **15** and **16** are less stable than NTO by 26.7 and 29.7 kcal/mol, respectively. It was recognized that NTO and its tautomers possess aromatic character to different degrees. For example, structures **12** and **14** are strongly aromatic, making them more stable than the other tautomers. The estimated C- NO_2 bond dissociation energy for NTO is 70 kcal/mol, which is comparable to that of nitrobenzene, as determined by laser induced homolysis in the gas phase [143b]. Meredith et al. [143a] studied all the proposed decomposition paths of NTO at CCSD//RHF/DZP (Scheme VIII) and concluded that the C- NO_2 bond dissociation path, requiring 67.1 kcal/mol, should be favored over all other

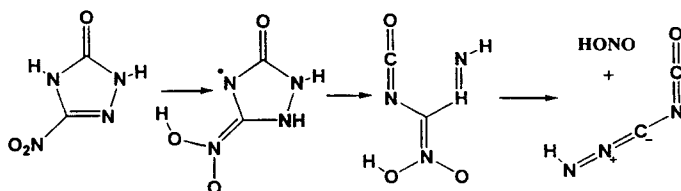
Scheme VIII



reaction channels. They computed that elimination of HONO would require 74.7 kcal/mol, ring scission 84.2 kcal/mol, and migration of the nitro group 86.3 kcal/mol.

Wang et al. [144] identified at MP2/6-31G** transition states for the unimolecular hydrogen transfer between various tautomers. They reported that the H-transfer from NTO to *aci*-nitro-NTO is the favored pathway with a barrier of 31.7 kcal/mol, which may therefore be considered as a dominant step in the decomposition process. They also reported that the bottleneck activation energies for C- NO_2 cleavage amounts to 80 kcal/mol, whereas that for cleaving C- NO_2H requires less (55-71 kcal/mol). This led them to suggest that the formation of an *aci*-nitro tautomer, given in Scheme VIII, with subsequent cleavage of its C- NO_2H bond is the favored reaction channel at lower temperatures and longer reaction times.

Scheme IX

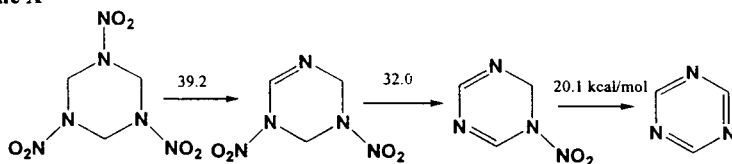


Yim and Liu [145] used a combined *ab initio* molecular dynamics (MD) study to reveal several new mechanistic paths that are energetically favored over dissociation of the C-NO₂ bond. Their study indicated dissociation of NTO via an *aci*-nitro tautomer followed by ring scission to a ketenimine intermediate as the most favorable pathway (Scheme IX), requiring only 38 kcal/mol as compared to the 62.5 kcal/mol needed for cleaving the C-NO₂ bond. Kohno et al. [151] conducted a theoretical study on the decomposition of the NTO dimer. They reported that HONO elimination is the last step of a cascade of reactions with a total barrier of 88 kcal/mol.

As discussed in this section, nitro \rightleftharpoons *aci*-nitro tautomerism plays a crucial role in the decomposition of the explosive NTO. Further studies are required to identify the importance of H-migration under bimolecular and solid state conditions.

b. Tautomerism in RDX: Cyclic nitramine hexahydro-1,3,5-trinitro-1,3,5-triazine (RDX) is an important high-energy compound for various propellants and explosives since it releases a large amount of energy in bulk decomposition [152-159]. The thermal decomposition of RDX has been shown to form simple products such as HCN, NO, N₂O, NO₂, CO, CO₂, H₂O, H₂CO, etc. [152-159]. N-NO₂ bond homolysis was found to compete with ring fission by infrared multiphoton dissociation (IRMPD) in a molecular beam experiment [152]. Fission of the CH₂N-NO₂ bond was shown to follow an 80 kcal/mol endothermic concerted reaction path. There is no direct experimental or theoretical evidence to support the involvement of an *aci*-nitro tautomer in the decomposition process of RDX. However, there is evidence to show that a concerted unimolecular HONO elimination is one of the primary processes, which does suggest that tautomerism is involved. Based on TG/MS and isotopic crossover experiments Behrens and Bulusu [158] suggested that the formation of oxy-s-triazine in the unimolecular reaction of RDX results from the elimination of HNO and two HONO molecules. Their studies on kinetic isotope effects

Scheme X

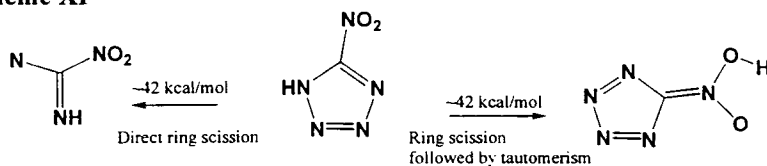


confirm the elimination of HONO to be the rate determining step. The laser induced photo-dissociation of RDX at 248 nm also suggested a concerted HONO elimination path [159].

The decomposition of RDX has also been the subject of theoretical analyses [160-167]. Our own study [160] and that of Rice and Chabalowski [161] showed RDX to have several conformations within an energy range of ca. 1 kcal/mol. The N-NO₂ and C-H bond dissociation energies were estimated at 42 and 85 kcal/mol, respectively (B3LYP/6-311G**), indicating their relative weakness and suggesting that the decomposition is initiated by N-N bond cleavage and propagated by hydrogen atom transfer. Wu and Fried showed that the N-NO₂ dissociation path is favored by 18.3 kcal/mol over a concerted ring fission that leads to methylenenitramine [164]. Goddard and co-workers studied the unimolecular decomposition of RDX extensively at B3LYP/6-31G*[166]. They found that the concerted decomposition of the ring to CH₂NNO₂ units is not an allowed pathway, requiring 59.4 kcal/mol. Homolytic N-NO₂ bond cleavage to give transient RDR has been estimated at 39.0 kcal/mol, but the subsequent decomposition requires 65-83 kcal/mol. Hence Goddard and co-workers suggested that the N-NO₂ bond cleavage may not be the most favored path. They proposed a new mechanism, which involves successive elimination of HONO from RDX with a threshold of 39.2 kcal/mol (Scheme X) [166-167]. They further conclude that HONO elimination is the most exothermic primary decomposition channel and that it may account for the energy release observed in the decomposition of RDX.

c. *Tautomerism in HMX*: Octahydro-1,3,5,7-tetranitro-1,3,5,7-tetrazocine (HMX) is another cyclic nitramine that is known as a potent explosive that is applied in rocket propellants [168-179]. The decomposition products of HMX are similar to those of RDX. Brill rationalized the experimental observations by suggesting that there are two competing reaction paths, one involving the initial release of HONO and the other involving the release of N₂O [169]. Recent laser-assisted self-oscillating burning experiments of HMX suggest that a multiple step reaction explains the data better [171]. Of the limited number of theoretical studies [180-183] Chakraborty et al. [183] addressed the mechanistic

Scheme XI



aspects of the decomposition. They concluded that the consecutive elimination of HONO is energetically preferred, similar to that for RDX, over other reaction channels such as a concerted decomposition, homolytic cleavage of the N-N bond, and O-migration from NO₂ to C with subsequent dissociation. These results indicate that nitro = *aci*-nitro tautomerization is involved in the initial stages of the decomposition of nitramines, even though the *aci*-nitro tautomer is not directly identified presumably because of its very modest kinetic stability.

d. *Tautomerism in 5-nitro-1H-Tetrazole*: Thermal decomposition of 5-nitro-1-hydrogen-tetrazole has been studied both experimentally and theoretically [184-190]. Although the explosive character of the system has not yet been thoroughly established, attempts are in process. Wang et al [190] studied the mechanism of the thermal decomposition with molecular dynamics simulations. Their calculations suggest that N₂-expulsion from the ring favored over nitro-*aci*-nitro tautomerism even though both processes require ca. 42 kcal/mol; they concluded that C-NO₂ bond breaking is less important. The direct ring scission by which N₂ is eliminated was shown to be highly exothermic and hence constitutes a very plausible decomposition pathway (Scheme XI).

REFERENCES

- [1] A.T. Nielson In *The Chemistry of the Nitro and Nitroso Groups*, H. Fueer, Ed. Interscience: New York, 1969, Part 1, p 349. (b) W.E. Noland, *Chem. Rev.* 55 (1955) 137. (c) *The Chemistry of Amine, Nitroso. and Nitro Compounds and Their Derivatives*. S. Patai, Ed.: Wiley: New York, 1982: H.A. Morrison, p 165, Y.L. Chow, p 181, L. Batt, p 417. (d) L.L. Davis and K.R. Brower, *Shock Compression Condens. Mat.* 1997, 699.
- [2] H. Schwarz and K. Levsen, In *The Chemistry of Amine, Nitroso and Their Derivatives*, S. Patai, Ed.; Wiley, New York, 1982 p. 85.
- [3] K. Lammertsma and B.V. Prasad, *J. Am. Chem. Soc.* 115 (1993) 2348 and references cited therein.
- [4] (a) J.T. Edward and P.H. Tremaine, *Can. J. Chem.* 49 (1971) 3483. (b) J.T. Edward and P.H. Tremaine, *Can. J. Chem.* 49 (1971) 3489.
- [5] G.N. Spokes and S.W. Benson, *J. Am. Chem. Soc.* 89 (1967) 6030.

- [6] (a) H. Bock, R. Dienelt, H. Schodel, Z. Havlas, E. Herdtweck and W.A. Herrmann, *Angew. Chem. Int. Ed. Engl.* 32 (1993) 1758. (b) F.A. Kang, C.L. Yin, and S.W. She, *J. Org. Chem.* 61 (1996) 5523.
- [7] (a) I. Erden, J.R. Keeffe, F.P. Xu and J.B. Yheng, *J. Am. Chem. Soc.* 115 (1993) 9834. (b) A.J. Kresge, *Chemtracts: Org. Chem.* 7 (1994) 187. (c) W. Cao, I. Erden and J.R. Keeffe, *Angew. Chem., Int. Ed. Engl.* 34 (1995) 1091.
- [8] T.B. Brill and K.J. James, *Chem. Rev.* 93 (1993) 2667.
- [9] P. Politzer, M.J. Seminario and P.R. Bolduc, *Chem. Phys. Lett.* 158 (1989) 463.
- [10] K.S. Sung, R.R. Wu and S.Y. Sun, *J. Phys. Org. Chem.* 15 (2002) 775 and references cited therein.
- [11] (a) C.C. Su, C.K. Lin, C.C. Wu and M.H. Lien, *J. Phys. Chem. A* 103 (1999) 3289. (b) B.J. Smith, M.T. Nguyen, W.J. Bouma and L. Radom, *J. Am. Chem. Soc.* 113 (1991) 6452.
- [12] Z. Rapport, (Ed.) *The Chemistry of Enols*; Wiley: Chichester, U.K., 1990.
- [13] K. Lammertsma and B.V. Prasad, *J. Am. Chem. Soc.* 116 (1994) 642.
- [14] J.F. Lin, C.C. Wu and M.H. Lien, *J. Phys. Chem.* 99 (1995) 16903.
- [15] L. Kozerski, B. Kwiecien, P. Krajewski, R. Kawecki, E. Bednarek, J. Sitkowski, W. Bocian, W. Kozminski and P.E. Hansen, *New J. Chem.* 26 (2002) 1060.
- [16] J.A. Long, N.J. Harris and K. Lammertsma, *J. Org. Chem.* 6 (2001), 6762.
- [17] D. Delaere, G. Raspoet and M.T. Nguyen, *J. Phys. Chem. A* 103 (1999) 171.
- [18] W.M. Wong, K.B. Wiberg and M.J. Frisch, *J. Am. Chem. Soc.* 114 (1992) 1645.
- [19] J. Albert, A. Gonzalez, J. Grannel, R. Moragas, X. Solans and M. Font-Bardia, *J. Chem. Soc., Dalton Trans.* 11 (1998) 1781
- [20] E. Nikiforov, *Russ. Chem. Rev.* 35 (1996) 817.
- [21] K. Lammertsma and P.V. Bharatam, *J. Org. Chem.* 65 (2000) 4662.
- [22] (a) Y.Z. He, J.P. Cui, W.G. Mallard and W. Tsang, *J. Am. Chem. Soc.* 110 (1988) 3754. (b) S.K. Chattopadhyay and B.B. Craig, *J. Phys. Chem.* 91, 1987, 323. (c) J.A. Menapace and J.E. Marlin, *J. Phys. Chem.* 94 (1990) 1906.
- [23] A.D. Cowan, N.W. Cant, B.S. Haynes and P.F. Nelson, *Catal.* 176 (1998) 329.
- [24] M. Akiba and Y. Sasaki, *Inorg. Chem. Commun.* 1 (1998) 61.
- [25] Y. Meah and V. Massey, *P. Natl. Acad. Sci. USA* 97 (2000) 10733.
- [26] C. Grewer, S. Abdollah, M. Mobarekeh, N. Watzke, T. Rauen and K. Schaper, *Biochemistry -US* 40 (2001) 232.
- [27] S. Bak, F.E. Tax, K.A. Feldmann, D.W. Galbraith and R. Feyereisen, *Plant Cell* 13 (2001) 101.
- [28] P.V. Bharatam and K. Lammertsma, unpublished work, manuscript under preparation.
- [29] H. Egsgaard, L. Carlsen, H. Florencio, T. Drewello and H. Schwarz, *Ber. Bunsenges. Phys. Chem.* 93 (1989) 76.
- [30] H. Egsgaard, L. Carlsen and S. Elbel, *Ber. Bunsenges. Phys. Chem.* 90 (1986) 369.
- [31] S.K. Hindawi, R.H. Fokkens, F.A. Pinkse and N.M.M. Nibbering, *Org. Mass Spectrom.* 21 (1986) 243.
- [32] P. Bilski, K. Reszka and C.R. Chignell, *J. Am. Chem. Soc.* 116 (1994) 9883.
- [33] P. Bilski, C.F. Chignell, J. Szychliński, A. Borkowski, E. Oleksy and K. Reszka, *J. Am. Chem. Soc.* 114 (1992) 549.
- [34] K. Reszka, C.F. Chignell, and P. Bilski, *J. Am. Chem. Soc.* 116 (1994) 4119.
- [35] (a) J.H.M. Beijersbergen, W.J.v.d. Zande, P.G. Kistemaker, J. Los, T. Drewello and N.M.M. Nibbering, *J. Phys. Chem.* 1992, 96, 9288. (b) K. Qian, A. Shukla and J. Futrell, *J. Am. Chem. Soc.* 113 (1991) 7121.
- [36] V.A. Rabinovich and Z.Y. Havin, (Eds.) *Brief Chemical Handbook*, Khimiya, Leningrad, 1978.

- [37] J.A. Dean, (Ed.) Lange's Handbook of chemistry, New York: Mc Graw-Hill.
- [38] (a) A.A. Kheir and J.F. Haw, J. Am. Chem. Soc. 116 (1994) 817. (b) A. Allouche, J. Phys. Chem. 100 (1996) 1820.
- [39] R. Engelke, W.L. Earl and C. McMichael-Rohlfing, J. Chem. Phys. 84 (1986) 142.
- [40] R. Engelke, W.L. Earl and C. McMichael-Rohlfing, J. Phys. Chem. 90 (1986) 545.
- [41] R. Engelke, D. Schiferl, C.B. Storm and W.L. Earl, J. Phys. Chem. 92 (1988) 6815.
- [42] (a) M.D. Cook and P.J. Haskins In Proceedings of the Ninth International Symposium on Detonation (Arlington, VA: Office of Naval Research), (1989) p 1027. (b) M.D. Cook and P.J. Haskins in Proceedings of the Tenth International Symposium on Detonation (Arlington, VA: Office of Naval Research), (1993) p 870.
- [43] A.M. Wodtke, E.J. Hintsa and Z.T. Lee, J. Chem. Phys. 84 (1986) 1044.
- [44] A.M. Wodtke, E.J. Hintsa and Y.T. Lee, J. Phys. Chem. 90, (1986) 3549.
- [45] B.H. Rockney and E.R. Grant, J. Chem. Phys. 79 (1983) 708.
- [46] A.P. Cox and S.J. Waring, J. Chem. Soc., Faraday Trans. 2 (1972) 1060.
- [47] G.O. Sorensen, T. Pederson, H. Dreiyler, A. Guarnieri and A.P. Cox, J. Mol. Struct. 97 (1983) 77.
- [48] D.C. McKean and R.A. Watt, J. Mol. Spectrosc. 61 (1976) 184.
- [49] C. Trinquecoste, M. Rey-Lafon and M.T. Forel, Spectrochim. Acta 30A (1974) 813.
- [50] K. Glanyer and J. Troe, Helv. Chim. Acta 55 (1972) 2884.
- [51] W.D. Taylor, T.D. Allston, M.J. Moscato, G.B. Fayekar, R. Koylowski and G. Takacs, Int. J. Chem. Kinet. 12 (1980) 231.
- [52] K. Honda, H. Mikuni and M. Takahasi, Bull. Chem. Soc. Jpn. 45 (1972) 3534.
- [53] H.S. Kilic, K.W.D. Ledingham, C. Kosmidis, T. McCanny, R.P. Singhal, S.L. Wang, D.J. Smith, A.J. Langley and W. Shaikh, J. Phys. Chem. A. 101 (1997) 817.
- [54] B.M. Rice and D.L. Thompson, J. Chem. Phys. 93 (1990) 7986 are references cited therein.
- [55] R.P. Saxon and M. Yoshimine, Can. J. Chem. 70 (1992) 572.
- [56] S. Roszak and J.J. Kaufman, J. Chem. Phys. 94 (1991) 6030.
- [57] P. Glarborg, A.B. Bendtsen and J.A. Miller, Int. J. Chem. Kinetics 31 (1999) 591.
- [58] Y.X. Zhang and S.H. Bauer, J. Phys. Chem. 101 (1997) 8717.
- [59] (a) Y.A. Gruzdkov and Y.M. Gupta, J. Phys. Chem. A. 102 (1998) 2322. (b) J.M. Winey and Y.M. Gupta, J. Phys. Chem. B. 101 (1997) 10733. (c) G.I. Pangilinan and Y.M. Gupta, J. Phys. Chem. 98 (1994) 4522. (d) C. P. Constantinou, J.M. Winey and Y.M. Gupta, 98, 1994, 7767. (e) J.M. Winey and Y.M. Gupta, J. Phys. Chem. B. 101 (1997) 9333.
- [60] M.R. Manaa and L.E. Fried, J. Phys. Chem. A. 102 (1998) 9884.
- [61] N.C. Blais, E. Ray and S.A. Sheffield, J. Phys. Chem A 101 (1997) 8285.
- [62] D. Margetis, E. Kaxiras, M. Elstner and M.R. Manaa, J. Chem. Phys. 117 (2002) 788.
- [63] R. Shaw, P.S. Decarli, D.S. Ross, E.L. Lee and H.D. Stromberg, Combust. Flame 35 (1979) 237; *ibid.* 50 (1983) 123.
- [64] M.L. McKee, J. Am. Chem. Soc. 108 (1986) 5784.
- [65] M. Head-Gordon and J.A. Pople, Chem. Phys. Lett. 173 (1990) 585.
- [66] B.S. Jursic, Int. J. Quantum Chem. 64 (1997) 263.
- [67] G.L. Gutsev and R.J. Bartlett, J. Chem. Phys. 105 (1996) 8785.
- [68] B.C. Gilbert and M. Trenwith, J. Chem. Soc., Perkin Trans. 2, (1973) 2010.
- [69] F. Romondo, Can. J. Chem. 70 (1992) 314.
- [70] R.F.M. Lobo, A.M.C. Moutinho, K. Lacmann and J. Los, J. Chem. Phys., 95 (1991) 166.
- [71] N.J. Harris and K. Lammertsma, J. Am. Chem. Soc. 118 (1996) 8048.
- [72] E. Tannenbaum, R.D. Johnson, R.J. Myers and W.D. Gwinn, J. Chem. Phys. 22 (1954) 949.

- [73] E. Tannenbaum, R.J. Myers and W.D. Gwinn, *J. Chem. Phys.* 25 (1956) 42.
- [74] S.F. Trevino, E. Prince and C.R. Hubbart, *J. Chem. Phys.* 73 (1980) 2996.
- [75] G.A. Jeffrey, J.R. Ruble, L.M. Wingert, J.H. Yates and R.K. McMullan, *J. Am. Chem. Soc.* 107 (1985) 6227.
- [76] M.W. Chase, Jr., C.A. Davies, J.R. Downey, Jr., D.J. Frurip, R.A. McDonald and A.N. Syverud, *J. Phys. Chem. Ref. Data*, 14 (1985) Suppl. 1.
- [77] W.F. Hu, T.J. He, D.M. Chen and F.C. Liu, *J. Phys. Chem. A* 106 (2002) 7294 and references cited therein.
- [78] M.L. McKee, *J. Phys. Chem.* 93 (1989) 7365.
- [79] M.L. McKee, *Chem. Phys. Lett.* 164 (1989) 520.
- [80] M.J.S. Dewar and J.P. Ritchie, *J. Org. Chem.* 50 (1985) 1031.
- [81] T.S. Dibble and J.S. Francisco, *J. Phys. Chem.* 98 (1994) 5010.
- [82] P. Politzer, J.M. Seminario and A.G. Zacarias, *Mol. Phys.* 89 (1996) 1511.
- [83] R. Bianco and J.T. Hynes, *J. Phys. Chem. A* 103 (1999) 3797.
- [84] G. Sartori, F. Bigi, R. Maggi and F. Tomasini, *Tet. Lett.* 35 (1994) 2393.
- [85] M. Cook, J. Fellows and P.J. Haskins, In *Decomposition, Combustion and Detonation Chemistry of Energetic Materials*, Materials Research Society, Symposium Proceedings, Vol. 418; Materials Research Society: Pittsburgh, 1996, pp 267-275.
- [86] R.D. Bardo, In *Eighth Symposium (International) on Detonation Naval Surface Weapons Center: White Oak, MD, 1985*, p 855.
- [87] R.D. Bardo, *Int. J. Quantum Chem. Symp.* 20 (1986) 455.
- [88] R.D. Bardo, In *Ninth Symposium (International) on Detonation Office of Naval Research: Arlington, VA, 1989*, p 235.
- [89] C.F. Bernasconi, P.J. Wenzel, J.R. Keeffe and S. Gronert, *J. Am. Chem. Soc.*, 1997, 119, 4008.
- [90] S. Odiet, M. Blain, E. Vauthier and S. Fliszar, *J. Mol. Struct. (Theochem)* 279 (1993) 233.
- [91] D. Beksic, J. Bertran, J.M. Lluch and J.T. Hynes, *J. Phys. Chem. A* 102 (1998) 3977.
- [92] G.N. Spokes and S.W. Benson, *J. Am. Chem. Soc.* 89 (1967) 6030.
- [93] W. Tsang, D. Robaugh and W.G. Mallard, *J. Phys. Chem.* 90 (1986) 5968.
- [94] A.C. Gonzalez, C.W. Larson, D.F. McMillen and D.M. Golden, *J. Phys. Chem.* 89 (1985) 4809.
- [95] K.E. Lesis, D.F. McMillen and D.M. Golden, *J. Phys. Chem.* 84 (1980) 226.
- [96] V.G. Matveev, V.V. Dubikhin and G.M. Nayin, *Izv. Akad. Nauk SSR, Ser. Khim*, 1978, 675.
- [97] (a) Y.Y. Maksimov, *Russ. J. Phys. Chem.* 1972, 46, 990. (b) Y.Y. Maksimov, E.N. Kogu, *Russ. J. Phys. Chem.* 1978, 52, 805.
- [98] (a) G. Wettermark, *J. Phys. Chem.* 1962, 66, 2560 (b) G. Wettermark and R. Ricci, *J. Chem. Phys.* 1963, 39, 1218. (c) G. Wettermark, E. Black and L. Dogliotti, *Photochem. Photobiol.* 4, (1965) 229.
- [99] H. Morrison and B.J. Migdalof, *J. org. Chem.* 30 ((1965) 3996.
- [100] K. Suryanarayanan and C. Capellos, *Int. J. Chem. Kinet.* 6, 1974, 89.
- [101] M. Coellen and C. Ruechardt, *Chem. Eur. J.* 1 (1995) 564.
- [102] T. Urbanski *Chemistry and Technology of Explosives*, Vol. 1. Pergamon Press, Oxford (1964)
- [103] J. Fan, Y. Gu, H. Xiao and H. Dong, *J. Phys. Org. Chem.* 11 (1998) 177.
- [104] P.C. Chen, W. Lo and S.C. Tzeng, *J. Mol. Struct. (THEOHEM)* 428 (1998) 257.
- [105] (a) M.J. Kamlet and H.G. Adolph, *Propellants Explos.* 4 (1979) 30. (b) D.E. Bliss, S.L. Christian and W.S. Wilson, *J. Energ. Mater.* 9 (1991) 319.

- [106] V.G. Mateev, V.V. Dubikhin and G.M. Nayin, *Izv. Akad. Nauk SSSR Ser. Khim.* 1978, 474.
- [107] J. Yinon, *Org. Mass Spectrom.* 22 (1987) 501.
- [108] S. Meyerson, I. Puskas and E.K. Fields, *J. Am. Chem. Soc.* 88 (1966) 4974.
- [109] A.D. Britt, W.B. Moniy, G.C. Chingas, D.W. Moore, C.A. Heller and C.L. Lo, *Propellant Explos.* 6 (1981) 94.
- [110] M.H. Miles, D. Gustaveson and K.L. Devries, *J. Mater. Sci.* 18 (1983) 3243.
- [111] H. Xiao, J. Fan, Z. Gu and H. Dong, *Chem. Phys.* 226 (1998) 15.
- [112] M.R. Manaa, R.H. Gee and L.E. Fried, *J. Phys. Chem. A* 2002, 106, 8806.
- [113] Y.V. Il'ichev and J. Wirz, *J. Phys. Chem. A* 104 (2000) 7856.
- [114] P.C. Chen and S.C. Chen, *Int. J. Quantum Chem.* 83 (2001) 332.
- [115] M. Schworer and J. Wirz, *Helv. Chim. Acta* 84 (2001) 1441.
- [116] M.E. Langmuir L. Dogliotti E.D. Black and G. Wettermark, *J. Am. Chem. Soc.* 91 (1969) 2204.
- [117] J.A. Sousa and J. Weinstein, *J. Org. Chem.* 27 (1962) 3155.
- [118] H. Sixl and R. Warta, *Chem. Phys.* 94 (1985) 147.
- [119] P.C. Chen and Y.C. Chieh *J. Mol. Struct. (Theochem)* 583 (2002) 173.
- [120] C.I. Sainz-Diaz, *J. Phys. Chem. A* 106 (2002) 6600.
- [121] B.M. Rice and J.J. Hare, *J. Phys. Chem. A* 106 (2002) 1770.
- [122] W.S. Wilson, D.E. Bliss, S.L. Christian and D.J. Knight, Navel Weapons Center Technical Report NWC TP 7073 (1990).
- [123] T.B. Brill and K.J. James *J. Phys. Chem.* 97 (1993) 8752.
- [124] P. Politzer, M.E. Grice and J.M. Seminario *Int. J. Quant. Chem.* 61 (1997) 389.
- [125] A.I. Vokin, L.V. Sherstyannikova, L.V. Kanitskaya, K.A. Abzaeva, V.A. Lopyrev and V.K. Turchaninov, *Russ. J. Gen. Chem.* 71 (2001) 1708.
- [126] A.I. Vokin, L.V. Sherstyannikova, K.A. Abzaeva, V.A. Lopyrev and V.K. Turchaninov, *Russ. J. Gen. Chem.* 72 (2002) 287.
- [127] D.C. Sorescu, C.M. Bennett and D.L. Thompson, *J. Phys. Chem. A* 102 (1998) 10348.
- [128] S. Ono, K. Okazaki, M. Sakurai and Y. Inoue *J. Phys. Chem. A* 101 (1997) 3769.
- [129] K.Y. Lee, L.B. Chapman and M.D. Coburn *J. Energ. Mater.* 5 (1987) 27.
- [130] (a) C. Zhao-Xu and X. Heming, *Int. J. Quant. Chem.* 79 (2000) 350. (b) G.T. Long, B.A. Brems and C.A. Wight, *J. Phys. Chem. B* 106 (2002) 4022.
- [131] (a) G.K. Williams and T.B. Brill, *J. Phys. Chem.* 99 (1995) 12536 (b) T.B. Brill, P.E. Gongwer and G.K. Williams *J. Phys. Chem.* 98 (1994) 12242.
- [132] B.C. Beard and J. Sharma *J. Energ. Mater.* 11 (1993) 325.
- [133] E.F. Rothgery, E.D. Audette, R.C. Wedlich and D.A. Csejka, *Thermochim. Acta* 189 (1991) 283.
- [134] K.V. Prabhakaran, S.R. Naidu and E.M. Kurian *Thermochim. Acta*, 241 (1994) 199.
- [135] (a) H. Ostmark, Thermal Decomposition of NTO. FOA Report D-201782.3rd National Defense Research Establishment; Sundbyberg Sweden, No.V (1991). (b) H. Ostmark, H. Bergman and G. Aqvist, *Thermochim. Acta* 213 (1993) 165.
- [136] J.A. Menapace, J.E. Marlin, D.R. Bruss and R.V. Dascher, *J. Phys. Chem.* 95 (1991) 5509.
- [137] G.K. Williams, S.F. Palopoli and T.B. Brill, *Combust. Flame* 98 (1994) 197.
- [138] J.C. Oxley, J.L. Smith, Y. Yhou and R.L. McKenny *J. Phys. Chem.* 99 (1995) 10383.
- [139] D.F. McMillen, D.C. Erlich, C. He, C.H. Becker and D.A. Shockey, *Compust. Flame* 111 (1997) 133.
- [140] N.L. Garland, H.D. Ladouceur and H.H. Nelson, *J. Phys. Chem. A* 101 (1997) 8508.
- [141] J.C. Oxley, J.L. Smith, K.E. Yeager, E. Rogers and X. Dong, *Mater. Res. Soc. Symp Proc.* 418 (1996) 135.

- [142] T.R. Botcher, D.J. Beardall, C.A. Wight, L. Fan and T.J. Burkey, *J. Phys. Chem.* 100 (1996) 8802.
- [143] (a) C. Meredith, T.R. Russell, R.C. Mowrey and J.R. McDonald, *J. Phys. Chem. A.* 102 (1998) 471. (b) A.M. Renlund and W.M. Trott, *Chem. Phys. Lett* 107 (1984) 555.
- [144] Y.M. Wang, C. Chen and S.T. Lin, *J. Mol. Struct. (Theochem)*, 460 (1999) 79.
- [145] W.L. Yim and Z.F. Liu, *J. Am. Chem. Soc.* 123 (2001) 2243.
- [146] M.D. Pace, L. Fan and T.J. Burkey, *Mater. Res. Soc. Symp. Proc.* 418 (1996) 127.
- [147] J. Ritchie, K.Y. Lee, D.T. Cromer, E.M. Kober and D.D. Lee, *J. Org. Chem.* 55 (1990) 1994.
- [148] D.C. Sorescu, T.R.L. Sutton, D.L. Thompson, D. Beardall and C.A. Wight, *J. Mol. Struct.* 384 (1996) 87.
- [149] D.C. Sorescu and D.L. Thompson, *J. Phys. Chem. B.* 101 (1997) 3605.
- [150] E.A. Zhurova and A.A. Pinkerton, *Acta Cryst. Sec. B* B57 (2001) 359.
- [151] Y. Kohno, O. Takasashi and K. Saito, *Phys. Chem. Chem. Phys.* 3 (2001) 2742.
- [152] X. Zhao, E.J. Hinst and Y.T. Lee, *J. Chem. Phys.* 88 (1988) 801.
- [153] C.C. Chambers and D.L. Thompson, *J. Phys. Chem.* 99 (1995) 15881.
- [154] T.R. Botcher and C.A. Wight, *J. Phys. Chem.* 98 (1994) 5441; 97 (1993) 9149.
- [155] M.D. Pace, *J. Phys. Chem.* 95 (1991) 5858.
- [156] M. Choi, H. Kim and C. Chung, *J. Phys. Chem.* 99 (1995) 15785.
- [157] C.F. Melius and J.S. Binkley, In *Chemistry and Physics and Energetic Materials*, S.N. Bulusu, Ed., Kulwer: Dordrecht, (1990) p 21.
- [158] R. Behrens, Jr. and S. N. Bulusu, *J. Phys. Chem.* 96 (1992) 8877, 8891 (b) R. Behrens Jr. and S.N. Bulusu, *J. Phys. Chgem.* 95 (1991) 5838. (c) R. Behrens, Jr., *J. Phys. Chem.* 94 (1990) 6706. (d) R. Behrens, In *Chemistry and Physics of Energetic Materials*; S.N. Bulusu, Ed.; Kulwer: Dordrecht, (1990) p 347.
- [159] C. Capellos, P. Papagiannakopoulos and Y.L. Liang, *Chem. Phys. Lett.* 164 (1989) 533.
- [160] N.J. Harris and K. Lammertsma, *J. Am. Chem. Soc.* 119 (1997) 6583.
- [161] B.M. Rice and C.F. Chabalowski, *J. Phys. Chem. A.* 101 (1997) 8720.
- [162] T.D. Sewell and D.L. Thompson, *J. Phys. Chem.* 95 (1991) 6228.
- [163] D. Habibollahzadeh, M. Grodzicki, J.M. Seminario and P. Politzer, *J. Phys. Chem.* 95 (1991) 7699
- [164] C.J. Wu and L.E. Fried, *J. Phys. Chem. A.* 101 (1997) 8675.
- [165] N.J. Harris and K. Lammertsma, *J. Phys. Chem.* 101 (1997) 1370.
- [166] D. Chakraborty, R.P. Muller, S. Dasgupta and W.A. Goddard, III, *J. Phys. Chem. A.* 104 (2000) 2261 and references cited therein.
- [167] D. Chakraborty, R. P. Muller, S. Dasgupta and W.A. Goddard, III, *J. Comp. Aided Mat. Design*, 8 (2001) 203.
- [168] B. Suryanarayana, R.J. Graybush and J.R. Autera, *Chem. Ind. London*, 52 (1967) 2177.
- [169] T.B. Brill, *J. Prop. Power* 11 (1995) 740.
- [170] C.J. Tang, Y.J. Lee, G. Kudva and T.A. Lityinger, *Combust. Flame* 117 (1999) 170.
- [171] C.J. Tang, Y.J. Lee and T.A. Lityinger, *J. Prop. Power* 15 (1999) 296.
- [172] G.D. Smith and R.K. Bharadwaj, *J. Phys. Chem. B.* 103 (1999) 3570.
- [173] H.V. Brand, R.L. Rabie, D.J. Funk, I. Diaz-Acosta, P. Pulay and T.K. Lippert, *J. Phys. Chem. B* 106 (2002) 10594.
- [174] M.R. Manaa, L.R. Fried, C.F. Melius, M. Elstner and T. Frauenheim, *J. Phys. Chem. A* 106 (2002) 9024.
- [175] L. Smilowitz, B.F. Henson, B.W. Asay and P.M. Dickson, *J. Chem. Phys.* 117 (2002) 3789.
- [176] M.R. Manaa, R.H. Gee and L.E. Fried, *J. Phys. Chem. A.* 106 (2002) 8806.

- [177] M.L. Batz, P.M. Garland, R.C. Reiter, M.D. Sanborn and C.D. Stevenson, *J. Org. Chem.* 62 (1997) 2045.
- [178] A.J. Abkowitz-Bienko, Z. Latajka, D.C. Bienko and D. Michalska, *Chem. Phys.* 250 (1999) 123.
- [179] C. I. Yainz-Diaz, *J. Phys. Chem. A.* 106 (2002) 6600.
- [180] D.C. Sorescu, B.M. Rice and D.L. Thompson, *J. Phys. Chem. B* 102 (1998) 6692.
- [181] D. C. Sorescu, B.M. Rice and D.L. Thompson, *J. Phys. Chem. B.* 103 (1999) 6783.
- [182] R. Pati, N. Sahoo and T.P. Das, *J. Phys. Chem. A.* 101 (1997) 8302.
- [183] D. Chakraborty, R.P. Muller, S. Dasgupta and W.A. Goddard III, *J. Phys. Chem.* 105 (2001) 1302 and references cited therein.
- [184] (a) A.R. Katritzky, C.W. Rees and E.F.V. Scriven, In *Comprehensive Heterocyclic Chemistry II*, Vol. 4, Pergamon Press Elmsford, NY, 1996.
- [185] O.A. Ivashkevich, P.N. Goponik, A.O. Koren, O.N. Bubel and E.V. Fronchek, *Inter. J. Quantum Chem.* 43 (1992) 813.
- [186] R.J. Spear, J.R. Bentley and M.G. Wolfson, *Combust. Flame* 50 (1983) 249.
- [187] A.S. Tompa, *Thermochim. Acta* 80 (1984) 367.
- [188] D.J. Whelan, R.J. Spear and R.W. Read, *Thermochim Acta* 80 (1984) 149.
- [189] A.E. Fogelzang, V.P. Sinditskii, V.Y. Egorshv and V.V. Serushkin, *Mater. Res. Soc. Symp. Proc.* (1996) 151.
- [190] J. Wang, J. Gu and A. Tian, *Chem. Phys. Lett.* 351 (2002) 459.

This Page Intentionally Left Blank

Chapter 4

Decomposition Mechanism of 1,1-Diamino Dinitroethylene (Fox-7): An Overview of the Quantum Chemical Calculation

Asta Gindulyte and Lou Massa[@]

Department of Chemistry, Hunter College, 695 Park Avenue, New York, New York 10021, and The Graduate School, City University of New York, 365 Fifth Avenue, New York, New York 10016. [@]CUNY CREST Center for Mesoscopic Modelling & Simulation.

Lulu Huang and Jerome Karle

Laboratory for the Structure of Matter, Naval Research Laboratory, Washington, D.C. 20375

We review the main features of our calculations leading to prediction of the molecular mechanism of detonation and decomposition of the recently discovered high energy, high density material diaminodinitroethylene (DADNE) also called FOX-7. We have investigated the unimolecular decomposition pathway of the high energy, high density molecule. Importantly, in order to facilitate the employment of DFT methods, their accuracy has been calibrated by means of *abinitio* calculations (MP2, MP4, G2) on a simpler but related molecule, nitroethylene. Four distinct pathways of unimolecular decomposition of nitroethylene, the C-NO₂ bond breaking, nitro-to-nitrite rearrangement, 1,2-elimination reaction and 1,1-elimination reaction, have been computationally investigated with *abinitio*, MP2, MP4, and G2 methods as well as with DFT methods. The nitro-to-nitrite rearrangement and 1,2-elimination reaction was found to give the lowest energy decomposition pathways for this molecule, about 15 kcal/mol lower than the cleavage of the nitro group. The computational calibration of our DFT method with nitroethylene simplified substantially our characterization of the entire decomposition reaction pathway of DADNE. Importantly, we find that the reaction is initiated by a nitro-to-nitrite rearrangement with a calculated energy barrier of magnitude 59.1 kcal/mol obtained by use of B3LYP (59.7 kcal/mol with B3P86). This is very close to the experimental

activation energy of 58 kcal/mol. Moreover, we have characterized every step in the decomposition reaction pathway leading to fragments NO, HONO, CO, NH₂, and HNC. These may interact to yield final stable products, CO, N₂, and H₂O, with an energy release that, on average, is adequate to initiate two additional DADNE molecular decompositions and, thus, sustain a chain reaction. The structural parameters we have calculated for DADNE are consistent with the known experimental crystallographic structure, and also with previous theoretical calculations. Additionally, we have obtained the structural parameters of the initial transition state, as well as each subsequent step along the decomposition pathway. Thus we consider the unimolecular decomposition of DADNE to be well characterized. Although our major purpose in this paper is to give an overview of our calculations revealing the mechanism of detonation and decomposition of DADNE, we also mention briefly a selection of the related work which rounds out our understanding of this new and promising candidate among insensitive munitions (IM).

1. INTRODUCTION

In recent years there has been a significant effort to develop new candidates which might lead to improved explosives in terms of performance, safety and other favorable properties. In this context DADNE [1-4] was synthesized and studied by members of the Swedish Defense Research Agency (FOI) and others who were able to show its utility as an insensitive munition (IM), having low sensitivity, and explosive performance that is only very slightly less favorable than the most widely used explosives. For this reason DADNE is an explosive receiving a good deal of attention. Its low sensitivity combined with high performance indicates it will be useful in a variety of differing applications. The most important properties of DADNE have been collected together [5], and are now reviewed. It is a high density material, as revealed by single crystal X-ray diffraction, which yields a density magnitude of 1.878g/cm³. Its experimental activation energy is 58 kcal/mole, a high value accounting in large part for its favorable insensitivity. This may be compared with, for example, RDX (40kcal/mole). Also favoring insensitivity is the manner in which DADNE packs into its crystal structure exhibiting a herringbone pattern held together with numerous intra and inter molecular hydrogen bonds. Such crystal packing is consistent with many of the favorable physical properties of the compound such as low solubility, low sensitivity to friction/impact (126 cm (2kg, BAM) and >35kp (Julius-Petri), respectively), and explicative of others such

as its absence of a well defined melting point. Another feature of DADNE, which augers well for its usefulness, is that it mixes well with a variety of polymers and plasticizers without incompatibility problems. The detonation velocity and detonation pressure of DADNE have values of 8870m/s and of 34GPa respectively, which compare favorably to other standard explosives, as for example, RDX (8930m/s and 34.6 GPa, respectively).

Thus Swedish scientists (at FOI) have very quickly synthesized, and established by their laboratory studies the favorable physical and chemical properties of DADNE, including its high performance and low sensitivity, resulting in a widely recognized useful new insensitive munition. Indeed, DADNE is now manufactured in quantity at NEXPLO-Bofors AB in Karlskoga.

Very much had been studied concerning the properties of DADNE by the time we had begun our investigation several years ago [6,7]. We were aware that the synthesis had been reported [1] and the crystal structure had been determined [2,3]. Its features as an explosive, including the activation energy, had been characterized experimentally [4]. The important properties such as C-NO₂ and C-NH₂ bond dissociation energies, heats of formation, vaporization, and sublimation had been calculated at the B3P86/6-31G+(d,p) level [8]. As Politzer *et al* [8] had pointed out, this compound has the same molecular stoichiometry as RDX, and HMX, which are among the most effective currently used explosives and monopropellants, and, upon complete decomposition to CO, N₂, and H₂O, all of these molecules would yield the same high value, 0.0405, for moles of gaseous product per gram of compound, one of the key determinants of explosive and propellant performance. We noted that the reported activation energy ($E_a = 58$ kcal/mol for temperature interval 210-250 °C) [4] for DADNE is higher than that of RDX ($E_a \sim 40$ kcal/mol) [9-11] and HMX ($E_a \sim 35$ kcal/mol) [12], which favors DADNE as an insensitive munition. It was this feature which motivated our interest and led us to calculate the activation energy E_a by means of a quantum chemical method, followed by a calculation of the decomposition pathway. An understanding of the decomposition mechanism can also play a useful role in the evaluation of an explosive.

The decomposition mechanism for DADNE can be expected to be quite different from that for RDX and HMX. Even though DADNE has the same stoichiometry as RDX and HMX, structurally it bears little similarity to these molecules. Thus, possible reaction pathways involving unimolecular decomposition of these compounds would differ from those studied in DADNE. Instead of C-NO₂, N-NO₂ bond dissociation would occur, and the ring geometries would present the possibility of symmetric ring fission.

Theoretical work investigating possible reaction pathways for RDX and HMX has been carried out [10,11,13-15]. Considerable experimental work has been performed with RDX and HMX in order to determine possible decomposition pathways and their relative importance [16-20].

We proceeded with the quantum chemical calculation of the initial activation energy and subsequent decomposition mechanism of DADNE, focusing on discovering the lowest energy decomposition pathway for a possible unimolecular decomposition of this compound. Because it is simpler we began with a consideration of the behavior of the nitro group in nitroethylene, as a model for the behavior of nitro groups in DADNE. In both cases a nitro group is adjacent to a carbon-carbon double bond. We wished to employ less complex DFT methods with a moderate size basis set to obtain a description of the energetic profile for the DADNE decomposition pathway. Thus we used rather more complex, and more accurate methods, to examine the simpler case of nitroethylene, with a view to calibrate the accuracy we could expect to obtain with the less complex DFT methods which we wanted to employ with the larger and more complicated case of DADNE. In nitroethylene, we studied [6] the effect of basis set size on relative energies. It has been found that DFT methods (especially those based upon the Becke three-parameter hybrid (B3) exchange functional) with a moderate basis set yielded good geometries [21]. For a given geometry, a way to obtain a more accurate evaluation of energy values is to carry out a single-point calculation with a larger basis set. In the case of nitroethylene, however, we found that larger basis sets did not significantly improve the energy values obtained with the moderate basis set that we intended to use with DADNE. In our nitroethylene study we employed the *ab initio* methods MP2, MP4, and also G2, which are expected to give highly accurate energy values, as well as DFT methods based upon B3 exchange and two different correlation energy functionals, viz., LYP and P86. In most decomposition steps, LYP performed better than P86, except for estimations of bond dissociation energies (BDE), as judged by comparison with *ab initio* results. With DADNE, we also applied both B3LYP and B3P86 to get a sense of the variability associated with different correlation energy functionals. We found that, while there are some quantitative differences between DFT and *ab initio* results, the qualitative trends are the same. Furthermore, we anticipated that the DFT error estimates, measured against G2 as a standard, which were obtained for nitroethylene might be applied to DADNE for those particular steps in the decomposition pathway which are essentially the same. Thus we found our rather extensive exploration of the simpler, but closely related problem of

nitroethylene, with the use of quite large basis sets and accurate quantum chemical methods, to be a valuable precursor to the study of DADNE. Calibrating our moderate basis and DFT method with larger bases and more highly reliable methods, with the use of the smaller molecule, gave us good insight concerning the accuracy that may be expected for the larger molecule, DADNE. Also we anticipated that the behavior in nitroethylene of the nitro group next to a CC double bond, might suggest how the analogous nitro groups in DADNE might behave. This turned out to be so.

In what follows we discuss first our studies of the simpler molecule nitroethylene, and subsequently proceed to calculations on the more complicated molecule DADNE.

2. NITROETHYLENE COMPUTATIONAL DETAILS [6]

Four distinct pathways of unimolecular decomposition of nitroethylene, the C-NO₂ bond breaking, nitro-to-nitrite rearrangement, 1,2-elimination reaction and 1,1-elimination reaction, have been computationally investigated with ab initio, MP2, MP4, and G2 methods as well as with DFT methods. The nitro-to-nitrite rearrangement and 1,2-elimination reaction are found to give the lowest energy decomposition pathways for this molecule, about 15 kcal/mol lower than the cleavage of the nitro group, as we shall indicate.

All quantum mechanical calculations were carried out with the *Gaussian 98* program package [22]. The reader is pointed to reference 23 for definitions of technical symbols. The geometries of all reactants, products, and transition states have been optimized at the MP2(FC)/6-31G(d,p) level of theory, where FC denotes the frozen core. When calculating the relative energies for the systems where radicals were involved, PMP2 (spin-projected MP2) rather than MP2 energies were used. Vibrational frequencies have been calculated using the same approximation for the characterization of the nature of stationary points and the determination of zero-point vibrational energy (ZPVE) corrections. To obtain more reliable energies for all of the structures involved, we performed single-point calculations at MP4(SDTQ)/6-311+G(d,p) level of theory. All of the stationary points have been positively identified for minimum energy with no imaginary frequencies and the transition states with one imaginary frequency. For anharmonicity correction [24], the calculated ZPVE values were scaled by 0.9608. Intrinsic reaction coordinate (IRC) analysis was carried out for each transition state to make sure that it is the transition

structure connecting the desired reactants and products. The calculated values of the vibrational frequencies are given as Supporting Information.

We also performed a G2 procedure as implemented in the *Gaussian* code for all of the structures involved. Differently from the standard G2 procedure, we used the ZPVE values obtained with MP2 rather than HF for anharmonicity corrections.

The same analysis as described for MP2 above was also carried out with two DFT methods. The Becke three-parameter hybrid (B3) [25] was used in conjunction with two correlation functionals, Perdew-86 (P86) [26] and Lee-Yang-Parr (LYP) [27]. The geometries of all reactants, products, and transition states have been optimized using B3P86/6-31+G(d,p) and B3LYP/6-31+G(d,p). For anharmonicity correction [24], the calculated ZPVE values were scaled by 0.9759 and 0.9806 for B3P86 and B3LYP, respectively. To obtain more reliable energies for all of the structures involved, we performed single point calculations at B3P86/6-311++G(3df,3pd) and B3LYP/6-311++G(3df,3pd) levels of theory, respectively.

3. NITROETHYLENE RESULTS [6]

We investigated four distinct pathways (A-D) of nitroethylene decomposition, shown in Figure 1.

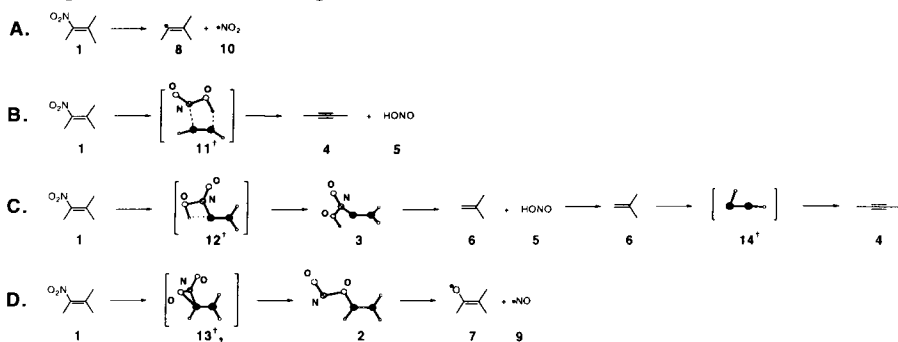


Figure 1 A scheme of pathways for the unimolecular decomposition of nitroethylene. (After figure 1, ref 6)

The structures and optimized geometrical parameters of all the species involved were obtained, as well as their corresponding absolute energies, and relative (to nitroethylene) energies. The reader is referred to our original publication [6] for extensive tabulation of these numerical results for

nitroethylene, as well as a detailed discussion of the calculations associated with each of the possible pathways (A-D). The reaction diagram of the decomposition pathways is displayed in Figure 2, in accordance with which we concluded that path D would be that favored by the decomposition of nitroethylene.

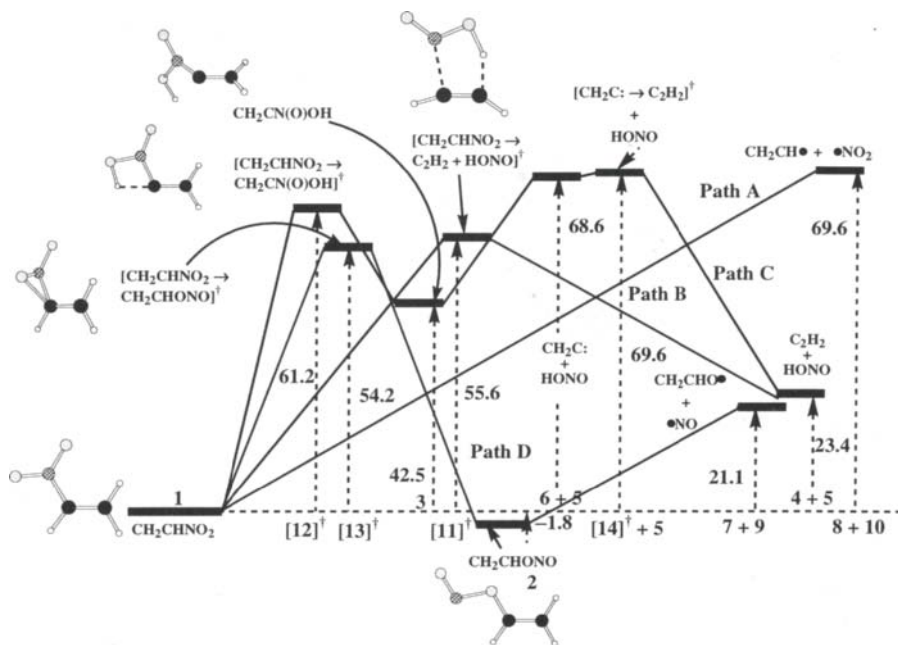


Figure 2. Energy diagram of nitroethylene decomposition pathways. The energy values are in units of kcal/mol and have been calculated by performing single-point energy calculations with the MP4/6-311+G(d,p) method and the use of optimized geometries obtained from the MP2(FC)/6-31G(d,p) calculations. The energy values were corrected for ZPVE obtained from the MP2(FC)/6-31G(d,p) calculations. (After figure 3, ref 6)

Pathway D is a nitro-to-nitrite rearrangement reaction. It proceeds through a triangular transition state $[13]^\ddagger$ in which a C-O bond is created and a C-N bond is elongated, while an NO_2 group is bent out from the $\text{C}=\text{CH}_2$ plane. The barrier is 57.9 kcal/mol as calculated with the G2 method, and the values obtained with other methods are very similar. The product is isonitrite, **2**. To avoid confusion, we mention in passing that it is likely both O_A and O_B are equally capable of forming the bond with C. IRC analysis of $[13]^\ddagger$ led to a reactant with the NO_2 group rotated perpendicularly to the C-

C-N plane. Thus, this group could then rotate either way.

While there are a few rotational isomers of the product, **2**, resulting from rotations around C-O and N-O bonds, the one that is depicted in Figure 1 was obtained by optimizing the final structure from an IRC calculation and was calculated to be the most stable. Product **2** may further decompose into NO and CH₂CHO radicals via the O-N bond dissociation. The BDE for this bond is rather low, 23.3 kcal/mol as calculated with the G2 method. B3LYP underestimates this value by almost 10 kcal/mol, while B3P86 performs somewhat better, underestimating this value by 3.3 kcal/mol.

We concluded that the HONO elimination reaction B and nitro-to-nitrite rearrangement D are the lowest energy decomposition channels for nitroethylene with the G2 calculated activation barriers of 57.3 and 57.9 kcal/mol, respectively. This is ~15 kcal/mol lower than the amount of energy required for the C-NO₂ bond cleavage.

We found that the DFT methods used, B3LYP and B3P86, were able to provide a realistic description of nitroethylene decomposition. While there are some quantitative differences between DFT and *ab initio* results, the trends are the same. It is known that DFT methods (especially those based upon the Becke three-parameter hybrid (B3) exchange functional) with a moderate basis set yield good geometries. It is often suggested that for a given geometry an efficient way to obtain more accurate evaluation of energy values is to carry out a single point calculation with a larger basis set. We found, however, that, in the case of nitroethylene, larger basis sets did not significantly improve the energy values obtained with the moderate basis set. In most decomposition steps B3LYP performed better than B3P86, except for estimations of BDE values, as judged by comparison to *abinitio* results.

Having obtained a satisfactory description of nitroethylene decomposition, and a calibration of how modest basis DFT calculations fared in comparison to higher level calculations, we set out to apply them to the unimolecular decomposition of DADNE, which we consider next.

4. DADNE COMPUTATIONAL DETAILS [7]

In a manner analogous to that described above for nitroethylene, again all quantum mechanical calculations for DADNE were performed with the *Gaussian 98* program package [22]. Intrinsic reaction coordinate (IRC) analysis was carried out for each transition state to make sure that it is the transition structure connecting the desired reactants and products. For all structures with an even number of electrons, a restricted (doubly occupied

orbitals) wave function was used. For the high-energy structure, transition state [2][†], in figures 3 and 4, however, an unrestricted wave function was also implemented to check the result. For all doublet structures an unrestricted wave function was used and examined for spin contamination, which was found to be inconsequential.

5. DADNE RESULTS AND DISCUSSION [7]

5.1 Initial Step of DADNE Decomposition

The initial step in thermal decomposition of nitro-containing compounds is often the cleavage of a C-NO₂ or N-NO₂ bond [28]. The C-NH₂ bond is known to have a very high bond dissociation energy [8]. Therefore, we calculated the C-NO₂ bond dissociation energy (BDE) for DADNE. Our B3P86 value of 68.9 kcal/mol is consistent with the result obtained by Politzer et al [8], by use of the same method. The BDE obtained with B3LYP is 62.9 kcal/mol. Both of these values may be underestimates. Our previous study of nitroethylene [6] showed that B3LYP and B3P86 underestimate the C-NO₂ bond dissociation energy for nitroethylene by ~8 and ~4 kcal/mol respectively, as compared to the G2 result. We thus predict that the BDE for DADNE should probably be around 73 kcal/mol, which is quite high compared to the experimental E_a of 58 kcal/mol [4], and therefore there must exist a lower energy process which is responsible for the initial decomposition step of this molecule.

We previously found that nitro-to-nitrite rearrangement is the lowest energy decomposition pathway (~15 kcal/mol lower than the C-NO₂ bond cleavage) for nitroethylene [6]. Investigation of the nitro-to-nitrite rearrangement in DADNE verified that the same is true for this molecule. The barrier for the rearrangement is 59.7 and 59.1 kcal/mol, as obtained with B3P86 and B3LYP methods, respectively. Furthermore, based on our investigation of the same reaction for nitroethylene, for which G2, B3LYP and B3P86 results agree very closely, we argue that the error of this calculation should be rather small. Note that this result compares very well to the experimental activation energy (E_a) of 58 kcal/mol [4].

The structures for DADNE, **1**, the transition state, $[2]^\ddagger$, and the isonitrite product, **3**, are shown in figure 3. The detailed geometrical parameters are tabulated in our original paper [7]. Note that DADNE is not a planar structure. Because of the repulsion between the two NO₂ groups, they are rotated by more than 20° with respect to the C1-C2-N plane. When further rotation of either NO₂ group occurs, a possibility of C-O bond formation and thus nitro-to-nitrite rearrangement emerges. In the transition state structure, $[2]^\ddagger$, a C-N bond is elongated to 1.536 Å from that of 1.432 Å in DADNE, and a new C-O bond of 1.785 Å is formed. Upon formation of the product, isonitrite, **3**, a C-N bond is broken, and the C-O bond shortens to 1.355 Å. To avoid confusion, we mention in passing that both similar atoms O are equally capable of forming a bond with the nearby atom C. IRC analysis of $[2]^\ddagger$ led to a reactant with the NO₂ group rotated perpendicularly to the C-C-N plane, and this group can subsequently rotate either way.

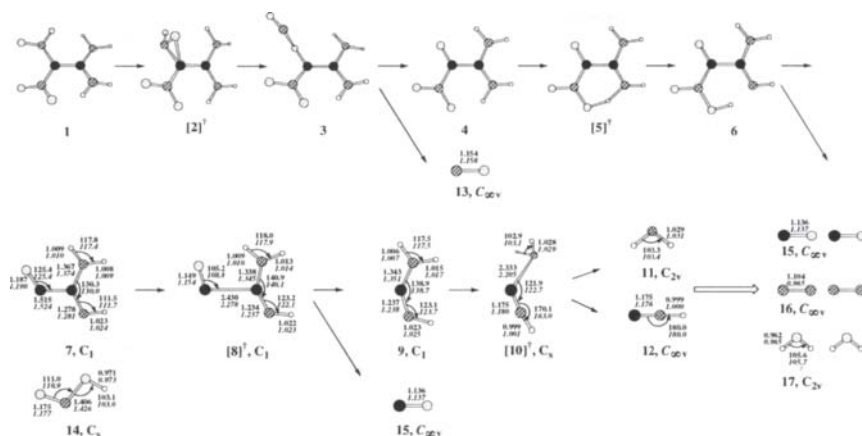


Figure 3. A scheme of unimolecular DADNE decomposition via the nitro-to-nitrite rearrangement pathway. The optimized geometrical parameters of species **1-3** and **4-6** are displayed in Tables 2 and 3, respectively of reference 7. The regular and italic fonts indicate the use of the B3P86/6-31+G(d,p) and the B3LYP/6-31+G(d,p) methods, respectively. (After figure 1, ref 7)

We now proceed, referring to figures 3 and 4, with a description of the DADNE decomposition steps following the nitro-to-nitrite rearrangement. Figure 3 provides a scheme of unimolecular DADNE decomposition, via the nitro-to-nitrite rearrangement pathway, through formation of small fragments, which can further react among themselves to form stable products, such as CO, N₂, and H₂O. In addition, the structures

and optimized geometrical parameters of species **7-17** are also shown in Figure 3. We refer the reader to our original publication [7] for a detailed tabulation of the structures and optimized geometrical parameters for species **1-3** and **4-6**, for lists of the calculated energies of all chemical species involved in the decomposition process, and for relative (to DADNE) energies at every step of the decomposition of DADNE. A depiction of the reaction diagram is given in Figure 4.

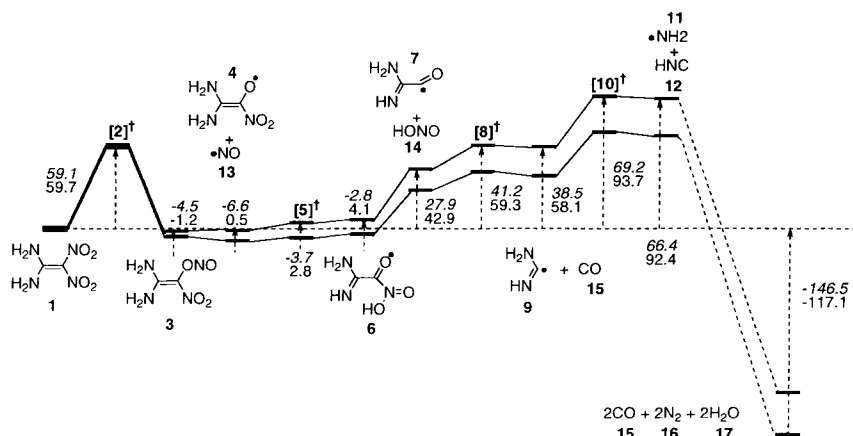


Figure 4. The energetic profile of DADNE decomposition via the nitro-to-nitrite rearrangement pathway. All of the energies are in reference to DADNE. The units are kcal/mol. The regular and italic fonts indicate the use of the B3P86/6-31+G(d,p) and the B3LYP/6-31+G(d,p) methods, respectively. (After figure 2, ref 7)

5.2 Isonitrite, 3

Energetically, this species lies lower than DADNE by some 1.2 and 4.5 kcal/mol as calculated with the B3P86 and B3LYP methods, respectively. It is, however, highly unstable, since it immediately loses an NO radical via the Obs-N2b bond dissociation. The BDE obtained with B3P86 is 0.5 kcal/mol as compared to the negative B3LYP value of -6.6 kcal/mol for this reaction. Obviously, the error of this calculation is quite substantial. It is interesting to note that the analogous process for nitroethylene requires some 18.2 kcal/mol as calculated with B3P86 and 13.6 kcal/mol as calculated with B3LYP [20]. The G2 method gives an even higher value of 23.3 kcal/mol [6]. As with the C-NO₂ BDE for DADNE, we expect that the DFT values

are underestimated for this process too. Our rough prediction by comparison to nitroethylene would be a BDE of ~4-5 kcal/mol.

5.3 Hydrogen Atom Migration from NH_2 to NO_2

The remaining radical, **4**, has a C-C bond length of 1.460 Å, as compared to 1.428 Å in **1**, as well as a C-NH₂ bond length at 1.336 Å versus 1.345 Å in **1**. It is possible for a hydrogen atom to readily migrate from the NH₂ group to the NO₂ group, because the transition state, **[5]**[‡], of this reaction lies only 2.3 and 3.1 kcal/mol above **4**, as calculated with B3P86 and B3LYP, respectively. The optimized geometrical parameters [7] for the radical **4**, the transition state structure, **[5]**[‡], and the isomeric product, **6**, are sketched in figure 3. All of these structures are planar. Product, **6**, lies energetically higher than the transition state, **[5]**[‡], if the ZPVE correction is made when calculating the differences in energy. If no ZPVE correction is made, **6** lies lower than **[5]**[‡] by 0.4 and 1.1 kcal/mol as calculated with B3P86 and B3LYP, respectively. This indicates that the calculations are not accurate. However, we may conclude that the differences in energy between species **4-6** are small and that **4** may easily be converted to **6** and vice versa.

5.4 HONO Elimination

We considered several possibilities of species **4** and **6** decomposition on a doublet potential energy surface (PES). Species **4** could undergo either NO₂ or NH₂ radical elimination, while species **6** could undergo NH₂ radical or HONO molecule elimination. However, only the HONO elimination from **6** would result in the formation of a reasonably stable conjugated structure, radical **7**. We were not able to locate the transition state for HONO elimination from **6**. We thus obtained a PES by optimizing the geometry at a series of fixed C-N bond lengths in **6**. The energy of the system increases with an increasing bond length at first and then reaches a plateau. Therefore, the barrier for this process is approximately equal to the differences in energy between the reactant, **6**, and the two products, **7** and **14**. We calculated this barrier to be 38.7 and 25.1 kcal/mol with the use of B3P86 and B3LYP, respectively.

The large difference between the values for this barrier obtained from the two methods merits a comment. While investigating the decomposition of nitroethylene [6], we found that the results obtained from the use of B3P86 and B3LYP were similar in almost all of the steps, except the ones which result in HONO formation. Moreover, the B3LYP results come

reasonably close to the G2 results, while the B3P86 results are overestimations as compared to the results obtained from the G2 method. Comparison of optimized geometrical parameters with the experimental ones also indicates that the B3LYP calculations are preferable. The experimental HO-N bond length is 1.433 Å versus 1.426 Å and 1.406 Å as calculated with B3LYP and B3P86, respectively. Thus, the B3LYP result appears to be somewhat more trustworthy here. Additional information on the performance of DFT methods, including the comparison of experimental and calculated geometrical parameters for the HONO system, can be found in a recent work by Jursic [29].

5.5 CO Elimination

The C-C bond appears to be the weakest spot in structure **7**. CO elimination may occur on a doublet PES with a barrier of only 16.4 and 13.3 kcal/mol as calculated with B3P86 and B3LYP, respectively. The transition state, **[8][†]**, has an extremely long C-C distance of 2.278 Å and one imaginary frequency of 198i. The products of this reaction are the radical, **9**, and CO, **15**, which is an extremely stable molecule.

5.6 NH₂ Radical Elimination

The remaining fragment, **9**, may further decompose into NH₂ radical, **11**, and HNC, **12**, via NH₂ radical elimination on a doublet PES. The barrier is 35.6 and 30.7 kcal/mol as calculated with B3P86 and B3LYP, respectively. The transition state, **[10][†]**, has a long C-NH₂ distance of 2.205 Å and one imaginary frequency of 236i.

5.7 Final Stages of DADNE Decomposition

So far we showed how unimolecular decomposition of DADNE may lead to the formation of the following fragments: NO radical, HONO, CO, NH₂ radical, and HNC. Clearly, these fragments may undergo collisions and thus react with other fragments and with yet unreacted molecules. The number of possibilities is large. We point out below, however, some of the most important and the most likely reactions to occur in the final stages of DADNE decomposition. They all have rather low activation energies (determined either experimentally and/or theoretically by various authors, see refs 29-32) and lead to stable products, N₂, CO, and H₂O.

- (a) [27] $\text{HONO} \rightarrow \bullet\text{NO} + \bullet\text{OH}$
- (b) [28] $\bullet\text{NO} + \bullet\text{NH}_2 \rightarrow \text{N}_2 + \text{H}_2\text{O}$
- (c) [29] $\text{HNC} + \bullet\text{OH} \rightarrow \bullet\text{CN} + \text{H}_2\text{O}$
- (d) [29] $\text{HNC} \rightarrow \text{HCN}$
- (e) [29] $\text{HCN} + \bullet\text{OH} \rightarrow \bullet\text{CN} + \text{H}_2\text{O}$
- (f) [30] $\bullet\text{CN} + \bullet\text{NO} \rightarrow \text{N}_2 + \text{CO}$

The two N_2 , two CO , and two H_2O molecules energetically lie below DADNE by an impressive 117.1 and 146.5 kcal/mol as obtained with B3P86 and B3LYP, respectively.

6. ADDITIONAL CHECK ON THE ACCURACY OF DFT CALCULATIONS

As mentioned earlier, we calibrated our use of the DFT methodology, applied in this paper, by comparing DFT results with ab initio results (MP2, MP4, G2) for the related molecule, nitroethylene. However, for purposes of having one additional check on the accuracy of DFT as applied to DADNE, and at the same time obtaining additional information concerning the first step of particular interest in the decomposition, we have carried out ab initio MP2 calculations on the structures **1**, **[2][†]**, and **3**, of figures 3 and 4, which define the first step in the nitro-to-nitrite rearrangement reaction pathway. We obtained energy values calculated by the MP2 method with two different basis sets, viz., 6-31G(d,p) (I) and 6-311+G(d,p) (II), at the B3LYP geometries, for these three structures. Recall that our DFT prediction for the crucial initial step in the nitro-to-nitrite rearrangement pathway was an activation energy of 59.7 and 59.1 kcal/mol, obtained with the B3P86 and B3LYP methods, respectively. This prediction is very close to and just above the experimental activation energy of 58 kcal/mol. Our MP2 predictions for the same activation energy are 56.9 and 55.9 kcal/mol with basis sets I and II, respectively, very close to and just below the experimental value. Thus, the assumed errors in the DFT methodology are not expected to change the conclusions associated with our calculated DFT results. The closeness of DFT to MP2 predictions of the activation energy lends support to the use of DFT calculations in the study of DADNE.

7. CONCLUDING REMARKS

The calculations made and the conclusions drawn concerning DADNE are based on DFT methodology. While there are errors to be expected in applying DFT calculations to the various steps in the reaction path studied,

we have relied upon our experience [6] with the simpler but related molecule nitroethylene to help characterize the magnitude of the errors. In the simpler case we made both *ab initio* (MP2, MP4, and G2) and DFT calculations. We used the simpler molecule to estimate the level of basis that would be adequate for reliable results. In that way, we chose the basis sets used here for DADNE. In those steps that are similar in both molecules, for example, the critical nitro-to-nitrite rearrangement, the errors associated with DFT, judged against the *ab initio* results as standard, were likely to be similar in both molecules. This permitted us to use relatively efficient DFT calculations to characterize the unimolecular decomposition of DADNE.

We have found that the initial step in the unimolecular decomposition of DADNE is a nitro-to-nitrite rearrangement. The calculated barrier to transition at 59.1 kcal/mol B3LYP (59.7 kcal/mol B3P86) compares very well with the experimental value of 58 kcal/mol, and with the single-point MP2 calculations performed at the B3LYP optimized geometry. Once the initial barrier is surmounted, the decomposition proceeds through a series of steps, all of which we were able to characterize, involving relatively low energy barriers, resulting in the production of fragments NO, HONO, CO, NH₂, and HNC. We pointed out how these fragments may plausibly interact to yield, as final stable products, CO, N₂, and H₂O. These final products lie below the original DADNE molecule by 146.5 kcal/mol B3LYP (117.1 kcal/mol B3P86). On average, the energy released by one DADNE molecule is sufficient to activate two additional molecules, and thus a chain reaction may be sustained.

The structural parameters that we have calculated for DADNE are consistent with the experimental crystallographic structure [2,3], and also with the previous calculations of Politzer et al [8]. Additionally, we have obtained the structural parameters for the initial transition state, as well as for each subsequent step along the decomposition pathway. Thus, the unimolecular decomposition of DADNE appears to be well characterized.

U. Bemm and H. Ostmark, their Swedish colleagues, and others have synthesized a novel explosive and have proven it to have low sensitivity and high performance [1-5]. Soon after its synthesis, the first theoretical investigation by Politzer et. al [8]. examined several properties of the molecule, including geometry, bond dissociation energies, heats of formation, vaporization, and sublimation. The DADNE calculations [7] we have reviewed above are consistent with the experimental characteristics that had been assigned to the compound.

We mention here certain interesting calculation results obtained by other groups, subsequent to our work, which added important additional

perspective to our understanding of DADNE. H. Dorsett [33] used *ab initio* calculations to study three possible DADNE reaction paths. These are Hydrogen transfer, scission of the C-nitro bond, and our nitro-nitrite rearrangement. It is suggested that which of the three initiation steps are to be preferred will be a function of the experimental conditions of initiation, e.g., thermolysis, shock or impact, and electronic excitation. Further study to correlate experimental behavior under varying initiation conditions with the variety of mechanisms available is indicated.

Sorescu et. al [34]. undertook first principles calculations to investigate structural and vibrational properties of DADNE, including solid state calculations using a plane wave basis. Their predicted crystal structure is in good agreement with the experimentally determined X-ray structure. They obtain an intermolecular potential to describe the crystal, allowing investigation of its response to a variety of perturbations such as heating or pressure. Their paper is replete with a wide variety of calculated crystal properties and their comparison to experimental results.

J. G. Fu et. al [35]., study DADNE structure and properties using *ab initio* calculations. Most interestingly, they study the relative stability of three different isomers of DADNE, and established their relative order of stability. They also calculate the vibration spectra of the molecule and find it compares favorably to the corresponding experimental results.

While there is considerably more work required, to complete the study of DADNE, in the short time since its synthesis, quantum theory and its computational implementation have done much to clarify our understanding of the molecule.

ACKNOWLEDGMENTS

L.M. acknowledges an IBM Shared University Research (SUR) grant, and an NSF CREST grant. L.H. and J.K. acknowledge support in part by the Office of Naval Research and in part by the National Institutes of Health Grant GM-30902.

SUPPORTING INFORMATION AVAILABLE [6,7]

Table of calculated values of the vibrational frequencies for each structure. This material is available free of charge via the Internet at <http://pubs.acs.org>.

REFERENCES

1. Latypov, N. V.; Bergman, J.; Langlet, A.; Wellmar, U.; Bemm, U. *Tetrahedron* **1998**, *54*, 11525.
2. Bemm, U.; Östmark, H. *Acta Crystallogr.* **1998**, *C54*, 1997.
3. Gilardi, R. Crystallographic data (excluding structure factors) for the DADNE structure have been deposited with the Cambridge Crystallographic Data Centre, 12 Union Road, Cambridge CB2 1EZ, U.K. (deposition number CCDC 127539).
4. Östmark, H.; Langlet, A.; Bergman, H.; Wingborg, U.; Wellmar, U.; Bemm, U. FOX-7 - A New Explosive with Low Sensitivity And High Performance; *11th International Symposium on Detonation*, 1998; <http://www.sainc.com/onr/detsymp/financemt.html>.
5. Bergman, H.; Edvinsson, H.; Ostmark, H.; Hahma, A.; Janzon, B.; Trends and development of New Energetic Materials, <http://www.verkstaderna.se/mtt/pdf/200102/energetic%20materials.pdf>.
6. Ab Initio Study of Unimolecular Decomposition of Nitroethylene Gindulyte, L. Massa, L. Huang, J. Karle, J. Phys. Chem. A; 1999; 103(50); 11040-11044.
7. PROPOSED Mechanism of 1,1-Diamino-Dinitroethylene Decomposition: A Density Functional Theory Study, A. Gindulyte, L. Massa, L. Huang, J. Karle, J. Phys. Chem. A; 1999; 103(50); 11045-11051.
8. Politzer, P.; Concha, M. C.; Grice, M. E.; Murray, J. S.; Lane, P. J. *Mol. Struct. (THEOCHEM)* **1998**, *452*, 75. Also refs 1 and 2 therein.
9. Zhao, X.; Hints, E. J.; Lee, Y. T. *J. Chem. Phys.* **1988**, *88*, 801.
10. Shalashilin, D. V.; Thompson, D. L. *J. Phys. Chem. A* **1997**, *101*, 961.
11. Wu, C. J.; Fried, L. E. *J. Phys. Chem. A* **1997**, *101*, 8675.
12. Lofy, P.; Wight, C. A. Thermal Decomposition of HMX (Octahydro-1,3,5,7-tetranitro-1,3,5,7-tetrazocine) Below its Melting Point; *Proceedings of the JANNAF Combustion and Hazards Meeting*, Tucson, Arizona, 1998.
13. Rice, B. M.; Chabalowski, C. F. *J. Phys. Chem. A* **1997**, *101*, 8720.
14. Melius, C. F. Thermochemical Modeling: I. Application to Decomposition of Energetic Materials. In *Chemistry and Physics of Energetic Materials*; Bulusu, S. N., Ed.; Kluwer Academic Publishers: The Netherlands, 1990; Vol. 301, pp 21-49.
15. Melius, C. F. Thermochemical Modeling: II. Application to Ignition and Combustion of Energetic Materials. In *Chemistry and Physics of*

Energetic Materials; Bulusu, S. N., Ed.; Kluwer Academic Publishers: The Netherlands, 1990; Vol. 301, pp 51-78.

16. Behrens, R., Jr. *J. Phys. Chem.* **1990**, *94*, 6707.
17. Behrens, R., Jr.; Bulusu, S. *J. Phys. Chem.* **1991**, *95*, 5838.
18. Behrens, R., Jr.; Bulusu, S. *J. Phys. Chem.* **1992**, *96*, 8877.
19. Behrens, R., Jr.; Bulusu, S. *J. Phys. Chem.* **1992**, *96*, 8891.
20. Behrens, R., Jr.; Mack, S.; Wood, J. Thermal Decomposition Mechanisms of HMX: The Interrelationship of Chemical and Physical Processes. *Proceedings of the JANNAF Combustion and Hazards Meeting*, Tucson, Arizona, 1998.
21. Hu, C.-H.; Chong, D. P. Density Functional Applications. In *Encyclopedia of Computational Chemistry*; Schleyer, P. v. R., Allinger, N. L., Clark, T., Gasteiger, J., Kollman, P. A., Schaefer, H. F., III, Schreiner, P. R., Eds.; John Wiley & Sons: New York, 1998; pp 664-678.
22. Frisch, M. J.; Trucks, G. W.; Schlegel, H. B.; Scuseria, G. E.; Robb, M. A.; Cheeseman, J. R.; Zakrzewski, V. G.; Montgomery, J. A., Jr.; Stratmann, R. E.; Burant, J. C.; Dapprich, S.; Millam, J. M.; Daniels, A. D.; Kudin, K. N.; Strain, M. C.; Farkas, O.; Tomasi, J.; Barone, V.; Cossi, M.; Cammi, R.; Mennucci, B.; Pomelli, C.; Adamo, C.; Clifford, S.; Ochterski, J.; Petersson, G. A.; Ayala, P. Y.; Cui, Q.; Morokuma, K.; Malick, D. K.; Rabuck, A. D.; Raghavachari, K.; Foresman, J. B.; Cioslowski, J.; Ortiz, J. V.; Stefanov, B. B.; Liu, G.; Liashenko, A.; Piskorz, P.; Komaromi, I.; Gomperts, R.; Martin, R. L.; Fox, D. J.; Keith, T.; Al-Laham, M. A.; Peng, C. Y.; Nanayakkara, A.; Gonzalez, C.; Challacombe, M.; Gill, P. M. W.; Johnson, B.; Chen, W.; Wong, M. W.; Andres, J. L.; Gonzalez, C.; Head-Gordon, M.; Replogle, E. S.; Pople, J. A. *Gaussian 98*, Revision A.6; Gaussian, Inc.: Pittsburgh, PA, 1998.
23. Foresman, J. B.; Frisch, A. *Exploring Chemistry with Electronic Structure Methods*, 2nd ed.; Gaussian, Inc.: Pittsburgh, 1996.
24. Scott A. P.; Radom L. *J. Phys. Chem.* **1996**, *100*, 16502.
25. Becke, A. D. *J. Chem. Phys.* **1993**, *98*, 5648.
26. Perdew, J. P. *Phys. Rev. B* **1986**, *33*, 8822.
27. Lee, C.; Yang, W.; Parr, R. G. *Phys. Rev. B* **1988**, *37*, 785.
28. Guirguis, R.; Hsu, D.; Bogan, D.; Oran, E. *Combust. Flame* **1985**, *61*, 51.
29. Jursic, B. S. *Chem. Phys. Lett.* **1999**, *299*, 334.
30. Wolf, M.; Yang D. L.; Durant, J. L. *J. Phys. Chem. A* **1997**, *101*, 6243.

31. Palma, A.; Semprini, E.; Stefani, F.; Talamo, A. *J. Chem. Phys.* **1996**, *105*, 5091.
32. Klippenstein, S. J.; Yang, D. L.; Yu, T.; Kristyan, S.; Lin, M. C.; Robertson, S. H. *J. Phys. Chem. A* **1998**, *102*, 6973.
33. Dorsett, H; Computational Studies of Fox-7, A New Insensitive Explosive, <http://65.105.56.185/master5/category32/A089483.html>
34. Sorescu, D.C.; Boatz, J.A.; Thompson, D.L.; Classical and Quantum Mechanical Studies of Crystalline FOX-7 (1,1-Diamino-2,2-dinitroethylene), *J. Phys. Chem. A* 2001, *105*, 5010-5021
35. FU, J.G.; Xiao, H.M.; Dong, H.S.; Gong, X.D.; Li, J.S.; Wang, Z.Y.; The Theoretical Study on Structure and property of Diamino-dinitroethylene, 59, No.1, 39-47 (2001)

This Page Intentionally Left Blank

Chapter 5

Quantum-Chemical Dynamics with the Slater-Roothaan Method

B. I. Dunlap

Theoretical Chemistry Section, Code 6189, US Naval Research Laboratory,
Washington, DC 20375, dunlap@nrl.navy.mil

1. Introduction

Slater invented the precursor to density-functional theory (DFT) to simplify and extend Hartree-Fock (HF) calculations [1]. In HF theory electrons in occupied orbitals see a potential due to one less than the total number of electrons, i.e., a potential due to every other electron, but electrons in unoccupied orbitals are repelled by every electron. Every electron is in either an occupied or a virtual level. HF theory is not defined for partially occupied orbitals that might be useful for describing the breaking and making of chemical bonds. In such situations multiconfiguration self-consistent-field (MCSCF) theory variationally mixes Slater determinants with and without the relevant bonding orbitals. Transforming to the natural orbitals, which diagonalize the first-order density matrix [2], generated by the MCSCF wavefunction show that the occupancy of those bonding and antibonding orbitals varies along the reaction path. In density-functional theory every electron moves in the same Kohn-Sham (KS) potential [3], and no distinction is made between occupied and unoccupied orbitals. Slater averaged the exchange potential of the homogeneous electron gas over all occupied orbitals to obtain a quantity that, by dimensional analysis alone, must be proportional to the cube root of the uniform density of the homogeneous-electron-gas problem, which approximately describes the electronic structure of a metal. Slater's average proportionality constant is reduced by a factor of 2/3 in a variational treatment [3,4] that samples only electrons at the Fermi energy, which separates the energy eigenvalues of occupied and virtual orbitals in DFT.

Schwarz [5] found the values of that proportionality constant, α , which give the HF energy of the atom for each element. Any general method capable of using various α is called an $X\alpha$ method. Any such method that uses Schwarz' values of α can be said to be variational, if variational is taken to mean bounding

the exact energy from above, because HF bounds the exact energy from above [6]. Indeed that bound is well above the exact energy, and it is perhaps useful to switch to a different definition of variational, as is done herein. The meaning of variational advocated in this work is mathematically variational, consistent Roothaan's work. For the rest of this work the term $X\alpha$ will be restricted to mean using the HF values of α .

Schwarz' values of α turn out to lie between Slater's value of one and the Gáspár-Kohn-Sham (GKS) value of $2/3$, as would those of a method constructed to give the total nonrelativistic atomic electronic energy. All values are used in the following spin density-functional expression for the exchange and correlation (XC) energy,

$$E_{xc} = \alpha \frac{9}{4} \left(\frac{3}{4\pi} \right)^{1/3} \int \rho_{\uparrow}^{4/3}(\mathbf{r}) + \rho_{\downarrow}^{4/3}(\mathbf{r}) d^3\mathbf{r}, \quad (1)$$

where $\rho_{\uparrow}(\mathbf{r})$ is the density of electrons with up spin. The standard functional for electronic Coulomb repulsion,

$$E_c = \iint \rho(\mathbf{r}_1)\rho(\mathbf{r}_2) d^3\mathbf{r}_1 d^3\mathbf{r}_2 / 2r_{12} \equiv \frac{1}{2} \langle \rho \| \rho \rangle, \quad (2)$$

where the density in this expression is the sum of the two spin densities, completes the description of the electron-electron interaction in DFT. The total electronic energy in $X\alpha$ theory is completed by the standard one-electron kinetic energy and nuclear-attraction part of the electronic Hamiltonian, h_1 ,

$$E_1 = \sum_i n_i \langle i | h_1 | i \rangle, \quad (3)$$

where n_i is the occupation number of orbital i . This last is not a density functional expression. The quantum mechanical kinetic operator is retained to allow chemical bonding.

These equations are easily solved for atoms using the central-field approximation. The original $X\alpha$ implementation for molecules used these atomic solutions within spheres (muffin-tins) around each atom. The method was quite promising because unlike most other quantum chemical methods molecules dissociated correctly if the muffin-tins were allowed to grow as the molecule dissociates [7]. The problem with multiple-scattering $X\alpha$ (MSX α) was that the potential is discontinuous at the muffin-tin edges. Thus a meaningful energy can not be defined, which means that the method can not be made mathematically variational.

Roothaan variationally determined finite linear-combination-of-atomic-orbital (LCAO) expansions of molecular spin-orbitals by minimizing the energy [8]. Limiting the length of atomic basis sets and using those small sets as a basis for expanding molecular orbitals makes quantum chemistry practical. Only if full atomic orbitals are used can molecules dissociate correctly in the LCAO approach. Accurate atomic orbitals decay exponentially near to and far from the nucleus. The most reliable quantum chemical calculations, however, use Gaussians, which decay too rapidly far from the molecule to yield accurate dissociated-atom limits. Their advantage lies in the fact that solid-harmonic Gaussian orbitals have the same functional form in position and momentum space. Thus the Gaussian functional form gives the minimum uncertainty expectation value, which means that it has the shortest range in quantum chemical calculations. Thus big, well-chosen Gaussian basis sets can be used without introducing numerical instability and enable calculations on large molecules through sparsity in the overlap matrix.

Similarly, expanding the KS potential in an LCAO expansion makes molecular density-functional calculations practical [9]. For metals and similar crystalline solids, it is best to expand the Kohn-Sham potential in momentum space via Fourier coefficients. For molecular solids various real-space methods are under investigation. For molecules studied with the big, well-chosen Gaussian basis sets of quantum chemistry, it is undoubtedly best to expand the KS potential in linear-combination-of-Gaussian-type-orbital (LCGTO) form [10].

If the KS potential is fitted, then a total Roothaan variation of the energy must include terms that account for how the fitted KS potential changes if a molecular spin-orbital is varied. In particular, even if the XC energy is fitted numerically to analytic form, then the variational orbital-optimization process introduces a numerical component into the Fock matrix, which must be iterated to give the optimal total energy [11]. Thus numerically fitting XC functional of the LCAO orbitals to make the calculation of the energy analytic and then fully varying the energy to optimize the orbitals reintroduces an effective KS potential that turns out to have a numerical component. This at least partially defeats the purpose of fitting in the first place. The only way around this problem appears to be to restrict one's attention to approximate density functionals that give LCAO energies without resort to numerical integration in any form. Fortunately methods have been developed to analytically fit KS potentials in a way that is commensurate with Roothaan's method for fitting molecular orbitals. Those fitting methods are called robust and variational. They are reviewed in the next Section. The third Section discusses orbital and fitting basis sets and calculations on a few hydrogen-containing molecules. The fourth Section discusses technical details concerned with using DFT in direct dynamics calculations. The fifth Section describes the chemistry of ONNO-ONNO collisions that are restricted to occur in two dimension. This chapter ends with a few conclusions.

2. ROBUST AND VARIATIONAL FITTING

In the LCTGTO approach to DFT it is obviously best to treat the KS potentials for both spins as if they were two additional orbitals. If they were spin-orbitals that were optimized by varying the energy, then changing their LCGTO coefficients in any way would not affect the energy to first order [8]. Requiring that the total energy have no error through first order if one or more of its components is fitted, ensures this important property. Such a fit is called robust because the fits can be altered slightly without affecting the total energy. Often this entails adding another term to the total energy. For example Sambe and Felton made an LCAO approximation, which by definition is single-center, to the two-center density, $\bar{\rho} \cong \rho$, to approximate E_c [10],

$$E_c = \frac{1}{2} \langle \rho \| \rho \rangle \cong \frac{1}{2} \langle \rho \| \bar{\rho} \rangle. \quad (4)$$

Unfortunately if any significant LCGTO coefficient in $\bar{\rho}$ changes by one part in 10^{10} then the Coulomb energy, which is on the order of the total energy, particularly for large systems, changes by one part in 10^{10} . In contrast the variational energy evaluated on a computer using double precision changes not at all if a significant orbital coefficient changes by one part in 10^{10} . In general, the computationally cheapest solution to this problem lies in adding a somewhat less accurate fit to the total energy that is constructed to remove the first-order error. One can add to the mix of ways the Coulomb energy can be calculated the Coulomb energy of the fit itself. The unique combination that has no first-order is easily determined [12],

$$E_c = \frac{1}{2} \langle \rho \| \rho \rangle \cong \langle \rho \| \bar{\rho} \rangle - \frac{1}{2} \langle \bar{\rho} \| \bar{\rho} \rangle. \quad (5)$$

Note that the added term, which involves the fit twice, is in that sense less accurate than Sambe and Felton's original term, which involves the fit only once. The point is, however, that if the fitted density is expressed as the exact density minus an error term, then the error in Eq. (5) is the Coulomb repulsion of the error with itself, which is always second order and positive [12]. This approach is readily extended to four-center Coulomb integrals [13],

$$\langle ab \| cd \rangle \cong \langle ab \| \bar{\rho}_{cd} \rangle + \langle \bar{\rho}_{ab} \| cd \rangle - \langle \bar{\rho}_{ab} \| \bar{\rho}_{cd} \rangle, \quad (6)$$

where $\bar{\rho}_{ab}(\mathbf{r})$ is the single-center fit to charge distribution $a(\mathbf{r})b(\mathbf{r})$, etc. Many other, but not yet all, DFT functionals can be fitted robustly in similar fashion [13].

In this case, and perhaps for all robust fits, if the fit is robust then its LCAO coefficients can be determined by variation of the energy. In that case the fit is said to be variational. Quantum chemists are beginning to use variational fits, but they do not yet include robust energies, in a method that they call resolution of the identity [14,15]. Equation (6), with $\bar{\rho}_{ab}$ replaced by $\bar{\rho}_{LM}$, where L and M are the usual multipole-moment quantum numbers, can also be used to remove the first order error from fast-multipole methods [16].

To evaluate Eq. (1) in a way that is analytic, robust and variational, it is first necessary to divide the density among the atoms. That is easy in any LCAO approach, where the only problem is to how to assign centers to the cross (two-center) terms of the density. The computationally most efficient way is to multiply each atomic orbital by $\alpha^{3/8}$, where α is the appropriate X α scaling factor for that atom. Then the scaled, and thus partitioned, density may be written

$$n(\mathbf{r}) = \sum_{iab} n_i c_a^{i*} c_b^i \alpha^{3/8}(a) \alpha^{3/8}(b) \phi_b^*(\mathbf{r}) \phi_b(\mathbf{r}), \quad (7)$$

where $\alpha(a)$ is the X α scaling factor of the nucleus that is the center of atomic orbital a . This is extremely efficient computationally because the multiplication by the 3/8 power of α can be moved out of all loops until the summation over different atomic centers. In fact, when both centers are the same then the integrand of Eq. (1) results, $n^{4/3}(\mathbf{r}) \rightarrow \alpha \rho^{4/3}(\mathbf{r})$. Thus MSX α and methods based on $n(\mathbf{r})$ go smoothly to separated-atom limits in which each atom can have an independent XC potential. Unlike MSX α energies, energies based on Eq. (7) are continuous and differentiable for all internuclear separations. On the other hand, MSX α alone is applicable to all functionals, including hybrid functionals.

The 4/3-power functional is not analytic about the origin; there are three cube roots of one. Nevertheless, the 4/3-power functional can be treated analytically using robust and variational fitting [17]. To do so it is convenient to define two new LCGTO functionals. The first functional approximates the cube root of the partitioned density,

$$X(\mathbf{r}) \cong n^{1/3}(\mathbf{r}). \quad (9)$$

The second approximates the 2/3 power of the partitioned density,

$$X^2(\mathbf{r}) \cong Y(\mathbf{r}) \cong n^{2/3}(\mathbf{r}). \quad (10)$$

Using X , Y and n a unique robust approximation to the $4/3$ power of the partitioned density can be constructed.

$$[n(\mathbf{r})]^{4/3} \cong 4[n(\mathbf{r})X(\mathbf{r}) - X^2(\mathbf{r})Y(\mathbf{r}) + Y^2(\mathbf{r})]/3. \quad (11)$$

It is easy to show that if X and Y each are in error then this equation is accurate through first order, i.e. the approximation is robust. The right-hand side of this equation is single valued; but we are only interested in solutions for which the scaled density is real and nonnegative. There is no guarantee that the mathematically simplest partitioning scheme Eq. (7) is chemically optimal. Without doubt it is not, but other partitioning schemes such as using Mulliken population analysis are easily implemented as noted above, but will not be explored in this work.

3. THE SLATER-ROOTHAAN METHOD

The Slater-Roothaan method uses solid-harmonic Gaussians [18] to fit the molecular orbitals and five other nonnegative quantities, namely the total density, the cube root of the partitioned density for both spins, and the $2/3$ power of the partitioned density for both spins. They are treated as five additional orbitals of the totally symmetric irreducible representation. Changing them slightly does not affect the robust energy at all.

As discussed above, variational fitting of the density is well established in density-functional and *ab-initio* quantum chemistry. DGauss [19] was the first commercial code to employ variational fitting of the density. It required three sets of Gaussian basis functions: two for fitting the orbitals and charge density (CD) variationally and a third for fitting the XC potential nonvariationally. These basis sets have been published for first-row atoms [20]. More elements are covered in a file, called BASIS, distributed with DGauss and deMon [21]. The fitting basis sets are uncontracted. Based on our work, those Gaussian exponents for fitting the XC potential are scaled by the factor $1/3$ from the CD exponents and for heavy atoms five p and 5 d fitting functions are used in both basis sets. Godout, *et al.*, have optimized those sets as well as 3- p and 3- d fitting basis sets for use with DGauss' valence double- ζ orbital basis sets. Only a bigger 4- p and 4- d basis is available from PNNL [22]. Even the smallest sets work very well with all orbital basis sets, and the difference between using any of the fitting basis sets discussed in this work is always less than the difference between using a double- ζ and a triple- ζ orbital basis set [16].

The commercial code Turbomole [23] uses variational, but not robust, fitting of the charge density. Therefore, it uses very large fitting bases, including g

functions for second-row atoms [14], however its *s*-type fitting functions are smaller than ours. We scale the *s*-type orbital exponents by two to fit the CD, by 2/3 to fit the XC potential [24], and by 4/3 to generate the *Y* basis. We also use bond-centered Gaussians of exponents of 1.0 for the CD and 0.3 for the other two fitting bases. In the following we use the biggest fitting basis sets and the 6-311G** orbital basis sets downloaded from PNNL [22], however using the smallest fitting basis sets would not change these results significantly. All fits are robust.

In a very influential study Becke showed conclusively that mixing exact, HF, exchange and local-density-functional (LDF) exchange led to a method that was impressively accurate [25]. Now, most quantum-chemical calculations use the hybrid B3LYP functional [26]. Mixing half exact and half LDF, the Becke Half & Half method, is less accurate, but is sufficiently exact to point the way toward making parameter-rich analytic $X\alpha$ accurate. Hydrogen is the element that is least accurately treated using DFT. Thus in Table 1 we collect the data for hydrogen containing molecules from Becke's work. All calculations include full geometry optimization in the highest symmetry for which the electronic structure is nondegenerate for both molecules and separated atoms. Becke did not publish directly his LDF energies, but they are easily obtained, and listed in the third column, from the first two columns of the table that he did publish directly.

The fourth column of the Table contains the $X\alpha$ atomization energies that result from using the elemental HF values of α that are tabulated for spin polarized calculations by Connolly [27], (Schwarz' calculations were spin restricted) and interpolated linearly when necessary. The next column uses a uniform $\alpha = 0.7$. That choice of α is the most practical for quantum methods that must have α constant throughout the molecule [9]. The last column uses the Gáspár-Kohn-Sham value of 2/3. The average values for all these molecules and electronic states are given in the last row. Universally the binding energies decrease across the last three columns. The XC energy is negative and proportional to α . Schwarz' HF values of α monotonically decrease with atomic number, and fall below 0.7 between Cd and Xe [27]. On average Becke's Half-&-Half atomization energies are best reproduced using $X\alpha$. This caused by the fact that the LDF significantly overbinds the right-hand-side of the periodic table [24]. For the lighter molecules the LDF and $X\alpha$ are more alike.

Numerous ways to improve upon $X\alpha$ come to mind. The first is related to the fact that HF favors states of high spin. Similarly, as the Table shows, the energetics of spin polarization in $X\alpha$ too strong, at least for molecules containing hydrogen. For example, singlet H_2 is not stable enough relative to two completely polarized hydrogen atoms. Thus an obvious improvement would reduce the scaling constant for minority spins to perhaps as small as the GKS value. As was mentioned above, it might be better at the same time to

Table 1 Atomization Energy (kcal/mol)

Molecule	Exact	Half & Half	LDF	X α	$\alpha = 0.7$	GKS
H ₂	101.8	125.2	85.1	85.1	82.8	81.8
LiH	53.1	74.0	37.6	37.6	34.7	33.6
BeH	55.9	65.7	55.9	55.9	49.7	46.9
CH	78.1	104.8	66.3	66.3	64.4	63.4
CH ₂ (³ B ₁)	185.0	226.9	191.0	191.0	179.9	173.4
CH ₂ (¹ A ₁)	167.7	220.0	155.8	155.8	148.6	144.7
CH ₃	294.1	363.4	294.3	294.3	279.4	271.1
CH ₄	396.6	492.3	401.6	401.6	381.8	371
NH	76.8	109.3	66.7	66.7	64.1	62.7
NH ₂	167.9	232.2	156.0	156.0	148.9	145.1
NH ₃	179.0	273.6	368.2	269.8	256.1	248.7
OH	62.0	99.4	136.8	97.2	93.8	91.5
H ₂ O	142.4	215.0	287.6	224.8	213.4	206.4
HF	91.0	132.2	173.4	142.1	135.4	130.5
C ₂ H ₂	275.6	384.7	493.8	416.0	394.3	382.3
C ₂ H ₄	395.0	534.8	674.6	561.8	533.1	516.9
C ₂ H ₆	503.8	674.4	845.0	700.1	663.6	643.3
HCN	185.8	290.6	395.4	312.1	300.3	292.9
HCO	168.2	264.2	360.2	300.4	288.3	280.1
H ₂ CO	235.8	351.4	467.0	386.8	369.4	358.5
CH ₃ OH	334.2	481.0	627.8	512.7	486.1	470.4
N ₂ H ₄	230.3	399.2	568.1	408.7	386.6	374
H ₂ O ₂	113.5	239.7	365.9	277.8	265.3	256.5
SiH ₂ (¹ A ₁)	100.9	144.0	187.1	125.6	119.1	116.5
SiH ₂ (³ B ₁)	95.2	128.1	161.0	120.0	114.0	110.3
SiH ₃	163.4	216.8	270.2	193.7	184.7	180.2
SiH ₄	233.3	305.9	378.5	281.2	266.9	260
PH ₂	96.0	146.0	196.0	125.1	120.1	118.1
PH ₃	152.8	226.0	299.2	202.1	193.8	190.3
H ₂ S	120.0	173.1	226.2	162.6	156.0	152.8
HCl	74.2	102.4	130.6	99.1	97.2	95
Si ₂ H ₆	379.4	506.1	632.8	472.8	450.3	438
CH ₃ Cl	272.3	374.9	477.5	391.6	373.9	362.5
H ₃ CSH	320.1	448.2	576.3	458.9	435.5	422.9
HOCl	66.5	149.3	232.1	169.2	161.7	156.1
Average	175.2	252.5	329.9	254.9	242.7	235.7

increase the majority scaling constant to give the total atomic energies rather than the just HF atomic energies. Such studies are beyond the scope of the work, the goal of which is a practical first-principles method for directly studying chemical dynamics on a computer. Toward that end, an apparently necessary simplification is to abandon bond-centered functions. That change has no effect when the remaining fitting basis sets are as big as those used in this work. A significant problem remains, however, having to do with the multiplicity of DFT solutions.

4. Symmetry and Balanced DFT Dynamics

I have been told that a major consideration in planning the Car-Parrinello code [28] was to specifically forbid the imposition of symmetry in those DFT calculations [29]. The problems with symmetry in DFT are well known [30]. It is less well known that they do not go away if symmetry is not enforced in the calculations. The essential problem concerns spin. As developed so far, DFT does not allow a simple single bond to be broken along the singlet surface. A simple extension allows one to obtain the singlet energy from two DFT calculations [31]. One can, of course, invert any such set of equations that give multiplet-splittings to obtain the energy in question and variationally minimize that target energy alone [32,33]. The problems with such "improvements" to DFT is that to apply them you need to know much about the electronic structure of the solution before you begin the calculation. These multiplicity problems are compounded in combustion and detonation where oxygen usually plays an important role. Despite the fact that both the oxygen atom and diatom are even-electron systems, but they both have triplet ground states. On the other hand, ozone, for example, has a singlet ground state. Thus collision-induced dissociation of two ozone molecules proceeds very differently depending on how the spin of the dynamics is constrained [34]. As we are interested in high-density phenomenon such as detonation, we have chosen to leave spin completely free in our dynamics. Such dynamics is impossible using HF and thus is impossible using hybrid methods such as B3LYP, with or without enforcing spatial symmetry. For a large enough set of interacting molecules that is either the correct dynamics or indistinguishable from it.

Spatial symmetry significantly speeds up calculations using good quantum-chemical codes [30]. Therefore we would like to use it to the greatest extent possible to facilitate obtaining as many different calculations as possible that might shed light on how to best study chemical dynamics using DFT. Clearly spatial symmetry constraints can affect dynamics, perhaps to remarkable extents. Our original studies of the NO system constrained the NO dimers to be in a one-dimensional (1-D) chain [35]. That constraint made the calculations very easy to perform and full collisions between two 1-D solids could be followed completely through the entire collision process. Unfortunately no exothermic

chemical reactions were seen. Thus that work is consistent with the possibility that 1-D NO will not detonate at collision velocities less than 20 km/sec despite the fact that linearization considerably weakens the bonds of the dimer.

The NO dimer, although slightly non-linear, is planar. Thus less constrained, 2-D dynamics will not affect the energetics of the isolated molecule. The number of different collision orientations is much greater in 2-D. In the most efficient 2-D DFT calculations all orbitals are either σ or π . The dimer is even under reflection. Isolated NO fragments have spin one half and can be either even or odd under reflection, depending on whether the anti-bonding π electron is in the plane or perpendicular to it. (Of course DFT calculations could be performed in which the $p\pi^*$ electron is oriented at arbitrary angle to the plane, but such calculations are not considered in this work.)

One can dissociate the NO dimer simply by increasing the N-N bond distance to infinity. One can also require that during that process the molecule remain on the singlet surface, which by definition has a wavefunction and thus density that has equal spin-up and spin-down components everywhere in space. We are not interested in spin-restricted dynamics. We are interested in the much more balanced chemical dynamics that treats each half of the dissociated dimer "correctly" in DFT via a spin-polarized calculation. This decision must be made independent of whether or not one wants to use spatial symmetry to reduce the cost of the calculation. Spin-unrestricted DFT chemical dynamics will be called balanced in the following.

The choice for balanced DFT dynamics has important consequences for how the calculations are actually performed. Beyond a certain N-N distance in $(\text{NO})_2$ there are two degenerate DFT solutions that are related to each other simply by flipping the spins. In a crowded, spin-polarized environment those two states might not be precisely degenerate and the system might be covered by the Hohenberg-Kohn theorem [36]. Independent of whether or not these states are precisely degenerate, which requires at least two different successful SCF calculations to determine, it seems practically impossible to prevent surface hopping. The term surface hopping will be used to describe flipping from one of these states to another. Certainly as systems get bigger and contain more and oxygen atoms and diatoms the number of such states grows and staying on one surface becomes ever more difficult.

One can increase the chances that the system remains on one surface by starting each SCF cycle at each new geometry using the converged SCF results from the previous time step. We go one step further and if there is a second previous time step, then we start the current SCF process using the KS potential that is twice the previous SCF KS potential minus the second previous SCF KS potential. (So far we have only used constant time steps.) While this method does allow practical dynamics, it does not seem to be a good idea. The problem

is easily seen by reconsidering symmetric $(\text{NO})_2$ dissociation again. One can travel out the singlet surface for a long way after the two spin-polarized solutions have dropped lower in energy. The problem of getting stuck high and dry is minimized by starting every second time step from a superposed-atom KS potential. In this work we use high energies (initial velocities) and a time step of 0.1 fs. Starting every third time step from scratch changes the dynamics in too many cases.

5. 2-D Chemical Dynamics

It does not seem practical to use bond-centered fitting functions in chemical dynamics calculations in which bonds are being broken and reformed. Thus our fitting functions are uncontracted and scaled from the 6-311G** orbital sets in the s manifold. The atomic $L > 0$ fitting functions are unscaled and contracted exactly as optimized for Turbomole calculations [14] except that the silicon basis is uncontracted. The calculations are performed in C_s symmetry.

Slater has shown that the $X\alpha$ eigenvalues are the precise derivatives of the energy with respect to occupation numbers [37]. Janak shows that the same theorem holds for Kohn-Sham DFT as it has come to be implemented computationally [38]. Thus at each time step our electronic structure is fully self-consistent and all of our orbitals are empty, singly occupied (σ states), doubly occupied (π states), or fractionally occupied if and only if their KS eigenvalue is precisely the Fermi energy at that time step. For the vast majority of times the SCF process converges in 120 iterations. If not, the SCF process is restarted from scratch with the superposed-atom potential, but with current occupation numbers. If that does not converge forces are computed as if it had. Those forces are used to update the nuclear positions according to the summed form of the velocity-verlet algorithm [39]. With a new geometry and forces, the new electronic energy is known. (There are no additional forces due to the use of precise fractional occupation numbers [40].) This gives a test that is weakly enforced now. We stop the code if the energy has changed by a Hartree more than we thought it should change. This basically tests for the total failure of the SCF process. The calculations rarely stop, but if they do, then they tend to stop over and over again on the same trajectory. An example of such a trajectory is given below. A trajectory is accepted as good if the total energy changes no more than a few times 0.01 Hartree over the course of the trajectory due to all causes. The most important such cause is travelling on an excited potential energy surface. Such discontinuous steps can be determined and the dynamics started again after exploring a few SCF solutions. But if the discontinuities are too small, caused, e.g., by reorienting the spin of oxygen atoms or dimers, then the dynamics if corrected will change very little and the original dynamics is accepted as good. Jumps of 0.01 Hartree are rather common and accepted as valid dynamics.

The number of π and σ electrons is not monitored during the dynamics, but the number of unpaired spins is. Most often the number of unpaired spins changes fractionally and thus slowly, but once a jump of six was seen for a few tens of steps with no noticeable accompanying error in the total energy.

The ONNO-ONNO “Van der Waal’s” distance was found by optimizing the geometry of that system. It is slightly more than 3 Ångstroms. So all collisions are started with all inter-dimer atomic distances greater than 3.5 Ångstroms.

For our $(\text{NO})_2$ on $(\text{NO})_2$ studies we used collision energies that are a bit too high to be chemically relevant [41], because our previous study was disappointing in that no chemical reactions were seen [35]. For the most part in this work the two dimers were launched at each other along the two center-of-masses of both dimers at a velocity of $\pm 10 \text{ km/sec}$. With this constraint and in 2-D there are many different possible collisions. We kept one molecule with its long axis perpendicular to its velocity and rotated the other relative to the orientation of the first. For the parallel collision the forward facing NNO knees knock off the opposing O atoms in direction perpendicular to the collision. For the 180° -collision the knees meet, invert and the adjacent oxygen atoms leave as dioxygen. It is possible that that the remaining NNO molecules in these two collision geometries might further fragment, but if so they do not before going through several vibrational periods. The 90° -collision orientation sends all of the atoms of the rotated dimer towards the weakened central bond of the other. That orientation breaks that bond but leads to a high-density mess with no other bonds clearly broken and atomic geometries that are very difficult, if not ultimately impossible, to converge. That trajectory was stopped because, unfortunately, our methods cannot converge atomic iron without being assisted by symmetry, a case that only has six partially filled orbitals at the Fermi energy.

The 45° -collision orientation is beautiful. The molecules collide. Two oxygen diatoms leave almost immediately and the remaining two dinitrogen molecules strongly interact but eventually leave in the direction from which they came. A similar final state occurs if one dimer is shifted perpendicular to the line of approach by 0.5 Å to give nonzero angular momentum to the collision. In this case the two nitrogen molecules react less strongly and follow the oxygen molecules more closely. These reactions are strongly dependent on initial conditions, however. Halving the initial velocity in the 45° -collision leads to incomplete reaction.

6. Conclusion

The $X\alpha$ method has been made analytic and variational via single-center, LCGTO, robust, and variational fitting. It is quite promising because, unlike empirical and semiempirical methods, it is applicable to all elements. In fact, it has an independent parameter for each element that can be optimized to give

some chemical property for each element and GTO orbital basis set. For hydrogen it should probably be adjusted to give the dissociation energy of H_2 . Despite that great flexibility the method behaves well for molecular dynamics involving more than one element, i.e., multiple α 's. Clearly our methods for converging fractional-occupation-number solutions need improvement.

The Office of Naval Research directly and through the Naval Research Laboratory supported this research.

REFERENCES

- [1] J. C. Slater, Phys. Rev. 81 (1951) 385.
- [2] E. R. Davidson, Rev. Mod. Phys. 44 (1972) 451.
- [3] W. Kohn and L. J. Sham, Phys. Rev. 140 (1965) A1133.
- [4] R. Gáspár, Acta Phys. Hung. 3 (1954) 263.
- [5] K. Schwarz, Phys. Rev. B 5 (1972) 2466.
- [6] M. A. Ratner and G. C. Schatz, Introduction to Quantum Mechanics in Chemistry, Prentice Hall, Upper Saddle River, New Jersey, 2001.
- [7] J. C. Slater, Quantum Theory of Molecules and Solids, Vol. IV, McGraw-Hill, New York, 1974.
- [8] C. C. J. Roothaan, Rev. Mod. Phys. 23 (1951) 69; 32 (1960) 179.
- [9] E. J. Baerends, D. E. Ellis and P. Ros, Chem. Phys. 2 (1973) 41.
- [10] H. Sambe and R. H. Felton, J. Chem. Phys. 61 (1974) 3862; 62 (1975) 1122.
- [11] B. I. Dunlap, J. Andzelm, and J.W. Mintmire, Phys. Rev. A 42 (1990) 6354. B. I. Dunlap and J. Andzelm, Phys. Rev. A 45 (1992) 81.
- [12] B. I. Dunlap, J. W. D. Connolly and J. R. Sabin, J. Chem. Phys. 71 (1979) 3396; 4993.
- [13] B. I. Dunlap, Phys. Chem. Chem. Phys. 2 2000 21, J. Mol. Struct. (Theochem) 501 (2000) 221; 529 (2000) 37.
- [14] K. Eichkorn, F. Weigend, Treutler, O.; Ahlrichs, R. Theor. Chem. Acc. 1997, 97, 119.
- [15] F. Weigend, Phys. Chem. Chem. Phys. 4 (2002) 4285.
- [16] B. I. Dunlap, unpublished.
- [17] B. I. Dunlap, J. Phys. Chem. 90 (1986) 5524.
- [18] Dunlap, B. I. Phys. Rev. A 42 (1990) 1127; Int. J. Quantum. Chem. 81 (2001) 373, Phys. Rev. A, 66 (2002) 032502.
- [19] J. Andzelm and E. Wimmer, J. Chem. Phys. 96 (1992) 1280.
- [20] N. Godbout, D. R. Salahub, J. Andzelm, E. Wimmer, Can. J. Chem. 70 (1992) 560.
- [21] A. St-Amant and D. R. Salahub, Chem. Phys. Lett. 169 (1990) 387. A. St-Amant, Ph.D. Thesis, Université de Montréal (1992).
- [22] www.emsl.pnl.gov:2080/forms/basisform.html
- [23] R. Ahlrichs, M. Bär, M. Häser, H. Horn, C. Kölmel, Chem. Phys. Lett. 162 (1989) 165.
- [24] B. I. Dunlap, J. W. D. Connolly, J. R. Sabin, J. Chem. Phys. 71 (1979) 3396, 4993.
- [25] A. D. Becke, J. Chem. Phys. 98 (1993) 1372.
- [26] A. D. Becke, J. Chem. Phys. 98 (1993) 5648.
- [27] J. W. D. Connolly, in: Modern Theoretical Chemistry, Vol. 7, Ed. G.A. Segal, Plenum, New York, 1977, p. 105. DeMon User Guide, Version 1.0 beta, Biosym Technologies, San Diego, 1992..
- [28] R. Car and M. Parrinello, Phys. Rev. Lett. 55 (1985) 2471.
- [29] Priya Vashishta, private communication.
- [30] B. I. Dunlap, Adv. Chem. Phys. 69 (1987) 287.
- [31] T. Ziegler, A. Rauk and E. J. Baerends, Theoret. Chim. Acta (Berl.) 43 (1977) 261.

- [32] B. I. Dunlap, Phys. Rev. A 29 (1984) 2902.
- [33] M. Filatov and S. Shaik, J. Chem. Phys. 110 (1999) 116, Chem. Phys. Lett. 304 (1999) 429, 332 (2000) 409.
- [34] R. W. Warren and B. I. Dunlap, Phys. Rev. A 57 (1998) 899.
- [35] B. I. Dunlap and R. W. Warren, Adv. Quantum Chem. 33 (1999) 167.
- [36] P. Hohenberg and W. Kohn, Phys. Rev. 136 (1964) B864.
- [37] J. C. Slater and J. H. Wood, Int. J. Quantum Chem. 4 (1971) 3.
- [38] J. F. Janak, Phys. Rev. B 18 (1978) 7165.
- [39] C. Swope, H. C. Anderson, P. H. Berens and K. R. Wilson. J. Chem Phys. 76 (1982) 637.
- [40] R. W. Warren and B. I. Dunlap, Chem. Phys. Lett. 262 (1996) 384.
- [41] C. T. White, private communication.

Chapter 6

MOLECULAR DYNAMICS SIMULATIONS OF ENERGETIC MATERIALS

Dan C. Sorescu*, Betsy M. Rice, and Donald L. Thompson*****

* U. S. Department of Energy, National Energy Technology Laboratory,
Pittsburgh, Pennsylvania 15236

**The U.S. Army Research Laboratory, Aberdeen Proving Ground,
Maryland 21005.

***Department of Chemistry, Oklahoma State University, Stillwater,
Oklahoma 74078.

A description of the method of molecular dynamics simulations and its applications to energetic materials research is provided. We present an overview of the development of both reactive and non-reactive interaction potentials used to describe the energetic materials in different phases. Limitations as well as performances of the current models are indicated, including recent advances in reactive model development. Applications of the method to both gas and condensed phases of energetic materials are given to illustrate current capabilities.

1. INTRODUCTION

An energetic material can be characterized as belonging to the class of chemical compounds that react rapidly and release significant amounts of energy and force. Extensive experimental and theoretical attempts have been made to unravel the mix of various fundamental chemical and physical processes that occur during the conversion of the energetic material to its final products, with the hope that the relative importance and contributions of each step in the overall process can be identified and understood. Such information will lead to an increased ability to design materials and/or applications with optimal performances. However, the chemically interesting aspects of these materials (i.e., rapid reactions with significant energy release) make elucidation of the fundamental processes virtually

impossible through experimental measurements alone. Thus, as are well described in several contributing chapters to this volume, models of varying degrees of sophistication have been developed to assist in the interpretation of experimental measurements that investigate the conversion of the material to final products. Many of these models could benefit from information produced through molecular dynamics (MD) simulations. For instance, the emerging multiphase models of ignition and combustion of energetic materials make many assumptions about the fundamental processes involved. These processes include condensed phase reactions, diffusion and transport phenomena, interactions or reactions of transient intermediates in the condensed phase, evaporation of species into the gas phase, and chemical reactions in the flame. Such information is often not available, due to difficulties in measurements or in interpretation of measurements. Molecular dynamics simulation results of these fundamental processes, therefore, could assist in assessing the validity of the assumptions used in the multiphase models. The results would also provide guidance on ways in which the models should be refined. MD results could also provide necessary inputs for the models that otherwise are not available. For example, flame models have been very successful in their predictive ability if the gas-phase kinetics used in modeling the flames is properly described. The flame models require rate data, often at elevated temperatures and pressures, and thus rely on either measured or theoretical chemical predictions of such information. In lieu of experimental information, the quantum mechanical mappings of the potential energy surface provide a first step in assessing the gas-phase kinetics of the problem. If the reaction under study involves only a single step in converting from reactants to products, rates of thermally activated processes can be determined using the quantum mechanical mappings and variational transition state theory (VTST). VTST has been applied with great success to a number of gas phase reactions, reactions in liquids, gas-surface and surface-diffusion processes [1]. The theory requires a statistical mechanical description of reactants in thermal equilibrium and assumes a single transition barrier between reactants and products. For more complicated reactions that involve multiple intermediates or for reactions where the thermal distribution of energy is not achieved during the reaction time, VTST cannot provide reaction rates. Unfortunately, quantum mechanical predictions of reaction paths for reactions of energetic materials often show a great deal of complexity in that intermediate species are formed, and there are competing reaction paths [2-4] that are accessible at the elevated temperatures associated with the flame. Even with experimental information, the identification of such transient

species and their effect on the overall kinetics would be extremely difficult to determine from measured results alone. For these cases, additional dynamic investigations are required in order to clarify the full kinetic problem associated with these systems. These could be accomplished using the method of molecular dynamics.

Another area that would benefit from molecular dynamics simulation is that of sub-continuum mesoscale modeling. One application of mesoscale modeling is to investigate the role of hot spots in the initiation of an energetic material. Initiation is the response of the energetic material to external stimuli resulting in the reactions that convert the material to its final products. It has long been assumed that hot spots (regions of local high temperature) control and influence initiation of an energetic material and its sensitivity to impact [5]. Although substantial effort has been invested in their characterization, hot spots have not been resolved or analyzed through direct experimental measurement. The critical sizes of hot spots leading to ignition of energetic materials are estimated to be within the micron-millimeter range [6], a spatial regime that is appropriately modeled through sub-continuum mesoscale simulations. The mesoscale models require as input the constitutive properties of an explosive, which are sometimes difficult to obtain through experiment. Molecular dynamics can be used to generate such information. Molecular dynamics can also be used to characterize and follow details of important time-dependent processes occurring within the localized region of microscopic defects that might result in the generation of a hot spot. Processes that can be followed include chemical reaction or coupling of the initiation energy (for example, the mechanical energy generated through shock impact) with the material corresponding to the defect and growth of a microscopic hot spot. The monitoring of these details at the atomic level might provide a portrait of the inception and expansion of a hot spot to critical sizes that might influence the sensitivity of the material.

In addition to providing information used by other models in the study of energetic materials, MD simulations can provide atomic-level details that cannot be obtained through measurement or the continuum-type models. One such process is detonation. A detonation is a reaction wave that proceeds through a material at supersonic speeds, and whose time and spatial regime is on the nanoscale. The speed and length scale of the reactions, the multiple concurrent chemical and physical processes and the extreme energies and pressures released during the events preclude direct experimental observations of the fundamental mechanisms that drive the

detonation wave. Molecular dynamics simulations, on the other hand, are not limited by the factors that make experimental observation so difficult. Another dynamical process ideally suited for investigation through molecular dynamics is that of energy transfer. The mapping of the transfer of energy through the various molecular and condensed phase modes (if applicable) would provide the energetic materials researcher important information related to how a material will respond to initiation events. Furthermore, there are a variety of stimuli that can initiate an energetic material, such as shock, impact, heating, electrical discharge, friction, and chemical incompatibility [7]. As the responses of a material to different stimuli are not always the same, the examination of the microscopic details of the material during the initiation events using molecular dynamics simulations could provide information about the different responses, and perhaps lead to ways in which the outcome of an initiation could be controlled.

These are but a few of important ways in which molecular dynamics can advance the field of energetic materials research. At this time, molecular dynamics is the most powerful theoretical technique to monitor atomic-level dynamic processes occurring in the conversion of an energetic material to products. The remainder of this chapter will describe the methods and the development of the force fields used to represent energetic materials. This chapter will review several molecular dynamics studies applied to energetic materials in the gas and condensed phases, and will illustrate how MD can be used to assist in interpretation of experimental results, complement other modeling results, calculate properties that are not amenable to measurement or other types of modeling, and to identify processes for which a fundamental understanding is not established. Throughout each topic, we hope to identify areas of research needed to advance this powerful method for the study of energetic materials.

2. THE GENERAL METHOD OF MOLECULAR DYNAMICS SIMULATIONS

The general method of molecular dynamics simulations is based on evaluation of the time history of positions and linear momenta for the ensemble of particles (atoms or molecules) subject to investigation. For classical systems it is assumed that the Born-Oppenheimer approximation for separation of the electronic and nuclear degrees of freedom is valid and the evolution of the system takes place without changes in the electronic

state of the system. In particular, in the majority of cases it is considered that the system is in its ground electronic state. The temporal evolution of the system can then be obtained by integration of the equations of motion using, for example, the Lagrangian or Hamiltonian formalisms [8]. Further reformulations of the Lagrangian equations of motion can be used to perform simulations in other statistical ensembles, for example in canonical or isothermal-isobaric ensembles [9-11].

The essential element of a classical molecular simulation is the potential energy surface, from which the atomic forces used in the equations of motion are obtained. The potential energy surface consists of an ensemble of functions that can be used to describe important regions of the phase space, for example, around the equilibrium configurations or the transition states. These functions are generally written in terms of valence coordinates. The earliest procedures to obtain such potential energy functions were based on empirical fits to experimental data. However, due to the enormous improvements in the accuracy and performances of the first principles methods, the fitting of the potential energy surfaces can now be done almost exclusively using the data provided by *ab initio* or density functional theory methods. The MD method and practical implementations of it for both gas- and condensed-phase molecular dynamics simulations (including those of detonation) have been well described in other reviews and will not be repeated here [12,13].

The immense progress of the *ab initio* methods from the past decade has allowed in turn the development of a new approach for simulation of molecular systems, namely *ab initio* molecular dynamics. In this case the forces between atoms are calculated directly from the electronic structure and consequently the need for development of potential energy surface functions is eliminated. For example, in the Car-Parrinello approach [14] to *ab initio* molecular dynamics, the electronic configuration is described using the Kohn-Sham formulation of the density functional theory with the Kohn-Sham orbitals expanded in plane-wave basis sets [15-17]. A specific characteristic of the Car-Parrinello approach is its use of a set of fictitious dynamical equations for the expansion coefficients that are propagated adiabatically with respect to the nuclei. As a result the system is in its electronic ground state and the electrons follow the nuclear motion adiabatically. The Car-Parrinello approach has so far had only limited application in simulations of energetic systems [18, 19] due to the very large computational requirements involved. However, it can be expected that further developments of the method and advances in computer hardware will

lead to growing use of the *ab initio* molecular dynamics methods to describe complex molecular systems.

A notable reformulation of the equations of motion was proposed by Maillet et al. [20] to address shock properties of materials and is called “uniaxial Hugoniot molecular dynamics.” This method efficiently evaluates the shock Hugoniot curve of a material using constrained molecular dynamics. The states of a material that comprise the Hugoniot curve provide structural and thermodynamic information of a material subjected to varying shock strengths, and are often used to provide insight into performances and behavior of an energetic material. The Hugoniot states are those that satisfy the Hugoniot relation [21]:

$$H = E - E_0 - \frac{1}{2}(P + P_0)(V_0 - V) = 0 \quad (1)$$

where E and V are the specific internal energy and volume, respectively, and P is the pressure. The term *specific* refers to the quantities normalized to unit mass and the subscript “o” denotes the quantity in the quiescent, unshocked material.

Two conventional methods exist for calculating the shock Hugoniot curve using molecular dynamics: The first involves using canonical or isothermal-isobaric molecular dynamics to evaluate the Equation of State (EOS) of the material over a range of T , V , and P and extracting the conditions for which Equation (1) is satisfied [22]. The second is a direct calculation of the state of the material behind the shock discontinuity in a large-scale microcanonical shock-wave simulation [23]. Both methods are straightforward, but can be extremely computationally demanding. For example, the first procedure requires several molecular dynamics simulations to generate a single point on the shock Hugoniot curve. Even though the size of the simulations can be relatively small (a few hundred atoms), the requirement of having to generate a large number of (T, V, P) points can lead to prohibitive computational costs. In the second procedure (the direct calculation of the state of the material behind the shock wave), a single simulation will provide the information needed for a point on the shock Hugoniot curve. However, this calculation requires that sufficient material exists to monitor a shock wave propagating through the material. Thus, such simulations require large numbers of particles. In the method introduced by Maillet et al. [20], the equations of motion for the system are formulated such that the system is constrained to produce time-averaged properties that lie on the shock Hugoniot curve. Since each point on the shock Hugoniot curve can be obtained in a single small-scale simulation using these equations of motion, this is a considerably more efficient method

to determine the shock properties of a material than through generating the EOS or simulating shock wave propagation through a material.

3. MOLECULAR DYNAMICS STUDIES OF ENERGETIC MATERIALS

3.1 Gas-Phase Reactions of Energetic Materials

Whether an energetic material decomposes gently (e.g., in a cook-off experiment) or violently (e.g., in a detonation), a lot of the chemistry, energy release, and certainly “useful work” involves gas-phase reactions. Thus, it is important to know the rates and mechanisms of the gas-phase reactions. A decomposing energetic material such as RDX emits a “vapor” comprising a variety of species (these include RDX molecules and large and small radicals) which then undergo unimolecular and bimolecular reactions. A burning solid or liquid energetic material comprises a complex “chemical soup” that is not easily probed, so experiments have been of limited benefit in exploring these reactions because of the speed at which they occur and because several key species are not detectable by the usual methods. Thus we still do not fully understand the chemical decomposition of even RDX, perhaps the most studied of all energetic materials. In fact, even the initial decomposition steps are not firmly established.

This chemistry presents an equally difficult challenge to theory; nevertheless, given the limitations of experiments, we must look to theory if we are to resolve the decomposition mechanisms of energetic materials. Reliable, accurate theoretical predictions of reaction rates are still limited to few-atom, few-electron systems, and the sizes of many of the species of interest in energetic materials are enormous in comparison. The first step for the theorist is to determine the potential energy surface, at least the critical points leading from reactants to products, although one would really like to know the full topology of the potential. The sizes of most energetic molecules precludes the use of the highest levels of *ab initio* methods and, of course, the very large number of degrees of freedom can mean a prohibitive number of energy points are needed to describe the potential energy surface. Nevertheless, as we will discuss below, much progress is being made here. Once the potential energy surface is known, there are various approximate methods for computing rates (rigorous quantum-mechanical treatments are not feasible except for few-atom reactions). If the critical points on the potential energy surface are well characterized (i.e., energies and frequencies are determined) and the statistical assumption is valid (and it often is), then

it is straightforward to compute rates with a transition-state theory (TST). The TST approaches provide rates for specific steps in an assumed mechanism and thus are useful in a mechanistic analysis of a complex decomposition process. Statistical rate calculations are especially useful in providing kinetic parameters needed in detailed phenomenological modeling of flames.

Molecular dynamics simulations are attractive because they can provide not only quantitative information about rates and pathways of reactions, but also valuable insight into the details of how the chemistry occurs. Furthermore, a dynamical treatment is required if the statistical assumption is not valid. Yet another reason for interest in explicit atomic-level simulations of the gas-phase reactions is that they contribute to the formulation of condensed-phase models and, of course, are needed if one is to include the initial stages of the vapor-phase chemistry in the simulations of the decomposition of energetic materials. These and other motivations have lead to a lot of efforts to develop realistic atomic-level models that can be used in MD simulations of the decomposition of gas-phase energetic molecules.

In this section we review the current status of efforts to determine potential energy surfaces and to use them to study the rates and mechanisms of key energetic materials. Given the wide range of chemical systems that can be classified as an *energetic material* we cannot exhaustively cover the field, thus we limit the review to those molecules for which, in our opinion, there is the greatest interest and ongoing research. Our focus is nitro and nitramine compounds. For the sake of providing a relatively clear theme for this complicated subject, we will concentrate first on hexahydro-1,3,5-trinitro-*s*-triazine (RDX) to illustrate the state of affairs for one of the most complex gas-phase chemical dynamics problems. We will then discuss octahydro-1,3,5,7-tetranitro-1,3,5,7-tetrazocine (HMX), dimethyl nitramine (DMNA) and nitromethane with the same strategy. Finally, we will discuss a few other relevant molecules and some of the decomposition products of energetic molecules.

3.1.1 RDX: Initial Decomposition Reactions

The energetic molecule that has received the most attention, due in large part to its practical importance (it certainly does not present easy kinetics problems!), is RDX. In spite of all the interest and attention it has received from both experimentalists and theorists, there is still uncertainty about the initial decomposition steps of RDX.

A brief sketch of what we know about the kinetics of RDX decomposition is needed for context for the discussion of the simulation studies. In most experiments the data are taken with little experimental control, with the observations complicated by the rapid release of large amounts of energy, and with the liquid or solid undergoing phase transitions and chemical reactions to form small gaseous molecules such as N_2O , H_2O , H_2CO , HCN , NO , NO_2 , CO , and CO_2 . The reaction mechanisms involve many sequential, branched pathways, which are strongly dependent on the experimental conditions. It is not our purpose here to try to sort out the mechanisms for the various conditions, but we do need, for foundation, to discuss the experimental observations relevant to the elementary gas-phase reactions.

The first experimental determination of the activation energy E_a was done in 1949 by Robertson [24]. His studies of liquid RDX yielded a value of 47.5 kcal/mol for E_a . Subsequent experiments seem to confirm that the E_a value is in the range 47 to 48 kcal/mol. Cosgrove and Owen [25] concluded that the decomposition occurs in the vapor phase based on experiments carried out near the melting point. In 1969 Rauch and Fanelli [26] reported that the liquid- and gas-phase reactions yield different products. They found that the gas-phase reaction produced NO_2 and the liquid-phase reaction N_2O and CO_2 . It has been widely accepted that N-N bond fission to yield NO_2 is the initial step in the decomposition. However, it has been difficult to firmly establish that as fact because of the difficulties in making kinetics measurements and the unreliability of *ab initio* predictions for molecules of this size.

In modeling studies of the decomposition it is usually assumed that RDX enters the vapor phase before dissociating [27-31]. These models usually assume a "global reaction" for the decomposition and thus are not dependent upon the details of the dissociation mechanism. Presumably the availability of such a mechanism could lead to refinement in the modeling.

Recently, Long *et al.* [32] reported the results of a series of experiments in which they studied RDX decomposition in open and closed ("pierced") containers to monitor the kinetics as a function of the extent of reaction. Heating RDX in a closed container causes decomposition to occur in the liquid phase; for which they found $E_a \sim 47.8$ kcal/mol, in accord with the accepted value for N-N bond fission. They also determined $E_a \sim 23.9$ kcal/mol for evaporation, a value well below the energy for most chemical decomposition reactions.

As this discussion shows, there is good reason to assume that the condensed-phase decomposition of RDX begins with simple N-N bond

fission to give NO_2 , and this appears to be generally accepted. However, it is not clear that this is the reaction that would dominate over all ranges of temperature and pressure. And, as we will see, there is evidence that this may not be the lowest-energy pathway in isolated RDX molecules. However, it does appear that the initial reaction is unimolecular. A number of initial reactions have been suggested; these include, in addition to N- NO_2 bond fission, nitro-to-nitrite isomerization, proton transfer followed by HONO elimination, concerted ring fission (triple C-N bond rupture) to give three methylene nitramine ($\text{H}_2\text{CN-NO}_2$) molecules, and others. The most clear cut experiments and certainly the most provocative experiments were those reported by Zhao *et al.* [33] in 1988.

Zhao, Hintsä, and Lee studied the infrared multiphoton dissociation (IRMPD) of RDX in a molecular beam. They concluded that the initial decomposition involves two competing reactions: simple N- NO_2 bond fission (in accord with the generally accepted mechanisms) and a concerted molecular elimination involving fission of three C-N ring bonds to give three methylene nitramine molecules. The branching favors ring fission over N-N bond fission by about two to one. They saw no evidence for HONO elimination, in conflict with an earlier IRMPD/molecular beam study by Zuckermann, Greenblatt, and Haas [34]. The Zhao *et al.* experiments provided strong motivation for theoretical studies of the gas-phase unimolecular decomposition of RDX.

In 1991 Sewell and Thompson [35] reported the results of a classical trajectory study of RDX unimolecular dissociation that attempted to model the Zhao *et al.* conditions. They constructed an empirical, analytical potential energy surface that was sufficiently flexible that they could vary the energy barrier for the ring fission pathway. The fundamental features of the potential energy surface were based on the limited spectroscopic, thermodynamic, and kinetic data that were available for RDX. The analytical form of the potential was based on valence force fields that describe the reactant and products with the values of the potential parameters smoothly varied by arbitrary "switching" functions. The mathematical forms of the switching functions and the parameters in them were selected to give the desired behavior of the surface as the molecule decomposes. When N- NO_2 bond dissociation energy was held fixed at 47.8 kcal/mol the computed results best reproduced the IRMPD-beam results, that is, approximately two for the ratio of rates for the symmetric ring fission and simple N-N bond fission reactions. They also computed the product rotational, vibrational, and translational energy partitioning which was in general agreement with the measured distributions. A subsequent study by

Chambers and Thompson [36] refined the Sewell-Thompson potential energy surface and extended the simulations to better define the energy dependencies of the two decomposition channels. This potential energy surface could now be further improved given the information, especially *ab initio* results, that have become available since it was developed.

It is useful to consider some of the practical aspects of these kinds of simulations. A problem in MD simulations of chemical reactions is that they must be carried out at relatively high energies and then the results extrapolated to the energy range of the experiments. In a classical dynamics simulation of unimolecular reactions a microcanonical ensemble of initial phase space points are selected by a Monte Carlo procedure and then propagated by numerical integration of the equations of motion [37,38]. Lifetimes of the molecules are calculated by using criteria that defines the boundary between the reactant and the products, and the rate constant k is determined by fitting the lifetimes to $\ln(N_t/N_0) = -kt$, where N_t is the number of unreacted molecules at time t and N_0 is the number of molecules at $t = 0$.

The problem is that the simulations must be done at energies sufficiently high that a statistically significant number of reactions occur. Thus, the energy range for the simulations is usually well above the reaction threshold and experimental energies. The dynamics at the higher energies can differ from the threshold behavior, which tends to be statistical—thus, simple extrapolations may not be valid. At low energies, near threshold, the reaction rate is slow compared to the rate of intramolecular vibrational energy redistribution (IVR), leading to “statistical” reaction rates. However, at high energies the rate of reaction can be sufficiently fast that the rate is actually controlled by the IVR rate; that is, the reaction rate is determined by the rate at which energy flows into the reaction coordinate modes. Bunker and Hase [39-42] referred to this as “intrinsic non-RRKM” behavior.

The trajectory calculations of the RDX decomposition rates were carried out over the energy range 200-450 kcal/mol while the energy range probed in the IRMPD experiments [33] was estimated to be 150-170 kcal/mol. Thus the comparisons mentioned above were based on the extrapolated value for the theoretical results. Since the rates at energies near the barrier height are expected to be statistical, Shalashilin and Thompson [43] computed the RDX dissociation rates using Monte Carlo variational transition-state theory (MCVTST) [44]. An advantage of MCVTST is that it allows for a direct comparison of statistical and dynamical rates for the same potential energy surface.

The microcanonical rate coefficient $k(E)$ is given by [45]

$$k(E) = \frac{\int d\Gamma \delta[H(\Gamma) - E] \delta[q_{RC} - q_c] |\dot{q}_{RC}|}{\int d\Gamma \delta[H(\Gamma) - E]}, \quad (2)$$

where Γ is the complete set of phase space coordinates, E is the energy, $H(\Gamma)$ is the Hamiltonian, q_{RC} is the reaction coordinate, q_c is the critical surface separating reactants and products, and $|\dot{q}_{RC}|$ is the average velocity of the reaction coordinate through q_c . The reaction coordinate, q_{RC} , is a function of some or all of the internal coordinates of the system. The integral in the denominator is over the reactant phase space while the one in the numerator is over only the region of the dividing surface. Thus, the rate coefficient is the ratio of the flux through the dividing surface to the total volume of phase space available to the system at a specified energy E .

Shalashilin and Thompson [43] used MCVTST to compute the statistical rates over the energy range 170-400 kcal/mol for both the simple N-N bond fission and ring fission reactions using the Chambers-Thompson [36] potential energy surface. The computed ratio of the rates at 170 kcal/mol is in good agreement with the Zhao *et al.* [33] value. But significantly, a comparison of the individual rates at high energy shows that as the energy decreases the reaction dynamics shifts from IVR-limited to reaction-limited at about 200 kcal/mol, well above the experimental energy of 170 kcal/mol. The statistical rates at high energy are, as expected, larger than the “dynamical” rates [See Fig. 5 of Ref. 43]. There are two caveats to consider. First, if classical mechanics is used to simulate chemical reactions in a molecule or material where it is necessary to do the calculations well in excess of the energy or temperature of interest, one cannot easily extrapolate the results. The other issue to keep in mind is that it may not be appropriate to use TST rates for conditions if the energies at which reaction is occurring are well in excess of the activation barriers since the true rates may be IVR-limited. Such energies and “temperatures” may apply for some of the extreme conditions for which one may wish to model an energetic material. This would mean that one would have to use MD simulations rather than the easier, cheaper TST approaches.

Shalashilin and Thompson [46-48] developed a method based on classical diffusion theory for calculating unimolecular reaction rates in the IVR-limited regime. This method, which they referred to as *intramolecular dynamics diffusion theory* (IDDT) requires the calculation of short-time (~fs) classical trajectories to determine the rate of energy transfer from the “bath” modes of the molecule to the reaction coordinate modes. This method, in conjunction with MCVTST, spans the full energy range from the statistical to the dynamical limits. It in essence provides a means of accurately

interpolating between these limits. Guo *et al.* [49] presented a simplified IDDT, based on Kramers' energy diffusion theory that predicts the behavior of rates over the full energy range by basing the IDDT parameters on only a single value of the rate above the statistical regime. They applied the method to N-N bond fission and the concerted molecular elimination reactions in RDX [50].

The finding by Zhao *et al.* [33] that the concerted ring fission reactions provides the lowest-energy pathway for the decomposition of RDX generated considerable interest and controversy since it seemed at odds with all the other observations. The IRMPD/molecular beam results provide the only evidence for this. It is important to remember that those experiments are for isolated RDX molecules, while, except for the Zuckermann *et al.* [33] experiments, all of the other data are for condensed phases and less "controlled" conditions. As a way of reconciling these observations, Wight and Botcher [51, 52] suggested that in condensed phases that the confinement of the reactions may lead to an inhibition of the ring fission reaction because of a large "volume of activation" effect. Guo and Thompson [53] studied the relative effects of "confinement" on the two reactions. Using the Chambers-Thompson RDX potential energy surface and simple pair-wise Lennard-Jones interactions, they performed MD simulation of the decomposition of RDX in liquid xenon as a function of pressure. Their results show that the concerted molecular elimination reaction is suppressed in the condensed phase. They calculated values of 30 cm³/mol and 19 cm³/mol for the volume of activation for the ring fission and simple bond-fission reactions, respectively, indicating that the former will be dampened in the liquid phase to a greater extent than will the latter reaction.

Recently, some additional empirical evidence that the ring fission is a relatively low-energy decomposition pathway is provided by some work by Long *et al.* [32]. They observed a "gas phase" decomposition reaction with $E_a \sim 33.5$ kcal/mol. They suggested that this might be due to the ring fission reaction observed by Zhao *et al.* [33], although there may be other explanations for the observations.

Although RDX strains the limits of accurate applicability of quantum chemistry methods, they have provided valuable information about the decomposition mechanism. Ultimately, it is expected that quantum chemistry will play a vital role in elucidating the elementary reaction mechanisms for energetic materials. In fact, given the experimental difficulties for molecules such as RDX we must look to quantum chemistry. While the quantum chemistry description of the fundamental properties and elementary reactions of RDX is still "a work in progress," much has been

accomplished. We will now briefly review the progress, beginning with the *ab initio* predictions of the spectroscopic properties and finishing with the predicted decomposition pathways.

The most basic information that is needed for constructing a global potential energy surface for gas phase MD simulations is the structures and vibrational frequencies. The earliest information about gas-phase RDX molecular structures was obtained from theoretical calculations [54-58]. In 1984 Karpowicz and Brill [59] reported Fourier transform infrared spectra for vapor-phase (and for the α - and β -phase) RDX in 1984, however, their data precluded a complete description of the molecular conformations and vibrational spectroscopy. More recently, Shishkov *et al.* [60] presented a more complete description based on electron-scattering data and molecular modeling. They concluded that the data were best reproduced by RDX in the chair conformation with all the nitro groups in axial positions.

Wallis and Thompson [61] developed a potential energy surface using these spectroscopic and theoretical data and used it in molecular dynamics simulations to study the chair-to-boat conformational inversion. They followed up this study with simulations of the RDX conformational changes in dense xenon gas as a function of concentration. Since then a great deal more has been learned about the details of the potential from quantum chemistry calculations and could be used to improve the Wallis-Thompson model.

Rice and Chabalowski, [62] Harris and Lammertsma [63], and Vladimiroff and Rice [64] have reported density functional theory (DFT) and second-order Moeller-Plesset (MP2) results that greatly clarify many of the structural details of the RDX gas-phase conformations, the energy barriers between them, and provide predictions of the vibrational frequencies.

Although these studies provide critical basic information necessary for simulating RDX, more germane are the *ab initio* calculations that explore the decomposition pathways. Unfortunately, although several studies have been reported, no definitive conclusions about the lowest-energy pathway have emerged. The first quantum chemistry prediction for the decomposition paths for RDX was reported in 1986 by Melius and Binkley [65, 66]. They predicted a detailed model for the decomposition of RDX based on the bond-additivity-corrected-Moeller-Plesset-fourth-order (BAC-MP4) method. They predicted that the first step is N-N bond fission eliminating NO₂, requiring ~48 kcal/mol, followed by breaking up of the resulting ring fragment to give H₂CN and 2H₂C=N-NO₂. This is not completely consistent with the Zhao *et al.* gas-phase experiment [33.] Also,

the concerted triple bond-fission molecular elimination pathway was beyond the scope of their method. The Zhao *et al.* [33] experiments prompted attempts by quantum chemists to resolve the mechanism. Habibollahzadeh *et al.* [57] reported semiempirical, *ab initio*, and DFT predictions of energy barrier for the concerted ring fission channel of 72-75 kcal/mol, clearly in disagreement with experiment [33]. Wu and Fried [67] reported a study in which they used gradient-corrected DFT to evaluate the energy barriers for simple N-N bond fission and ring fission. They computed values of 34.2 and 52.5 kcal/mol, respectively, for the energy barriers. They used simple transition-state theory to predict the Arrhenius frequency factors and found that they differ only by a factor of seven, thus they predict that the NO₂ elimination channel is dominant. Yet another DFT study has been reported by Chakraborty *et al.* [2]. They computed (zero-point energy corrected) values of 39 and 59 kcal/mol for, respectively, the N-N bond and ring fission channels. They also investigated the HONO elimination path and found it to be competitive with NO₂ elimination, with a zero-point energy corrected barrier of 40 kcal/mol.

The mechanism for the gas-phase decomposition of this important energetic molecule remains unresolved and controversial. Only one well-defined experiment has been done [33]. The quantum chemistry studies have yet to resolve the matter.

3.1.2 HMX: Initial Decomposition Reactions

There have been no experimental studies of the gas-phase decomposition of HMX, although a few theoretical studies have been reported. Melius [65, 66] used BAC-MP4 to predict that NO₂ loss is the dominant initial reaction with an energy barrier ~48 kcal/mol. Zhang and Truong [68] carried out rate calculations using a direct *ab initio* method. The potential energy was computed using hybrid nonlocal B3LYP DFT and the rates were calculated based on variational transition-state theory for the microcanonical and canonical distributions. The computed temperature dependence of the rate constant differs somewhat from that obtained by Melius [65, 66], which is in accord with some experimental data while the Zhang-Truong prediction agrees with other data. The theoretical calculations are for isolated HMX molecules while the experimental data are for condensed-phase HMX. Zhang and Truong [69] followed up their first study of HMX with one, using the same level of theory, in which they used a master equation approach to examine both the NO₂ and HONO elimination channels. They calculated barriers of 44.17 and 47 kcal/mol, respectively, for these pathways. Almost concurrently, Chakraborty *et al.* [3] published

DFT calculations that predict that the dominant initial decomposition pathway is consecutive HONO eliminations. Their calculations also predict that NO_2 elimination and the concerted ring fission are significant channels.

3.1.3 DMNA: A Prototypical Nitramine

Dimethylnitramine has been used as a simple model for cyclic nitramines because it is easier to deal with experimentally and theoretically than RDX and HMX, and it undergoes some of the same kinds of reactions: N- NO_2 bond fission, nitro-nitrite isomerization (which can be followed by NO elimination), and HONO elimination. However, even though it seemingly presents fewer problems than do the large nitramines, its decomposition mechanism is not fully resolved.

Sumpter and Thompson [70] used DMNA as a prototypical nitramine in one of the earliest molecular dynamics simulations of gas-phase decompositions via competing pathways. The studies focused on practical aspects of simulating unimolecular reactions in large molecules (e.g., the influence of the details of the potential energy surface) and the fundamental dynamics (e.g., IVR) on the decomposition reactions. They carried out simulations using various models for the potential energy surfaces and for various initial energy distributions.

The focus in the reaction dynamics studies was on the NO_2 elimination channel, but they also studied the HONO elimination reactions [70]. They based the potential energy surface on experimental data but performed some minimal basis set *ab initio* calculations to determine geometries, force fields, torsional potentials, and some information about the reaction paths. The representations of the global potential energy surfaces were based on valence force fields for equilibrium structures with arbitrary switching functions operating on the potential parameters to effect smooth and (assumed) proper behavior along the reaction paths. Based on the available experiments [71-73], they assumed that the primary decomposition reaction is simple N-N bond rupture to eliminate NO_2 .

One of the more significant results of the Sumpter and Thompson [70] study was that the N-N bond fission results were about the same for two quite different potential energy surfaces. Most of the calculations were done using a "realistic" potential in which the interactions for all the motions were represented as accurately as possible. The N-N bond energy was taken to be 46 kcal/mol and represented by a Morse function. The torsional motion of the nitro group (i.e., the CNNO dihedral) has a very low frequency and was treated as a free rotor, an approximation they checked by comparing IVR results with and without a barrier to the rotation. The

methyl torsion was represented by a six-term cosine series with the parameter values based on 4-31G *ab initio* calculations. In the most realistic model they studied, all the bonds were represented by Morse functions and the bond angle bending motions by a quartic potential. They compared the N-N bond fission rates for this potential and for one in which all the angles and all the bonds except the N-N were treated as harmonic oscillators. They found insignificant differences in the rates for the two potentials. This was consistent with the results of their earlier study of IVR in DMNA [74]. The fact that the computed reaction rate is not significantly affected by treating the molecular modes not directly involved in the reaction coordinate as harmonic means that realistic simulations are possible with relatively simple models so long as the reaction coordinate mode is accurately described and correctly coupled to the “bath” modes. The harmonic assumption greatly reduces the potential energy surface problem. That this is a generally applicable approximation is shown by dynamics studies of other systems [75]. Also, it is the basis of successful theories such as RRKM and the *reaction path Hamiltonian* approach [76-78].

They also studied the competition between the simple N-N bond rupture and HONO molecular elimination channels as a function of initial energy distribution. In addition to these reactions the potential also allowed for bond fissions leading to other products, although at energies well above those for these two main pathways. The trajectory results predicted that HONO elimination *may* play a role in DMNA decomposition, however, given the qualitative nature of their characterization of the energetic and reaction coordinate (proton transfer followed by N-N bond fission) this conclusion has to be treated as tentative. Furthermore, the prediction must be qualified because they were not able (due to prohibitive computer time costs at the time for systems of this size) to study large ensembles. Yet another aspect of the study that qualifies the conclusion is that they only observed about 5% of the trajectories resulting in HONO elimination (for a barrier of 38 kcal/mol) for random distributions of energy; although they found significant enhancement in the rate for certain kinds of nonstatistical initial energy distributions, e.g., CH stretch excitations.

The lack of accurate experimental and *ab initio* information about the reaction pathways at the time limited the Sumpter and Thompson [70] studies. Since then quantum chemistry calculations have better defined the energetics and reaction coordinates for the decomposition of DMNA. Politzer *et al.* [79] studied DMNA using DFT. They predicted the N-N bond energy to be 43.8 kcal/mol, in excellent agreement with the experimental value of 43.3 kcal/mol [80]. Harris and Lammertsma [81] computed the

zero-point-energy corrected energy for the N-N bond fission to be 41.08 kcal/mol and, more recently, Johnson and Truong [82] computed the value to be 41.6 kcal/mol. The calculation shows that the transition state geometry for HONO elimination is a five-member near-planar ring with a barrier height of at least 38 kcal/mol. The fact that HONO elimination has not been seen in experimental studies may be due to the entropy requirements for it relative to that for the simple bond fission reaction.

3.1.4 Nitromethane Decomposition

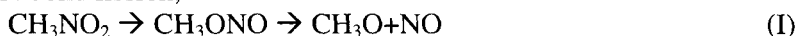
Nitromethane is the simplest and perhaps the most studied prototypical energetic material. It has been subjected to most of the applicable experimental techniques and its chemical and physical properties have been investigated for the solid, liquid, and gas phases. Significant progress in theoretically modeling of nitromethane in the various phases is being made. It appears that the initial steps in the chemical decomposition mechanisms are the same in the liquid and gas phases [83].

The initial decomposition chemistry involves unimolecular reactions. This was the conclusion of the first gas-phase kinetics study [84] and has been repeatedly confirmed by subsequent bulb and shock-tube experiments [85, 86]. That first study used shock heating to induce thermal decomposition [84]. The data were interpreted in terms of simple C-N bond fission to give CH_3 and NO_2 . A more extensive and definitive shock-tube study was reported by Zhang and Bauer in 1997 [85]. Zhang and Bauer presented a detailed kinetics model based on 99 chemical reactions that reproduced their own data and that of other shock-tube experiments [84, 86]. An interesting conclusion is that about 40% of the nitromethane is lost in secondary reactions.

Although the mechanism is far from completely determined (which is not surprising given its complexity), there are sufficient details to invite attempts to simulate the chemistry of this prototypical energetic material. Its size permits accurate *ab initio* calculations to determine the potential energy surface of the reactions in the proposed mechanism; many of the secondary reactions are of interest in other combustion systems and have been studied by various experimental and theoretical approaches. Even a cursory discussion of the theoretical studies of secondary reactions involved in the decomposition of nitromethane is beyond the scope of this chapter; we limit the discussion to the initial decomposition steps.

The most explicit and definitive study of the decomposition of isolated nitromethane molecules is that by Wodtke, Hints, and Lee [87, 88]. They used infrared multiphoton excitation to dissociate nitromethane in a

molecular beam. They concluded that nitro-nitrite isomerization followed by O-N bond fission,



is competitive with simple C-N bond fission,



They determined the branching ratio of reaction I to reaction II to be 0.6 ± 0.2 . By modeling the reactions with RRKM theory they estimated the barrier to the nitro-nitrite rearrangement to be 55.5 ± 1.5 kcal/mol, which is about 4 kcal/mol lower than that for C-N bond rupture. Previously, there had been *ab initio* predictions of the energy barrier to nitro-nitrite isomerization [89-91], but the values were significantly higher (by 20-30 kcal/mol) than that estimated by Wodtke *et al.* based on their data, as were the values published subsequently [92, 93].

Rice and Thompson [94] developed global potential energy surfaces and performed extensive classical trajectory calculations in an effort to elucidate the initial decomposition mechanism. They considered three potential energy surfaces that differed mainly in the transition state regions, especially in the barrier heights to isomerization. The C-N bond-fission barrier was taken to be 60 kcal/mol and the barrier to isomerization for the three surfaces were 216.4, 55.1, and 47.6 kcal/mol. The purpose of the study of the surface with the very high barrier to isomerization (216.4 kcal/mol) was to examine a case in which isomerization via a saddle-point transition state was not allowed – *ab initio* calculations had predicted a high barrier (~70 kcal/mol). In spite of this extremely high barrier they observed a few cases where methyl nitrite was formed by C-N bond rupture followed by “recombination” of the CH_3 and NO_2 radical. The surface with the 55.1 kcal/mol barrier, corresponding to the value estimated by Wodtke *et al.* [88], gave a value for the branching ratio that differed from the experimental value by an order of magnitude. The surface with the barrier of 47.6 kcal/mol gave a branching ratio in agreement with experiment. This value for the barrier had been previously predicted by a semi-empirical MINDO calculation by Dewar and Ritchie [90].

In their study of the decomposition of nitromethane, Rice and Thompson [94] introduced a new approach for constructing potential energy surfaces for many-atoms systems that react via multiple pathways. The basic idea of the approach is to construct potentials that accurately describe the various equilibrium regions, e.g., reactants and products, and then write the overall global potential as $V_{\text{total}} = \sum S_i V_i$; where i denotes the various “stable” species, the V_i are the analytical potentials for those species, and the S_i are weighting functions that effect a “switching” between the potentials

V_i . The main advantage of this formalism is that it allows one to link various component surfaces to build more complex ones. Thus when an accurate, tested potential exists for some segment of a branching, sequential reaction it can be incorporated into the “new” overall potential. The forms of S_i and the values of the parameters in them must be carefully selected to ensure proper behavior along the various reaction paths. Rice and Thompson had little information about the regions of the nitromethane potential between the reactant and the products except for estimates of the barrier heights. More accurate and sophisticated switching function than they used could be developed to fit detailed information, e.g., frequencies and energies, along the reaction paths. This is an ad hoc, but more flexible and practical, method of the same spirit as the *empirical valence bond* (EVB) formalism introduced by Warshel [95]. The EVB formalism is more straightforward, but is most applicable to double-well potentials. The method has been widely used, especially with the modification introduced by Chang and Miller [96]. It can be easily applied to many-atom reactions, however, there can be complications if the potential involves more than one transition-state. An application relevant to energetic materials is a recent study of the unimolecular decomposition of HONO [97].

More accurate quantum chemistry methods for large molecules have become feasible since the Rice and Thompson [94] analytical potential was developed. The capabilities were illustrated by Manaa and Fried [98] in a DFT and *ab initio* study of the C-N bond dissociation energy for the singlet and triplet states of nitromethane.

3.1.5 Methylene Nitramine Decomposition

It is likely that theoretical methods, both *ab initio* and MD simulations, will be needed to resolve the complicated chemical decomposition of energetic materials. There are species and steps in the branching, sequential reactions that cannot be studied by extant experimental techniques. Even when experiments can provide some information it is often inferred or incomplete. The fate of methylene nitramine, a primary product observed by Zhao *et al.* [33] in their IRMPD/molecular beam experiments on RDX, is a prime example. Rice *et al.* [99, 100] performed extensive classical dynamics simulations of the unimolecular decomposition of methylene nitramine in an effort to help clarify its role in the mechanism for the gas-phase decomposition of RDX.

Zhao *et al.* [33] detected a product with mass 74 amu, which they identified as CH_2NNO_2 . There had been earlier predictions that it is formed in the dissociation of cyclic nitramines [101, 102], but this was the best

evidence that it plays a key role in the mechanism. Since it has not been isolated in the laboratory, theory could provide the only information about it.

Mowrey *et al.* [103] performed *ab initio* calculations to determine the structures, energies, and frequencies at the critical point of the possible dissociation pathways for methylene nitramine. There are three possible routes for H_2CNNO_2 decomposition. The calculations predict that simple bond fission



requires 35 ± 4 kcal/mol. Zhao *et al.* [33] did not see evidence for this reaction in their experiments. The analysis of the experiments indicated that the dissociation is mainly due to



which proceeds via a five-center transition state. Mowrey *et al.* predicted the barrier for this reaction to be 31 ± 4 kcal/mol. The third dissociation reaction is



which is the most exothermic (by ~ 75 kcal/mol) but has the highest barrier (~ 38 kcal/mol). Recently, Chakraborty and Lin [104] have performed *ab initio* calculations that predict that the HONO elimination barrier is 32.7 kcal/mol, which is lower than that for N-N fission and contrary to the Mowrey *et al.* prediction.

Rice *et al.* [99] developed a global potential energy surface based on the Mowrey *et al.* [103] results and performed extensive classical trajectory calculations to study the dynamics of the CH_2NNO_2 dissociation reactions. They calculated rates for reactions (III) and (IV) with classical barriers of 35 and 37 kcal/mol, respectively. They found that N-N bond fission dominates at low energy but that HONO elimination is competitive. Chakraborty and Lin [104] predict the opposite on the basis of their *ab initio* barriers and RRKM theory calculations. The two dissociations channels are closely competitive and it is not clear that *ab initio* methods are sufficiently reliable to distinguish between two reactions that have such similar energy requirements. Also, the Zhao *et al.* results [33] are not in accord with the theoretical predictions.

A strong motivation for the Rice *et al.* [99] simulations was to try to interpret the Zhao *et al.* [33] observations that the HONO elimination channel dominates while the N-N bond rupture reaction does not occur. A possible explanation is that the nascent CH_2NNO_2 product of the RDX ring fission reaction is highly excited and has a nonstatistical distribution of energy. Sewell and Thompson [35] estimated that it may be formed with 55 to 65 kcal/mol of energy, which is well in excess of the predicted energy

barriers to dissociation. Furthermore, the Sewell and Thompson [35] trajectory study predicted that the excitation energy is mostly confined in the vibrational modes of the CH_2NNO_2 . Rice, Grosh, and Thompson [100] used the Rice-Adams-Page-Thompson [99] potential energy surface to examine the influence of nonstatistical distributions of 57.7 kcal/mol of excitation energy on the branching ratio of the N-N bond fission and HONO elimination dissociation reactions. They computed rates for initial conditions in which the excitation energy was selectively deposited in various vibrational modes of CH_2NNO_2 . Their results show that the HONO elimination would dominate if the CH_2NNO_2 is formed with the excitation energy in vibrational modes that are strongly coupled to the reaction coordinate.

3.2 Condensed Phase Studies

3.2.1 Non-reactive Models

3.2.1.1 Early Simplified Models

The most recent approaches for developing classical force fields for molecular dynamics simulations of non-reactive processes in the condensed phase usually combine quantum mechanical information for isolated molecules with measured condensed phase properties to parameterize simple descriptions of interactions among the atoms in the system. Before the 1990s, however, computational resources required for the quantum mechanical descriptions used in developing these force fields were limited to very small molecules. Since most energetic materials are fairly large polyatomic molecules, early molecular dynamics studies of energetic materials used extremely simple models that did not represent any known material. However, when used in MD studies of processes associated with energetic materials, many of these simple models produced results that were physically realistic and consequently, they have been able to aid in interpretation of experimental results of real energetic materials. Also, molecular dynamics studies using these simple models have been valuable for developing simulation techniques for energetic materials (e.g. shock and detonation). For example, MD studies have been performed to examine shock propagation through a variety of materials described by simple models [105].

Examples of the utility of simple models for providing atomic-level details of processes occurring in energetic materials are evident in a number of MD studies performed by Tsai and co-workers [106-108]. For instance,

Tsai et al. [106] performed a series of MD simulations to identify the mechanism of growth and heating of localized hot spots associated with defects in materials. The first study examined localized heating in a rapidly-compressed monatomic BCC solid that contained vacancy clusters. The form of potential describing the interactions among the atoms in this model monatomic crystal was a simple Morse function. Peaks in the potential energy distributions were centered over the vacancy cluster, representing the strain energy associated with defect sites. Compression of the vacancy-containing lattices, applied uniformly at rates corresponding to that of shock compression, showed that the structural relaxation associated with the compression resulted in the contribution of additional potential energy to atoms surrounding the vacancy cluster. Subsequent integration of the equations of motion caused a redistribution of the excess potential energy associated with the vacancy site into kinetic energy of adjacent atoms, resulting in the localized heating of the region surrounding with the defect site. Additionally, the nascent hot spot was larger in size than that of the original vacancy. The same mechanism of hot spot heating was observed for a variety of simulations in which the relaxed lattice was compressed in one, two or three dimensions or in which the crystal was heated and again allowed to relax.

Subsequent studies were performed for a more complex crystal that consisted of cubic molecules containing eight atoms [107, 108]. This investigation supplemented the earlier study of the monatomic crystal, by exploring the mechanism of hot spot heating in molecular crystals. In this study, a three-dimensional FCC lattice consisting of the cubic molecules was subjected to a one-dimensional compression along one of the three crystal axes. As in the earlier study, the interatomic potential had a simple Morse form; however, the parameter that determines the well depth for each atom pair is dependent on whether the pair is included in the same or different cubic molecules. Defects of the lattice are introduced by removing whole molecules from the lattice. As seen in the earlier study of the monatomic crystal [106], energy due to the mechanical compression of the lattice couples with the existing strain energy at the defect sites. As structural relaxation proceeds, this excess energy is converted to kinetic energy, resulting in substantial heating of the atoms adjacent to the vacancy. The study also showed that other defects, such as kinks and slip planes, were generated during structural relaxation after compression of the lattice, resulting in additional sites of localized heating. Uniaxial compression of the FCC crystal using this model resulted in hot spots that had higher

temperatures when compressed along the [110] direction compared to uniaxial compression in the [100] direction. Such a result is consistent with experimental findings for the high explosive PETN [109].

A third study [108], using the FCC crystal consisting of cubic molecules as described in Tsai and Armstrong [107], examined transfer of energy into the internal modes of the molecules upon excitation of the translational degrees of freedom. One of the goals of this paper was to examine energy equilibration within the perfect and vacancy-filled lattice upon excitation of the translational modes of the crystal. Of particular interest is the mechanism of energy transfer due to the passage of a shock wave. In order to mimic excitation of the normal modes of a crystal that would be excited by passage of a shock wave, a sinusoidal mass velocity distribution was assigned to all (100) molecular lattice planes after thermal equilibration of a lattice compressed by 10% along the [100] direction. The results of simulations using these initial conditions showed that for crystals at low temperatures, relaxation of the excited translational modes was not efficient. At higher temperatures, however, energy transfer was faster, and the time required for the relaxation of the excited translational modes decreased with increasing temperature. Simulations performed at various temperatures and different phonon excitations consistently showed that the mechanism of energy transfer is through anharmonic scattering of molecular vibrations, and that coupling between the phonon and internal molecular modes is not great.

Another goal of the third study [108] was to determine if the energy equilibration in defect-containing crystals is consistent with the “up-pumping” theory of initiation to detonation [110]. This theory suggests that initiation to detonation is due to the thermal excitation of internal vibrational modes leading to reaction, caused by the “up-pumping” of energy transferred from shock-excited phonon modes to “door-way” modes in the reacting molecule. This theory asserts that energy transfer from the translational modes to the internal modes would be more efficient at the defect sites, due to enhancement of anharmonic coupling between the translational and molecular modes. To examine this hypothesis using the simple molecular model, Tsai [108] performed a simulation in which a lattice containing a single vacancy defect is rapidly compressed along one axis. Excitation of the lattice translational degrees of freedom resulted from relaxation of the compressed lattice and equilibration with the molecular degrees of freedom was faster than the time required for the overall structural relaxation to complete. In these simulations, the vibrational

modes of one of the molecules adjacent to the vacancy were excited directly when the compressed molecule expanded into the adjacent vacancy site. Consequently, a hot spot resulted from heating at the vacancy site due to the expansion of the compressed molecule into it. Also, the temperature of the hot spot is augmented by the heating resulting from conversion of the strain energy at the defect site, as seen in the earlier studies [106,107].

While the simulations performed by Tsai *et al.* [106-108] were designed to study hot spot formation and energy sharing between internal molecular modes and phonon modes that would be excited upon shock wave passage, these simulations did not include descriptions of the conversion of the mechanical energy of a shock wave to the potential energy associated with compression, and the effect on the subsequent excitation of phonon modes, energy exchange, structural relaxation and hot spot formation. Such a study was undertaken by Mintmire, Robertson, and White [111]. In this, three-dimensional molecular dynamics simulations were performed using a homonuclear diatomic molecular crystal with molecular centers located at FCC lattice sites. The intramolecular interaction of each diatom was modeled by a harmonic oscillator with all intermolecular interactions described by a Morse functional form. A cylindrically shaped void was introduced into this lattice by removing a number of diatoms. Also, the axis of the cylindrical void was oriented perpendicular to the direction of the shock wave propagation. Shock waves of different strengths were generated through simulated flyer-plate impact, resulting in void collapse and subsequent hot spot formation after shock wave passage. The results of these simulations indicated that for weak shock waves propagating through the crystal, the void collapses in a smooth fashion with little local vibrational heating. For the case of strong shock waves, the collapse of the void is described as “turbulent,” with molecules at the front of the void wall being ejected into the cavity upon shock wave passage. The ejected molecules strike the rear wall of the void with high velocities leading to significant excitation of the vibrational energy of the molecules at the rear wall. The results also show that, as in the Tsai study [108], that the coupling between the phonon and intramolecular modes is weak, resulting in a prolonged lifetime of the nascent hot spot generated by void collapse.

With the advent of first principles computational methods, highly scalable software and parallel computer architectures, more elaborate and accurate classical force fields than those discussed in the preceding section are being developed for predictions of physical and chemical properties of energetic solids. As indicated in section 2 of this chapter there are several

areas in which accurate atomistic models are needed. Among those of particular importance is the possibility to predict through molecular dynamics or Monte Carlo simulations the phase diagram of the energetic materials as function of a large variety of external stimuli at different conditions of temperature and pressure. Moreover, in the case of solid explosives it is important to understand the relationship between molecular structure, molecular interactions, and the corresponding crystal packing. This need is due to the fact that energetic materials have larger densities, of the order of $1.8\text{--}2.0\text{ g/cm}^3$, than do ordinary C-O-N-H organic compounds, which have values in the range $1.1\text{--}1.4\text{ g/cm}^3$. Consequently, it is of primary importance to understand why the crystal packing efficiency of energetic materials are higher than for the other ordinary organic crystals or how new energetic crystals with increased densities can be designed.

Development of the general atomistic models requires the use of classical potentials to describe both the intramolecular as well as the intermolecular interactions of the molecules of a crystal. For the intramolecular part, several potential functions have been used to describe the stretching of the interatomic bonds, the bond angle bending and the torsion of groups of four atoms or the out-of-plane motion of an atom or a group of atoms. The typical functions used to describe such intramolecular motions are Morse-type potentials for bond stretching, harmonic oscillators for angles bending and wag motions, and cosine series to describe torsional motions. The intermolecular interactions are usually assumed to be pair-additive functions that can be decomposed into van der Waals and electrostatic types of interactions. A more detailed description of the parameterization procedure and validation of different sets of force fields developed for simulation of non-reactive processes in energetic materials are detailed in the next sections.

3. 2. 1. 2. 1. Approximation of Rigid Molecular Models.

An important step toward an accurate atomistic description of the energetic molecular crystals was accomplished through the development of classical intermolecular force fields between such molecules. In a series of studies, Sorescu, Rice, and Thompson [112-117] have shown how such potentials can be parameterized successfully for use in rigid-molecule simulations of energetic materials. In this approximation the molecules are considered rigid entities with the geometry taken from experimental crystallographic data. As a result, simulations of such systems require only the availability of intermolecular potentials without considering the intramolecular interactions.

There are several areas of research where such intermolecular force fields can be useful. First, they can be used to reproduce the structural and elastic properties of crystals in different polymorphic phases [120,121]. Additionally, as the lattice energies can be obtained through direct energy minimization, these force fields can be used to determine the contributions of different types of non-bonded interactions to the total lattice energy as well as the relative stability of the lattices of different polymorphic phases. Furthermore, various regions of the phase diagram can be investigated using such potentials, particularly for temperatures and pressures close to normal conditions where the intramolecular deformations are expected to not be important [112]. The degree of usefulness of such potentials is directly dependent on the number and the types of chemical compounds that can be simulated, particularly when a general force field for different classes of compounds is envisioned. The advantage of having a robust force field, capable of reproducing the structural and energetic properties of different classes of energetic compounds leads in turn to new application areas. For example, such force fields can be used to *ab initio* predict the properties of various crystals without any prior knowledge of their experimental structure [122,123]. Such applications open the possibility to design new crystals, to test large libraries of crystal compounds for which the structural and energetic properties will be predicted without any experimental input.

In the development of the set of intermolecular potentials for the nitramine crystals Sorescu, Rice, and Thompson [112-115] have considered as the starting point the general principles of atom-atom potentials, proven to be successful in modeling a large number of organic crystals [120,123]. Particularly, it was assumed that intermolecular interactions can be separated into dispersive-repulsive interactions of van der Waals and electrostatic interactions. An additional simplification has been made by assuming that the intermolecular interactions depend only on the interatomic distances and that the same type of van der Waals potential parameters can be used for the same type of atoms, independent of their valence state. The non-electric interactions between molecules have been represented by Buckingham exp-6 functions,

$$V_{\alpha\beta}(r) = A_{\alpha\beta} \exp(-B_{\alpha\beta}r) - C/r_{\alpha\beta}^6, \quad (3)$$

while the electrostatic interactions have been assumed to be represented by simple Coulombic potentials,

$$V_{\alpha\beta}(r) = q_{\alpha}q_{\beta} / (4\pi\epsilon_0 r_{\alpha\beta}). \quad (4)$$

The atom-centered monopole charges have been determined by fitting the quantum mechanically derived electrostatic potential in the region

surrounding the van der Waals surface of the molecule of interest using CHELPG method proposed by Breneman and Wiberg [124].

In the original article dedicated to development of a force field for crystalline hexahydro-1,3,5-trinitro-1,3,5-s-triazine (RDX) [112], the Buckingham potential parameters have been obtained by fitting both the crystallographic and energetic parameters of the RDX crystal. The optimal set of potential parameters has been obtained using the procedure introduced by Williams [125] by minimizing a weighted superposition function of forces and torques plus the square of the difference between the calculated lattice energy and the corresponding experimental measured value. The number of parameters to be fitted was further reduced by using traditional combination rules to obtain the heteroatom parameters from homoatom parameters:

$$A_{\alpha\beta} = \sqrt{A_{\alpha\alpha} A_{\beta\beta}} , \quad (5)$$

$$B_{\alpha\beta} = (B_{\alpha\alpha} + B_{\beta\beta}) / 2 , \quad (6)$$

$$C_{\alpha\beta} = \sqrt{C_{\alpha\alpha} C_{\beta\beta}} . \quad (7)$$

Based on molecular packing calculations with and without symmetry constraints the lattice dimensions for RDX crystal have been reproduced to within 0.9% deviation relative to experimental results and with a very small translation and rotation (less than 1.1°) of the molecules inside the unit cell. Additionally, the lattice energy was found to be practically identical to the static lattice energy estimated based on the experimental enthalpy of sublimation ($E \approx \Delta H_0^{subl} + 2RT$).

As molecular packing calculations involve just simple lattice energy minimizations another set of tests have focused on the finite temperature effects. For this purpose, Sorescu *et al.* [112] have performed isothermal-isobaric Monte Carlo and molecular dynamics simulations in the temperature range 4.2-325 K, at ambient pressure. It was found that the calculated crystal structures at 300 K were in outstanding agreement with experiment within 2% for lattice dimensions and almost no rotational and translational disorder of the molecules in the unit cell. Moreover, the space group symmetry was maintained throughout the simulations. Finally, the calculated expansion coefficients were determined to be in reasonable accord with experiment.

In two subsequent studies Sorescu *et al.* [113,114] have shown that the intermolecular energy function developed for the RDX crystal can be used successfully to simulate two other nitramine crystals, the polycyclic

nitramine 2,4,6,8,10,12-hexanitrohexaazaiso-wurtzitane (HNIW) [113] and the monocyclic nitramine 1,3,5,7-tetranitro-1,3,5,7-tetraazacyclooctane (HMX) [114]. Both these crystals have various polymorphic phases. Particularly, the phases ϵ , β , and γ of the HNIW crystal and β , α , and δ of the HMX crystal have been considered in simulations. In all these cases the 6-exp potential parameters were those developed for the RDX crystal [112] while the Coulombic charges were fitted to the quantum mechanically derived electrostatic potentials of the individual molecules corresponding to different polymorphs. Both molecular packing and isothermal-isobaric molecular dynamics simulations (NPT-MD) predicted geometrical parameters in good agreement with experimental values for different polymorphic phases. Moreover, the calculated lattice energies for different polymorphs were found to agree with the experimentally determined ranking order. In particular, for HNIW the calculated lattice energies per molecule support the polymorph stability ranking $\epsilon > \beta > \gamma$ given by Russell *et al.* [126] while for the HMX crystal the stability ranking $\beta > \alpha > \delta$ was found in agreement with that determined experimentally by McCrone [127]. These results indicate that the proposed set of force fields is accurate not only to predict the crystallographic structure of these energetic materials but at the same time the corresponding lattice energies of different polymorphic phases.

A further study to determine the limits of transferability of their interaction potentials has been done by Sorescu, Rice, and Thompson [115] for a set of 30 nitramines crystals. This set of crystals was composed of various monocyclic, polycyclic, and acyclic nitramine molecules (see Figure 1), representative for energetic material applications. Again, through molecular packing calculations it was proved that the Buckingham potential terms obtained for RDX [112] can be successfully used to simulate the crystallographic structures and lattice energies of this set of nitramines. For most of the crystals included in the probe set, the predicted structural lattice parameters differ by less than 2% from the experimental structures with small rotations and practically no translations of the molecules in the asymmetric unit cell. Additionally, it was determined that the lattice energies are strongly dependent on the electrostatic model used. In particular, it was found that the best agreement of the calculated lattice energies with experimental data is obtained when the electrostatic charges are determined using *ab initio* methods that include electron correlation effects, such as second-order Möller-Plesset (MP2) and density functional theory (DFT) using the Becke-Lee-Yang-Parr (B3LYP) exchange correlation functional. The lattice energies calculated using the B3LYP

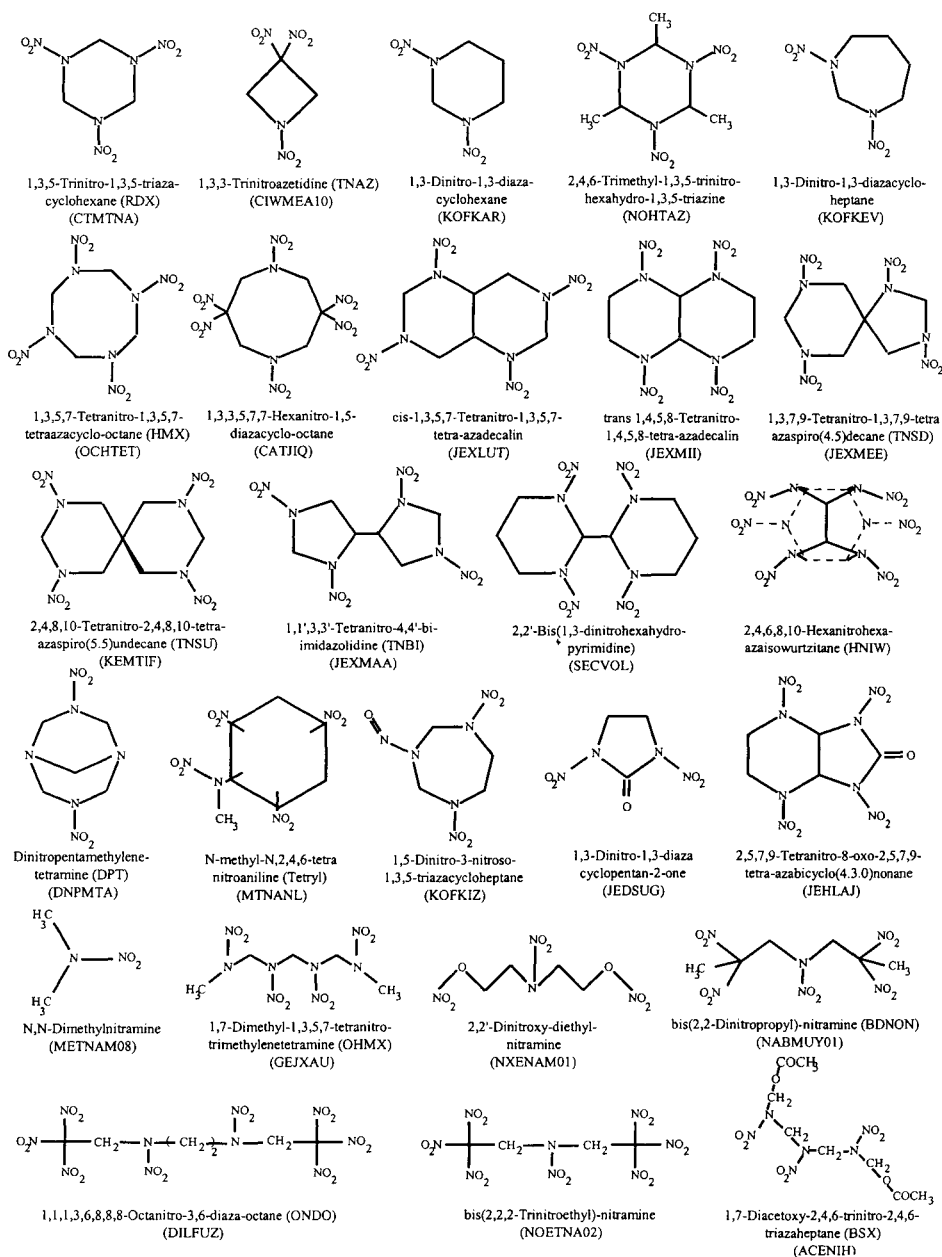


Figure 1. Illustration of the set of 30 nitramine molecules for which crystal structures were calculated. The common abbreviation of the crystal name is given in the first set of parentheses, and the *refcode* entry of the Cambridge Structural Database [118] is given in the second set of parentheses. Reproduced with permission from J. Phys. Chem. A 1998, 102, 8386-8392. Copyright 1998 Am. Chem. Soc.

charges overestimate the MP2 energies by about 2.6% while the overestimation in the case of Hartree-Fock charges is about 12.8% [115].

In a subsequent study, Sorescu, Rice, and Thompson [116] have shown that the proposed intermolecular force field for nitramine crystals can be extended beyond the class of nitramines to other energetic compounds. In this case the transferability analysis has been done for a set of 51 nitro compounds which include nitroalkanes, nitroaromatic, nitrocubanes, polynitro-adamantanes, polynitropolycyclo-undecanes, polynitropolycyclododecanes, hydroxynitro derivatives, nitrobenzonitriles, nitrobenzotriazoles, and nitrate esters (see Figure 2). As in the previous studies [112-115] the Coulombic interaction terms have been obtained through fitting of partial charges centered on each atom in the experimental arrangement of the corresponding molecules to a quantum mechanically derived electrostatic potential while the Buckingham potential terms have been transferred from the RDX case. The overall results were generally accurate for prediction of either crystallographic structures or lattice energies. As in the case of nitramine crystals, it was found that the *ab initio* method used to evaluate the set of charges has an important effect upon the total lattice energy, while the crystallographic parameters are less influenced by the set of charges used. Overall, the best agreement with experiment has been obtained for the case of the *ab initio* methods that use electron correlated techniques.

Further testing of the proposed intermolecular potential has been done by Sorescu *et al.* [116] based on NPT-MD simulations for the temperature dependence of the crystallographic parameters for two important energetic crystals, the monoclinic phase of the 2,4,6-trinitrotoluene (TNT) and the polymorphic phase I of pentaerythritol tetranitrate (PETN) crystals. In both cases, the results of molecular dynamics simulations indicate that the average structure of the crystals maintains the same group symmetry as seen experimentally and there is a good agreement between the calculated crystallographic parameters and the experimental values.

A final set of tests of this series of investigations focused on the analysis of hydrostatic compression of some representative energetic materials. Sorescu *et al.* [117] have considered the case of nitramine RDX (α -phase), HMX (β -phase), and HNIW (ϵ -phase) and the non-nitramine PETN crystal. These studies have been performed based on NPT-MD simulations at room temperature over the pressure ranges: 0-4 GPa for RDX, 0-7.5 GPa for HMX, 0-3.5 GPa for HNIW, and 0-9 GPa for PETN. In the case of the RDX, HMX, and HNIW crystals, the results indicate that the proposed potential model is able to reproduce accurately the changes in the

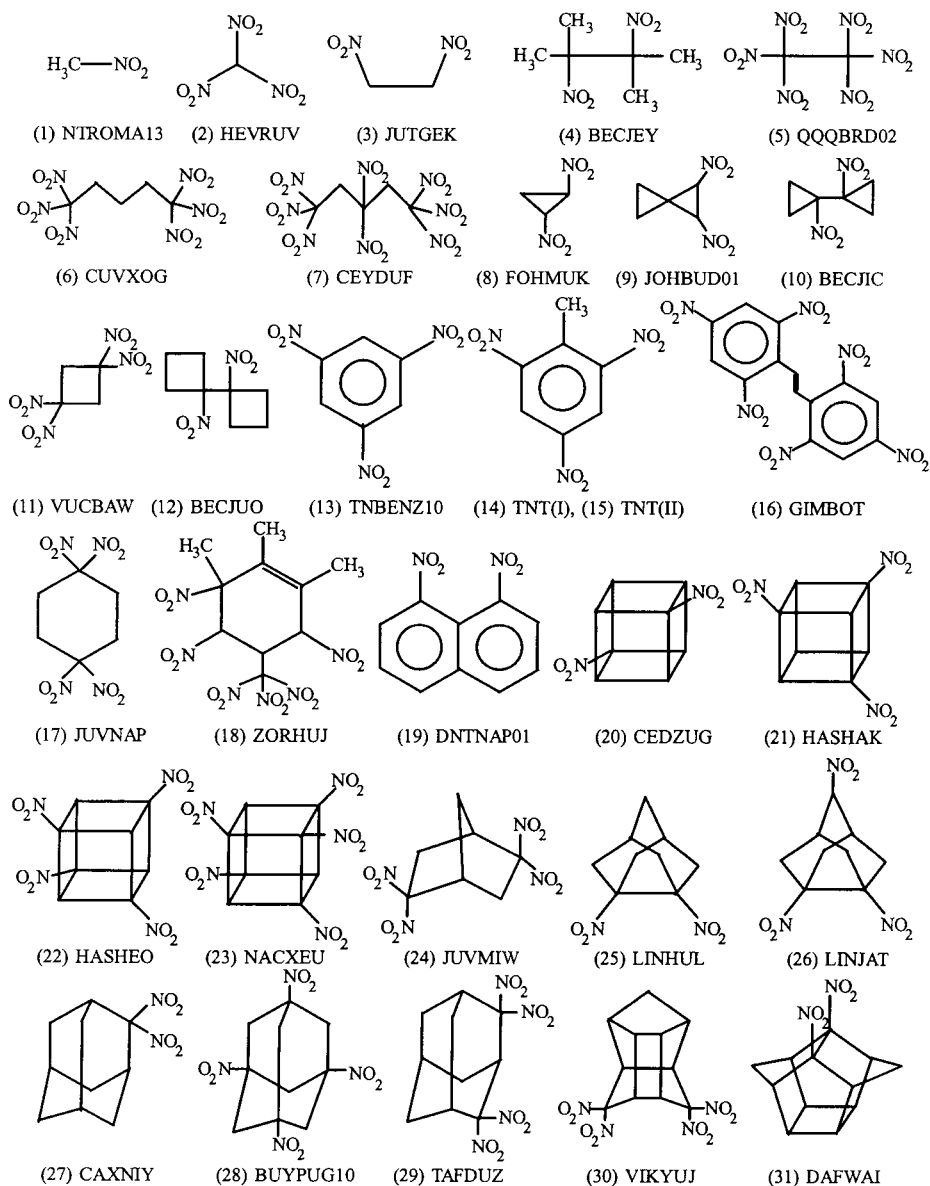


Figure 2. Illustration of the molecules whose crystal structures were studied. Where available, the corresponding *refcode* entry in the Cambridge Structural Database [118] is indicated. The corresponding names of the molecules are given in ref. 119. Reproduced with permission from J. Phys. Chem. A 1999, 103, 989-998. Copyright 1999 Am. Chem. Soc.

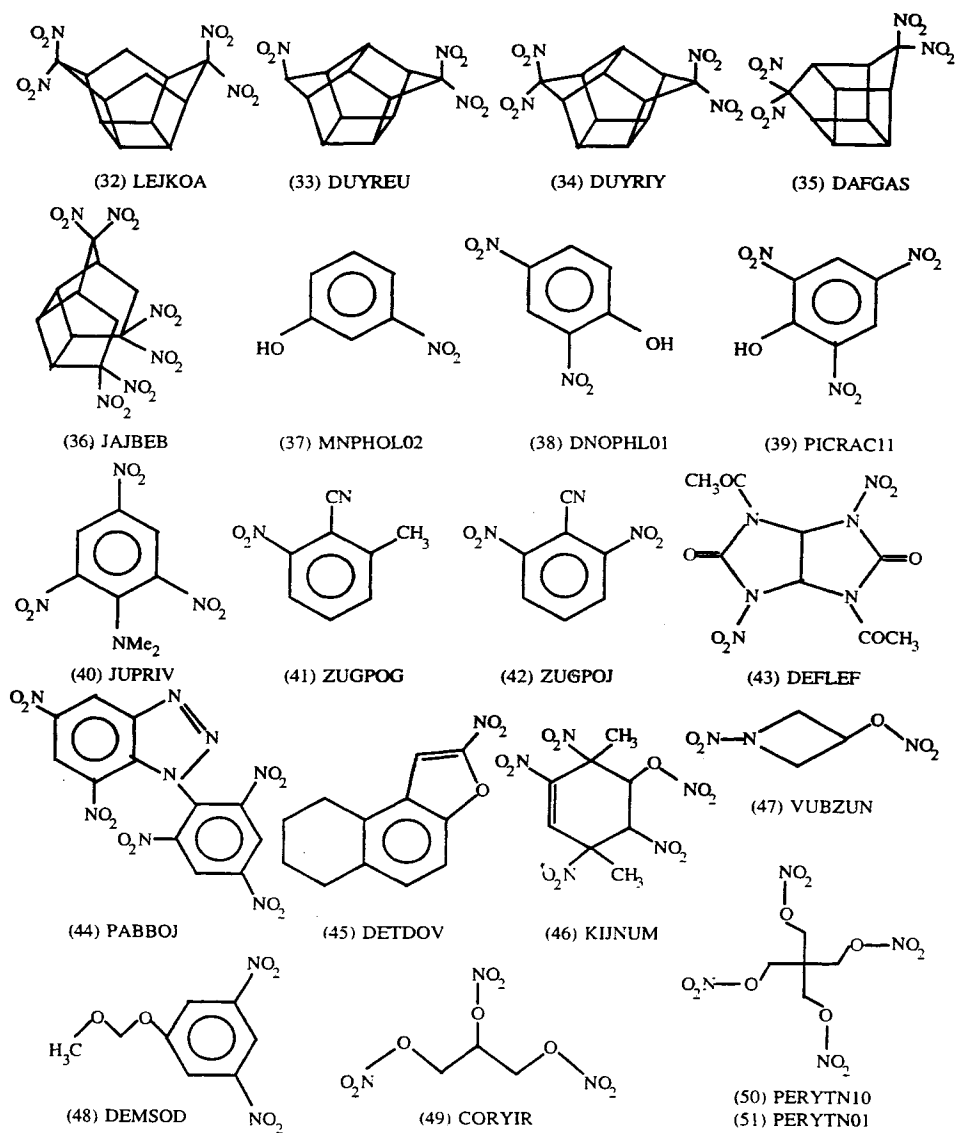


Figure 2 (continued).

structural crystallographic parameters as functions of pressure for the entire range of pressures that has been investigated experimentally. For example, the calculated bulk moduli for RDX and HMX were found to be 12.93 and 14.53 GPa in very good agreement with the corresponding values of 13.0 and 13.5 GPa, respectively [117]. In the case of the PETN crystal, the crystallographic parameters have been reproduced accurately up to about 5 GPa. Above this pressure, there have been noticed larger deviations from the experimental results which have been attributed to the limitations of the rigid-molecule approximation used for a floppy molecule such as PETN. Based on these results it was concluded that the rigid-molecule approximation can be used in the regime of lower pressures where the main effect of the initial compression is represented by the reduction of the intermolecular distances without significant molecular deformation. The corresponding pressure range depends on the type of molecular systems considered, being larger (up to 7.5 GPa) for more rigid systems such as polycyclic nitramines RDX, HMX or HNIW or smaller (up to 5 GPa) for the floppy PETN molecule.

Overall, this entire set of atomistic investigations [112-117] has demonstrated that the proposed set of intermolecular potentials can be used in conjunction with the rigid-molecule approximation as an effective tool to describe through molecular packing or molecular dynamics simulations the structural properties of energetic molecular crystals, their corresponding lattice energies and the relative stability order in the case when several polymorphic phases are present. Furthermore, it was shown that not only the low temperature structures but also the ambient equilibrium configurations or the effects of hydrostatic compression in a pressure range below 7.5 GPa can be predicted.

Despite the significant success of the above described intermolecular potentials to simulate the equilibrium properties of crystalline energetic materials there have also been identified limitations of this set of potentials. Such an example is the case of the new explosive 1,1-diamino-2,2-dinitroethylene (FOX-7) crystal. In this case the molecular geometry is characterized by extensive π conjugation, with two intramolecular hydrogen bonds between the nitro-O and the amino-H atoms. The molecular arrangement inside the crystal is that of two-dimensional wave-shaped layers with extensive intermolecular hydrogen bonding within the layers and with simple van der Waals interactions between the layers. Sorescu *et al.* [128] have shown that simple transferability of the previous nitramine force field to this system is not valid. However, an accurate description of the FOX-7 crystal in the approximation of the rigid molecules can be obtained by

keeping unmodified the H-H and C-C used in the case of nitramine crystals but refitting the attractive-repulsive N-N and O-O potential terms. Only simple charge-charge interactions have been considered to describe the electrostatic interactions in this crystal. These results indicate that transferability of the original proposed potential for nitramines crystals is limited when applied to crystals with extensive hydrogen bonding. In such cases simple electrostatic atomic monopole models might be inadequate. One way to overcome this inadequacy is to include higher electrostatic multipoles. For example, more elaborated electrostatic models to include higher electrostatic multipoles have proven to be successfully to describe hydrogen-bonded structures, π - π interactions or polar crystals [129,130].

3. 2. 1. 2. 2. Flexible Molecular Models

As the majority of physical and chemical processes of most interest for energetic materials applications take place in the regime of high temperatures and pressures in both solid and liquid phases where the molecular conformational changes become important it follows that further developments of the interaction potentials beyond the rigid-body approximation are necessary. Such developments should include both the intramolecular and intermolecular interactions which allow not only the molecular deformations but are able to describe both vibrational excitation and energy flow. Electrostatic interactions are usually considered of Coulombic type with the point charges centered on atomic nuclei being fitted to electrostatic potentials generated in quantum mechanical calculations. However, more elaborated electrostatic models to include higher electrostatic multipoles have also been used [130].

The intermolecular interactions are usually assumed to be pair-additive functions such as the Lennard-Jones 12-6 or 9-6 potentials or the Buckingham exponential-6 type of potentials and are parameterized using methods similar to those described in the previous paragraph to reproduce the crystallographic structure and the lattice energy. For the case of liquid systems the parameterization of non-bonded interactions can be done to reproduce the liquid densities and the heats of vaporization.

In order to describe intramolecular motion typical functions used are Morse-type potentials of the form

$$D_{\alpha\beta} \left[\left\{ 1 - \exp \left[-a_{\alpha\beta} (r - r_0) \right] \right\}^2 - 1 \right], \quad (8)$$

or a power-series expansion of bond distances

$$\sum_n k_n (r - r_0)^n, \quad (9)$$

for bond stretching motion, harmonic oscillators or a power series expansion

$$\sum_n k_\theta (\theta - \theta_0)^n \quad (10)$$

for bond angle bending, cosine series expansion

$$\sum_n k_{\phi,n} [1 + \cos(n\Phi - \delta)] \quad (11)$$

to describe torsional motions and various types of bond-bond,

$$k_{\alpha\beta} (r_\alpha - r_{\alpha,0})(r_\beta - r_{\beta,0}) \quad (12)$$

and stretch-bend coupling terms.

$$k_{\alpha\beta} (r_\alpha - r_{\alpha,0})(\theta_\beta - \theta_{\beta,0}). \quad (13)$$

Typically, the parameterization of the intramolecular (valence terms) force constants is done iteratively based on a set of *ab initio* data [131-133]. Such sets might include the electrostatic potentials, the energies and the first and second derivatives of the energies.

To date a handful of molecular dynamics simulations based on the use of intramolecular and intermolecular potentials have been reported for simulations of crystalline energetic materials. We will focus first on the development of the intermolecular force field for nitramine and non-nitramine systems [112-117] presented in the previous section to include the intramolecular interactions. Sorescu, Rice, and Thompson [134] have made this extension for the particular case of the prototypical explosive, nitromethane. This has been done by taking the intramolecular part of the potential as superposition of bond stretching, bond bending and torsional angles terms. In particular, Morse potentials have been used to represent bond stretches while harmonic and cosine type of potentials have been used to simulate the bending and torsional motions. These terms were parameterized based on the geometric and vibrational frequencies and the corresponding eigenvectors data obtained from *ab initio* molecular orbital calculations for the isolated molecule. The intermolecular potential was chosen as in previous studies [112-117] of the Buckingham 6-exp form plus Coulombic interactions. Molecular packing calculations using the proposed potential indicate that an accurate prediction of the crystallographic parameters with deviations less than 1.2% for the lattice edges. Moreover, NPT-MD simulations performed over the temperature range 4.2-228 K and pressure range 0.3-7.0 GPa indicate that the crystallographic parameters are well reproduced for the entire range of temperatures and pressures simulated. Furthermore, it was determined that the present potential predicts correctly an experimentally-observed 45° change in methyl group orientation in the high pressure regime relative to the low-temperature configuration. Excellent agreement was found for the calculated bulk

modules of nitromethane (6.78 GPa) with the experimental data (7.0 GPa). The agreement was confirmed not only for the structural lattice parameters but also for the distribution of H-C-N-O dihedral angles of nitromethane. The corresponding predicted values as function of either temperature or pressure reproduce very well the experimental data obtained by neutron diffraction techniques [135] or by X-ray diffraction [136]. Also, the corresponding activation energy for methyl rotation was found to be in the range of the reported experimental activation energies.

In a subsequent study, Sorescu *et al.* [137] have analyzed the transferability of the general intra- and inter-molecular potential developed for crystalline nitromethane to the liquid phase of nitromethane by computing various physical properties of the liquid as functions of temperature and pressure. A large set of static and dynamic properties of liquid nitromethane have been considered in these tests including the heat of vaporization, the variation of density with temperature (over the range 255-374 K) and pressure (over the range 0-14.2 GPa), the thermal expansion coefficient, the self-diffusion coefficients, the viscosity coefficient, the dielectric constant, the bulk modulus, and the variation of vibrational frequencies with pressure. The analyses performed using NPT-MD simulations show that the great majority of these structural, energetic and spectroscopic are well reproduced. The only exception is the dielectric permittivity, which was underestimated. This limitation was attributed to the lack of polarization effects in the intermolecular interactions.

Due to its success describing both the solid and liquid phases of nitromethane as well as its reliability and transferability for a large number of important energetic materials, Sorescu *et al.* [137] indicated that this set of potentials can be further extended to investigate the energy transfer, the solid-liquid phase transitions, or different reactions in condensed phase.

Other flexible molecular models of nitromethane were developed by Politzer *et al.* [131,132]. In these, parameters for classical force fields that describe intramolecular and intermolecular motion are adjusted at intervals during a condensed phase molecular dynamics simulation until experimental properties are reproduced. In their first study, these authors used quantum-mechanically calculated force constants for an isolated nitromethane molecule for the intramolecular interaction terms. Coulombic interactions were treated using partial charges centered on the nuclei of the atoms, and determined from fitting to the quantum mechanical electrostatic potential surrounding the molecule. After an equilibration trajectory in which the final temperature had been scaled to the desired value (300 K), a cluster of nine molecules was selected for a density function calculation from which

the atomic partial charges were determined. The force field was then updated by using the new charges calculated for the central molecule of the nine-cluster set. There is no indication that the intramolecular force constants were updated at this point. Radial distribution functions for CC, CN, and NN pairs in the system were evaluated and used in a subsequent calculation. In the second procedure, a potential energy function used by the CHARMM molecular dynamics software package [138] is assumed, in which covalent bonds and bond angles are treated as harmonic oscillators. No other intramolecular motions were explicitly treated. Intermolecular interactions were described using a standard Lennard-Jones 6-12 interaction potential plus Coulombic interactions. Partial charges were determined in the same fashion as the earlier calculation and initial force field parameters corresponded to those in the CHARMM protein library [138]. In the first step of the iterative adjustment of the force field, a series of NVT calculations were performed for nitromethane at 300 K, with the Lennard-Jones parameters adjusted until the observed heat of vaporization at 298 K and the radial distribution functions generated in the earlier calculations are reproduced. Next, the intramolecular force constants were varied until the vibrational frequencies of the isolated molecule were reproduced. A subsequent molecular dynamics simulation using the refined parameters was performed for liquid nitromethane, and the radial distribution functions and heat of vaporization were calculated. This adjustment procedure was repeated until the desired liquid state properties are reproduced. This model was then used to predict a variety of liquid phase properties, including the heat capacity, density, dielectric constant and collective dipole reorientation times.

Bunte and Sun [133] parameterized a nitrate ester force field using valence and non-bonded terms available in the COMPASS (Condensed-phase Optimized Molecular Potentials for Atomistic Simulation Studies) [139] force field. Parameterization of the force field was accomplished by performing a series of quantum mechanical calculations for two model nitrate ester compounds, methyl nitrate and ethyl nitrate, at various configurations near local minima on their respective potential energy surfaces. Energies and energy derivatives were then used to fit valence parameters, and coulombic interactions were represented by partial charges derived from a constrained fitting of the electrostatic potential. The van der Waals interactions are represented by the Lennard-Jones 9-6 function, and parameterized using condensed phase data. A series of molecular dynamics calculations were used to adjust the Lennard-Jones parameters to reproduce the cohesive energies for liquid methyl, ethyl, propyl, isopropyl, and butyl

nitrate at specified temperatures and pressures. Validation of the predictive capabilities of this model was accomplished through NPT simulations of the five nitrate ester compounds used in parameterizing the van der Waals terms. Predicted densities using this force field are within 3% for all systems. The force field was also applied to predict liquid phase properties of nitroglycerine (NG) and diethylenediglycol dinitrate (DEGDN). Densities for NG and DEGDN were within 2.0 and 0.1% of experiment at room temperatures, respectively. This force field was also used in NPT-MD simulations of crystalline Pentaerythritol Tetranitrate (PETN). Both energy minimizations and NPT-MD at $T=293$ K, 1 atm were performed. The results of both calculations are in good agreement with experimental information, particularly the NPT-MD simulations; these results predict a density with 1% of the experimental value. Predicted sublimation energy (40.49 kcal/mol) is also in good agreement with experiment (35.95 kcal/mol). This model was then applied to predict condensed phase properties of a triple-base gun propellant, JA2, the components of which are all nitrate esters [140]: 15% (by weight) NG, 25% DEGDN and 60% of nitrocellulose (with a 13.1 percent nitration level). A simulation cell representing this mix was subjected to NPT molecular dynamics at ambient conditions. The resulting density, (1.595 g/cc) averaged over ten simulations, was 1.6% greater than the measured density (1.57 g/cc).

Flexible molecule force fields were developed for nitramines DMNA [141] and HMX [142] using simple functions to describe valence, dispersion, repulsion and coulombic terms. Valence terms were parameterized with information generated using *ab initio* calculations. The repulsive and dispersive interactions are modeled using an exponential six potential form, and the parameters for C, H and O were those used in earlier molecular mechanics studies of polyethylene and poly(oxymethylene) [143,144]. Parameters for nitrogen were adjusted to reproduce the gas-phase second virial coefficient of trimethylamine as a function of temperature. Non-bonded interactions are applied to all atoms separated by three or more covalent bonds. The model was parametrized to MP2 level predictions of isolated DMNA, including the ground state structure, and portions of the PES associated with inversion and rotational motion of the nitro and methyl groups within the molecule. Coulombic interactions were described by atom-centered partial charges, determined by fitting to the MP2 electrostatic potential surrounding the molecule. A harmonic oscillator is used to describe the bond stretches, valence bends, out-of-plane wags, and the parameters were fitted to scaled SCF force constants. A simple cosine

function is used to describe torsional motions associated with methyl and nitro group rotations in DMNA, with parameters chosen to reproduce the quantum mechanically determined features of these rotations. The same model, with the exception of the values of the atomic charges, was used to model isolated HMX molecules for comparison of conformer geometries and relative energies with density functional theory predictions. For HMX, additional potential terms were included to treat vibrational motions associated with the ring, such as the N-C-N bending motion, or rotations about the C-N-C-N and N-C-N-C dihedral angles. As for DMNA, atomic charges were determined through fitting partial charges centered on each atom in the HMX conformers to the quantum-mechanically calculated electrostatic potential.

Sewell and co workers [145-148] have performed molecular dynamics simulations using the HMX model developed by Smith and Bharadwaj [142] to predict thermophysical and mechanical properties of HMX for use in mesoscale simulations of HMX-containing plastic-bonded explosives. Since much of the information needed for the mesoscale models cannot readily be obtained through experimental measurement, Menikoff and Sewell [145] demonstrate how information on HMX generated through molecular dynamics simulation supplement the available experimental information to provide the necessary data for the mesoscale models. The information generated from molecular dynamics simulations of HMX using the Smith and Bharadwaj model [142] includes shear viscosity, self-diffusion [146] and thermal conductivity [147] of liquid HMX. Sewell et al. have also assessed the validity of the HMX flexible model proposed by Smith and Bharadwaj in molecular dynamics studies of HMX crystalline polymorphs. [148].

3. 2. 1. 2. 3. Models for Simulation of Ionic Crystals

The atomistic models presented in the previous sections can also be applied to the case of ionic energetic materials. Sorescu and Thompson have illustrated this for the case of crystalline ammonium dinitramide (ADN) [149] and the low temperature phase of ammonium nitrate (AN) [150]. In the ADN case, an intermolecular potential that describes the structure of the crystal has been developed under the assumption of rigid ions. The potential is composed by pairwise 12-6 Lennard-Jones terms, hydrogen bonding terms of 12-10 form and Coulombic potential terms. The assignment of the atom-centered monopole charges has been made by fitting the quantum

mechanically derived electrostatic potential calculated over grid points surrounding the van der Waals surface of the dinitramine and ammonium ions, respectively. The potential parameters have been fitted to reproduce the lattice parameters and the experimental lattice energy of the crystal. Tests of this potential based on NPT-MD simulations in the temperature range 4.2-350 K indicated that the experimental structures can be reproduced within 3.4%. Additionally, little translational disorder occurs in thermal trajectories. However, the increase of temperature leads to the increase of rotational disorder of the ammonium ions. Based on the calculated thermal expansion coefficients it was concluded that there is an anisotropic thermal behavior of the crystal with the largest expansion along the *b* crystallographic axis.

This intermolecular potential for ADN ionic crystal has further been developed to describe the lowest phase of ammonium nitrate (phase V) [150]. The intermolecular potential contains similar potential terms as for the ADN crystal. This potential was extended to include intramolecular potential terms for bond stretches, bond bending and torsional motions. The corresponding set of force constants used in the intramolecular part of the potential was parameterized based on the *ab initio* calculated vibrational frequencies of the isolated ammonium and nitrate ions. The temperature dependence of the structural parameters indicate that experimental unit cell dimensions can be well reproduced, with little translational and rotational disorder of the ions in the crystal over the temperature range 4.2-250 K. Moreover, the anisotropic expansion of the lattice dimensions, predominantly along *a* and *b* axes were also found in agreement with experimental data. These were interpreted as being due to the out-of-plane motions of the nitrate ions which are positions perpendicular on both these axes.

The progress over the last few years in the field of atomistic simulations of energetic materials indicate that we are at the stage when general force fields for different classes of energetic materials such as nitramines [116] or non-nitramines systems [117] is possible and that potential transferability among such classes is achievable. This indicates that new areas of research such as design of new energetic materials through *ab initio* means are now within our reach. Moreover, it is now possible to develop both intra and intermolecular force fields able to reproduce the main structural, energetic, spectral and elastic properties of different phases of these materials. In turn this allows description of the temperature and pressure dependence of the physical properties, the transport properties and the corresponding transition among various phases of these materials. The

main missing part from the atomistic methodology is description of the reactions that can take place in the condensed phase. Some recent developments in this area are emphasized in the next section.

3.2.2 Reactive Models

Most models used in molecular dynamics simulations of reactions of energetic materials in the condensed phase were developed for detonation simulations, and usually represent crystals of small (typically diatomic) molecules. The functional descriptions of the interatomic interactions are simple and the exothermal formation of final products typically involves only one step rather than a sequence of reactions [151]. In reality, pure explosives tend to be large organic molecules (the majority of which consist only of carbon, nitrogen, hydrogen, and oxygen). Further they are believed to form reactive fragments in the initiation step of a detonation. The fragments then undergo a series of sequential reactions, forming many intermediate species that subsequently react before forming the final products of a detonation, which are usually simple combustion gases (in the case of CHNO explosives, these include CO, N₂, H₂, CO₂, and H₂O) [152]. Unfortunately experimental and theoretical methods have not advanced to the point of identifying the initiation step or features of the intermediate steps of these condensed phase reactions, thus information for use in developing interaction potential models for molecular dynamics simulation is not available. Also, until recently, computational limitations precluded the use of extremely complex descriptions of interaction potentials for systems in which there were large numbers of degrees of freedom. Thus, most of the models used in the detonation simulations to date are highly idealized and lack complexity in form. However, they have been extremely useful in providing guidance on simulation design and showing types of information that can be gained through molecular dynamics simulation.

The earliest models used in molecular dynamics simulation of detonation were extremely simple representations of heat release reactions [153-160]. In these, the equilibrium for each reactant diatomic molecule in the crystal corresponds to a local shallow energy minimum on the potential energy surface. This minimum is higher in energy than that of the dissociated atoms. The energy release reaction is a simple unimolecular decomposition to form atoms. While it is possible to simulate a steady reaction wave using these predissociative models [160], these models do not correctly mimic energy release reactions of real explosives. In a real explosive the initiation step is endothermic, as in the predissociative models, but the energy release is due to exothermal formation of products resulting

from association of fragments or reaction intermediates created in and after the initiation step.

More realistic models were subsequently developed to incorporate many-body effects and realistic reaction mechanisms. Implementation of these in reduced dimensionality, small-scale simulations demonstrated the importance of the inclusion of these effects [161,162]; however, the complexity of the functions and accompanying computational requirements prevent their use in large-scale molecular dynamics simulations in the condensed phase.

In the early 1990s, Brenner and coworkers [163] developed interaction potentials for model explosives that include realistic chemical reaction steps (i.e., endothermic bond rupture and exothermic product formation) and many-body effects. This potential, called the Reactive Empirical Bond Order (REBO) potential, has been used in molecular dynamics simulations by numerous groups to explore atomic-level details of self-sustained reaction waves propagating through a crystal [163-171]. The potential is based on ideas first proposed by Abell [172] and implemented for covalent solids by Tersoff [173]. It introduces many-body effects through modification of the pair-additive attractive term by an empirical bond-order function whose value is dependent on the local atomic environment. The form that has been used in the detonation simulations assumes that the total energy of a system of N atoms is:

$$V = \sum_{i=1}^{N-1} \sum_{j>i}^N \{f_c(r_{ij})[V_R - \bar{B}_{ij}V_A] + V_{NB}\} \quad (14)$$

where V_{NB} represents intermolecular interactions and the terms in the brackets denote repulsive and attractive interactions, respectively. The bond order function, \bar{B}_{ij} , has the form:

$$\bar{B}_{ij} = \frac{1}{2}(B_{ij} + B_{ji}) \quad (15)$$

where

$$B_{ij} = \left\{ 1 + G \sum_{k \neq i,j} f_c(r_{ik}) \exp[m(r_{ij} - r_{ik})] \right\}. \quad (16)$$

The range for both the intramolecular interaction term and the bond-order function is very small (in most models 3 Å) and attenuates to zero at the intramolecular cutoff distance through a switching function f_c .

The intermolecular potential term is represented by a simple Lennard-Jones function that is attenuated at short interatomic distances by a cubic spline so that at small (covalent) internuclear distances, the description of the interaction is that of the intramolecular term only. The original form of

the potential was developed to describe a simple AB molecular system, in which possible reactions include exothermal formation of homonuclear diatomic products or exchange reactions to form heteronuclear diatomic products with no net energy release. In the original Brenner model [163], the binding energy of the AB molecule is 2 eV, whereas the binding energies for the AA and BB products are 5.0 eV. Reaction of the AB molecules to form the homonuclear products results in a net energy release of 3 eV for each AB molecule.

Molecular dynamics simulations performed on diatomic 2-D and 3-D crystals using the REBO potential show that self-sustained reaction waves could be generated from shock-initiation of a flyer plate [163-167]. In these studies, a shock wave is produced by hitting one edge of a low-temperature crystal consisting of the A-B reactant molecules with a small flyer-plate consisting of layers of product molecules. The composition of the flyer plate was selected so that reactions of the flyer plate molecules would not contribute to the mechanical energy that is transferred to the reactant crystal upon impact. To simulate flyer-plate impact, the molecules in the flyer plate, located at one edge of the reactant crystal, are given an initial large velocity in the direction of shock wave propagation, and the equations of motion are integrated. The position of the shock front is monitored as a function of time during these simulations, to determine the speed of the propagating wave through the material. The initial stages of the simulation show a compression of the flyer plate molecules and edge of reactant crystal, and the subsequent initiation of a shock wave. These simulations show that with sufficient energy of the flyer plate, reactions occur behind the nascent shock front and the reaction wave proceeds, powered by the accompanying energy release. If the flyer plate velocity is too low, not enough reactions occur to sustain the reaction wave, and the speed of the shock front slows. For those simulations in which self-sustained reaction waves are generated, the speed of the shock wave propagation reaches a constant value. Further, the velocity of the shock wave is independent of the flyer-plate impact velocities above a threshold value. The threshold velocity needed to initiate self-sustained reaction waves for a fixed-size flyer plate is dependent on the size of the flyer plate. In another study [166], the equation of state of a REBO model was calculated and used to calculate its shock Hugoniot using the classical conservation equations that relate the mass, momentum and energy of a quiescent crystal with the state behind the shock wave. Outstanding agreement was found between hydrodynamic predictions of the Chapman-Jouguet state and the material properties calculated behind the shock front in a self-sustained reaction wave simulated using the REBO

potential. Construction of the shock Hugoniot of the REBO crystal has also been accomplished using calculated properties behind the shock discontinuity in shock wave simulations [168].

Since a key controversy in the initiation community has been whether initiation is a thermal or an electronic process, Rice *et al.* [167] investigated the mechanism of initiation and self-sustained detonation using the REBO potential and found, through monitoring vibrational, rotational and translational energies and atomic forces experienced by all unreacted molecules in the shock front, that this model suggests an electronic mechanism for initiation. Molecular dynamics simulations show that within a very small region immediately behind the shock discontinuity of a self-sustained detonation wave, the atoms within the mix experience completely repulsive interactions, even though the internuclear distances between the atoms are of the order of covalent bond lengths. At regions of the material with lower densities (and thus larger internuclear separations), such as in the rarefaction region of the shocked material or in the quiescent crystal, the atoms experience both attractive and repulsive interactions, depending on the local bonding environment [see Eq. (14)]. The lack of attractive interactions among the atoms immediately behind the shock discontinuity indicates that the mechanism leading to the heat release reaction in this model is, therefore, pressure-induced atomization, followed by exothermal formation of the energetically-favored product species through association of the atoms in the mix. In investigating thermal aspects, Haskins and Cook [165] subjected the 2D and 3D model material described by the REBO potential to thermal initiation and found that the reaction rates of the uncompressed crystal are significantly slower than those resulting from shock initiation. Compression of the model crystals to densities up to twice that of the uncompressed crystal resulted in reaction rates that were in closer agreement to those obtained through shock-initiated reaction. These results are all consistent with the form of the REBO potential, in which the bond order function mimics weakening of covalent bonds upon compression.

A subsequent molecular dynamics study using the REBO potential was used to demonstrate how information on reaction mechanisms gleaned from MD simulations can be used to design an explosive with specific performance properties [169]. Because the first step of the initiation reactions requires that a critical degree of compression must be attained in order for the material to atomize, there is an implication that a REBO crystal can be tailored in such a way that this critical degree of compression cannot be reached. Rice *et al.* [169] used molecular dynamics and REBO crystals that included heavy inert

diluent to test this hypothesis. The diluent molecule is a homonuclear diatomic denoted C_2 and is described by the REBO potential. However, the diluent molecule has a mass that is an order of magnitude larger than that of the A-B reactant. Also, the bond dissociation energy of the isolated C_2 molecule is set to be the same as the A-A product molecule. This bond dissociation energy was selected to ensure that formation of C-B is endothermic and formation of C-A or exchange to form C_2 result in no net energy change. The first set of simulations in this study used REBO crystals in which slabs of the heavy inert diluent molecules are inserted in between layers of pure explosive. Detonation of this tailored crystal is initiated through flyer plate impact on one edge of the layered crystal. The flyer plate first strikes the layer of pure AB explosive, whose molecules are arranged in the equilibrium position. The crystal was constructed so that there is enough pure explosive in this layer to allow the propagating reaction wave to reach its steady state velocity well before the shock front arrives at the layer containing the heavy inert diluent. After the propagating shock wave traverses the slab of diluent, it enters a second layer of pure explosive, whose molecules are arranged in the equilibrium configuration. The simulations indicated that there is a threshold size of the diluent layer beyond which detonation could not be resumed after the shock wave traversed the slab of diluent. For diluent layers whose size was below the threshold value, the shock wave that emerged from the diluent layer was strong enough to compress the pure explosive to the critical value needed to atomize the material, thus initiating the reaction sequence leading to the resumption of the self-sustained detonation. The energy of shock waves emanating from diluent layers whose sizes exceeded this threshold were insufficient to reestablish detonation, and the shock wave energy was continually dissipated as it proceeded through unreacted pure explosive. A second series of simulations investigated the detonation properties of a solid solution of AB and C_2 molecules described by the REBO potential. In these, the A-B explosive is mixed with varying concentrations of diluent to form the solid solution (25, 34 and 37% diluent concentrations). Self-sustained detonation could be initiated through flyer-plate impact for the solutions with 25 and 34% diluent concentrations; detonation could be not sustained for the solution containing 37% diluent concentration.

Haskins and coworkers [170] also examined mixed systems, in which the solid contained equimolar mixtures of AB and CD molecules, all characterized by the REBO potential. In this study, the CD molecules were identical to the AB molecules except for the values used to describe the binding energies of both reactants and products. The results showed that addition of more strongly-bound CD molecules increased the shock initiation

threshold considerably. Haskins and Cook performed additional molecular simulations to examine effects due to changes in activation barriers and reaction exothermicities through modification of the REBO parameters [170,171]. These changes can be accomplished by modifying the binding energies of the reactant and/or product diatomics. The results indicate that the sensitivity of the REBO crystal to impact was significantly reduced with decreasing reaction exothermicity. The results also indicated either extremely thick flyer plates or very large flyer plate velocities were required to initiate self-sustained detonation in REBO crystals whose reaction exothermicities were below a threshold value. The critical width of a charge (the minimum dimension for self-sustained propagation of the reaction wave) as a function of the reaction exothermicity of the REBO model was also determined by Haskins and Cook [170]. This was accomplished using results of MD simulations in which periodic boundaries were not imposed on the crystal. The simulations showed the development of a curved shock front subsequent to flyer plate impact. The curvature of the shock increased with time for systems below the critical width of the charge. This increase in curvature merely reflects the increasing amount of unreacted material behind the propagating shock front. In the early stages of the simulation, most of the unreacted material behind the shock front is located at the edges of the crystal whose directions are perpendicular to the direction of shock propagation. However, as the simulation proceeds, the amount of unreacted material increases inwardly from the edges toward the center of the material behind the shock front. Eventually, the material behind the shock front consists almost completely of unreacted material. At this point, there are not enough heat release reactions occurring behind the shock front to drive the detonation wave; thus, the detonation is quenched. This study showed that the critical width of the charge increases exponentially as the reaction exothermicity is reduced, a result observed in liquid explosives diluted with inert additives. Finally, these showed that the square of the detonation velocity is proportional to the reaction exothermicity, in agreement with classical hydrodynamic theory.

Although features of self-sustained reaction waves generated using these models are observed in detonations, the model is not representative of or parameterized to any known explosive. However, Raz and Levine [174] compared features of the REBO potential energy surface with that of a LEPS potential used to study the $\text{N}_2 + \text{O}_2$ reaction. They found that the barrier to formation of NO was remarkably comparable, and that the REBO model predicted a local energy minimum corresponding to a stable N_2O species, although the energy required to break the N-N bond of this molecule is too

small. Another REBO potential was parameterized to describe the ozone reaction $2\text{O}_3 \rightarrow 3\text{O}_2$, but it appears this model was parameterized to gas phase information only [175,176]. There is no indication that the crystal structure of solid ozone was reproduced in molecular dynamics simulations, nor any other solid state property. This model was used to study effects of nanoscale void defects on initiation; the results indicate that the initiation threshold is reduced by the incorporation of voids into the crystal lattice [175,176]. The authors suggest this reduction could be due to formation of hot spots created at the voids assuming the mechanism observed in their earlier MD study of a non-reactive diatomic solid [111]; that is, upon void collapse initiated by propagating shock wave, molecules at the void front are ejected to the back of the void wall resulting in vibrational excitation and, in this case, chemical reaction. The heat release of these reactions, coupled with relaxation of the lattice upon void collapse, would provide energy that would drive the detonation wave.

Clearly MD simulations using the simple REBO descriptions of di- and triatomic molecular crystals have been useful in developing computational methods to simulate multifaceted and complicated events (e.g. shock-initiated detonation) and have given insight into the complexity of processes occurring during such an event. However, more realistic representations of reactions are required in order to significantly advance our understanding of the basic processes that occur in shock and thermal initiation of energetic molecules. Currently, new models that represent reactions of molecules in the condensed phase are emerging to meet this need. Brenner has extended the REBO-type methodology to hydrocarbons and carbon [177,178]. As for the REBO potentials described earlier, the potential is based on the Abell-Tersoff bond formalism, in which many body effects are introduced into pair functions by bond-order functions whose values depend on local coordination and bond angles. The bond order functions were parameterized to adjust the attractive pair terms according to local coordination, bond angles, radical character and conjugation of unsaturated bonds. The functions have been shown to be transferable between bonding types and allow for breaking and formation of covalent bonds [179-181]. A recently re-parameterized form of the function provides a significantly better description of bond energies, lengths, and force constants for hydrocarbon molecules, as well as elastic properties, interstitial defect energies, and surface energies for diamond [182]. This model holds substantial promise for use in molecular simulations of explosives upon proper parameterization to account for chemical functionality.

Another reactive force field that is dependent on bond-order was developed by van Duin, Dasgupta, Loran, and Goddard [183] for hydrocarbons. The configurational energy is described as the sum of energy contributions from internal modes as well as non-bonding van der Waals and Coulombic interactions, but the parameters of the functions that describe each contribution is dependent upon the bond order of atoms involved in each description. It is assumed that the bond order between an atom pair is dependent on the interatomic separation. While this model has been used to predict bond dissociation energies, heats of formation and structures of simple hydrocarbons, it was not applied to predict condensed phase properties. However, the form of the potential should allow for condensed phase studies.

3.2.3 First Principles Simulation Models

As the computational architectures and methods advance, large-scale direct dynamics calculations using *ab initio* force fields will be used to study reactions of energetic materials. A few calculations have been performed to date using this methodology, but due to the large computational requirements and constraints on the computational methodologies, the molecular dynamics studies are limited in scope. For example, Klein and co-workers applied the Car-Parinello *ab initio* molecular dynamics method [14] to solid nitromethane [18, 19]. These studies focused on reproducing structural information and dynamics information about the methyl group rotation in nitromethane and did not investigate changes in crystallographic parameters with initial state. A more recent *ab initio* molecular dynamics study on nitromethane was performed in order to investigate electronic processes that might support a proposed initiation mechanism due to electronic excitation [184]. An earlier CASSCF study on an isolated nitromethane molecule showed that a nonradiative transition to electronic excited states is possible if the molecule is significantly distorted [185]. Density functional theory calculations of the molecular crystal under conditions of hydrostatic and uniaxial compression, shear and including molecular defects predicted structural relaxations of the crystal within which the molecular structure is not significantly deformed [184]. Under these conditions, the crystalline band gap was not reduced to the point that initiation via an electronic mechanism would be possible. *Ab initio* molecular dynamics simulations of rapid shock compression of a nitromethane crystal, molecular collisions associated with shock wave propagation, and crystal shearing were next performed to determine if dynamic effects will cause significant molecular distortion that would lead

to the reduction or closing of the crystalline band gap. While the band gap was reduced in these simulations, the reduction was not large enough to allow for significant thermal population of excited states. The authors note that little molecular deformation occurred in these simulations. Direct rupture of the C-N bond in nitromethane was observed in one simulation of high velocity molecular collisions along the c-axis of nitromethane; this same process was observed in simulations of crystal shearing. The authors conclude that closure of the crystalline band gap would require high velocity collisions between molecules at defect sites or during shearing of the crystal. To perform *ab initio* molecular dynamics simulations of such a defect-containing crystal would be extremely computationally intensive and perhaps not possible at this time.

While *ab initio* molecular dynamics simulations of condensed phase system hold great promise for accurate modeling of condensed phase processes, we anticipate that their use in large-scale simulations of reactions of energetic materials will not be feasible for several years. Therefore, until the computational limitations are eased, then molecular dynamics simulations of energetic materials in the condensed phase will be restricted to classical descriptions of reactions.

REFERENCES

- [1] T. C. Allison and D. G. Truhlar, in D. L. Thompson (Ed.), *Modern Methods for Multidimensional Dynamics Computations in Chemistry*, World Scientific, Singapore, 1998.
- [2] D. Chakraborty, R. P. Muller, S. Dasgupta, and W. A. Goddard III, *J. Phys. Chem. A* 104, (2000) 2261.
- [3] D. Chakraborty, R. P. Muller, S. Dasgupta, and W. A. Goddard III, *J. Phys. Chem. A* 105 (2001) 1302.
- [4] S. W. Bunte, B. M. Rice, and C. F. Chabalowski, *J. Phys. Chem.* 101 (1997) 9430.
- [5] F. P. Bowden and A. D. Yoffee, *Initiation and Growth of Explosions in Liquids and Solids*; Cambridge University Press, Cambridge, 1952.
- [6] C. M. Tarver, S. K. Chidester, and A. L. Nichols III, *J. Phys. Chem.* 100 (1996) 5794.
- [7] J. Van Deuren, T. Lloyd, S. Chhetry, R. Liou, J. Peck, *Remediation Technologies Screening Matrix and Reference Guide*, 4th Edition, SFIM-AEC-ET-CR-97053, U.S. Army Environmental Center, Attn: SFIM-AEC-PCT (Scott Hill/Richard Williams Building E4460, Beal Road, Aberdeen Proving Ground, MD 21010-5401).

- [8] H. Goldstein, *Classical Mechanics*, 2nd Ed., Addison-Wesley, Massachusetts, 1980.
- [9] S. Nosé, *J. Chem. Phys.* 81 (1984) 511.
- [10] W. G. Hoover, *Phys. Rev. A* 31 (1985) 1696.
- [11] W. G. Hoover, *Phys. Rev. A* 34 (1996) 2499.
- [12] D. Frenkel, B. Smith, *Understanding Molecular Simulation*, Academic Press: New York, 1996.
- [13] D. L. Thompson, Ed., *Modern Methods for Multidimensional Molecular Dynamics Computations in Chemistry*, World Scientific Pub., New Jersey, 1998.
- [14] R. Car and M. Parrinello, *Phys. Rev. Lett.* 55 (1985) 2471.
- [15] W. Kohn and L. J. Sham, *Phys. Rev.* 140 (1965) A1133.
- [16] P. Hohenber, W. Kohn *Phys. Rev.* 136 (1964) B86.
- [17] R. G. Parr, W. Yang *Density-Functional Theory of Atoms and Molecules*, Oxford University Press, New York, 1989.
- [18] M. E. Tuckerman, P. J. Ungar, T. von Rosenvinge, and M. L. Klein, *J. Phys. Chem.* 100 (1996) 12878.
- [19] M. E. Tuckerman and M. L. Klein, *Chem. Phys. Lett.* 283 (1998) 147.
- [20] J.-B. Maillet, M. Mareschal, L. Souldard, R. Ravelo, P. S. Lomdahl, T. C. Germann and B. L. Holian, *Physical Review E*, Vol. 63 (2000) 016121.
- [21] Y. B. Zeldovich and Y. P. Raizer, *Physics of Shock Waves and High-Temperature Hydrodynamic Phenomena*, Academic Press, New York, 1966.
- [22] See, for example, J. J. Erpenbeck, *Phys. Rev. A* 46 (1992) 6406.
- [23] D. R. Swanson, J. W. Mintmire, D. H. Robertson and C. T. White, *Chem. Phys. Repts.* 18 (2000) 1871.
- [24] A. J. B. Robertson, *Trans. Faraday Soc.* 45 (1949) 85.
- [25] J. D. Cosgrove and A. J. Owen, *Chem. Comm.* (1968) 286.
- [26] F. C. Rauch and A. J. Fanelli, *J. Phys. Chem.* 73 (1969) 1604.
- [27] C. F. Melius, in *Chemistry and Physics of Energetic Materials*, edited by S. Bulusu, NATO ASI 309 (1990) 51.
- [28] Y. – C. Liao and V. Yang, *J. Propulsion and Power* 11 (1995) 729.
- [29] K. Prasad, R. A. Yetter, and M. D. Smooke, *Comb. Sci. Tech.* 124 (1997) 35.
- [30] J. E. Davidson and M. W. Beckstead, *J. Propulsion and Power* 13 (1997) 375.
- [31] M. S. Miller and W. R. Anderson, in *Solid Propellant Combustion Chemistry, Combustion, and Motor Interior Ballistics*, edited by V. Yang, T. B. Brill, and W. Z. Ren, Vol. 185, of *Progress in*

Astronautics and Aeronautics, P. Zarchan, Editor in Chief (American Institute of Aeronautics and Astronautics, Reston, VA, 2000, pp. 501-531.

- [32] G. T. Long, S. Vyazovkia, B. A. Brems, and C. A. Wight, *J. Phys. Chem. A* 104, (2000) 2570.
- [33] X. Zhao, E. J. Hints, and Y. T. Lee, *J. Chem. Phys.* 88 (1988) 801.
- [34] H. Zuckermann, G. D. Greenblatt, and Y. Haas, *J. Phys. Chem.* 91 (1987) 5159.
- [35] T. D. Sewell and D. L. Thompson, *J. Phys. Chem.* 95 (1991) 6228.
- [36] C. C. Chambers and D. L. Thompson, *J. Phys. Chem.* 59 (1995) 15881.
- [37] See, e.g., L. M. Raff and D. L. Thompson in, *Theory of Chemical Reaction Dynamics*, Vol. 3, Edited by M. Baer (CRC Press, Boca Raton, FL., 1985), p. 1.
- [38] T. D. Sewell and D. L. Thompson, *Int. J. Mod. Phys. B* 11 (1997) 1067.
- [39] D. L. Bunker and W. L. Hase, *J. Chem. Phys.* 59 (1973) 4673.
- [40] D. L. Bunker and W. L. Hase, *ibid.*, 69 (1978) 4711.
- [41] W. L. Hase, in *Potential Energy Surfaces and Dynamical Calculations*, edited by D. G. Truhlar (Plenum, New York, 1981), p. 1.
- [42] W. L. Hase, in *Dynamics of Molecular Collisions*, edited by W. H. Miller, Plenum, New York, 1976, Vol. VIIB, p. 121.
- [43] D. V. Shalashilin and D. L. Thompson, *J. Phys. Chem. A* 101 (1997) 961.
- [44] R. Viswanathan, L. M. Raff, and D. L. Thompson, *J. Chem. Phys.* 81 (1984) 828; *ibid.* (1984) 3118; and references therein.
- [45] J. C. Keck, *Adv. Chem. Phys.* 13 (1967) 85.
- [46] D. V. Shalashilin and D. L. Thompson, *J. Chem. Phys.* 105 (1996) 1833.
- [47] D. V. Shalashilin and D. L. Thompson, *J. Chem. Phys.* 107 (1997) 6204.
- [48] D. V. Shalashilin and D. L. Thompson, in *Highly Excited Molecules: Relaxation, Reaction, and Structure*, edited by A. S. Mullin and G. C. Schatz, American Chemical Society, Washington, D.C., 1997, pp. 81-98.
- [49] Y. Guo, D. V. Shalashilin, J. A. Krouse, and D. L. Thompson, *J. Chem. Phys.* 110, (1999) 5514.
- [50] Y. Guo, D. V. Shalashilin, J. A. Krouse, and D. L. Thompson, *J. Chem. Phys.* 110 (1999) 5521.

- [51] C. A. Wight and T. R. Botcher, *J. Am. Chem. Soc.* 114 (1992) 8303.
- [52] C. A. Wight and T. R. Botcher, *J. Phys. Chem.* 97 (1993) 9149.
- [53] Y. Guo and D. L. Thompson, *J. Phys. Chem. B* 103 (1999) 10599.
- [54] M. K. Orloff, P. A. Mullen, and F. C. Rauch, *J. Phys. Chem.* 74 (1970) 2189.
- [55] A. Filhol, C. Clement, M. T. Forel, J. Paviot, M. Rey-Lefon, G. Richoux, P. A. Mullen, and F. C. Rauch, *J. Phys. Chem.* 74 (1970) 2189.
- [56] P. Politzer, N. Sukumar, K. Jayasuriya, and S. Ranganathan, *J. Am. Chem. Soc.* 110 (1988) 3425.
- [57] D. Habibollahzadeh, M. Grodzicki, J. M. Seminario, and P. Politzer, *J. Phys. Chem.* 95 (1991) 7699.
- [58] D. Habibollahzadeh, J. S. Murray, P. C. Redfern, and P. Politzer, *J. Phys. Chem.* 95 (1991) 7702.
- [59] R. J. Karpowicz and T. B. Brill, *J. Phys. Chem.* 88 (1984) 348.
- [60] I. F. Shishkov, L. V. Vilkov, M. Kolonits, and B. Rozsondai, *Struct. Chem.* 2 (1991) 57.
- [61] E. P. Wallis and D. L. Thompson, *Chem. Phys. Letters* 189 (1992) 363.
- [62] B. M. Rice and C. F. Chabalowski, *J. Phys. Chem. A* 101, (1997) 8720.
- [63] N. J. Harris and K. Lammertsma, *J. Am. Chem. Soc.* 119 (1997) 6583.
- [64] T. Vladimiroff and B. M. Rice, *J. Phys. Chem. A* 106 (2002) 10437.
- [65] C. F. Melius and J. S. Binkley, *Symp. (Int.) Comust. [Proc.]*, 21st, (1986) p. 1953.
- [66] C. F. Melius in *Chemistry and Physics of Energetic Materials*, edited by S. N. Bulusu, Kluwer, Dordrecht, 1990, p. 21.
- [67] C. J. Wu and L. E. Fried, *J. Phys. Chem. A* 101 (1997) 8675.
- [68] S. Zhang and T. N. Truong, *J. Phys. Chem.* 104 (2000) 7304.
- [69] S. Zhang and T. N. Truong, *J. Phys. Chem. A* 105 (2001) 2427.
- [70] B. G. Sumpter and D. L. Thompson, *J. Chem. Phys.* 88 (1988) 6889.
- [71] J. M. Flournoy, *J. Chem. Phys.* 36 (1962) 1106.
- [72] S. A. Lloyd, M. E. Umstead, and M. C. Lin, *J. Energetic Materials* 3 (1985) 187.
- [73] J. C. Mailocq and J. C. Stephenson, *Chem. Phys. Letters* 123 (1986) 390.
- [74] B. G. Sumpter and D. L. Thompson, *J. Chem. Phys.* 86 (1987)
- [75] See, e.g., K. L. Bintz, D. L. Thompson, and J. W. Brady, *Chem. Phys. Letters* 131 (1986) 398.
- [76] T. Carrington Jr. and W. H. Miller, *J. Chem. Phys.* 84 (1986) 4364.

- [77] R. A. Marcus, J. Chem. Phys. 45 (1966) 4493 ; *ibid.* 49, (1968) 2610.
- [78] K. Fukui, Accounts Chem. Res. 14 (1981) 363.
- [79] P. Politzer, P. Lane, M. E. Grice, M. C. Concha, and P. C. Redfern, J. Mol. Struct. (Theochem) 338 (1995) 249.
- [80] S. A. Lloyd, M. E. Umstead, and M. C. Lin, J. Energy Mater. 3 (1985) 187.
- [81] N. J. Harris and K. Lammertsma, J. Phys. Chem. 101 (1997) 1370.
- [82] M. A. Johnson and T. N. Truong, J. Phys. Chem. A 103 (1999) 8840.
- [83] See, e.g., E. Woods III, Y. Dessiaterik, R. E. Miller, and T. Baer, J. Phys. A 105 (2001) 8273.
- [84] K. Glänzer and J. Troe, Helv. Chim. Acta 55 (1972) 2884.
- [85] Y.-X. Zhang and S. H. Bauer, J. Phys. Chem. B 101 (1997) 8717.
- [86] D. S. V. Hsu and M. C. Lin, J. Energ. Materials 3 (1985) 95.
- [87] A. M. Wodtke, E. J. Hints, and Y. T. Lee, J. Chem. Phys. 84 (1986) 1044.
- [88] A. M. Wodtke, E. J. Hints, and Y. T. Lee, J. Phys Chem.. 90 (1986) 3549.
- [89] M. L. McKee, J. Am. Chem. Soc. 107 (1985) 1900.
- [90] M. J. S. Dewar and J. P. Ritchie, J. Org. Chem. 50 (1985) 1031.
- [91] M. L. McKee, J. Am. Chem. Soc. 108 (1986) 5784.
- [92] R. P. Saxon and M. Yoshimine, Can. J. Chem. 70 (1992) 572.
- [93] M. L. McKee, J. Phys. Chem. 93 (1989) 7365.
- [94] B. M. Rice and D. L. Thompson, J. Chem. Phys. 93 (1990) 7983.
- [95] A. Warshel, Acc. Chem. Res. 14 (1981) 284.
- [96] Y. T. Chang and W. H. Miller, J. Phys. Chem. 94 (1992) 5884.
- [97] Y. Yin and D. L. Thompson, J. Chem. Phys., in press.
- [98] M. R. Manaa and L. E. Fried, J. Phys. Chem. A 102 (1998) 9884.
- [99] B. M. Rice, G. F. Adams, M. Page, and D. L. Thompson, J. Phys. Chem. 99 (1995) 5016.
- [100] B. M. Rice, J. Grosh, and D. L. Thompson, J. Chem. Phys. 102 (1995) 8790.
- [101] M. Farber and R. D. Srivastava, Chem. Phys. Letters 64 (1979) 307.
- [102] M. A. Schroeder, Proceeding of the 18th JANNAF Combustion Meeting, Vol. II, (1981) p. 395.
- [103] R. C. Mowrey, M. Page, G. F. Adams, and B. H. Lengsfeld III, J. Chem. Phys. 93 (1990) 1857.
- [104] D. Chakraborty and M. C. Lin, in Solid Propellant Chemistry, Combustion, and Motor Interior Ballistics, vol. 185, Progress in Astronautics and Aeronautics, edited by V. Yang, T. B. Brill and W.-

- Z. Ren , American Institute of Aeronautics and Astronautics, Inc., Reston, VA, (2000) pp. 33-71.
- [105] B. L. Holian, Shock Waves, 5 (1995) 149.
- [106] D. H. Tsai, J. Chem. Phys. 95(1991) 7497.
- [107] D. H. Tsai and R. W. Armstrong, J. Phys. Chem. 98 (1994) 10997.
- [108] D. H. Tsai, Proceedings of the Materials Research Society Symposium on Decomposition, Combustion and Detonation Chemistry of Energetic Materials", 418, Pittsburgh, PA, (1996) p. 281.
- [109] J. J. Dick, Proceedings of the Materials Research Society Symposium on Structure and Properties of Energetic Materials, 296, Pittsburgh, PA, (1993) p. 75.
- [110] S. Chen, W. A. Tolbert, and D. D. Dlott, J. Phys. Chem. 98 (1994) 7759.
- [111] J. W. Mintmire, D. H. Robertson and C. T. White, Physical Rev. B, 49 (1994) 14859.
- [112] D. C. Sorescu, B. M. Rice and D. L. Thompson, J. Phys. Chem. B 101 (1997) 798.
- [113] D. C. Sorescu, B. M. Rice, and D. L. Thompson, J. Phys. Chem. B 102 (1998) 948.
- [114] D. C. Sorescu, B. M. Rice, and D. L. Thompson, J. Phys. Chem. B 102 (1998) 6692.
- [115] D. C. Sorescu, B. M. Rice, and D. L. Thompson, J. Phys. Chem. A 102 (1998) 8386.
- [116] D. C. Sorescu, B. M. Rice, and D. L. Thompson, J. Phys. Chem. A 103 (1999) 989.
- [117] D. C. Sorescu, B. M. Rice, and D. L. Thompson, J. Phys. Chem. B 103 (1999) 6783.
- [118] F. H. Allen and O. Kennard, Chem. Des. Autom. News. 8 (1993) 31.
- [119] (1) Trideutero-nitromethane (NTROMA13). (2) Trinitromethane (HEVRUV). (3) 1,2-Dinitroethane (JUTGEK). (4) 2,3-Dimethyl-2,3-dinitrobutane (BECJEY). (5) Hexanitroethane (QQBRD02). (6) 1,1,1,3,5,5,5-Heptanitropentane (CUVXOG). (7) 1,1,1,3,3,5,5,5-Octanitropentane (CEYDUF). (8) trans-1,2-Dinitrocyclopropane (FOHMUK). (9) trans-1,2-Dinitro(2,2)spiro-pentane (JOHBUD01). (10) 1,1'-Dinitrobicyclopentyl (BECJIC). (11) 1,1,3,3-Tetranitrocyclobutane (VUCBAW). (12) 1,1'-Dinitrobicyclobutyl (BECJUO). (13) 1,3,5-Trinitrobenzene (TNBENZ10). (14) 2,4,6-Trinitrotoluene, orthorhombic form. (15) 2,4,6-Trinitrotoluene, monoclinic form. (16) 2,2',4,4',6,6'-

Hexanitrostilbene (GIMBOT). (17) 1,1,4,4 Tetranitrocyclohexane (JUVNAP). (18) 1,2,3-Trimethyl-r-3,c-4,c-6-trinitro-t-5-trinitro-methylcylohex-1-ene (ZORHUI). (19) 1,8-Dinitronaphthalene (DNTNAP01). (20) 1,4-Dinitrocubane (CEDZUG). (21) 1,3,5-Trinitrocubane (HASHAK). (22) 1,3,5,7-Tetranitrocubane (HASHEO). (23) 1,2,3,5,7-Pentanitrocubane (NACXEU). (24) 2,2,5,5-Tetranitrobicyclo(2.2.1)heptane (JUVMIW). (25) 3,7-Dinitronoradamantane (LINHUL). (26) 3,7,9-Trinitronor-adamantane (LINJAT). (27) 2,2-Dinitroadamantane (CAXNIY). (28) 1,3,5,7-Tetranitroadamantane (BUYPUG10). (29) 2,2,4,4-Tetranitroadamantane (TAFDUZ). (30) 8,8,11,11-Tetranitropentacyclo(5.4.0.0^{2,6}.0^{3,10}.0^{5,9})undecane (VIKYUJ). (31) 2,6-Dinitrohexacyclo(5.4.1.0^{2,6}.0^{3,10}.0^{5,9}.0^{8,11})dodecane (DAFWAI). (32) Decahydro-2,2,5,5-tetranitro-1,6:3,4-dimethano-cyclobuta(1,2:3,4)dicyclopentene (LEJKO). (33) 5,5,11-Trinitrohexacyclo(5.4.1.0^{2,6}.0^{3,10}.0^{4,8}.0^{9,12})dodecane Trinitro-1,3-bis(homopentaprismene) (DUYREU). (34) 5,5,11,11-Tetranitrohexacyclo(5.4.1.0^{2,6}.0^{3,10}.0^{4,8}.0^{9,12})dodecane (DUYRIY). (35) 6,6,10,10-Tetranitropenta-cyclo(5.3.0.0^{2,5}.0^{3,9}.0^{4,8})decane (DAFGAS). (36) 4,4,8,8, 11,11-Hexanitropentacyclo(5.4.0.0^{2,6}.0^{3,10}.0^{5,9})undecane (JAJBEB). (37) m-Nitrophenol, monoclinic form (MNPOL02). (38) 2,4-Dinitrophenol (DNOPHL01). (39) 2,4,6-Trinitrophenol (Picric acid) (PICRAC11). (40) N,N-Dimethyl-2,4,6-trinitroaniline (JUPRIV). (41) 6-Methyl-2-nitrobenzonitrile (ZUGPOG). (42) 2,6-Dinitrobenzonitrile (ZUGPOJ). (43) 1,4-Diacetyl-3,6-dinitrotetrahydro-imidazo-(4,5-d)imidazole-2,5(1H,3H)-dione,3,6-Diacetyl-1,4-dinitro-glycoluril (DEFLEF). (44) 5,7-Dinitro-1-picrylbenzotriazole (PABBOJ). (45) 2-Nitro-6,7,8,9-tetrahydronaphtho(2,1-b)furan (DETDOV). (46) 3,6-Dimethyl-c-5-nitrato-1,r-3,t-4,c-6-tetranitrocyclohexene (KIJNUM). (47) 3-Nitrato-1-nitroazetidine (VUBZUN). (48) 1-Methoxymethoxy-3,5-dinitrobenzene (DEMSOD). (49) 1,2,3-Propanetriol trinitrate, beta modification (CORYIR). (50) Pentaerythritol tetranitrate (PETN), form I (PERYTN10). (51) Pentaerythritol tetranitrate, form II (PERYTN01).

[120] A. J. Pertsin and A. I. Kitaigorodsky, *The Atom-Atom Potential Method, Applications to Organic Molecular Solids*; Springer-Verlag: Berlin, 1987.

[121] D. E. Williams in *Crystal Cohesion and Conformational Energies*, Metzger, R. M., Ed.; Springer-Verlag: Berlin, 1981: p. 3-40.

- [122] J. R. Holden, Z. Y. Du, and H. L. Ammon, *J. Comput. Chem.* 14 (1993) 422.
- [123] D. E. Williams, *Acta Cryst.* 1996, A52, 326.
- [124] C. M. Breneman and K. B. Wiberg, *J. Comput. Chem.* 8 (1987) 894.
- [125] L.-Y. Hsu and D. E. Williams, *Acta Crystallogr.* 1980, A36, 277.
- [126] T. P. Russell, P. J. Miller, G. J. Piermarini, S. Block, R. Gilardi, and C. George. AD-C048 931 (92-0134), p. 155, Apr. 91, CPIA Abstract. No. 92, 0149, AD D604 542, C-D, Chemical Propulsion Information Agency, 10630 Little Patuxent Parkway, Suite 202, Columbia, MD 21044-3200.
- [127] W. C. McCrone in *Physics and Chemistry of the Organic Solid State*, D. Fox, M. M. Labes, A. Weissberger, Eds., Wiley: New York, 1965, vol II, p.726.
- [128] D. C. Sorescu, J. A. Boatz, and D. L. Thompson, *J. Phys. Chem. A* 105 (2001) 5010.
- [129] S. L. Price and A. J. Stone, *Mol. Phys.* 51 (1987) 569.
- [130] D. J. Willock, S. L. Price, M. Leslie, and C. R. A. Catlow, *J. Comput. Chem.* 16 (1995) 628.
- [131] J. Seminario, M. C. Concha, and P. Politzer, *J. Chem. Phys.* 102 (1995) 8281.
- [132] H. E. Alper, F. Abu-Awwad, and P. Politzer, *J. Phys. Chem. B* 103 (1999) 9738
- [133] S. W. Bunte and H. Sun, *J. Phys. Chem. B* 104 (2000) 2477.
- [134] D. C. Sorescu, B. M. Rice, and D. L. Thompson, *J. Phys. Chem. B* 104 (2000) 8406.
- [135] S. F. Trevino and W. H. Rymes, *J. Chem. Phys.* 73 (1980) 3001.
- [136] D. T. Cromer, R. R. Ryan, and D. Schiferl, *J. Phys. Chem.* 89 (1985) 2315.
- [137] D. C. Sorescu, B. M. Rice, and D. L. Thompson, *J. Phys. Chem. B* 105 (2001) 9336.
- [138] B. R. Brooks, R. E. Bruccoleri, B. D. Olafson, D. J. States, S. Swaminathan, and M. Karplus, *J. Comp. Chem.* 4 (1983) 187.
- [139] H. Sun, *J. Phys. Chem. B*, 102 (1998) 7338.
- [140] S. W. Bunte and M. S. Miller, Army Research Laboratory Technical Report , ARL-TR-2496, Aberdeen Proving Ground, MD 21005, (2001).
- [141] Smith, G.D., R.K. Bharadwaj, D. Bedrov and C. Ayyagari, *J. Phys. Chem. B* 103 (1999), 705.
- [142] Smith, G.D. and R.K. Baharadwaj, *J. Phys. Chem. B* 103 (1999) 3570.

- [143] R. A. Sorensen, W. B. Liao, L. Kesner and R. H. Boyd, *Macromolecules* 21, (1998) 200.
- [144] R. A. Sorensen, W. B. Liao, L. Kesner and R. H. Boyd, *Macromolecules* 21 (1988) 200.
- [145] R. Menikoff and T. D. Sewell, *Combustion Theory and Modelling* 6 (2002) 103.
- [146] D. Bedrov, G. D. Smith, and T. Sewell, *J. Chem. Phys.* 112 (2000) 7203.
- [147] D. Bedrov, G. D. Smith, and T. D. Sewell, *Chem. Phys. Lett.* 324 (2000) 64.
- [148] D. Bedrov, C. Ayyagari, G. D. Smith, T. D. Sewell, R. Menikoff, and J. M. Zaugg, *J. Computer-Aided Materials Design* 8 (2002) 77.
- [149] D. C. Sorescu and D. L. Thompson, *J. Phys. Chem. B* 103 (1999) 6774.
- [150] D. C. Sorescu and D. L. Thompson, *J. Phys. Chem. A* 105 (2001) 720.
- [151] D. W. Brenner, "Molecular Potentials for Simulating Shock-Induced Chemistry" in *Shock Compression of Condensed Matter*, S. C. Schmidt, R. D. Dick, J. W. Forbes and D. G. Tasker, Eds. (North-Holland, Amsterdam), (1992) 115.
- [152] M. J. Kamlet and S. J. Jacobs, *J. Chem. Phys.* 48 (1968) 23.
- [153] A. M. Karo, J. R. Hardy, and F. E. Walker, *Acta Astronautica* 5 (1978) 1041.
- [154] D. H. Tsai and S. F. Trevino, *J. Chem. Phys.* 81 (1984) 5636.
- [155] D. H. Tsai in "Chemistry and Physics of Energetic Materials", ed. S. N. Bulusu (Kluwer Academic Publishers, Netherlands (1990) pp. 195-227.
- [156] M. Peyrard, S. Odier, E. Lavenir, and J. M. Schnur, *J. Appl. Phys.* 57 (1985) 2626.
- [157] M. Peyrard, S. Odier, E. Oran, J. Boris, and J. Schnur, *Phys. Rev. B* 33 (1986) 2350.
- [158] A. V. Utkin, I. F. Golovnev, W. M. Fomin, in *Proceedings of the Third Russian-Korean International Symposium on Science and Technology, KORUS'99*; Piscataway, NJ, USA, IEEE 1999, Vol. 2, p. 585.
- [159] P. Maffre and M. Peyrard, *Phys. Rev. B* 45 (1992) 9551.
- [160] S. G. Lambrakos, M. Peyrard, E. S. Oran, and J. P. Boris, *Phys. Rev. B* 39 (1989) 993.
- [161] M. L. Elert, D. M. Deaven, D. W. Brenner, and C. T. White, *Phys. Rev. B* 39 (1989) 1453.
- [162] N. C. Blais and J. R. Stine, *J. Chem. Phys.* 93 (1990) 7914.

- [163] D. W. Brenner, D. H. Robertson, M. L. Elert, and C. T. White, Phys. Rev. Lett. 70 (1993) 2174; *ibid*, Phys. Rev. Lett 76 (1996) 2202.
- [164] P. J. Haskins and M. D. Cook, in *Proceedings of the Joint International Association for Research and Advancement of High Pressure Science and Technology and American Physical Society Topical Group on Shock Compression of Condensed Matter*, ed. S. C. Schmidt, AIP Press, New York (1994) pp.1341-1344).
- [165] P. J. Haskins and M. D. Cook, *Proceedings of the Conference of the American Physical Society Topical Group on Shock Compression of Condensed Matter*, eds. S. C. Schmidt and W. C. Tao ,AIP Press, NY (1996) pp. 195-198.
- [166] B. M. Rice, W. Mattson, J. Grosh, and S. F. Trevino, Phys. Rev. E 53 (1996) 611.
- [167] B. M. Rice, W. Mattson, J. Grosh, and S. F. Trevino, Phys. Rev. E 53 (1996) 623.
- [168] D. R. Swanson, J. W. Mintmire, D. H. Robertson, and C. T. White, Chem. Phys. Reps. 18 (2000) 1871.
- [169] B. M. Rice, W. Mattson, and S. F. Trevino, Phys. Rev. E 57 (1998) 5106.
- [170] P. J. Haskins, M. D. Cook, J. Fellows, and A. Wood, *Proceedings 6th Symposium (International) on Detonation*, Snowmass, Colorado (2000) 897.
- [171] P. J. Haskins and M. D. Cook, in *Proceedings of the APS Topical Conference on Shock Compression of Condensed Matter* (1993) pp. 1341-1344.
- [172] G. C. Abell, Phys. Rev. B 31 (1985) 6184 .
- [173] J. Tersoff, Phys. Rev. Lett. 61 (1988) 2879; *ibid* Phys. Rev. B 39 (1989) 5566.
- [174] T. Raz and R. D. Levin, Chem. Phys. Lett. 246 (1995) 405.
- [175] J. J. C. Barrett, D. W. Brenner, D. H. Robertson, and C. T. White, *Shock Compression of Condensed Matter* (1996) 370.
- [176] J. J. C. Barrett, D. H. Robertson, and C. T. White, Chem. Phys. Reports 18 (2000) 1969.
- [177] D. W. Brenner, Phys. Rev. B 42 (1990) 9458.
- [178] D. W. Brenner, O. A. Shenderova, J. A. Harrison, S. J. Stuart, B. Ni, and S. B. Sinnott, J. Phys.: Condens. Matter 14 (2002) 783.
- [179] D. W. Brenner, Materials Research Society Bulletin 21 (1996) 36.
- [180] D. W. Brenner, O. A. Shenderova, and D. A. Areshkin, Rev. Comp. Chem., K. B. Lipkowitz and D. B. Boyd, Eds., VCH Publishers, New York (1998) pp. 213-245.

- [181] D. W. Brenner, *Physica Status Solidi B* 217 (2000) 23.
- [182] D. W. Brenner, O. A. Shenderova, J. A. Harrison, S. J. Stuart, B. Ni, and S. B. Sinnott, *Journal of Physics-Condensed Matter* 14 (2002) 783.
- [183] A. C. T. van Duin, S. Dasgupta, F. Lorant, and W. A. Goddard III, *J. Phys. Chem. A* 105 (2001) 9396.
- [184] E. J. Reed, J. D. Joannopoulos, and L. E. Fried, *Phys. Rev. B* 62 (2000) 16500.
- [185] M. R. Manaa and L. E. Fried, *J. Phys. Chem.* 103 (1999) 9349.

Chapter 7

Structure and density predictions for energetic materials

James R. Holden, Zuyue Du and Herman L. Ammon

Department of Chemistry and Biochemistry
University of Maryland, College Park, MD 20742, USA

The discovery of new energetic materials could be facilitated, accelerated and made more cost effective with the use of computer modeling and simulations for the identification of compounds with significant advantages over materials currently in use. The quantitative estimation of properties, such as the heat of formation, density, detonation velocity, detonation pressure and sensitivity, to screen potential energetic candidates would permit the selection of only the most promising substances [1] for laboratory synthesis, measurement of properties, scale-up, testing, etc. The most significant properties or characteristics of a high performance energetic material are the molecular structure, elemental composition, heat of formation, solid-state density and microstructure. Performance characteristics such as the detonation velocity and pressure are proportional to the density. The detonation velocity, for example, increases linearly with density while the Chapman-Jouguet pressure is proportional to the square of the initial density [2]. An increase in the solid-state density also is desirable in terms of the amount of material that can be packed into a volume-limited warhead or propulsion configuration. Density has been termed “the primary physical parameter in detonation performance” [3]. Microstructure is a catchall term that refers to the three-dimensional structure with various dislocation motifs and imperfections. The sensitivity of a material in response to impact or shock stimuli is associated with a number of factors, among which are the molecular and micro structures.

This chapter will not provide reviews of density and structure prediction, but rather focus on our work and its emphasis on predictions for energetic materials. Because of the importance of crystal density in the performance of energetic materials, our initial efforts were directed to this area in general and to volume additivity techniques in particular.

Without question, the simplest method for estimating the density of a compound is by so-called “group or volume additivity.” This is truly a back-of-the-envelope or spreadsheet calculation. Appropriate atom and functional group

volumes are summed to provide an effective volume (V_{VA}) for the molecule in a crystal which is an approximation of the observed crystal volume (V_{OBS}) per molecule. The volume comprises the actual molecular volume (V_{MOL}) plus an average amount of unoccupied space (V_{VOID}) in the solid ($V_{VA} \approx V_{OBS} = V_{MOL} + V_{VOID}$) and is combined with the molecular weight for an estimation of the crystal density. A number of volume additivity studies have been published over the years. They are basically similar and differ primarily in the numbers and types of crystal structures contained in the data bases used to derive the atom and group volume parameters. For example, the 1971 study by Immirzi and Perini [4] used a 500 structure data base and restricted cyclic compounds to those containing benzene or naphthalene rings, the Tarver [5] investigation in 1979 employed a data base of 188 explosives and related compounds and the Cichra, Holden, and Dickinson report [6] used 807 substances biased toward high energy compounds. The more extensive investigation of Stine in 1981 [7] used 2,051 supposedly "error-free" crystal structure data to determine 34 atomic volumes for C, H, N, O and F. In 1998, we published [8] new parameterizations based on more than 11,000 high quality, error-free crystal structures to provide 78 atom and group volumes for C, H, N, O and F-containing materials.

This study was followed [9] by the determination of 96 volumes for C, H, N, O, F, P, S, Cl and Br from approximately 21,000 organic structures. Three sets of atom/group terms were determined. (1) The crystal volume (V_{VA}) of a molecule was assumed to be the linear sum of appropriate atom and group volumes (V_j 's) determined from experimental crystal unit cell volumes per molecule (V_{OBS}) by minimization of Δ_L . The V_j are called "linear volumes" because V_{VA} is a linear function of the V_j component volumes. (2) An alternative approach was to determine the V_j 's by minimization of Δ_{NL} , which uses the observed and calculated densities (ρ_{OBS} , ρ_{VA}). Here the V_j 's are referred to as "nonlinear volumes" because ρ_{VA} is a nonlinear function of the V_j 's. (3) A third approach was the determination of atom and group densities (q_{VA}) by minimization of Δ_ρ ; these are termed "linear densities." Use of the V_j 's to calculate crystal-molecular volumes and densities for about 2,200 structures not present in the original parameterization gave an average percent volume difference ($100|V_{OBS} - V_{VA}|/V_{OBS}$) of 2.1%. Generally, the q_{VA} 's are least reliable in estimating crystal densities.

The volume and density data and component atoms and groups are not shown here and interested readers are directed to Table 1 in Ref. 9. Improvements in the general accuracy of volume additivity predictions can be achieved, for example, by the use of separate parameters for the same kind of atom in different structural environments. For example, the parameters in Ref. 9 contain separate entries for CH_3 linked to C, N, O and S ($V_j = 32.2, 30.5, 28.8, 32.1 \text{ \AA}^3$) and for HO bonded to sp^3 and sp^2 C ($V_j = 12.9, 14.8 \text{ \AA}^3$). Numerous

improvements are possible and might include, for example, separate parameters for H linked to amine, amide and imide N's or for CH₃ bonded to sp³ and sp² C.

$$\Delta_L = \sum_{i=1}^N [(V_{\text{OBS}})_i - (V_{\text{VA}})_i]^2; \quad V_{\text{VA}} = \sum_{j=1}^n (V_j)$$

$$\Delta_{\text{NL}} = \sum_{i=1}^N [(\rho_{\text{OBS}})_i - (\rho_{\text{VA}})_i]^2; \quad \rho_{\text{VA}} = M_{\text{MOL}}/0.6022V_{\text{VA}}$$

$$\Delta_{\rho} = \sum_{i=1}^N [(\rho_{\text{OBS}})_i - (\rho_{\text{VA}})_i]^2; \quad \rho_{\text{VA}} = (1/M_{\text{MOL}}) / \sum_{j=1}^n (q_{\text{VA}})_j$$

V = volume (Å³); ρ = density (g cm⁻³)

M_{MOL} = gram-molecular weight (g mol⁻¹)

N = number of structures; n = number of atoms in a molecule

A disadvantage of the usual atom/group procedure is the need to anticipate the atoms and groups that will be found in a database, such as the Cambridge Structural Database (CSD). Some molecules will be excluded simply because they contain functionality not recognized in the defined list. This pre-knowledge requirement was circumvented [9] by the concept of an "atom code", which consists of (1) the name of the (primary) atom, (2) the names of (secondary) atoms bonded to the primary atom, (3) the number of atoms bonded to each secondary atom and (4) by allowing the structures in the CSD to define the necessary codes. This approach will not be further discussed here and interested readers are again directed to Ref. 9.

However many different atoms, groups or codes are introduced to improve the overall volume additivity parameterization, the technique does not readily account for either molecular conformation or crystal packing efficiency. The nitramine explosives RDX and the HMX polymorphs, which have CH₂NNO₂ as the basic structural unit are a case in point, with experimental crystal densities of 1.806 (RDX), 1.839 (α -HMX), 1.902 (β -HMX) and 1.759 (δ -HMX) g cm⁻³. The additivity densities [9], of 1.838 and 1.847 g cm⁻³ for the six and eight-membered ring nitramines, are somewhat differentiated by the use of separate CH₂ parameters for different ring sizes (V_j 's for sp³ C in 6 and 8-membered rings are 12.28 and 12.17 Å³, respectively). It should be noted also that the experimental densities are due in part to the molecular conformations in the crystals reflected by the point group symmetries of C_s for RDX and C₂, C_i and C_{2v} for the three HMX's. Additionally, volume additivity cannot readily handle positional isomerism such as one finds in 3-aminobenzenecarbonitrile (ρ_{OBS} =

1.145 g cm⁻³) and the 4-amino isomer ($\rho_{\text{OBS}} = 1.219 \text{ g cm}^{-3}$).

An improvement on the basic volume additivity approach has been implemented by Blaive and co-workers with the use of molecular mechanics and atomic radii to estimate molecular volumes and both liquid and crystal densities. [10]

Crystal density, while valuable for the calculation of various performance properties, is limited in its information content. A procedure to predict the most likely crystal structure for a substance would be more generally useful and also provide an estimation of crystal density. Additionally, the crystal structure prediction to density step would have several advantages over volume additivity by itself. (1) Information on the molecular structure, conformation and positional isomerism automatically are introduced because the three dimensional structure of a molecule forms the essential starting point. (2) The procedure routinely handles (different) packing efficiencies. The packing coefficient or efficiency (Kitaigorodski [11]) is defined as $PC = V_{\text{MOL}}/V_{\text{OBS}}$, the ratio of the molecular volume to the crystal volume per molecule. PC's typically are in the 0.6-0.85 range with reasonable atomic/molecular volumes. The molecular and crystal density relationships of $\rho_{\text{MOL}} = M_{\text{MOL}}/V_{\text{MOL}}$ and $\rho_{\text{CRY}} = PC \cdot \rho_{\text{MOL}}$ point up that the highest density crystals will have both high packing efficiencies and molecular densities.

This chapter will focus on our procedures that have evolved over a period of about 20 years. Excellent reviews of the state-of-the-art in organic structure prediction are available from two blind test investigations hosted in 1999 and 2001 by the Cambridge Crystallographic Data Center and a recent dissertation [12].

The development of MOLPAK (MOLEcular PAcKing)

A crystal structure usually is described by the unit cell dimensions, space group and coordinates of the atoms (or orientation and position of the molecules) in the asymmetric unit. This, in fact, is the order in which the information is obtained when a crystal structure is determined by X-ray or neutron diffraction experiments. However, an equivalent way to describe a structure is to place the center of a molecule at the origin of an orthogonal coordinate system and to specify its molecular surroundings. This alternative is especially powerful in crystals with one molecule per asymmetric unit because the orientations of the surrounding molecules are related to the central molecule by crystallographic symmetry. The "coordination sphere" or environment of the structure then is defined as those surrounding molecules which are in van der Waals contact, or nearly in contact, with the central molecule.

Therefore, the first step in developing a method for predicting crystal structures was to characterize the coordination spheres found in known structures. This was limited to compounds of moderate molecular weight

containing only C, H, N, O and F in the triclinic, monoclinic, and $Z = 4$ orthorhombic space groups. An initial survey of coordination sphere information used crystal structure information for 136 carbon to fluorine-containing materials and was later expanded to 267 [13]. Two programs, MOLCON and MOLPAN (MOLEcular CONformation; MOLEcular Packing ANalysis), were written to facilitate collection and analysis of the coordination information. The analyses used standard van der Waals radii ($C = 1.70$, $H = 1.10$, $N = 1.55$, $O = 1.52$ and $F = 1.50$ Å [14]) to determine the minimum distances between the van der Waals envelopes of a central molecule and the surrounding molecules. For each structure, the distances were arranged in ascending order and plots of distance vs. sequence number (Fig. 1) typically showed a sizable break of 1-2 Å (DNOPHL01) at sequence numbers of about 12-14. The inner molecules, those before the gap, were taken as members of the coordination sphere. Fig. 1 also shows an example (GEMZAZ) of a “break less” type of plot produced in some instances; a cutoff minimum distance of 0.75 Å was used in these instances. With this information and other considerations, 14 was established as the most probable number of molecules in a coordination sphere; summaries for the 267 structures [13] and

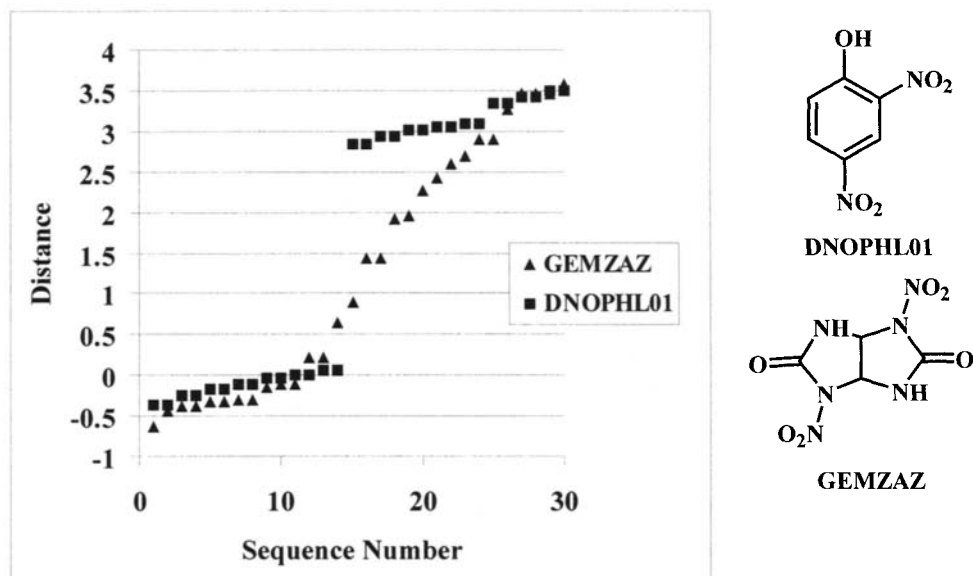


Fig. 1. Distance (Å) vs. sequence number for two molecules

from a recent survey of 13,851 structures are given in Table 1.

The composition of each coordination sphere (the molecules are Identity or Initial, Plane, Axis and Center) is characteristic of the space group and the three-dimensional relationships between the molecules fall into a limited

number of patterns and sub-patterns. The simplest space group, P1 with one molecule per unit cell, indicates why 14 is a natural number. With an **I** molecule at the origin, the unit cell distorts to place two **I**'s along each of the three cell axes (6); two along each of the three face diagonals (6); and two along the shortest body diagonal for a total of 14. Perhaps a better view of this

Table 1

Data for the determination of the most probable number of molecules in the coordination spheres of C, H, N, O and F-containing structures

Break	N*	%*	Break* Dist (Å)	N**	%*	Break* Dist (Å)
19-20				142	1.0	1.05
18-19				727	5.2	1.38
17-18				381	2.8	1.20
16-17	20	7.5	1.43	2501	18.1	1.59
15-16	18	6.7	1.18	825	6.0	1.35
14-15	152	56.9	1.74	7147	51.6	1.84
13-14	27	10.1	1.33	969	7.0	1.27
12-13	42	15.7	1.26	1053	7.6	1.30
11-12	2	0.7	1.62	63	0.5	1.00
10-11	4	1.5	1.03	53	0.4	0.95
9-10	1	0.4	2.40	3	0.02	1.27
8-9	1	0.4	1.80	5	0.04	0.59

*Ref [13] data for 267 structures.

**Data for 13,851 structures. 107 structures with breaks at 7-8 or smaller and 55 Fdd2 (Z = 16) structures were eliminated from the original data set. The original CCSD search yielded 19,351 hits after removing structures containing tertiary N, D and carboxylates.

Approximately 3,500 structures were removed because of missing atoms (usually H) in the coordinate sets, atoms with incorrect valences (usually H with 0 or more than one bond) and bad bond angles. Finally, duplicate structures were removed to leave just the lowest R-factor entry. The space groups included in the analysis are given in Table 2.

coordination sphere, in terms of pattern building, is that it contains six **I** molecules in the plane of the central **I** molecule with four **I** molecules in offset planes above and below the central plane. There is a similar pattern in P-1, but with four **C** molecules above and four below in the offset planes in place of the **I** molecules.

The compositions of the coordination spheres for known structures in the Z = 1, 2 or 4 triclinic, monoclinic and orthorhombic space groups plus a few important Z = 8 orthorhombic space groups were analyzed and characterized with the MOLCON and MOLPAN programs. From this analysis, the MOLPAK program was written to build hypothetical crystal structures from a 3-D model for an **I** molecule and appropriate coordination

sphere information. The coordination sphere patterns and analysis are summarized in Table 3 and described briefly here.

The first column (Code) in Table 3 is the two-letter code assigned to that coordination sphere type and the second column (Sub) indicates which MOLPAK subroutine contains the procedure to build coordination spheres of that type. Some procedures employ common steps and more than one procedure may be contained in a particular subroutine. Columns 3 and 4 give the crystal system (CS) and Z value, respectively. The remainder of each row identifies the relationships of the molecules in the coordination sphere to the central molecule and their distribution in an orthogonal coordinate space. The symbols are

Table 2

Crystal structure space groups, numbers of structures (N) and percentages used in the Table 1 analysis

Space group			Space group		
#	Symbol	N	#	Symbol	N
1	P1	58	21	C222	1
2	P-1	1747	23	I222	2
4	P21	1507	29	P21ab	137
5	C2	125	33	Pna21	253
7	Pc	46	34	Pnn2	2
9	Cc	135	41	Aba2	10
13	P2/c	12	45	Iba2	9
14	P21/c	5157	52	Pncn	1
15	C2/c	557	56	Pccn	35
18	P21212	57	60	Pnca	62
19	P212121	3210	61	Pbca	714
20	C2221	14			

defined at the end of Table 3. Code and subroutine information are given in Table 4 for molecules on special positions.

The MOLPAK computer program was developed and rewritten over a number of years and various accounts have been published by Holden and Dickinson [15], Cromer, Ammon and Holden [16] and Holden, Du and Ammon [13]. Its operation is based on the assumption that molecules will pack into the smallest volume consistent with their size and conformation. That is, the coordination sphere will collapse inward until stopped by repulsion between atoms in the surrounding and central molecules. MOLPAK contains a different procedure for building each of the coordination sphere types listed in Table 3.

Table 3
Coordination Sphere Patterns for Triclinic, Monoclinic and Orthorhombic Space Groups

Code	Sub	Space group	CS	Z	Coordination Sphere Contents*
AA	TA	P1	T	1	6 I in plane-1,2; 4 I above; 4 I below
AB	TA	P-1	T	2	6 I in plane-1,2; 4 C above; 4 C below
CA	TC	P-1	T	2	6 I on all axes; 4 C above; 4 C below
AC	TA	Pm	M	2	6 I in plane-1,2; 4 P3 above; 4 P3 below
AD	TA	Pc	M	2	6 I in plane-1,2; 4 P3 1 above; 4 P3 1 below
AE	TB	P2	M	2	6 I in plane-1,3; 4 A3 right; 4 A3 left
AF	TB	P21	M	2	6 I in plane-1,3; 4 S3 right; 4 S3 left
AG	TB	Pc	M	2	6 I in plane-1,3; 4 P3 2 right; 4 P3 2 left
AH	TA	P21	M	2	6 I in plane-1,2; 4 S3 above; 4 S3 below
AI	FA	P21/c ⁺	M	4	2 I on axis-3; 4 P3 1; 4 S3; 4 C
AJ	FA	P2/c ⁺	M	4	2 I on axis-3; 4 P3 1; 4 A3; 4 C
AK	FA	P21/c	M	4	2 I on axis-3; 4 P3 1; 4 S3; 4 C
AL	FA	P2/c	M	4	2 I on axis-3; 4 P3 1; 4 A3; 4 C
AM	FB	P21/c	M	4	2 I on axis-1; 4 P3 2; 4 S3; 4 C
AN	FC	P21/m	M	4	2 I on axis-1; 4 P3 ; 4 S3; 4 C
AO	FC	P2/m	M	4	2 I on axis-1; 4 P3 ; 4 A3; 4 C
FA	FD	P21/c	M	4	6 I in plane-1,2; 4 C above; 4 P3 1 below
FB	FD	P21/m	M	4	6 I in plane-1,2; 4 C above; 4 P3 below
FC	FE	P21/c	M	4	6 I in plane-1,3; 4 S3 right; 4 C left
FD	FE	P2/c	M	4	6 I in plane-1,3; 4 A3 right; 4 C left
AP	OA	P21212	O	4	2 I on axis-3; 4 S1; 4 S2; 4 A3
AQ	OA	P212121	O	4	2 I on axis-3; 4 S1; 4 S2; 4 S3
AR	OB	Pnn2	O	4	2 I on axis-3; 4 P1 n; 4 P2 n; 4 A3
AS	OB	Pna21	O	4	2 I on axis-3; 4 P1 2; 4 P2 n; 4 S3
AT	OB	Pnn2	O	4	2 I on axis-3; 4 P2 n; 4 P3 n; 4 A1
AU	OB	Pna21	O	4	2 I on axis-3; 4 P2 n; 4 P3 2; 4 S1
AV	OB	Pna21	O	4	2 I on axis-3; 4 P1 n; 4 P2 1; 4 S3
AW	OB	Pba2	O	4	2 I on axis-3; 4 P1 2; 4 P2 1; 4 A3
AX	OB	Pnc2	O	4	2 I on axis-3; 4 P2 1; 4 P3 n; 4 A1
AY	OB	Pca21	O	4	2 I on axis-3; 4 P2 1; 4 P3 2; 4 S1
AZ	OC	P212121	O	4	6 I in plane-2,3; 4 S2; 4 S3
BA	OC	P21212	O	4	6 I in plane-2,3; 4 S2; 4 A3
BB	OC	P21212	O	4	6 I in plane-2,3; 4 A2; 4 S3
BC	OC	P2221	O	4	6 I in plane-2,3; 4 A2; 4 A3
BD	OC	Pna21	O	4	6 I in plane-2,3; 4 P1 n; 4 S3
BE	OC	Pnn2	O	4	6 I in plane-2,3; 4 P1 n; 4 A3
BF	OC	Pna21	O	4	6 I in plane-2,3; 4 P1 2; 4 S3
BG	OC	Pba2	O	4	6 I in plane-2,3; 4 P1 2; 4 A3
BH	OC	Pca21	O	4	6 I in plane-2,3; 4 P1 3; 4 S3
BI	OC	Pnc2	O	4	6 I in plane-2,3; 4 P1 3; 4 A3 (continued on next page)

BJ	OC	Pmn21	O	4	6 I in plane-2,3; 4 P1 -; 4 S3
BK	OC	Pma2	O	4	6 I in plane-2,3; 4 P1; 4 A3
CB	EA	Pbca	O	8	2 P1 2; 2 P2 3; 2 P3 1; 2 A1; 2 A2; 2 A3; 2 C
CC	EA	Pbca	O	8	2 I on axis-1; 4 P1 2; 2 P3 1; 2 A1; 2 A2; 2 C
CD	EB	Pbcn	O	8	2 P1 2; 2 P2 3; 2 P3 n; 2 S1; 2 A2; 2 S3; 2 C
CE	EB	Pbcn	O	8	2 I on axis-2; 2 P1 2; 4 P2 3; 2 A2; 2 S3; 2 C
CF	XX	Pnma	O	8	Limited to molecules on mirror, Z = 4; see SO and SP
DA	NA	Cc	M	4	6 I in C plane-1,3; 4 P3 2 right; 4 P3 2 left
DB	NA	C2	M	4	6 I in C plane-1,3; 4 A3 right; 4 A3 left
DC	NA	C2/c	M	8	4-6 I in C plane-1,3; 3-4 A3; 0-1 P3 2; 4 C
DD	NA	C2/c	M	8	2 I on C diagonal-1,3; 4 P3 2; 4 A3; 4 C
DE	NA	C2/c	M	8	2 I on axis-3; 4 P3 2; 4 A3; 4 C
DF	NC	Fdd2	O	16	Limited to molecules on axis, Z = 8; see ST and SU
DG	NC	Fdd2	O	16	Limited to molecules on axis, Z = 8; see ST and SU
SA	SA	A-P2 ⁺ or P-Pm	M	1	6 I in plane-1,2; 4 I above; 4 I below
SB	SA	C-P21/m	M	2	6 I in plane-1,2; 4 X3 above; 4 X3 below
SC	SA	C-P21/c	M	2	6 I in plane-1,2; 4 X3 1 above; 4 X3 1 below
SD	SB	C-P21/c	M	2	6 I in plane-1,3; 4 Z3 2 right; 4 Z3 2 left
SE	SB	C-P2/c	M	2	6 I in plane-1,3; 4 Y3 2 right; 4 Y3 2 left
SF	SC	A-21212	O	2	6 I in plane-1,2; 4 Z1 3 above; 4 Z1 3 below
SG	SC	A-P2221	O	2	6 I in plane-1,2; 4 Y1 3 above; 4 Y1 3 below
SH	SD	A-Pnn2	O	2	6 I in plane-1,3; 4 X1 n right; 4 X1 n left
SI	SD	A-Pba2	O	2	6 I in plane-1,3; 4 X1 3 right; 4 X1 3 left
SJ	SD	A-Pma2	O	2	6 I in plane-1,3; 4 W1 3 right; 4 W1 3 left
SK	SE	A-Pnc2	O	2	6 I in plane-1,2; 4 X1 3 above; 4 X1 3 below
SL	SF	P-Pmn21	O	2	6 I in plane-1,3; 4 X2 1 right; 4 X2 1 left
SM	SF	P-Pma2	O	2	6 I in plane-1,3; 4 X2 right; 4 X2 left
SN	SG	C-Pbca	O	4	2 I on axis-3; 4 Z1 3; 4 Z2 1; 4 Z3 2
SO	SH	P-Pnma	O	4	2 I on axis-2; 4 P2 n; 4 S2; 4 C
SP	SH	P-Pnma	O	4	2 I on axis-1; 4 P2 n; 4 S2; 4 C
SQ	SI	A-Pbcn	O	4	2 I on axis-2; 4 P2 3; 4 S2; 4 C
SR	SI	A-Pbcn	O	4	2 I on axis-3; 4 P2 3; 4 S2; 4 C
SS	SI	A-Pbcn	O	4	2 I on axis-1; 4 P2 3; 4 S2; 4 C
ST	SJ	A-Fdd2	O	8	2 I on axis-3; 4 T13; 2 d; 2 d23; 2 d13; 2 d12
SU	SJ	A-Fdd2	O	8	2 I on axis-1; 4 T13; 2 d; 2 d23; 2 d13; 2 d12

* Axis-1, axis-2, and axis-3 refer to the Eulerian rotation axes used in the MOLPAK search routines. The unique axis (b) in monoclinic space groups is along axis-3. The various symbols refer to molecules related to the origin molecule by the following operations:

I is an identity; same as origin molecule

C is related by center of symmetry

Plane-ij is the plane containing axis-i and axis-j

Pi j is a glide plane perpendicular to axis-i with an axis-j translation

Pi n is a glide plane perpendicular to axis-i with a diagonal translation

Pi is a mirror plane perpendicular to axis-i

Si is a two-fold screw axis parallel to axis-i

(continued on next page)

A_i is a two-fold rotation axis parallel to axis- i
 $X_i j$ is a glide plane with a $\frac{1}{2}$ axis- i offset and axis- j translation
 X_i is a mirror plane with a $\frac{1}{2}$ axis- i offset
 $W_i j$ is a glide plane with zero axis- i offset and axis- j translation
 $Y_i j$ is a two-fold axis parallel to axis- i with an intersection on axis- j
 $Z_i j$ is a two-fold screw axis parallel to axis- i with an intersection on axis- j
 $T13$ is an identity translated by $\frac{1}{2}$ along axis-1 and axis-3
 D is a P1 with a $\frac{1}{4}$ glide along all three axes
 $d23$ has an additional translation of $\frac{1}{2}$ along axis-2 and axis-3
 "above" and "below" refer to directions along axis-3
 "left" and "right" refer to directions along axis-2

[†]The lead C, A, or P before the space group designations for symmetric molecules means that the molecule contains an internal center of symmetry, two-fold axis, or mirror plane. For example, C-P21/c is the reduced space group for P21/c containing centric molecules. W and X refer to mirror and glide plane related molecules whose positions are restricted to preserve the symmetry of the original symmetric molecule. Y and Z refer to two-fold axis and screw axis related molecules whose positions are restricted for the same reason.

[‡]AI and AJ are special cases of AK and AL, respectively, with pairs of P3 1 along axis-3; this accelerates the MOLPAK search routines.

Three procedures are outlined below. Most coordination spheres are constructed in steps involving the three orthogonal axes, called axis-1, axis-2 and axis-3. (1) A line of molecules is established along axis-1 by moving a second molecule toward the central (origin) molecule until some repulsion criterion is met. (2) A two-dimensional grid is established by moving a line of molecules with the spacing established in step 1 toward the central molecule from the direction of axis-2. This step may require sliding the line parallel to axis-1, to locate the minimum distance allowed by a second repulsion threshold. (3) A two-dimensional grid with the spacings established in steps 1 and 2 is placed parallel to the central grid and moved toward the central molecule along axis-3. Location of the minimum axis-3 distance allowed by a third repulsion threshold may require shifting this grid along both the axis-1 and axis-2 directions.

The repulsion energy between two (or more) molecules is computed as the sum of all pair-wise atom-to-atom interactions. These energies are evaluated with the modified 6-12 function described in a following section. The threshold used for the axis-1 search is the maximum allowable repulsion between any pair of molecules in the structure. Twice this value is used for the step 2 search because the central molecule generally is in contact with two molecules in a line. In step 3, the central molecule is usually in contact with four molecules in a plane above (or below) the central plane and thus four times the threshold energy is used in this search. The threshold energy was derived from known structures by searching for values which reproduced the true unit cell volume with the central molecule in the orientation of the known structure. Most were in the 0.2 - 1.0 kcal mol⁻¹ range and 0.5 kcal mol⁻¹ is used as the molecule to

molecule threshold energy in the construction of unknown structures.

In the triclinic, monoclinic and orthorhombic space groups, the types of symmetry operations that alter a molecule's orientation are planes (mirror and glide), two-fold axes (rotation and screw) and centers of symmetry. These operations involve changing the signs of one, two or all three of the coordinates of the atomic positions. The unique direction of a plane or axis must be parallel

Table 4

Additional routines called for molecules with C_i , C_2 and C_s internal symmetry

C_i		C_2		C_s	
Entered	Called	Entered	Called	Entered	Called
AB	AA	AE	SA	AC	SA
CA	AA	AJ	AG	AN	AF+AH
AI	SD	AL	AG	AO	AE
AJ	SE	AO	AC	BJ	SL
AK	SD	AP	SF	BK	SM
AL	SE	AR	SH	CF	SO+SP
AM	SC+SD	AT	SH	FB	AE
AN	SB	AW	SI		
FA	SC+SD	AX	SK		
FB	SB	BA	SF		
FC	SC+SD	BB	SF		
FD	SE	BC	SG		
CB	SN	BE	SH		
CC	SN	BG	SI		
DC	DB	BI	SK		
DD	DB	BK	SJ		
DE	DB	CD	SQ+SR+SS		
		CE	SQ		
		DC	DA		
		DD	DA		
		DE	DA		
		DF	ST		
		DG	ST		
		FD	AG		

to a cell axis which is perpendicular to the other two axes, such as the **b** axis in monoclinic. An associated translation that moves a molecule along the direction of an unchanged coordinate (no sign change) must be either 0 or 1/2 of a unit cell translation. These restrictions often simplify steps 2 and 3 that involve the placement of lines and two-dimensional grids in the development of the coordination environment.

Examples of Coordination Sphere Building Procedures

The manner in which MOLPAK derives coordination spheres is illustrated by three examples, one for P-1 and two for P2₁/c, the most important of the space groups for light atom containing organic substances. The procedure for each type is unique, but these examples show some of the techniques developed.

Triclinic, P-1, AB Coordination Geometry. The coordination sphere contains 6 **I** molecules positioned with the step 1 and step 2 procedures. The **a** cell axis length is determined as described in step 1, approach of an **I** molecule along axis-1. This establishes the repeat vector along the axis-1 direction for all molecules, not only **I** molecules. Next, the **b** axis length is determined as described for step 2 and involves the approach of a line of **I** molecules along axis-2. Because axis **a** is not perpendicular to axis **b**, the line must be shifted along the axis-1 direction to the position which allows the closest approach in the axis-2 direction. The **b** axis is then the vector between the central molecule (the origin) and the center of one of the **I** molecules in the line, thus the γ angle between **a** and **b** is also determined. All of the repeat vectors established in the axis-1/axis-2 plane apply to all molecules, not only **I**'s. The remaining cell parameters are determined by two applications of the procedure described as step 3, the approach of a two-dimensional grid of molecules along axis-3. First, a grid of **C** molecules with the spacings derived for **I**'s in steps 1 and 2 approaches the central molecule along positive axis-3. Because the **c** axis is not perpendicular to either **a** or **b**, adjustments must be made in both the axis-1 and axis-2 directions. Then an identical **C** grid approaches along negative axis-3 and is suitably adjusted. The **c** axis of the unit cell is a vector from a **C** molecule in the lower grid to a **C** molecule in the upper grid.

Monoclinic, P2₁/c, AI Coordination Geometry. The coordination sphere contains only 2 **I**'s whose positions are determined in step 1, this time along axis-3. This determines the **b** cell axis length. In this coordination sphere type, **P** molecules have a **c** axis glide and occur in pairs along axis-3. Therefore, the **c** axis length and the **P** molecule offset (along **b**) are determined by a step 2 approach of a line of **P** molecules along axis-1 with adjustment along axis-3. The length of the **c** axis is equal to twice the approach distance of the **P** line, because the **P** glide is equal to **c**/2.

The **a** axis length and β angle are determined by two step 3 procedures along positive and negative directions of axis-2. The approach plane contains both **A** and **C** molecules. Since the unit cell contains a screw axis, the **A** molecules are halfway along the **b** axis direction (axis-3) and the vector between each **A** and **C** pair is the same as that between the central **I** molecule and a **P** molecule. (A **P3** conversion alters the signs of the axis-3 coordinates of all of the atoms and turns an **A3** into a **C** molecule.) Because the axis-3 coordinates of the **A**'s are fixed, the **A/C** grid must be adjusted only along the axis-1 direction. The **a** cell axis is a vector from an **A** molecule on the minus side to an **A** molecule on the plus

side.

Monoclinic, P2₁/c, AK Coordination Geometry. This coordination sphere type is similar to AI, except that the **P**'s are not in contacting pairs along axis-3. Therefore, the unit cell must be determined by an iterative procedure in which the offset of the glide plane molecules along **b** (axis-3) is arbitrarily set and then refined. The **b** axis length is determined by a step 1 procedure along axis-3. The range of possible **b** offsets for the **P** (glide plane) molecules is from zero to the **b** axis length. This range is covered by a number of equal steps (usually 8) and then refined to a specified fraction (usually 1/128) of the **b** axis length.

With the offset arbitrarily set at the first step, a tentative value of the **c** cell axis length is determined by applying the approach of a line of **P** molecules along axis-1. However, in this case, the **P** molecule offset along **b** (axis-3) is not adjusted, because only one **P** is in contact with the central **I**. The corresponding values of **a** and β are determined by approaches of grids of **A**, **C** and **P** (the other **P**) molecules along positive and negative axis-2. The **P** offset is stepped and refined to the value which produces the smallest unit cell volume. This procedure is iterative and may require significantly more calculation time.

MOLPAK Overview and Structure Prediction

MOLPAK creates a minimum volume packing arrangement for a given coordination geometry and orientation of the search probe (a model of the molecule of interest). It has been extensively tested for the space groups (numbers of coordination geometries per space group in parentheses) P1 (1), P-1 (2), P2₁ (2), P2₁/c (5), Cc (1), C2 (1), C2/c(3), P2₁2₁2 (3), P2₁2₁2₁ (2), Pca2₁(2), Pna2₁ (3), Pbca (2) and Pbcn (2). Models with C_i, C₂ and C_s point group symmetries can be examined in space groups in which the model and space groups symmetries coincide. The 29 coordination geometries presently encoded (and tested) can fit the known structures of approximately 94% of all C-H-N-O-F containing compounds with one molecule per asymmetric unit.

The optimum orientation of the probe with respect to space group symmetry is unknown beforehand and, therefore, it is necessary to calculate a three-dimensional minimum volume map as a function of the unique set of orientations of the probe. The orientations are accomplished by rotation of the probe about three Eulerian axes from -90° to +90° in (usually) 10° steps for 6,869 (19³) orientations, and each must be converted into a minimum volume packing arrangement which represents an energy compromise. The use of an ordinary intermolecular potential, such as a Lennard-Jones 6-12 or Buckingham 6-exp, to determine the minimum energy between molecules can be time-consuming because of the large number of atom-to-atom interactions that require evaluation.

Among the most important computational aspects of MOLPAK are replacement of the standard interatomic potential by a repulsion-only potential

and the introduction of docking thresholds. An ordinary Lennard-Jones 6-12 potential (E_{ij}) is modified with the addition of an E_{\min} correction to make the energy at the usual minimum energy distance (d_{\min}) equal to zero. This shifts the

$$E_{ij} = C_1/r_{ij}^6 + C_2/r_{ij}^{12} + |E_{\min}|$$

entire potential by $|E_{\min}|$. Additionally, intermolecular distances (r_{ij}) larger than d_{\min} are ignored and only those smaller are used to obtain a repulsion energy. With the use of pre-determined repulsion thresholds, a summation between two molecules, for example, is terminated when the energy sum exceeds the threshold. The C_1 and C_2 coefficients were taken primarily from the work of Giglio [17] and Holden and Dickinson [18] with some MOLPAK-specific adjustments. Test calculations showed that, in agreement with Kitaigorodsky, fine details of an intermolecular fit could be adequately represented by repulsion.

Numerous other tricks were used to speed the calculations, such as the initial calculation of an E_{ij} vs. r_{ij}^2 table for atom ij pairs and a table look-up based on the r_{ij}^2 between atoms. This avoided the repeated calculation of E_{ij} and the need to take square roots to obtain r_{ij} .

Structure Prediction

The overall procedure contains three steps. (1) Construction of a reasonable three-dimensional model for the compound of interest (the search probe) followed by *ab initio* quantum mechanical geometry optimization. The optimizations invariably are done with density functional theory (DFT) and a 6-31G* basis set (B3LYP/6-31G* option) with the Gaussian 98 [19] or Spartan 02 [20] programs on Unix/Linux workstations or G98W or Spartan 02 on Windows workstations. (2) Determination of possible hypothetical crystal structure with MOLPAK for all 29 coordination geometries. (3) The best 100-500 (smallest volume) structures from each of the coordination geometries are refined by lattice energy minimization to adjust the unit cell parameters, search probe orientation and position.

A number of programs are available for calculating the crystal lattice energy (energy sum of all atom-to-atom interactions between a central molecule and the surroundings) and performing the step (3) optimizations, but we primarily use the WMIN [21] and DMAREL [22] procedures and programs. The WMIN (E_{WMIN}) intermolecular potential contains a simple Coulombic and standard 6-exp terms for attraction and repulsion; e_i is a point charge on atom i from electrostatic potential calculations (6-31g* basis set), r_{ij} is the atom i to atom j distance; $A_{ij} = (A_i * A_j)^{1/2}$, $B_{ij} = (B_i * B_j)^{1/2}$, A_i and B_i are empirical coefficients for atom i ; C_i is similar to a van der Waals radius. The DMAREL potential is similar, but with a distributed multipole electrostatic term (6-31G** basis set) in place of the WMIN monopole. The A and B coefficients (C 's are fixed at

literature values) in both potentials are obtained by fitting calculated to experimental structures with the use of observed quantities such as the unit cell parameters, intermolecular distances, crystal densities and heats of sublimation where available. The coefficients are listed in Table 5.

$$E_{\text{WMIN}} = \sum_{(i \neq j)} e_i e_j / r_{ij} - (A_{ij}) / r_{ij}^6 + (B_{ij}) \exp[-r_{ij} / (C_i + C_j)]$$

Ideally, a single A (or B) coefficient would be appropriate for each element type such as one A_{H} for all hydrogens. It has been our experience, however, that atoms of the same element often require different coefficients in different functional groups. There would be, for example, different A_{H} 's for H in H-O , H-NR_2 , $\text{H-C}(\text{sp}^2)$, $\text{H-C}(\text{sp}^3)$, etc. Other complications may involve separate cross terms for each of the atom i – atom j interactions. For a simple molecule such as formaldehyde (H_2CO), the A_{ij} cross terms are handled in WMIN with three A_{H} , A_{C} and A_{O} coefficients that are used to form the six possible cross terms. But other programs, (e.g. DMAREL) may require cross terms that encompass the A_{HH} , A_{HO} , A_{HC} , A_{CC} , A_{CO} and A_{OO} possibilities. This is undoubtedly more flexible and possibly more accurate but does have the disadvantage of requiring the evaluation of many cross term coefficients. Of course, in cases with separate cross terms, one can always use the WMIN simplification of $A_{\text{HO}} = (A_{\text{H}} * A_{\text{O}})^{1/2}$, etc.

Several examples of the MOLPAK + WMIN structure prediction procedures are given in the next sections. The problem of identifying the correct crystal structure from literally thousands of possible structures remains. The “which is the best/correct solution” was an important topic during the 1999 and 2001 CCDC sponsored blind tests [12]. Calculated lattice energies are adequate in many cases, but in others small lattice energy differences make it difficult to separate the wheat from the chaff. Other criteria, such as good or bad patterns of intermolecular contacts in comparison with known crystal structures could be helpful.

Examples of MOLPAK + WMIN predictions

The utility of the MOLPAK + WMIN procedure for identifying the correct crystal structure is illustrated by the data in Figs. 2 and 3 and more detailed discussions for NOHTAZ, β -HMX, HNFx and octanitrocubane follow. Our ability to identify the correct structure from literally thousands of possibilities, while quite gratifying, is not yet at a level of 100%. The problem is one of recognizing the correct (best) structure from a number of good structures whose calculated lattice energies and densities may differ by only a few $0.1 \text{ kcal mol}^{-1}$ and a few 0.01 g cm^{-3} , respectively. The 35 structures shown in Fig 2 are examples in which the lowest lattice energies corresponded to the correct (experimental) structures. Whereas, the seven structures shown in Fig. 3 are

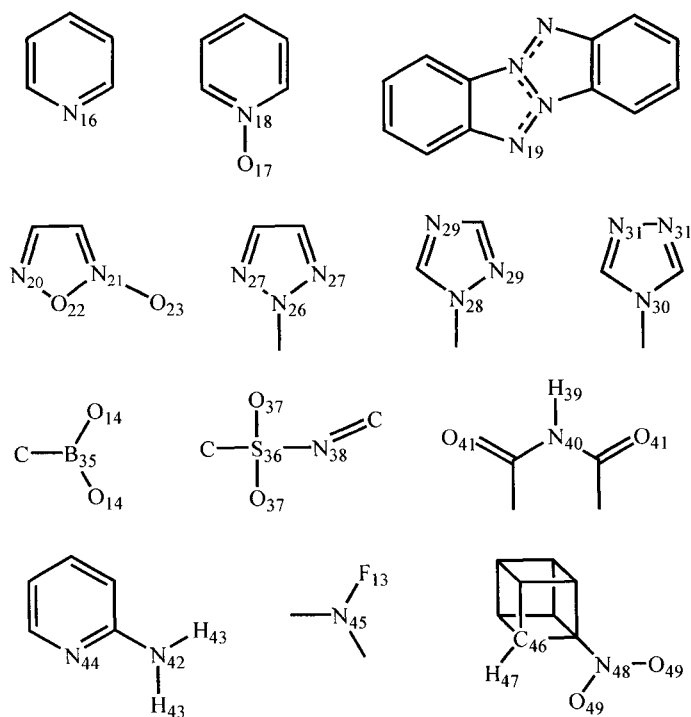
Table 5

Coefficients for lattice energy calculations with WMIN and 631G* electrostatic potential charges‡

#	Atom	A (kcal Å ⁶ mol ⁻¹)	B (kcal mol ⁻¹)	C (Å)
1	H (CH)	7.605	53.807	1.87
2	H (CH ₃ , CH ₂)	6.756	51.583	1.87
3	H (NH ₂)	7.60	54.90	1.87
4	C (sp ²)	20.761	283.021	1.80
5	C (sp ³)	21.091	291.427	1.80
6	O (NO ₂)	14.537	241.828	1.98
7	N (NO ₂)	19.377	248.336	1.89
8	N (<u>N</u> -NO ₂)	35.50	267.0	1.89
9	N (C-N(CH ₃) ₂)	32.50	282.0	1.89
10	N (NH ₂)	32.50	282.0	1.89
12	Br	91.241	841.761	1.66
13	F (NF ₂)	15.690	350.222	2.08
14	O (ethers)	19.10	251.5	1.98
15	O (ketones)	18.70	252.5	1.98
16	N (pyridines)	20.50	237.0	1.89
17	O (pyridine N-oxides)	18.50	153.0	1.98
18	N (pyridine N-oxides)	26.20	338.2	1.89
19	N (tetraaza-pentalenes)	21.0	243.0	1.89
20	N (1,2,5-oxadiazole)	24.20	332.0	1.89
21	N (1,2,5-oxadiazole)	26.00	338.0	1.89
22	O (1,2,5-oxadiazole)	18.10	269.0	1.98
23	O (1,2,5-oxadiazole)	17.50	285.0	1.98
24	N (nitroso)	18.00	343.0	1.89
25	O (nitroso)	18.00	253.0	1.98
26	N (1,2,3-triazole)	25.00	315.0	1.89
27	N (1,2,3-triazole)	24.50	315.0	1.89
28	N (1,2,4-triazole)	30.00	300.0	1.89
29	N (1,2,4-triazole)	24.00	334.0	1.89
30	N (1,3,4-triazole)	30.50	299.0	1.89
31	N (1,3,4-triazole)	24.50	324.0	1.89
32	N (azide N=N=N)	20.00	247.0	1.89
33	N (nitrile)	18.00	240.0	1.89
34	C (nitrile)	19.50	280.0	1.80
35	B (boron)	23.289	228.918	1.75
36	S (-O ₂ S-N=)	23.707	708.544	1.76
37	O (-O ₂ S-N=)	20.143	256.297	1.98
38	N (-O ₂ S-N=)	15.118	170.908	1.89
39	H (imides)	7.709	52.136	1.87
40	N (imides)	29.509	288.974	1.89
41	O (imides)	17.352	258.962	1.98

(continued next page)

42	N (amines)	17.858	287.599	1.89
43	H (amines)	6.891	44.930	1.87
44	N (amines)	5.686	87.829	1.89
45	N (NF ₂)	25.245	289.628	1.89
46	C (cubane)	23.068	273.735	1.80
47	H (cubane)	5.361	47.495	1.87
48	N (cubane-NO ₂)	19.637	269.325	1.89
49	O (cubane-NO ₂) [†]	13.463	197.934	1.98



[†]Nitrocubane O's are given a separate O---O B coefficient of 234.643. kcal mol⁻¹.

[‡]Crystal structure bond lengths can have substantial variability and the following adjustments are made before charge calculation: C(sp³)-H = 1.098, C(sp²)-H = 1.084, N-H = 1.01, N-O = 1.22 and N-F = 1.40 Å.

examples in which the experimental structure did not correspond to the lowest lattice energy solution. For these materials, the data in parentheses indicate the energy rank of the correct structure and the energy difference between the lowest energy and correct structures. In the case of KOFKAR, for example, the correct structure was the sixth lowest in energy and the lattice energy was 1.3 kcal mol⁻¹ larger than the lowest energy structure.

The last structure (GEJXAU) in Fig. 3, illustrates the potential importance of a packing procedure that can address problems of conformational flexibility.

The CCDC entry did not contain coordinates for the hydrogen atoms which were generated subsequently with the Chem3D program [23]. Chem3D oriented the methyl H's with a C-H bond eclipsing the nearby C-N bond. No further adjustments were made to this model and its use as the rigid body search probe for the MOLPAK + WMIN procedure led to the correct crystal structure (energy rank #3) outlined in Fig. 3. However, the use of a Gaussian-98 B3LYP/631G* model/search probe failed to produce a correct solution. This failure is presumably due to relatively minor differences in the X-ray and optimized model N-CH₃ conformations. In Fig 4, the two structures plus an overlay are shown which graphically demonstrate the very small differences between success and failure.

A Good Example: NOHTAZ, P2₁2₁2₁, $\rho_{\text{obs}} = 1.580 \text{ g cm}^{-3}$. The structure of NOHTAZ, essentially a trimethyl derivative of RDX, is shown in Fig. 2. As in all cases, the C-H and N-O distances in the X-ray model were adjusted to the standard values of 1.098 and 1.22 Å, respectively, before electrostatic potential calculations of the atomic charges. This adjusted model with charges constitutes the search probe. The standard 180° Eulerian axis orientations in 10° increments of the search probe were used for MOLPAK calculations with each of the 29 coordination geometries. The 400 smallest volume hypothetical structures for each geometry were passed to WMIN for structure optimization. The data in Table 5 summarize the lowest energy prediction for each geometry and are sorted on the basis of energy from lowest to highest. This clearly is a very favorable example with the correct structure having both the lowest energy and highest density. Additionally, the lattice energy difference of +2.6 kcal mol⁻¹ between the best and next best predicted structures is substantial by comparison with most predictions.

A Good Example: β -HMX, P2₁/c, Z' = 0.5, $\rho_{\text{obs}} = 1.893 \text{ g cm}^{-3}$. The α , β and δ -polymorphs of HMX have been well characterized by diffraction experiments. Certainly, the most important and the one with the highest crystal density is the β -form. The polymorph crystallizes in the monoclinic P2₁/c space group with two molecules per unit cell; the molecule has C_i point group symmetry and is positioned on a crystallographic inversion center. MOLPAK + WMIN Structure predictions were performed for coordination geometries in space groups with centers of symmetry, P-1, P2₁/c, C2/c, Pbca and Pbcn. The predicted structure with the smallest lattice energy corresponded to the experimental structure: P2₁/c, E = -45.14 kcal mol⁻¹, $\rho_{\text{calcd}} = 1.890 \text{ g cm}^{-3}$. The second lowest energy structure was Pbca, E = -44.56 kcal mol⁻¹, $\rho_{\text{calcd}} = 1.887 \text{ g cm}^{-3}$. The reduced cell parameters for the predicted structure and percent differences from experiment (in parentheses) are a = 6.525 (-0.2%), b = 7.478 (+1.4), c = 10.864 Å (-1.7), $\gamma = 101.06^\circ$ (-1.7).

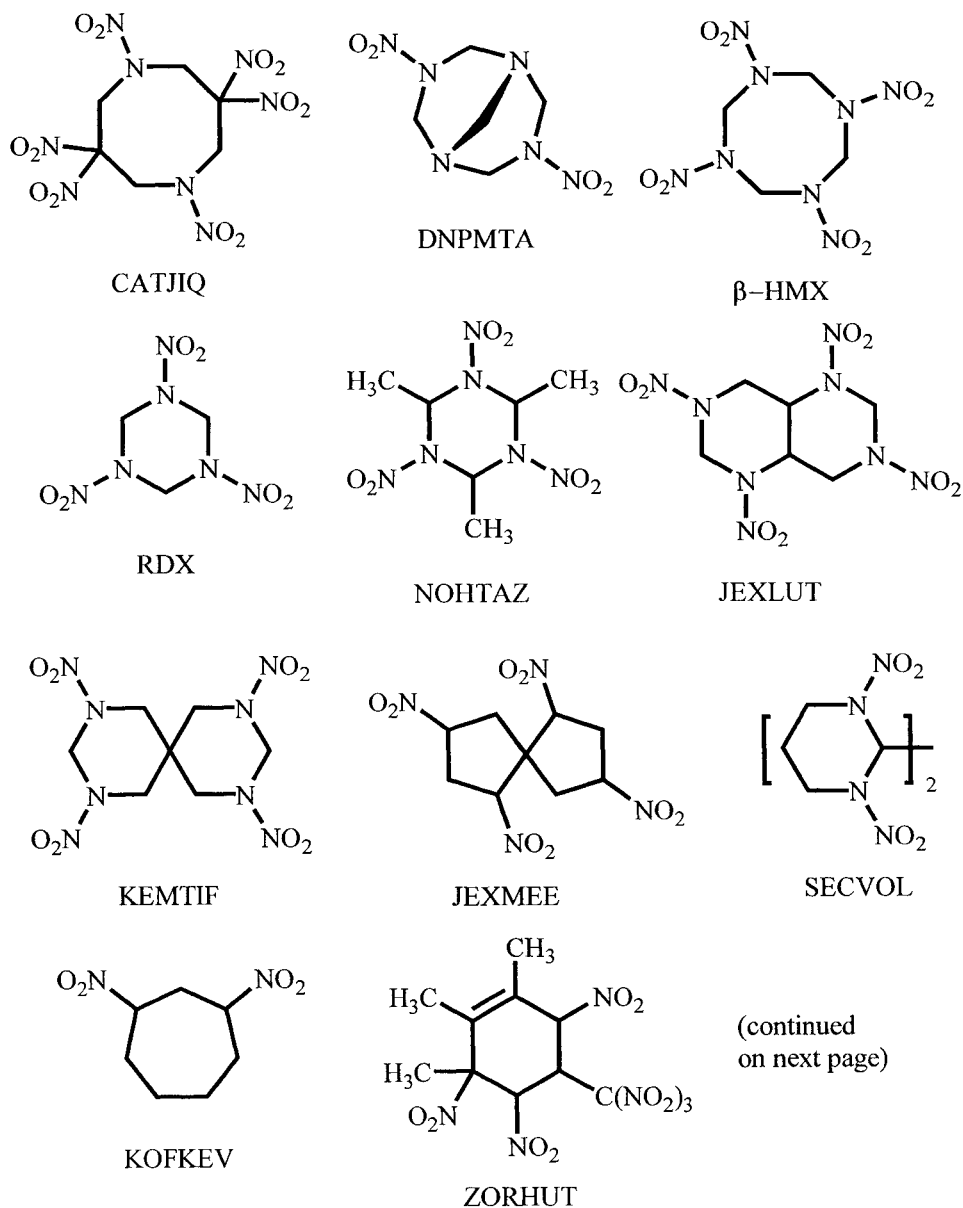
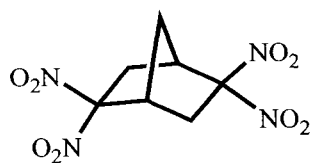
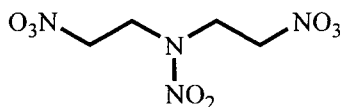


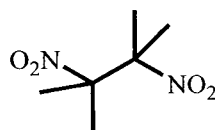
Figure 2. Drawings and reference codes for examples of MOLPAK + WMIN structure predictions; lowest energy prediction corresponds to the observed X-ray structure.



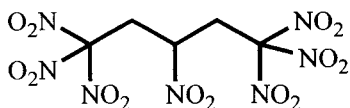
JUVMIW



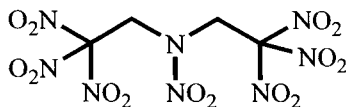
NXENAM



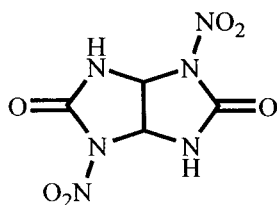
BECJEY (LT)



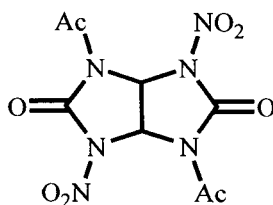
CUVXOG



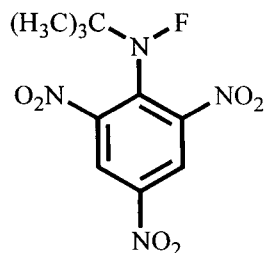
NOETNA



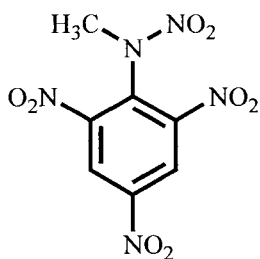
GEMZAZ



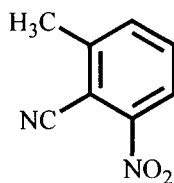
DEFLEF



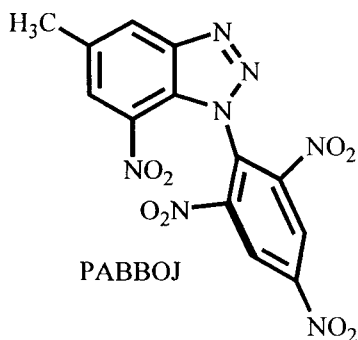
FBATNB



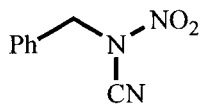
MTNANL



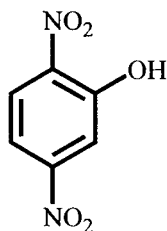
ZUGPOG



PABBOJ

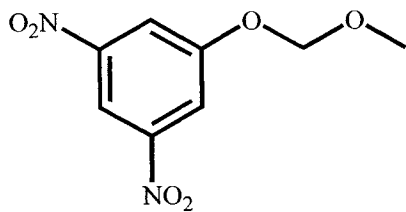


KASBAH (LT)

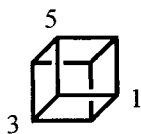


DNOPHL

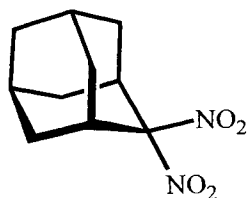
(continued
on next page)



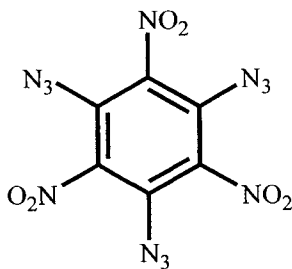
DEMSOD



CEDZUG; 1,4-(NO₂)₂
 HASHAK; 1,3,5-(NO₂)₃
 NACXEQ; 1,2,3,5,7-(NO₂)₇
 CUGCOW; (NO₂)₇
 CUGDIR; (NO₂)₈



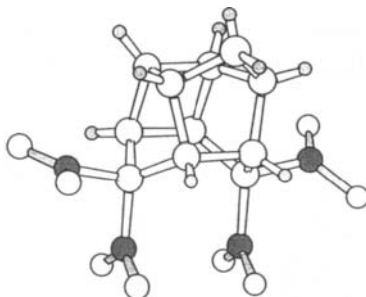
CAXNIY



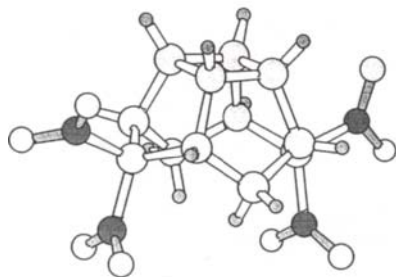
AZNIBZ



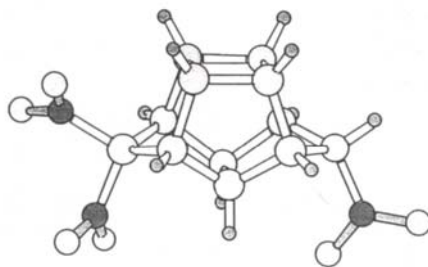
ε-CL20



VIKYUJ

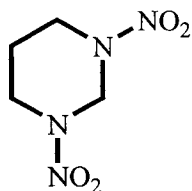


KEJKOA

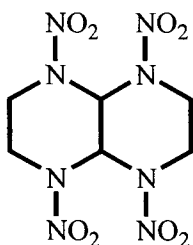


DUYREU (LT)

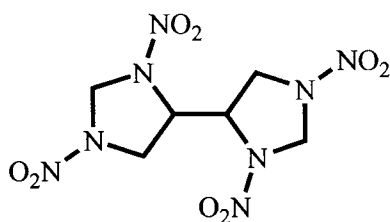
AZNIBZ Xray coordinates supplied by Prof. Klapotke, see Ref. [24].



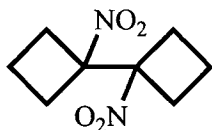
KOFKAR
(#6, 1.3
kcal mol⁻¹)



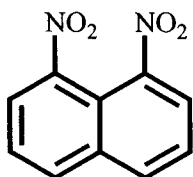
JEXMII
(#2, 0.6)



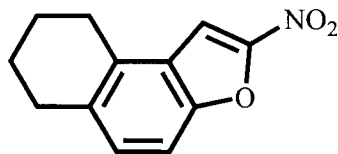
JEXMAA
(#6, 0.6)



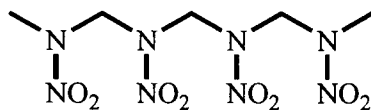
BECJUO
(#3, 0.2)



DNTNAP
(#6, 0.5)



DETDOV
(#3, 0.4)



GEJXAU
(#3, 0.6)

The hatched number gives the energy rank. In GEJXAU, for example, the correct structure had the third lowest (# 3) energy; and the energy was 0.6 kcal mol⁻¹ higher than the lowest energy structure.

Figure 3. Drawings and reference codes for materials used for MOLPAK + WMIN structure predictions in which the predicted structure with the smallest lattice energy did not correspond to the correct structure.

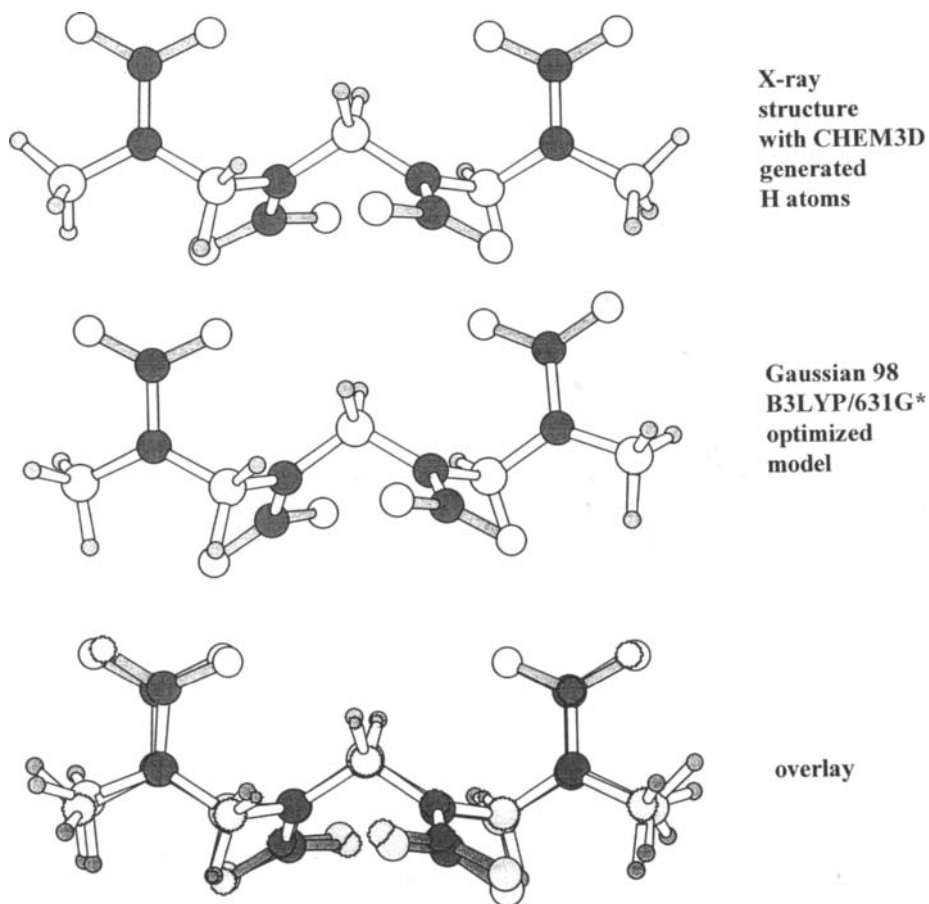


Figure 4. Drawings for two GEJXAU structures plus an overlay to illustrate differences between the X-ray and B3LYP/6-31G* optimized models.

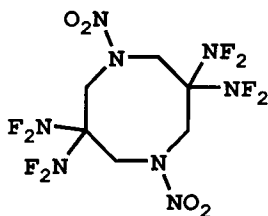
Table 6

Summary of predictions for NOHTAZ with predicted densities* (ρ ; g cm^{-3}), lattice energies (E ; kcal mol^{-1}) and space groups

#	ρ	E	Space group	#	ρ	E	Space group
1	1.590	-34.81	P212121	16	1.517	29.69	P21
2	1.584	-32.20	P21/c	17	1.504	29.64	Pbca
3	1.587	-31.99	P21/c	18	1.515	29.33	P21212
4	1.553	-31.42	Pna21	19	1.515	29.33	P21212
5	1.542	-31.03	P21/c	20	1.515	29.33	P21212
6	1.542	-31.03	P21/c	21	1.509	29.18	Pbcn
7	1.538	-30.96	Pbca	22	1.497	28.47	Pbcn
8	1.565	-30.94	P-1	23	1.515	28.15	Cc
9	1.565	-30.94	P-1	24	1.530	28.10	P21
10	1.505	-30.64	P212121	25	1.494	28.06	Pca21
11	1.547	30.50	P21/c	26	1.494	28.06	Pca21
12	1.590	30.28	C2/c	27	1.485	27.86	Pna21
13	1.537	30.22	C2/c	28	1.523	27.75	Pna21
14	1.537	30.21	C2/c	29	1.515	27.19	P1
15	1.523	30.03	C2				

*Volume additivity density = 1.560 g cm^{-3} .

Is There Something Better?: HNFX, R-3, $\rho_{\text{obs}} = 1.807 \text{ g cm}^{-3}$. Difluoroamino compounds are of interest because of their potential high density and energy and properties as solid propellant oxidizers. An X-ray crystallographic determination [25] of the promising HNFX [26] revealed the disappointingly



low density of 1.807 g cm^{-3} . The crystal structure “shows an interesting, unpredicted feature: channels, with a 3-fold axis of symmetry surrounded by HNFX molecules.” [25] Our calculations and predictions, outlined in Table 7, show that the experimental crystal structure in space group R-3 indeed is not the lowest energy at $-39.7 \text{ kcal mol}^{-1}$. Rather, we suggest there is an unknown

polymorph in space group $P2_1/c$ with a substantially lower energy of about -44 kcal mol⁻¹ and higher density of about 2.03 g cm⁻³.

Table 7

Various HNFx models, space groups, lattice energies (E, kcal mol⁻¹) and densities (ρ , g cm⁻³)

Model geometry	Space group	E	ρ
C _i , Xray model*	R-3	-39.71	1.789
C _i , Xray model in general position	Pca2 ₁	-41.19	1.945
C _i , Xray model on center of symmetry	P2 ₁ /c	-43.39	2.049
C _i , optimized model† on center of symmetry	P2 ₁ /c	-44.77	2.027
C _i , optimized model† in general position	Pca2 ₁ or P2 ₁ 2 ₁ 2 ₁	-41.03	1.963
C ₂ , model** in general position	Cc	-39.38	1.944
C ₂ , model* on 2-fold axis	C2/c	-33.33	1.760
C ₁ model	P2 ₁ /c	-37.72	1.917

* The two unique NF₂ groups show two-fold disorder in the experimental X-ray structure.

The minor conformations were removed for the calculations: $\rho_{\text{obs}} = 1.807$ g cm⁻³; $\rho_{\text{VA}} = 1.915$ g cm⁻³. †Model from Gaussian-98, B3LYP/631G* optimization.

A Good Example: Octanitrocubane, C2/c, Z' = 0.5, $\rho_{\text{obs}} = 1.979$ g cm⁻³.

Earlier predictions of the density ranged from 2.1 to more than 2.2 g cm⁻³. The plot (Fig. 5) of crystal density vs. number of nitro groups suggests that extrapolation of the cubane to tetranitrocubane data would give a value of 2.2 g cm⁻³ or perhaps larger for ONC. However, beyond five nitro groups the slope eases and has become almost flat in the 6-8 nitro group range. The successful synthesis and subsequent X-ray structure determination [27] in 2000 showed a disappointing crystal density of less than 2 g cm⁻³. Extensive calculations, performed with the MOLPAK + WMIN procedures are summarized in Table 8. The predicted densities with both an X-ray model and Gaussian 98 optimized model for the search probe are in good agreement with experiment. The predicted structure for geometry DC corresponds to the experimental X-ray structure and is only 0.01 kcal mol⁻¹ higher than the lowest energy structure. Geometry DA, space group Cc, also corresponds to the experimental structure

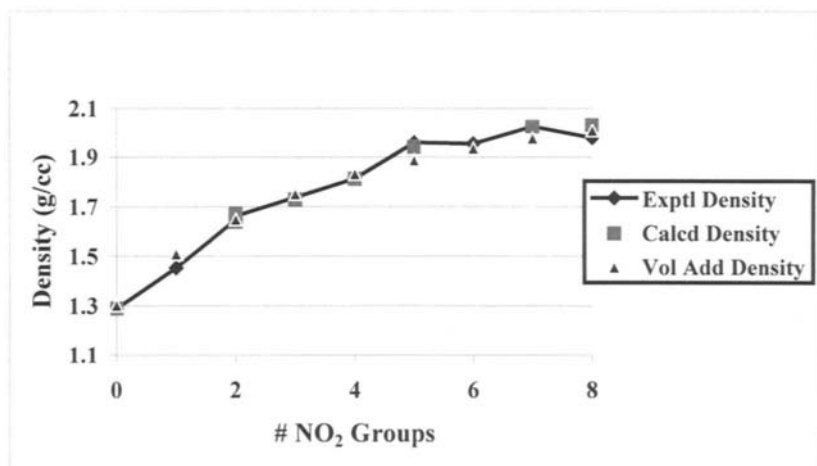


Fig. 5. Crystal density vs number of nitro groups for various cubanes

Table 8

Summary of MOLPAK + WMIN predictions for octanitrocubane with lattice energies (E , kcal mol⁻¹) and densities (ρ , g cm⁻³); Gaussian 98 B3LYP/631G** model with C_2 symmetry

Coord geom.	ρ	E	Space group
AB	2.003	-23.27	P-1
AK	2.003	-23.27	P21/c
DC	2.003	-23.26	C2/c ← molecule on 2-fold axis
DA	2.003	-23.24	Cc ← molecule in general position
AM	2.002	-23.24	P21/c
AH	1.898	-21.34	P21
AQ	1.883	-21.08	P212121
....	geometries deleted
BF	1.732	-18.16	Pna21
BB	1.764	-16.99	P21212
AP	1.647	-15.19	P21212 ← molecule on 2-fold axis

with the search probe's C_2 axis aligned to generate an effective $C2/c$ space group. Use of the X-ray structure as the search probe gave DC (experimental) as the lowest energy structure.

Summary and Challenges. Because of the expense, labor, time requirements and possible danger (both to personnel and the environment) of synthesizing new energetic materials, it is important to pre-select only materials which have the potential for substantially better performance than compounds currently in use. In this chapter, our procedures for crystal structure (and density) prediction were detailed. Crystal structure prediction provides an entry into other important areas such as sensitivity and crystal habit.

Structure prediction has made great strides within the last few years. Although there still remains the problem of identifying the correct structure from among thousands of possibilities, this no longer is a serious impediment in many instances. Conformational flexibility can be handled by some existing codes, but this aspect remains a work in progress. Additionally, handling crystals with more than one molecule per asymmetric unit and structures with different molecules per asymmetric unit requires substantially more development. We look forward to better and faster procedures for lattice energy calculation and structure refinement and will devote substantially more time to the complete parameterization of codes such as DMAREL. Comparisons with *ab initio* crystal calculations will be helpful.

Acknowledgements. This work has been supported over the years by the Office of Naval Research. Our thanks to program managers Drs. Richard Miller (retired) and Judah Goldwasser. Current work is supported in part by ONR and a MURI (Multidisciplinary Research Program of the University Research Initiative) grant titled "Energetic Materials Design for Improved Performance/Low Life Cycle Cost," U. S. Army Research Office under contract/grant number DAAD19-02-1-0176. Our thanks to program managers Drs. Robert Shaw and David Mann.

References

- [1] R. J. Spear and W. S. Wilson, *J. Energetic Materials*, 2 (1984) 61.
- [2] M. J. Kamlet and S. J. Jacobs, *J. Chem. Phys.*, 4 (1968) 23.
- [3] C. L. Mader in "Organic Energetic Compounds," P. L. Markinas, ed., Nova Science Publishers, Commack, NY, p. 193, 1996
- [4] A. Immirzi and B. Perini, *Acta Cryst.*, A33 (1977) 216.
- [5] C. M. Tarver, *J. Chem. Eng. Data*, 24 (1979) 136.
- [6] D. A. Cichra, J. R. Holden, and C. Dickinson, Estimation of "Normal" Densities of Explosive Compounds from Empirical Atomic Volumes, Naval Surface Weapons Center, Silver Spring, MD (1980)
- [7] J. R. Stine, Predictions of Crystal Densities of Organic Explosives by Group Additivity, Report LA-8920, Los Alamos National Laboratory, Los Alamos, NM (1981).

-
- [8] H. L. Ammon and S. Mitchell, *Propellants Explosives Pyrotechnics*, 23 (1998) 260.
- [9] H. L. Ammon, *Structural Chem.*, 21 (2001) 205.
- [10] G. Piacenza, B. Jacob, H. Graindorge, B. Blaive and R. Gallo, *Combustion and Detonation Jahrestagung 1997*, Fraunhofer ICT and Verlag GMgh, Karlsruhe, pp 1-14, (1997).
- [11] A. I. Kitaigorodsky, *Organic Chemical Crystallography*, Consultants Bureau, New York, pp 106-7 (1973).
- [12] W. D. S. Motherwell, H. L. Ammon, J. D. Dunitz, A. Dzyabchenko, P. Erk, A. Gavezzotti, D. W. M. Hofmann, F. J. J. Leusen, J. P. M. Lommerse, W. T. M. Mooji, S. L. Price, H. Scheraga, B. Schweizer, M. U. Schmidt, B. P. van Eijck, P. Verwer and D. E. Williams, *Acta Cryst.*, B58, (2002) 647; J. P. M. Lommerse, W. D. S. Motherwell, H. L. Ammon, J. D. Dunitz, A. Gavezzotti, D. W. M. Hofmann, F. J. J. Leusen, W. T. M. Mooji, S. L. Price, B. Schweizer, M. U. Schmidt, B. P. van Eijck, P. Verwer and D. E. Williams, *Acta Cryst.*, B56 (2000) 697; W. T. M. Mooji, *Ab Initio Prediction of Crystal Structures*, Ph.D. Dissertation, Utrecht University, The Netherlands (2000).
- [13] J. R. Holden, Z. Du and H. L. Ammon, *J. Comp. Chem.*, 14 (1993) 422.
- [14] L. Pauling, L., *The Nature of the Chemical Bond*, 3rd ed., Cornell University Press, NY, p. 260, 1960; W. H. Baur, *Acta Cryst.*, B28 (1973) 1456; A. Bondi, *J. Phys. Chem.*, 68 (1964) 441. T. R. Stouch and P. C. Jurs, *J. Chem. Inf. Comput. Sci.*, 26 (1986) 4.
- [15] J. R. Holden and C. Dickinson, *J. Phys. Chem.*, 81 (1977) 1505.
- [16] D. T. Cromer, H. L. Ammon and J. R. Holden, *A Procedure of Estimating the Crystal Densities of Organic Explosives*, Report LA-11142-MS, Los Alamos Scientific Laboratory, Los Alamos, NM (1981).
- [17] E. Giglio, *Nature*, 222 (1969) 339.
- [18] J. R. Holden and C. Dickinson, *J. Phys. Chem.*, 81 (1977) 1505.
- [19] Gaussian 98 (Revision A.11), M. J. Frisch, G. W. Trucks, H. B. Schlegel, G. E. Scuseria, M. A. Robb, J. R. Cheeseman, V. G. Zakrzewski, J. A. Montgomery, Jr., R. E. Stratmann, J. C. Burant, S. Dapprich, J. M. Millam, A. D. Daniels, K. N. Kudin, M. C. Strain, O. Farkas, J. Tomasi, V. Barone, M. Cossi, R. Cammi, B. Mennucci, C. Pomelli, C. Adamo, S. Clifford, J. Ochterski, G. A. Petersson, P. Y. Ayala, Q. Cui, K. Morokuma, P. Salvador, J. J. Dannenberg, D. K. Malick, A. D. Rabuck, K. Raghavachari, J. B. Foresman, J. Cioslowski, J. V. Ortiz, A. G. Baboul, B. B. Stefanov, G. Liu, A. Liashenko, P. Piskorz, I. Komaromi, R. Gomperts, R. L. Martin, D. J. Fox, T. Keith, M. A. Al-Laham, C. Y. Peng, A. Nanayakkara, M. Challacombe, P. M. W. Gill, B. Johnson, W. Chen, M. W. Wong, J. L. Andres, C. Gonzalez, M. Head-Gordon, E. S. Replogle, and J. A. Pople, Gaussian, Inc., Pittsburgh PA (2001).

-
- [20] Spartan 02, Wavefunction, Inc., Irvine, CA (2001).
- [21] W. R. Busing, WMIN, A Computer Program to Model Molecules and Crystals in Terms of Potential Energy Functions, Report ORNL-5747, Oak Ridge National Laboratory, Oak Ridge, TN (1981).
- [22] D. J. Willock, S. L. Price, M. Leslie and C. R. A. Catlow, *J. Comput. Chem.*, 16 (1995) 628.
- [23] Chem3D, Molecular Modeling and Analysis Program, CambridgeSoft Corp., Cambridge, MA (1999).
- [24] D. Adam, K. Karaghiosoff, T. M. Klapotke, G. Holl and M. Kaiser, *Propellants, Explosives, Pyrotechnics*, 27 (2002) 7; thanks to Prof. Klapotke for a CIF file with the Xray crystallographic details.
- [25] R. D. Chapman, R. D. Gilardi, M. F. Welker and C. B. Kreutzberger, *J. Org. Chem.* 64, (1999) 960.
- [26] R. D. Chapman, M. F. Welker and C. B. Kreutzberger, *J. Org. Chem.*, 63 (1998) 1566.
- [27] M. Zhang, P. E. Eaton and R. Gilardi, *Angew. Chem. Int. Ed.*, 39 (2000) 404; P. E. Eaton, M. Zhang, R. Gilardi, N. Gelber, S. Iyer and R. Surapaneni, *Propellants, Explosives, Pyrotechnics*, 27 (2002) 1.

This Page Intentionally Left Blank

Chapter 8

X-ray crystallography – beyond structure in energetic materials

A. Alan Pinkerton, Elizabeth A. Zhurova and Yu-Sheng Chen

Department of Chemistry, University of Toledo, Toledo, OH, USA

X-ray crystallography may be used to obtain details of the chemical structure of energetic materials that goes far beyond the simple determination of the atomic positions and derived geometrical structure. X-rays are scattered by electrons, hence, if diffraction data of sufficient quality are obtained, it is possible to map the entire electron density distribution. This may be used in a variety of ways. In the simplest application, partial charges may be assigned to atoms. By comparison with a promolecule composed of neutral spherical atoms, the deformation of the electron density on bond and molecule formation may be obtained. From the analysis of the topology of the total electron density, chemical bond orders may be cleanly characterized, and partial charges defined according to the Bader Atoms in Molecules approach. Calculation of the Laplacian of the electron density provides an additional parameter to characterize chemical bonding interactions. From the location of the nuclei (assumed to be at the center of the core electron density) and the electron density distribution, the electrostatic potential may be mapped for a molecule. From the electron density distribution and the Laplacian, the kinetic and potential energy density distribution may be obtained, thus giving a measure of energy storage in the molecules themselves (especially when compared with a promolecule), and the interaction energies between neighbors. The methodologies used to obtain these parameters are presented along with examples taken from recent studies on energetic molecules.

1. INTRODUCTION

In recent years, there has been growing interest in the development of new solid energetic materials, especially those with low shock sensitivity and propellants with low signatures. Empirical studies suggest that desired properties for this class of compounds are a halogen-free, nitrogen- and oxygen-rich molecular composition, high densities and a high heat of formation [1]. In order to relate

their properties to more fundamental parameters, we have initiated a program to experimentally and theoretically map the electron density distributions in energetic materials, to use this information to characterize the chemical bonding, and to derive other one-electron properties as well as to identify the energy rich regions in the molecules of such compounds.

The utility of X-ray crystallography depends on the scattering of X-rays by the periodic electron density distribution that exists in crystals. The ability to measure extensive, accurate X-ray diffraction data sets at low temperature has allowed the crystallographer to go beyond the determination of the atomic positions (concentration of electron density) in molecules and to examine the distribution of electron density related to chemical bonding. This type of study is far removed from routine structure determination; however, the necessary experimental protocols for this type of study using modern diffraction equipment, along with the computational techniques required have now been well established [2]. Typically data must be taken at low temperature to minimize thermal motion and thermal diffuse scattering thus increasing the observable data at high orders and allowing the deconvolution of thermal motion from non-spherical electron density distribution associated with bonded atoms.

The following sections will describe the experimental protocols, the important steps of data reduction, the model used to describe the electron density distribution, the current methods of analyzing this distribution, and the properties that may be derived from such analyses. In all cases, the discussion will be illustrated by examples of studies of energetic molecules either taken from the literature or from unpublished results taken from our own laboratory.

2. EXPERIMENTAL PROTOCOL

From kinematic theory, the electron density distribution in a crystal may be represented by a Fourier series,

$$\rho(\mathbf{r}) = \frac{1}{V} \sum_{\mathbf{H}} F_{\mathbf{H}} \exp(-2\pi i \mathbf{H} \cdot \mathbf{r}) \quad (1)$$

where V is the volume of the unit cell, $F_{\mathbf{H}}$ are structure factors derived from the observed diffracted X-ray intensities, and \mathbf{H} and \mathbf{r} are vectors in reciprocal and direct space respectively [3]. Clearly the precision with which we can know $\rho(\mathbf{r})$ depends on how well we measure $F_{\mathbf{H}}$ and how many terms are in the summation. In addition, the electron density is smeared by thermal motion; hence, to interpret the valence density distribution it is necessary to deconvolute the non-spherical atomic electron density from the anisotropic motion of the atoms themselves. Ideally, data should be collected at absolute zero. In practice, although there are devices that allow experiments to be carried out at 10 – 20 K

using helium as the cryogen [4,5], it is much more common for experiments to be carried out at 85 – 100 K using nitrogen. In order to effect the deconvolution, advantage is taken of the fact that the compact atomic cores scatter to much higher diffraction angles than the more diffuse valence electrons, hence data obtained at sufficiently high angles is almost entirely due to thermally smeared core electron density, whereas the low angle data has a large contribution from the valence electrons also.

In order to minimize systematic errors, and also to improve the accuracy of the data set, it is common to measure a highly redundant data set, either by collecting symmetry equivalent Bragg reflections or by multiple measurements of the same reflections using different settings of the crystal on the diffractometer. At the present time, diffractometers that use area detectors, most commonly based on CCD technology, have largely replaced point detectors; hence many Bragg reflections may be recorded at the same time [6].

A typical experiment on NTO used the following experimental protocol [7]. A transparent, colorless single crystal of the β -phase of NTO was mounted on a 0.1 mm capillary with epoxy resin and slowly cooled down to 100K with an Oxford Cryostream. The X-ray diffraction experiment was performed with a Bruker platform diffractometer [8] with a 2K CCD detector using $\text{Ag-K}\alpha$ radiation. 0.3° ω -scans were performed at a detector distance of 3.44 cm, and using a series of different φ settings, which produced a data set with approximately ten-fold redundancy. Details of the data collection strategy are shown in Table 1. The exposure time of 160 sec allowed the use of the full dynamic range of the detector. No intensity decay was observed during the experiment. Other experimental details are in Table 2.

Table 1

Data collection strategy for β -NTO

Run No.	2θ	ω_{start}	φ	No. of frames
1	0	350	0	530
2	0	350	45	530
3	0	350	90	530
4	0	350	180	530
5	0	350	270	530
6	-45	300	0	500
7	-45	300	30	500
8	-45	300	90	500
9	-45	300	135	500
10	-45	300	225	500
11	-45	300	315	500
12	0	350	0	100

2θ is the swing angle of the detector, φ is the fixed angle for each run (set of frames).

Table 2

Experimental details for β -NTO

Chemical formula	$C_2H_2N_4O_3$
Chemical formula weight	130.08
Space group	$P2_1/c$
a (Å)	9.3255(1)
b (Å)	5.4503(1)
c (Å)	9.0400(1)
β (°)	101.474(1)
V (Å ³)	450.29
Z	4
D_x (Mg m ⁻³)	1.919
Radiation type	Ag K α
Wavelength (Å)	0.56086
No. of reflections for cell parameters	8330
θ range (°)	0 - 27
μ (mm ⁻¹)	0.1
Temperature (K)	100(1)
Crystal size (mm)	0.12 x 0.12 x 0.4
No. of measured reflections	68989
θ_{min} (°)	1.76
θ_{max} (°)	43.69
Criterion for observed reflections	$I > 2 \sigma(I)$ for $\sin \theta/\lambda < 1.0 \text{ Å}^{-1}$ $I > 6 \sigma(I)$ for $\sin \theta/\lambda > 1.0 \text{ Å}^{-1}$
No. of observed reflections	43381
No. of independent reflections	4080
R_{int}	0.0215

3. DATA REDUCTION

In order to obtain the best quality data, it is essential to obtain the best possible unit cell parameters along with the associated orientation matrix. This typically requires repeated integrations of the data set until the optimum parameters are empirically obtained based on statistical evaluation of the data. In the case of the β -NTO data presented above, the integration of the intensity data was performed with the program SAINT [9]. An empirically chosen integration box size of $1.69 \times 1.82 \times 0.864^\circ$, and a profile fitting procedure for the weak reflections based on the profiles of strong ($I > 30\sigma(I)$) reflections allowed us to obtain the best internal consistency ($R_{int}=0.0215$) and preliminary (spherical atom model) refinement R factors. After the integration process, the unit cell parameters were

refined from the centroids of all reflections with $\sin\theta/\lambda < 0.8 \text{ \AA}^{-1}$, since all of the high-angle reflections were relatively weak. The integration process was repeated 3 times until total convergence in cell parameters was obtained.

Additional corrections need to be applied to the data at this time to remove systematic errors. Typically the most important of these are for absorption and possible inhomogeneity of the X-ray beam. When using area detector data, either the program SADABS [10] or SORTAV [11] have been used for this purpose. In the case of β -NTO, no absorption correction was needed ($\mu=0.1 \text{ mm}^{-1}$), however, SADABS [10] was used to correct the data for possible inhomogeneity of the X-ray beam. At this time it is typical to average the data, and to remove any outliers detected in the data set. This can also be conveniently done with the program SORTAV [11], and the quality of the data analyzed from the output statistics. The most important parameters are the internal consistency of the data, the maximum resolution of the data and the $I/\sigma(I)$ ratio. The results for a typical experiment, in this case for HMX [12], are reported in Table 3. As expected, the strongest reflections have the best internal agreement, the highest $I/\sigma(I)$ ratios and appear at the lower diffraction angles. Although the intensity of the data falls off with increasing Bragg angle, there are still significant observations obtained with $\sin\theta/\lambda > 1.0 \text{ \AA}^{-1}$. The need for data which extends over such a wide range of reciprocal space, is due to the fact that the valence electrons only have significant scattering at relatively low angles whereas the most important effects of thermal motion are obtained from data at high angles.

Table 3

Data statistics for HMX as a function of $Q = I/\sigma(I)$ and as a function of $S = \sin\theta/\lambda$.

Intensity-significance intervals ($Q_{\min} < Q < Q_{\max}$)				
	NTERMS	NMEANS	$\langle N \rangle$	R1
$-1 < Q < 0$	706	269	2.6	1.1226
$0 < Q < 1$	1713	616	2.8	1.1006
$1 < Q < 2$	1335	474	2.8	0.5833
$2 < Q < 3$	1021	378	2.7	0.3765
$3 < Q < 4$	789	281	2.8	0.2691
$4 < Q < 6$	1688	547	3.1	0.1938
$6 < Q < 8$	1404	469	3.0	0.1389
$8 < Q < 10$	1351	455	3.0	0.1024
$10 < Q < 20$	5581	1666	3.3	0.0612
$20 < Q < 30$	4839	1152	4.2	0.0394
$30 < Q < 50$	4213	754	5.6	0.0280
$50 < Q < 100$	477	93	5.1	0.0180

Table 3 contd.

Resolution shells ($S_{\min} < S < S_{\max}$)				
	NTERMS	NMEANS	<N>	R1
$S < 0.050$	2	1	2.0	0.2682
$0.050 < S < 0.063$	0	0	0.0	0.0000
$0.063 < S < 0.083$	2	1	2.0	0.0478
$0.083 < S < 0.125$	30	8	3.8	0.0230
$0.125 < S < 0.143$	12	3	4.0	0.0446
$0.143 < S < 0.167$	35	9	3.9	0.0153
$0.167 < S < 0.200$	57	13	4.4	0.0192
$0.200 < S < 0.250$	210	38	5.5	0.0264
$0.250 < S < 0.333$	658	95	6.9	0.0256
$0.333 < S < 0.500$	3001	399	7.5	0.0283
$0.500 < S < 0.667$	5346	746	7.2	0.0348
$0.667 < S < 1.000$	7550	2537	3.0	0.0427
$1.000 < S < 1.250$	6593	2629	2.5	0.0732
$1.250 < S < 1.428$	1711	711	2.4	0.1519

4. DATA ANALYSIS

X-ray crystallography seeks to obtain the best model to describe the periodic electron density in a crystal by a least squares fit of the parameters of the model (used to calculate structure factors) against the observed structure factors derived from the diffraction experiment. All models used are atomic in nature, but vary in the complexity of the description of the atomic electron density.

4.1 Structure model – spherical atom

In normal, routine structure determination experiments, the atomic scattering factors (f_i) used are derived from spherically averaged ground state electronic configurations of neutral atoms. The positions of these scattering centers convoluted with thermal motion are then used to calculate structure factors (F_H), which are compared with observed structure factors derived from the observed Bragg intensities [3].

$$F_H = \sum_i [f_i]_T \exp(2\pi i \mathbf{H} \cdot \mathbf{r}) \quad (2)$$

Treating the positional parameters and the elements of the thermal displacement tensor as variables, a best fit of the observed to the calculated structure factors in a least squares sense is determined. As this is a non-linear procedure, it is essential to over determine the problem. For a routine structure

determination, the reported parameters are the fractional atomic coordinates within the unit cell along with the atomic displacement parameters. These results are typically summarized in an ORTEP plot [13] as shown in Fig. 1 for the trinitrodiazapentalene, TNDAP [15]. These results were obtained with the SHELXTL program suite [16].

Given the quality of data described above, it is possible to go beyond the neutral spherical atom model, and to determine the redistribution of valence electrons due to chemical bonding. In other words, we can develop a description of the electron density distribution that includes charge transfer and non-spherical atoms.

4.2 Structure model – atom centered multipole model

Although it is possible to determine the complete electron density distribution using the Fourier transform of the observed structure factors, Eq. (1), the errors inherent in the structure factor amplitudes and, in the case of non-centrosymmetric structures, the errors in their phases introduce significant noise and bias into the result. Because of this, it has become normal practice to model the electron density by a series of pseudo-atoms consisting of a frozen, spherical core and an atom centered multipole expansion to represent the valence electron density [2,17].

$$\rho_{atomic}(\mathbf{r}) = \rho_{core}(r) + P_v \kappa'^3 \rho_{valence}(\kappa' r) + \sum_{l=1}^4 \kappa''^3 R_l(\kappa'' r) \sum_{m=-l}^l P_{lm} y_{lm}(\mathbf{r}/r) \quad (3)$$

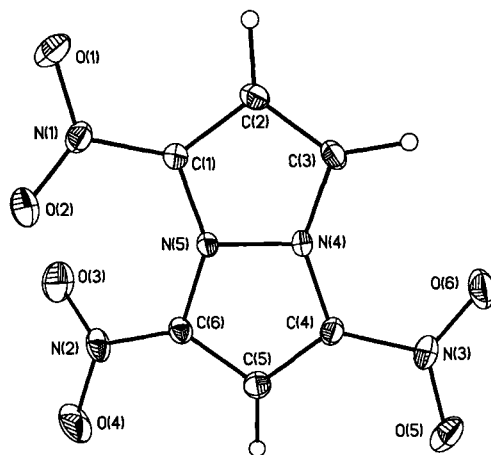


Fig. 1. The TNDAP molecule showing 75% probability thermal ellipsoids.

Here P_v and P_{lm} are monopole and higher multipole populations; R_i are normalized Slater-type radial functions; y_{lm} are real spherical harmonic angular functions; κ' and κ'' are the valence shell expansion /contraction parameters. Hartree-Fock electron densities are used for the spherically averaged core and valence shells. This atom centered multipole model may also be refined against the observed data using the XD program suite [18], where the additional variables are the population and expansion/contraction parameters. If only the monopole is considered, this reduces to a spherical atom model with charge transfer and expansion/contraction of the valence shell. This is commonly referred to as a kappa refinement [19].

An example of a kappa refinement for β -NTO is given below in Table 4. Clearly, the electronegative oxygen atoms have gained electrons with a concomitant expansion of the valence shell, whereas the more electropositive atoms have lost electrons and the valence shell is contracted.

Population of functions other than the monopole does not modify the charge on the pseudo-atom, but redistributes it in a non-spherical manner. Examples of the angular functions showing their symmetry for a selected number of poles are shown in Fig. 2 below. Although one must be careful not to confuse the various multipoles with atomic orbitals, their shapes are the same, i.e. the monopole is a spherical function like an s orbital, the three dipoles resemble p orbitals, etc.

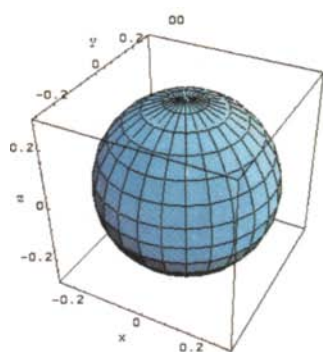
As we are dealing with spherical harmonics, and as we are trying to model the aspherical atomic electron density, the orientation of the local atom centered coordinate system is, in principle, arbitrary, appropriate linear combinations always giving the same result. However, in practice it is helpful to choose a local coordinate system such that the multipoles are oriented in rational directions, and thus the most important multipole populations will lie in directions that would be expected to represent chemical bonds or lone pairs [2,20], e.g. for an sp^2 hybridized atom, defining one bond as the x direction, the trigonal plane as the xy plane, and z perpendicular defines three lobes of the $3p_z$

Table 4

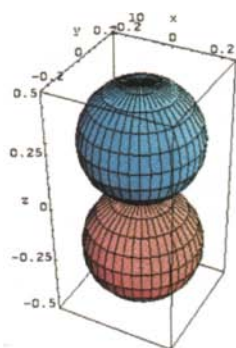
β -NTO: the results of the κ -refinement where q is the atomic charge derived from the monopole population

	q, e	κ'		q, e	κ'
N(1)	-0.06(4)	1.013(5)	O(6)	-0.19(4)	1.002(4)
N(2)	-0.20(4)	1.006(5)	C(3)	+0.37(6)	1.058(9)
N(4)	-0.35(5)	1.004(5)	C(5)	+0.21(7)	1.048(9)
N(5)	+0.32(6)	1.034(6)	H(2)	+0.23(2)	1.22(3)*
O(3)	-0.48(5)	0.981(4)	H(4)	+0.30(2)	1.22(3)
O(5)	-0.14(4)	1.005(4)			

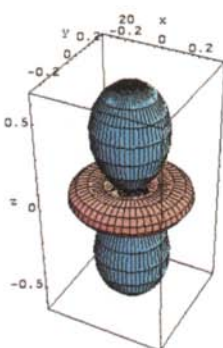
* The same κ' was used for both hydrogen atoms



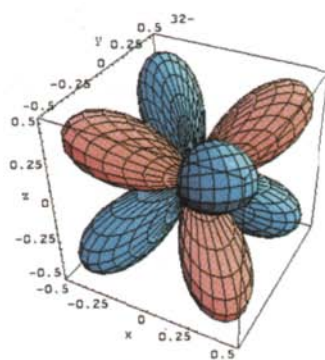
00 monopole



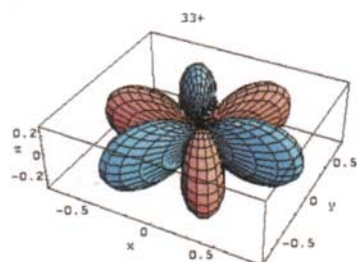
10 dipole



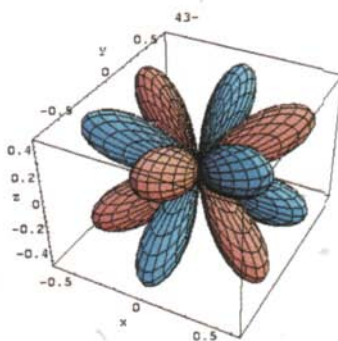
20 quadrupole



32- octupole



33+ octupole



43- hexadecapole

Fig. 2. Examples of multipoles, blue representing positive electron density and red, negative density

octupole along the bonding directions and the 20 quadrupole with lobes perpendicular to the plane to account for π -bonding density, or, for sp^3 atoms, defining x, y and z as the orthogonal two-fold axes of the tetrahedron (the bond bisectors) allows the use of a single 32- octupole to represent the four bonding directions. In this way the deviations from idealized bonding directions will only show up as perturbations from other multipoles with minor populations. There are additional benefits to this approach beyond that of simple visualization; using only a small number of additional variables in the early stages of least squares refinement renders the calculation more stable, and the use of rational directions allows the use of additional local symmetry based on the chemistry in the case of large molecules.

The local coordinate system chosen for β - NTO is shown in Fig. 3.

5. REFINEMENTS

Typically the refinement is carried out in a series of steps. For example, for β - NTO [7], first the scale factor, extinction, valence monopole population, P_v , positional and displacement parameters were refined with the whole data set. Second, the positional and displacement parameters for non-hydrogen atoms were refined with high-angle reflections ($\sin \theta/\lambda > 0.7 \text{ \AA}^{-1}$) and fixed. Third, P_v , κ' - parameters and extinction were refined with low-angle ($\sin \theta/\lambda < 1.0 \text{ \AA}^{-1}$)

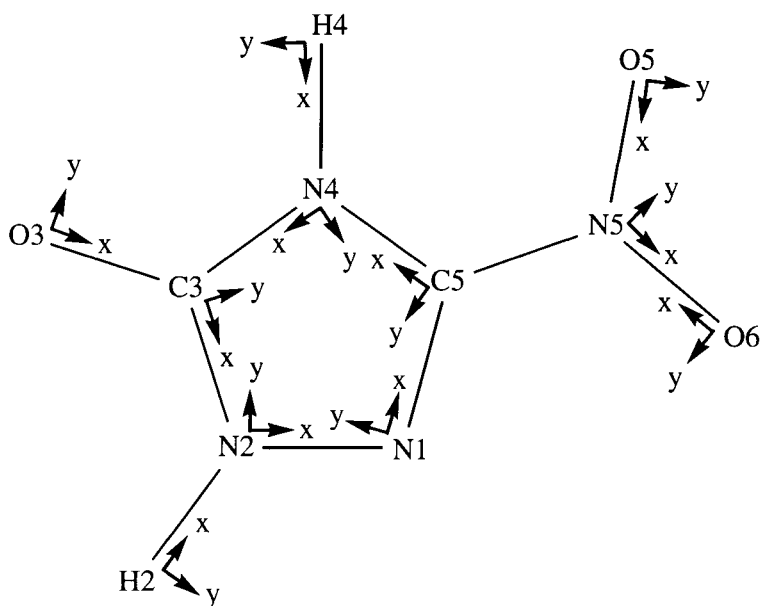


Fig. 3. Local coordinate system used for β -NTO, z being orthogonal to x and y.

reflections. Then, after scale factor refinement with all reflections, the procedure was repeated until total convergence of the refined parameters was obtained. At this point, the positional and displacement parameters for the hydrogen atoms, were refined using reflections with $\sin \theta/\lambda < 0.5 \text{ \AA}^{-1}$. Then, the N-H bond lengths were extended and fixed to the tabulated neutron values [21]. After that, P_v and κ' were fixed, and the multipole parameters P_{lm} and κ'' were refined alternately with scale, positional and displacement parameters as described above. For the heavy atoms the multipole refinement was performed up to the hexadecapole level ($l_{\max}=4$), for hydrogens only dipole populations were refined. Electroneutrality of the molecule was imposed during the refinement. In the final cycles, parameters with values that refined to less than one standard uncertainty were fixed at zero. Different κ -sets were used for each of the atoms except the hydrogens. The same κ' and κ'' values were applied for both H-atoms. For the initial approximation of κ' (H(2), H(4)) a value of 1.2 was taken. Isotropic secondary extinction was described according to Becker and Coppens [22]. The final residuals were $R(\text{all data}) = 0.0333$, $R(\sin \theta/\lambda < 1.0 \text{ \AA}^{-1}) = 0.0245$. The multipole populations from the final refinement are reported in Table 5.

6. ELECTRON DENSITY DISTRIBUTIONS

6.1 Residuals

Although the quality of the refinement may be judged in the usual way from the crystallographic agreement factors, it is essential to confirm that all of the features of the electron density present in the data have been accounted for. To this end a difference Fourier ($\delta\rho_{\text{resid}} = \rho_{\text{exper}} - \rho_{\text{mult}}$) or residual map is calculated, which should be featureless, the random noise representing the inherent errors in the data. Fig. 4 presents such a residual map in the plane of a nitro group in HMX after the multipole refinement [12]. The largest residual is a minimum of -0.15 e\AA^{-3} , however, there are no maxima greater than 0.05 e\AA^{-3} . These values can be compared with the deformation densities described below, and give a measure of the errors associated with the map in Fig. 5.

6.2 Deformation densities

The redistribution of the valence electron density due to chemical bonding may be obtained from summing the multipole populations or Fourier transforming appropriately calculated structure factors, having removed the contribution from neutral spherical atoms, to produce a so-called deformation density map [2]. This function was introduced by Roux et al. [23] and has been widely used since then. The deformation electron density represents the difference between the electron density of the system, $\rho(\mathbf{r})$, and the electron

Table 5

Final refined multipole populations for β -NTO

	N(1)	N(2)	N(4)	N(5)	C(3)	C(5)	O(3)	O(5)	O(6)	H(2)	H(4)
00	5.06(4)	5.20(4)	5.35(5)	4.68(6)	3.63(6)	3.79(7)	6.48(5)	6.14(4)	6.19(4)	0.77(2)	0.70(2)
10	0	0	0.015(6)	0.028(8)	0	0.035(8)	0	0	0	-0.028(8)	0
11+	-0.051(7)	-0.030(6)	0	-0.018(8)	-0.041(10)	0	-0.090(10)	-0.067(9)	-0.066(8)	0.063(7)	0.039(7)
11-	-0.143(8)	-0.013(6)	-0.040(6)	0.015(8)	-0.071(10)	0.087(10)	0.019(7)	-0.021(7)	0	0	0.022(8)
20	-0.099(8)	0	-0.060(7)	-0.173(10)	-0.216(11)	-0.124(10)	-0.022(8)	-0.048(8)	-0.041(7)		
21+	0	0.013(6)	0	0.015(7)	0	0	0	0	0		
21-	0	0.016(6)	0.020(6)	0	0	0	0.011(7)	-0.018(8)	0.012(7)		
22+	0.066(7)	-0.047(6)	-0.019(7)	0.026(8)	-0.027(9)	-0.045(9)	-0.056(9)	-0.137(10)	-0.066(7)		
22-	0.083(8)	0.011(6)	0.046(7)	-0.064(8)	0.103(9)	-0.036(10)	-0.021(8)	0	-0.096(7)		
30	0.015(9)	0	0	0	0	0	0	-0.016(10)	0		
31+	-0.035(9)	-0.014(8)	0	0.012(10)	0.033(11)	0	0	-0.048(9)	-0.012(9)		
31-	-0.040(9)	0.018(8)	0	0	0	0.034(11)	0	0	0		
32+	0	0	0	0	0.025(11)	-0.012(11)	0	-0.017(9)	0.015(9)		
32-	0	0.014(8)	0	0.015(10)	-0.012(11)	-0.013(11)	0	-0.017(10)	0		
33+	0.107(10)	0.174(11)	0.159(10)	0.281(15)	0.236(15)	0.287(15)	0.035(10)	0.029(9)	0.018(8)		
33-	-0.075(9)	-0.018(8)	-0.045(9)	0.035(11)	-0.105(12)	-0.117(13)	0	0.014(9)	0.038(8)		
40	0	-0.012(11)	0	0	0.022(14)	0.041(16)	0	0	0		
41+	0.021(11)	-0.016(10)	0.053(10)	0	0	0	0	0.034(12)	0		
41-	0	0	0	-0.035(12)	-0.019(13)	0	-0.022(12)	0	0		
42+	0	0	0	0.032(12)	-0.031(13)	0.035(14)	0.031(13)	0	-0.020(11)		
42-	0	0.044(10)	0	0	-0.011(13)	-0.052(14)	0	0	0		
43+	-0.024(11)	0	0.011(10)	0.025(12)	0	-0.037(14)	0.014(11)	0	-0.030(11)		
43-	0.013(12)	-0.018(10)	0	0.036(14)	0	0.033(14)	-0.026(12)	0	-0.026(11)		
44+	0.032(11)	0.011(9)	0.029(10)	-0.020(12)	0.067(16)	0	0.026(12)	-0.015(12)	0		
44-	0	0.027(10)	0	0	0	-0.023(15)	0.022(11)	0	0		
κ'	1.013(5)	1.006(5)	1.004(5)	1.034(6)	1.058(9)	1.048(9)	0.981(4)	1.005(4)	1.002(4)	1.22(3)	1.22(3)
κ''	0.98(2)	1.09(4)	1.03(3)	0.93(2)	1.01(2)	0.98(2)	0.80(4)	0.84(3)	1.02(5)	1.29(4)	1.29(4)

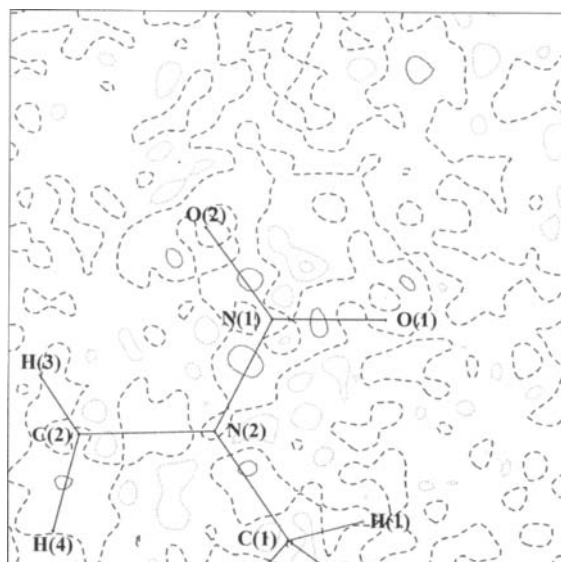


Fig. 4. Residual map in the plane of a nitro group in HMX after the final multipole refinement. Solid contours are positive, dotted contours are negative, and dashed contours are zero. Contour interval is $0.05 \text{ e}\text{\AA}^{-3}$.

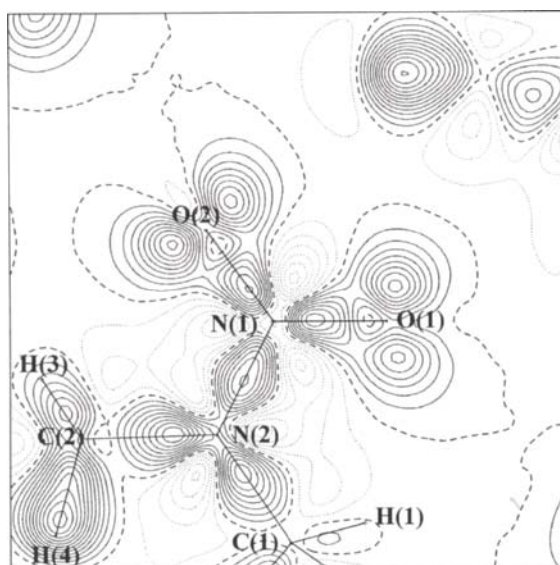


Fig. 5. Deformation electron density map in the N(1), O(1), O(2) plane for HMX. Solid contours are positive, dotted contours are negative, and dashed contours are zero. Contour interval is $0.05 \text{ e}\text{\AA}^{-3}$.

density of a set of spherically averaged non-interacting neutral atoms (procrystal), placed at the same positions as the atoms of the system under study undergoing the same thermal motion: $\delta\rho_{\text{mult}} = \rho_{\text{mult}} - \rho_{\text{sph}}$. Thus, it describes the redistribution of electrons after neutral atoms combine to form the crystal (or molecule). One can thus expect deformation electron density maxima associated with electron concentration in the chemical bonds, lone pairs, etc.

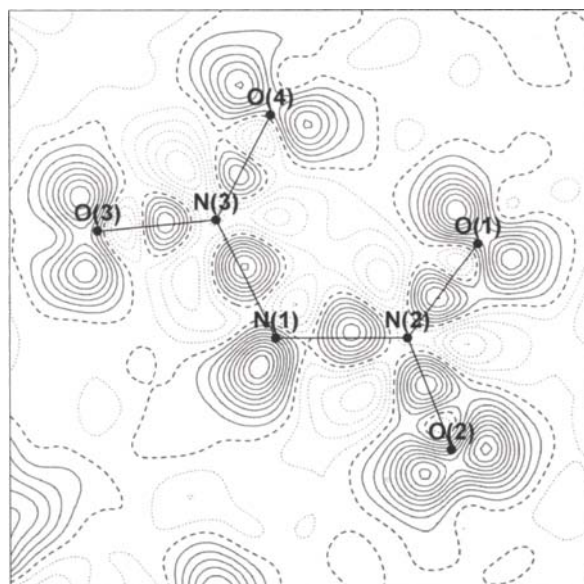
Two examples are shown. In Fig. 5 above, the deformation electron density in the plane of one of the nitro groups in HMX is shown [12]. There is clear evidence of concentration of electron density in all of the covalent bonds. Particularly striking is the form of the lone pairs associated with the oxygen atoms. Not only are they localized in the plane of the nitro group, they are also almost perpendicular to the N – O bonds. A similar situation is observed below in Fig. 6a for the dinitramide anion in biguanidinium dinitramide, (BIGH)(DN) [14]. In addition to the deformation density observed in the bonds and the lone pairs on oxygens, the lone pair associated with the bridging nitrogen atom of the dinitramide anion is also seen. This lone pair is significantly extended perpendicular to the N2, N1, N3 plane as shown in Fig. 6b, however, only one maximum is observed.

6.3 Laplacian of the electron density

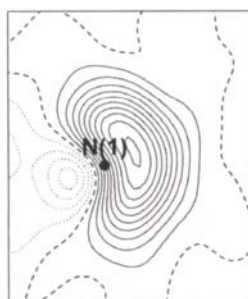
The spatial distribution of the Laplacian of the electron density, $\nabla^2\rho(\mathbf{r})$, characterizes regions of concentration and depletion of electrons [24]. This accumulation is mostly concentrated around the atoms along the chemical bonds and in the non-bonding directions associated with lone pairs. This is shown in Fig. 7, where the accumulation of electron density due to covalent bonding and the lone pair regions of a nitro group in HMX are clearly demonstrated [12]. In the view of the local virial theorem [25], $\nabla^2\rho(\mathbf{r})$ can be interpreted as the local balance between the kinetic and potential energy of a molecule. The sign of the Laplacian at the bond (3,-1) critical point, obtained from summing the principal curvatures of the electron density at the critical point, reflects the character of the atomic interactions. If the electrons are locally concentrated in the bond critical point ($\nabla^2\rho(\mathbf{r}_c) < 0$), then electron density is shared by both nuclei, typical for covalent bonds. If electrons are concentrated in each of the atomic basins separately ($\nabla^2\rho(\mathbf{r}_c) > 0$), the interaction type is closed-shell, typical for ionic and hydrogen bonds, as well as van der Waals interactions [25,26].

7. TOPOLOGICAL ANALYSIS

A plot of the total electron density for β - NTO is shown in Fig. 8. The plot has been truncated at the atomic positions to accentuate the bonding features.



a)



b)

Fig. 6. a) Deformation electron density map of the DN anion of (BIGH)(DN) in the N(1)-N(2)-N(3) plane, b) Lone pair region of the DN anion perpendicular to the N(1)-N(2)-N(3) plane and bisecting the angle at N(1). Solid contours are positive, dotted contours are negative, and dashed contours are zero. Contour interval is $0.05 \text{ e}\text{\AA}^{-3}$.

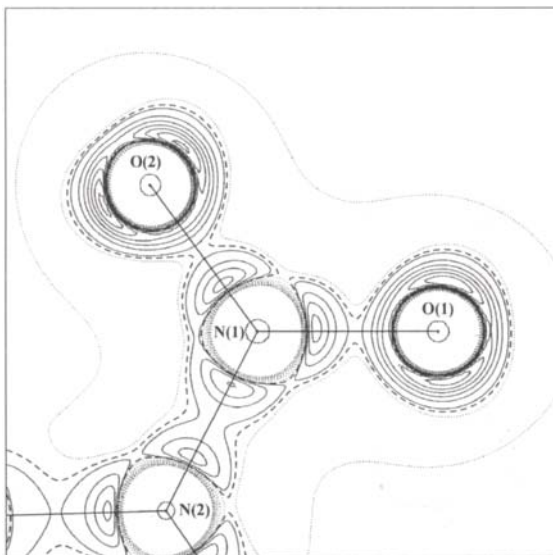


Fig. 7. Negative Laplacian of the total electron density of HMX for atoms in the plane of N(1), O(1) and O(2). Contour intervals are +6, +26, +46, +66, +86, +106, +126, +146 $\text{e}\text{\AA}^{-5}$ (solid line), and -6, -26, -46, -66, -86, -106, -126, -146 $\text{e}\text{\AA}^{-5}$ (dotted line), and zero (dashed line)

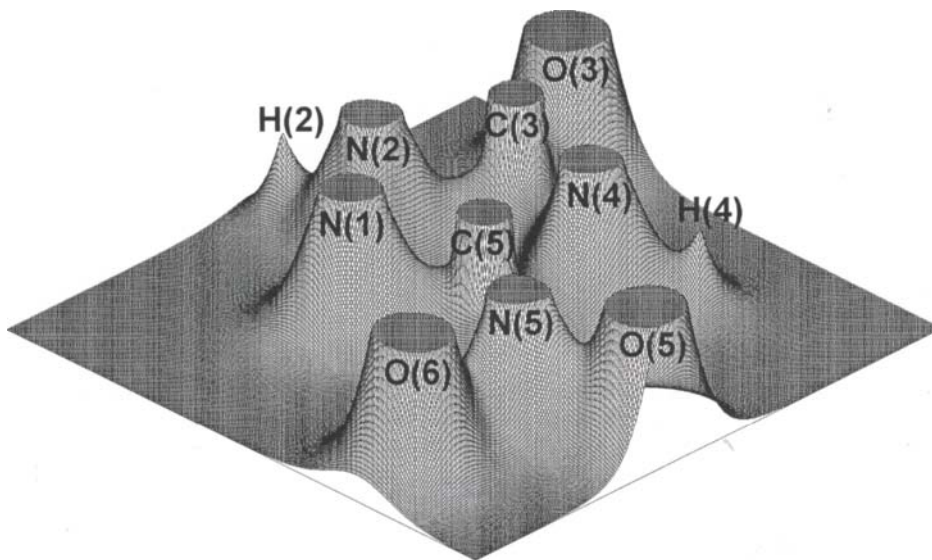


Fig. 8. Relief map of the total electron density in β -NTO truncated close to the nuclear positions for clarity.

In the past decade the analysis of the total electron density using the theory of atoms in molecules (AIM) has gained popularity [27]. This theory describes a crystal in terms of the electron density, $\rho(\mathbf{r})$, its gradient vector field, $\nabla\rho(\mathbf{r})$, electron density curvature, critical point ($\nabla\rho(\mathbf{r}_c)=0$) positions and their characteristics [28]. A critical point is defined by rank, the number of non-zero eigenvalues of the diagonalized Hessian matrix λ_i , and signature, the sum of the algebraic signs of λ_i . The electron density exhibits four kinds of non-degenerate critical points of rank 3, with a (3,-1) saddle point corresponding to a chemical bond in the crystal or molecule. In the $\nabla\rho(\mathbf{r})$ field, pairs of gradient lines originating at a (3,-1) critical point and terminating at two neighboring nuclei (determined by the eigenvector corresponding to the only positive eigenvalue of the Hessian, λ_3 , at the critical point) form the atomic interaction lines along which the electron density decreases for any lateral displacement. At equilibrium, this line is named a bond path containing the associated (3,-1) bond critical point. By plotting the gradient lines away from the nuclear positions, the zero flux surface uniquely defines the atomic boundaries in terms of the electron density. The analysis for β -NTO in the molecular plane in Fig. 9 clearly shows the atomic space partitioning and the critical points. The strength of the bond may be inferred from the total electron density at the (3,-1) critical points or from the corresponding Laplacian. The location of the critical point measures the polarization of the bond, and the ellipticity of the electron density at the critical point gives a measure of π bonding.

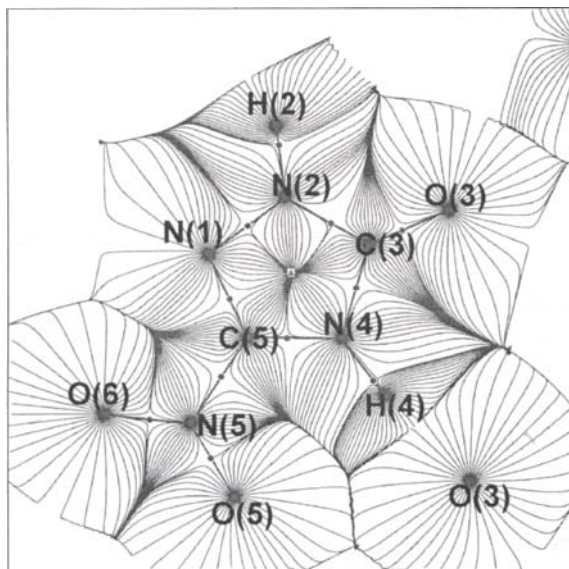


Fig. 9. The $\nabla\rho(\mathbf{r})$ field for β -NTO showing the atomic positions and the bond critical points. Note that there is also a (3,+1) critical point in the center of the ring.

7.1 Atomic charges

The atomic basin boundaries were defined for TNDAP [12,15], and the atomic charges integrated within the basins with the TOPXD program [30]. The integrated atomic charge $q(\Omega)$ over the atomic basin Ω is defined as a difference between nuclear Z_Ω and electronic $N(\Omega)$ charges:

$$q(\Omega) = Z_\Omega - N(\Omega), \quad (4)$$

$$N(\Omega) = \int_{\Omega} \rho(\mathbf{r}) d\tau, \quad (5)$$

where $\rho(\mathbf{r})$ is the electron density.

The atomic charges thus derived are shown in Fig. 10 and compared with those obtained from the kappa refinement described previously. The atomic charges, calculated from AIM theory are generally higher [30] than those obtained from the spherical atom model. This is because the AIM charges take into account the complete electron distribution, whereas the kappa refinement only considers charge transfer measured for the monopole populations. Thus, AIM gives a more rigorous definition of the atomic charges. Every charge, shown in Fig. 10 has a reasonable value and sign expected for this type of compound. Thus the oxygen atoms are negative, the hydrogen atoms are positive, nitrogen bound to oxygen is positive whereas nitrogen bound to carbon is negative, and all the carbons are negative except when bound to nitro groups.

7.2 Bond critical point properties

The topological analysis of the electron density for β -NTO [7] corresponding to Fig. 8 was performed with the XD [18] and TOPXD [30] programs. The properties for all the (3,-1) critical points found in the molecule are listed in Table 6. The trend in the properties at the critical points is in agreement with anticipated bond strengths and types. The electron density value at the critical point is greater for the nitro-group N(5)-O(5,6) than for the rest of the molecule, and the least negative Laplacian value is for the N(1)-N(2) bond. The positions of the critical points indicate polarization of N-H, N-C and C-O bonds. For example, the critical point on the C(3)-O(3) bond is closer to the C(3) atom (0.4959 Å) than to O(3) (0.7384 Å), i.e. electrons are shifted towards oxygen, the more electronegative atom. Analysis of the chemical bonds in the triazolone ring indicates significant conjugation in all cases based both on the electron density and the ellipticity. N(1)-C(5) has the highest electron density value at the bond critical point and the most negative Laplacian and thus is the best candidate for the bond in the ring to be considered as a 'double bond'. The critical point on the C(3)-O(3) bond has even higher values for the electron

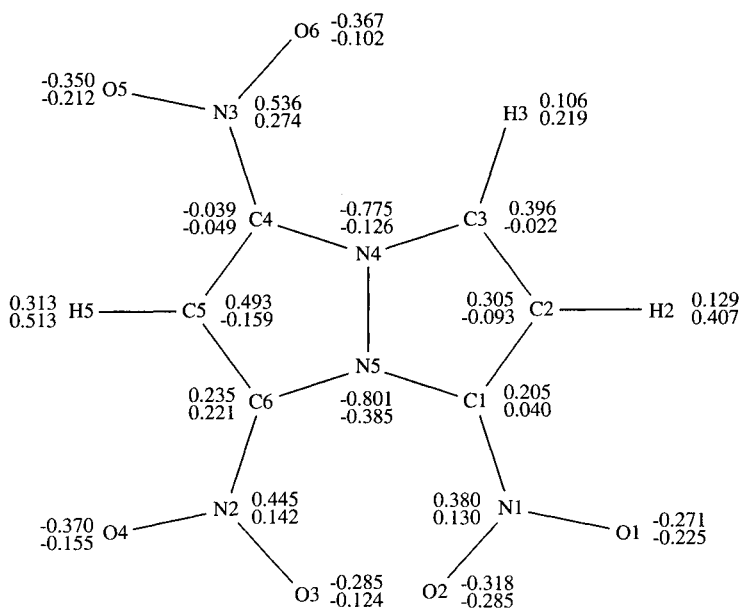


Fig. 10. Atomic charges for TNDAP – upper number from AIM analysis, lower from kappa refinement.

density and Laplacian, so the whole picture is exactly as expected from the point of view of conventional bonding theory. Although the values of ρ and $\nabla^2\rho$ at the critical point on the double C(3)-O(3) bond are in the expected range, the ellipticity of this bond is very low (0.06), however, the ellipticity of C=O bonds can vary from 0.07 to 0.14 for different types of compounds [31].

The electron density values at the critical points on the N-O bonds in β -NTO are relatively high: 3.39 and 3.27 $\text{e}\text{\AA}^{-3}$, though the absolute values of the Laplacian are less compared to other bonds: -6.8 and -4.7 $\text{e}\text{\AA}^{-5}$. The properties at the critical point on the N(1)-N(2) bond have similar features to the above. Although the electron density value (2.30 $\text{e}\text{\AA}^{-3}$) is quite similar to other bonds in the ring (2.17–2.67 $\text{e}\text{\AA}^{-3}$), the absolute value of the Laplacian is significantly less: -3.32 $\text{e}\text{\AA}^{-5}$ compared to -27.5 – -17.4 $\text{e}\text{\AA}^{-5}$. The λ_1 and λ_2 negative Hessian eigenvalues, showing the contraction of electron density towards the bond in the perpendicular directions are approximately the same as for all the other bonds in the triazolone ring, however the positive λ_3 eigenvalue, showing the depletion along the bond direction is much greater: 33.62 $\text{e}\text{\AA}^{-5}$ compared to 17.11–21.12 $\text{e}\text{\AA}^{-5}$ for the other bonds in the ring.

Table 6
Bond Critical Points in β -NTO.

Bond	ρ	$\nabla^2\rho$	λ_1	λ_2	λ_3	R_{ij}	d_1	d_2	$\varepsilon=\lambda_1/\lambda_2-1$
N(2)-H(2)	1.98(2)	-15.34(7)	-25.97	-23.99	34.63	1.009	0.748	0.261	0.08
N(2)-N(1)	2.30(2)	-3.32(7)	-19.94	-17.00	33.62	1.366	0.702	0.664	0.16
N(2)-C(3)	2.23(3)	-20.8(1)	-21.27	-16.94	17.45	1.374	0.793	0.581	0.26
C(3)-O(3)	2.90(3)	-30.1(2)	-26.43	-24.84	21.12	1.234	0.496	0.738	0.06
N(1)-C(5)	2.67(3)	-27.5(1)	-24.71	-19.76	16.96	1.299	0.751	0.548	0.25
N(4)-H(4)	1.93(1)	-17.47(4)	-26.34	-25.42	34.29	1.009	0.770	0.239	0.04
C(3)-N(4)	2.17(2)	-17.4(1)	-19.34	-16.07	18.00	1.380	0.589	0.791	0.21
C(5)-N(4)	2.23(3)	-17.9(1)	-19.60	-15.43	17.11	1.357	0.577	0.780	0.27
N(5)-C(5)	2.01(2)	-16.97(9)	-18.51	-16.08	17.62	1.443	0.803	0.640	0.14
N(5)-O(5)	3.39(2)	-6.8(1)	-33.02	-30.98	57.21	1.225	0.602	0.623	0.06
N(5)-O(6)	3.27(3)	-4.7(1)	-31.67	-27.90	54.84	1.228	0.598	0.630	0.12

8. PROPERTIES

Given the complete description of the structure in terms of pseudo atoms as described above, it is possible to derive additional properties that provide insight into the chemical and physical properties of energetic materials. Two of these are described below, the molecular electrostatic potential and the energy density distribution.

8.1 Electrostatic potential

The electrostatic potential at any point, $V(r)$, is the energy required to bring a single positive charge from infinity to that point. As each pseudo atom in the refined model consists of the nucleus and the electron density distribution described by the multipole expansion parameters, the electrostatic potential may be calculated by the evaluation of

$$V(r) = \sum_A \frac{Z_A}{|R_A - r|} - \int \frac{\rho(r')dr'}{|r' - r|} \quad (6)$$

where Z_A is the charge on nucleus A located at R_A [26,32]. Thus, possible sites for electrophilic or nucleophilic attack may easily be identified, and a measure

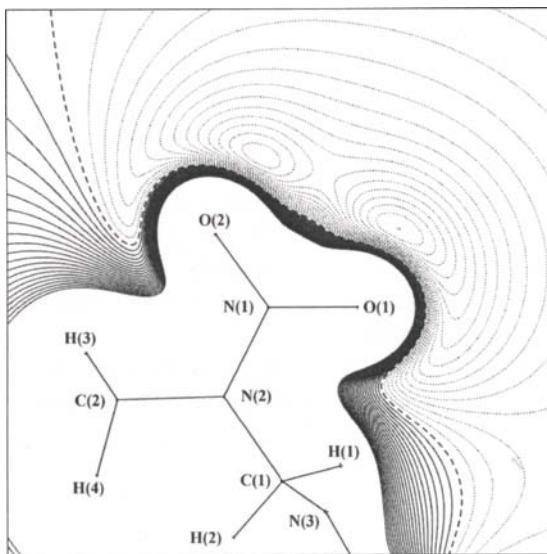


Fig. 11. The total electrostatic potential for an HMX molecule isolated from the crystal structure in the N(1), O(1), O(2) plane. Contour intervals are $+0.01\text{e}\text{\AA}^{-1}$ (solid line), $-0.01\text{e}\text{\AA}^{-1}$ (dotted line), and zero (dashed line).

of the interaction of the molecule with its environment obtained. The electrostatic potential around a nitro group in HMX in Fig. 11 clearly shows the negative potential associated with the electronegative oxygen atoms [12].

8.2 Energy density distribution

The density of the electronic energy is the sum of the kinetic, $g(\mathbf{r})$, and potential, $v(\mathbf{r})$, energy density [33]

$$h_e(\mathbf{r}) = g(\mathbf{r}) + v(\mathbf{r}), \quad (7)$$

and may be obtained from the local virial theorem

$$2g(\mathbf{r}) + v(\mathbf{r}) = (1/4)\nabla^2\rho(\mathbf{r}), \quad (8)$$

which shows that $\nabla^2\rho(\mathbf{r})$ characterizes the local balance between the kinetic, $g(\mathbf{r}) > 0$, and potential, $v(\mathbf{r}) < 0$, energy densities of a system. It has also been demonstrated that the Thomas-Fermi model may be used to obtain the kinetic energy, $g(\mathbf{r})$, directly from the electron density derived from the X-ray diffraction experiment [34,35]:

$$g(\mathbf{r}) = (3/10) (3\pi^2)^{2/3} \rho(\mathbf{r})^{5/3} + (1/72) [\nabla\rho(\mathbf{r})]^2/\rho(\mathbf{r}) + (1/6)\nabla^2\rho(\mathbf{r}) \quad (9)$$

No repulsive potential energy exists in a system at equilibrium. Each virial path, a line of maximally negative potential energy density, is homeomorphically mirrored by a bond path linking the same nuclei [36]. The corresponding electron accumulation leads to the balancing of the Hellmann-Feynman forces and results in the equilibrium of the system. Therefore, the presence of a bond path and its associated virial path provide a 'universal indicator of bonding between atoms' [37]. The network of the virial and bond paths linking neighboring nuclei is an intrinsic property of each compound. Thus, consideration of the local energies provides a direct approach to the study of bonding in molecules and crystals.

Thus, if it is assumed that the local virial theorem is valid for the model electron densities fitted to the experimental structure factors, the kinetic, $g(\mathbf{r})$, and potential, $v(\mathbf{r})$, energy densities may be mapped, as well as the energy characteristics of the (3,-1) bond critical points evaluated [38].

In the following, this approach has been used to study the energy features of β -NTO [29]. The kinetic, $g(\mathbf{r})$, and potential, $v(\mathbf{r})$, energy density maps have been calculated from the experimental electron densities with the *WinXPRO* program package [39] using the approach described above, as well as their difference with respect to atomic procystals with no chemical bonds. Critical point characteristics have also been similarly analyzed.

The potential energy density, $v(\mathbf{r})$, maps reveal explicitly that the NO_2 -group is the most potential energy-rich area in the molecule (Fig. 12b). This is confirmed by the analysis of the local energies at the bond critical points (see below). The kinetic energy densities, $g(\mathbf{r})$, are also higher for these groups (Fig. 12a).

In order to reveal the subtle changes in the energy distributions caused by the crystal/molecule formation, we have calculated the deformation kinetic and potential energy densities [34,40]:

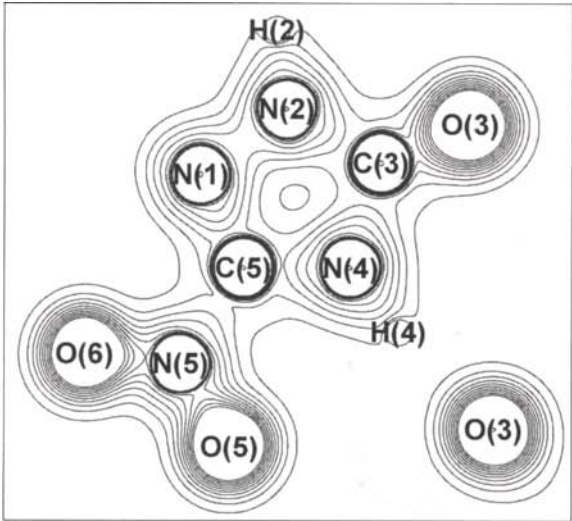
$$\delta g(\mathbf{r}) = g(\mathbf{r}) - g_{\text{procrystal}}(\mathbf{r}) \quad (10)$$

$$\delta v(\mathbf{r}) = v(\mathbf{r}) - v_{\text{procrystal}}(\mathbf{r}) \quad (11)$$

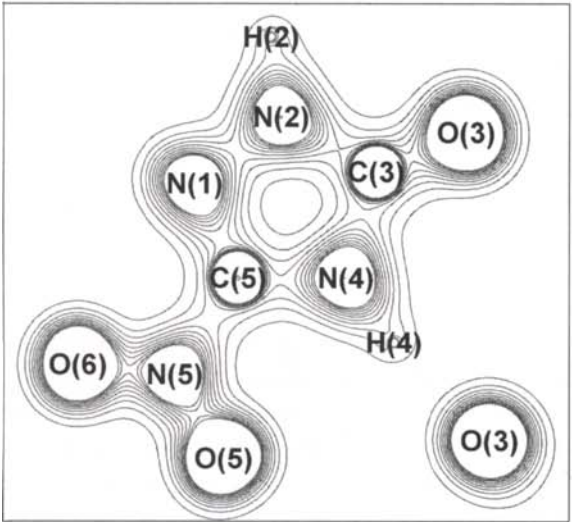
Here $g(\mathbf{r})/v(\mathbf{r})$ are the kinetic/potential energy densities in a crystal, whereas $g_{\text{procrystal}}(\mathbf{r})/v_{\text{procrystal}}(\mathbf{r})$ are the distributions of the kinetic/potential energy density of the atomic procrystal. The corresponding $\delta g(\mathbf{r})$ and $\delta v(\mathbf{r})$ maps for the β -NTO crystal are shown in Fig. 13. Although, during the formation of the crystal from the unbound atoms, the potential energy is enhanced for every covalent bond (Table 7), this enhancement is different for different parts of the molecule. Being bond-localized, it is maximal around the nitrogen atoms and for the oxygen lone pairs. At the same time, although the kinetic energy in a crystal is generally greater than in the atomic procrystal (Table 7), no significant delocalized changes in the kinetic energy density $\delta g(\mathbf{r})$ were found (Fig. 13a). The $\delta g(\mathbf{r})$ and $\delta v(\mathbf{r})$ distributions demonstrate the details of the stabilizing enhancement in the local potential energy, and destabilizing increase in the local kinetic energy resulting from formation of a crystal/molecule from neutral unbound atoms.

8.3 Energy density critical points

The density of the electronic energy at the bond critical points provides an additional characterization of the atomic interaction type: $h_e(\mathbf{r}_{\text{cp}}) < 0$ is observed for shared-type atomic interactions, while $h_e(\mathbf{r}_{\text{cp}}) > 0$ is observed for closed-shell interactions [41,42]. The analysis of the local energies at the bond critical points (Table 7) for β -NTO shows that the highest $g(\mathbf{r}_{\text{cp}})$, $v(\mathbf{r}_{\text{cp}})$ and $h_e(\mathbf{r}_{\text{cp}})$ values are observed for the N-O bonds in the NO_2 group. The next are the values for the 'double' C-O and C-N bonds. It is worth noting that the values of $\rho(\mathbf{r}_{\text{cp}})$, $g(\mathbf{r}_{\text{cp}})$, $v(\mathbf{r}_{\text{cp}})$ and $h_e(\mathbf{r}_{\text{cp}})$ for crystalline β -NTO correctly reflect the tendency of the chemical decomposition of this molecule. According to theoretical calculations [43], the C(5)-N(5) and N-H bonds should be the first to break during chemical decomposition. In agreement with this prediction, we observe that the electron

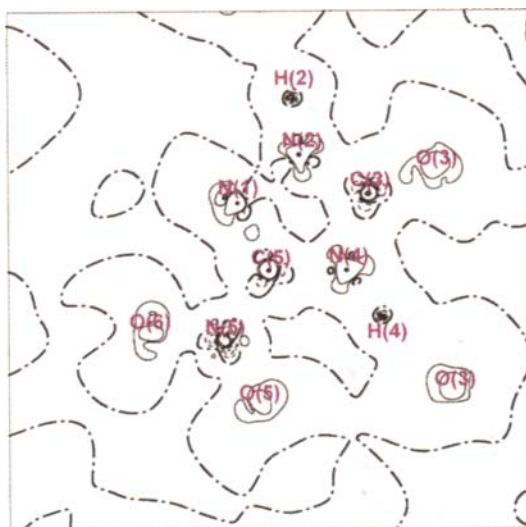


a)



b)

Fig. 12. a) The kinetic energy density, $g(\mathbf{r})$, (the contour interval is 0.1 a.u., all contours being positive), b) the potential energy density, $v(\mathbf{r})$, (the contour interval is 0.2 a.u., all contours being negative), in β -NTO .



a)



b)

Fig. 13. a) The deformation kinetic energy density, $\delta g(\mathbf{r})$; and b) the deformation potential energy density, $\delta v(\mathbf{r})$, in the β -NTO crystal. Contour interval is 0.1 a.u.

Table 7

 β -NTO: bond critical points in the electron density and energy density

Bond path	ρ , eÅ ⁻³	$\nabla^2\rho$, eÅ ⁻⁵	g , a.u.	v , a.u.	h_e , a.u.	R , Å
N(2)-H(2)	1.98(2)	-15.34(7)	0.2672	-0.6934	-0.4263	1.0090
	1.56	-8.66	0.1901	-0.4701	-0.2800	
N(2)-N(1)	2.30(2)	-3.32(7)	0.4552	-0.9449	-0.4896	1.3658
	2.05	8.62	0.4538	-0.8181	-0.3643	
N(2)-C(3)	2.23(3)	-20.8(1)	0.3089	-0.8332	-0.5243	1.3737
	1.69	-1.43	0.2758	-0.5664	-0.2906	
C(3)-O(3)	2.90(3)	-30.1(2)	0.4934	-1.2994	-0.8061	1.2343
	2.11	5.37	0.4507	-0.8457	-0.3950	
N(1)-C(5)	2.67(3)	-27.5(1)	0.4201	-1.1255	-0.7055	1.2987
	1.91	-5.93	0.3093	-0.6801	-0.3708	
N(4)-H(4)	1.93(1)	-17.47(4)	0.2360	-0.6531	-0.4172	1.0090
	1.56	-8.63	0.1903	-0.4702	-0.2798	
C(3)-N(4)	2.17(2)	-17.4(1)	0.3136	-0.8078	-0.4942	1.3795
	1.68	-1.16	0.2749	-0.5617	-0.2869	
C(5)-N(4)	2.23(3)	-17.9(1)	0.3303	-0.8464	-0.5161	1.3556
	1.75	-2.58	0.2849	-0.5967	-0.3117	
N(5)-C(5)	2.01(2)	-16.97(9)	0.2640	-0.7041	-0.4401	1.4430
	1.49	1.64	0.2429	-0.4689	-0.2259	
N(5)-O(6)	3.39(2)	-6.8(1)	0.8645	-1.7994	-0.9350	1.2253
	2.92	8.10	0.7668	-1.4495	-0.6827	
N(5)-O(5)	3.27(3)	-4.7(1)	0.8269	-1.7029	-0.8760	1.2279
	2.91	8.32	0.7642	-1.4422	-0.6779	

The first line lists the experimental result; the second line- the atomic procrystal; ρ is the electron density; $\nabla^2\rho$ is the Laplacian, g , v and h_e are the kinetic, potential and total electronic energies at the critical point; R is the bond path length.

density, kinetic, potential and total electronic energy values at the critical points on these bonds are the lowest of all bonds in the molecule. Thus, it might be supposed that local energy characteristics give information to help predict the initial mechanism of the decomposition of energetic molecules.

The comparison of the properties at the critical points in the β -NTO electron density with those in the atomic procrystals (Table 6) reveals the contraction of the electron density towards the shared interaction lines during crystal/molecule formation. This contraction is accompanied by a significant enhancement of the local kinetic, potential and electronic energies (Table 7).

Thus, the analysis of energy density distributions should prove to be a useful tool in the study of the fundamental properties of energetic materials.

8.4 Hydrogen bonding

In many energetic materials, significant hydrogen bonding is observed. This is particularly true of a number of salts of the dinitramide anion. In

biguanidinium bis(dinitramide), $(\text{BIGH}_2)(\text{DN})_2$, where the cation is located on a crystallographic twofold axis, most of the hydrogen atoms from the cation are involved in two hydrogen bonds with different oxygen atoms of the anion and vice versa, as well as with the bridging nitrogen atom of the anion [14]. A plot of the deformation electron density and the corresponding Laplacian through the hydrogen bond to the bridging nitrogen, the shortest hydrogen bond in this structure, is shown in Fig. 14. The analysis of the properties of the (3,-1) critical points in the electron density is reported in Table 8 for all of the hydrogen bonds in this structure. The values of $\rho(\mathbf{r}_c)$ at the hydrogen bond critical points are significantly lower than for covalent bonds as expected. The positive values of the Laplacian are indicative of the closed-shell type of these interactions.

Following Espinosa et al. [38], the dissociation energies for the hydrogen bonds have been estimated as:

$$D = -v(\mathbf{r}_c)/2 \quad (12)$$

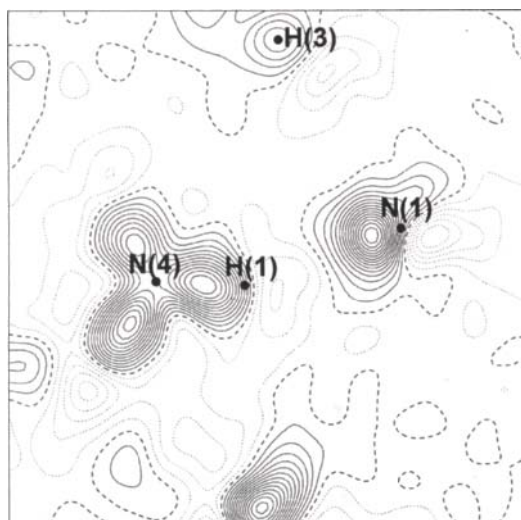
Here $v(\mathbf{r}_c)$ is a potential energy density at the critical point, which was calculated as in the previous section. The correlation between the length of the hydrogen bond, $\rho(\mathbf{r}_c)$, $\nabla^2\rho(\mathbf{r}_c)$, and dissociation energy are striking.

9. CONCLUSION

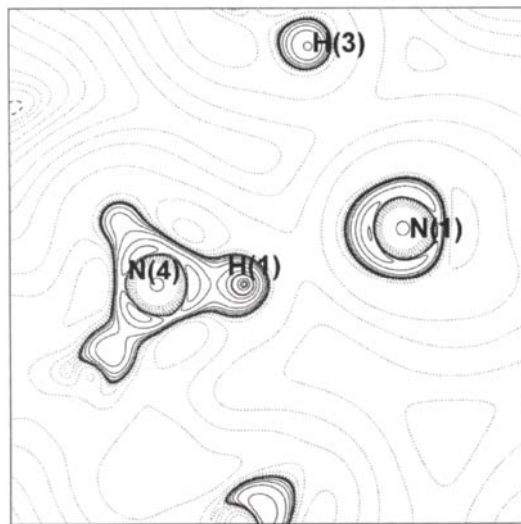
Although X-ray crystallography has mainly been used for structure determination in the past, the diffraction data, especially if measured carefully and to high orders, contain information about the total electron density distribution in the crystal. This may be analyzed to provide essential information about the chemical properties of molecules, in particular the characterization of covalent and hydrogen bonds, both from the point of view of the valence electron density, the Laplacian of the density and derived energy density distribution. In addition, calculation of the molecular electrostatic potential indicates direction of chemical attack as well as how molecules can interact with their environment.

Acknowledgments

The authors thank Dr. A. Volkov and Prof. P. Coppens for making the TOPXD program, and Dr. A. Stash and Prof. V.G. Tsirelson for making the WinXPRO program available to us, as well as for helpful discussions. We also gratefully acknowledge financial support from the Office of Naval Research under contracts N00014-95-1-0013 and N00014-99-1-0392.



a)



b)

Fig. 14. a) The multipole deformation electron density and b) the negative Laplacian of the electron density in the N(1)...H(1) hydrogen bond region in (BIGH₂)(DN)₂. Contour interval is 0.05 eÅ⁻³ for a) and $2,4,8 \times 10^{-3} \cdot +^3$ eÅ⁻³ plus a contour of 70 eÅ⁻³ for b). Solid contours are positive, dotted ones are negative, and dashed ones are zero.

biguanidinium bis(dinitramide), $(\text{BIGH}_2)(\text{DN})_2$, where the cation is located on a crystallographic twofold axis, most of the hydrogen atoms from the cation are involved in two hydrogen bonds with different oxygen atoms of the anion and vice versa, as well as with the bridging nitrogen atom of the anion [14]. A plot of the deformation electron density and the corresponding Laplacian through the hydrogen bond to the bridging nitrogen, the shortest hydrogen bond in this structure, is shown in Fig. 14. The analysis of the properties of the (3,-1) critical points in the electron density is reported in Table 8 for all of the hydrogen bonds in this structure. The values of $\rho(\mathbf{r}_c)$ at the hydrogen bond critical points are significantly lower than for covalent bonds as expected. The positive values of the Laplacian are indicative of the closed-shell type of these interactions.

Following Espinosa et al. [38], the dissociation energies for the hydrogen bonds have been estimated as:

$$D = -v(\mathbf{r}_c)/2 \quad (12)$$

Here $v(\mathbf{r}_c)$ is a potential energy density at the critical point, which was calculated as in the previous section. The correlation between the length of the hydrogen bond, $\rho(\mathbf{r}_c)$, $\nabla^2\rho(\mathbf{r}_c)$, and dissociation energy are striking.

9. CONCLUSION

Although X-ray crystallography has mainly been used for structure determination in the past, the diffraction data, especially if measured carefully and to high orders, contain information about the total electron density distribution in the crystal. This may be analyzed to provide essential information about the chemical properties of molecules, in particular the characterization of covalent and hydrogen bonds, both from the point of view of the valence electron density, the Laplacian of the density and derived energy density distribution. In addition, calculation of the molecular electrostatic potential indicates direction of chemical attack as well as how molecules can interact with their environment.

Acknowledgments

The authors thank Dr. A. Volkov and Prof. P. Coppens for making the TOPXD program, and Dr. A. Stash and Prof. V.G. Tsirelson for making the WinXPRO program available to us, as well as for helpful discussions. We also gratefully acknowledge financial support from the Office of Naval Research under contracts N00014-95-1-0013 and N00014-99-1-0392.

REFERENCES

- [1] G.A. Olah and D.R. Squire, "Chemistry of Energetic Materials," Academic Press, 1991.
- [2] P. Coppens, "X-ray Charge Densities and Chemical Bonding," Oxford University Press, 1997; V.G. Tsirelson and R.P. Ozerov, "Electron Density and Bonding in Crystals," Bristol and Philadelphia: Institute of Physics, 1996
- [3] International Tables for Crystallography, Vol. C, Kluwer Academic Publishers, Dordrecht, 1999.
- [4] F.K. Larsen, *Acta Crystallogr.*, B51 (1995) 468.
- [5] M.J. Hardie, K. Kirschbaum, A. Martin and A.A. Pinkerton, *J. Appl. Crystallogr.*, 31 (1998) 815.
- [6] A. Martin and A.A. Pinkerton, *Acta Crystallogr.*, B54 (1998) 471.
- [7] E.A. Zhurova and A.A. Pinkerton, *Acta Crystallogr.*, B57 (2001) 359.
- [8] Bruker, SMART 5.622. Bruker Analytical X-ray Instruments Inc.: Madison, Wisconsin, USA (2001).
- [9] Bruker, SAINT-Plus 6.02a. Bruker Analytical X-ray Instruments Inc.: Madison, Wisconsin, USA (2000).
- [10] G.M. Sheldrick, SADABS, University of Göttingen (1996).
- [11] R.H. Blessing, SORTAV, *Crystallogr. Rev.*, 1 (1987) 3-58.
- [12] Y.-S. Chen and A.A. Pinkerton, to be published.
- [13] C.K. Johnson, ORTEP, Report ORNL-3794, Oak Ridge National Laboratory, Tennessee, USA (1971).
- [14] E.A. Zhurova, A. Martin and A.A. Pinkerton, *J. Am. Chem. Soc.*, 124 (2002) 8741.
- [15] J.C. Bottaro, to be published.
- [16] G.M. Sheldrick, SHELXTL Vers.5.1. An Integrated System for Solving, Refining and Displaying Crystal Structures from Diffraction Data, University of Göttingen: Germany (1997).
- [17] N. Hansen and P. Coppens, *Acta Crystallogr.*, A34 (1978) 909.
- [18] T. Koritsanszky, S. Howard, P.R. Mallison, Z. Su, T. Ritcher and N.K. Hansen, XD, A computer Program Package for Multipole Refinement and Analysis of Electron Densities from Diffraction Data, User's Manual, University of Berlin, Germany (1995).
- [19] P. Coppens, T.N. Guru Row, P. Leung, E.D. Stevens, P.J. Becker and Y.W. Yang, *Acta Crystallogr.*, A35 (1979) 63.
- [20] V. Pichon-Pesme, C. Lecomte and H. Lachekar, *J. Phys. Chem.*, 99 (1995) 6242.
- [21] F.H. Allen, O. Kennard, D.G. Watson, L. Brammer, A.G. Orpen and R. Taylor, *J. Chem. Soc. Perkin Trans. 2*, (1987) S1.
- [22] P.J. Becker and P. Coppens, *Acta Cryst.*, A30 (1974) 129.
- [23] M. Roux, S. Besnainou and R. Daudel, *J. Chem. Phys.*, 53 (1956) 218.
- [24] R.F.W. Bader and H.J. Essen, *Chem. Phys.* 80 (1984) 1943.
- [25] M.A. Pendas, A. Costales and V. Luana, *Phys. Rev.*, B55, (1997) 4275.
- [26] V.G. Tsirelson, Yu. Ivanov, E.A. Zhurova, V.V. Zhurov and K. Tanaka, *Acta Crystallogr.*, B56, (2000) 197.
- [27] R.F.W. Bader, "Atoms in Molecules: A Quantum Theory," The International Series of Monographs of Chemistry, J. Halpen and M.L.H. Green (eds.). Oxford: Clarendon Press, p.1-438 (1990).
- [28] V.G. Tsirelson, *Can. J. Chem.*, 74 (1996) 1171.
- [29] E.A. Zhurova and A.A. Pinkerton, to be published.
- [30] A. Volkov, C. Gatti, Yu. Abramov and P. Coppens, *Acta Crystallogr.*, A56 (2000) 252.
- [31] F. Benabicha, V. Pichon-Pesme, C. Jelsch, C. Lecomte and A. Khmou, *Acta Crystallogr.*, B56 (2000) 155.
- [32] R.F. Stewart, *God. Jugosl. Cent. Kristallogr.*, 17 (1982) 1.
- [33] R.F.W. Bader and P.M. Beddal, *J. Chem. Phys.*, 56 (1972) 3320.
- [34] V.G. Tsirelson, *Acta Crystallogr.*, B58 (2002) 632.
- [35] D.A. Kirzhnits, *Sov. Phys. JETP* 1957, 5, 64.

- [36] T.A. Keith, R.F.W. Bader and Y. Aray, Intern. Journal of Quantum Chem., 57 (1996) 183.
- [37] R.F.W. Bader, J. Phys. Chem., A102 (1998) 7314.
- [38] E. Espinosa, E. Molins and C. Lecomte, Chem. Phys. Letts., 285 (1998) 170.
- [39] A. Stash and V.G. Tsirelson, J. Appl. Crystallogr., 35 (2002) 371.
- [40] R.F.W. Bader and H.J.T. Preston, Intern. J. Quant. Chem., 3 (1969) 327.
- [41] D. Cramer and E. Kraka, Croatica Chemica Acta, 57 (1984) 1259.
- [42] R.G.A. Bone and R.F.W. Bader, J. Phys. Chem., B100 (1996) 10892.
- [43] N.J. Harris and K. Lammertsma, J. Am. Chem. Soc., 118 (1996) 8048.

This Page Intentionally Left Blank

Chapter 9

Computational approaches to heats of formation

Peter Politzer, Pat Lane and Monica C. Concha

Department of Chemistry, University of New Orleans, New Orleans, LA 70148, USA

1. INTRODUCTION

In assessing the potential value of a proposed energetic compound, important measures of performance are detonation velocity and pressure for explosives and specific impulse for propellants. One of the key factors in determining these properties is the energy that is produced in the decomposition or combustion process [1-4]. This can normally be estimated if the compound's heat of formation, ΔH_f , is known. (There are also indications that the energy of decomposition is related to sensitivity toward initiation of detonation [5,6].) Thus a reliable value for ΔH_f is essential to the evaluation of a compound. If the latter has not yet been synthesized, then its heat of formation must necessarily be obtained by a computational procedure. This may be true as well if only a very small amount has been prepared, or if the laboratory determination presents difficulties [7].

Heats of formation are of course of great practical importance in thermochemistry in general. Since experimental values are available for less than 0.1% of the more than ten million compounds known [8], considerable effort has been expended upon developing computational approaches. These range from empirical, e.g. group additivity, to semi-empirical molecular orbital to ab initio and density functional techniques; for an excellent overview, see Irikura and Frurip [9]. The empirical and semi-empirical methods, while often yielding good results, require extensive parametrization and are not designed for the rather atypical molecules – metastable, energy-rich – that are characteristic of energetic materials. For example, a recent survey found that the largest mean errors in ΔH_f produced by the semi-empirical MNDO, AM1 and PM3 methods (7 - 9 kcal/mole) were for C/H/N/O-type molecules [10], the category that encompasses most explosives. Sometimes the errors are sufficiently systematic that they can largely be taken into account, within series of

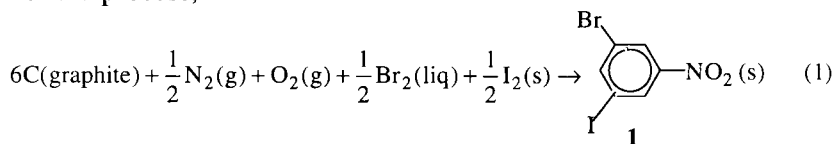
similar molecules, by correction terms [11,12]. Thus Chen and Wu showed, for a group of nitroaromatics, that the experimental ΔH_f correlated well with the AM1 and PM3 calculated values when the latter were corrected by a multiple of the number of nitro groups [11]; the mean errors decreased to 1.7 (AM1) and 1.4 (PM3) kcal/mole, in contrast to the original 15.1 and 4.3 kcal/mole, respectively.

The use of density functional and high-level *ab initio* procedures to calculate ΔH_f , which shall be the focus of this chapter, has been increasing steadily in recent years, despite the considerable demands that they (especially the *ab initio*) place upon computer resources. This barrier is gradually being diminished (although it is far from being overcome) by the advances in methodology, software and particularly processor technology that have occurred over approximately the past decade. While limitations upon molecular size continue to exist, although much less so for the density functional techniques, it is becoming ever more feasible to compute heats of formation with good accuracy (± 3 kcal/mole) for a variety of systems of practical importance in the area of energetic materials.

Within the density functional/*ab initio* framework, several different approaches have been used to find ΔH_f . These shall now be briefly described.

2. SPECIFIC APPROACHES TO ΔH_f

The most direct route to calculating the heat of formation of a compound is to simply apply the definition of ΔH_f : it is ΔH for the reaction (often hypothetical) whereby the compound is formed from its elements. The latter should be in whatever are their most stable states at the temperature in question; tabulated ΔH_f are generally at 25°C (298.15 K). (The pressure is typically one bar, i.e. standard state, although that is normally not a factor in computing ΔH_f .) Thus ΔH_f for 3-iodo-5-bromonitrobenzene, **1**, is ΔH for the process,



The first step then is to compute the energy at 0 K for the carbon atom and for the N_2 , O_2 , Br_2 , I_2 and **1** molecules. Next the zero-point vibrational contributions are added to the molecular energies, plus the thermal corrections to convert each $E(0 \text{ K})$ to $H(T)$, whatever is the temperature of interest. (We will assume it to be 298 K.) Finally the heat of vaporization of Br_2 and the heats of sublimation of graphite, I_2 and **1** must be included

in order that the reactants and product be in the states indicated in eq. (1). The heats of phase transitions are generally known experimentally for the elements but probably not for the product compound, so that computed heats of formation have usually been restricted to the latter being in the gas phase. However there are now available widely-applicable procedures for predicting heats of vaporization [13] and sublimation [14] from the properties of the calculated electrostatic potentials on molecular surfaces; thus it has become quite feasible to obtain liquid and solid phase heats of formation to satisfactory accuracy, as shall be discussed in section 4.

The vibrational thermal contribution to the total energy, as given by eq. (2), requires that the vibration frequencies be determined [15]. (These are generally multiplied by a corrective scaling factor that depends upon the computational technique that was used [16].) However since these corrections are relatively small in magnitude, this time-consuming step is often carried out at a lower computational level. Calculating the vibration frequencies of the product compound also serves the purpose of establishing, by the absence of imaginary values, that its computed structure corresponds to an energy minimum [15]. This is of course important if the compound has not yet been synthesized and its stability is open to question. If this is not an issue, then a time-saving alternative is to estimate the zero-point plus vibrational thermal energy from the molecular stoichiometry [17,18], which can be done to within an average absolute error of 1.0 kcal/mole. Finally, the other thermal terms (rotational and translational) and the conversion of energy to enthalpy are easily handled by means of the ideal gas model [15]. Thus,

$$E_{\text{vib}} = \frac{1}{2}h \sum_i \nu_i + N_A h \sum_i \nu_i [\exp(h\nu_i / kT) - 1]^{-1} \quad (2)$$

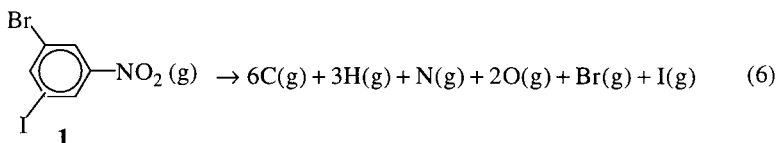
$$E_{\text{rot}} = \frac{3}{2}RT \text{ (non-linear molecule), } E_{\text{rot}} = RT \text{ (linear molecule)} \quad (3)$$

$$E_{\text{trans}} = \frac{3}{2}RT \quad (4)$$

$$H(T) = E(T) + RT \quad (5)$$

In eqs. (2) - (5), ν_i is the vibration frequency of the i^{th} normal mode and N_A is Avogadro's number. The other constants have their usual meanings.

A modified version of this approach to computing heats of formation is to calculate ΔH not for the formation of the compound but rather for its atomization, i.e. separation of the gas phase molecule into the individual atoms. For 1, this is the process,

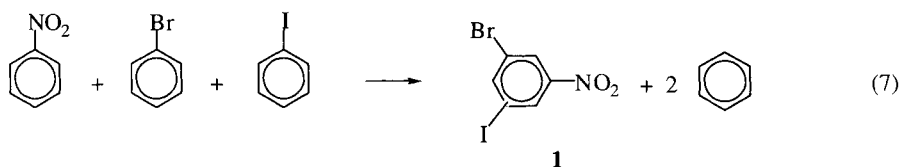


This $\Delta H(298 \text{ K})$, when appropriately combined with the experimental dissociation enthalpies of $\text{H}_2(\text{g})$, $\text{N}_2(\text{g})$, $\text{O}_2(\text{g})$, $\text{Br}_2(\text{g})$ and $\text{I}_2(\text{g})$, the heat of vaporization of $\text{Br}_2(\text{liq})$ and the heats of sublimation of graphite, $\text{I}_2(\text{s})$ and **1** will yield the *negative* of the heat of formation of the last-named compound. This approach to ΔH_f avoids the need for computing the energies of molecular elements.

The use of formation or atomization reactions, eqs. (1) and (6), as the basis for determining ΔH_f is rigorous and well-defined in that there is no arbitrariness; there is only one possible formation process, and only one possible atomization, for each compound. Obtaining accurate results by either of these procedures, however, is computationally challenging, because the products and reactants are likely to be quite different, as will therefore be their electronic correlation energies. In eq. (1), for example, a neutral nitrogen atom that is involved in a triple bond is being transformed into one with a formal positive charge that is participating in three bonds, with differing degrees of polarity and double-bond character. Analogous observations can be made for the other atoms. Dealing properly with the corresponding changes in electronic correlation will require a high computational level. This is illustrated by the work of Schlegel and Skancke [19], who used both formation and atomization reactions to find ΔH_f for NH_2 , NH_3 and N_2H_4 . With Hartree-Fock methodology, which takes no account of correlation, the results are very poor; the average absolute error is 70 kcal/mole. This improves somewhat with the inclusion of the lowest-order perturbation theory correction term (MP2), but only to 35 kcal/mole. However the highly-correlated G2 technique (to be discussed later) produces an average error of only 1.3 kcal/mole.

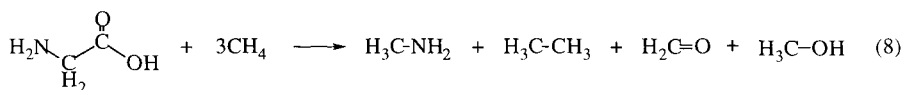
An indirect means of dealing with the correlation problem when the molecule is too large to be treated by advanced methods such as the G2 is to include it in a reaction (often hypothetical) in which the reactants and products are similar in terms of one or more of several electronic and structural factors, e.g. number of electron pairs, types of bonds, atom environments, etc. [15,20,21]. It is hoped that in computing $\Delta H(298 \text{ K})$ for such a process, the errors for the reactants and products will largely cancel. The desired ΔH_f can then be obtained if the ΔH_f of all of the other species are known. There are several categories of such reactions; isogyric ones conserve the number of electron pairs, isodesmic maintain unchanged

the numbers of both electron pairs and bonds of each formal type, while homodesmotic extend this to include the number of atoms with each set of neighbors. An example of the last category that could be used to find ΔH_f for **1** is,



This approach to calculating heats of formation is in principle as rigorous as using formation or atomization processes, although there is certainly an element of arbitrariness now, in choosing the reaction. Sometimes it may be difficult to find a reasonable one. Certainly the extent of cancellation of correlation errors is likely to differ somewhat among possible candidates. An important consideration is that the experimental ΔH_f of some of the other participants in the reaction may not be known accurately.

A proposed way of avoiding arbitrariness is by using "bond separation" isodesmic reactions [15,20]. These involve separation of the molecule into the simplest smaller ones having each formal bond type between non-hydrogen atoms; for example, for glycine this would be,



This has the additional advantage that reliable ΔH_f will usually be available for the small molecules. On the other hand, a problem arises when the molecule of interest has two or more significant resonance structures, so that some of the bonds cannot be classified as single, double or triple; benzene and nitro derivatives are obvious examples. Furthermore, as pointed out by Petersson *et al* [22], a relatively large molecule may require several of some of the smaller ones, so that the error in the latter is multiplied; e.g., octanitrocubane would need 8 ethanes. Fishtik *et al* have suggested an alternative scheme, based on "response reactions" [23].

The three routes to ΔH_f that have been described are all intrinsically rigorous, meaning that exact computed energies plus highly accurate experimental data where needed would yield an exact ΔH_f for the compound of interest. There have also been developed a number of procedures that combine an *ab initio* or density functional technique with some empirical feature(s). These will be described after a brief survey of some *ab initio* and density functional techniques.

3. COMPUTATIONAL METHODOLOGIES

The essential question that we address in this section is: How well can the various types of *ab initio* and density functional calculations predict heats of formation? However an important caveat must be added: Our eventual interest will not be in “normal, typical” molecules, but rather in those metastable ones that show potential as energetic materials. The present discussion will focus upon gas phase ΔH_f ; we will return later to the conversion to liquid and solid phase values.

3.1 *Ab Initio*

The Hartree-Fock method has the advantage that it can be applied to relatively large molecules, e.g. octanitrocubane, with a reasonably good basis set, such as 6-31G**. Since no electronic correlation is taken into account, Hartree-Fock calculations of heats of formation should be attempted only in conjunction with an isodesmic or homodesmotic reaction [24]. If suitable ones are chosen, satisfactory results may be obtained [25,26]. On the other hand, an isodesmic reaction produced an HF/6-31G* ΔH_f of 166.1 kcal/mole for cubane, while a homodesmotic one yielded 133.4 kcal/mole [25]. The experimental value is 148.7 kcal/mole [27]. One must also be wary of a fortuitous element: the same homodesmotic reaction produced an excellent 149.7 kcal/mole with the very small STO-3G basis set [28].

The most widely-used manner of introducing some degree of electronic correlation is via Moeller-Plesset (MP) perturbation theory, to various orders. Although this takes considerable correlation into account, it is still best to work with isodesmic or homodesmotic processes [24]. The ΔH_f are usually more reliable than the Hartree-Fock values [25,26], but molecular size now becomes a more important issue; furthermore, the general effectiveness of the MP approach has recently been questioned [29,30]. Proceeding to a higher level, coupled-cluster calculations including triple excitations, CCSD(T), can reach very good accuracy [24,31-33] (although not invariably [34]), but are limited to molecules with four or five first-row atoms.

An important development in recent years has been the emergence of composite *ab initio* procedures, the most prominent being the Gn (Gaussian-n) [35,36] and the CBS (complete basis set) [37,38]. One of their objectives is to calculate thermochemical properties to an accuracy of ± 2 kcal/mole for molecules equivalent in size to about 10 - 14 first-row atoms. This is to be achieved by a sequence of single-point higher-order energy corrections following an initial Hartree-Fock (HF) or MP2 geometry

optimization. Since these corrections, while time-consuming, are relatively small, they may be determined using only moderately-sized basis sets. As the Gn and CBS methodologies have evolved, various modifications have been introduced in successive generations, seeking to improve accuracy and/or computational efficiency. For example, there are now versions that use density functional rather than HF or MP2 geometry optimization: G3(B3LYP) [39] and CBS-QB3 [40]. It should be noted that both the Gn and the CBS procedures do involve some molecule-independent empirical parameters (a point that has been criticized [41]).

These composite approaches have been, overall, very successful. For example, recent variants of G3 give the heats of formation of a test set of 222 molecules, many having second-row atoms, with overall mean absolute deviations of about 1 kcal/mole [42,43]. Atomization reactions were used. The results are nearly as good when third-row atoms are included [44]. Similarly, the CBS-QB3 procedure, for 147 first- and second-row molecules, produced a mean average deviation of 1.08 kcal/mole [38]. A few molecules, often containing halogens, do give problems [38,42-44], but the errors are rarely more than 5 kcal/mole. However the size limitations mentioned above must be kept in mind.

3.2 Density Functional

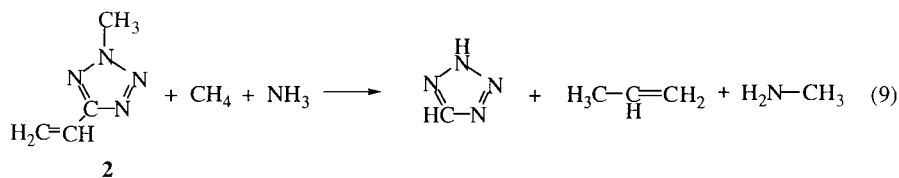
During the past 10 - 15 years, Kohn-Sham density functional theory has been a major factor in a dramatic expansion of the scope of computational chemistry and its capability for treating systems of practical importance [45-51]. Density functional methodology includes electronic correlation, so that the energies are more accurate than Hartree-Fock; however the Kohn-Sham formalism is similar to the latter, as are therefore the demands upon computer resources. It is therefore feasible to treat relatively large systems at a reasonably high (post-Hartree-Fock) level.

Within the Kohn-Sham framework, various formulations have been proposed for the exchange and correlation contributions to the energy [48-50]. These originally invoked the uniform electron gas model (local density approximation, LDA), which is quite effective for certain purposes but greatly overestimates bond-breaking energies. A major advance was the introduction of functionals that involve the gradient of the electronic density. Currently the most widely-used technique is Becke's three-parameter hybrid (B3, [52]), which consists of five terms: LDA exchange and correlation, gradient corrections to each, and finally Hartree-Fock exchange. The relative weights of these contributions are governed by three empirical parameters which were determined by fitting to experimental data [52] (atomization and ionization energies and electron and proton affinities). The gradient correction used for exchange is

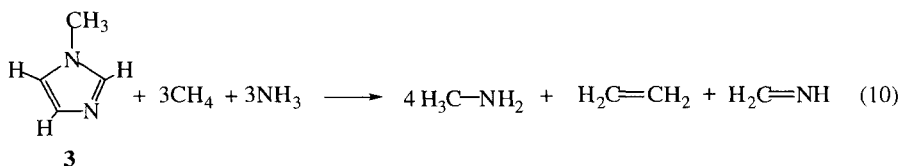
generally Becke's 1988 expression [53], while the most popular ones for correlation are those due to Lee, Yang and Parr (LYP, [54]), Perdew (P86, [55]) and Perdew and Wang (PW91, [56]). Thus these three functional combinations are designated B3LYP, B3P86 and B3PW91. There are of course continuing efforts to achieve further improvement; see, for example, Schmider and Becke [57].

How effective are these procedures in computing heats of formation and other thermochemical quantities? For a group of 40 small hydrocarbons and their oxygen and nitrogen derivatives, Raghavachari *et al* found mean absolute deviations of 2.7 kcal/mole (B3LYP), 3.7 kcal/mole (B3PW91) and 33.3 kcal/mole (B3P86) in ΔH_f obtained from atomization processes [58], using the relatively large 6-311+G(3df,2p) basis set. These improved to 1.5 (B3LYP), 3.3 (B3PW91) and – particularly striking – 1.7 kcal/mole (B3P86) when bond separation isodesmic reactions were used. In a more stringent test involving 148 molecules, many with second-row atoms, atomization-based ΔH_f had average absolute deviations of 3.11 kcal/mole (B3LYP), 3.51 kcal/mole (B3PW91) and 17.97 kcal/mole (B3P86) [59]. The basis set was again 6-311+G(3df,2p). There were seven instances of the B3LYP and B3PW91 errors being greater than 10 kcal/mole (usually not the same molecule). When the database was expanded to 222 molecules, the B3LYP mean absolute deviation became 4.81 kcal/mol [42], with 32 errors of more than 10 kcal/mole. For the same molecules, the G3 mean absolute deviations were about 1 kcal/mole. On the other hand, for 19 molecules containing third-row atoms, the B3LYP and B3PW91 average absolute deviations in the atomization energies were 3.32 and 2.06 kcal/mole [60], with no errors greater than 6.2 kcal/mole.

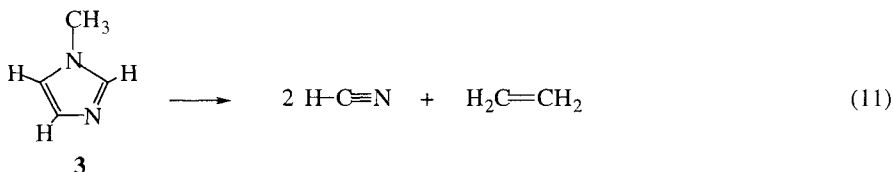
Two recent studies are of particular interest in the present context because they present B3LYP heats of formation for some nitroheterocycles, which provide the basic framework for many energetic molecules. Chen *et al* used homodesmic reactions to obtain ΔH_f for five tetrazoles with an average absolute error of only 2.0 kcal/mole [61]. They had the advantage of having available reliable ΔH_f for the two parent molecules, so that they needed to model only the bonds to the substituents; thus ΔH_f for 2-methyl-5-ethenyltetrazole (**2**) was predicted with an error of only 0.45 kcal/mole from eq. (9):



By analogous reasoning, eq. (7) should provide a good means of computing ΔH_f for **1**, given accurate ΔH_f for the three monosubstituted benzenes. Rather unexpected, however, are the results of Mo *et al* for ten imidazoles and pyrazoles [62]. Atomization processes gave unsatisfactory ΔH_f with an average absolute error of 5.2 kcal/mole. Mo *et al* suggested that a reasonable set of isodesmic reactions would have involved methylenimine, $H_2C=NH$; e.g. for 1-methylimidazole (**3**),



However they noted that experimental measurements of ΔH_f for $H_2C=NH$ cover a range of 40 kcal/mole. Accordingly they selected $H-C\equiv N$ to model the $C=N$ double bond:



Since reactions such as eq. (11) do not adhere to the isodesmic principle of conserving formal bond type, they were termed “quasiisodesmic” by Mo *et al* [62]. Surprisingly, the average absolute error for the ten imidazoles and pyrazoles was only 2.5 kcal/mole. On the other hand, Mo *et al* subsequently obtained poorer results for a group of alkyl and aryl benzenes [63]. Bond separation isodesmic processes, using $H_2C=CH_2$ and H_3C-CH_3 to model the bonds in the benzene ring, produced average absolute errors of 4.3 kcal/mole; most puzzling is that this *increased* to 5.7 kcal/mole for reactions that included the parent benzene molecule! Thus, density functional calculation of heats of formation via isodesmic and homodesmic reactions has some seemingly contradictory aspects. Nevertheless, it warrants further investigation.

Accordingly, we recently undertook the determination, by means of homodesmic reactions, of the gas and solid phase ΔH_f of six energetic nitroaromatic compounds for which the experimental $\Delta H_f(\text{solid})$ are ambiguous, i.e. two or more values differ by at least 6 kcal/mole [64]. Nitroaromatics should be particularly well suited for modeling by means of homodesmic reactions, since all of the participants in these can have the

basic aromatic framework and differ only in the substituents that are interacting with it; this can be seen in eq. (7). We kept the coefficients of the smaller molecules as low as possible, never as large as 3, in order to minimize error magnification (the point raised by Petersson *et al* [22]). Following the recommendations of Sicre and Cobos [65] and Ventura *et al* [66], we used the B3PW91 procedure (with the 6-31G** basis set) to find ΔH ; this has the important advantage that it was the PW91 correlation correction that Becke utilized in parametrizing the B3 hybrid functional [52]. $\Delta H(\text{solid})$ was obtained from $\Delta H(\text{gas})$ by the method to be described in section 4. Our results are encouraging. For four test cases, the average absolute error was only 1.3 kcal/mole; for the six nitroaromatics of interest, our calculated $\Delta H_f(\text{solid})$ clearly support some of the experimental values over the others. Given the appropriate circumstances, therefore, it appears that homodesmotic reactions can provide an effective approach to estimating the heat of formation.

Finally, in the context of B3 density functional methodology, we would like to return to the fact that the relative weights that Becke assigned to the contributing terms in his hybrid expression were determined empirically, by fitting to certain experimental data that Becke selected [52]. While his values have proven to be remarkably successful for a variety of systems and properties, there is no reason why they cannot be changed, using an appropriate database, so as to be more effective for specific objectives; i.e. the technique could be attuned to its particular purpose. Such reparametrization has been suggested in the past [67-71], and was indeed tested for (a) approximating electronic ionization potentials by Kohn-Sham orbital energies [69], (b) treating transition metal diatomics [71], and (c) computing the heats of formation of hypervalent molecules [71]. The results have been encouraging, and have confirmed that hybrid functionals can be tailored to the need. Thus it is possible that they could also be designed to produce improved heats of formation (or other desired properties) for the types of H/C/N/O/NO₂/NF₂ molecules that are of interest for energetic materials.

3.3 *Ab Initio*/Empirical and Density Functional/Empirical Combinations

First, it must be acknowledged that the Gn, CBS and B3 procedures discussed in the preceding two sections do contain some empirical parameters, and therefore should perhaps not be termed “pure” *ab initio* and density functional methods. (But has not their purity already been sullied by the presence of Planck’s constant?) In response, it can be argued that these parameters are few in number and are universal, i.e. independent of any particular atom, group, molecule, etc. (This statement would of

course have to be modified if the B3 functional were reparametrized to fit the objective, as suggested in the last paragraph of section 3.2.)

The techniques to be described now involve larger numbers of empirical parameters, and they are atom-, group- and/or bond-dependent. Many of these approaches require computing only $E(0\text{ K})$ for the molecule for which ΔH_f is desired; since one of the aims is to be able to treat relatively large systems, this may be done at Hartree-Fock [72-77] or density functional [77-80] levels. This energy is converted to $\Delta H_f(298\text{ K})$ by subtracting empirical parameters, often called "equivalents," corresponding to the atoms, groups and/or bonds of which the molecule is comprised. The results can achieve quite a good level of accuracy, but this is limited by the range and versatility of the parametrization.

A second category of procedures obtains ΔH_f from formation, atomization or isodesmic reactions, but improves it by imposing empirical corrections [22,81-86]. Three of these are of particular interest because they have been applied successfully to energetic molecules. Melius and his collaborators calculate ΔH_f from atomization processes, computing MP4 energies for the molecule and its constituent atoms [81,86]. "Bond additivity corrections" (BAC) are then added, which depend upon the types of bonds and their lengths. The ΔH_f are generally quite accurate, with errors usually less than 2 kcal/mole, but are restricted to rather small molecules due to the use of MP4. BAC-MP4 studies have been carried out for a number of combustion and energetic molecule decomposition reactions [87]. (Irikura has proposed some CCSD(T)-based techniques, including a variant of BAC-MP4, which involve only 1 - 4 parameters [34], but they are again limited to small molecules.)

We have developed a density functional scheme, which involves computing the B3P86/6-31+G** $\Delta H(298\text{ K})$ for the formation process and then adding correction terms for the carbons, nitrogens and oxygens in the molecule of interest [83,84]. Rice *et al* find $\Delta H_f(298\text{ K})$ by computing the B3LYP/6-31G* molecular energy and then subtracting atom equivalents determined specifically for H/C/N/O energetic molecules [85]. These two density functional procedures have been applied to more than 150 energetic molecules, containing as many as 30 first-row atoms. In most instances, the gas phase values were used to obtain liquid and/or solid phase ΔH_f , via relationships based upon molecular surface electrostatic potentials [13,14,85] (section 4). The results will be discussed, and some of them presented, in section 5.2.

4. LIQUID AND SOLID PHASE HEATS OF FORMATION

Computational procedures typically produce gas phase ΔH_f , whereas energetic compounds are generally liquids or solids. For molecular liquids and solids, ΔH_f can readily be obtained from the gas phase values if the heats of vaporization and sublimation, ΔH_{vap} and ΔH_{sub} , are known:

$$\Delta H_f (\text{liquid}) = \Delta H_f (\text{gas}) - \Delta H_{\text{vap}} \quad (12)$$

$$\Delta H_f (\text{solid}) = \Delta H_f (\text{gas}) - \Delta H_{\text{sub}} \quad (13)$$

In a series of studies, reviewed on several occasions [13,88,89], we have found that a variety of physical properties that depend upon noncovalent interactions, including ΔH_{vap} and ΔH_{sub} , can be related quantitatively to certain features of the electrostatic potentials on molecular surfaces. The electrostatic potential $V(\mathbf{r})$ that the electrons and nuclei of a molecule create at any point \mathbf{r} is given by,

$$V(\mathbf{r}) = \sum_A \frac{Z_A}{|\mathbf{R}_A - \mathbf{r}|} - \int \frac{\rho(\mathbf{r}')d\mathbf{r}'}{|\mathbf{r}' - \mathbf{r}|} \quad (14)$$

in which Z_A is the charge on nucleus A, located at \mathbf{R}_A , and $\rho(\mathbf{r})$ is the electronic density. The molecular surface is taken to be the 0.001 electrons/bohr³ contour of $\rho(\mathbf{r})$ [90]. For present purposes, we calculate the total variance σ_{tot}^2 of $V(\mathbf{r})$ on the surface, which indicates its variability or range, and a parameter v that is a measure of the degree of balances between positive and negative regions:

$$\sigma_{\text{tot}}^2 = \sigma_+^2 + \sigma_-^2 = \frac{1}{m} \sum_{i=1}^m [V_S^+(\mathbf{r}_i) - \bar{V}_S^+]^2 + \frac{1}{n} \sum_{j=1}^n [V_S^-(\mathbf{r}_j) - \bar{V}_S^-]^2 \quad (15)$$

$$v = \frac{\sigma_+^2 \sigma_-^2}{[\sigma_{\text{tot}}^2]^2} \quad (16)$$

In eqs. (15) and (16), $V_S^+(\mathbf{r}_i)$ and $V_S^-(\mathbf{r}_j)$ are the positive and negative values of $V(\mathbf{r})$ on the surface and \bar{V}_S^+ and \bar{V}_S^- are their averages.

We have shown that ΔH_{vap} [13] and ΔH_{sub} [14] can be expressed as,

$$\Delta H_{\text{vap}} = \alpha_1(\text{surface area})^{0.5} + \alpha_2(v\sigma_{\text{tot}}^2)^{0.5} + \alpha_3 \quad (17)$$

and

$$\Delta H_{\text{sub}} = \beta_1(\text{surface area})^2 + \beta_2(v\sigma_{\text{tot}}^2)^{0.5} + \beta_3 \quad (18)$$

We determined the coefficients in eqs. (17) and (18) by fitting to general databases of experimental ΔH_{vap} and ΔH_{sub} , using Hartree-Fock electrostatic potentials [13,14]; however Rice *et al* reparametrized these equations at the B3LYP/6-31G* level in terms of data pertaining specifically to energetic compounds [85]. Their average absolute deviations for ΔH_{vap} and ΔH_{sub} were 1.2 and 2.7 kcal/mole, respectively.

For compounds that are ionic rather than molecular solids, ΔH_f can be calculated by appropriately combining the heats of formation of the gas phase ions (computed or experimental) with the lattice energy (converted to enthalpy [91]). We have developed formulas for lattice energies in terms of properties of the electrostatic potentials on the anions' surfaces [92], for any of three possible cations: NH_4^+ , Na^+ and K^+ .

5. APPLICATIONS AND DISCUSSION

5.1 Boron and Aluminum Combustion Products

In conjunction with extensive studies of the combustion of boron- and aluminum-based propellant formulations in oxygen/nitrogen/fluorine environments, we have computed the gas phase heats of formation for more than 70 likely products of these processes, as well as ΔH and ΔG at 298 K and 2000 K for numerous possible reaction steps [93-97]. Transition states and activation barriers were found for some of these.

The molecules involved are relatively small, so that CBS procedures were feasible for these calculations. For boron combustion, we initially used both the CBS-Q and the B3PW91 techniques [93], but changed to the superior CBS-QB3 when it became available [94-96], and continued with it for the aluminum work [97]. At this level, the average absolute error in ΔH_f (determined from formation reactions) was less than 2.0 kcal/mole [96,97]. The same accuracy was achieved for $\Delta H(298 \text{ K})$, $\Delta H(2000 \text{ K})$ and $\Delta G(298 \text{ K})$ for the combustion steps examined. It was observed that ΔH changes very little, by an average of less than 2.0 kcal/mole, in going from 298 K to 2000 K. In contrast, $\Delta G(2000 \text{ K})$ can differ quite significantly from $\Delta G(298 \text{ K})$, and tends to be less accurate. (Fortunately

the greater uncertainty in ΔG at 2000 K does not produce an equivalent one in the resulting equilibrium constant [97].)

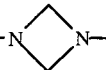
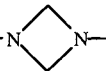


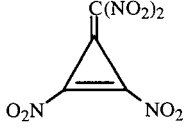
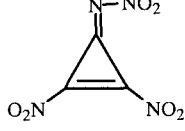
5.2 H/C/N/O/F Energetic Compounds

As mentioned in section 3.3, we have been determining the heats of formation of relatively large energetic molecules by computing $\Delta H(298\text{ K})$ for the formation reaction, initially at the BP86/6-31G** level [83] and subsequently B3P86/6-31+G** [84], and then adding correction terms, obtained by fitting to experimental ΔH_f , that depend upon the coordination states of the carbons, nitrogens and oxygens. The zero-point and vibrational thermal energy often came from our stoichiometry-based relationship [18], in order to avoid the very lengthy calculation of vibration frequencies. In many instances, the gas phase ΔH_f were converted to liquid and/or solid values by means of eqs. (12) and (13), using ΔH_{vap} and ΔH_{sub} from eqs. (17) and (18). Nearly all of this work has been carried out with the Gaussian codes, most recently Gaussian 98 [98]. In comparisons with experimental data, our average absolute errors have been, overall, about 3 kcal/mole.

In the context of energetic materials, we have applied this procedure to more than 80 compounds for which experimental ΔH_f were not available, and which in many instances have not even been prepared. Some had been proposed for evaluation prior to undertaking synthesis efforts; others were of interest for purposes of comparison. A portion of these results are presented in Tables 1 and 2. Table 1 contains only gas phase values; these were computed, for the most part, before we had developed the capability of predicting ΔH_{vap} and ΔH_{sub} and hence the condensed phase ΔH_f . In Table 2 are given gas, liquid and solid phase heats of formation. All of these data are in cal/g as well as kcal/mole, since the formulas for detonation velocity, detonation pressure and specific impulse require that the energy produced in decomposition or combustion be given on a gram basis [1-4]. For the solids in Table 2, we also give the heat release, Q , which is $\Delta H(298\text{ K})$ for the process in which the compound decomposes only to some combination of the stable gaseous products N_2 , CO , CO_2 , H_2O and HF . Q is calculated using the solid phase $\Delta H_f(298\text{ K})$ and the experimental heats of formation of the product gases [27]. While the actual decomposition is likely to differ to some extent from this idealized one, the heat release of the latter is an indication of the energy potentially available from the compound. (If its stoichiometry is such that products other than these five would be necessary, no value is given for Q .)

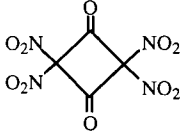
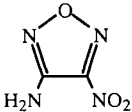
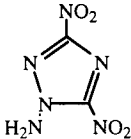
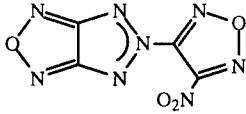
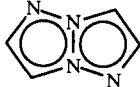

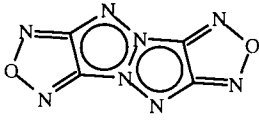
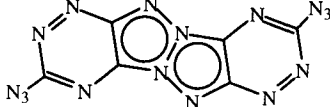
Certain trends can be seen in Tables 1 and 2. A particularly interesting one concerns the effect of substituting the NF_2 (difluoramine)

Table 1.
Calculated gas phase heats of formation.^a

Compound	$\Delta H_f(298\text{ K}),$ kcal/mole	$\Delta H_f(298\text{ K}),$ cal/g	Ref.
4 $(\text{H}_3\text{C})_2\text{N}-\text{NO}_2$ DMNA	-3	-30	b
5 $(\text{H}_3\text{C})_2\text{N}-\text{NF}_2$	-20	-206	b
6 	44	297	b
7 	29	186	b
8 	7	38	c
9 $\text{HN}(\text{NO}_2)_2$	19	178	d
10 $\text{O}_2\text{N}-\text{C}\equiv\text{C}-\text{NO}_2$	89	763	c,e
11 $\text{O}_2\text{N}-\text{C}\equiv\text{C}-\text{NF}_2$	74	606	c,e
12 $\text{O}_2\text{N}-\text{C}\equiv\text{C}-\text{NO}$	100	1004	c,e
13 $\text{F}_2\text{N}-\text{C}\equiv\text{C}-\text{NO}$	95	901	c,e
14 $\text{O}_2\text{N}-\text{N}=\text{C}=\text{N}-\text{NO}_2$	87	659	c,e
15 	102	465	c
16 	130	559	c
17 	135	716	c

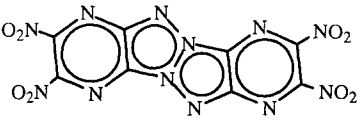
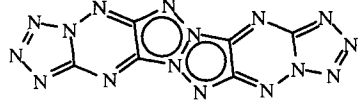
(continued)

Table 1.
Calculated gas phase heats of formation (continued).

Compound		$\Delta H_f(298\text{ K})$, kcal/mole	$\Delta H_f(298\text{ K})$, cal/g	Ref.
18		9	35	c
19		43	330	c
20 ADNT		87	502	c
21 NOTO		202	903	c,f
22		124	1151	c,f
23		125	1158	c,f
24		253	1318	c,f
25		426	1439	c,f

(continued)

Table 1.
Calculated gas phase heats of formation (continued).

Compound	$\Delta H_f(298\text{ K})$, kcal/mole	$\Delta H_f(298\text{ K})$, cal/g	Ref.
26 	247	630	c
27 	442	1493	f

^aValues are given to the nearest kcal or cal.

^bRef. 99.

^cRef. 100.

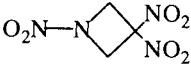
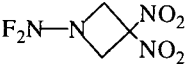
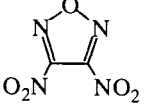
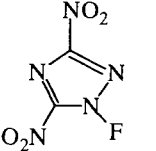
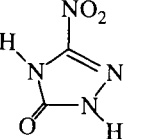
^dObtained from isodesmic reactions, Ref. 101.

^eRef. 102.

^fRef. 103.

Table 2.

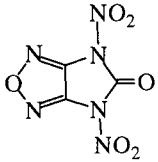
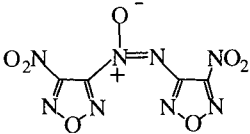
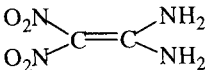
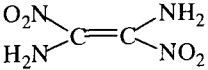
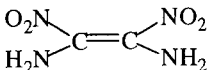
Calculated gas, liquid and/or solid phase heats of formation and solid phase heat releases.^a

Compound		$\Delta H_f(298\text{ K}), \text{ gas}$		$\Delta H_f(298\text{ K}), \text{ liquid}$		$\Delta H_f(298\text{ K}), \text{ solid}$		$Q, \text{ solid}$		Ref.
		kcal/mole	cal/g	kcal/mole	cal/g	kcal/mole	cal/g	kcal/mole	cal/g	
31 TNAZ		31	160	---	---	8	43	-271	-1410	b,c,d
32		16	79	---	---	-6	-30	-261	-1321	c,e
33		67	420	---	---	49	304	-237	-1480	f
34		77	435	---	---	56	316	---	---	e
35 NTO		-6	-44	---	---	-25	-194	-85	-657	b,d

(continued)

Table 2.

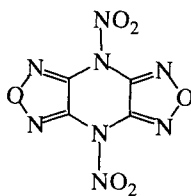
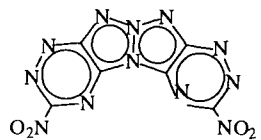
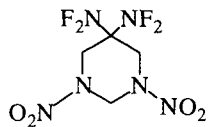
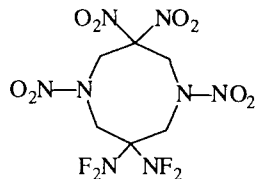
Calculated gas, liquid and/or solid phase heats of formation and solid phase heat releases (continued).^a

Compound	$\Delta H_f(298\text{ K}), \text{ gas}$		$\Delta H_f(298\text{ K}), \text{ liquid}$		$\Delta H_f(298\text{ K}), \text{ solid}$		$Q, \text{ solid}$		Ref.
	kcal/mole	cal/g	kcal/mole	cal/g	kcal/mole	cal/g	kcal/mole	cal/g	
36 	74	341	60	278	50	231	-332	-1536	f
37 DNAF 	169	621	155	570	137	504	-446	-1638	d
28 FOX-7 DADNE 	-1	-8	-16	-109	-27	-183	-141	-954	g
29 	1	7	-11	-74	-19	-125	-150	-1012	g
30 	15	101	2	14	-7	-45	-162	-1093	g

(continued)

Table 2.

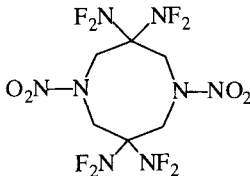
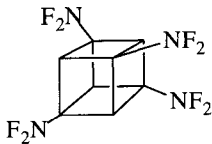
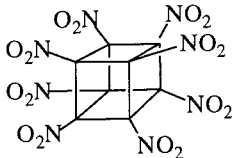
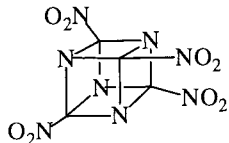
Calculated gas, liquid and/or solid phase heats of formation and solid phase heat releases (continued).^a

Compound	$\Delta H_f(298\text{ K}), \text{ gas}$		$\Delta H_f(298\text{ K}), \text{ liquid}$		$\Delta H_f(298\text{ K}), \text{ solid}$		$Q, \text{ solid}$		Ref.
	kcal/mole	cal/g	kcal/mole	cal/g	kcal/mole	cal/g	kcal/mole	cal/g	
38 	155	604	139	544	126	491	-367	-1432	f
39 	300	985	282	926	260	855	---	---	f
40 	11	40	---	---	-21	-76	---	---	e
41 	5	12	---	---	-39	-98	-496	-1253	e

(continued)

Table 2.

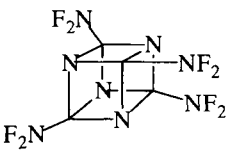
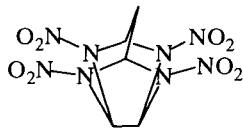
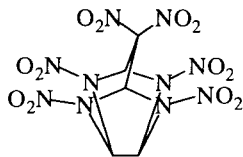
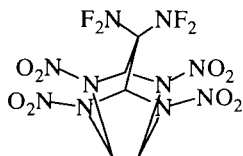
Calculated gas, liquid and/or solid phase heats of formation and solid phase heat releases (continued).^a

	Compound	$\Delta H_f(298\text{ K}), \text{ gas}$		$\Delta H_f(298\text{ K}), \text{ liquid}$		$\Delta H_f(298\text{ K}), \text{ solid}$		$Q, \text{ solid}$		Ref.
		kcal/mole	cal/g	kcal/mole	cal/g	kcal/mole	cal/g	kcal/mole	cal/g	
42		-24	-58	---	---	-67	-165	---	---	e
43		73	237	58	188	43	141	---	---	e
44	ONC 	197	424	179	385	144	310	-896	-1931	h
45		216	750	202	701	189	656	-565	-1962	h

(continued)

Table 2.

Calculated gas, liquid and/or solid phase heats of formation and solid phase heat releases (continued).^a

	Compound	$\Delta H_f(298\text{ K}), \text{ gas}$		$\Delta H_f(298\text{ K}), \text{ liquid}$		$\Delta H_f(298\text{ K}), \text{ solid}$		$Q, \text{ solid}$		Ref.
		kcal/mole	cal/g	kcal/mole	cal/g	kcal/mole	cal/g	kcal/mole	cal/g	
46		141	452	127	407	114	365	---	---	e
47		81	263	64	210	46	150	-351	-1147	f
48		104	264	88	221	62	157	-648	-1636	f
49		96	236	79	194	54	132	-649	-1591	f

(continued)

Table 2.

Calculated gas, liquid and/or solid phase heats of formation and solid phase heat releases (continued).^a

Compound	<u>$\Delta H_f(298\text{ K})$, gas</u>		<u>$\Delta H_f(298\text{ K})$, liquid</u>		<u>$\Delta H_f(298\text{ K})$, solid</u>		<u>Q, solid</u>		Ref.
	kcal/mole	cal/g	kcal/mole	cal/g	kcal/mole	cal/g	kcal/mole	cal/g	
50 $\text{NH}_4^+\text{O}_2^-$ (ionic)	---	---	---	---	-39	-780	-77	-1540	i
51 $\text{NH}_4^+\text{O}_3^-$ (ionic)	---	---	---	---	-37	-561	---	---	i

^aValues are given to nearest kcal or cal.^bRef. 14.^cRef. 99.^dRef. 100.^eRef. 105.^fRef. 84.^gRef. 104.^hRef. 106.ⁱRef. 107.

group for NO_2 . This is an attractive possibility because it is likely to produce a higher density [105,108], a larger number of moles of gaseous products per gram of compound [2,105] and more efficient ignition/combustion of boron- and aluminum-based propellant formulations [108-110]. There is concern, however, regarding the stabilities of difluoramines [99,105,111-114]. Furthermore, as has been pointed out earlier [99,100,102,105,115] and can be seen again in Tables 1 and 2, replacing NO_2 by NF_2 lowers the heat of formation, whether this occurs on a carbon (compare **10** and **11**, **12** and **13**) or nitrogen (compare **4** and **5**, **6** and **7**) and as well in the liquid and solid as the gas phase (**31** vs. **32**, **45** vs. **46**, **48** vs. **49**). On the other hand, nitroso derivatives have higher ΔH_f than do their nitro counterparts; this is seen in comparing **10** vs. **12** and **11** vs. **13**, and is confirmed by experimental gas- and solid-phase data [85].

From the standpoint of energetic performance, the most important quantity given in Table 2 is the heat release in cal/g, keeping in mind however that it refers to an idealized process. There are numerous examples showing that Q (cal/g) does not show the same trends as ΔH_f , whether the latter be in kcal/mole or cal/g; compare, for instance, **36** and **38**. Indeed, even a negative heat of formation does not preclude a large heat release; good examples are the ionic NH_4O_2 , **50**, and the difluoramine **32**.

Among the compounds in Table 2, by far the largest energy output in cal/g would be anticipated from octanitrocubane (ONC), **44**, and its tetraazacounterpart, **45**. ONC has recently been synthesized [116], after years of effort, and is expected to show excellent detonation performance [117]. The tetraaza compound, **45**, has not yet been prepared; however its potential as an energetic compound was pointed out already some years ago [118].

The procedure that we used to compute the heats of formation in Tables 1 and 2 was intended to be a general one; the C/N/O corrections and the coefficients in the ΔH_{vap} and ΔH_{sub} expressions, eqs. (17) and (18), were determined by fitting to experimental databases that included a wide variety of compounds [83,84]. In contrast, Rice *et al* parametrized their approach explicitly for energetic compounds [85]. They compute $E(0 \text{ K})$ for the molecule and then directly produce $\Delta H_f(298 \text{ K})$ by subtracting empirical atom equivalents for the hydrogens, carbons, nitrogens and oxygens that depend upon whether the atom is involved in single or multiple bonds. Rice *et al* obtained these atom equivalents, as well as their coefficients for eqs. (17) and (18), by fitting to measured ΔH_f , ΔH_{vap} and ΔH_{sub} of H/C/N/O energetic compounds [27]. Thus their method should be particularly effective for this category. Their results, overall, bear this out. For a group of 69 energetic compounds, 19 of which had not been included in the parametrization, the average absolute deviations from the

available experimental values are: ΔH_{vap} , 1.2 kcal/mole; ΔH_{sub} , 2.7 kcal/mole; $\Delta H_f(\text{gas})$, 2.4 kcal/mole; $\Delta H_f(\text{liquid})$, 2.5 kcal/mole; $\Delta H_f(\text{solid})$, 6.1 kcal/mole. The relatively poor results for solid heats of formation are somewhat misleading, since some of the experimental data are clearly unreliable. For each of seven compounds, several $\Delta H_f(\text{solid})$ differing by more than 6 kcal/mole have been reported [27]; for 2,4,6-trinitroresorcinol, they range from -103.5 to -129.76 kcal/mole, for 1,3,5-triamino-2,4,6-trinitrobenzene (TATB), from -17.854 to -36.9 kcal/mole. These ambiguities in the literature motivated us to estimate the heats of formation of six of these compounds, all nitroaromatics, via homodesmotic reactions at the B3PW91/6-31G** computational level [64]. This work is described in detail in section 3.2. The results clearly support certain of the experimental $\Delta H_f(\text{solid})$, and not others. When the latter are not used in calculating Rice *et al*'s average absolute deviation for $\Delta H_f(\text{solid})$, it decreases from 6.1 to 5.5 kcal/mole.

6. SUMMARY AND CONCLUSIONS

With the continuing improvements in computer technology, it can be anticipated that accurate Gn and CBS calculations of ΔH_f from (non-arbitrary) formation and atomization processes, will be feasible for molecules of increasing size. It should be noted, however, that even with these techniques, better results are sometimes obtained by means of isodesmotic reactions [65,119,120].

For molecules of energetic interest that are too large for Gn or CBS methodology, the two density functional/empirical procedures discussed in section 5.2 are good options, although they do occasionally produce relatively large errors. Appropriate homodesmotic reactions, if possible, can be a useful alternative, or better yet, serve as a check, provided that the required experimental $\Delta H_f(\text{gas})$ are known with sufficient accuracy. We suggest that the B3PW91 technique be utilized.

The two density functional/empirical methodologies are based on, respectively, B3P86 and B3LYP computations. In view of our [64] and others' [65,66] success with B3PW91, and the fact that the PW91 correlation correction was the one used in parametrizing the B3 hybrid functional [52], it seems reasonable to develop a new, B3PW91 density functional/empirical approach to heats of formation. We are in the process of doing so.

ACKNOWLEDGEMENT

We greatly appreciate the financial support of the Office of Naval Research, Contract No. N00014-99-1-0393, Project Officer Dr. Judah M. Goldwasser.

REFERENCES

- [1] M. J. Kamlet and S. J. Jacobs, *J. Chem. Phys.*, 48 (1968) 23.
- [2] P. Politzer, J. S. Murray, M. E. Grice and P. Sjöberg, in: G. A. Olah and D. R. Squire (eds.), *Chemistry of Energetic Materials*, Academic Press, New York, 1991, ch. 4.
- [3] J. Kohler and R. Meyer, *Explosives*, 4th ed., VCH, Weinheim (Germany), 1993.
- [4] C. L. Mader, *Numerical Modeling of Explosives and Propellants*, 2nd ed., CRC Press, New York, 1998.
- [5] C. J. Wu and L. E. Fried, *Proc. Symp. Detonation*, 6 (2000) 490.
- [6] B. M. Rice and J. J. Hare, *J. Phys. Chem. A*, 106 (2002) 1770.
- [7] K. B. Wiberg, in: J. F. Liebman and A. Greenberg (eds.), *Molecular Structure and Energetics*, Vol. 2, Physical Measurements, VCH, New York, 1987, ch. 4.
- [8] H. Y. Afeefy and J. F. Liebman, in: K. K. Irikura and D. J. Frurip (eds.), *Computational Thermochemistry*, ACS Symposium Series 677, American Chemical Society, Washington, 1998, ch. 5.
- [9] K. K. Irikura and D. J. Frurip, in: K. K. Irikura and D. J. Frurip (eds.), *Computational Thermochemistry*, ACS Symposium Series 677, American Chemical Society, Washington, 1998, ch. 1.
- [10] W. Thiel, in: K. K. Irikura and D. J. Frurip (eds.), *Computational Thermochemistry*, ACS Symposium Series 677, American Chemical Society, Washington, 1998, ch. 8.
- [11] C. Chen and J. C. Wu, *Comput. Chem.*, 25 (2001) 117.
- [12] P. C. Chen, J. C. Wu and S. C. Chen, *Comput. Chem.* 25 (2001) 439.
- [13] J. S. Murray and P. Politzer, in: J. S. Murray and P. Politzer (eds.), *Quantitative Treatments of Solute/Solvent Interactions*, Elsevier, Amsterdam, 1994, ch. 8.
- [14] P. Politzer, J. S. Murray, M. E. Grice, M. DeSalvo and E. Miller, *Mol. Phys.*, 91 (1997) 923.
- [15] W. J. Hehre, L. Radom, P. v. R. Schleyer and J. A. Pople, *Ab Initio Molecular Orbital Theory*, Wiley-Interscience, New York, 1986.
- [16] A. P. Scott and L. Radom, *J. Phys. Chem.*, 100 (1996) 16502.

- [17] M. R. Ibrahim and Z. A. Fataftah, *Chem. Phys. Lett.*, 125 (1986) 149.
- [18] M. E. Grice and P. Politzer, *Chem. Phys. Lett.*, 244 (1995) 295.
- [19] H. B. Schlegel and A. Skancke, *J. Am. Chem. Soc.*, 115 (1993) 7465.
- [20] W. J. Hehre, R. Ditchfield, L. Radom and J. A. Pople, *J. Am. Chem. Soc.*, 92 (1970) 4796.
- [21] P. George, M. Trachtman, A. M. Brett and C. W. Bock, *J. Chem. Soc., Perkin Trans. 2*, (1977) 1036.
- [22] G. A. Petersson, D. K. Malick, W. G. Wilson, J. W. Ochterski, J. A. Montgomery, Jr. and M. J. Frisch, *J. Chem. Phys.*, 109 (1998) 10570.
- [23] I. Fishtik, R. Datta and J. F. Liebman, *J. Phys. Chem. A*, 107 (2003) 695.
- [24] K. L. Bak, P. Jorgensen, J. Olsen, T. Helgaker and W. Klopper, *J. Chem. Phys.*, 112 (2000) 9229.
- [25] R. L. Disch, J. M. Schulman and M. L. Sabio, *J. Am. Chem. Soc.*, 107 (1985) 1904.
- [26] M. Sana, G. Leroy, D. Peeters and C. Wilante, *J. Mol. Struct. (Theochem)*, 164 (1988) 249.
- [27] W. G. Mallard and P. J. Linstrom (eds.), *NIST Chemistry Webbook, NIST Standard Reference Database No. 69*, NIST, Gaithersburg, MD, 1998 (<http://webbook.nist.gov>).
- [28] J. M. Schulman and R. L. Disch, *J. Am. Chem. Soc.*, 106 (1984) 1202.
- [29] T. H. Dunning, Jr., *J. Phys. Chem. A*, 104 (2000) 9062.
- [30] M. L. Leininger, W. D. Allen, H. F. Schaefer III and C. D. Sherrill, *J. Chem. Phys.*, 112 (2000) 9213.
- [31] J. Noga, P. Valiron and W. Klopper, *J. Chem. Phys.*, 115 (2001) 2022.
- [32] N. L. Haworth and G. B. Bacskay, *J. Chem. Phys.*, 117 (2002) 11175.
- [33] D. Feller, K. A. Peterson, W. A. de Jong and D. A. Dixon, *J. Chem. Phys.*, 118 (2003) 3510, and references cited.
- [34] K. K. Irikura, *J. Phys. Chem. A*, 106 (2002) 9910.
- [35] J. A. Pople, M. Head-Gordon, D. J. Fox, K. Raghavachari and L. A. Curtiss, *J. Chem. Phys.*, 90 (1989) 5622.
- [36] L. A. Curtiss, K. Raghavachari, P. C. Redfern and J. A. Pople, *J. Chem. Phys.*, 112 (2000) 1125, and references cited.
- [37] G. A. Petersson, A. Bennett, T. G. Tensfeldt, M. A. Al-Laham, W. A. Shirley and J. Mantzaris, *J. Chem. Phys.*, 89 (1988) 2193.
- [38] J. A. Montgomery, Jr., M. J. Frisch, J. W. Ochterski and G. A. Petersson, *J. Chem. Phys.*, 112 (2000) 6532, and references cited.
- [39] A. G. Baboul, L. A. Curtiss, P. C. Redfern and K. Raghavachari, *J. Chem. Phys.*, 110 (1999) 7650.

- [40] J. A. Montgomery, Jr., M. J. Frisch, J. W. Ochterski and G. A. Petersson, *J. Chem. Phys.*, 110 (1999) 2822.
- [41] G. N. Merrill and M. S. Gordon, *J. Chem. Phys.*, 110 (1999) 6154.
- [42] L. A. Curtiss, K. Raghavachari, P. C. Redfern and J. A. Pople, *J. Chem. Phys.*, 112 (2000) 7374.
- [43] L. A. Curtiss, P. C. Redfern, K. Raghavachari and J. A. Pople, *J. Chem. Phys.*, 114 (2001) 108.
- [44] L. A. Curtiss, P. C. Redfern, V. Rassolov, G. Kedziora and J. A. Pople, *J. Chem. Phys.*, 114 (2001) 9287.
- [45] J. K. Labanowski and J. W. Andzelm (eds.), *Density Functional Methods in Chemistry*, Springer, New York, 1991.
- [46] T. Ziegler, *Chem. Rev.*, 91 (1991) 651.
- [47] P. Politzer and J. M. Seminario, *Trends Phys. Chem.*, 3 (1992) 175.
- [48] J. M. Seminario and P. Politzer (eds.), *Modern Density Functional Theory*, Elsevier, Amsterdam, 1995.
- [49] R. G. Parr, *Annu. Rev. Phys. Chem.*, 46 (1995) 701.
- [50] J. M. Seminario (ed.), *Recent Developments and Applications of Modern Density Functional Theory*, Elsevier, Amsterdam, 1996.
- [51] M. Springborg (ed.), *Density-Functional Methods in Chemistry and Materials Science*, Wiley, New York, 1997.
- [52] A. D. Becke, *J. Chem. Phys.*, 98 (1993) 5648.
- [53] A. D. Becke, *Phys. Rev. A*, 38 (1988) 3098.
- [54] C. Lee, W. Yang and R. G. Parr, *Phys. Rev. B*, 37 (1988) 785.
- [55] J. P. Perdew, *Phys. Rev. B*, 33 (1986) 8822.
- [56] J. P. Perdew, J. A. Chevary, S. H. Vosko, K. A. Jackson, M. R. Pederson, D. J. Singh and C. Fiolhais, *Phys. Rev. B*, 46 (1992) 6671.
- [57] H. L. Schmider and A. D. Becke, *J. Chem. Phys.*, 109 (1998) 8188.
- [58] K. Raghavachari, B. B. Stefanov and L. A. Curtiss, *Mol. Phys.*, 91 (1997) 555.
- [59] L. A. Curtiss, K. Raghavachari, P. C. Redfern and J. A. Pople, *J. Chem. Phys.*, 106 (1997) 1063.
- [60] P. C. Redfern, J.-P. Blaudeau and L. A. Curtiss, *J. Phys. Chem. A*, 101 (1997) 8701.
- [61] Z. X. Chen, J. M. Xiao, H. M. Xiao and Y. N. Chiu, *J. Phys. Chem. A*, 103 (1999) 8062.
- [62] O. Mo, M. Yanez, M. V. Roux, P. Jimenez, J. Z. Davalos, M. A. V. Ribeiro da Silva, M. Das Dores M. C. Ribeiro da Silva, M. Agostinha R. Matos, L. M. P. F. Amaral, A. Sanchez-Migallon, P. Cabildo, R. Claramunt, J. Elguero and J. F. Liebman, *J. Phys. Chem. A*, 103 (1999) 9336.
- [63] O. Mo, M. Yanez, J. Elguero, M. V. Roux, P. Jimenez, J. Z. Davalos, M. A. V. Ribeiro da Silva, M. das Dores M. C. Ribeiro da Silva, P. Cabildo and R. Claramunt, *J. Phys. Chem. A*, 107 (2003) 366.

- [64] P. Politzer, P. Lane and M. C. Concha, *Struct. Chem.*, in press.
- [65] J. E. Sicre and C. J. Cobos, *J. Mol. Struct. (Theochem)*, 620 (2003) 215.
- [66] O. N. Ventura, M. Kieninger and P. A. Denis, *J. Phys. Chem. A*, 107 (2003) 518.
- [67] C. W. Bauschlicher, Jr. and H. Partridge, *Chem. Phys. Lett.*, 231 (1994) 277.
- [68] E. J. Thomas III, J. S. Murray, C. J. O'Connor and P. Politzer, *J. Mol. Struct. (Theochem)*, 487 (1999) 177.
- [69] F. Abu-Awwad and P. Politzer, *J. Comp. Chem.*, 21 (2000) 227.
- [70] C. J. Barden, J. C. Rienstra-Kiracofe and H. F. Schaefer III, *J. Chem. Phys.*, 113 (2000) 690.
- [71] P. Politzer, P. Lane, E. J. Thomas III, F. Abu-Awwad and C. J. O'Connor, *Recent Res. Devel. Quantum Chem.*, 2 (2001) 41.
- [72] K. B. Wiberg, *J. Comp. Chem.*, 5 (1984) 197.
- [73] M. J. S. Dewar and D. M. Storch, *J. Am. Chem. Soc.*, 107 (1985) 3898.
- [74] M. R. Ibrahim and P. v. R. Schleyer, *J. Comp. Chem.*, 6 (1985) 157.
- [75] Z. Yala, *J. Mol. Struct. (Theochem)*, 207 (1990) 217.
- [76] E. A. Castro, *J. Mol. Struct. (Theochem)*, 304 (1994) 93.
- [77] J. Cioslowski, G. Liu and P. Piskorz, *J. Phys. Chem. A*, 102 (1998) 9890.
- [78] S. J. Mole, X. Zhou and R. Liu, *J. Phys. Chem.*, 100 (1996) 14665.
- [79] J. Cioslowski, M. Schimeczek, G. Liu and V. Stoyanov, *J. Chem. Phys.*, 113 (2000) 9377.
- [80] J. P. Guthrie, *J. Phys. Chem. A*, 105 (2001) 9196.
- [81] P. Ho, M. E. Coltrin, J. S. Binkley and C. F. Melius, *J. Phys. Chem.*, 89 (1985) 4647; 90 (1986) 3399.
- [82] A. Fortunelli and M. Selmi, *J. Mol. Struct. (Theochem)*, 337 (1995) 25.
- [83] D. Habibollahzadeh, M. E. Grice, M. C. Concha, J. S. Murray and P. Politzer, *J. Comp. Chem.*, 16 (1995) 654.
- [84] P. Politzer, M. E. Grice and J. S. Murray, *Recent Res. Devel. Phys. Chem.*, 3 (1999) 95.
- [85] B. M. Rice, S. V. Pai and J. Hare, *Combust. Flame*, 118 (1999) 445.
- [86] M. R. Zachariah and C. F. Melius, in: K. K. Irikura and D. J. Frurip (eds.), *Computational Thermochemistry*, ACS Symposium Series 677, American Chemical Society, Washington, 1998, ch. 9, and references cited.
- [87] C. F. Melius, in: S. N. Bulusu (ed.), *Chemistry and Physics of Energetic Materials*, Kluwer, Dordrecht (The Netherlands), 1990, chpts. 3, 4.

- [88] J. S. Murray and P. Politzer, *J. Mol. Struct. (Theochem)*, 425 (1998) 107.
- [89] P. Politzer and J. S. Murray, *Trends Chem. Phys.*, 7 (1999) 157.
- [90] R. F. W. Bader, M. T. Carroll, J. R. Cheeseman and C. Chang, *J. Am. Chem. Soc.*, 109 (1987) 7968.
- [91] D. R. Lide (ed.), *Handbook of Chemistry and Physics*, 78th ed., CRC Press, New York, 1997.
- [92] P. Politzer and J. S. Murray, *J. Phys. Chem. A*, 102 (1998) 1018.
- [93] P. Politzer, P. Lane and M. C. Concha, *J. Phys. Chem. A*, 103 (1999) 1419.
- [94] P. Politzer, M. C. Concha and P. Lane, *J. Mol. Struct. (Theochem)*, 529 (2000) 41.
- [95] P. Politzer, P. Lane and M. C. Concha, *Proc. 36th JANNAF Combust. Subcomm. Mtg.*, Vol. II, CPIA Publ. 691, 2000, p. 331.
- [96] P. Politzer, P. Lane and M. Concha, *Recent Res. Devel. Phys. Chem.* 4 (2000) 319.
- [97] P. Politzer, P. Lane and M. E. Grice, *J. Phys. Chem. A*, 105 (2001) 7473.
- [98] M. J. Frisch, G. W. Trucks, H. B. Schlegel, G. E. Scuseria, M. A. Robb, J. R. Cheeseman, V. G. Zakrzewski, J. A. Montgomery, R. E. Stratmann, J. C. Burant, S. Dappich, J. M. Millam, A. D. Daniels, K. N. Kudin, M. C. Strain, O. Farkas, J. Tomasi, V. Barone, M. Cossi, R. Cammi, B. Mennucci, C. Pomelli, C. Adamo, S. Clifford, J. Ochterski, G. Petersson, P. Y. Aayala, Q. Cui, K. Morokuma, D. K. Malick, A. D. Rubuck, K. Raghavachari, J. B. Foresman, J. Cioslowski, J. V. Ortiz, B. B. Stefanov, G. Liu, A. Liashenko, P. Piskorz, I. Komaromi, R. Gomperts, R. L. Martin, D. J. Fox, T. Keith, M. A. Al-Laham, C. Y. Peng, A. Nanayakkara, C. Gonzalez, M. Challacombe, P. M. W. Gill, B. G. Johnson, W. Chen, M. W. Wong, J. L. Andres, M. Head-Gordon, E. S. Replogle and J. A. Pople, *Gaussian 98, Revision A.5*, Gaussian, Inc.: Pittsburgh, PA, 1998.
- [99] P. Politzer, P. Lane, M. E. Grice, M. C. Concha and P. C. Redfern, *J. Mol. Struct. (Theochem)*, 338 (1995) 249.
- [100] P. Politzer, J. S. Murray and M. E. Grice, *Mater. Res. Soc. Symp. Proc.*, 418 (1996) 55.
- [101] P. Politzer, J. M. Seminario and M. C. Concha, *J. Mol. Struct. (Theochem)*, 427 (1998) 123.
- [102] P. Politzer, P. Lane, P. Sjöberg, M. E. Grice and H. Shechter, *Struct. Chem.*, 6 (1995) 217.
- [103] M. E. Grice and P. Politzer, *J. Mol. Struct. (Theochem)*, 358 (1995) 63.

- [104] P. Politzer, M. C. Concha, M. E. Grice, J. S. Murray, P. Lane and D. Habibollahzadeh, *J. Mol. Struct. (Theochem)*, 452 (1998) 75.
- [105] P. Politzer and P. Lane, *Adv. Mol. Struct. Res.*, 3 (1997) 269.
- [106] P. Politzer, P. Lane and J. J. M. Wiener, in: K. K. Laali (ed.), *Carbocyclic and Heterocyclic Cage Compounds and Their Building Blocks*, JAI Press, Stamford, CT, 1999, p. 73.
- [107] P. Politzer, J. S. Murray, M. E. Grice and T. Brinck, *J. Energ. Mater.*, 18 (2000) 89.
- [108] R. S. Miller, *Mater. Res. Soc. Symp. Proc.*, 418 (1996) 3.
- [109] W. Zhou, R. A. Yetter, F. L. Dryer, H. Rabitz, R. C. Brown and C. E. Kolb, *Combust. Flame*, 112 (1998) 507.
- [110] D. P. Belyung, G. T. Dalakos, J.-D. R. Rocha and A. Fontijn, *Twenty-Seventh Symposium (International) on Combustion*, vol. 1, The Combustion Institute, Pittsburgh, 1998, p. 227.
- [111] P. Politzer and M. E. Grice, *J. Chem. Res.*, (1995) 296.
- [112] P. Politzer, P. Lane and M. E. Grice, *J. Mol. Struct. (Theochem)*, 365 (1996) 89.
- [113] P. Politzer and P. Lane, *J. Mol. Struct. (Theochem)*, 388 (1996) 51.
- [114] P. Politzer, J. S. Murray, J. M. Seminario, P. Lane, M. E. Grice and M. C. Concha, *J. Mol. Struct. (Theochem)*, 573 (2001) 1.
- [115] G. Leroy, M. Sana, C. Wilante, D. Peeters and S. Bourasseau, *J. Mol. Struct. (Theochem)*, 187 (1989) 251.
- [116] M.-X. Zhang, P. E. Eaton and R. Gilardi, *Angew. Chem. Int. Ed.*, 39 (2000) 401.
- [117] P. E. Eaton, R. L. Gilardi and M.-X. Zhang, *Adv. Mater.*, 12 (2000) 1143.
- [118] J. S. Murray, J. M. Seminario and P. Politzer, *Struct. Chem.*, 2 (1991) 153.
- [119] R. J. Berry, D. R. F. Burgess, Jr., M. R. Nyden, M. R. Zachariah and M. Schwartz, *J. Phys. Chem.*, 99 (1995) 17145.
- [120] L. A. Curtiss, K. Raghavachari, P. C. Redfern and B. B. Stefanov, *J. Chem. Phys.*, 108 (1998) 692.

This Page Intentionally Left Blank

Chapter 10

Thermodynamic and mechanical properties of HMX from atomistic simulations

Dmitry Bedrov^a, Grant D. Smith^{a,b}, and Thomas D. Sewell^c

^aDepartment of Materials Science and Engineering, University of Utah,
122 S. Central Campus Drive, EMRO 304, Salt Lake City, Utah 84112, USA

^bDepartment of Chemical and Fuels Engineering, University of Utah,
50 S. Central Campus Drive, MEB 3290, Salt Lake City, Utah 84112, USA

^cTheoretical Division, Detonation Theory and Application Group, Mail Stop B-214, Los Alamos National Laboratory, Los Alamos, NM 87545, USA

1. INTRODUCTION

Mesomechanics simulations, in which microstructure in a heterogeneous material is spatially resolved within a continuum hydrodynamic computational framework, are increasingly used to understand the physical response of plastic-bonded high explosives (PBXs) under various loading scenarios, *e.g.*, thermal localization (hot spots) under weak shock stimuli [1,2]. The goal of such studies is to identify and characterize the essential dissipative processes that must be captured in order to provide reliable, physically-based subgrid physics models for use in predictive, macroscale engineering codes. The development and parameterization of mesomechanical models for high explosives presents a significant challenge, given the expense and practical difficulties with measurements of explosive properties for many thermodynamic conditions of interest.

The high explosive octahydro-1,3,5,7-tetranitro-1,3,5,7-tetrazocine (HMX, Fig. 1) is the energetic material in a number of high performance military explosive and propellant formulations [3]. HMX exhibits three crystal polymorphs at ambient pressure denoted β - [4,5], α - [6], and δ -HMX [7] and listed in terms of stability with increasing temperature. At temperature $T \sim 550$ K the crystalline structure become unstable and HMX begins to melt. The liquid phase of HMX is very unstable and therefore no direct measurements of

thermophysical properties of liquid HMX have been conducted. Nevertheless, melt properties as well as mechanical and thermodynamic properties of crystalline HMX are believed to be crucial for a complete modeling of HMX decomposition under external stimuli, for example, rapid heating due to accidental fire [8].

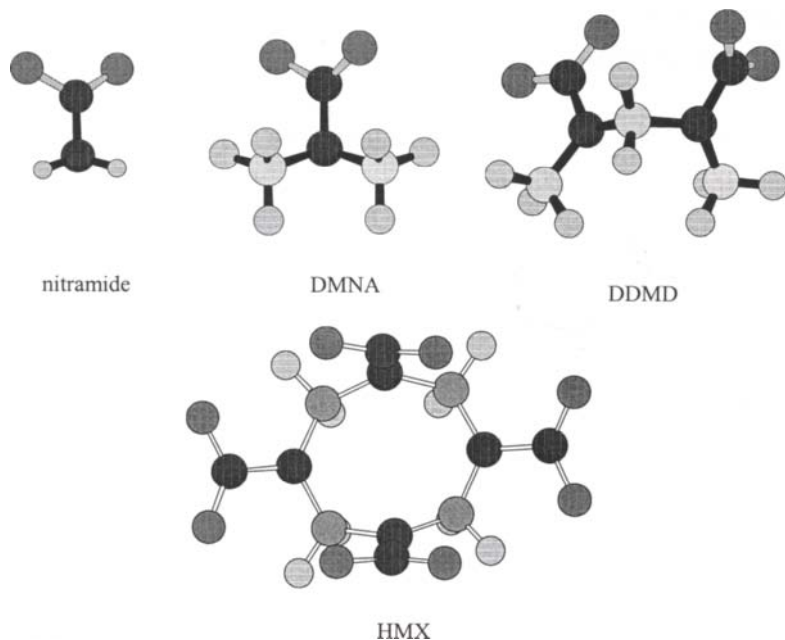


Fig. 1. Molecular structure of several nitramine compounds discussed in this chapter.

We think that judicious application of molecular simulation tools for the calculation of thermophysical and mechanical properties is a viable strategy for obtaining some of the information required as input to mesoscale equations of state. Given a validated potential-energy surface, simulations can serve as a complement to experimental data by extending intervals in pressure and temperature for which information is available. Furthermore, in many cases, simulations provide the only realistic means to obtain key properties; *e.g.*, for explosives that decompose upon melting, measurement of liquid-state properties is extremely difficult, if not impossible, due to extremely fast reaction rates, which nevertheless correspond to time scales that must be resolved in mesoscale simulations of explosive shock initiation. By contrast, molecular dynamics simulations can provide converged values for those properties on time scales below the chemical reaction induction times. Finally,

since computational protocols can be designed to mimic experiments, simulations can be used to interpret discrepancies between experimental results, or to determine which among competing analysis methods is most appropriate.

In this chapter we focus on atomistic predictions of thermophysical and mechanical properties of HMX crystals and liquid important to the development of reliable mesoscale equations of state. The outline of the remainder of the chapter is as follows: In section 2 we describe briefly the philosophy and overall approach we have taken to force field development, including the results of quantum chemistry calculations for HMX and smaller model compounds that were used in the force field parameterization. The focus of section 3 is on the properties of liquid HMX, for which experimental data are completely lacking. Structural, thermal, and mechanical properties of the three pure crystal polymorphs of HMX are presented in section 4, where the results are compared to the available experimental data. At the ends of sections 3 and 4 we discuss briefly the importance of the various properties with mesoscale models of high explosives, with an emphasis on conditions relevant to weak shock initiation. We conclude in section 5, and provide our opinions (and justifications, based on our interactions with mesoscale modelers) regarding which HMX properties and phenomena should comprise the next targets for study via atomistic simulation.

2. FORCE FIELD

2.1 General philosophy

It is now generally accepted that, given a sufficiently accurate classical force field, molecular dynamics (MD) simulations are capable of predicting thermophysical, structural, dynamical and mechanical properties in quantitative agreement with experiment for a wide variety of materials, including liquids and their mixtures [9-12], polymer melts [13-18], polymer solutions [19-21], polymer electrolytes [22-24] and liquid electrolyte solutions [25].

Over the last decade we have successfully applied quantum chemistry (QC) calculations to model compounds containing from several to a few dozen atoms to obtain optimized geometries, conformational energetics and dimer binding energies. These were subsequently used to parameterize atomistic potential functions (or force fields) for use in classical molecular dynamics (MD) simulations of polymer-containing materials, including polymer melts [26-30], polymer and ionic solutions [31,32] and polymer electrolytes [33]. We found that, when a systematic investigation of the influence of level of theory and basis sets is conducted, MD simulations performed using force fields fitted to reproduce accurate, sufficiently converged QC data are usually in excellent

agreement with experiments, without the need for additional empirical adjustments. Our QC calculations are usually performed for isolated gas-phase molecules or small clusters; thus, one might question their applicability to force fields intended for use in studies of condensed-phase systems. However, our extensive comparison between results of MD simulations using the QC-based force fields and corresponding experimental data [9-25] indicate that this is not the case. Moreover, it appears that the QC-based force fields usually have a correct “balance” between various types of interactions, leading to improved overall predictive capability compared to force fields that were adjusted empirically to reproduce a particular set of experimental data (e.g., densities and heats of vaporization/sublimation).

2.2 Quantum chemistry

We have adopted a strategy similar to that used in our development of polymer force fields in parameterization of an atomistic potential function for HMX. Specifically, we have undertaken a systematic investigation of conformational and intermolecular binding energies in model nitramine compounds (i.e., those containing the C_2N-NO_2 moiety) using high-level QC calculations. In the case of HMX, a QC-based force field is the only realistic option due to insufficient spectroscopic data that would facilitate force field parameterization.

The relatively large size of the HMX molecule (20 heavy atoms) makes it impractical to perform a thorough investigation of the influence of level of theory and basis set employed on the results of QC calculations. To resolve these issues we considered smaller and hence computationally less demanding nitramine compounds, including nitramide [34], dimethylnitramine [34] (DMNA) and 1,3-dimethyl-1,3-dinitro methyldiamine (DDMD) [35] (see Fig 1). Despite their relatively small size and simple structure, the nitramide and DMNA molecules possess important features such as inversion about the amine nitrogen and conformational flexibility for rotation of the nitro group around the N-N bond which are typical for all nitramines including HMX. Moreover, for nitramide there is an experimental estimate of the inversion barrier available; this provides a good validation point for determining what level of theory and basis set is required in the QC calculations to reproduce properties for geometries away from equilibrium. Based upon our systematic study of the influence of basis set and electron correlation on molecular geometries, nitro group rotational energies, and inversion energies about the amine nitrogen for nitramide and DMNA, we concluded that geometry optimizations at the B3LYP/6-311G** level and subsequent single point energy calculations at the MP2/6-311G** level are sufficient to obtain accurate conformational energies and geometries in nitramine compounds. We also found that while the barrier

for rotation of the nitro group is large (around 10 kcal/mol), the amine nitrogen inversion barrier is less than 1 kcal/mol.

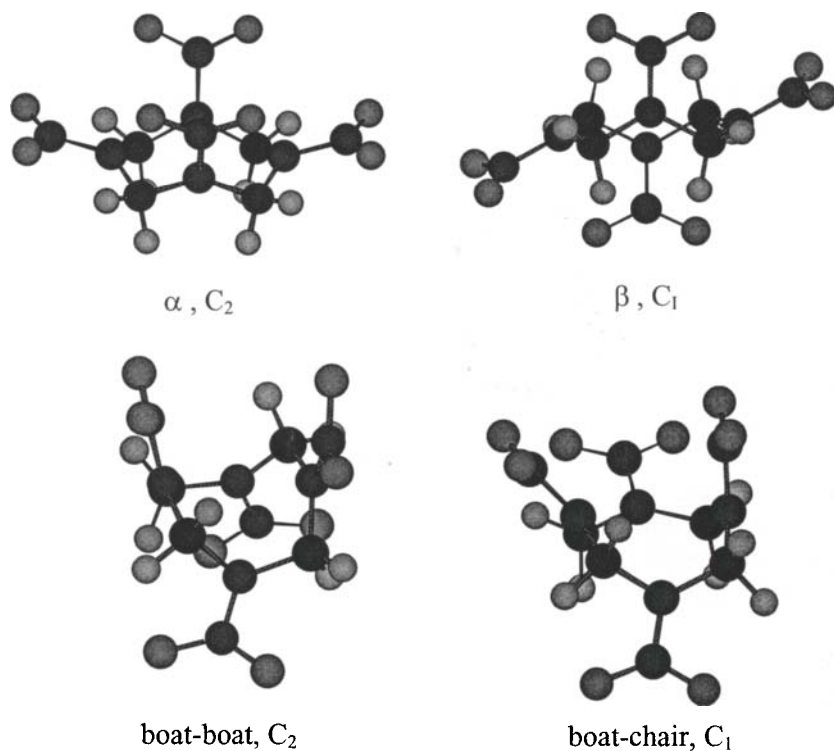


Fig. 2. Geometries of the low-energy HMX conformers.

Having determined an adequate level of theory based on QC calculations for nitramide and DMNA, we focused on the conformational energetics for HMX and DDMD molecules. The low energy conformers of HMX determined at the B3LYP/6-311G** level are illustrated in Fig. 2, and the ring dihedral angles and out-of-plane bending angles at the amine nitrogen are tabulated in Table 1. The relative conformer energies, determined at the B3LYP/6-311G**//MP2/6-311G** geometry/energy level, are also tabulated in Table 1. The " α " conformer, with C_2 symmetry, corresponds to the geometry found in the α polymorph of crystalline HMX, and is quite similar to the HMX conformations in γ and δ forms; whereas the " β " conformer with C_1 symmetry

corresponds to the geometry in β -HMX. In addition to these conformers, we found two low-energy conformations of HMX not seen in the crystalline phases. The global minimum boat-chair (BC) conformer has C_1 symmetry, while the boat-boat (BB) conformer has C_2 symmetry. Comparison of the ring conformations and out-of-plane bending angles for the α and β conformers obtained from B3LYP/6-311G** optimization with experimentally determined geometries for the molecules in the respective crystal polymorphs reveals good agreement, as shown in Table 1. This agreement supports our contention that the B3LYP/6-311G** level of theory is adequate for geometry optimizations in nitramine compounds. The agreement also indicates that the molecular geometries of HMX in the crystalline polymorphs are not greatly distorted from the optimized gas-phase geometries, i.e., that condensed-phase effects in the crystalline phase do not strongly perturb the conformational geometry of HMX. However, the fact that the lowest energy gas-phase conformers (boat-boat and boat-chair) are not found in the crystal phases indicates that intermolecular interactions do play some role in determining the conformations of molecules in the stable crystalline structures.

DDMD, illustrated in Fig. 3, is the ideal model compound for studying the rotational energetics of the C-N—C-N dihedrals that form the cyclic structure of HMX: both the conformer energies and geometries as well as the energies and geometries of the rotational energy barriers can be more readily determined from QC calculations for this smaller molecule than for the computationally demanding HMX molecule. The low energy conformers and saddle points (rotational energy barriers) for DDMD are summarized in Table 2 and are illustrated in Fig. 3. Fig. 4 is a plot of ϕ_2 vs. ϕ_1 for the C-N—C—N-C dihedral pairs (denoted in Fig. 3) for the DDMD conformers and rotational energy barriers as well as for the α , β and BC and BB conformers of HMX (denoted in Fig. 2) obtained at the B3LYP/6-311G** level. It can be seen that dihedral pair conformations similar to the lowest energy DDMD conformer (Min-1) are found only in the lowest energy HMX conformers, BC and BB. These conformations are not seen in crystalline HMX (see discussion above). Conformations resembling those found in the higher energy DDMD minima (Min-2 and Min-3) are found in each of the HMX conformers except BB. Table 2 shows the energy of DDMD constrained to the conformation (as determined from quantum chemistry) of representative torsional pairs in both α and β HMX. The resulting DDMD energies are quite similar to those of the Min-2 and Min-3 conformers of DDMD.

Table 1.

HMX conformer energies and geometries

con	source	Energy	ring dihedral angles								out-of-plane angles			
		kcal/mol	ϕ_1	ϕ_2	ϕ_3	ϕ_4	ϕ_5	ϕ_6	ϕ_7	ϕ_8	δ_1	δ_2	δ_3	δ_4
α	exp ^a	--- ^b	-105.5	99.4	-63.8	69.5	-105.0	100.7	-64.7	68.2	12.3	3.6	13.4	3.2
α	q.c. ^c	4.3 (2.9)	-94.9	94.9	-70.3	70.3	-94.9	94.9	-70.3	70.3	19.2	4.1	19.2	4.1
α	f.f. ^d	3.2	-98.6	109.1	-69.4	61.9	-97.6	96.2	-58.0	58.3	17.9	9.4	7.2	1.2
β	exp ^e	---	-18.1	-43.4	117.1	-101.6	18.1	43.4	-117.2	101.7	8.5	21.3	8.5	21.3
β	q.c.	0.8 (0.8)	-20.6	-41.9	113.8	-100.9	20.6	41.9	-113.8	100.9	7.5	19.4	7.5	19.4
β	f.f.	0.6	-23.6	-48.9	116.7	-85.2	2.3	57.5	-102.0	92.0	4.1	18.2	2.1	5.7
BC	q.c.	0.0 (0.0)	63.6	-55.7	96.3	-56.3	-61.2	73.3	36.1	-98.5	21.5	1.8	18.5	14.0
BC	f.f.	0.0	58.1	-59.2	106.8	-59.4	-54.3	64.2	44.8	-100.2	8.1	2.5	5.8	18.0
BB	q.c.	0.5 (1.4)	-26.4	73.3	26.4	-73.3	-26.4	73.3	26.4	-73.3	10.0	10.0	10.0	10.0
BB	f.f.	-0.6	-40.5	71.4	36.6	-73.3	-32.3	67.6	36.5	-65.9	14.7	11.6	0.9	0.1

^aRef. [6]. ^bSingle molecule energies are not available. ^cQuantum chemistry MP2(B3LYP) energies. ^dForce field energies. ^eRef. [4].

Examination of Fig. 4 reveals that conformations of the C-N—C-N dihedrals in the low energy conformers of DDMD and HMX are restricted to $|\phi| \leq 120^\circ$. The trans conformation of the C-N—C-N dihedral leads to strong steric interference between a nitro oxygen atom and the amine nitrogen of the neighboring nitramine group. This interaction can be only partially relieved by out-of-plane distortion of the nitro group. Complete relief of the interaction would require significant rotation of the nitro group, which is energetically unfavorable. A consequence of the nitro oxygen-amine nitrogen steric interaction is that the barrier for rotation from Min-1 to Min-2 is significantly higher through Sad-2 than through Sad-5 (see Fig. 3 and Table 2). It can also be seen that all methylene centered dihedral pairs in the HMX conformers lie closer to the cis-cis origin of Fig. 4 than in the low energy conformers of DDMD. This is a consequence of conformational restrictions in the cyclic HMX molecule. However, the similarity between the energies obtained for the DDMD conformers constrained to α and β HMX dihedral angles and the fully relaxed Min-2 and Min-3 DDMD conformers indicate that the ring conformations of α and β HMX are not highly strained relative to the latter DDMD conformers. (It should be remembered that the Min-2 and Min-3 conformers of DDMD are already significantly higher in energy than the global Min-1 conformer).

Table 2.

Conformers and rotational energy barriers for DDMD

Conformer	B3LYP/6-311G** Geometry		Energy (kcal/mol)	
	ϕ_1	ϕ_2	BL3YP/6-311G**	MP2/6-311G**
Min-1	81.5 (70) ^a	104.3 (70)	0.00	0.00 (0.0)
Min-2	38.2 (45)	-126.5 (-96)	4.82	3.59 (2.9)
Min-3	58.9	-121.3	5.49	5.30
Sad-1	63.5	-88.5	6.28	5.66
Sad-2	85.7 (80)	153.6 (170)	9.46	8.61 (7.5)
Sad-3	88.9	88.9		0.54
Sad-4	68.6	-68.6	6.35	6.43
Sad-5	19.5 (-15)	-97.1 (-70)	6.06	6.12 (3.5)
α^b	70.3	-94.86	5.68	5.51 (2.9) ^c
β^b	113.8	-41.6	4.96	4.25 (3.3) ^c

^aNumbers in parentheses are from force field calculations discussed below. ^bTypical angles for a methylene centered dihedral pair for the respective HMX conformer from quantum chemistry geometries. ^cDihedral angles were constrained to the quantum chemistry values.

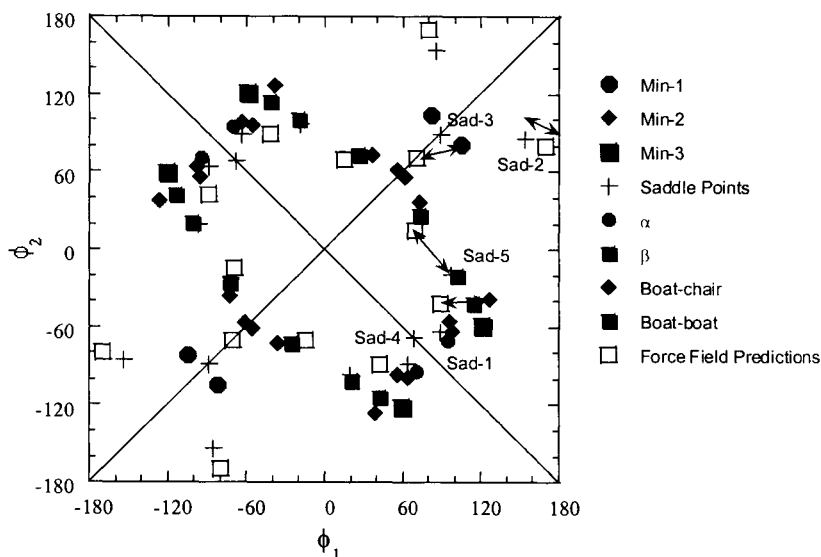


Fig. 4. Dihedral geometry of the low-energy conformers of DDMD and the rotational energy barriers between them. Also shown are the geometries for methylene-centered dihedral pairs in the low-energy conformers of HMX.

2.3 Force field parameterization and validation

Some of the previous potential functions for HMX [36,37] have considered rigid molecules, and hence have been concerned only with the intermolecular potential. While it is reasonable to assume that the rigid-molecule approach will be useful in predicting some static properties of crystalline HMX, we think that a reasonable representation of conformational flexibility is required in order to accurately predict liquid phase thermophysical and transport properties from atomistic simulations, and will be important for predicting static properties of crystalline HMX under compression, at elevated temperatures and during phase transitions. A requirement for our atomistic, fully flexible molecule force field is that it accurately reproduce the results of QC calculations on HMX and the model compounds identified above. Keeping this in mind we approached the task of fitting a potential function for HMX and other nitramine compounds which has a general form:

$$U = U^{bond} + U^{bend} + U^{torsion} + U^{out-of-plane} + U^{nonbonded} + U^{coulomb} \quad (1)$$

In the following we describe briefly the procedure for fitting force field parameters, and provide comparisons between force-field and QC predictions. A more detailed discussion of the force field parameterization can be found in Refs. [34] and [35].

Partial atomic charges. Partial atomic charges were determined for each of the low energy DDMD conformers, and for the α , β , and BC conformers of HMX, according to the following algorithm. The electrostatic potential at a grid of 30,000 to 70,000 points (depending upon the compound) lying within 4.0 Å of any atom but excluding points within the van der Waals radius of any atom was determined for each conformer from the MP2 wave functions. The set of partial atomic charges that best reproduced the electrostatic potential at the grid points, and the molecular dipole moment, was determined with the constraint that "like" atoms had equal charges. The charges, which were quite similar for each conformer, were averaged to obtain the average charges shown in Table 3. As can be seen in Table 4, the charges do a good job overall in reproducing the molecular dipole moments of each conformer, indicating that the charges are not strongly conformation dependent. The charges for DDMD are quite similar to those for HMX. For the purpose of investigating the accuracy of the potential function for DDMD, and for optimizing transferability of the potential function, the HMX charges were used in describing DDMD, with the methyl carbon charge set to be equal to the methylene carbon charge minus a hydrogen charge. These charges are also given in Table 3. In practice, the conformational energies of DDMD were found to be only weakly sensitive to which set of DDMD charges was employed.

Upon conducting MD simulations of liquid DMNA we found that, in order to reproduce adequately the thermodynamic properties of DMNA liquid, the partial atomic charges should be increased by 25% to account for strong polarization (induced dipolar) effects that have significant contributions in condensed phases (crystalline and liquid) due to relatively larger molecular dipole moments in nitramine compounds such as HMX, DMNA, and DDMD. In the simulations of crystalline and liquid phases (see below) we used these larger charges which are also reported in the right-most column of Table 3.

Table 3.

Partial atomic charges for HMX and DDMD

Atom	DDMD	DDMD(HMX)	HMX-gas	HMX-cond
C	-0.4166	----	----	----
C (methylene)	----	-0.4320	-0.4320	-0.540000
C (methyl)	----	-0.6480	----	----
N (amine)	0.1598	0.0451	0.0451	0.056375
N (nitro)	0.5601	0.6885	0.6881	0.860125

O	-0.3599	-0.3668	-0.3668	-0.458500
H	0.1562	0.2160	0.2160	0.270000

Table 4
Dipole moments of HMX and DDMD conformers

Conformer	Molecular Dipole Moment (Debye)	
	MP2/6-311G**	Force Field
DDMD Min-1	2.17	1.76
DDMD Min-2	6.41	6.77
DDMD Min-3	6.13	6.25
HMX α	8.41	8.78
HMX β	0.0	0.0
HMX BC	5.45	5.45

Nonbonded parameters. All dispersion interactions were modeled by an exponential-6 potential with parameters taken from previous work [38,39]. The parameters for carbon, hydrogen, and oxygen were taken from Sorensen et al [38]. The nonbonded parameters for nitrogen were determined so as to accurately reproduce the gas-phase second virial coefficient of trimethylamine as a function of temperature [39]. In calibrating the N-N potential, the potential parameters for C, H, and O were taken from previous work [38]. Standard combining rules were employed in describing interactions between different atom pairs except for C-H.

Valence parameters. The stretching force constants were obtained from normal-mode analysis of DMNA at the SCF/6-311G** level for the ground-state geometry. The force constants were scaled by 0.80 to account for deficiencies in the SCF force constants and anharmonic effects. The equilibrium bond lengths were determined so as to match the MP2/6-311G** ground state geometry of the DMNA molecule, with a slight increase to account for anharmonic effects. The bending force constants are consistent with the internal coordinate force constants obtained at the SCF/6-311G** level, except for the N-C-H and H-C-H, where constants were obtained from the MOLBD3 [40] database. The equilibrium angle parameters were adjusted to give the best representation of the ground state and inversion barrier geometries for DMNA and to reproduce the inversion energy in DMNA. The force field yields a value of 0.81 for the inversion barrier which is in good agreement with the quantum chemistry value of 0.89 kcal/mol. The bending parameters for the N-C-N bend were determined from the quantum chemistry geometry and force constants for DDMD.

Torsional potential function. The torsional parameters were adjusted to give the best representation of the methyl and nitro group rotation in DMNA.

The three-fold H-C-N-N function allows for exact reproduction of the methyl group rotational barrier of 1.63 kcal/mol. The ability of the force field to represent the nitro group rotation is illustrated in Fig. 5. Emphasis was placed on accurate representation of the conformational energy in the vicinity of the minima, which tend to be highly populated due to the very high barrier (11.50 kcal/mol from the force field vs. 10.58 kcal/mol from quantum chemistry). In addition, an improper torsion, or out-of-plane bending, function for the nitro group was parameterized to reproduce the distortion energy of the nitro group obtained from ab initio studies. The only additional potential parameters required to complete the description of HMX and DDMD are the torsional parameters for rotations about the C-N—C-N (or N-C—N-C) dihedrals. These were determined by obtaining the best representation of the quantum chemistry conformer energies and geometries for the α , β , boat-boat and boat-chair conformers of HMX while at the same time maintaining a reasonable description of the conformational energies and rotational energy barriers in DDMD.

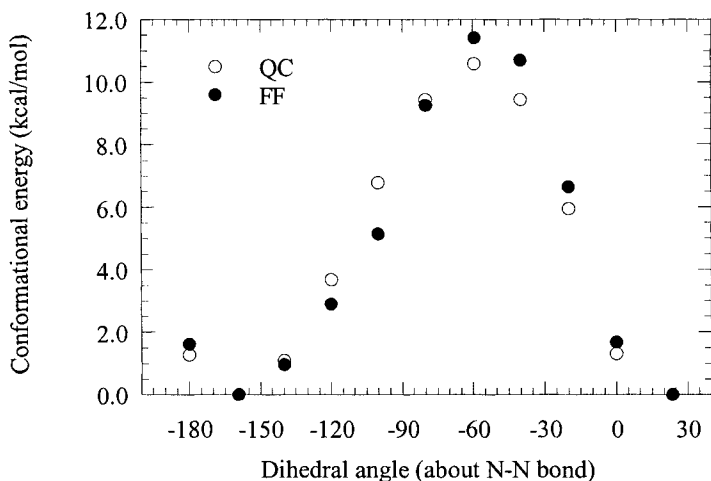


Fig. 5. Conformational energy of DMNA as a function of O-N-N-C dihedral, determined from QC and molecular mechanics using QC-based force field.

The force field energies and geometries for the low energy conformers of HMX are given in Table 1. The force field does a credible job in reproducing the quantum chemistry conformational energies and geometries for HMX. Relative to the global minimum boat-chair conformer, the force field accurately reproduces the energy of the β conformer while yielding an energy for the

α conformer which lies between the MP2 and B3LYP values. In contrast to quantum chemistry, the force field yields an energy for the boat-boat conformer that is lower than that of the boat-chair. For application of the force field to crystalline HMX it is important that the difference in energy between the α and β conformers is well represented. According to our quantum chemistry calculations, this difference is 3.5 ± 1.0 [41] kcal/mol at the MP2 level and 2.1 kcal/mol at the B3LYP level, while the force field yields 2.6 kcal/mol. If the ring dihedrals are constrained to the quantum chemistry values, the force field yields (relative to a fully relaxed boat-chair conformation) 4.9 kcal/mol and 1.6 kcal/mol, respectively, for the α and β conformers, with a corresponding energy difference of 3.3 kcal/mol.

The conformer energies and geometries for DDMD from the force field are given in Table 2 and illustrated in Fig. 4. The force field does a reasonable job in representing the geometries and energies of the Min-1 and Min-2 conformers as well as the high energy saddle point Sad-2. Min-1 is found to be a single minimum with C_2 symmetry as opposed to split minima separated by a low energy saddle point as predicted by quantum chemistry. No conformer corresponding to Min-3 exists on the DDMD conformational energy surface. The low energy saddle point (Sad-5) separating Min-1 and Min-2 is not as well represented by the force field, lying only 0.7 kcal/mol above the energy of Min-2 as opposed to 2.5 and 1.2 kcal/mol predicted by quantum chemistry at the MP2 and B3LYP levels, respectively.

Force field validation. In addition to ensuring that the force field reproduces results of QC calculations we have compared predictions of MD simulations using this force field with the available experimental data. Gas phase MD simulations using the quantum-chemistry based force field accurately reproduced the gas phase structure of DMNA as determined from electron diffraction studies. Liquid phase MD simulations of DMNA predicted the densities and solubility parameter as well as the activation energy and correlation times associated with molecular reorientation that are in good agreement with experimental data [34]. As we will show in Section 4, comparison to structural and thermal data for the three pure crystalline polymorphs of HMX support the overall validity of our formulation and parameterization.

3. SIMULATIONS OF LIQUID HMX

3.1. Viscosity and self-diffusion coefficient

Methodology. Equilibrium MD simulations were carried out at six different temperatures (550-800 K, at 50 K intervals) and atmospheric pressure.

Isothermal-isobaric (NpT) simulations were performed for 4.0 ns in order to establish the equilibrium density, using the final configuration from a higher-temperature equilibration as the starting point for the next lower temperature. Isothermal-isochoric (NVT) production runs of 10-30 ns duration (depending upon temperature) were performed using the Nose-Hoover thermostat [42] with an integration step size of 1.0 fs. Simulations were performed in the cubic cell with periodic boundary conditions. The standard Shake algorithm [43] was used to constrain bond lengths. The Ewald summation method [44] was employed to evaluate long-range electrostatic interactions. All simulation cells contained 50 HMX molecules.

Calculation and results. For each temperature we calculated the HMX molecular center-of-mass self-diffusion coefficient determined as:

$$D = \lim_{t \rightarrow \infty} \frac{\langle [R_{cm}(t) - R_{cm}(0)]^2 \rangle}{6t} \quad (2)$$

where $R_{cm}(t) - R_{cm}(0)$ is the time dependent center-of-mass displacement of a given molecule. Following Mondello and Grest [45] the shear viscosity was calculated using the Einstein relation:

$$\eta = \lim_{t \rightarrow \infty} \frac{V}{20k_B T t} \left\langle \sum_{\alpha} \sum_{\beta} [A_{\alpha\beta}(t) - A_{\alpha\beta}(0)]^2 \right\rangle = \lim_{t \rightarrow \infty} \frac{V}{20k_B T t} \left\langle \sum_{\alpha} \sum_{\beta} [\Delta A_{\alpha\beta}(t)]^2 \right\rangle \quad (3)$$

where

$$\Delta A_{\alpha\beta}(t) = \int_0^t P_{\alpha\beta}(t') dt' \quad (4)$$

and $(P_{\alpha\beta})$ is a stress tensor defined as:

$$P_{\alpha\beta} = (\sigma_{\alpha\beta} + \sigma_{\beta\alpha}) / 2 - \frac{\delta_{\alpha\beta}}{3} \left(\sum_{\gamma} \sigma_{\gamma\gamma} \right) \quad (5)$$

where $\delta_{\alpha\beta}$ is the Kronecker delta.

With the exception of 550 K, each trajectory was at least 45 times longer than the largest molecular relaxation time at a given temperature. The system at 550 K would have required upwards of 70 ns by these criteria, which is beyond the practical limits imposed by our computational resources. Therefore we stopped the simulations at this temperature after 20 ns, which was sufficient to

accurately calculate the self-diffusion coefficient. The atmospheric pressure, temperature dependent shear viscosity and self-diffusion coefficients for liquid HMX in the temperature interval $550 \text{ K} \leq T \leq 800 \text{ K}$ are summarized in Table 5. The shear viscosity is predicted to range from $0.0055 \text{ Pa}\cdot\text{s}$ at 800 K up to $0.45 \text{ Pa}\cdot\text{s}$ at 550 K .

Table 5.

Relaxation times and transport coefficients of liquid HMX obtained from MD simulations.

$T \text{ K}$	$\rho [\text{kg m}^{-3}]$	$\tau_R [\text{ps}]$	$\tau_D [\text{ps}]$	$D^*10^9 [\text{m}^2\text{s}^{-1}]$	$\eta [\text{Pa s}]$	$\lambda \times 10^4 [\text{cal cm}^{-1} \text{s}^{-1} \text{K}^{-1}]$
550	1650.9	310.0	1664	0.006	0.450	9.28
600	1614.4	70.0	675	0.018	0.120	7.51
650	1586.9	33.6	304	0.040	0.040	6.90
700	1554.5	20.7	129	0.094	0.022	6.24
750	1520.1	12.9	54	0.225	0.010	6.30
800	1488.2	9.5	37	0.325	0.0055	6.40

The temperature dependence of the shear viscosity and self-diffusion coefficients can be well described by Arrhenius expressions, as shown in Fig. 6. There is no evidence for the onset of non-Arrhenius behavior over the temperature interval considered, which extends down to near the melting point of HMX. The calculated apparent activation energies are 14.4 kcal/mol and 14.5 kcal/mol for self-diffusion and shear viscosity, respectively. The Eyring rate expression for dense fluids [46] indicates that the viscosity activation energy is proportional to the energy of vaporization. For more than one hundred substances including associated liquids the simple relation $(\Delta E_{vap} = n\Delta E_{vis})$, where $2 \leq n \leq 5$) holds [46]. Assuming that the energy of vaporization is approximately equal to the cohesive energy it is possible to compare ΔE_{vap} and ΔE_{vis} as determined directly from MD simulations. We obtain $\Delta E_{vap} = 36.3 \text{ kcal/mol}$ from simulation (800 K), yielding a ratio $\Delta E_{vap}/\Delta E_{vis} = 2.5$. The large value for the viscosity activation energy is consistent with the high energy of vaporization of HMX.

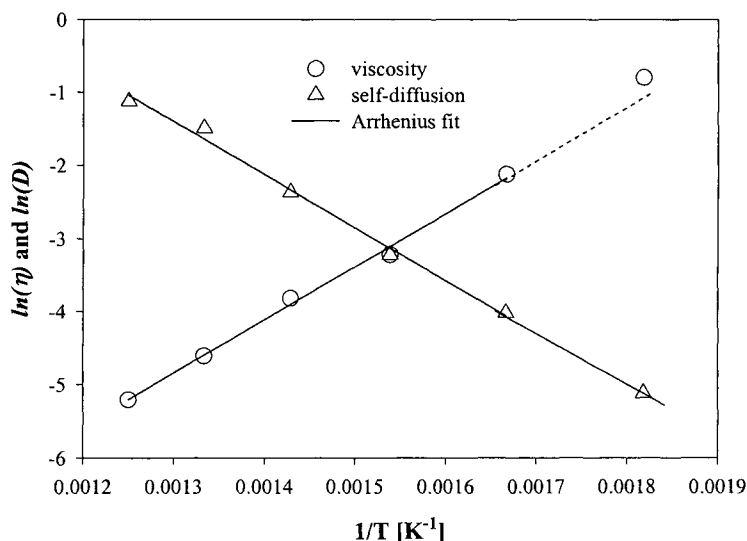


Fig. 6. Arrhenius fit (solid lines) of viscosity in the temperature interval 600-800 K and self-diffusion in the temperature interval 550-800 K obtained from MD simulations (symbols) and extrapolation of viscosity fit to 550K (dashed line)

Correlation of viscosity with diffusion and rotation of HMX. It is informative to examine correlations between the temperature dependence of viscosity with that of other dynamic properties, in particular self diffusion and rotational diffusion. For each temperature we have calculated the rotational correlation time (τ_R), obtained by fitting the “end-to-end” vector autocorrelation function ($T_1 = \langle \cos \theta(t) \rangle$) for nitro group nitrogen atoms on opposite sides of the molecule to a simple exponential decay law:

$$T_1 = \exp\left(-\frac{t}{2\tau_R}\right); \quad (6)$$

and diffusion relaxation time (τ_D) calculated as:

$$\tau_D = \frac{\langle R_g^2 \rangle}{6D} \quad (7)$$

where $\langle R_g^2 \rangle$ is the average radius of gyration (7.3 \AA^2) and D is the molecular self-diffusion coefficient. Rotational and diffusion relaxation times as well as equilibrium density for each temperature are also reported in Table 5.

There are many empirical, semi-empirical, and theoretically-based relations to describe correlation between dynamical properties and shear viscosity. Most of these correlations can be represented as

$$\eta_D = K \frac{\rho T}{D} \quad (8)$$

or

$$\eta_{\tau_R} = K \rho T \tau_R \quad (9)$$

where K is a constant which depends on the particular model involved in the derivation of the relation. If we have an accurate value of viscosity at some temperature T_0 (η_0), then the temperature dependence of the viscosity can be established from the temperature dependence of the self-diffusion coefficient (D) or rotational diffusion time (τ_R) using one of the following relationships

$$\eta_{D_1} = \eta_{D_0} \frac{\rho_1 T_1 D_0}{\rho_0 T_0 D_1} \quad (10)$$

or

$$\eta_{\tau_1} = \eta_{\tau_0} \frac{\rho_1 T_1 \tau_{R1}}{\rho_0 T_0 \tau_{R0}} \quad (11)$$

The practical advantage of these relations is that, in MD simulations, single molecule properties like the self-diffusion coefficient and rotational relaxation times converge much faster than system properties due to additional averaging over the number of molecules in the ensemble. We applied eqs. 10 and 11 to our MD results using data at 800 K as a reference point in order to predict the viscosity over the entire temperature interval. In Fig. 7 we compare the predicted values with those obtained from simulation. It appears that in the temperature interval 600 K to 800 K predictions of Eq. (10) are more consistent with MD results than are the predictions of Eq. (11). This leads us to conclude that the viscosity temperature dependence in liquid HMX is more correlated

with molecular center-of-mass diffusion than with the molecular rotational relaxation time.

Also shown in Fig. 7 is the prediction of viscosity by the Arrhenius equation

$$\eta = \eta_0 \exp\left(-\frac{\Delta E_{vis}}{RT}\right) \quad (12)$$

with parameters (E_{vis} and η_0) determined using MD simulation viscosity results at 800 K and 750 K. This allows us to test how accurately the low-temperature viscosity can be predicted based on the faster converging MD simulations at higher temperature if Arrhenius behavior is assumed. It is clear that in the temperature interval 600 K to 800 K the predictions from the Arrhenius equation are in essentially quantitative agreement with results obtained from MD simulations. Since our simulation at 550 K is too short to estimate the uncertainty in the viscosity, we have more confidence in the viscosity value obtained using Eq. (12) at this temperature.

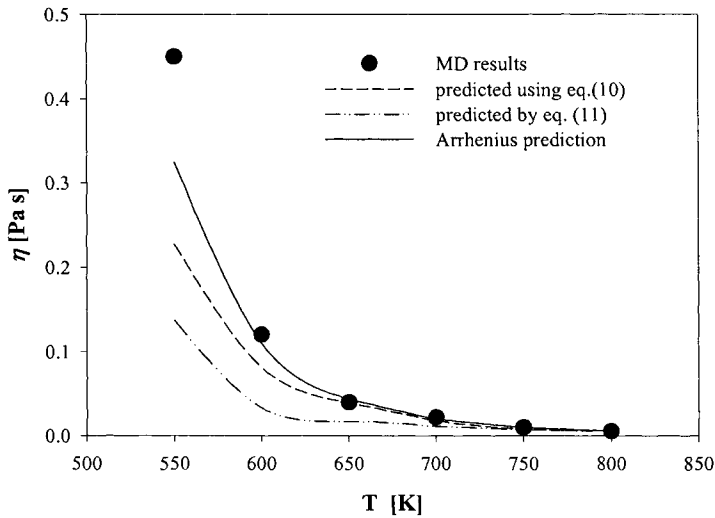


Fig. 7. Temperature dependence of viscosity obtained from the MD simulations.

The shear viscosities calculated for liquid HMX, 0.055-4.5 Poise, are orders of magnitude smaller than values for the solid phase (ca. 1000 Poise) [47]. As a consequence, viscous heating in the melt phase will be comparatively small unless the associated shear strain is large. Large shear strains can only occur in thin layers. Menikoff and Sewell [47] have estimated that the thickness of a shear layer in HMX is only about 300 molecules wide, and that large shear strains ($\epsilon \sim 300$) can occur. At atmospheric pressure and using HMX physical parameters appropriate for $T=550$ K, they estimated that the maximum increase in temperature ΔT_{max} due to viscous heating in liquid HMX is 1.2×10^4 K; using parameter values appropriate for 800 K, ΔT_{max} is reduced to 210 K. The shear viscosity increases significantly with pressure. Thus increased pressure due to heating would partially offset the rapid decrease in shear viscosity, and thus in ΔT_{max} , with increasing temperature.

One scenario in which thin shear layers and large shear strains can occur in plastic-bonded explosives is at the interface between grains sliding past one another or along closed cracks within a grain. These processes have been postulated by Dienes [48] as the dominant dissipative mechanism for generating “hot spots” in plastic-bonded explosives, and have been incorporated into the Statistical Crack Mechanics (SCRAM) model for high-explosive response.

3.2. Thermal conductivity

Methodology. While equilibrium MD simulations allowed us to calculate directly most of the thermophysical and dynamical properties of liquid HMX, calculations of thermal conductivity using equilibrium MD techniques can suffer significant difficulties due to complications in determining the microscopic heat flux $J(t)$ [49], especially for molecular fluids, which are often characterized by long-range interactions (e.g., Coulomb). While the microscopic definitions of mass flux (self-diffusion) and momentum flux (viscosity) involve only self-particle or self- and interparticle static correlations, respectively, the heat flux involves interparticle dynamic correlations requiring evaluation of pair velocities [49,50]. Long-range static correlations can be effectively treated using Ewald and related methods; however, no equivalent method exists for handling long-range dynamic correlations. Since the force field for HMX contains partial atomic charges and therefore includes long-range interactions (and perhaps long-range correlations) we chose to employ a non-equilibrium MD (NEMD) simulation method that does not involve calculation of the microscopic heat flux and hence does not suffer from the complications mentioned above.

Recently, Müller-Plathe suggested a NEMD method [51] for calculation of thermal conductivity in atomic fluids that was subsequently adapted and applied

by us to molecular liquids with long-range interactions [52]. The gist of the method is to impose an exactly known heat flux on the system and then “measure” the resulting steady-state temperature gradient in the direction parallel to the heat flux. The thermal conductivity λ can be expressed as

$$\lambda = \frac{\langle J_z(t) \rangle}{2tA \langle dT/dz \rangle}, \quad (13)$$

where $\langle J_z(t) \rangle$ is cumulative heat flux imposed in the z direction during the simulation, $\langle dT/dz \rangle$ is the resultant temperature gradient in this direction, A is the surface area perpendicular to the z -axis, and t is the total simulation time. The heat flux is created by exchanging the center-of-mass velocities of molecules in “cold” and “hot” slabs located in the middle of the simulation box and adjacent to one of the simulation box boundaries [52]. Specifically, the velocity exchange involves the “hottest” molecule in the cold slab and the “coldest” molecule in the hot slab, where “temperature” is defined by molecular center-of-mass velocities. Performing this exchange with a frequency W results in the heating up of the hot slab and cooling down of the cold slab and eventually yields a steady-state temperature gradient in the z direction due to thermal conduction through slabs separating the cold and hot slabs. The temperature gradient can be easily measured by calculating the local temperature in each slab. The imposed heat flux is given exactly by the relationship

$$\langle J_z(t) \rangle = \sum_{\text{transfers}} \frac{m}{2} (v_c^2 - v_h^2), \quad (14)$$

where v_c and v_h are the translational velocities of the identical mass molecules that participate in the exchange procedure in the cold and hot slabs, respectively. The reader is referred to Refs. [51] and [52] for more details about the methodology and implementation of the imposed heat flux NEMD method.

Using the imposed heat flux method, we carried out NEMD simulations for the HMX melt at six temperatures (550 K - 800 K, in 50 K intervals) and atmospheric pressure. The simulation methodology was similar to the one described above for equilibrium MD simulations with a few exceptions. Each system contained 100 HMX molecules. The orthorhombic simulation box, extended in the z direction, was subdivided into 10 equal slabs with width of about 5.0 Å and cross-sectional area of about 625.0 Å². The molecular center-of-mass velocities were exchanged every 500 fs ($W=0.002$ fs⁻¹) for pairs of molecules belonging to the cold and hot slabs. This choice of the W was based on our previous experience with simulations of liquid n-butane and water [52],

where the same value of W was found to provide accurate predictions of thermal conductivity over a wide temperature interval.

Simulation results. The thermal conductivity of liquid HMX at atmospheric pressure is summarized in Table 5. The thermal conductivity exhibits a much weaker temperature dependence than was found for the other transport properties. Whereas the shear viscosity and self-diffusion coefficients vary by orders of magnitude between 550 and 800 K, the thermal conductivity only varies by $\sim 40\%$ over the same temperature interval. Such behavior is consistent with experimental data on aromatic hydrocarbons [53] and can be explained by differences in the energy, momentum and mass transfer mechanisms. In order to transport energy, a molecule need only oscillate in its local “cage”, interacting with its neighboring molecules without disrupting the local structure. As the primary mechanism for energy transport does not involve long-range molecular transport, the thermal conductivity is relatively insensitive to temperature. In contrast, (zero frequency) momentum and mass transfer require hopping of the molecules from cage to cage, a process involving severe disruption of the local structure. This process is thermally activated with a large activation energy (14.5 kcal/mol), resulting in a strong temperature dependence of the viscosity and self-diffusion coefficients.

In Fig. 8 we show a comparison of the thermal conductivity for liquid HMX obtained from our NEMD simulations with measured values for crystalline HMX [54] as well as values used in combustion models for HMX [55]. Despite being weak, the temperature dependence of the thermal conductivity of liquid HMX is not featureless. The thermal conductivity exhibits a sharp drop in the temperature interval from the melting point (550 K) up to 650 K. At higher temperatures the thermal conductivity exhibits almost no temperature dependence. The predicted value at 550 K is consistent with the HMX crystal data [54]. The thermal conductivity used in some combustion models [55] agrees to within about 25% with our NEMD predictions over the entire temperature interval.

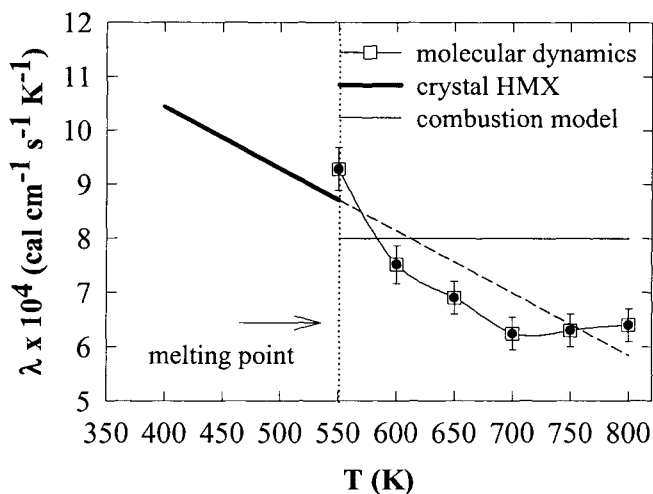


Fig. 8. The thermal conductivity of HMX as a function of temperature. Symbols: this work (liquid phase); solid bold line: experiment (crystal phase); solid thin line: semi-empirical form used in some combustion models. The dashed line is an extrapolation of the experimental data for HMX crystal into liquid region.

The importance of thermal conductivity in high explosives initiation is quite scenario-dependent [47]. On a microsecond time scale comparable to the chemical reaction induction time for a hot spot, heat conduction is only relevant over very small distances (micron or less). By contrast, heat conduction affects distances of the order of centimeters over the hours-long time scale of a cookoff experiment. Menikoff and Sewell have presented arguments indicating that heat conduction is not a suitable mechanism for growth of hot spots in an explosive, nor is it the mechanism for steady detonation propagation. It is, however, an important factor in low-to-moderate speed deflagration waves (mm/sec to cm/sec). At higher speeds, convection of hot gases through pores in the material exceeds heat conduction as the dominant mechanism. Finally, thermal conduction is inversely proportional to the maximum temperature increase ΔT_{max} attainable via viscous shear in the melt.

We close our discussion of thermal conductivity with the observation that experimental determinations of this property at elevated temperatures have large error bars. Indeed, the two measurements of which we are aware differ by roughly 50%. (The “experimental” line in Fig. 8 is the recommended linear

form published by Hanson-Parr and Parr in Ref. [54] Part of the complication at elevated temperatures arises due to chemical reaction, as well as issues of whether phase changes have gone to completion throughout the sample (kinetics versus thermodynamics, as well as the possibility of complicated stress states within a pressed sample “resisting” transformation from one polymorph to another). The non-equilibrium molecular dynamics simulation described above can be extended to yield temperature-dependent thermal conductivities of each solid phase of HMX. We think such simulations would be useful, in light of experimental difficulties. Simulations of the solid would yield thermal conductivity tensors, but anisotropic values could be obtained via suitable averaging.

4. CRYSTALLINE HMX

4.1. Structural properties

Simulation methodology. Isothermal-isobaric (NpT) MD simulations [56] were performed at atmospheric pressure for each phase using the Rahman-Parrinello approach [57] with primary simulation cells corresponding to 24 ($4 \times 2 \times 3$), 8 ($2 \times 1 \times 4$), and 16 ($4 \times 4 \times 1$) unit cells for β -, α - and δ -HMX, respectively. A systematic investigation of the influence of frequencies for the barostat (w_b) and thermostat (w_t) on the volume and enthalpy fluctuations was performed to determine a range of these frequencies for which the average structural properties are independent of the values chosen; values of $w_b=8.0 \times 10^{-4} \text{ fs}^{-1}$ for barostat and $w_t=1.0 \times 10^{-2} \text{ fs}^{-1}$ for thermostat were used for all simulations reported here. Experimental crystal structures [5,6,7] were used to define initial configurations for the simulations. For each system, an equilibration run of 0.5 ns duration was performed, followed by a 1.0 ns production run (5ns at 295 K); the integration step size and sampling interval were 1 fs and 10 fs, respectively. Nonbonded interactions were truncated at 10.0 Å; the standard Ewald summation [44] was used to handle long-range electrostatics. Intramolecular bond lengths were constrained using the SHAKE algorithm [43].

Cell parameters. In Table 6 we report atmospheric pressure lattice parameters and unit cell volumes for β -, α -, and δ -HMX as obtained from MD simulations at 295 K. Also shown for comparison are the experimental results at the same temperature. It can be seen that the simulation results are in good agreement with experiment. The largest percent error in unit cell volume, 1.4%, occurs for α -HMX. The lattice angles are essentially exact with the exception of β -HMX, for which the monoclinic angle β is 3.6% too small. This error is compensated by errors of -4.7% and 3.7% in lattice lengths b and c ,

respectively, to yield nearly perfect agreement with experiment for the unit cell volume. (The errors in those two lattice parameters are the largest obtained in the present work.) Overall, the current predictions are more accurate than those based on the force field of Dzyabchenko *et al* [58], and comparable to those reported by Sorescu *et al* [36]. More detailed comparisons among the force fields are somewhat problematic, however, since in the former case molecular packing was used while in the latter case the temperatures at which the isothermal-isobaric calculations were performed for α - and δ -HMX did not correspond to those for which experimental structural determinations have been reported (295 K).

Coefficients of thermal expansion. In order to determine the coefficients of thermal expansion (CTEs), simulations for each polymorph were performed at several temperatures in the associated stability domains [59], as well as at 295 K; we used $250 < T < 350$ K (250, 280, 295, 320, and 350 K) for β -HMX, $295 < T < 450$ K (295, 350, 380, 400, 420, and 450 K) for α -HMX and $295 < T < 520$ K (295, 480, 500, and 520 K) for δ -HMX. The resulting temperature dependencies of the lattice parameters were adequately described by straight lines; thus, the CTE χ_X for a given lattice parameter at 295 K was determined from $\chi_{X,295K} = 1/X_{295K}(\partial X/\partial T)$ where $X=a, b, c$, and V . The CTEs thus obtained are reported in Table 6 and are in generally good agreement with the experimental data at 295 K [60-62], which are included for comparison. The largest deviation of the predicted χ_V from experimental data is observed for β -HMX and is 11.4%. The CTEs of the individual cell parameters are in best agreement with experiment for α - and δ -HMX, and somewhat less so for β -HMX [63]. In Fig. 9 we compare CTEs predicted in this work with experimental data [60-62] and from previous simulations with a rigid molecule force field [36]. The current CTEs are of comparable or even better accuracy than the values obtained from the rigid-molecule force field.

We note that the results of the two independent experimental investigations for β - and δ -HMX are in serious disagreement for some of the expansion coefficients. Moreover, Saw [62] observed significant differences in some of the CTEs depending on particle size. (This is somewhat surprising to us since the measurements were obtained using x-ray diffraction.) While it is not clear which of the two experiments is most reliable, the results of the two simulation studies suggest that the results due to Herrmann *et al* are likely the more accurate. Resolution of the discrepancy is important since knowledge of the thermal expansion is required to transform between parameters in different thermodynamic ensembles, *e.g.*, isothermal/isentropic or isobaric/isochoric. In some cases, such as C_p and C_V , only the volumetric coefficient is required, *viz.*,

$$C_V = C_p - \beta^2 VTK_T \quad (15)$$

whereas in others, such as the isothermal and isentropic elastic coefficients, the complete thermal expansion tensor $\bar{\beta} = \left(\frac{\partial \bar{\epsilon}}{\partial T} \right)_{\text{stress}}$ is required, *e.g.*,

$$\bar{C}_S = \bar{C}_T + \frac{VT}{c_\epsilon} (\bar{C}_T : \bar{\beta}) \otimes (\bar{C}_T : \bar{\beta}). \quad (16)$$

Here, V denotes specific volume, K denotes bulk modulus, subscripts P, V, S and T denote isobaric, isochoric, isentropic and isothermal conditions, respectively; ϵ is the second-rank strain tensor, and \bar{C} is the fourth-rank elastic tensor.

Table 6

Properties of HMX polymorphs from MD simulations and experiments at 295 K.

Property	β -HMX		α -HMX		δ -HMX	
	MD	exp	MD	exp	MD	exp
a [Å]	6.531	6.535 ^a	14.991	15.14 ^c	7.620	7.711 ^f
b [Å]	10.509	11.030 ^a	23.908	23.89 ^c	7.610	7.711 ^f
c [Å]	7.625	7.3549 ^a	6.0531	5.913 ^c	33.534	32.553 ^f
α	89.999	90.0 ^a	89.990	90.0 ^c	89.999	90.0 ^f
β	98.946	102.69 ^a	90.000	90.0 ^c	89.994	90.0 ^f
γ	90.000	90.0 ^a	89.999	90.0 ^c	120.170	120.0 ^f
volume [Å ³]	516.86	517.16 ^a	2168.86	2138.7 ^c	1681.85	1676.3 ^f
$\chi_a \times 10^5$ [K ⁻¹]	2.07	-0.29 ^b 3.8 ^c	3.65	3.65 ^b	4.02	4.1 ^b 8.0 ^c
$\chi_b \times 10^5$ [K ⁻¹]	7.2	11.6 ^b 15.0 ^c	4.26	4.86 ^b	4.19	4.1 ^b 8.0 ^c
$\chi_c \times 10^5$ [K ⁻¹]	2.56	2.30 ^b 0.9 ^c	1.44	1.21 ^b	3.94	2.6 ^b 2.1 ^c
$\chi_V \times 10^5$ [K ⁻¹]	11.60	13.1 ^b 20.5 ^c	9.34	9.6 ^b	12.76	13.5 ^b 18.5 ^c
ΔH_{sub} [kcal/mol]	45.5	44.16 ^d	44.2	---	41.0	42.04 ^d
ΔE_{inter} [kcal/mol]	48.0		53.0		53.0	
ΔE_{intra} [kcal/mol]	-0.8		-7.0		-10.0	

^a Ref.[5]; ^bRefs.[60,61]; ^cRef.[62]; ^dRef.[65]; ^eRef. [6]; ^fRef. [7]

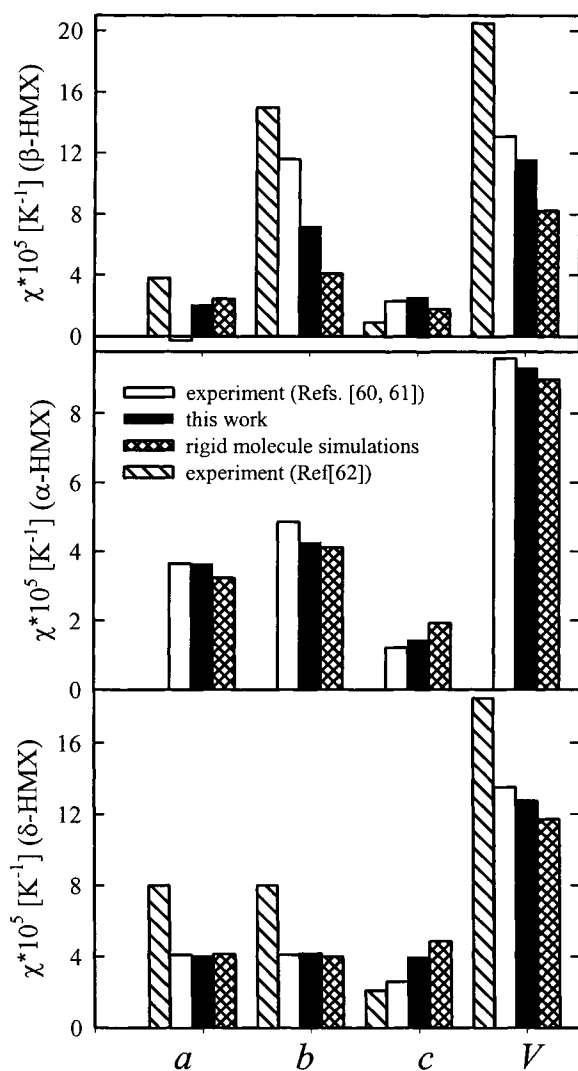


Fig. 9. Coefficients of thermal expansion of linear cell dimensions and unit cell volume for three HMX polymorphs as obtained from experiments and simulations.

4.2 Enthalpy of sublimation

The accuracy with which a force field predicts enthalpies of sublimation is another useful test of its overall validity. The sublimation enthalpy can be determined as:

$$\Delta H_{sub} = H_{gas} - H_{solid} = RT + \Delta E_{inter} + \Delta E_{intra} \quad (17)$$

where ΔE_{inter} and ΔE_{intra} are the differences in intermolecular and intramolecular potential energies of HMX molecules in the ideal gas and relevant crystal phases, respectively. We note that for HMX ΔE_{intra} is not negligible: quantum chemistry calculations at the B3LYP/6-311G** level indicate that the energy difference between the lowest energy gas-phase geometry and that of an optimized gas-phase molecule in the nominal α -HMX conformation is 3.5 kcal/mol. Also, in the crystal phase, bends and torsions of a particular conformer can be distorted from the optimal values of the corresponding gas-phase conformer due to condensed-phase effects. While the difference in intramolecular energies of gas- and solid-phase molecules can make a significant contribution to ΔH_{sub} , this effect has been ignored in the assessment of other force fields [58,36]. In order to obtain the intramolecular energy difference in the present work, simulations of an HMX ideal gas were performed at 295 K using a stochastic dynamics algorithm described elsewhere [64]. The calculated sublimation energies for each polymorph are provided in Table 6, where they are compared (for β - and δ -HMX) to values derived by Lyman *et al* [65] based on a combined analysis of experimental data due to others [66,67]. Good agreement between experimental and MD predicted enthalpies is obtained. The predicted ΔH_{sub} for α -HMX lies in between the values of β - and δ -HMX, which is consistent with the polymorph stability ranking [59] ($\beta > \alpha > \delta$) at room temperature. The ΔE_{inter} and ΔE_{intra} contributions to ΔH_{sub} obtained from MD simulations are also reported in Table 6. ΔE_{intra} makes an important contribution to the ΔH_{sub} of α - and δ -HMX (7.0 and 10.0 kcal/mol, respectively) and is only about 0.8 kcal/mol for β -HMX. It is worth noting that the polymorph dependence of the intermolecular energy contribution to ΔH_{sub} is opposite to that of ΔH_{sub} itself, *i.e.*, the intermolecular interactions for δ - and α -HMX are more favorable than for β -HMX. However, this relative “stabilization” of δ - and α -HMX due to intermolecular interactions is compensated by the unfavorable intramolecular energy of HMX molecules in these phases, resulting in smaller enthalpies of sublimation relative to β -HMX.

4.3 Hydrostatic compression

Isotherm fitting forms. There are two published measurements of the room temperature isotherm for β -HMX. As part of a series of experiments to determine isotherms for various explosive crystals, Olinger, Roof, and Cady reported in 1978 an x-ray determination of the room temperature lattice parameters of β -HMX in the pressure interval $0 < p < 7.47$ GPa [68]. They fit the isotherm to an equation of state (EOS)

$$p(V) = \frac{V_0 - V}{[V_0 - s(V_0 - V)]^2} c^2 \quad (18)$$

based on the hugoniot jump conditions [69],

$$\begin{aligned} \frac{V}{V_0} &= 1 - \frac{U_p}{U_s}, \\ p &= p_0 + \rho_0 U_p U_s, \end{aligned} \quad (19)$$

where V is specific volume, U_s and U_p are the pseudo shock velocity and pseudo particle velocity, respectively; ρ is density; and “0” denotes the reference state (atmospheric pressure in the present case). The fitting parameters c and s are related to the bulk modulus K_0 and its pressure derivative K_0' as $K_0 = \rho_0 c^2$ and $K_0' = 4s - 1$, respectively. In their analysis, Olinger *et al.* observed a linear relation between U_s and U_p , $U_s = c + sU_p$, and obtained $K_0 = 13.5$ GPa and $K_0' = 9.3$.

In 1999, Yoo and Cynn revisited the β -HMX isotherm [70]. Their synchrotron x-ray determination of the pressure dependent lattice parameters employed a diamond anvil cell, and extended out to 43 GPa. They analyzed their data using the third-order Birch-Murnaghan (BM) EOS [71]

$$p(V) = 1.5K_0 \left[\eta^{-7/3} - \eta^{-5/3} \right] \left[1 + 0.75(K_0' - 4)(\eta^{-2/3} - 1) \right] \quad (20)$$

where $\eta = V/V_0$ is the compression ratio at pressure p . Yoo and Cynn reported $K_0 = 12.4$ GPa and $K_0' = 10.4$, for pressures below 27 GPa. Although it is unclear in detail how Yoo and Cynn fit their isotherm to Eq. 20, we note that the third-order BM EOS can be written as a linear function in K_0' and $K_0 K_0'$ via the transformation

$$x=[\eta^{-2/3}-1]^{-1}-3 \quad (21)$$

$$y=2p(V)\{3[\eta^{-7/3}-\eta^{-5/3}][\eta^{-2/3}-1]\}^{-1},$$

for which the slope and intercept are K_o and $3K_oK_o'/4$, respectively. We refer to this form of the BM EOS as BM-linear. In this plane, low-pressure data points are more heavily weighted than high pressure ones. We think that fits to obtain the initial (zero pressure) bulk modulus and pressure derivative using Eq. 20 should employ this weighting scheme rather than a direct fit in the p - V plane, for which all data points are weighted equally, regardless of pressure.

Menikoff and Sewell [72] reported recently a re-analysis of the Olinger *et al.* and Yoo and Cynn experiments, applying both equations of state (Eqs. 18 and 21) to both data sets, to determine which data set and fitting form combination is most consistent with the preponderance of other data for HMX and HMX-based plastic-bonded explosives [73]. In the case of the Yoo-Cynn experiment, they also considered the sensitivity in the predicted values of K_o and K_o' to the interval of the data used, due to the presence of phase transitions in the data.

We applied all three fitting forms (Eqs. 18, 20, and 21) to isotherms for β -, α -, and δ -HMX obtained from simulation and to the two simulation β -HMX isotherms extracted from Fig. 3b of Sorescu *et al.* [74]. We also fit the two experimental β -HMX isotherms directly to Eq. 20, since this was not included in the work of Menikoff and Sewell.

Simulation methodology. Our initial approach was to perform all simulations using the Rahman-Parrinello isothermal-isobaric approach to MD simulations [57], as we described in section 4.1, in which lattice degrees of freedom for the primary cell are explicitly coupled to an external barostat *via* the stress tensor. However, this requires specification of a parameter corresponding to the strength of coupling to the barostat. We found that, while the mean values of the lattice parameters and thermodynamic properties discussed above were independent of the specific value chosen for this parameter, higher moments of the distributions did vary with the barostat coupling, at least for the 2-5 nanosecond simulation times considered in our preliminary studies. This sensitivity is troublesome for our purposes, since calculation of the elastic tensor (discussed below) is based on a fluctuation analysis of the microscopic strain tensor. While the results may become independent of the barostat parameter chosen for sufficiently long simulations, it was not practical for us to perform a careful study of this behavior given the anticipated computational expense. Therefore, for all simulations discussed in this and subsequent sections we employed an approach in which isothermal-isochoric (NVT) molecular dynamics of the simulation cell contents was

interspersed with isothermal-isobaric (NpT) Monte Carlo (MC) variations of the cell shape and volume. This is valid based on the parametric separability of the partition function in the isothermal-isobaric ensemble [75],

$$Z_{NpT} = \int dV \exp(-\beta pV) \int dq \exp[-\beta E(q; V)] = \int dV \exp(-\beta pV) Q_{NVT}, \quad (22)$$

where $\beta=1/\kappa T$ and Q_{NVT} is the partition function in the NVT ensemble.

We used NVT MD to sample the contents of the simulation cell, and an NpT MC algorithm to vary its shape and volume. The latter moves were carried out within a rigid-molecule framework as described previously [76], using the atomic positions at the end of the preceding flexible molecule NVT MD segment. In practice, 1 ps of NVT MD simulation was followed by a sequence of 100 NpT MC steps. The Monte Carlo step size for a given thermodynamic state was adjusted to yield an acceptance probability of 40-50%.

Predicted isotherms. The measured β -HMX isotherms and the one predicted from our combined MD-MC simulations are shown in Fig. 10. The solid line passing through the simulation results is a fit of the third-order BM-linear equation of state to the data using Eq. 21. The agreement between experiment and simulation at a given pressure is reasonably good: at the highest pressure considered here, 10.6 GPa, the percent difference between our compression ratio and the measurements of Yoo and Cynn is 4.6%, with the simulated isotherm being somewhat stiffer than experiment. The comparison is significantly less favorable if we instead compare predicted pressure at a given compression ratio. For example, at $\eta=0.8$, the predicted pressure and that reported by Yoo and Cynn differ by approximately 40%. We point out the sizeable discrepancy between the two experimental results, and that our predictions and those of Sorescu et al. are closer to the results of Olinger et al. However upon consideration of all data, Menikoff and Sewell [72] concluded that the Yoo and Cynn isotherm is likely the more accurate of the two.

Application of Eq. 19 to the β -HMX isotherm from simulations leads to the U_s-U_p curve shown in Fig. 11, where negative curvature in the simulation results is clearly evident (filled circles). While such behavior would be anomalous for metals, it is actually expected for pressures below about one GPa in the case of polyatomic molecular crystals, due to complicated molecular packings and intramolecular flexibility, and has in fact been reported for the high explosives pentaerythritol tetranitrate (PETN) where careful studies were performed for low levels of compression [77]. By contrast, the experimental results for β -HMX in the U_s-U_p plane do not exhibit significant curvature due to lack of data at pressures below about one GPa [78]. Thus, estimates of isothermal sound speeds, and hence isothermal bulk moduli, based on

extrapolation of these data are likely to be too large. The consequence of employing a linear fit and the lack of low-pressure data on the calculated isothermal bulk modulus can be seen in Fig. 11 by comparing a linear fit ($U_s = c + sU_p$, dashed lines) to the simulation data over the experimental pressure range ($p > 1.6$ GPa) to a quadratic fit ($U_s = c + sU_p + tU_p^2$, solid line) to the same data over the entire pressure range. The $U_p = 0$ intercepts, which yield c and hence the initial isothermal bulk modulus ($K_o = \rho_o c^2$), differ considerably between the two fits. Hence, the details are important when the goal is to make comparison to ambient sound speed data.

There are no experimental determinations or previous theoretical predictions of the isotherms for α - and δ -HMX. Our results are shown in Fig. 12, where we also include the calculated β -HMX isotherm for comparison. The β - and δ -HMX isotherms are smooth over the entire interval. By contrast, there is a clear break in the isotherm for α -HMX that occurs between 0.2 and 0.5 GPa, indicating a pressure-induced phase transition $\alpha \rightarrow \alpha'$ for that polymorph. The phase transformation preserves molecular point group, but involves a change in molecular packing motif and a shift from an orthorhombic to a monoclinic lattice, with abrupt changes in the lattice parameters. In light of this, we restrict the equation of state fits for α -HMX to pressures less than 0.2 GPa. While there is no apparent discontinuity in the δ -HMX isotherm, examination of the individual lattice parameters indicated a gradual, symmetry-class preserving shift that occurs between 1.0 and 2.4 GPa. For this reason, and in analogy with restricting our fits of the Yoo and Cynn data to pressures below 12 GPa, we restrict our fits for δ -HMX to 1.0 GPa and below. We point out that pressure-induced phase changes are common in organic crystals, and have been identified for the high explosives β -HMX [70] and hexahydro-1,3,5-trinitro-1,3,5-triazine (RDX) [79]. This is unsurprising, since anisotropy leads to significant shear strains even under hydrostatic loading.

Bulk moduli and pressure derivatives. Results for the bulk modulus and its pressure derivative for all three HMX polymorphs obtained from fitting simulation-predicted isotherms to the equations of state discussed above are summarized in Table 7. For all data sets, we include fits to the U_s - U_p form (Eq. 18) and both weighting schemes for the third-order Birch-Murnaghan equation of state (Eqs. 20 and 21). In the case of the experimental data for β -HMX, values for the moduli based on Eqs. 18 and 20 were taken from the re-analysis of Menikoff and Sewell. Two sets of results are included in the case of Yoo and Cynn, since they reported on the basis of shifts in the Raman spectra a phase transition with zero volume change at 12 GPa. Simulation data of the β -HMX isotherm due to Sorescu *et al.* were extracted by hand from Fig. 3b of their work.

A few general observations are in order. First, tabulated values of the initial bulk modulus vary by almost a factor of two, from 8.4 to 17.5 GPa, while values of the pressure derivative vary by almost a factor of *five*; even within a given data set, there is significant scatter in these parameters. In practice, the fits are most sensitive at ambient conditions; for high pressures, the differences among them are lessened. This underscores the need for high-precision data, with information extending down to low pressures if the objective is accurate predictions of the initial bulk modulus.

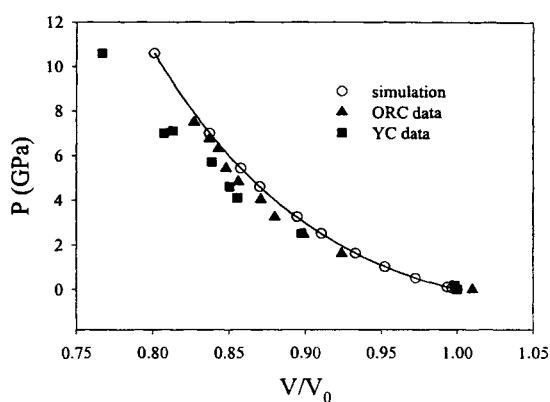


Fig. 10. Isotherms for β -HMX. Open circles: simulation; triangles: Olinger *et al.* (Ref.[77]); squares: Yoo and Cynn (Ref. [70]). Solid line is third-order Birch-Murnaghan fit (Eq. 20) to simulation results, fit via Eq. 21.

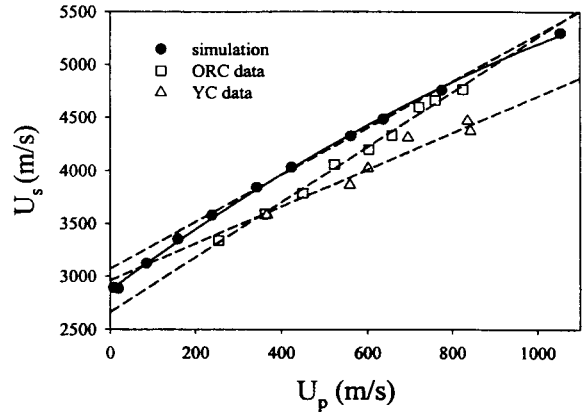


Fig. 11. β -HMX isotherms in the psuedo- (U_s, U_p) plane (Eq. 19). Solid line is a quadratic fit to the simulation results. Dashed lines are linear fits to Eq. 19.

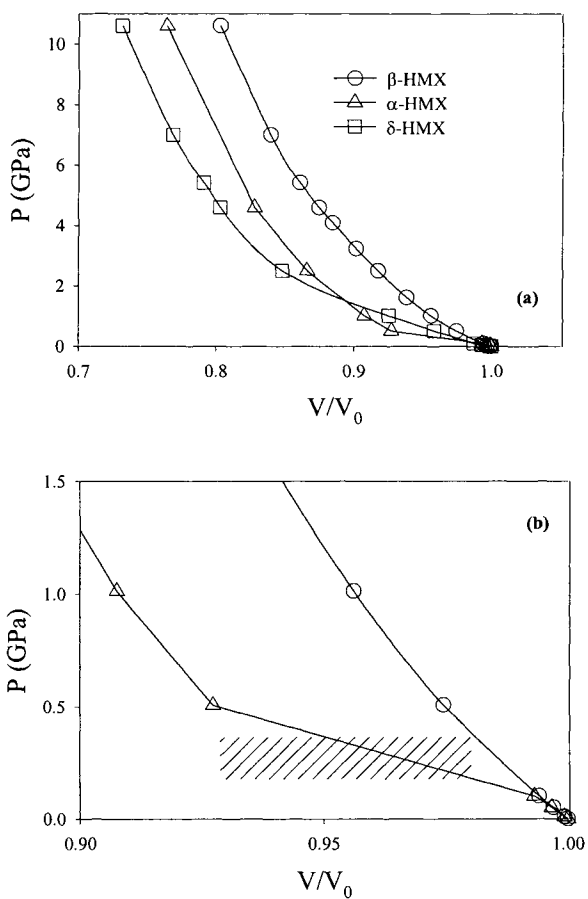


Fig. 12. Panel (a): Calculated isotherms for HMX polymorphs, $p < 10.6$ GPa. Circles: β -HMX; triangles: α -HMX; squares: δ -HMX. Lines connecting data points are only intended as a guide for the eye. Panel (b): blow-up of low-pressure isotherms for β -HMX (circles) and α -HMX (triangles), showing break in α -HMX result corresponding to pressure-induced phase transition.

Table 7.
Bulk modulus and its pressure derivative for HMX polymorphs.^a

Source	Method ^b	β		α		δ	
		K_o	K_o'	K_o	K_o'	K_o	K_o'
<i>Experiment</i>							
ORC	BM	8.4	26.2				
	BM-linear	10.6	18.1				
	U_s - U_p	13.4	9.4				
YC (<12 GPa)	BM	16.7	6.8				
	BM-linear	16.0	7.3				
	U_s - U_p	17.2	5.7				
YC (< 27 GPa)	BM	14.5	8.7				
	BM-linear	14.7	8.6				
	U_s - U_p	17.5	5.6				
<i>Simulation</i>							
Sorescu <i>et al.</i> P_{21}/c	BM	9.6	22.0				
	BM-linear	10.9	18.4				
	U_s - U_p	12.2	11.8				
Sorescu <i>et al.</i> P_{21}/n	BM	11.6	20.9				
	BM-linear	13.4	16.6				
	U_s - U_p	14.8	10.8				
Evans <i>et al.</i>	QC	12.5		38.6		48.0	
This work	fluctuations	15.1		14.1		11.8	
	BM	16.3	11.4	15.5	-13.9	14.1	0.4
	BM-linear	15.5	12.1	14.3	14.0	12.0	8.1
	U_s - U_p	15.6	11.0	14.1	16.8	12.3	4.7

^a K_o in GPa, K_o' is dimensionless. ^bBM = from Birch-Murnaghan EOS (Eq. 20). BM-linear = from Birch-Murnaghan EOS (Eq. 21). U_s-U_p = from U_s-U_p EOS (Eq. 19). QC = from quantum chemical calculations (Ref.[82]). Fluctuations = from equilibrium volume fluctuations (Eq. 25) or, equivalently, the equilibrium elastic tensor (using Eq. 24) at atmospheric pressure.

Among the experimental sets, the Yoo and Cynn β -HMX isotherm leads to more consistent predictions for both K_o and K_o' . Menikoff and Sewell [72] provided a thorough discussion of the two experimental isotherms. Although they obtained values of K_o and K_o' that disagreed significantly with those reported by Yoo and Cynn, they found that their data, fit using the third-order Birch-Murnaghan equation of state *via* Eq. 21, leads to better overall agreement with the other HMX data than does the set of Olinger *et al*. In particular, the β -HMX isotherm of Olinger *et al* leads to the prediction of a stiffer equation of state than is obtained from shock hugoniot data [80] for pressed HMX. As our interest is in the initial bulk modulus and pressure derivative, we make our principal comparisons between the Yoo and Cynn results for $p < 12$ GPa, for which $16.0 < K_o < 17.2$ GPa and $5.7 < K_o' < 7.3$.

Results obtained using the two calculated isotherms of Sorescu *et al* and from the quantum chemistry-based cold curve calculations of Evans *et al* yield predictions of the β -HMX bulk modulus $9.6 < K_o < 14.8$. These values are generally consistent with values derived from the Olinger *et al* isotherm, *i.e.*, roughly 3 GPa lower than the Yoo and Cynn results for $p < 27$ GPa. An interesting observation is that the isotherms of Sorescu *et al* are sensitive to whether the $P_{21/c}$ or $P_{21/n}$ space group setting is chosen, even though the two are formally equivalent. This is apparently due to the use of independent crystal structure determinations for the two space groups, with associated small differences in measured molecular geometries, that were used as input to their rigid-molecule simulations. These differences led in turn to slightly different partial atomic charges in the potential-energy functions for the two cases [81].

Bulk moduli for β -HMX obtained from the present simulations yield moduli consistent with the Yoo and Cynn results, namely, $15.1 < K_o < 16.3$ GPa, and $11.0 < K_o' < 12.1$. The calculated pressure derivative is somewhat higher than the Yoo and Cynn set, consistent with the stiffer overall isotherm predicted from the simulations. Values of the bulk modulus extracted from the α - and δ -HMX isotherms, with fits restricted to the specified intervals, are included in Table 7. There is an approximately linear correlation between bulk modulus and crystal density, with $K_{o\beta} > K_{o\alpha} (\approx 0.93 K_{o\beta}) > K_{o\delta} (\approx 0.78 K_{o\beta})$. This stands in contrast to the quantum chemistry-based predictions of Evans *et al* [82], who obtained zero Kelvin values $K_{o\beta} = 10.2$ -12.5 GPa, $K_{o\alpha} = 38.6$ GPa and $K_{o\delta} = 48.0$ GPa from a fit of the cold curve to $K = V^{-1} d^2 E / dV^2$, where V is the specific volume and E is potential energy. Evans *et al* [82] cautioned that their predictions should only be regarded as rough estimates due to geometric constraints on crystal lattice parameters imposed in their study, which would be expected in general to lead to overestimates of the bulk moduli. The values reported in the present work should be much more reliable.

The isotropic moduli, particularly the initial bulk modulus and its pressure derivative, are key ingredients in specifying the mechanical equation of state. As noted above, determination of these properties from experimental hydrostatic compression data is difficult due to issues with acquisition of high precision at low pressures and particular sensitivity in the choice of equation of state fitting form to data below about one GPa. Alternative routes to this information at low pressures included impulsive stimulated light scattering (ISLS) and resonant ultrasound spectroscopy (RUS), which can in principle provide the complete elastic tensor (ISLS) and isotropic bulk and shear moduli (RUS).

Sampling difficulties are less acute using simulations; indeed, determination of the bulk modulus from an analysis of either volume fluctuations or explicitly from the elastic tensor yields computed at one atmosphere pressure yields the “correct” value, which can be used as a gauge against which equation of state fitting schemes based on extrapolation isotherm data taken at higher pressures can be assessed. It is important to recognize, however, that current force fields apparently somewhat overestimate the stiffness of the isotherm at high pressures if one accepts the conclusions of Menikoff and Sewell that the Yoo and Cynn experimental isotherm is probably more reliable than the one due to Olinger, Roof, and Cady.

4.4. Anisotropic elasticity

Elastic Tensor, Volume Fluctuations, and Isotropic Moduli. Rahman and Parrinello [83] showed that the fourth-rank elastic tensor for an anisotropic crystalline solid can be calculated using fluctuations of the microscopic strain tensor:

$$S_{ijkl} = \frac{\langle V \rangle}{\kappa T} \langle \varepsilon_{ij} \varepsilon_{kl} \rangle, \quad (23)$$

where S_{ijkl} are elements of the elastic compliance tensor, κ is the Boltzmann constant, and $\langle V \rangle$ is the average volume at a given temperature T (and, implicitly, pressure p). Following the definitions of stress, strain, and Voigt contraction scheme as prescribed by Tsai [84], the elements of the compliance tensor \mathbf{S} and elastic tensor \mathbf{C} are related simply as matrix inverses of one another, *i.e.*, $\mathbf{S} = \mathbf{C}^{-1}$. Eq. 23 is readily constructed from a suitably large set of observations from an isothermal-isobaric simulation. The particular form expected for \mathbf{C} is determined by the symmetry class for a given crystal (*e.g.*, monoclinic, orthorhombic, and hexagonal for β -, α - and δ -HMX, respectively), and can be used as a partial check for convergence of the simulation results.

Given the elastic tensor we can obtain Reuss average, isotropic bulk and shear moduli

$$K_R^{-1} = [S_{11} + S_{22} + S_{33} + 2(S_{12} + S_{13} + S_{23})] \quad (24)$$

$$G_R^{-1} = \frac{4}{15} \left[S_{11} + S_{22} + S_{33} - (S_{12} + S_{13} + S_{23}) + \frac{3}{4}(S_{44} + S_{55} + S_{66}) \right],$$

corresponding to conditions of uniform stress (the appropriate choice for comparison to isotherm data). The bulk modulus can also be expressed directly from the volume fluctuations,

$$K_V = \frac{\langle V \rangle \kappa T}{\sigma_V^2}, \quad (25)$$

where σ_V is the variance of the volume distribution corresponding to a given pressure and temperature obtained directly from simulations. Volume distributions for all three polymorphs were described accurately by Gaussian functions, indicating that finite-size effects on the predicted moduli are small.

Elastic tensor. Published information about the elastic tensor for β -HMX is limited to a partial determination, due to Zaug, at two temperatures [85]. By fitting to isentropic sound speeds determined from Impulsive Stimulated Light Scattering (ISLS) measurements, Zaug was able to obtain a set of isentropic elastic coefficients. With only two experimental samples of similar orientations available, however, the number of elastic coefficients projecting strongly onto the observed sound speeds was limited; indeed, only five of the thirteen non-zero elastic constants could be accurately determined (C_{11} , C_{15} , C_{33} , C_{35} and C_{55}). To determine a complete set of elastic coefficients corresponding to a globally optimized fit would require additional measurements for different crystal orientations. We note that the fitted values were adjusted to yield agreement with isentropic sound speeds, but were normalized using the isothermal bulk modulus $K_o=12.5$ GPa reported in a conference proceeding by Yoo and Cynn [86], which would appear to be too small based on the analysis due to Menikoff and Sewell [72].

The calculated isothermal elastic tensor for β -HMX is compared in Table 8 to the one reported by Zaug (isentropic conditions). Uncertainties in the calculated elastic coefficients represent one standard deviation in values predicted from five contiguous two nanosecond simulation sequences from the overall ten nanosecond simulation. As mentioned above, Zaug's experiments sufficed to determine uniquely five of the thirteen elastic constants (*modulo* the

need to specify a target value for the bulk modulus). These coefficients -- C_{11} , C_{33} , C_{55} , C_{15} , and C_{35} -- are indicated in bold in the experimental column, and the comparison between the two sets is most meaningful for those particular C_{ij} . Acceptable agreement (percent difference of *ca.* 20% or less) is obtained for C_{11} , C_{33} , and C_{35} . The agreement is less good for C_{55} , where the experimental value is only 55% of the calculated one. Similar discrepancies are seen in for some of the other elements of the elastic tensor and, while it is of interest to understand why this is the case, we do not have an explanation at the present time.

Table 8.
Elastic coefficients and isotropic shear modulus (G) for HMX polymorphs^a

	β Exp. ^b	β	α	δ^c
C_{11}	20.8	22.2±0.3	30.6±0.5	14.5±0.7 ($C_{11}=C_{22}$)
C_{22}	26.9	23.9±0.5	23.3±0.8	14.0±0.8 ($C_{22}=C_{11}$)
C_{33}	18.5	23.4±0.5	31.4±0.2	18.0±0.9
C_{44}	4.2	9.2±0.2	0.80±0.04	4.4±0.2 ($C_{44}=C_{55}$)
C_{55}	6.1	11.1±0.1	3.3±0.1	4.4±0.2 ($C_{55}=C_{44}$)
C_{66}	2.5	10.1±0.1	3.3±0.2	2.3±0.4 ($C_{66}=C_{11}-C_{12}$)
C_{12}	4.8	9.6±0.7	5.7±0.7	10.3±0.5
C_{13}	12.5	13.2±0.3	13.8±0.7	10.6±0.7 ($C_{13}=C_{23}$)
C_{23}	5.8	13.0±0.2	6.0±0.3	10.3±0.4 ($C_{23}=C_{13}$)
C_{15}	-0.5	-0.1±0.3		
C_{25}	-1.9	4.7±0.2		
C_{35}	1.9	1.6±0.2		
C_{46}	2.9	2.5±0.3		
G		7.0	2.4	2.9

^a In GPa. For α -HMX, a , b , and c are directed along the \hat{x} , \hat{y} , and \hat{z} axes, respectively, in a right-handed cartesian frame. For β -HMX, a is directed along \hat{x} , b is along \hat{y} , and c is in the $\hat{x}\hat{z}$ plane. For δ -HMX, a is directed along \hat{x} , b is in the $\hat{x}\hat{y}$ plane, and c is along the \hat{z} axis.

^b Well-determined experimental values (see text) are in bold.

^c Symmetry-dictated equivalencies of the elastic coefficients for δ -HMX (hexagonal crystal lattice) are indicated.

Room temperature elastic tensors for α - and δ -HMX are also given in Table 8. There are no previous reports concerning the elastic coefficients for

those polymorphs. The results indicate considerable anisotropy in the diagonal elements of the tensor for α -HMX ($C_{11} \approx C_{33} \sim 1.3 C_{22}$; $C_{55} \approx C_{66} \sim 5 C_{44}$), in contrast to the case of β -HMX where strong anisotropy is not observed. This difference presumably arises due to the qualitatively different molecular packing in the two polymorphs and, insofar as anisotropies in the elastic tensor may have similarities in plastic deformation mechanisms, they may have ramifications for the energetics of slip systems in the two materials. This is an issue with practical importance, since differences in mechanical slip systems within a given crystal polymorph have been considered in attempts to explain orientational dependencies of elastic-plastic wave profiles and shock-induced detonation thresholds in HMX [87], PETN [88], and nitromethane [89]. For δ -HMX, which is of hexagonal symmetry, formal symmetry-based relations exist among the elements of the elastic tensor. These are indicated in Table 8, and expectations are fulfilled with the exception of C_{66} , for which the predicted value 2.3 GPa differs by -1.6 GPa from the expected value.

Bulk moduli obtained from the elastic tensor, via Eq. 24, and from volume fluctuations of the simulation cell, Eq. 25, agree to within 0.1 GPa and are also shown in Table 7 (only a single value is shown). Values obtained in this way should represent the “true” initial bulk modulus, since they sample microscopic fluctuations at one atmosphere. This is borne out by the fits to the isotherm. Moreover, fitting forms that emphasize the low-pressure regions of the equation of state (i.e., Eq. 21) yield values of the bulk modulus in closer agreement to the fluctuation-based values than does the Birch-Murnaghan fit using Eq. 20 directly. That this trend is not upheld in the simulation data of Sorescu et al. probably arises because they did not include low-pressure states in their study. (Their main objective was to validate their potential against the isotherm of Olinger et al., so no low-pressure simulations were performed.) As for β -HMX, the bulk moduli extracted from the α - and δ -HMX isotherms are consistent with values derived from the elastic tensor and analysis of volume fluctuations.

Isotropic shear moduli calculated using Eq. 24 for all three HMX polymorphs are included at the bottom of Table 8. Interestingly, the predicted shear moduli for α - and δ -HMX are significantly smaller, by more than a factor of two, than the value for β -HMX. In a forthcoming conference proceeding, Tappan *et al*[90] report resonant ultrasound measurements of the longitudinal and transverse sound speeds in pressed samples of HMX (*not* single crystal). The longitudinal and shear wave sound speeds, c_l and c_s , respectively, are related to the bulk and shear moduli *via* $K = c_l^2 \rho$ and $G = c_s^2 \rho$. The value Tappan *et al*[90] obtained for the bulk modulus of β -HMX at room temperature, 3.7 GPa under a constant load of 5.6 MPa, is significantly smaller than any reported value for a single crystal. This is not surprising since their pressed

sample had a porosity of about 4.4%, and sound speeds are highly sensitive to porosity. It is interesting, however, that they observed a significant decrease in the apparent bulk and shear moduli upon transformation from β - to δ -HMX at ~ 185 C. This is consistent with the present results, and may be of interest with respect to understanding the increased shock sensitivity of δ -HMX relative to β -HMX.

To the best of our knowledge, anisotropic elastic response has been ignored in all mesomechanical simulations of plastic-bonded explosives to date, due in part to difficulties of complete tensoral elasticity within existing code frameworks and also due to the substantial increase in memory that would be required to carry tensoral information about material properties within a continuum simulation framework. One possible step to approximate anisotropy would be to choose a distribution of isotropic moduli for individual grains, depending on their initial orientation within the sample simulation volume. This would provide some, qualitative, indication of the probable effects of anisotropic elastic response, since wave speeds in the direction of loading would reflect the initial distribution of grain orientations. This in turn would presumably lead to increased dissipation of the wave on fine length scales. Whether such effects would become manifest at larger scales is unclear.

5. CONCLUSIONS

In addition to the properties discussed above, there are several others whose determination would be of great use within a mesoscopic modeling framework. Among these are the melt curve $T_{melt}=T_{melt}(p)$, the temperature and pressure dependent specific heat, initial efforts towards understanding plastic response, and studies of solid-solid phase transitions.

Melt curve. Shear heating and plastic work in the solid are among the dissipative mechanisms that lead to hot-spot formation. Upon melting, however, the yield strength vanishes and the shear viscosity decreases by orders of magnitude. Thus, melting significantly limits the maximum hot-spot temperature that can be reached by those two mechanisms. Given the extreme sensitivity of reaction rates to temperature, the dependence of the melting point on pressure is an important, but unknown quantity. For HMX, not even the form is known; two approximations are sometimes used. Linearization of the melt curve can be done in volume using the Kraut-Kennedy relation,

$$T_m = T_{m,0} \left(1 + a \frac{\Delta V}{V_0} \right), \quad (26)$$

where the coefficient a is given by

$$a = 2\left(\Gamma - \frac{1}{3}\right) \quad (27)$$

or, from thermodynamics,

$$a = \frac{VK_s - \Gamma^2 C_V T}{L - (\Delta V/V) \Gamma C_V T} \frac{\Delta V}{V}, \quad (28)$$

where L is the latent heat of melting. Alternatively, the melt curve can be linearized in terms of pressure,

$$T_m = T_{m,0} + bp, \quad (29)$$

where $b = aT_{m,0} / K_T$. Clearly, these two forms will behave differently at high pressures. Indeed, they lead to qualitatively different conclusions concerning the state of HMX under shock loading. With extrapolation in volume, melting is predicted for shock pressures greater than 19 GPa, whereas extrapolation in pressures leads to the prediction that melting will not occur for any shock pressure. Although it would be a significant challenge, calculation of the melt curve, or at least elucidation of its qualitative form to discriminate between the two extrapolation schemes, would be a worthwhile endeavor.

Specific heat and Gruneisen coefficient. The temperature behind a shock can be written as

$$T(V, e) = T_0 \left(\frac{V_0}{V} \right)^\Gamma + \frac{e - e_s(V)}{C_V}, \quad (30)$$

where the first and second terms correspond to isentropic compression and dissipative heating, respectively; the Gruneisen parameter Γ is given by

$$\Gamma / V = K_s \beta / C_V = (\partial p / \partial T)_{|V} C_V^{-1} \quad (31)$$

where V is specific volume, β is the volumetric thermal expansion coefficient, and K_s is the isentropic bulk modulus; s denotes a value on the initial isentrope and C_V is the specific heat at constant volume. For pressures up to 10 GPa, the heating contribution from isentropic compression is less than 100 K. For fast reaction temperatures of at least 700 K are required. Thus, a temperature rise of at least 400 K above room temperature is required, and most of this must come from dissipative heating. Since dissipative heating is

inversely proportional to the specific heat, knowledge of this parameter as functions of pressure and temperature is critical if we are to make accurate predictions of temperature in shocked HMX, and the ability to do so is a prerequisite to making predictions of chemistry using real reaction rates.

Goddard and co-workers have reported the temperature dependent specific heat C_V for β -HMX for temperatures between 0 and 3000 K, based on a weighted integration of the density of states obtained from a molecular dynamics trajectory. They predict that the specific heat is a monotonically increasing function of temperature; the value at 1000 K is about 40% larger than at ambient conditions. By contrast, most equations of state used for HMX assume a constant specific heat, using a value corresponding to the melting point. This introduces a significant error into the calculation of hot-spot temperature. Thus, calculations of the specific heat should be extended to other volumes. Additionally, calculations should be performed for the δ polymorph and liquid state of HMX. These new results should be incorporated into improved equations of state currently under development. Similar remarks apply to calculation of the Grüneisen parameter.

Twinning and plastic yield. Microscopic examination of β -HMX in PBX-9501 reveals significant twinning. It is known that, for sufficiently low stress, the twinning is reversible, whereas the twins become permanent above some critical applied stress. The twin directions are known, although they have not been studied theoretically. It would be of interest to model twinning behavior in β -HMX from molecular mechanics and molecular dynamics, to obtain theoretical understanding of the process. In the not-too-distant future, it might be possible to extend simulations to study local plastic yield in shock loaded HMX, as a function of orientation. If successful, such studies would provide useful, although probably qualitative, insight into the anisotropic yield surface in the material.

Solid-solid phase transitions. The β - δ phase transition has received a lot of attention over the years, primarily from experimentalists. While theoretical models of the transition exist, no simulations of the process have been reported. This is not surprising, since the β - δ transition involves significant conformational rearrangement of the molecular structure and is generally accompanied by significant damage which presumably arises due to incommensurate structures. These factors, coupled to the large size of HMX and the relatively large numbers of molecules per unit cell in δ -HMX, suggest that direct simulation of the β - δ transition might be prohibitively difficult in the near term. We note, however, that the molecular point group in δ -HMX and α -HMX is essentially the same. Thus, study of the α - δ transition would seem to be preferable to the β - δ case, in that the transition in the former case is dominated by orientational rearrangement and change of crystal lattice class,

without significant molecular conformational change. Even so, we suspect that direct simulation of this process will present formidable challenges to existing technologies developed for the study of simpler systems.

AKNOWLEDGEMENTS

DB and GDS are funded by the University of Utah Center for the Simulation of Accidental Fires and Explosions (C-SAFE), funded by the Department of Energy, Lawrence Livermore National Laboratory, under subcontract B341493. TDS is supported by the U.S. Department of Energy under the auspices of the Los Alamos ASCI High Explosives Project.

REFERENCES

- [1] M.R. Baer, *Thermochim. Acta* 38 (2002) 351.
- [2] S.G. Bardenhagen, J.U. Brackbill, and D. Sulsky, *Phys. Rev. E* 62 (2000) 3882.
- [3] T.R. Gibbs, and A. Popolato, *LASL Explosive Property Data*, University of California, Berkeley, 1980.
- [4] C.S. Choi and H.P. Boutin, *Acta Crystallogr. B* 26 (1970) 1235.
- [5] Y. Kohno, K. Maekawa, N. Azuma, T. Tsuchioka, T. Hashizume, and A. Imamura, *Kogyo Kayako* 53 (1992) 227.
- [6] H.H. Cady, A.C. Larson, and D.T. Cromer, *Acta Cryst.* 16 (1963) 617. Note that the “y” fractional coordinate for atom N_i in Table 2 should have a negative sign.
- [7] R.E. Cobblestick, and R.W.H. Small, *Acta Cryst. B* 30 (1974) 1918.
- [8] www.csafe.utah.edu
- [9] D. Bedrov and G.D. Smith, *J. Phys. Chem. B.*, 103 (1999) 3791.
- [10] G.D. Smith, R.K. Bharadwaj, D. Bedrov, and C. Ayyagari, *J. Phys. Chem. B*, 103, (1999) 705.
- [11] D. Bedrov, G.D. Smith, and T. Sewell, *J. Chem. Phys.*, 112 (2000) 7203.
- [12] D. Bedrov and G.D. Smith, *J. Chem. Phys.*, 113 (2000) 8080.
- [13] W. Paul, G.D. Smith, and D.Y. Yoon, *Macromolecules*, 30 (1997) 7772.
- [14] G.D. Smith, W. Paul, D.Y. Yoon, A. Zirkel, J. Hendricks, D. Richter, and H. Schober, *J. Chem. Phys.*, 107 (1997) 4751.
- [15] G.D. Smith, D.Y. Yoon, C.G. Wade, D. O’Leary, A. Chen, and R.L. Jaffe, *J. Chem. Phys.*, 106 (1997) 3798.
- [16] G.D. Smith, W. Paul, M. Monkenbusch, L. Willner, D. Richter, X.H. Qiu, and M.D. Ediger, *Macromolecules*, 32 (1999) 8857.
- [17] C. Ayyagari, D. Bedrov, and G.D. Smith, *Macromolecules*, 33 (2000) 6194.
- [18] P. Ahlström, G. Wahnström, P. Carlsson, O. Borodin, and G. D. Smith, *J. Chem. Phys.*, 112 (2000) 10669.
- [19] O. Borodin, F. Trouw, D. Bedrov, and G.D. Smith, *J. Phys. Chem. B*, 106 (2002) 5184.
- [20] O. Borodin, D. Bedrov, and G.D. Smith, *Macromolecules*, 35 (2002) 2410.
- [21] O. Borodin, D. Bedrov, and G.D. Smith, *J. Phys. Chem. B*, 106 (2002) 5194.
- [22] O. Borodin and G.D. Smith, *Macromolecules*, 31 (1998) 8396.
- [23] O. Borodin and G.D. Smith, *Macromolecules*, 33 (2000) 2273.

-
- [24] B.K. Annis, H.M. Kim, G.D. Wignall, O. Borodin, and G.D. Smith, *Macromolecules*, 33 (2000) 7544.
- [25] O. Borodin, R.L. Bell, Y. Li, D. Bedrov, and G.D. Smith, *Chem. Phys. Lett.* 336 (2001) 292.
- [26] G.D. Smith and W. Paul, *J. Phys. Chem. A.*, 102, (1998) 102, 1200.
- [27] O.G. Bytner and G.D. Smith, *Macromolecules*, 33 (2000) 4264.
- [28] G.D. Smith, R.L. Jaffe, and D.Y. Yoon, *J. Phys. Chem.*, 97 (1993) 12752.
- [29] G.D. Smith, O. Borodin, and D. Bedrov, *J. Phys. Chem. A*, 102 (1998) 10318.
- [30] O. Borodin, G.D. Smith, and D. Bedrov, *J. Phys. Chem. B*, 106 (2002) 9912.
- [31] D. Bedrov, M. Pekny, and G.D. Smith, *J. Phys. Chem. B*, 102 (1998) 996; G.D. Smith, O. Borodin, and D. Bedrov, *J. Comp. Chem.*, in press 2003
- [32] O. Borodin, R.L. Bell, Y. Li, D. Bedrov, and G.D. Smith, *Chem. Phys. Lett.*, 336 (2001) 292
- [33] O. Borodin, G.D. Smith, and R.L. Jaffe, *J. Comp. Chem.*, 22 (2001) 641
- [34] G.D. Smith, R.K. Bharadwaj, D. Bedrov, and C. Ayyagari, *J. Phys. Chem. B*, 103 (1999) 705.
- [35] G.D. Smith and R.K. Bharadwaj, *J. Phys. Chem. B*, 103 (1999) 3570.
- [36] D.C. Sorescu, B.M. Rice, and D.L. Thompson, *J. Phys. Chem. B*, 102 (1998) 6692.
- [37] T.D. Sewell, *AIP Conference Proceedings 0094-243X* 429 (1998) 269 .
- [38] R.A. Sorensen, W.B. Liao, K. Kesner, and R.H. Boyd, *Macromolecules*, 21 (1988) 200.
- [39] G.D. Smith, in *Computational Materials research*, Hinkley, J.A. and Gates, T. S. eds., NASA Conference Publication 10190, Williamsburg, Virginia, January 4-5, 1996.
- [40] The MOLBD3 force field is available in the POLYMER module of the SYBYL simulation software of the Tripos Co., St. Louis MO.
- [41] Based upon the basis set dependence of conformational energies in nitramide and DMNA, we estimate the uncertainties in the conformational energies of HMX from the B3LYP/6-311G**//MP2/6-311G** quantum chemistry calculations to be around 1 kcal/mol.
- [42] S. Nose, *J. Chem. Phys.*, 81 (1984) 511.
- [43] J. Ryckaert, G. Ciccotti, and H.J.C. Berendsen, *J. Comp. Phys.* 23 (1977) 327.
- [44] M.P. Allen and D.T. Tildesley, *Computer Simulation of Liquids*, Oxford, NY, 1987.
- [45] M. Mondello and G.S. Grest, *J. Chem. Phys.* 106 (1997) 9327.
- [46] S. Glasstone, K.J. Laidler, and H. Eyring, *The Theory of Rate Processes*, McGraw-Hill, New-York, 1941.
- [47] R. Menikoff and T.D. Sewell, *Combustion Theory and Modeling* 6, (2002) 103.
- [48] J.K. Dienes, "A unified theory of flow, hot spots, and fragmentation with an application to explosive sensitivity," in *High-Pressure Shock Compression of Solids II: Dynamic Fracture and Fragmentation*, L. Davison, D. Grady, and M. Shahinpoor Eds. Springer, New York, 1996.
- [49] C. Hoheisel, in *Transport Properties of Fluids: Their Correlation, Prediction and Estimation*, J. Millat, J.H. Dymond, C.A. Nieto de Castro, eds., Cambridge University Press, N.Y., 1996.
- [50] G. Marechal and J.P. Ryckaert, *Chem. Phys. Lett.*, 101 (1983) 548.
- [51] F. Müller-Plathe, *J. Chem. Phys.* 106 (1997) 6082.
- [52] D. Bedrov and G.D. Smith, *J. Chem. Phys.*, 113 (2000) 8080.

-
- [53] E. McLaughlin, in Thermal Conductivity R.P. Tye ed., vol. 2, Academic Press, NY, 1969.
- [54] D.M. Hanson-Parr and T.P. Parr, J. Energetic Materials 17 (1999) 1.
- [55] M.W. Beckstead, personal communication. Values were obtained by adjusting them to reproduce the experimental thickness of the melt-layer in deflagrating HMX.
- [56] G.J. Martyna, M.E. Tuckerman, D.J. Tobias, and M.L. Klein, Mol. Phys. 87 (1996) 1117.
- [57] M. Parrinello and A. Rahman, A., J. Appl. Phys. 52 (1981) 7182.
- [58] A.V. Dzyabchenko, T.S. Pivina, and E.A. Arnautova, J. Mol. Structure 378 (1996) 67.
- [59] W.C. McCrone, in Physics and Chemistry of the Organic Solid State; D. Fox, D., M.M. Labes, and A. Weissberger, eds., Vol. II, Wiley, NY, 1965.
- [60] M. Herrmann, W. Engel, and N. Eisenreich, Propellants Explosives Polytechnics, 17 (1992) 190.
- [61] M. Herrmann, W. Engel, and N. Eisenreich, Z. Kristall. 204 (1993) 121.
- [62] C.K. Saw, "Kinetics of HMX and Phase Transitions: Effects of Grain Size at Elevated Temperature", to appear in Proceedings of the 12th International Detonation Symposium; August 11-16, 2002; San Diego, CA.
- [63] We note that the linear and volumetric CTEs in Refs.60 and 61 are not self-consistent in that the latter do not follow from the former according to the formal expression (for a monoclinic cell) $\chi_v = \chi_a + \chi_b + \chi_c + (\cos\beta/\sin\beta)\beta\chi_\beta$. The reason for this is that χ_v was determined from a direct fit to the temperature dependent unit cell volume rather than from the linear CTEs (M. Herrmann, private communication). Although the same approach was used here, we obtained self-consistency to the percent level.
- [64] G.D. Smith, D.Y. Yoon, and R.L Jaffe, Macromolecules 26 (1993) 298.
- [65] J.L. Lyman, Y-C. Liau, and H.V. Brand, Combustion and Flame 130 (2002) 185.
- [66] J.M. Rosen and C. Dickinson, J. Chem. & Eng. Data 14 (1969) 120.
- [67] J.W. Taylor, and R.J. Crookes, J. Chem. Soc., Faraday Trans. 72 (1976) 723.
- [68] B. Olinger, B. Roof, and H. Cady, in: Proc. Symposium (Intern.) on High Dynamic Pressures, C.E.A. Paris, France, 1978.
- [69] W.Fickett and W.C.Davis, Detonations, University of California, Berkeley, 1979.
- [70] C.-S. Yoo and H. Cynn, J. Chem. Phys. 111 (1999) 10229.
- [71] J.-P. Poirier, Introduction to the Physics of the Earth's Interior, Cambridge University Press, Cambridge, UK, 1999.
- [72] R. Menikoff and T.D. Sewell, High Press. Res. 21 (2001) 121.
- [73] Menikoff and Sewell (Ref.72) performed the fit to Eq. 23 in the p - V plane by writing $p(V) = af_1(V) + bf_2(V)$ and minimizing the residual $R = \sum (\Delta P)^2 = \sum [P_i - af_1(V_i) - bf_2(V_i)]^2$ with respect to a and b , where $a = K_0$ and $b = K_0 K_0'$.
- [74] D.C. Sorescu, B.M. Rice, and D.L. Thompson, J. Phys. Chem. B 103 (1999) 6783.
- [75] For example, W.W. Wood, in Physics of Simple Fluids, H.N.V. Temperley, J.S. Rowlinson, and G.S. Rushbrooke, eds. North-Holland, Amsterdam, 1968.
- [76] T.D. Sewell, J. Appl. Phys. 83 (1998) 4142.
- [77] B. Olinger, P.M. Halleck, and H.H. Cady, J. Chem. Phys. 62 (1975) 4480.
- [78] Following Menikoff and Sewell (Ref. 72), we ignore the Yoo and Cynn (Ref. 70) data point at 0.20 GPa, since it leads to the aphysical prediction of a non-monotonic U_s - U_p curve.
- [79] B.J. Baer, J. Oxley, and M. Nicol, High. Press. Res. 2 (1990) 99.
- [80] S.P. Marsh (ed.), LASL Shock Hugoniot Data, University of California, Berkeley, 1980.

-
- [81] D.C. Sorescu, private communication.
 - [82] R.B. Evans, J.P. Lewis, T.D. Sewell, R.B. Evans, and G.A. Voth, *J. Phys. Chem. B*, 104 (2000) 1009.
 - [83] M. Parrinello, and A. Rahman, *J. Chem. Phys.* 76 (1982) 2662.
 - [84] S.W. Tsai, *Mechanics of Composite Materials, Part II, Theoretical Aspects*, AFML Tech. Rept. AFML-TR-66-149, November 1966.
 - [85] J.M. Zaug in *Proceedings of the 11th International Detonation Symposium*, J.M.Short, ed., Snowmass Village, CO, 1998.
 - [86] C.-S. Yoo, H. Cynn, W.M. Howard, and N. Holmes, in *Proceedings of the 11th International Detonation Symposium*, J.M.Short, ed., Snowmass Village, CO, 1998.
 - [87] J.J. Dick, A.R. Martinez, and R.S. Hixson, Technical report LA-13426-MS, Los Alamos National Laboratory (1998)
 - [88] J.J. Dick and J.P. Ritchie, *J. Physique IV* 4 (1994) 393.
 - [89] J.J. Dick, *J. Phys. Chem.* 97 (1993) 6193.
 - [90] A.S. Tappan, A.M. Renlund, J.C. Stachowiak, J.C. Miller, and M.S. Oliver, to appear in *Proceedings of the 12th International Detonation Symposium*, San Diego, CA, 2002.

Chapter 11

Optical absorption in PETN and RDX

Warren F. Perger

Electrical Engineering and Physics Depts, Michigan Tech Univ, Houghton,
MI 49931-1295, USA

The theoretical procedure for obtaining optical absorption spectra for PETN and RDX is presented. This procedure utilizes the Crystal [1] program to generate the eigenvalues and eigenvectors of the time-independent problem, then time-dependent perturbation theory to calculate the imaginary part of the complex permittivity which, with the Kramers-Kronig relationship, provides the optical absorption spectrum. The stand-alone computer program, most of which was generated with a computer algebra system to calculate the various matrix elements, is described. The imaginary part of the complex permittivity is calculated for both PETN and RDX, using both Hartree-Fock and density-functional methods. Suggestions for improving optical absorption studies in energetic molecular crystals are given.

1. BACKGROUND

The theoretical prediction of the optical absorption profile of a solid using first-principles methods has produced results in reasonable agreement with experiment for a variety of systems [2-4]. For example, several ionic crystals were studied extensively, generally using the Hartree-Fock one-electron approximation [5], through the extreme-ultraviolet. Lithium fluoride was the focus of a particularly detailed comparison [6-8], providing excellent confirmation of the applicability of the band theory of solids for optical absorption.

It was therefore a natural progression for one of these pioneering investigators, A. B. Kunz, to attempt to extend this approach to energetic materials, specifically RDX ($C_3H_6N_6O_6$, cyclotrimethylene trinitramine) [9,10]. The work described here is a continuation of that effort. RDX has been studied for a variety of properties. X-ray structure factors and bulk modulus have been calculated using the Crystal [1] program as a starting point [11], and with defects [12]. Sewell and Bennett [13,14] used a Monte

Carlo approach to calculate the physical and mechanical properties of RDX. Rice and Chabalowski used a density function theory (DFT) and second-order Moller-Plesset (MP2) for geometry optimization and normal-mode analyzes of the RDX molecule. For the solid state, with improvements in computer hardware and software, the basis sets employed can now be more robust while simultaneously improving correlation which has been shown to improve the band gaps with respect to experiment [15]. In spite of the rapid progress in computational power, energetic materials still pose a formidable challenge due to the hundreds of electrons often required in a unit cell. In RDX, for example, the unit cell has 168 atoms, 912 electrons, and over a thousand orbitals for even a simple basis set. This issue represents a serious computational and theoretical challenge, forcing difficult choices in approximations on the theoretical side and placing a premium on the judicious choice of computational tactics which do not compromise the quality of the final result, in this case the optical absorption profile.

2. THE APPROACH

The formal approach used in this work is based on the seminal work of Ehrenreich and Cohen [16], with other excellent, more modern, expositions available [17,18]. The strategy employed here is to utilize the well-known capabilities of the Crystal [1] program in order to generate the eigenvectors and energy eigenvalues necessary for a stand-alone program which, after picking up these eigenvectors and eigenvalues, calculates the relevant matrix elements for an optical transition, then sorts these according to energy of the incoming photon, resulting in an optical absorption spectrum.

2.1 Optical absorption and the use of Crystal program

When an electromagnetic wave, described by an electric field, \mathbf{E} , impinges on a material, the absorption of the electromagnetic wave as a function of z behaves as $|\mathbf{E}| \sim \exp^{-az/2}$, so the intensity falls off as $I \sim \exp^{-az}$. The immediate goal is to relate this classical absorption coefficient, α , which is the quantity of experimental interest, to the theory, wherein the quantum-mechanical mechanism responsible for absorbing a photon of a given frequency is found. To do this, α is defined as: [18]

$$\alpha \equiv \frac{\text{Power absorbed per volume}}{\text{Incident power per area}} \quad (1)$$

or:

$$\alpha = \frac{\hbar\omega W(\omega)}{\frac{1}{2}v\epsilon_r\epsilon_o |\mathbf{E}|^2} \quad (2)$$

where v is the velocity of the electromagnetic wave in the medium, $\frac{1}{2}\epsilon_r\epsilon_o|\mathbf{E}|^2$ is the energy per volume of the classical electromagnetic field, and $W(\omega)$ is the number of photons absorbed per unit volume per unit time (so that $\hbar\omega W(\omega)$ is the total power absorbed per volume). The frequency-dependent complex permittivity is defined as:

$$\epsilon_r(\omega) \equiv \epsilon_1(\omega) + i\epsilon_2(\omega) \quad (3)$$

The real and imaginary parts of Eq. (3) are related by the Kramers-Kronig relationship [19]:

$$\begin{aligned} \epsilon_1(\omega) &= 1 + \frac{2}{\pi} PV \int_0^\infty \frac{\omega' \epsilon_2(\omega')}{\omega'^2 - \omega^2} d\omega' \\ \epsilon_2(\omega) &= -\frac{2\omega}{\pi} PV \int_0^\infty \frac{\epsilon_1(\omega') - 1}{\omega'^2 - \omega^2} d\omega' \end{aligned} \quad (4)$$

In optics, the complex refractive index is defined as $N = n + ik = (\epsilon_r(\omega))^{1/2}$, where the real index of refraction, n , and extinction coefficient, k , are related to the real and imaginary parts of the complex dielectric constant by:

$$\epsilon_1(\omega) = n^2 - k^2 \text{ and } \epsilon_2(\omega) = 2nk. \quad (5)$$

A plane wave propagating in the z -direction would therefore have an electric field given by:

$$\begin{aligned} \mathbf{E} &= \mathbf{e} E_o e^{N \frac{\omega}{c} z - i\omega t} \\ &= \mathbf{e} E_o e^{-\frac{\alpha k}{c} z} e^{i(\frac{\omega}{c} z - \omega t)} \end{aligned} \quad (6)$$

where \mathbf{e} is the polarization vector and the absorption coefficient is given by the decaying exponential term in Eq. (6):

$$\alpha = 2 \frac{\omega k}{c}. \quad (7)$$

Because the magnetic vector potential, \mathbf{A} , is more naturally suited for including in the quantum-mechanical Hamiltonian [20, vII, pg 15-8], the incident light is represented mathematically by the magnetic vector potential:

$$\mathbf{A}(\mathbf{r}, t) = \mathbf{e} A_o e^{i(N\omega z/c - \omega t)} + c.c. \quad (8)$$

The electric field is then related to the magnetic vector potential by:

$$\mathbf{E} = -\frac{\partial \mathbf{A}}{\partial t}. \quad (9)$$

Combining Eqs. (2), (8), and (9) into Eq. (7) gives:

$$\alpha = \frac{2\hbar}{\varepsilon_o n c \omega A_o^2} W(\omega), \quad (10)$$

From Eqs. (5), (7), and (10),

$$\varepsilon_2 = \frac{2\hbar}{\varepsilon_o \omega^2 A_o^2} W(\omega). \quad (11)$$

Eq. (11) is now in a form of constants, the photon frequency, ω , and $W(\omega)$, the number of photons absorbed per unit time per unit volume. The typical procedure is to calculate $\varepsilon_2(\omega)$, then $\varepsilon_1(\omega)$ via Eq. (4), and finally $\alpha(\omega)$ by taking the real part of $N = \text{Re}[(\varepsilon_1(\omega) + i\varepsilon_2(\omega))^{1/2}]$.

In order to obtain the function $W(\omega)$, the time-dependent Schrödinger equation is used:

$$\left[\frac{1}{2m} \left(\mathbf{p} + \frac{e}{c} \mathbf{A} \right)^2 + V(\mathbf{r}) \right] \Psi(\mathbf{r}, t) = i\hbar \frac{\partial \Psi(\mathbf{r}, t)}{\partial t}, \quad (12)$$

where the information about the incoming photon field is provided by \mathbf{A} . The Hamiltonian in Eq. (12) is split into the unperturbed part, H_o , and the time-dependent perturbation, H' : [21]

$$H = H_o(\mathbf{r}) + H' = H_o(\mathbf{r}) + \frac{e}{mc} \mathbf{p} \cdot \mathbf{A}, \quad (13)$$

neglecting the effects of the small A^2 term. The wavefunction of Eq. (12) can be represented as a product of a position-dependent part and a time-dependent part:

$$\Psi(\mathbf{r}, t) = \sum_{\mathbf{n}\mathbf{k}} a_n(\mathbf{k}, t) \exp\left(-\frac{i}{\hbar} E_n(\mathbf{k})t\right) \psi_n(\mathbf{k}, \mathbf{r}). \quad (14)$$

In Eq. (14), the position-dependent wavefunctions, $\psi_n(\mathbf{k}, \mathbf{r})$, and the eigenvalues, E_n , are both obtained from the unperturbed, time-independent problem:

$$H_o \psi_n(\mathbf{k}, \mathbf{r}) = E_n \psi_n(\mathbf{k}, \mathbf{r}). \quad (15)$$

The coefficients a_n in Eq. (14) are found by substitution of Eq. (14) into Eq. (12), multiplying from the left by $\exp[(i/\hbar)E_m(\mathbf{k}')t] \psi_m^*(\mathbf{k}')$ and integrating over all space yielding: [22]

$$\frac{da_m(\mathbf{k}', t)}{dt} = \frac{1}{i\hbar} \sum_{\mathbf{n}\mathbf{k}} a_n(\mathbf{k}, t) \exp\left(\frac{i}{\hbar} [E_m(\mathbf{k}') - E_n(\mathbf{k})]t\right) \langle m, \mathbf{k}' | H' | n, \mathbf{k} \rangle \quad (16)$$

where the notation $\langle m | H' | n \rangle$ is understood to represent an integration of states m , and n and the operator, H' , over all space. The procedure to find

these time-dependent coefficients is to set $a_j(t=0)=1$ and all other $a_n(t=0)=0$, then assume that the electron undergoing excitation is in the j th band described by Eq. (12) [22]. The probability, $W(j, j', \omega, t)$, that at time t the electron will be in the state ψ_i is then $|a_i(t)|^2$. After integration over the Wigner-Seitz cells, this leads to [18]:

$$W(j, j', \omega, t) = \frac{e^2 A_0^2}{m^2} |M_{jj'}|^2 2\pi \hbar t \delta(E_{j'} - E_j - \hbar \omega). \quad (17)$$

The total number of transitions per unit volume and time from Eq. (17) is obtained by dividing by t and summing over j (occupied bands) and j' (unoccupied bands). Integrating over the Brillouin zone gives:

$$W(\omega) = \sum_{jj'} \frac{2}{t(2\pi)^3} \int W(j, j', \omega, t) d\tau. \quad (18)$$

This produces the desired result for the imaginary part of the dielectric constant in Eq. (5):

$$\varepsilon_2 = \frac{4\pi e^2 \hbar^2}{\varepsilon_0 m^2 \omega^2} \sum_{jj'} \frac{2}{(2\pi)^3} \int |\langle j' | \mathbf{e} \cdot \nabla | j \rangle|^2 \delta(E_{j'} - E_j - \hbar \omega) d\tau \quad (19)$$

Defining the joint density of states, $g_{jj'}(\omega)$, as the number of pairs of states in bands j and j' separated by energy, $\hbar \omega$, one obtains:

$$\varepsilon_2 = \frac{4\pi e^2 \hbar^2}{\varepsilon_0 m^2 \omega^2} \sum_{jj'} \frac{2}{(2\pi)^3} |\langle j' | \mathbf{e} \cdot \nabla | j \rangle|^2 g_{jj'}(\omega). \quad (20)$$

2.2 Computational procedure

The first computational consideration is that of obtaining the solutions of the unperturbed problem, Eq. (15), and the approach taken in the present study is to utilize the Crystal program [1] as it has been successfully used for studies in molecular crystals [10-12,15]. A given crystalline orbital, $\psi_n(\mathbf{k}, \mathbf{r})$, such as that required for the matrix elements necessary given by the integral in Eq. (16), is expressed as a linear combination of Bloch functions, $a_{\mu,i}(\mathbf{k})$ and atomic orbitals, $\phi_\mu(\mathbf{k}, \mathbf{r})$: [1]

$$\psi_i(\mathbf{k}, \mathbf{r}) = \sum_{\mu} a_{\mu,i}(\mathbf{k}) \phi_{\mu}(\mathbf{k}, \mathbf{r}) \quad (21)$$

$$\phi_{\mu}(\mathbf{k}, \mathbf{r}) = \sum_{\mathbf{g}} \zeta_{\mu}(\mathbf{r} - \mathbf{A}_{\mu} - \mathbf{g}) e^{i\mathbf{k} \cdot \mathbf{g}}. \quad (22)$$

The local functions, $\zeta_\mu(\mathbf{k}, \mathbf{r})$ are in turn defined by a linear combination of n_G Gaussian-type orbitals (GTO's):

$$\zeta_\mu(\mathbf{r} - \mathbf{A}_\mu - \mathbf{g}) = \sum_j^{n_G} d_j G(\alpha_j; \mathbf{r} - \mathbf{A}_\mu - \mathbf{g}). \quad (23)$$

An examination of Eq. (20) and Eqs. (21)-(23) indicates that a large number of integrals involving GTO's of various symmetries must be taken. To accomplish this, the computer algebra system, MAPLE, was used to symbolically generate the analytic expressions for these matrix element integrals, then Fortran code was created directly from these MAPLE expressions, resulting in syntactically-correct and efficient Fortran subroutines. These subroutines were then compiled and linked as a part of a stand-alone program. This program was written to operate as a "back-end" to the Crystal program. That is, the sequence of steps is to prepare the appropriate Crystal input file, including a request for writing onto a file the eigenvalues and eigenvectors over \mathbf{k} -space, then run the Crystal program, followed by a run of this stand-alone program which automatically reads in the relevant information of the Gaussian basis set orbital parameters, eigenvalues, and eigenvectors, assembling the terms of Eq. (20). This approach has proven to produce efficient, error-free, code capable of producing optical absorption spectra.

3. RESULTS FOR PETN AND RDX

PETN, $[C(CH_2ONO_2)_4]$ is a molecular crystal with 29 atoms per molecule, with two molecules per unit cell, and belongs to the tetragonal $P\bar{4}2_1c$ space group. The internal co-ordinates used were from Kitaigorodskii [23]. RDX, $[(CH_2NNO_2)_3]$ has 21 atoms per molecule, 8 molecules per unit cell, and belongs to the orthorhombic $Pbca$ space group, with internal co-ordinates from Choi and Prince [24]. This results in 1176 atomic orbitals for the 168 atoms per unit cell and for this size of a system, it becomes especially important to utilize efficient numerical techniques and accurate physical models in order to obtain results in a reasonable time-frame.

Once the geometry data is chosen, the next, very important, step is to choose the basis set. The Crystal program offers the choice of Slater-type orbitals (STO's) or GTO's, with the latter being chosen for reasons of simpler calculation of the two-electron integrals [25]. A Gaussian basis set was chosen, a $s(6)sp(2)sp(1)$ set for the carbon, nitrogen, and oxygen atoms and a $s(2)s(1)$ set for the hydrogen atom ("6-21G"), as it had been successfully used previously for RDX [11,15] and PETN [15].

The last requirement is to choose a potential which retains effects of exchange and correlation, while still being efficient and practical for solving the Schrödinger equation. Because prior work has shown an improved bandgap using density-functional theory (DFT) and, in particular, the B3LYP hybrid potential [15,26], this approach was chosen for the optical absorption spectra of PETN and RDX in addition to the more common Hartree-Fock potential. The B3LYP potential has the form:

$$E_{xc} = E_{xc}^{LSDA} + 0.2(E_{xc}^{Fock} - E_{xc}^{LSDA}) + 0.72\Delta E_{xc}^{GGA}, \quad (24)$$

where *LSDA* is the local spin-density approximation and *GGA* is the generalized gradient approximation and the parameters were determined by Becke [27] to optimize atomization energies, ionization potentials, and proton affinities were several molecules. The B3LYP hybrid functional combines Becke's three-parameter functional [27] for the exchange with the non-local correlation potential of Lee-Yang-Parr [28]. The Crystal98 [1] program explicitly evaluates the non-local Fock energy, then blends 20% of that value into the hybrid functional, as shown in Eq. (24).

3.1 PETN

For PETN, the joint-density of states (JDOS), $g_{jj}(\omega)$, of Eq. (20) is plotted in Fig. 1 for the Hartree-Fock (HF) potential, with $\varepsilon_2(\omega)$ given in Fig. 2. As can be observed from those two figures, the HF potential produces a bandgap of over 14eV, and optical absorption edge is found there. Although the JDOS increases with energies above the optical bandgap, the optical absorption decreases, due in part to the $1/\omega^2$ term in Eq. (20), and due also to the matrix elements present.

3.2 RDX

The experimental value of the optical bandgap for RDX is 3.4eV [29], well below the HF value of about 14eV shown in Fig. 5 or 6. Figs. 7 and 8, obtained from a DFT-B3LYP potential, exhibit the same trend of a substantial narrowing of the optical bandgap, as was shown for PETN; the DFT-B3LYP value of 5.5eV is considerably closer to the experimental value. In the absence of experimental data with which to compare, the ε_2 absorption spectra is in acceptable agreement with the preliminary work of Zwitter, *et al.* [9].

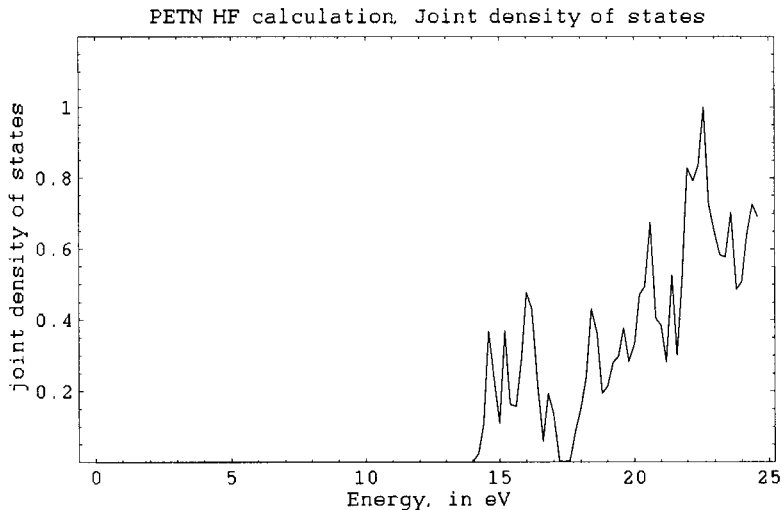


Figure 1 Joint density of states for PETN using HF approximation, as a function of energy.

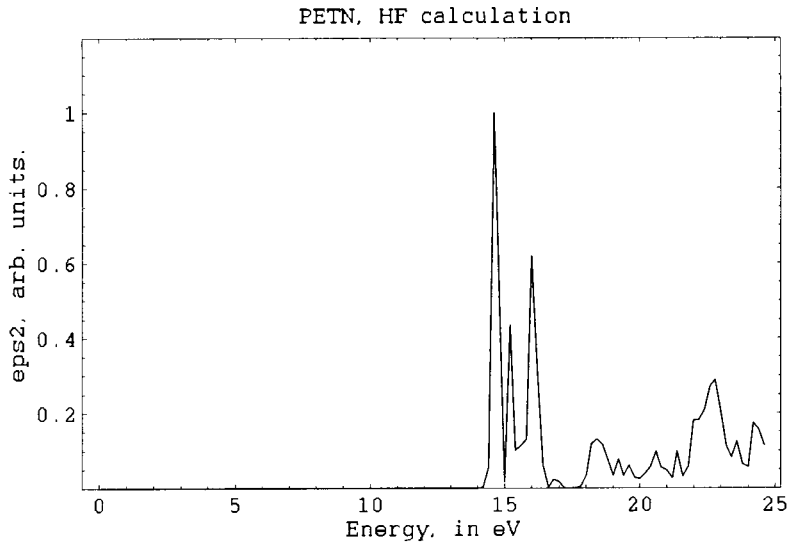


Figure 2 Imaginary part of the complex permittivity for PETN, using the Hartree-Fock approximation, as a function of energy.

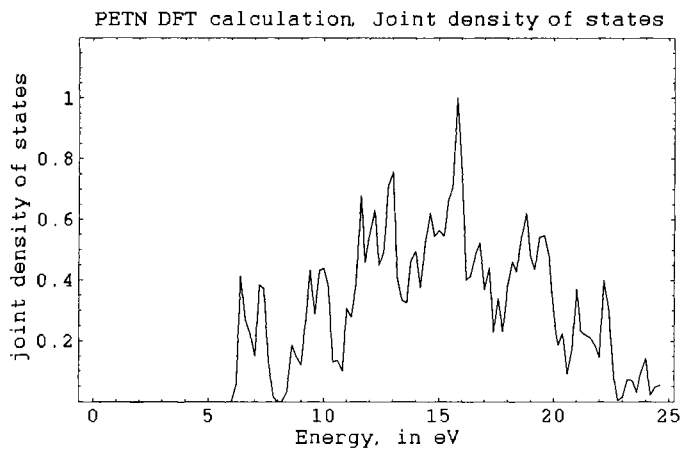


Figure 3 Joint density of states for PETN using DFT-B3LYP approximation, as a function of energy.

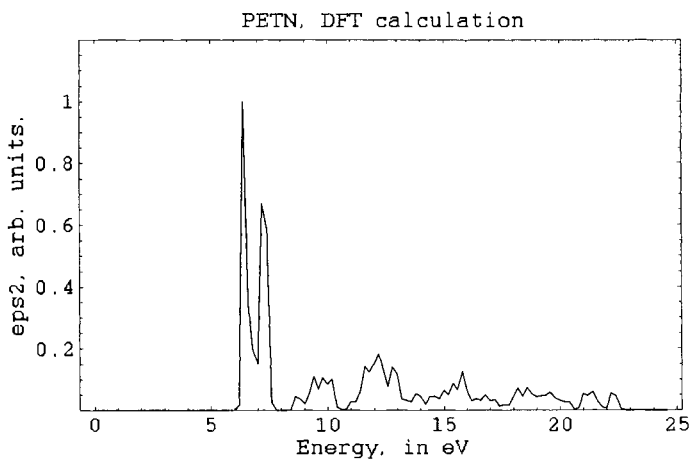


Figure 4 Imaginary part of the complex permittivity for PETN, using the DFT-B3LYP approximation, as a function of energy.

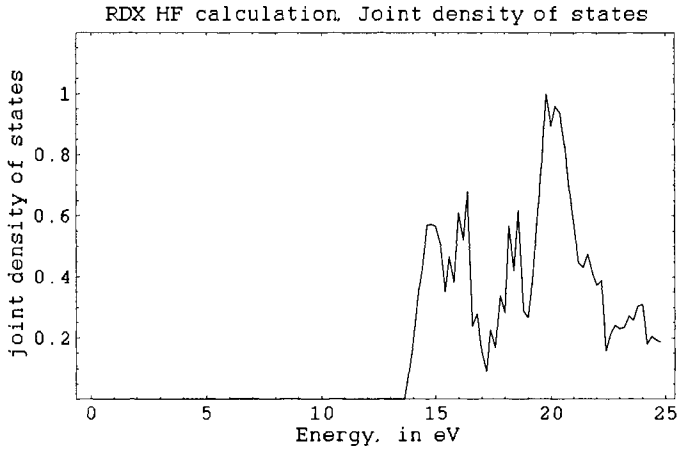


Figure 5 Joint density of states for RDX using the Hartree-Fock approximation, as a function of energy.

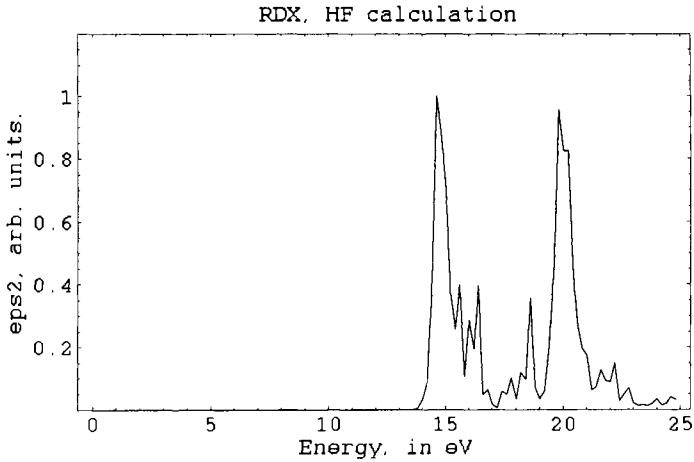


Figure 6 Imaginary part of the complex permittivity for RDX, using the Hartree-Fock approximation, as a function of energy.

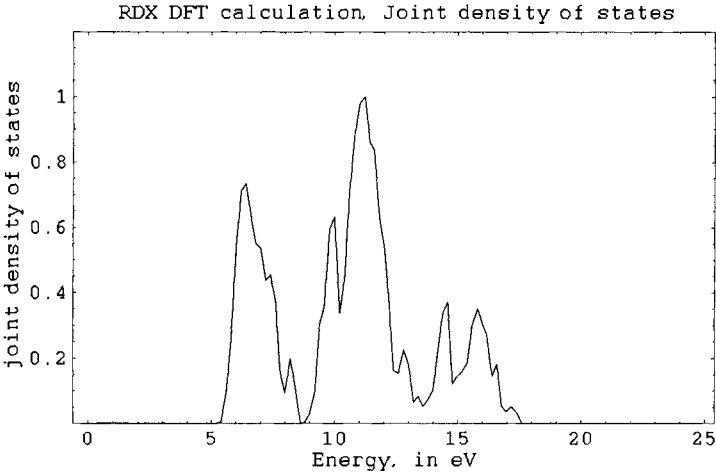


Figure 7 Joint density of states for RDX using DFT-B3LYP approximation as a function of energy.

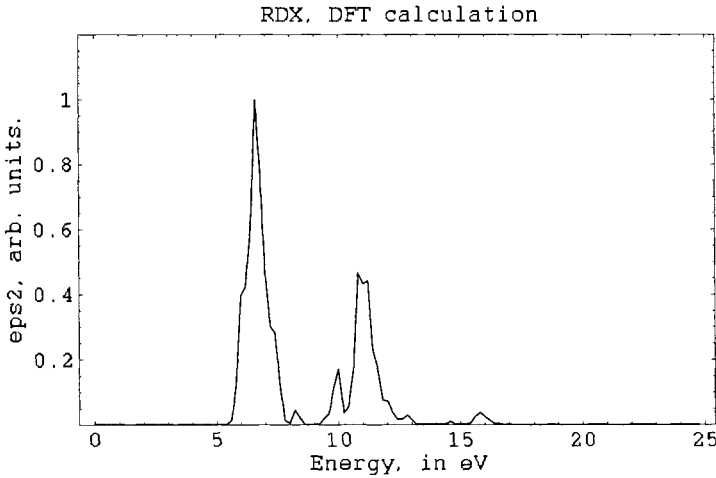


Figure 8 Imaginary part of the complex permittivity for RDX, using the DFT-B3LYP approximation, as a function of energy.

4. CONCLUSIONS AND FUTURE WORK

The topic of optical absorption in energetic materials has room for improvement in at least two distinct areas: “technological” and theoretical advances and, in some sense, the two cannot be cleanly separated. On the technological side has been, until recently, the lack of adequate computational power, in the form of memory, disk storage, and CPU speed. Using a 6-311G* Gaussian basis set, for example, for PETN requires tens of Gigabytes of disk storage for just the bi-electronic integrals, which is now readily achievable on an inexpensive Linux machine. The basis set chosen, which is at the heart of accurately representing the quantum-mechanical wavefunction, while an important consideration, is now more-or-less a problem with a technological solution, and much is now understood about both Gaussian and plane-wave basis sets [25]. The use of *ab initio* methods for the calculation of important properties of energetic crystals is admittedly in a primitive state relative to, for example, the quantum chemistry of the constituent molecules. However, a reasonable approach for solving the solid-state problems would seem to be to utilize as much as possible from the corresponding quantum chemistry. For example, the development of high-quality basis sets and correlation techniques, employed in quantum chemistry for over a decade, can be applied to the subject of molecular crystals, owing to the fact that the intra-molecular bonds are typically much stronger than the intermolecular crystalline field.

On the theoretical side, regarding correlation, as discussed by Fulde [30], the Hartree-Fock approximation is often adequate for cases where the correlation is not strong, and molecular crystals could generally fit this description, but certainly continued effort for improving correlation in molecular crystals will benefit the associated properties, such as optical absorption. A separate issue concerns the fact that although there is strong historical evidence, cited at the beginning of this chapter, supporting the model for optical absorption presented here, it is important to realize that optical absorption is inherently a time-dependent process, and a rigorous excited-state treatment is warranted, an effort that has only recently received much attention [8]. Emerging as a viable approach is the Green’s function method and could, in principle, be applied to optical absorption studies in energetic molecular crystals.

ACKNOWLEDGMENTS

The author is deeply indebted to Dr. A. Barry Kunz, who initiated this project and co-authored the first generation of the computer program used in this study, prior to his death in February, 2001. The author also gratefully acknowledges the efforts of Ms. D. Zwitter. Finally, the author would like to acknowledge the financial support of the US Office of Naval Research (MURI program) for this work and the extended visits at and collaboration with the Institute for Shock Physics, Washington State University, where Dr. Y. Gupta, *et al.*, provided motivation for this work.

REFERENCES

- [1] V. R. Saunders, R. Dovesi, C. Roetti, M. Causa, N. M. Harrison, R. Orlando, C. M. Zicovich-Wilson, CRYSTAL98 User's Manual, University of Torino, Torino, Italy, 1998.
- [2] R. C. Chaney, E. E. Lafon, C. C. Lin, Phys. Rev. B. 4 (1971) 2734.
- [3] R. C. Chaney, C. C. Lin, E. E. Lafon, Phys. Rev. B. 3 (1971) 459.
- [4] J. Callaway, C. S. Wang, Phys. Rev. B. 7 (1973) 1096.
- [5] F. C. Brown, C. Gahwiller, H. Fajita, A. B. Kunz, W. Schiefly, N. Carrera, Phys. Rev. B. 2 (6) (1970) 2126-2138.
- [6] W. P. Menzel, C. C. Lin, D. F. Fouquet, E. E. Lafon, R. Chaney, Phys. Rev. Lett. 30 (26) (1973) 1313-1315.
- [7] D. J. Mickish, A. B. Kunz, T. C. Collins, Phys. Rev. B. 9 (10) (1974) 4461-4467.
- [8] R. Rohlfing, S. G. Louie, "Quasiparticle and optical excitations in solids and clusters," in: A. Gonis, N. Kioussis, N. Ciftan (Eds.), Electron Correlations and Materials Properties, Kluwer Academic/Plenum Publishers, New York, 1999, pp. 309-328.
- [9] D. E. Zwitter, M. M. Kuklja, and A. B. Kunz, "A computation of the frequency dependent dielectric function for energetic materials," in: M. D. Furnish, L. C. Chhabildas, R. S. Hixson (Eds.), Shock Compression of Condensed Matter, American Physical Society, Snowbird, UT, 2000, pp. 405-408.
- [10] M. M. Kuklja, A. B. Kunz, J. Appl. Phys. 89 (9) (2001) 4962-4970.
- [11] A. B. Kunz, Phys. Rev. B. 53 (15) (1996) 9733-9738.
- [12] M. M. Kuklja, A. B. Kunz, J. Appl. Phys. 86 (8) (1999) 4428-4434.
- [13] T. D. Sewell, J. Appl. Phys. 83 (8) (1998) 4142-4145.
- [14] T. D. Sewell, C. M. Bennett, J. Appl. Phys. 88 (1) (2000) 88-95.
- [15] W. F. Perger, Chem. Phys. Lett. 368/3-4 (2003) 319-323.

- [16] H. Ehrenreich, M. H. Cohen, *Phys. Rev.* 115 (4) (1959) 786-790.
- [17] F. Wooten, *Optical Properties of Solids*, Academic Press, New York, 1972.
- [18] O. Madelung, *Introduction to Solid-State Theory*, Springer-Verlag, Berlin, 1978.
- [19] J. D. Jackson, *Classical Electrodynamics*, 3rd Edition, John Wiley and Sons, New York, 1999.
- [20] R. P. Feynman, R. B. Leighton, M. Sands, *The Feynman Lectures on Physics*, California Institute of Technology, Pasadena, CA, 1964.
- [21] A. S. Davydov, *Quantum Mechanics*, 2nd Edition, Pergamon Press, Oxford, 1976.
- [22] L. I. Schiff, *Quantum Mechanics*, McGraw-Hill Publishing Company, New York, 1968.
- [23] A. I. Kitaigorodskii, *Organic Chemical Crystallography*, Constants Bureau Enterprises, New York, 1961.
- [24] C. S. Choi, *Acta Cryst. B* 28 (1972) 2857-2862.
- [25] C. Pisani, *Ab initio approaches to the quantum-mechanical treatment of periodic systems*, in: C. Pisani (Ed.), *Lecture Notes in Chemistry*, Springer-Verlag, Berlin, 1996, pp. 47-75.
- [26] J. Muscat, A. Wander, N. M. Harrison, *Chem. Phys. Lett.* 342 (2001) 397-401.
- [27] A. D. Becke, *J. Chem. Phys.* 98 (1993) 5648-5652.
- [28] C. Lee, W. Yang, R. G. Parr, *Phys. Rev. B.* 37 (1988) 785.
- [29] P. L. Marinkas, *J. Lumin.* 15 (1977) 57.
- [30] P. Fulde, *Electron Correlations in Molecules and Solids*, Springer-Verlag, Berlin, 1991.

Chapter 12

Interactions of model organic species and explosives with clay minerals

A. Michalkova^{a,b}, L. Gorb^b and J. Leszczynski^b

^aInstitute of Inorganic Chemistry, Slovak Academy of Sciences, Dubravská Cesta 9, 842 36 Bratislava, Slovak Republic

^bComputational Center for Molecular Structure and Interactions, Department of Chemistry, Jackson State University, 1400 J. R. Lynch Street, P. O. Box 17910, Jackson, MS 39217, USA

1. INTRODUCTION

Energetic materials are important not only because of their obvious technological applications as explosives and propellants, but also for their inherently interesting molecular properties. In addition, many energetic compounds are also used in the synthesis of fungicides, insecticides, herbicides, pharmaceuticals, and dyes. Energetic materials, by their very nature, are metastable and will decompose at some rate under every condition. Therefore, the properties of energetic materials are controlled by reaction kinetics. These materials are susceptible to initiation, or self-sustained energy release, when present in sufficient quantities and exposed to stimuli such as heat, shock, friction, chemical incompatibility, or electrostatic discharge. Each of these materials reacts differently to the aforementioned stimuli; all will burn, but explosives and propellants can detonate under certain conditions (e.g., confinement) [1].

Explosives are classified as primary or secondary, based on their susceptibility to initiation. Primary explosives, which include lead azide and lead styphnate, are highly susceptible to initiation. Primary explosives often are referred to as initiating explosives because they can be used to ignite secondary explosives. Secondary explosives, which include 2,4,6-trinitrotoluene (TNT), hexahydro-1,3,5-trinitro-1,3,5-triazine (RDX or cyclonite), high melting explosives (HMX) like octahydro-1,3,5,7-tetranitro-1,3,5,7-tetrazine (HMX),

and N-methyl-N,2,4,6-tetranitroaniline (tetryl), are much more prevalent at military sites than are primary explosives. Because they are formulated to detonate only under specific circumstances, secondary explosives often are used as main charge or bolstering explosives. Secondary explosives can be loosely categorized into melt-pour explosives, which are based on TNT, and plastic-bonded explosives (PBX), which are based on a binder and a crystalline explosive such as RDX. Secondary explosives also can be classified according to their chemical structure as: 1. nitroaromatics (TNT, 2,4-dinitrotoluene (2,4-DNT), 2,4,6-trinitrophenol (picric acid, ammonium picrate), tetryl); 2. nitrate esters (nitroglycerine (glycerol trinitrate), nitrocellulose, propylene-, diethylene- and triethylene-glycol dinitrates, trimethylolethane trinitrate, hydroxylammonium-, trimethylammonium-, isopropylammonium, triethanolammonium-nitrates, triaminoguanidine nitrate, pentaerythritol tetranitrate (PETN)); 3. nitramines (RDX (NO_2 groups in the RDX molecule are bonded to nitrogens) and N-acetylated RDX, HMX and N-acetylated HMX, nitroguanidine) [2].

Propellants include both rocket and gun propellants. Most rocket propellants are either Hazard Class 1.3 composites, which are based on a rubber binder, and ammonium perchlorate (AP) oxidizer, and a powdered aluminum (Al) fuel; or Hazard Class 1.1 composites, which are based on a nitrate ester, usually nitroglycerine (NG), nitrocellulose (NC), HMX, AP, or polymer-bound NC. If a binder is used, it usually is an isocyanate-cured polyester or polyether. Some propellants contain combustion modifiers, such as lead oxide.

Gun propellants usually are single base (NC), double base (NC and NG), or triple base (NC, NG, and nitroguanidine (NQ)). Some of the newer, lower vulnerability gun propellants contain binders and crystalline explosives and thus are similar to PBX.

Pyrotechnics include illuminating flares, signaling flares, colored and white smoke generators, tracers, incendiary delays, fuses, and photo-flash compounds. Pyrotechnics usually are composed of an inorganic oxidizer and metal powder in a binder. Illuminating flares contain sodium nitrate, magnesium, and a binder. Signaling flares contain barium, strontium, or other metal nitrates [1].

The most studied kinds of explosives are nitroaromatic explosives and their metabolites. Therefore, the emphasis of this review is on properties of nitroaromatic explosives, rather than propellants, pyrotechnics, or munitions, and their interactions with soils. Nitroaromatic explosives are toxic, and their environmental transformation products, including arylamines, arylhydroxylamines, and condensed products such azoxy- and azo-compounds, are equally or more toxic than the parent nitroaromatic [3]. Aromatic amines and hydroxylamines are implicated as carcinogenic intermediates as a result of nitrenium ions formed by enzymatic oxidation [4]. Aromatic nitro compounds

are resistant to chemical or biological oxidation and to hydrolysis because of their electron-withdrawing nitro groups [5]. Consequently, they are environmentally persistent, and remediation of waste streams and contaminated ground water is difficult. In addition, TNT has very low mobility once adsorbed to soil [6].

Nitroaromatic explosives are found as contaminants in sludges, soils, surfaces and ground waters. The production and use of nitroaromatic explosives for military operations have resulted in their dissemination into the environment, where their presence in waterways and soil poses an ecological and health hazard. Many US Department of Army and other Department of Defense (DoD) installations have soil, sediment, surface water, and ground water contaminated with nitroaromatic explosives. Environmental contamination by nitro compounds is a problem because of the scale on which explosives have been manufactured, used, and tested. Contamination by TNT, RDX, and HMX explosives is often associated with explosives manufacturing and with loading, assembling, and packing of explosives into munitions items [7]. The United States DoD has identified that >95% of all contaminated sites with energetic compounds are contaminated with TNT and 87% exceeded permissible ground water contaminant levels [8]. U. S. Army Environmental Center (USAEC) has developed protocols for identifying sites that require explosives safety precautions and for handling explosives wastes at these sites. Under its current protocol, USAEC can determine quickly and inexpensively whether materials are susceptible to initiation and propagation by analyzing the composition of samples from the site [1].

1.1 Interactions of energetic materials with soils

The most polluted soils were contaminated many years ago. The problem of pollution of soils caused a widespread concern regarding environmental deterioration, and strict regulations were established. However, the high cost of remediation becomes evident. Nevertheless, assessments of the hazards from those sites have not taken into account slow processes that may take place and possibly reduce the impact of toxic compounds deposited in the soil, particularly those compounds that do not leach out to contaminate underlying aquifers. It was known that soils could be used as adsorbents and catalysts in various industrial applications such as purification and recycling of water systems, disposal of heavy metals and radioactive elements from water and soils and many others [9-12]. Unique properties such as being widespread in the earth and having high adsorption and catalytic ability have resulted in the use of natural adsorbents in the development of clean-up technologies. Therefore, in recent years, evidence has accumulated that the availability of certain organic

compounds changes as the compounds reside in soil for some time. Data have also been collected suggesting that organic molecules slowly become sequestered within the soil matrix. The declining availability and sequestration appear to be related, and a consideration of the declining bioavailability and the occurrence of chemical sequestration have great relevance to assessing toxicity, determining risk, and establishing meaningful regulations for the cleanup of sites containing hazardous wastes. Such findings suggest that the hazard and risk from toxic chemicals diminish as the compounds persist in soil. These findings lead to the fact that soils are currently being considered for remediation for organic energetic compounds [13].

For an accurate prediction of the fates of organic pollutants in the environment (e.g. long-term sequestering, chemical transformation, complexation, release to groundwater, etc.), or to design effective remediation strategies, it is important to have a fundamental knowledge of the chemico-physical behaviors of energetic organic molecules in soil. One potentially valuable aspect of understanding this fundamental behavior and, we believe, a valuable property for characterizing the environmental fate of organic energetic compounds is the detailed study of interactions of these compounds with soils. Therefore, the fundamental chemistry controlling these interactions should be understood in order to develop the best strategy in the management of contaminated soils and sediments. Remediation and risk management of contaminated sites requires knowledge of the fate and transport of energetic materials and their transformation products in the environment.

In general, soil is an unconsolidated combination of inorganic and organic materials. The inorganic components of soil are principally the products of rocks and minerals that have been gradually broken down by weather, chemical action, and other natural processes. Soil particles, also known as soil separates, are divided into three main size groups: sand, silt, and clay minerals [14].

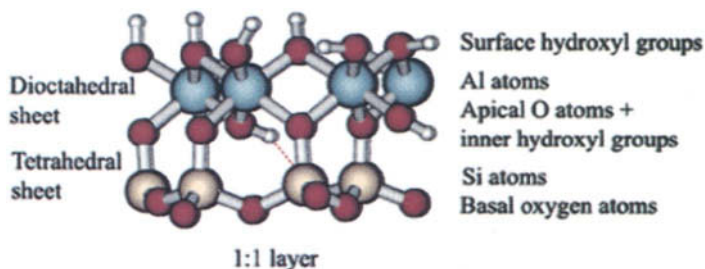


Fig. 1 The part of 1:1 layer of clay minerals, which contains one tetrahedral and one octahedral sheet (concretely dioctahedral sheet).

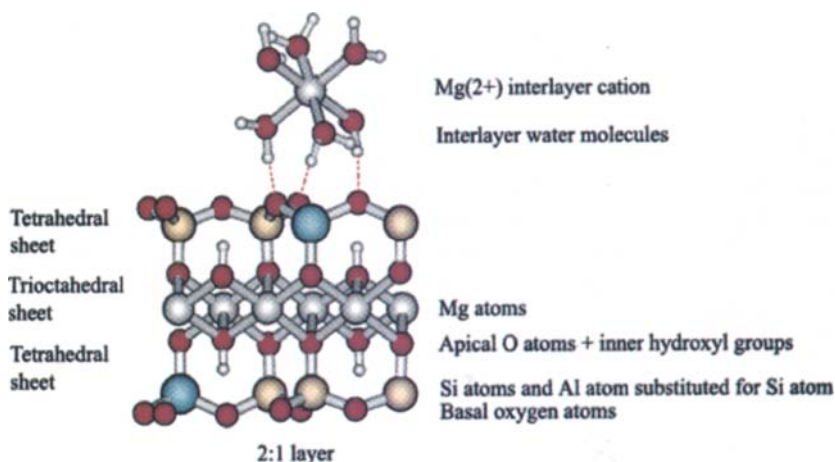


Fig. 2 The part of 2:1 layer of clay minerals with one octahedral sheet (concretely trioctahedral) between two tetrahedral sheets with exchangeable Mg^{2+} cation and interlayer water molecules.

Clay minerals are crystalline, hydrous aluminosilicates with layered structures. Figs. 1 and 2 illustrate the part of 1:1 and 2:1 layer of clay minerals with exchangeable cation and interlayer water molecules (in the case 2:1 layer). An individual layer consists of two connected sheets – a tetrahedral sheet formed from T_2O_5 tetrahedra sharing corners (the basal oxygens) (T-tetrahedral cation, normally Si^{4+} , Al^{3+} or Fe^{3+}) and an octahedral sheet consisting of MO_6 octahedra sharing edges (M-octahedral cation, normally Mg^{2+} , Al^{3+} , Fe^{2+} and Fe^{3+}). The common plane between the tetrahedral and octahedral sheets consists of the shared apical oxygens and unshared OH groups (see Figs. 1, 2). The smallest structural unit contains three octahedra. If all three octahedra are occupied (possess three cations in their centers) the sheet is classified as trioctahedral. If only two octahedra are occupied and the third octahedron is vacant, the sheet is classified as dioctahedral [15]. Depending how the tetrahedral and octahedral sheets are connected, the clays are subdivided into groups according to the structural types (1:1, 2:1, 2:1:1 clay minerals, etc.) (see Figs. 1, 2). The structure of the clay minerals described above is idealized and practically never exists in nature. Most of the clay minerals have extremely defective structures because of the isomeric substitution of the Mg atoms for the Al atoms (octahedrons) and the Al atoms for the Si atoms (tetrahedrons) [11, 12, 16-18]. The negative charge of the lattice that appears as result of isomeric substitution is compensated by exchangeable cations (Li^+ , Na^+ , K^+ , etc.) which in the case of dehydrated clays are located mainly in the ditrigonal cavities of the clay's basal plane [19].

Minerals of the kaolinite group (typical representatives are kaolinite and dickite) have a 1:1 dioctahedral structure with a common chemical formula $\text{Al}_2\text{Si}_2\text{O}_5(\text{OH})_4$. Dickite and kaolinite differ in the layer stacking. The unit cell of dickite consists of two kaolinite layers and is twice as large as the unit cell of kaolinite. The tetrahedral side of the layer is characterized by ditrigonal cavities. Minerals of the kaolinite group are very often used for preparation of intercalated materials. They form intercalates relatively easily since in the ideal case the layers are not charged and their interlayer space does not contain another material. The layers are kept together via hydrogen bridges between surface hydroxyl groups of the octahedral side and the basal oxygen atoms of the tetrahedral side [15, 17].

Smectite minerals possess a 2:1 layered structure such that one octahedral sheet is lying between two tetrahedral sheets, sharing the valences of their oxygen atoms. Layers of smectite are not electrostatically neutral because of the isomeric substitution of the Mg atoms for the Al atoms in the octahedral sheet and the Al atoms for the Si atoms in the tetrahedral sheet. The excess layer charge is neutralized by hydrated cations located in the interlayer space. Montmorillonite is a dioctahedral type of smectite. The layers are held together by bonding between divalent cations and water with basal oxygen atoms of the tetrahedral sheets. The formula for montmorillonite is $(\text{Si}_{7.8}\text{Al}_{0.2})^{4+}(\text{Al}_{3.4}\text{Mg}_{0.6})^{6+}\text{O}_{20}(\text{OH})_4$. This formula indicates that there is substitution for Si^{4+} by Al^{3+} in the tetrahedral sheet and for Al^{3+} by Mg^{2+} in the octahedral sheet [15, 17].

2. COMPUTATIONAL METHODS

Predicting and understanding the properties and behavior of energetic material systems is of great importance both from technological and academic points of view. An understanding of properties of energetic materials and reactions with soils and water at the atomistic level is vital for the development of methods and technologies for decontamination. Experimental studies contribute to clarification of these problems. However, energetic materials are typically degraded very slowly in environmental systems. Observation of mineralization in the environment and experimental studies of properties of energetic materials from the point of view of interactions with soils are complicated by this slow rate [20]. In addition, despite the existence of many experiments and the combination of several experimental methods continually some discrepancies were found in the position of the organic molecule on the surface of clay minerals, the mechanism of adsorption of nitroaromatic explosives on the surface of clay minerals, and especially interactions between the organic molecule and the layers of mineral.

In the last several years, a new approach has emerged which relies heavily on the use of predictive simulations of clay-energetic material systems. The computational methods are now commonly applied to the study of these species. Such studies will clarify above described discrepancies by means of precise interpretation of experimentally unclear data.

Theoretical simulations can be divided into two groups: 1. molecular dynamic and Monte Carlo simulations; 2. quantum chemical simulations.

1. The methods of the first group are very useful to provide detailed insight into the thermodynamic properties of calculated systems. Two general methods are available: Monte Carlo (MC) (classical, quantum, path-integral, volumetric) and molecular dynamic simulation (MD) (classical, tight binding, quantum). Molecular simulation serves as a method to assess the various models used in fitting experimental data. The results of MC and MD simulation calculations can be used to predict thermally averaged structures, reaction rate constants, free energies, dielectric constants, compressibility, heat capacities, phase transition temperatures [21]. MC and MD simulations using optimized interatomic potentials are successful in reproducing known structural and physical properties of calculated systems. The underlying philosophy of MC and MD simulations is to construct a mathematical description of interactions represented as potential functions and then sample the configuration of a manageable system of molecules in order to ascertain its properties [22]. A big advantage of these simulations is that the temperature is controllable. The disadvantage of MC and MD simulation methods is that their accuracy is dependent on the choice of suitable potential functions [23].

2. Quantum chemical *ab initio* calculations are much more reliable because they do not suffer from parameter-fitting problems. With the advent of supercomputers, *ab initio* quantum chemistry is now feasible also for large systems that include more than 100 heavy atoms. Quantum-chemical calculations complement experimental observations.

Two specific approximations were developed to solve the problems of surface chemistry: the periodic approximation, where quantum-chemical methods employ a periodic structure of the calculated system, and the cluster approximation, where the model of solid phase of finite size is created as a cutoff from the system of solid phase (it produces unsaturated dangling bonds at the border of cluster). The cluster approximation has been widely used for studying the interactions of molecules with all types of solids and their surfaces [24]. This approach is powerful in calculations of systems with deviations from the ideal periodic structure like doping and defects. Clay minerals are typical systems having such properties.

The most important disadvantage of the cluster model is the relatively small size of the considered system. The embedded and dipped cluster models

are usually used to overcome this problem. They are considered not only because the cluster models need corrections for neglected interactions with their surrounding but also because they are a promising alternative to the calculation of large cells ("supercells") [24]. The extension of the model and the inclusion of interaction of the cluster with its surroundings into the calculation is realized by different ways depending on the kind of phase (ionic, covalent solids, metals) [25]. For example, in the case of ionic crystals, the surrounding is represented by a crystal field with the main long-distance electrostatic part, or by discrete point, charges placed surrounding of the cluster instead of rest of crystal [26, 27]. For clusters of molecular crystals, it is possible to perform calculations of large clusters by assuming that all significant interactions are included. It is also possible to use a supermolecular approach [28]. Embedding techniques at various levels have been suggested to close the gap between the cluster and the periodic treatment.

Another way of performing calculations using the cluster model is the use of a hybrid method. It is a theoretical method, which uses different approaches for different parts of the molecular system. The ONIOM method is one of the hybrid methods developed quite recently to facilitate accurate *ab initio* calculations of large chemical species. The ONIOM method (n-layered integrated molecular orbital and molecular mechanics approach) [29] is a multi-level extrapolation method, in which the studied molecular system is divided into two or more parts or layers. The most important part of the system from the chemical point of view (the inner part, IP) is treated at a "high" level of theory (the HL method - a high level of *ab initio* molecular orbital method) and the rest of the system is described by a computationally less demanding method (the LL method - the lowest *ab initio* approximation or even semiempirical or molecular mechanic approximations) [30].

This chapter reviews results of experimental and theoretical works devoted to the properties of model systems and energetic materials interacting with clay minerals. We will summarize the information concerning these interactions, identify significant data deficiencies, and briefly discuss the directions of future research in this area. The review could lead to obtaining enough information to consider and select practical remedial alternatives of energetic contaminants in soils and groundwater.

3. INTERACTIONS OF CLAY MINERALS WITH WATER MOLECULES

Clay minerals can contain water molecules and exchangeable cations (see Section 2.). The presence of water and exchangeable cations affects the interactions between the adsorbed energetic material and the clay mineral.

Therefore, the energetic materials could interact with water molecules or with exchangeable cations in the interlayer space of mineral. These interactions are considered as one of many possibilities for the remediation of highly contaminated soils by energetic materials [31]. This is the reason why the understanding of phenomena of hydration of clay minerals is the crucial aspect, which could help to find a possible way of decontamination.

3.1. Experimental study

The experimental studies of water interactions with clay minerals are very extensive. The structure, dynamics and interactions of interlayer water with the surface of clay minerals were reviewed in several papers [32, 33] and described in a number of books [15, 34, 35]. Therefore, we will review only the most important studies concerning experimental investigations of the structure and interactions of water molecules on clays.

The experimental investigations of the role of water in clay minerals are often devoted to the study of properties and the structure of water molecules using several experimental techniques like neutron and X-ray diffraction, incoherent neutron scattering, IR, NMR and ESR spectroscopy, and dielectric relaxation. Among these methods, neutron diffraction, neutron scattering and NMR techniques have become the most powerful techniques in the study of this phenomenon.

Neutron diffraction experiments with substitution of deuterium (D) for hydrogen (H) used to determine the structure of interlayer water in Na-, Ni, Ca- and Li-vermiculite [36-38] have revealed that each interlayer cation is differently coordinated according to the kind of ion and the phase of the vermiculite. For example, Ni ion is coordinated octahedrally to six water molecules with all waters forming H-bonds with the adjacent clay surface. In the case of the 14.96 Å phase of Na-vermiculite there is an average of 4.9 interlayer water molecules per cation. About half of these water molecules are oriented to form a hydrogen bond to one of the clay surfaces. In the 11.78 Å phase of Na-vermiculite, there is an average of 2.1 water molecules per interlayer cation [36]. In addition, the difference in orientation of coordinated molecules that causes a distinct formation of hydrogen bonds to the adjacent clay surface was investigated. The recent study [39] suggested that the counterion density reaches a maximum at the center of the interlayer region of vermiculite.

The important role of the exchangeable cation in determining the structure of adsorbed water on smectites was discussed in the review of experimental studies of the structure of water adsorbed on smectites [32]. It was concluded that the spatial arrangement of the adsorbed water molecules indeed derives mainly from the solvation of exchangeable cations. Despite the great

significance of the exchangeable cations for the structure of adsorbed water on smectite, the role of the silicate surface cannot be neglected.

The structural differences are created by an epitaxy of the molecules in the first and second adsorbed monolayers, with a transition to an essentially liquid water state thereafter. This point of view, which has been emphasized by Tarasevich [40], is in agreement with the limited near-IR and NMR spectroscopic data available [41]. The adsorbed water molecules maintain preferred orientations relative to the opposing planes of oxygen atoms bounding the interlayer space.

The results of studies of Na- and Li-montmorillonite D₂O hydrates using neutron diffraction [42-44] and IR spectroscopy and X-ray diffraction [45] show qualitatively that the interlayer water has a liquid-like structure. The interlayer water in the Li-montmorillonite adopts a liquid-type structure and the clay surface does not prevent the interlayer water from adopting a highly hydrogen-bonded configuration. The formation of extensive H-bonding between the water molecules and the layers of mineral in Li- and Na-montmorillonite was also indicated using the neutron diffraction [46] and in Na⁺, K⁺, Co²⁺, and Cu²⁺-montmorillonite using FTIR techniques [47]. For the two-layer Li-montmorillonite hydrates, there is no evidence for disruption of hydrogen bonding in the interlayer space due to interactions with the clay surface. Lithium counterions are located midway between the clay plates and they form octahedral hydration complexes with six water molecules. The behavior of lithium is therefore rather different from that of the larger alkali-metal ions: sodium, potassium, and cesium. These ions prefer to bind directly to vermiculite clay surfaces, rather than fully solvate. Since only lithium-substituted vermiculites will swell macroscopically when soaked in water, it was concluded that interlayer cations must detach themselves from the clay surface if the particles are expanding colloidally [38].

In addition to diffraction methods, also spectroscopic techniques, especially NMR spectroscopy, are extensively used to study the complex interaction of water and the clay mineral surfaces. NMR spectroscopy has become a valuable tool to investigate the dynamics of water [41, 48-54]. The study of interaction of water with clays using NMR techniques has primarily involved measurements of ¹H and ²H spin-lattice relaxation and lineshape analysis of ¹H and ²H in water molecules adsorbed on clays [32, 41, 51-54]. Based upon the results of such studies, it is possible to calculate the distribution, orientation, and diffusion rates of water molecules bound to clays. It was found that water molecules have a preferential orientation on clays with low water contents at temperatures near 298K [52, 54].

In addition to studies which focused primarily on clay-water suspensions [55-58], Weiss and Gerasimowicz [59] have investigated using ²H NMR the

interactions between water molecules and a series of $\text{Ca}^{2+}/\text{Na}^+$, $\text{Ca}^{2+}/\text{NH}_4^+$, and $\text{NH}_4^+/\text{Na}^+$ exchanged hectorite and saponite in water- and clay-dominated systems with very low water content. The positions, orientations and interactions of water molecules in the interlayer space of minerals are more influenced by the cation than by the particular clay; this is consistent with earlier work [32]. It was found that an increase of the number of divalent ions near the clay surface causes the water molecules bonded next to the clay switch from rotation around the stronger divalent metal to the rotation around the hydrogen bond [55]. The rotation of water molecules around hydrogen bonds and those around the divalent metal have different signs. These findings concerning rotation of the water molecule agree with earlier studies [32] showing that the adsorbed water molecules in the first cation solvation layer in the interlayer space of smectites rotate around their C_2 axis.

^2H NMR study of clay suspensions was used to monitor the orientation of water molecules near the solid surface [60]. The location of cation isomorphous substitution and the $\text{Ca}^{2+}/\text{Na}^+$ molar ratio of exchangeable cations modulate their relative importance. In an agreement with these results, Sposito and Prost [32] conclude that the nature of the interaction between the silicate surface and water molecules depends on the degree of localization of charge deficits created by isomorphous substitutions in the smectite. If the deficit originates in the octahedral sheet, the excess negative charge tends to be delocalized around the oxygen atoms forming the ditrigonal cavities in the silicate surface and water molecules can form proton bonds through this charge distribution. If the deficit occurs in the tetrahedral sheet, the excess negative charge tends to be delocalized on single oxygen atoms, and conventional hydrogen bonding between a water molecule and the surface is possible.

3.2. Theoretical study

Considerable advances in the understanding of the structure of interlayer water in both smectites and vermiculites have been also achieved by means of computational simulations [61].

Sposito and co-workers employed a rigid framework for the clay lattice that has been used successfully to predict $d(001)$ layer spacing, interlayer structure, and water self-diffusion coefficients [62-80]. Calculated layer spacings and thermodynamic properties, as well as interlayer water configurations and interlayer-species self-diffusion coefficients are in agreement with available experimental data.

Calculations of water-talc interactions using atomic pair potentials [71] show that the binding energy of water in the 10 Å phase of talc amounts to 21.8 kcal/mol (only 8.4 kcal/mol is due to the hydrogen bonding between the water

and the surface hydroxyl group). The results of calculations also indicate that most of the clay surface is relatively hydrophobic.

MC and MD studies of hydrated smectites with monovalent counterions Li^+ , Na^+ , K^+ , Cs^+ were also performed [62, 63, 69, 70, 72, 77-80]. An increase of the simulation cell size of 2:1 Na-saturated clay or alternation of its shape from rectangular did not have a significant effect on the calculated interlayer properties [70]. It has been revealed that the mechanism of swelling and hydration depends upon the interlayer ion charge. Also the greater role of the clay mineral surface in organizing interlayer water in the case of K-montmorillonite with a weakly solvating counterion was concluded [64, 68].

Sposito et al. [76] have found that MC simulations of the first-order difference total radial distribution function for interlayer water in Na- and Li-montmorillonite hydrates were in good agreement with published experimental data [42-44]. The radial distribution function of K-montmorillonite differs from those for Na- and Li-montmorillonite hydrates. As the water content is increased, both Li^+ and Na^+ ions can be hydrated, thereby becoming detached from the clay surface. In contrast, K^+ ions migrate and they bond to the clay surface [79]. Therefore, K^+ ions screen the negatively charged, mutually repelling clay surfaces more effectively than Na^+ and Li^+ ions do. Two distinct populations of sodium ions can be identified within the clay pores [63, 79]. The water molecules have a strong tendency to solvate the sodium counterion, and to form hydrogen bonds to the clay surface. The interlayer water molecules in Li-montmorillonite hydrates tend to solvate Li^+ , although some ions were entrapped within cavities in the montmorillonite surface [77].

Simulations of three representative Cs-smectites revealed interlayer Cs^+ to be strongly bound as inner sphere surface complexes, in agreement with published bulk diffusion coefficients [78]. Spectroscopic and surface chemistry methods have provided data suggesting that in stable 12.4 Å Cs-smectite hydrates the interlayer water content is less than one-half monolayer. However, Smith [81] showed using molecular simulations of dry and hydrated Cs-montmorillonite that a 12.4 Å simulation layer spacing was predicted at about one full water monolayer. The results of MD computer simulations of Na-, Cs- and Sr-substituted montmorillonites also provide evidence for a constant water content swelling transition between one-layer and two-layer spacings [82].

Skipper et al. [65, 66] and Refson et al. [67] have performed comparable investigations of water-smectite systems with bivalent and monovalent counterions. Hydrolysis in the case of Mg-montmorillonite is similar in that it was found in several experimental studies for Li-montmorillonite [42-44]. Calculations of the one- and two-layer hydrates of Mg-montmorillonite revealed an equilibrium distribution of counterions on the interlayer midplane, with each Mg^{2+} surrounded by an octahedral solvation shell. Extensive

hydrogen bonding between nonsolvating water molecules and the siloxane surface of the clay mineral was also observed, as were water molecules attracted into the ditrigonal cavities of the surface. Overall, Mg^{2+} -water interactions strongly influenced the interlayer water configuration.

The interlayer configuration in two-layer hydrate of Mg-beidelite [74] is consistent with results of previous simulations of Mg-smectites [66, 67]. The Mg^{2+} cations are situated at the midplane solvated by three water molecules each above and below in agreement with a number of experimental studies [15, 34]. Nonsolvating water molecules form H-bonds with surface O atoms of beidelite. However, water molecules in Mg-beidelite show a greater tendency to occupy ditrigonal cavities in the siloxane surface than in the case of Mg-montmorillonite.

Using MC simulations Delville and co-workers have investigated the clay-water interface [83-87]. The number of hydration layers (2-3) increases suddenly during the swelling process [85]. For hydrated montmorillonite with interlayer sodium counterions it was determined that the water content of the pore is a function of the interlamellar distance. Water molecules are layered in successive shells, whose number (1-4) depends on the available interlayer space [87]. The MD study of structure of water in kaolinite [88] has indicated two types of adsorbed water molecules according to different orientations with respect to the structure of clay sheets with HH vector parallel or perpendicular to the surface.

Teppen et al. [89] have used a flexible model for clay minerals that allows full movement of the M-O-M bonds in the clay structure, where M represents Si, Al, or other cations in the octahedral sheet. This model was used in MD simulations of interactions of hydrated clay minerals with trichloroethene [90, 91]. The simulations suggest that at least three distinct mechanisms coexist for trichloroethene sorption on clay minerals [90]. The most stable interactions of trichloroethene with clay surfaces are by full molecular contact, coplanar with the basal surface. The second type more reversible, less stable is adsorption through single-atom contact between one chlorine atom and the surface. In a third mechanism, trichloroethene interacts with the first water layer and does not interact with clay surface directly. Using MC and MD simulation the structure and dynamics of methane in hydrated Na-smectite were studied [92]. Methane particles are solvated by approximately 12-13 water molecules, with six oxygen atoms from the clay surface completing the coordination shell.

In addition to MC and MD simulations, several quantum-chemical studies of hydrated clay minerals with or without exchangeable cations in the interlayer space have been performed at the *ab initio* and semiempirical level of theory. The total energy of hydrated layered silicates (talc and pyrophyllite) without exchangeable counterions, the position and interactions of interlayer water

obtained using the DFT level with pseudopotentials and plane wave basis set have been reported [93]. Calculated atomic coordinates are in good agreement with experimental data [94]. However, in contrast to the result of Skipper *et al* [71], Bridgeman and co-workers [93] have not investigated interactions of water molecules with OH groups of the octahedral site of the mineral. The most favorable position of a water molecule in the interlayer space of clays has been found in the midplane between the upper and lower layer, so that hydrogen atoms are located parallel to the layer.

Several DFT studies are devoted to the study of hydrated Na-smectites [95, 96, 97]. It was found that the interlayer Na^+ cation is more stabilized in montmorillonite in comparison to beidelite [95]. The locations of Na^+ cations over the clay surface are governed by the presence of charge centers in the respective clay material. This is consistent with experimental data [32]. The location of interlayer Na^+ cations in smectites depends on the isomorphous substitution [96, 97] that also corresponds with results of MC simulations [63, 77]. The calculation of a discontinuous model for adsorbed water [96] shows the presence of two kinds of water molecules, one corresponding to water molecules which hydrate the exchangeable cation, and the second adsorbed on the surface. These conclusions are supported by experiments performed in the near IR range [35]. A DFT study [97] shows that among all orientations of water the lowest energy is obtained when two hydrogen atoms of the water molecule point towards the clay surface and the oxygen atom is extending away from the clay surface, while the maximum energy is obtained when the oxygen of the water molecule is pointed towards the clay surface.

A DFT calculation of the chemical states of Cs^+ cation adsorbed on smectites (montmorillonite, montmorillonite-beidelite, Fe-montmorillonite, nontronite) [98] shows agreement with results of MD simulation study [78] that Cs^+ ion is adsorbed strongly on a basal oxygen hexagonal hole.

In a quantum-chemical MNDO-PM3 level study of the hydration of the Mg^{2+} cation located in a ditrigonal cavity of the basal surface of clays [99], the most favorable area of Mg^{2+} cation location was predicted to be in the vicinity of the AlO_4 tetrahedron formed by the isomorphous substitution of Si for Al in the silica-oxygen sheet. The authors have showed the important role of the hydrogen bond formation between the water molecules and the oxygen atoms of the silica-oxygen sheet in the Mg-ion hydration. This was confirmed in several MC simulation studies [65, 66].

In addition, several quantum chemical calculations of hydrated clay minerals with organic molecules using small cluster models of minerals, which consist of only several Al, Si, O, and H atoms, were published. Using small molecular models, aqueous aluminum acetate complexes [100, 101] and hydrolysis of a three-membered aluminosilicate ring were studied [102]. Using

ATR-FTIR and the HF/3-21G(d,p) level of theory [103], it was predicted that salicylic acid is adsorbed strongly onto illite. Salicylate forms surface complexes predominantly with the Al^{3+} octahedra located on the edges of the illite grains. The authors of DFT studies [104, 105] show that the ordering for the best sorption of dioxine and furane on the surface of smectites follows the order: $\text{Mg}^{2+} > \text{Fe}^{2+} > \text{Fe}^{3+} > \text{Li}^+$, which was obtained also in the case of adsorption of nitrogen heterocyclics on smectites [106].

Using a two-layered ONIOM approach and a model which consists of one octahedral ring and one tetrahedral ring of one 1:1 layer of mineral [107], it was ascertained that the formation of hydrogen bridges between the hydroxyl groups of the octahedral surface and the water molecule occur, with an adsorption energy about -8 kcal/mol. This is in agreement with the results of the simulation study of uncharged talc sheet and water molecules (-8.4 kcal/mol) [71]. The carboxylate group of the acetate anion also binds to the octahedral surface hydroxyls via hydrogen bridges (interaction energy amounts to about -70 kcal/mol). The water molecule and the acetic acid molecule interact with the tetrahedral surface through weaker hydrogen bonds (in comparison with those with the octahedral side). Adsorption energies are about -3 and -4 kcal/mol in these cases. This finding is in contrast to the conclusion of the MD simulation of interlayer water in kaolinite [88] where water molecules form weak hydrogen bonds with hydroxyls of the octahedral sheet and strongly interact with the siloxane surface.

3.3. Summary

Both experimental and quantum chemical studies have showed the structure, dynamic and interaction of interlayer water in clay minerals e.g. smectites, and vermiculite. The interlayer counterion has a significant effect on the location and interactions of water molecules. Despite of great significance of the exchangeable cations for the structure of adsorbed water on smectite also the role of the silicate surface can not be neglected. However, the water is more influenced by the cation than by the particular clay. The influence of different kinds of counterions and mineral surfaces results in different orientations of water molecules and a distinct formation of hydrogen bonds to the adjacent clay surface. The counterion density reaches a maximum at the center of the interlayer region of clay mineral. Further, the nature of the interaction between the silicate surface and water molecules depends on the degree of localization of charge deficits created by isomorphous substitutions in smectite.

MD and MC simulations have provided data on layer spacings, thermodynamic properties, as well as interlayer water configurations, interlayer-species self-diffusion coefficients, and total radial distribution functions that are consistent with experimental data. Most of the clay surface is relatively

hydrophobic. Increasing the simulation cell size or altering its shape from a rectangular has an insignificant effect on the calculated interlayer properties. The mechanism of swelling and hydration depends upon the interlayer ion charge.

4. INTERACTIONS OF CLAY MINERALS WITH SMALL ORGANIC MOLECULES

It was found that sorption of organic compounds on soils is one of the key factors affecting the fate of hazardous organic waste with energetic materials [108]. The adsorption of organic compounds onto minerals can affect bonding between clay minerals and organic contaminants. Therefore, understanding the interactions between natural organic matter and clays is an important step toward understanding the chemistry controlling the fate of organic energetic compounds in soils. Moreover, to examine possible bonding mechanisms of energetic materials to clays, at first it is necessary to know adsorption mechanisms of natural organic molecules on the surface. Understanding this mechanism could guide researchers into possible techniques for removing of organic energetic contaminants from soils.

4.1. Experimental study

The experimental studies of interactions of organic molecules adsorbed or intercalated in the interlayer space of clay minerals are very extensive. These experimental investigations were reviewed in several monographs [15-17]. In this part, we will review only experimental studies concerning systems of kaolinitic minerals (specifically dickite and kaolinite) with formamide (FA), N-methylformamide (MFA) and dimethylsulfoxide (DMSO) since theoretical studies of interactions of small organic molecules with clay minerals are devoted to intercalates and adsorbates of kaolinitic minerals with these organic molecules. This will allow to compare theoretical results with available experimental data.

Many experimental investigations of intercalates dickite-FA (D-FA), dickite-MFA (D-MFA) and kaolinite-DMSO (K-DMSO) applied IR and Raman spectroscopy, NMR technique and X-ray diffraction. These works are mostly devoted to the study of the position of the organic molecule in the interlayer space of kaolinite, interactions between the organic molecule and the layers of dickite and kaolinite, and the influence of mineral structure to the intercalation capability.

4.1.1. *D-FA and D-MFA systems*

The orientation of FA and MFA molecules in the interlayer space of dickite was revealed by experimental studies [109-114]. The FA molecule is located so that bond C-N is almost parallel with the surface of mineral. The oxygen atom of the FA and MFA molecule is directed to the center of the octahedral cavity of mineral and the N-H group of the MFA molecule is directed to the ditrigonal cavity of the mineral.

The formation of several hydrogen bonds between the oxygen atom of the FA or MFA molecule and the octahedral side of mineral, and between the amino group of the FA molecule and tetrahedral side of mineral was revealed using diffraction techniques [109-114] and NMR method [115, 116]. The formation of strong hydrogen bonds between the carbonyl oxygen atom of the FA molecule and the surface OH groups of the mineral in intercalation systems dickite and kaolinite with FA, MFA and N,N-dimethylformamide (DMF) molecules was confirmed in IR studies [117, 118]. However, there is no general accepted point of view on the participation of the amino group of formamide in the formation of hydrogen bonds with the mineral layers. Several studies considered this type of the hydrogen bonds with octahedral side [110-112] and tetrahedral surfaces of clay minerals [112] (for alternative point of view see the studies [115, 116]).

The intercalation capability of clay mineral decreases with increasing molecular volume of intercalated material [119]. The speed of intercalation of the MFA molecule decreases with increasing number of defects in the structure of mineral [120]. It corresponds with results of the study of Frost and co-workers [121] where highly ordered kaolinites easily intercalate which is in notable difference with high disordered kaolinites. The intercalation of formamide into kaolinite results in the changes in the vibrational spectra of both kaolinite and the target molecule [122-126]. The FA-intercalated kaolinite remains expanded after formamide desorption with a $d(001)$ spacing of 10.09 Å [127-129].

4.1.2. *K-DMSO system*

The position of the intercalated DMSO molecule in the interlayer space of kaolinite is such that the first S-C group is almost parallel with the surface of kaolinite and the second S-C group is directed into the tetrahedral cavity of kaolinite [130, 131]. The S=O group has 40.3° inclination to the basal surface of kaolinite. The methyl group of DMSO is influenced by both the opposing mineral surfaces. In addition, the intercalation of DMSO molecule results in the expansion of kaolinite from 7.2 to 11.19 Å phase [132]. The formation of H-bonds between DMSO and surface OH groups of the octahedral side and weak H-bonds with the tetrahedral side of kaolinite was suggested [133-139].

The intercalated DMSO molecule has different orientations in low and high defect kaolinite [132, 140]. This suggests different interactions between DMSO and these kinds of kaolinite. Heller-Kallai *et al.* [141] confirmed the same results. The authors have concluded that the way of placement of the DMSO molecule in the interlayer space of kaolinite depends on the number of defects in the structure of kaolinite.

The value of the reaction enthalpy of decomposition of the kaolinite-DMSO intercalate is -12 kcal/mol [142] and the enthalpy of formation of hydrogen bonds is about -10 kcal/mol [143].

It is proposed that the intercalation of kaolinite with DMSO depends on the presence of water molecules in the interlayer space of mineral [132, 140, 144]. The water molecules are in well-defined positions within the intercalation structure. The evidence of the existence of two types of intercalated water in the DMSO-intercalation complex was obtained [132].

Several papers studying the comparison of properties of intercalates of dickite and kaolinite with FA, MFA and DMSO molecules have been published. In these works [112, 119, 145, 146], it was indicated that the size of the intercalated molecule, its dipole moment, and also the temperature of running of intercalation influences the changes in the structure of mineral and in the formation of hydrogen bonds between the organic molecule and the layers of mineral. The next factor is the orientation and position of organic molecules in the interlayer space of mineral. Xie and Hayashi [115, 116] have indicated the following order of mobility of intercalated FA, MFA and DMF molecules in the interlayer space of kaolinitic minerals: FA < MFA < DMF. Thompson [135] has showed using NMR technique and IR spectroscopy that the strength of interaction between the layers of kaolinite and intercalated molecule decreases in the order from FA to DMSO. Lipsicas *et al* [147], who applied NMR and EPR techniques in combination with IR spectroscopy to investigate intercalates of kaolinite with FA, MFA and DMSO molecules, confirmed it.

4.2. Theoretical study

The theoretical studies applying cluster model approach [148, 149] and periodic approximation [150] devoted to the description of interaction of dickite and kaolinite with the FA, MFA and DMSO molecules have been performed. These works have studied the position and the orientation of the adsorbed and intercalated organic molecules with respect to the surface of mineral, interaction between the organic molecule and the mineral, interaction energy, the influence of the intercalation and adsorption on changes of geometry parameters, electron structures of organic molecules, and the surfaces of the minerals.

4.2.1. D-FA and D-MFA systems

In the study by Michalkova and co-workers [148] the intercalated and adsorbed D-FA and D-MFA systems using the B3LYP/3-21G* method and representative cluster models were investigated. Fig. 3 presents the optimized structure of intercalated molecules FA and MFA in the D-FA and D-MFA system. The intercalation and adsorption of FA molecule on dickite have also been studied using a two-layered ONIOM method and bigger cluster models [149]. The model was divided into two parts where the high level part was calculated at the B3LYP/3-21G* level of theory and low level part was calculated using PM3 semiempirical method (see Fig. 4 which presents the optimized structure of intercalated FA molecules in the D-FA system with illustration of partition of the model into the low and high level parts).

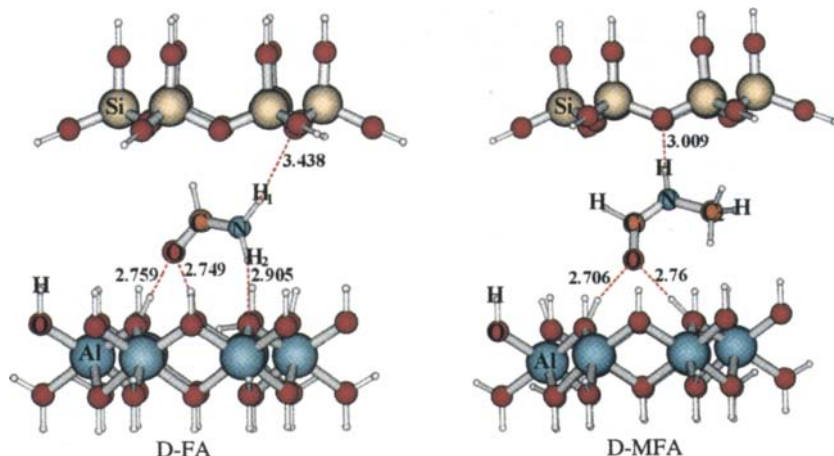


Fig. 3 The optimized structure of the intercalated FA and MFA molecule in the D-FA and D-MFA system obtained using B3LYP/3-21G* method [148].

It was found that for D-FA system the calculations using the ONIOM method and bigger models provide results in agreement with the B3LYP/3-21G* level predictions using smaller models.

Intercalation and adsorption lead to changes of structural parameters of intercalated and adsorbed organic molecule in comparison with the isolated species [148, 149] as is presented in Table 1 for the FA. Changes of bond angles of the intercalated and adsorbed molecule correspond to the effort to form maximum attractive contacts with the surface of the mineral. The length of bonds of atoms of the intercalated/adsorbed FA, and MFA molecules directly involving in the formation of the hydrogen bonds are enlarged in comparison with the isolated species.

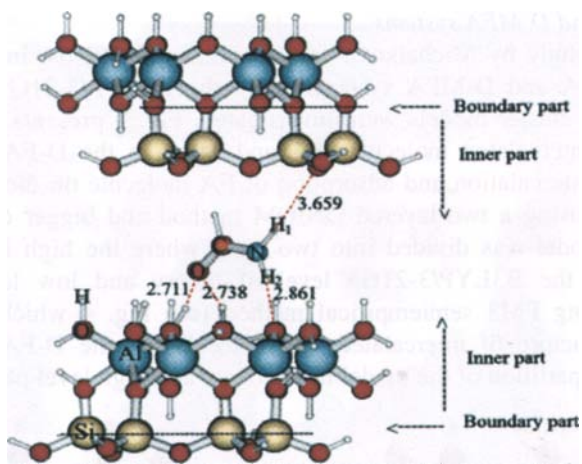


Fig. 4 The optimized structure of the FA intercalated molecule in the D-FA system obtained using ONIOM(B3LYP/3-21G*:PM3) method [149].

Table 1

Calculated geometrical parameters using B3LYP/3-21G* [148] and ONIOM(B3LYP/3-21G*:PM3) [149] method for isolated, intercalated and adsorbed FA molecule, and experimental data for intercalated FA molecule

Parameter ^a	Free FA	D-FA(ads)		D-FA(int)		Exp ^b
		ONIOM	B3LYP	ONIOM	B3LYP	
d(H ₁ -N)	1.013	1.015	1.015	1.018	1.021	-
d(H ₂ -N)	1.015	1.054	1.065	1.049	1.042	-
d(C-N)	1.367	1.336	1.338	1.336	1.340	1.36(12)
d(C=O)	1.234	1.264	1.263	1.272	1.272	1.20(11)
α(H ₁ -N-C)	121.8	118.6	120.3	119.3	119.8	-
α(H ₂ -N-C)	119.3	123.1	118.2	119.7	118.0	-
α(N-C-O)	125.4	125.5	125.0	123.8	123.8	113.5

^a Bond lengths (d) are in Å, angles (α) are in degrees, ^b Ref. [109].

The position of interacting molecules with respect to the surface of mineral was revealed [148, 149]. In the intercalated dickite-FA and dickite-MFA systems, the organic molecule is located above the octahedral ring so that the oxygen atom points into the center of the octahedral cavity (see Figs. 3, 4). These results are in a good agreement with experimentally found position and orientation of organic molecules in intercalated dickite-FA, dickite-MFA systems [109, 114]. The adsorbed FA and MFA molecules have the same position and orientation was found for the intercalated ones [148, 149].

The formation of hydrogen bonds between the organic molecule and the layers of dickite in which the carbonyl oxygen atom plays the central role was indicated [148, 149]. The carbonyl oxygen atom interacts as a proton acceptor for two H-bonds with the surface hydroxyl groups of the mineral (see Figs. 3, 4) which is in agreement with the results of several experimental studies [109, 110, 114-118]. The hydrogen bonds are stronger in the intercalation systems in comparison with the adsorption systems [148, 149]. The -NH_2 group of the FA molecule creates as proton donor the additional hydrogen bridge with the oxygen atom of the octahedral surface (proton acceptor) (see Figs. 3, 4) [148, 149]. Moreover, in the intercalated system the FA molecule forms a weaker hydrogen bridge between the second amide proton and one of the basal oxygen atoms. This observation is not consistent with conclusions from NMR experiments [115, 116] where authors suggest that both amide protons weakly interact with the silica sheet of the adjacent layer. However, calculation shows that more energetically favorable is the formation of the hydrogen bond between the second proton of the -NH_2 group and the oxygen atom of one surface hydroxyl group, since surface hydroxyl groups are very flexible and can be easily tilted out [148]. The proton of the =NH group of the MFA molecule forms H-bond of the length of 2.00 \AA (calculated value) with one of the basal oxygen atoms of the adjacent layer [148, 149]. The same formation of hydrogen bonds in kaolinite-MFA intercalate was predicted in the experimental study [112]. However, the calculated results are different from the conclusions of experimental studies [114-116]. They did not suppose the formation of any H-bond between tetrahedral surface and the proton of the =NH group.

The surface hydroxyl groups surrounding the octahedral hole are influenced by the formation of hydrogen bridges with the organic molecule [149]. The bond lengths of OH groups of intercalated and adsorbed dickite are enlarged in comparison with a pure mineral.

Atomic charges of the D-FA system calculated using Mulliken population analysis and ChelpG scheme by fitting to electrostatic potentials have been predicted at the B3LYP/3-21G* level of theory [149]. They are presented in Tables 2a, b. The intercalation and adsorption lead to certain reordering of electron structure of the adsorbed and intercalated molecule and the surface of dickite. The estimation of this effect can be obtained from comparison of atomic charges of isolated and intercalated or adsorbed dickite. One can see that the intercalation/adsorption lead to the polarization of the intercalated/adsorbed molecule and the OH groups of the mineral according to the participation in the formation of H-bonds (see Tables 2a, b). The polarization is more significant in the case of the intercalated system in comparison with the adsorbed system as consequence of larger redistribution of electron density under the influence of the upper layer of dickite.

Table 2

Atomic charges [$|e|$] of the FA molecule, octahedral -OH groups participating in the formation of hydrogen bond with the FA molecule in the D-FA system obtained using ChelpG scheme [149]

a/ FA molecule

Atom	Free FA	D-FA(adsorbed)	D-FA(intercalated)
O	-0.494	-0.670	-0.719
N	-0.843	-0.804	-0.998
H(C-H)	0.029	0.014	-0.059
H(N-H ₁) ^a	0.372	0.378	0.464
H(N-H ₂) ^b	0.397	0.366	0.433
C	0.319	0.635	0.813

^a hydrogen atom participating in the formation of H-bond with tetrahedral sheet, ^b hydrogen atom participating in the formation of H-bond with octahedral sheet.

b/ Mineral

Atom	Adsorbed		Intercalated	
	dickite	D-FA	dickite	D-FA
O	-0.799	-1.043	-0.959	-1.036
O	-0.876	-0.647	-0.799	-1.018
O	-0.959	-1.066	-0.876	-0.667
H	0.437	0.594	0.487	0.570
H	0.384	0.294	0.437	0.565
H	0.487	0.597	0.384	0.379

Table 3

BSSE corrected interaction energies (kcal/mol) of D-FA, D-MFA and K-DMSO systems calculated at the B3LYP/3-21G* level of the theory, and using ONIOM(B3LYP/3-21G*:PM3) method [148,149]

System	Adsorbed		Intercalated	
	B3LYP/3-21G*	ONIOM	B3LYP/3-21G*	ONIOM
D-FA	-14.6	-15.2	-20.2	-20.2
D-MFA	-3.7	-	-14.4	-
K-DMSO	-2.7	-	-9.6	-

Table 3 contains interaction energies of dickite-FA and dickite-MFA systems calculated using the cluster model at B3LYP/3-21G* level of theory and with ONIOM(B3LYP/3-21G*:PM3) method corrected by the BSSE. The adsorption energy is lower than intercalation energy of calculated systems. This difference represents the additional stabilization of the intercalated FA and MFA molecule in the interlayer space in comparison with adsorbed one. The adsorption and intercalation energy of D-FA system is higher in comparison with interaction energy of the D-MFA system [148, 149]. It is the consequence

of the presence of the methyl group and the lower number of hydrogen atoms of the MFA molecule available to form hydrogen bridges. It results in lower stabilization of the MFA molecule with respect to the surface of dickite in comparison with the FA molecule.

4.2.2. K-DMSO system

The intercalated and adsorbed K-DMSO system was studied using cluster models [148] and also applying periodic approximation [150]. Three periodic models of intercalated K-DMSO system were calculated using DFT with PW91 functional and plane-wave basis set as they are implemented in the Vienna *ab initio* program package (VASP) [151]. Models were constructed so that the unit cell of the intercalated K-DMSO system with twice as large *a* and *b* cell parameters contains one DMSO molecule (K-DMSO(1)), two DMSO molecules (K-DMSO(2)) and four DMSO molecules (K-DMSO(4)) in the interlayer space of kaolinite. Fig. 5 presents the optimized structure of the intercalated DMSO molecule in the K-DMSO system obtained using the cluster and the periodic model.

The periodic calculations show good agreement with results of cluster calculations, with small deviations in the geometry parameters of the intercalated molecules and in the distances of hydrogen bonds as a consequence of distinct mutual interactions of intercalated DMSO molecules or interactions between the DMSO molecules and the surface of kaolinite.

The adsorption and intercalation lead to more significant changes of geometrical parameters of the DMSO molecule in the K-DMSO system in comparison with intercalated and adsorbed FA and MFA molecules in dickite-FA and dickite-MFA systems [148, 150]. For example, the S=O bond of the DMSO is enlarged about 0.035 Å in the adsorbed system and 0.05 Å in the intercalated system [148].

The different orientation of the intercalated and adsorbed DMSO molecule with respect to the surface of kaolinite was found [148]. In the adsorbed system, the molecular C-O-C plane of DMSO is almost parallel with the basal surface of dickite. In the intercalated system, one of the methyl groups directs towards the center of the tetrahedral cavity and the second S-C bond is almost parallel with the plane of basal oxygen atoms (see Fig. 5). These positions and orientations are in agreement with the NMR experiments [130, 131, 137] where the existence of two non-equivalent methyl groups of the interlayer DMSO molecules in kaolinite was confirmed.

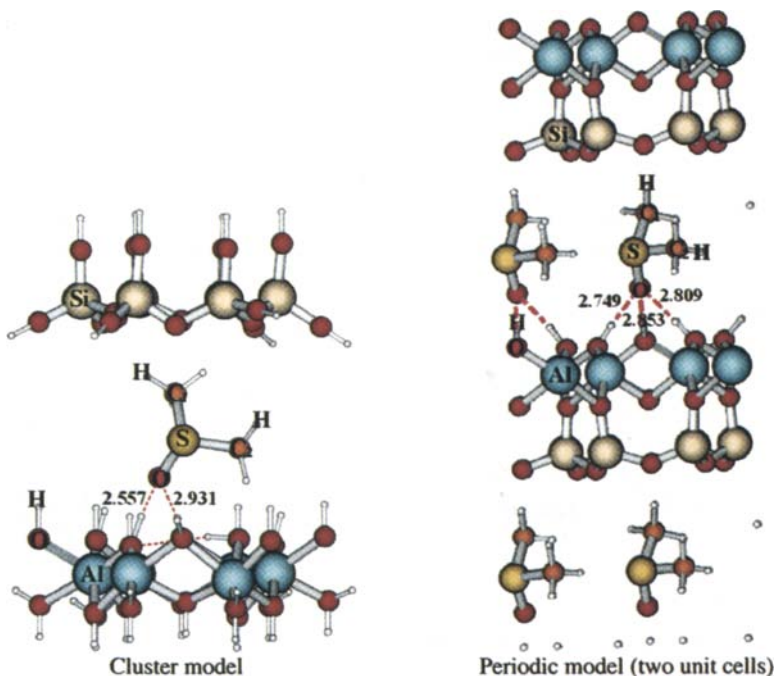


Fig. 5 The optimized structure of the DMSO intercalated molecule in the K-DMSO system calculated using cluster model at the B3LYP/3-21G* level of theory [148], and periodic model calculated using the DFT method, PW91 potential and plane waves basis set [150] (K-DMSO(4) model).

The oxygen atom of the DMSO molecule forms hydrogen bridges with the surface hydroxyl groups (see Fig. 5) [148, 150] that is consistent with results of several experimental works [136, 137, 147]. One can also see the formation of weak hydrogen bonds between the methyl group of the DMSO and basal oxygen atoms of the tetrahedral sheet of kaolinite [148]. This formation of hydrogen bonds between the DMSO and both tetrahedral and octahedral surface of kaolinite is confirmed by experimental studies [133, 134, 137].

The angle between the OH groups and the surface of kaolinite participating in the formation of hydrogen bonds with the DMSO molecule is $40\text{--}50^\circ$ [150]. Calculated geometry parameters of the octahedral OH groups of the intercalated K-DMSO system are in agreement with experimental data [134].

Calculated interaction energies for K-DMSO systems are significantly lower in comparison with two other studied systems (e.g., it is about 50 % comparing with the D-FA system) (see Table 3). It reflects the fact that the DMSO molecule is less stabilized with respect to the surface of the mineral than

are the FA and MFA molecules. The difference between the intercalation and adsorption energy of the K-DMSO system is large, which indicates a large contribution of the energy to the specific interactions between the rest of the DMSO molecule and both adjacent sheets in the intercalated system.

Different interaction energies of the K-DMSO system were found using periodic models, depending on the number of DMSO molecules present [150]. The calculated values of interaction energies are as follows: -21.69 kcal/mol (K-DMSO(1)), -17.90 kcal/mol (K-DMSO(2)), -15.88 kcal/mol (K-DMSO(4)) (the interaction energies are recalculated per one DMSO molecule). The interaction energy that corresponds to mutual interactions of intercalated DMSO molecules in the interlayer space of kaolinite is about 2.43 kcal/mol.

Table 4

Correlation between calculated interaction energies of intercalated systems at the B3LYP/3-21G* and the number of H-bonds, experimental interlayer distances [109, 114, 134] and calculated (B3LYP/3-21G*) molecular volumes of intercalated molecules

System	Energy (kcal/mol)	Number of H-bonds	Interlayer distance (Å)	Molecular volume (Å ³)
D-FA(int)	-20.23	4	10.083	45.25
D-MFA(int)	-14.43	3	10.716	54.66
K-DMSO(int)	-9.64	2	11.220	95.06

The interaction energy of neighboring DMSO molecules in the same interlayer space is about 0.95 kcal/mol. Despite these mutual interactions between DMSO molecules in the interlayer space of kaolinite, it was found that the interactions between the molecule and the surface of the kaolinite are the major contributors to the stabilization of the molecule.

In the study by Michalkova and co-workers [148] it was found that the stabilization of the investigated intercalated and adsorbed molecules in the interlayer space of the host mineral follows the order: FA > MFA > DMSO. This observation is in good agreement with conclusions of experimental works [115, 116, 135, 147]. The calculated interaction energy is directly proportional to the number of the formed hydrogen bonds. This is displayed in Table 4. One can see that decreasing the number of H-bonds causes lowering of the interaction energy (in absolute value). Slight increasing of the interlayer distance corresponds to the rise of the molecular volume of the intercalated molecule (see Table 4). Similar dependence between the molecular size and the interlayer distance was revealed for intercalates of kaolinite with amides [119].

4.3. Summary

Diffraction studies have determined positions of intercalated formamide, N-methylformamide and dimethylsulfoxide molecules in the interlayer space of

kaolinitic minerals. However, the role of hydrogen atoms in forming of hydrogen bridges between intercalated molecule and the surface hydroxyl groups is not fully understood. The changes in the structure of mineral and in the formation of hydrogen bonds between the organic molecule and the layers of mineral are dependent on the size of the intercalated molecule, its dipole moment, and also temperature of intercalation process. The intercalation capability of minerals decreases as the molecular volume of the intercalated material increases and as the number of defects in the structure of the mineral increases.

Cluster and periodic calculations allow predicting not only the position of organic molecules on the surface of clay minerals but also the types of chemical bonds that are formed between the adsorbed molecules and the surface of clay minerals. The adsorption leads to the changes of geometrical parameters and to the polarization of organic molecules and the surface OH groups of mineral. The C=O, -NH₂ and S=O groups of organic molecules form several hydrogen bonds with surface hydroxyl groups of mineral. Moreover, target molecules create the H-bonds with basal oxygen atoms of the adjacent layer. The calculated interaction energies are proportional to the number of formed hydrogen bonds between the organic molecule and the mineral layers, molecular volume of organic molecules and the interlayer distance. The order of the stabilization of these systems is following: D-FA > D-MFA > K-DMSO. The calculated adsorption energies on the octahedral surface of the mineral are smaller than the intercalation energies.

5. INTERACTIONS OF CLAY MINERALS WITH ENERGETIC MATERIALS

In this part of the review, we will describe the experimental and theoretical studies that are devoted to the investigation of properties of energetic materials interacting with soils. Since the key factor in the transformation of various energetic materials in soils is specific adsorption [152], our emphasis is on studies of adsorption of nitroaromatic explosives on the surface of clay minerals.

5.1. Experimental study

The treatment methods for remediation of energetic materials from soils are divided on *in situ* and *ex situ* biological (bioremediation, phytoremediation, composting), *in situ* and *ex situ* physico-chemical (adsorption, oxidation, electrokinetic separation, extraction, solidification, reduction, soil washing), *in situ* and *ex situ* thermal (pyrolysis, desorption) [1]. Among the above described

methods, the most extensive research has been devoted to define the adsorption of nitroaromatic compounds (NACs) on clay minerals.

The most powerful methods for the study of adsorption mechanism of nitroaromatic compounds on clay minerals have become *in situ* spectroscopic investigations. Handerlein et al. [152, 153] and Weissmahr et al. [154-156] have investigated the adsorption of NACs particularly on illites, montmorillonites and homoionic kaolinites. The substituted nitrobenzenes on the surface of smectites were investigated by Boyd et al. [157, 158]. The main focus in the experimental study of adsorption of NACs on the surface of clay minerals is: the influence of the type of clay mineral, the effect of exchangeable cation of the mineral, the effect of the structure and the kind of substituents of NAC compound on the position and orientation of NACs to the surface of mineral, the character of interaction between NACs and the surface of mineral, the adsorption energy.

The adsorption of NACs takes place primarily at the basal siloxane surface of kaolinite [153]. Adsorbed NACs are oriented coplanar to the siloxane layers, and they exhibit a high degree of mobility. It indicates fast, specific and reversible sorption with siloxane surface sites [153, 154].

The large negative adsorption enthalpies ($H_{\text{ads}} = -9.56 \pm 1.2$ kcal/mol) have been found for 4-Me-2NP (4-methyl-2-nitrophenol) and for four other NACs (3-Me-NB (3-nitrotoluene), 4-Me-NB (4-nitrotoluene), 4-Cl-NB (4-chloronitrobenzene), 4-CHO-NB (4-nitrobenzaldehyde)) for the adsorption on Cs^+ -kaolinite [153].

The type of clay mineral, depending on its abundance and degree of K^+ (or NH_4^+) saturation, may control the adsorption, phase distribution and thus the mobility and (bio)availability of NACs in soils [152]. The affinity of adsorption capacity of the clays for NACs increase in the order: kaolinite < illite < montmorillonite [152].

There are two points of view on adsorption mechanism of NACs on the siloxane surface of clay minerals. The first one proposes that the formation of electron donor-acceptor (EDA) complexes between oxygens of the siloxane surface and a given NAC [152-154]. Such EDA complexes could possess a significant impact on the transport and the fate of NACs (and probably of other organic pollutants exhibiting electron acceptor properties) in the subsurface environment. The major factor controlling the ability of clay minerals to form EDA complexes is the n-donor property of siloxane oxygens and the accessibility of these sites for π -acceptors. Isomorphic substitutions in layers of clay minerals enhance electron donor properties of siloxane oxygens [159]. The electron donor (mineral) – acceptor (substituted nitrobenzene) mechanism of adsorption of a series of *para*- and *meta*-substituted nitrobenzenes on K-smectite corroborate results of the experimental study of Boyd et al. [157]. They

have suggested that EDA complex formation at clays may control the transport of NACs in the subsurface, and also their reactivity concerning reductive transformation processes. They have found that other adsorption mechanisms such as H-bonding or direct coordination of NO₂ groups to surface sites were not important in aqueous environments, but contributed to the adsorption of NACs from apolar solvents.

The second viewpoint concerning the adsorption mechanism, published in earlier studies [160-164], does not consider the EDA complex formation as a potential adsorption mechanism. The different executions of sorption experiments in these works resulted in the different sorption mechanism. In these studies H-bonding of NACs to water ligands of exchangeable cations or direct coordination of NO₂ groups to such cations were identified as adsorption mechanism of NACs in clay minerals. Direct evidence of site-specific interaction between the NO₂ group of the NAC and the exchangeable cation was suggested [165-167].

The authors of some studies [157, 158] have criticized other published results [154], because of prior IR studies of NAC sorption to smectites using nonaqueous solvents [160-162]. After inspection of data published in this study [154] within the context of related IR studies of NACs [161, 168-175], Boyd and Johnston with co-workers have showed that the shifts of characteristic vibrational frequencies of 1,3,5-TNB associated with the NO₂ groups reported by Weissmahr *et al* [154] are significant. It indicates that the NO₂ groups are involved in specific interactions with K⁺ and Cs⁺ or water molecules surrounding these cations. Therefore, they suggest performing a more relevant comparison between a strongly hydrated cation (e.g., Mg²⁺) and a weakly hydrated cation (e.g., K⁺ and Cs⁺), as presented in the study [154] to address the influence of exchangeable cations.

The strength of adsorption of NACs on the siloxane surface of clay mineral depends on the type of exchangeable cation [152-154, 158]. In the presence of strongly hydrated cations (e.g., Li⁺, Na⁺, Mg²⁺, Ca²⁺, Al³⁺), no significant specific adsorption of NACs is observed. In the case of more weakly hydrated cations (e.g., NH₄⁺, K⁺, Rb⁺, Cs⁺), the distribution coefficient, K_d, of a given NAC, increases with decreasing free energy of hydration of the cation [152, 153]. According to results of the study [155] cation exchange on phyllosilicates is a crucial geochemical process that controls the accessibility of their siloxane sites to π -acceptors due to the different sizes of the hydrated cations. It was also indicated [176] that the TNT is bonded more strongly to K-montmorillonite in comparison with Ca-montmorillonite. It causes greater Lewis basicity and/or provides more available binding sites of K-montmorillonite relative to Ca-montmorillonite. Also authors of studies [160, 162, 164] have ascertained that in the case of nitrophenol sorbed on smectite the positions of the NO₂ stretching

bands were influenced by the type of exchangeable cation (e.g., Li, Na, K, Mg, and Al).

The adsorption of NACs on clay minerals is controlled by the structure of the nitroaromatic compound (i.e., number, type, and position of substituent). The highest adsorption coefficients are found for polynitroaromatic compounds, including some important contaminants such as explosives (e.g., trinitrotoluene, trinitrobenzene, and dinitrotoluidines) and dinitrophenol herbicides (e.g., 6-methyl-2,4-dinitrophenol (DNOC) and 6-*sec*-butyl-2,4-dinitrophenol (DINOSEB) [152]. No significant correlation between the K_d and hydrophobicity of substituents was observed. Substituents with strong electron-withdrawing and electron-delocalizing characteristics (e.g., NO_2 , CHO, COCH_3 , and CN) strongly enhance sorption.

In agreement with above described results, Boyd *et al* [157] and Johnston *et al* [158] have found for all of the compounds (1,3-dinitrobenzene (DNB), 1,3,5-trinitrobenzene (TNB), 1,4-DNB, DINOSEB, DNOC) adsorbed on smectites that the sorption of these species is strongly dependent on steric effects. The presence of two or more NO_2 substituents on the aromatic ring clearly enhances sorption of substituted nitrobenzenes. The potential for adsorption of substituted nitrobenzenes (SNB) by K-smectite is determined largely by the additive interactions of the NO_2 groups and the secondary substituent with K^+ interlayer cations [157]. It was indicated that NO_2 groups effectively complex K^+ ions in the interlayer space of smectites. The substituted nitrobenzenes which contain functional groups interacting with K^+ (e.g., $-\text{COOCH}_3$, $-\text{CN}$, and $-\text{NO}_2$) cause higher degree of sorption. The presence of functional groups unable to complex K^+ ($-\text{H}$, $-\text{NH}_2$ and $-\text{OCH}_3$) reduce adsorption of these substituted nitrobenzenes. Moreover, the adsorption is controlled by the aqueous solubility of substituted nitrobenzenes [157].

Substitution in the *para* position to the nitro group always has larger effect on K_d as compared to *meta* substitution [152]. These results are conformed in the study of intercalation of nitroanilines into kaolinite [177]. The authors have found that *meta*-nitroaniline (*m*NA) cannot intercalate into the interlayer space of kaolinite in contrast with *ortho*- and *para*-nitroanilines (*o*NA and *p*NA) which form intercalates relatively easily. *p*NA adopts a monolayer arrangement with the long axis inclined to the layers of kaolinite. *o*NA molecules also adopt a monolayer arrangement though the orientation is not well ordered. This indicates noncentrosymmetric arrangements of *p*NA and *o*NA, and such orientations are induced by the asymmetric environment of the interlayer region of kaolinite. In the case of adsorption of substituted nitrobenzenes on the siloxane surface of K-smectites it was found [157] that the *p*-dinitrobenzene interacts with K^+ ions in several ways: First, both oxygen atoms of one $-\text{NO}_2$ group are directly coordinated to a single K^+ ions, and second $-\text{NO}_2$ group's

oxygen atoms are coordinated to a different K^+ ion (inner complexes). Transition states exist in which $-NO_2$ groups are indirectly coordinated to K^+ ions through intermediation water (outer complex). In the case of *m*-dinitrobenzene, similar mix of inner and outer complexes was found [157].

In addition to adsorption of NACs on the surface of clay minerals, also the possibility of intercalation of these compounds in the interlayer space of clay minerals was studied. The XRD experiments indicate that NACs not only adsorb at external surfaces but also may penetrate the interlayer regions of smectites [154]. This causes the increasing of interlayer spacing of the mineral. Also according to the results of the study [178] partial intercalation of TNB into interlayer space of clay minerals was detected. Intercalation of nitroanilines into kaolinite was studied in the work of Takenawa et al. [177]. The authors have found by using the MAS NMR technique in the interlayer space of kaolinite, *para*-nitroaniline adopts a specific orientation where the amino groups interact with the tetrahedral site of kaolinite and the nitro groups interact with the OH groups of the octahedral groups. *Ortho*-nitroaniline is not oriented in such an ordered way as it was found for *p*NA. These spontaneous orientations are induced by the asymmetric interlayer region, which characterize the uniqueness of kaolinite.

Several more experimental investigations of interactions of soils with explosives, especially with nitroaromatic explosives, using several physico-chemical methods, were published [179-187]. It was found that the major factor affecting the fate and transport of TNT in the subsurface are transformation, sorption, and irreversible soil binding [179]. The next important factors according to the review of Pennington and Brannon [180] are immobilization of TNT in soils that could be a quantitative process descriptor for modeling of explosives fate and transport. Interpretation of sorption data for explosives, especially TNT, is confounded by the formation of TNT transformation products including 2-amino-4,6-dinitrotoluene (2ADNT), 4-amino-2,6-dinitrotoluene (4ADNT), 2,4-diamino-6-nitrotoluene (2,4DANT), and 2,6-diamino-4-nitrotoluene (2,6DANT) [181]. TNT reductive transformation products have been measured in laboratory and field studies [182-185]. TNT transformations are significantly enhanced under anaerobic conditions [186]. In contrast to the soil from long-term anaerobic treatment, no significant reduction of aminodinitrotoluene to diaminonitrotoluene was observed after short-term anaerobic treatment and metabolites remained in soils [187].

There are a number of works that indicate that the presence of Fe ions in soils enhance the transport and fate of NAC explosives. When sterilized and unsterilized soils were used [188], transformations were observed under both conditions biologically and abiotically, suggesting the presence of a purely abiotic transformation component. TNT has been demonstrated to disappear in

the presence of montmorillonite or kaolinite when Fe^{2+} ions are added [186]. Also according to the results of Hundal et al. [189] Fe^0 alone, Fe^0 followed by H_2O_2 , or Fe^0 in combination with biotic treatment can be used for effective remediation of munitions-contaminated water and soil. Abiotic reduction of NACs (other than TNT) to amino products by adsorbed Fe^{2+} has been shown to occur [190-192]. It was indicated that the transformation of TNT in soils is significantly dependent on pH in the presence of Fe ions. It is in contrast with findings of studies of adsorption of substituted nitrobenzenes and nitrophenols on the mineral surface [153] where it was indicated that the values of K_d distribution coefficient for the neutral NACs are unaffected even by substantial changes in pH.

Redox potential strongly affects the rate and products resulting from explosives transformation [193]. This effect was found for RDX in the study of adsorption and transformation of RDX in low-carbon aquifer soils [194]. In this context, it is interesting to note that nonaromatic polynitro compounds such as RDX do not show any tendency to adsorb specifically on clay mineral.

Little is known regarding the transformation and sorption of HMX. In laboratory studies it was found that HMX is stable under a broad range of redox and pH conditions [195]. Transformation products of HMX have rarely been detected in environmental samples. HMX is apparently sorbed less by soils than is TNT [179, 195, 196]. pH conditions affect the sorption characteristics of HMX. Highly anaerobic conditions decrease sorption of HMX into soil.

5.1.1. Summary

NACs adsorb preferentially to the siloxane surface of the mineral. The adsorbed NACs on the siloxane site are oriented coplanar to the surface. There are two points of view on the adsorption mechanism: the formation of electron donor-acceptor (EDA) complexes between basal oxygens of the siloxane surface and nitroaromatic compound and on the other side H-bonding of NACs to water ligands of exchangeable cations or direct coordination of NO_2 groups to such cations. The strength of adsorption depends on the structure of the mineral and the characteristics of compound (i.e., number, type and position of substituent) as well as on the type of exchangeable cation of the mineral.

The major factors affecting the fate and transport of TNT in soils are transformation, sorption, and irreversible soil binding and immobilization. TNT, RDX and HMX transformations are significantly enhanced under anaerobic conditions. The addition of Fe ions to soils is considered as the resource of transport and fate of NACs explosives where TNT transformation in soils can occur both biologically and abiotically. The transformation of TNT in soils is significantly dependent on pH in the presence of Fe ions.

5.2. Theoretical study

5.2.1. Interaction of 1,3,5-trinitrobenzene with nonhydrated surface of clay minerals

As we mention above the study of the interaction of nitroaromatic compounds with nonhydrated surface of clay minerals has been initiated by the hypothesis about the possibility for the adsorption of nitroaromatic compound on nonhydrated siloxane surface of clay minerals [152-158, 160-164]. This type of adsorption of 1,3,5-trinitrobenzene (TNB) on the siloxane surface of the mineral has been investigated theoretically by Pel'menschikov et al. [197] and Gorb with co-workers [198]. Since most of results of these studies supplement each other let us to discuss them together.

The calculations of molecular models of siloxane sites of clay minerals with adsorbed TNB at the SCF, DFT (B3LYP) and MP2 levels of theory have been recently carried out [197]. A series of basis sets was used from the smallest 6-31G(d) up to the 6-311+G(d) set of atomic orbitals.

To investigate adsorption of TNB on the siloxane surface also the ONIOM technique has been applied [198] using bigger cluster models. The models of siloxane adsorption sites used in these studies are presented in Fig. 6. They have different sizes starting from the simplest one just having only silicon-oxygen hexagonal ring and up to the molecular system, which possesses the $\text{Al}_{22}\text{Si}_{13}\text{O}_{81}\text{H}_{44}$ stoichiometry. Depending on the size of the system, the adsorption complex of TNB on siloxane sites, the target cluster has been subdivided into the high level part calculated at the MP2/6-31G(d) or HF/6-31G(d) level of theory, the middle level part calculated at the HF/6-31G(d) level and the low level part calculated at the HF/3-21G or HF/STO-3G level of theory.

According to experimental data [153, 154] the NAC compounds adsorb on the nonhydrated siloxane surface coplanar to the plane of surface oxygens. Therefore, initially it has been shown that TNB molecule significantly interacts with the siloxane surface only in planar orientation with respect to the plane of basal oxygen atoms [197, 198]. Then only the coplanar orientation of TNB with respect to the siloxane surface was considered. Two views on the typical structure of such adsorption complexes are illustrated in Fig. 7.

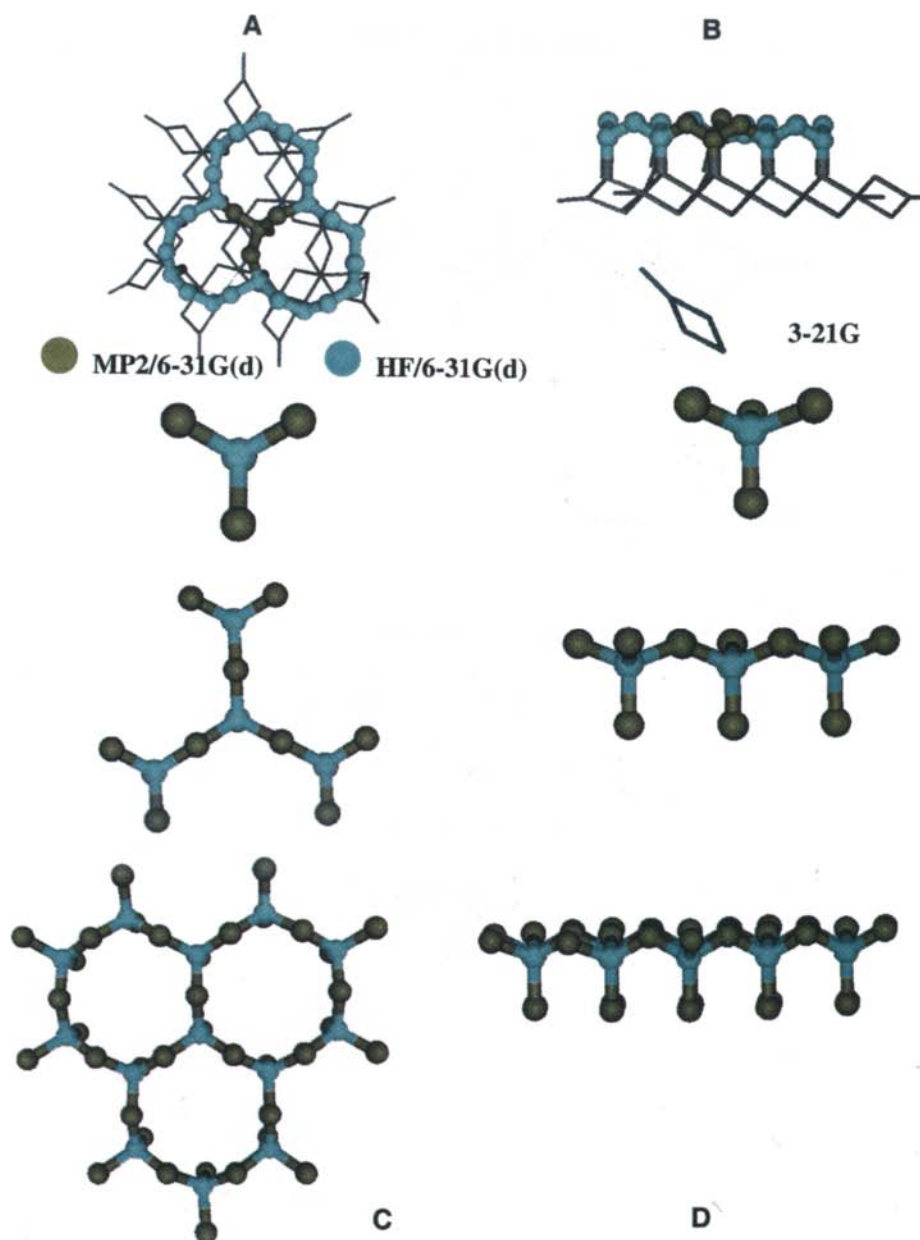


Fig.6 Clusters mimicking the ditrigonal cavities of clay minerals: A and B – used for ONIOM model; C and D – used for canonic *ab initio* calculations.

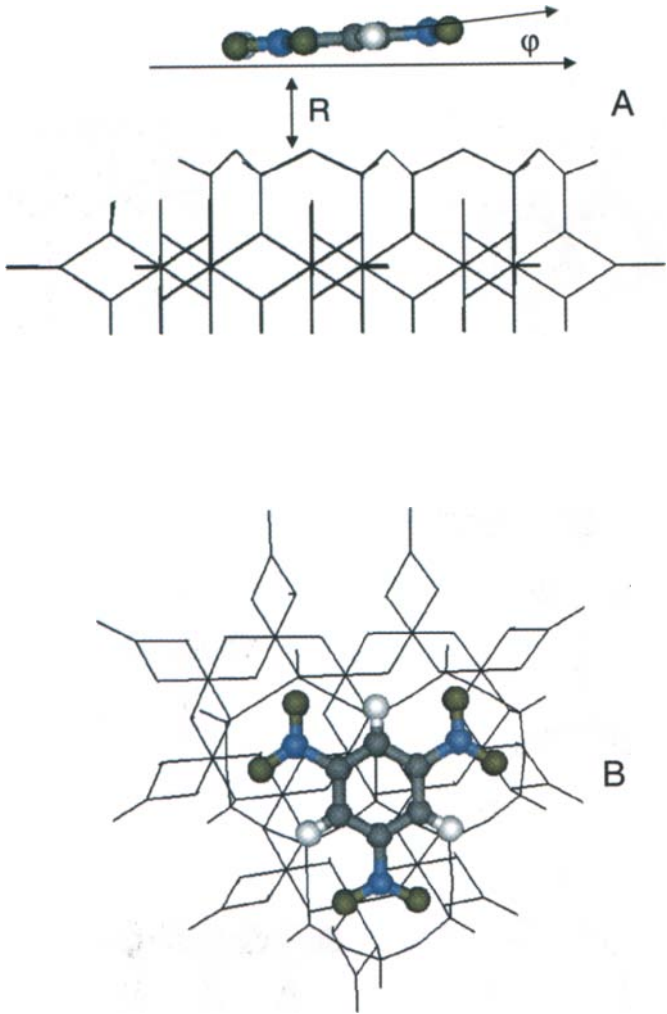


Fig. 7 The optimized structure of adsorbed TNB molecule on the siloxane surface of the mineral [198].

Let us first analyze the results of the calculations of geometrical parameters. The most important outcome of these investigations could be summarized as follows (see Table 5, which presents BSSE corrected interaction energies of TNB adsorption on the siloxane surface) [197, 198].

- i) The TNB molecule can be adsorbed in a virtually coplanar orientation of its plane with respect to the surface of the siloxane sites (see Fig. 7).
- ii) The vertical intermolecular distance between the oxygen plane and the TNB plane does not depend significantly on the size of cluster and the method of calculations. It amounts to ca. 3.2 – 3.4 Å. However, when electronic correlation is taken into account, it decreases to ca. 3.1 – 3.3 Å (see Table 5).
- iii) The oxygen atom of the clay surface is placed practically under the center of symmetry of the TNB molecule.

Table 5

BSSE corrected interaction energy (kcal/mol) of TNB adsorption on the siloxane surface and distances (Å) between the TNB plane and the siloxane surface calculated at the HF and DFT level of theory and using the ONIOM method [197, 198]

Cluster	Method	Basis set	Distance	Energy
Si ₁₃ O ₃₇ H ₂₂	HF	6-31G(d)	3.4	5.5
		6-31+G(d)	3.3	5.1
Al ₂₂ Si ₁₃ O ₈₁ H ₄₄	ONIOM(HF)	6-31G(d):6-31G(d):STO-3G	3.3	5.0
		6-31G(d):6-31G(d):3-21G	3.2	4.4
		6-31+G(d):6-31G(d):STO-3G	3.3	3.5
		6-31+G(d):6-31G(d):3-21G	3.3	3.1
Si ₄ O ₁₃ H ₁₀	DFT	6-31G	3.3	5.7
		6-31G(d)	3.5	4.1
		6-311G(d)	3.5	4.3
		6-311G(df,p)	3.5	3.8
Si ₄ O ₁₃ H ₁₀	MP2	6-31G	3.2	6.7
		6-31+G	3.2	7.9
		6-31G(d)	3.3	6.0
		6-311G(d)	3.3	6.5
Al ₂₂ Si ₁₃ O ₈₁ H ₄₄	ONIOM(HF)	6-311+G(d)	3.3	7.4
		MP2/6-31G(d):6-31G(d):STO-3G	3.3	6.8
		MP2/6-31G(d):6-31G(d):3-21G	3.1	7.1

Table 6

The interaction energy components calculated using ONIOM(MP2/6-31G(d):HF/6-31G(d)) method. All values are in kcal/mol

Interacting System	$\epsilon_{el}^{(1)}$	$\epsilon_{ex}^{(1)}$	$\Delta\epsilon_{del}$	ΔE_{SCF}	$\epsilon_{MP}^{(2)}$	ΔE_{MP2}
Trinitrobenzene...Siloxane	-7.8	4.4	-2.1	-5.5	-6.9	-12.4

Recently a comprehensive analysis of the adsorption energies of the TNB-siloxane surface systems has been published [197, 198]. The results are collected in Table 5. The following point needs to be highlighted: the data obtained at MP2 level of theory are always considerably higher than the ones obtained at the HF and DFT levels. Therefore, there is a significant contribution of electron correlation energy to the total value of interaction energy. Thus, it has been concluded [197] that two physical forces, presumably electrostatic and dispersion interactions, mostly contribute to the interaction between TNB and the siloxane surface of clay minerals.

For a better understanding of the nature of the adsorption forces between TNB and the siloxane surface of clay minerals, the decomposition scheme of Sokalski et al. [199] was applied. The results of such energy decomposition are presented in Table 6. They are in complete agreement with qualitative conclusions presented above. One may see that two dominant attractive contributions govern the adsorption of TNB. As it is expected, one is an electrostatic contribution, and the other one is contribution, which includes components that originate from the electronic correlation. The electronic correlation related contributions include the dispersion component and a correlation correction to electrostatic, exchange, and delocalization terms of the interaction energy.

In summary, the attractive term of the adsorption energy consists of two commensurable contributions. The first is the electrostatic interaction. It has specific character. This interaction is responsible for the orientation of the absorbed nitroaromatic compounds. Another stabilizing interaction originates from dispersion energy. The dispersion interaction does not have a specific character. However, it has been found that significant part of the adsorption energy contributes to the specific interaction between TNB and the siloxane sites of clay minerals.

The maps of electrostatic potential for TNB and for the siloxane surface were also published [198] (see Fig. 8). The area of positive electrostatic potential covers the whole TNB molecule with maximum in the center of symmetry of TNB. This is due to the strong electron acceptor influence of the nitro-groups. For the siloxane surface, the positive charges of the silicon atoms are screened by the negative charge of oxygens. It results in an area of negative electrostatic potential, which covers practically the whole of basal silicon-oxygen plane. Thus authors predicted that the superposition of the maxima for positive (TNB) and negative (siloxane) values of the potential results in the same orientation of the adsorbed TNB molecule as it was revealed by the ONIOM and canonic *ab initio* calculations.

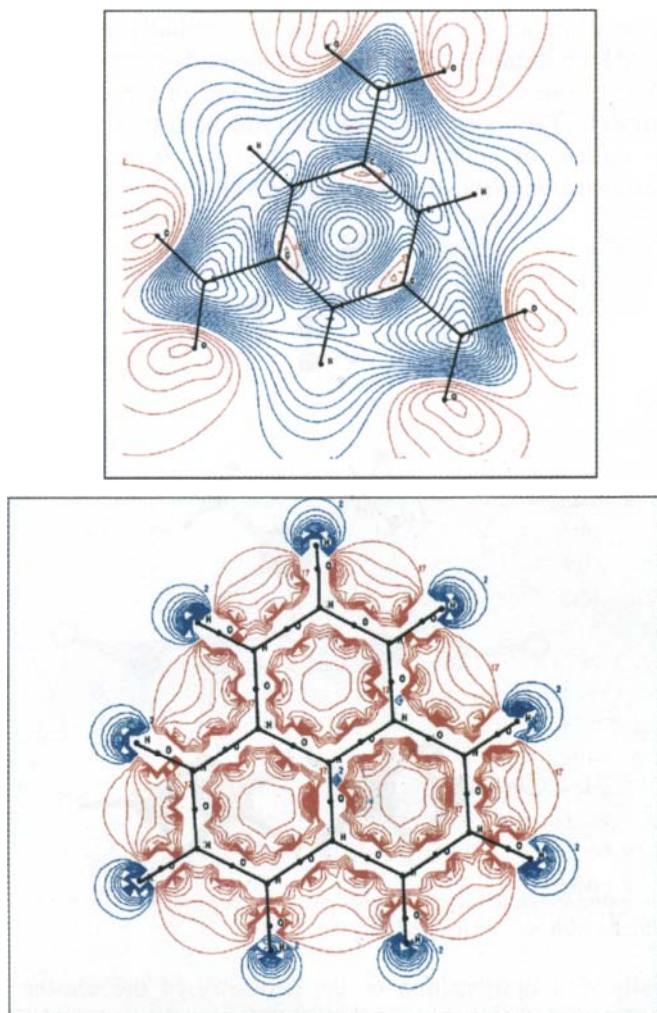


Fig. 8 The maps of electrostatic potential: A – 1,3,5-trinitrobenzene; B – siloxane site of clay minerals. Red color – area of negative electrostatic potential; blue color – area of positive electrostatic potential.

5.2.2. Interaction of 1,3,5-trinitrobenzene with hydrated surface of clay minerals

The investigations of the interactions of NACs with the partially hydrated basal surface of the mineral have been reported in [200]. Authors have calculated the geometry and interaction energy of nitrobenzene (NB) with the

hydrated basal surface of montmorillonite. The partially hydrated Na^+ cation has compensated the negative charge, which appears as consequence of isomorphic substitution of one Mg^{2+} cation for Al^{3+} cation in the octahedral part of the cluster model. The optimized structure of adsorbed nitrobenzene on the hydrated surface of montmorillonite with two water molecules and Na^+ exchangeable cation is illustrated in Fig. 9 [200].

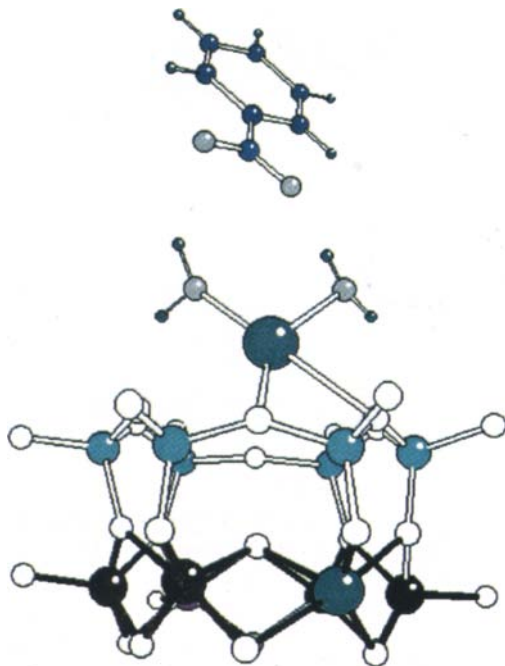


Fig. 9 The optimized structure of adsorbed nitrobenzene molecule on the hydrated surface of montmorillonite with Na^+ exchangeable cation [200].

Initially, full optimization of the geometry of the cluster with formula $\text{Si}_6\text{Al}_6\text{O}_{30}\text{H}_{18}$ has been carried out at the HF level of theory with 6-31G(d) basis set to check the suitability of this model to reproduce the average geometry parameters of the clay minerals. Quantum chemically calculated geometry parameters are in good agreement with an averaged experimentally Si-O and Al-O bond lengths and the Si-O-Al bond angle [201]. These calculations were followed by the calculation of electrostatic potential in the plane, which is parallel to the basal plane to find the most favorable position of the Na^+ exchangeable cation above the tetrahedral cavity. The Na^+ exchangeable cation has been placed in the middle of area with the most negative electrostatic potential in the basal plane of the cluster model. The calculated interaction

energy between the negatively charged aluminosilicate matrix and Na^+ is around 100 kcal/mol.

Additionally, the interactions of the adsorbed water molecules with the surface basal oxygen atoms of the tetrahedral sheet were investigated [201]. The authors have calculated the interaction of the Na^+ exchangeable cation with one and two water molecules on the surface of cluster model. The results of this *ab initio* calculations show the formation of hydrogen bonds between the water molecules and the surface basal oxygen atoms that was also suggested experimentally [12, 32]. This interaction could be considered as one of the sources of nonadditivity in the properties of the clay minerals having different degrees of humidity. Previously, this point was supported based on the results of the semiempirical calculations where the exchangeable cations have been hydrated by up to four water molecules [99]. A clear tendency of a decrease of the interatomic H...O distance when the number of water molecules is increased was found. The calculated geometrical parameters are in very good agreement with experimental data [12, 32]. Also, the stepwise interaction of water molecules is accompanied by an increase of the Na^+ -O bond length and the vertical distance between the Na^+ ion and the basal lattice plane. This is in agreement with experimental data [12, 17] suggesting that the hydrated exchangeable cations are leaving the ditrigonal cavities, and they are located in the interlayer space. It was also found that the stepwise interaction energy of the water molecules with Na^+ exchangeable cation amounts to 18 and 14 kcal/mol for an interaction with the first and second water molecules, respectively.

It has been finally revealed [200] that the NACs are adsorbed on the siloxane hydrated surface with Na^+ exchangeable cation by forming two H-bonds between oxygen atoms of $-\text{NO}_2$ group of the organic molecule and hydrogen atoms of the water molecules (see Fig. 9). As it should be expected, this process leads to the stretching of interatomic distances of hydrogen bond between the water molecules and the basal oxygens of mineral, the length of the Na^+ -O bonds, and the vertical distance between Na^+ ion and the surface. The interaction between nitrobenzene and a hydrated surface of kaolinite is 11.4 kcal/mol at the HF/6-31G(d) level of theory and 11.8 kcal/mol at the DFT(B3LYP)/6-31G(d) level of theory. Both values of interaction energy are in a good agreement with experimentally estimated adsorption energy of NACs on the surface of clay minerals (about 10 kcal/mol) [153]. It suggests that this type of adsorption of nitroaromatic compounds should be at least as effective as the adsorption, which includes the donor-acceptor type of interactions with a nonhydrated silicon-oxygen surface.

In addition to above described theoretical studies we also would like to mention very simple quantum chemical calculations of complexes 1,3-DNB and 1,3,5-TNB with two and three K^+ ions formed by placing K^+ ions in the plane of

each molecule and bisecting each O-N-O angle. These studies were performed at the B3LYP/6-311G** level of theory [157, 158]. The quantum chemical results follow the same trends as the experimental data. In these studies, also MD simulations of K^+ -smectites with *m*- and *p*-DNB in the interlayer space were executed in order to explore possible steric effect in the interlayer space [158]. The clay model has $K_{12}(Al_{36}Mg_{12})Si_{96}O_{240}(OH)_{48}$ composition. One molecule of either *m*- or *p*-DNB was added to the unit cell, with its molecular plane perpendicular to the basal planes of the clay. Fifty water molecules were also added. The formation of EDA complex between NACs and the siloxane surface was not supported by this study. It was found that the sorption of NACs to smectite surfaces is controlled largely by the hydration characteristics of the exchangeable cation, which regulates the cation-nitroaromatic complexation and swelling of the smectite. It was also shown that substituted nitrobenzenes adsorbed on K-smectite could directly interact with K^+ exchangeable ions or indirectly through coordinated water molecules. One or both these favorable interactions occur in the interlayer space of K^+ -smectite and contribute to the stabilization of the organic molecule-clay complexes. The K-O₂N interaction causes the N-O bonds to be somewhat weakened (lengthened, with less double-bond character) while C-N bonds are somewhat strengthened (shortened, with more double-bond character), relative to isolated, uncomplexed nitroaromatic molecules.

5.2.3. Summary

The obtained results enable the following conclusion. The calculated value of interaction energy between the nitrobenzene molecule and the partially hydrated surface of the clay minerals is very close to the interaction energy between the NAC molecules and the nonhydrated surface. This finding combined with the experimental data of the adsorption of nitroaromatic compounds on the hydrated surface of clay minerals indicates that this type of adsorption should be at least as effective as the adsorption, which includes coplanar interactions of TNB with nonhydrated silicon-oxygen surfaces.

The interaction energy of adsorption system TNB on the nonhydrated siloxane surface of clay minerals consists of two commensurable contributions. The first is the electrostatic interaction, which is responsible for the orientation of the absorbed nitroaromatic compounds. Another stabilizing interaction originates from dispersion energy.

The calculated values of interaction energies of TNB molecule on the surface of clay minerals are in good agreement with an experimental value.

6. GENERAL CONCLUSIONS AND FUTURE RESEARCH AREA

Recent theoretical studies of adsorption of nitroaromatic compounds on the surface of clay minerals provide a qualitative and quantitative understanding of the interactions between the organic molecule and the surface of the mineral that occur in soils and aquifer materials. The theoretical results lead to elucidation of experimental findings. Further, results of such theoretical studies could contribute to an understanding of the adsorption processes of nitroaromatic compounds that may be occurring in other environments. On the other hand, despite several theoretical studies performed it is necessary to continue calculations of systems of other nitroaromatic compounds with clay minerals, which will lead to an understanding of general trends of interactions of energetic materials with soils and so could facilitate development of possible procedures of decontamination of soils and ground water.

Based on results of recent experimental and theoretical studies we can suggest several problems, which would be interesting to study using computational methods. Among them are:

- the intercalation of nitroaromatic compounds in the interlayer space of clay minerals;
- the dependence of adsorption and intercalation on the type of nitroaromatic compounds;
- the effect of the type of exchangeable cation and the type of clay mineral on the different parameters of adsorption process;
- adsorption on the octahedral surface of clay minerals;
- the influence of the nature of the clay minerals surface on the adsorption or intercalation.

ACKNOWLEDGEMENT

This work was facilitated by the support of ARO grant No. DAAG55-98-1-0247, by the support of CREST grant No. 9805465 & 9706268, by the support of Department of the Army grant No. DACA42-02-C-0057 through the MACERAC Project, and by the support of the Army High Performance Computing Research Center under the auspices of the Department of the Army, Army Research Laboratory Cooperative agreement number DAAH04-95-2-0003/contract number DAAH04-95-C-0008, the content of which does not necessarily reflect the position or the policy of the government, and no official endorsement should be inferred.

REFERENCES

- [1] http://www.frtr.gov/matrix2/section2/2_10_1.html, Federal Remediation Technologies Roundtable, Remediation Technologies Screening Matrix and Reference Guide, Version 4.0, Section 2.10.
- [2] D.L. Kaplan, Biotechnology and Bioremediation for Organic Energetic Compounds, In: P. Markins (eds.), Organic Energetic Compounds, Nova Science Publishers, Inc., New York, 1993.
- [3] J. Hawari, J. Halasz, S. Beaudet, L. Paquet, G. Ampleman and S. Thoboutot, Appl. Environ. Microbiol., 65 (1999) 2977.
- [4] NDCEE Pink Water Treatment Options: National Defense Center for Environmental Excellence Pink Water Treatment Options, Technical Report, Contact No. DAAA21-93-C-0046, 1995, pp. 1-42.
- [5] P.G. Rieger and H.-J. Knackmuss, Basic Knowledge and Perspectives on Biodegradation of 2,4,6-trinitrotoluene and Related Compounds in Contaminated Soil, In: J. Spain (eds.), Biodegradation of Nitroaromatic compounds, Plenum Press, New York, 1995, pp. 1-18.
- [6] M.E. Walsh, T.F. Jenkins and P.G. Thorne, Analytical Methods for Characterization of Explosives Contaminated Sites on US Army Installations, ETHA-TECR-89205, SPIE 2504, (1990), pp. 342-349.
- [7] R.F. Spauling and J.W. Fulton, J. Contamin. Hydrol., 2(9) (1988) 139.
- [8] M.E. Walsh, T.F. Jenkins, P.S. Schnitker, J.W. Elwell and M.H. Stutz, USA Cold Regions Research and Engineering Laboratory CRREL Special Report 93-5, Hanover N. H, 1993, pp. 1-17.
- [9] R.L. Bates, Stone, Clay, Glasses: How Building Materials are Found and Used, Erslow, New York, 1987.
- [10] R.E. Grim, Clay Mineralogy, Mc Graw-Hill, New York, 1953.
- [11] G. Millot, Geology of Clays: Weathering, Sedimentation, Geochemistry, Springer, New York, 1970.
- [12] N.G. Vasyliov and V.V. Gonacharuk, The Natural Silicates: Structure, Properties and the Reaction Ability, Naukova dumka, Kiev, 1992 (in Russian).
- [13] M. Alexander, Environ. Sci. Technol., 29 (1995) 2713.
- [14] <http://encarta.msn.com/encnet/refpages/refarticle.aspx?refid=761576446>, Christopher King, B.A., M.J. "Soil," Microsoft® Encarta®, Online Encyclopedia, 2002, <http://encarta.msn.com> © 1997-2002.
- [15] S.W. Bailey, Structures of Layered Silicates, In: G.W. Brindley and G. Brown (eds.), Crystal Structures of Clay Minerals and their X-ray Identification, Mineralogical Society, London, 1980, pp. 6-28.
- [16] L. Pauling (ed.), The Nature of the Chemical Bond, Cornell University Press, New York, 1967.
- [17] A.C.D. Newman (ed.), The Chemistry of Clays and Clay Minerals (Mineralogical Society Monograph No. 6), Longman Scientific and Technical, London, 1987.
- [18] G. Wagelhard, U. Lohse and M. Magi, Structure and Reactivity of Modified Zeolites, Elsevier, Amsterdam, 1984.
- [19] A. Weiss and J. Russov, Proc. Int. Clay Conf., Stockholm 1 (1963) 203.
- [20] C. Achtnich, Environ. Sci. Technol., 33(19) (1999) 3421.
- [21] D. Frenkel and B. Smit, Understanding Molecular Simulation: From Algorithms to Applications, Academic Press, ISBN, 2nd edition, New York, 2001.

- [22] M.P. Allen and D.J. Tildesley, *Computer Simulation of Liquids*, Clarendon Press: Oxford, (1987), pp. 1, 205.
- [23] T. Schlick, *Molecular Modeling and Simulation, An Interdisciplinary guide*, Series: *Interdisciplinary Mathematics*, Vol. 21, Springer Verlag, New York, 2002.
- [24] J. Sauer, *Chem. Rev.*, 94 (1994) 2095.
- [25] J. Sauer, *Chem. Rev.*, 89 (1989) 199.
- [26] C. Pisani, R. Orlando and R. Nada, *Cluster Models for Surface and Bulk Phenomena*, G. Pacchoni (ed.), Plenum Press, New York, 1992, 221.
- [27] C. Pisani, R. Orlando and F. Cora, *J. Phys. Chem.*, 97 (1992) 4195.
- [28] M.D. Newton, *J. Phys. Chem.*, 87 (1983) 4288.
- [29] M. Svensson, S. Humbel, R.D.J. Froese, T. Matsubara, S. Sieber and K.J. Morokuma, *J. Phys. Chem.*, 100 (1996) 19357.
- [30] S. Daprich, I. Komaromi, K.S. Byun, K. Morokuma and M.J. Frisch, *J. Mol. Struct. (Theochem)*, 462 (1999) 1.
- [31] A.J.M. Lagadec, D.J. Miller, A.V. Lilke and S.B. Hawthorne, *Environ. Sci. Technol.*, 34 (2000) 1542.
- [32] G. Sposito and R. Prost, *Chem. Rev.*, 82(6) (1982) 571.
- [33] H. Othaki and T. Randnai, *Chem. Rev.*, 93 (1993) 1157.
- [34] C. de la Calle and H. Suquet, In: S.W. Bailey (eds.), *Reviews in Mineralogy*, Mineralogical Society of America, Washington, DC, 1988, 476.
- [35] W.A.P. Luck, In *Water: a Comprehensive Treatise. Water in Crystalline Hydrates. Aqueous Solution of Simple Nonelectrolytes*, Plenum Press, New York, 1973.
- [36] N.T. Skipper, A.K. Soper and J.D.C. McConnell, *J. Chem. Phys.*, 94 (1991) 5751.
- [37] N.T. Skipper, A.K. Soper and M.V. Smalley, *J. Phys. Chem.*, 98 (1994) 942.
- [38] N.T. Skipper, M.V. Smalley, G.D. Williams, A.K. Soper and C.H. Thompson, *J. Phys. Chem.*, 99 (1995) 14201.
- [39] G.D. Williams, A.K. Soper, N.T. Skipper and M.V. Smalley, *J. Phys. Chem. B*, 102 (1998) 8945.
- [40] Yu. Tarasevich, I. Khim. Teknol. Vody, 2 (1980) 99.
- [41] D.E. Woessner, *J. Magn. Reson.*, 39 (1980) 297.
- [42] D.H. Powell, K. Tongkhao, S.J. Kennedy and P.G. Slade, *Clays and Clay Miner.*, 45 (1997) 290.
- [43] D.H. Powell, K. Tongkhao, S.J. Kennedy and P.G. Slade, *Physica B*, 241-243 (1998) 387.
- [44] D.H. Powell, H.E. Fisher and N.T. Skipper, *J. Phys. Chem. B*, 102 (1998) 10899.
- [45] M.H. Fu, Z.Z. Zhang and P.F. Low, *Clays and Clay Miner.*, 38 (1990) 485.
- [46] C. Pitteloud, D.H. Powell, A.K. Soper and C.J. Benmore, *Physica B*, 276-278 (2000) 236.
- [47] C.T. Johnston, G. Sposito and C. Erickson, *Clays and Clay Miner.*, 40 (1992) 722.
- [48] D.E. Woessner, *J. Magn. Reson.*, 16 (1974) 483.
- [49] D.E. Woessner, *NMR Studies of Preferentially Oriented Water at Interface*. In: R. Haque and F.J. Biras (eds.) *Mass Spectrometry and NMR Spectroscopy in Pesticide Chemistry*, Plenum Press, New York, 1974, pp. 279-304.
- [50] D.E. Woessner, *Molec. Phys.*, 34 (1977) 899.
- [51] J. Hougardy, W.E.E. Stone and J.J. Fripiat, *J. Chem. Phys.*, 64, (1976) 3840.
- [52] D.E. Woessner and B.S. Snowden, *J. Colloid Interface Sci.*, 30 (1969) 54.
- [53] J.J. Fripiat and M. Lettelier, *J. Mag. Res.*, 57 (1984) 279.
- [54] A.-M. Hecht and E. Geissler, *J. Colloid Interface Sci.*, 34 (1970) 32.

- [55] J. Grandjean and P. Laszlo, *Clays and Clay Miner.*, 37 (1989) 403.
- [56] J. Grandjean and P. Laszlo, *J. Mag. Res.*, 83 (1990) 128.
- [57] J. Grandjean and P. Laszlo, *J. Mag. Res.*, 92 (1991) 404.
- [58] A. Delville, J. Grandjean and P. Laszlo, *J. Phys. Chem.*, 95 (1991) 1383.
- [59] C.A. Weiss Jr. and W.V. Gerasimowicz, *Geoch. Et Cosmoch. Acta*, 60 (1996) 265.
- [60] J. Grandjean, *J. Colloid Interface Sci.*, 185(2) (1997) 554.
- [61] S. Karaborni, B. Smith, W. Heidug, J. Urai and E. van Oort, *Science*, 271 (1996) 1102.
- [62] E.S. Boek, P.V. Coveney and N.T. Skipper, *Langmuir*, 11 (1995) 4629.
- [63] F.-R.C. Chang, N.T. Skipper and G. Sposito, *Langmuir*, 11 (1995) 2734.
- [64] F.-R.C. Chang, N.T. Skipper, K. Refson, J.A. Greathouse and G. Sposito, In: D.L. Sparks and T. Grundl. (eds.), *Mineral-Water Interface Reactions*, American Chemical Society, Washington, DC, 1998, Chapter 6.
- [65] N.T. Skipper, K. Refson and J.D.C. McConnell, *J. Chem. Hys.*, 94 (1991) 7434.
- [66] N.T. Skipper, K. Refson and J.D.C. McConnell, In: D. C. Manning, P. L. Hall and C. R. Hughs (eds.), *Geochemistry of Clay-Pore Fluid Interactions*, Chapman and Hall, London, 1993, Chapter 2.
- [67] K. Refson, N.T. Skipper and J.D.C. McConnell, In: D.C. Manning, P.L. Hall and C.R. Hughs (eds.), *Geochemistry of Clay-Pore Fluid Interactions*, Chapman and Hall, London, 1993, Chapter 3.
- [68] G. Sposito, N.T. Skipper, R. Sutton, S.-H. Park, A.K. Soper, J.A. Greathouse, *Proc. Natl. Acad. Sci. USA*, 96 (1999) 3358.
- [69] J.A. Greathouse and G. Sposito, *J. Phys. Chem. B*, 102 (1998) 2406.
- [70] N.T. Skipper, F.-R.C. Chang and G. Sposito, *Clays and Clay Miner.*, 43 (1995) 285.
- [71] N.T. Skipper, K. Refson and J.D.C. McConnell, *Clay Miner.*, 24 (1989) 411.
- [72] S.-H. Park and G. Sposito, *J. Phys. Chem. B*, 104 (2000) 4642.
- [73] F.-R.C. Chang, N.T. Skipper and G. Sposito, *Langmuir*, 14 (1998) 1201.
- [74] J.A. Greathouse, K. Refson and G. Sposito, *J. Am. Chem. Soc.*, 122 (2000) 11459.
- [75] N.T. Skipper, A.K. Soper, J.D.C. McConnell and K. Refson, *Chem. Phys. Lett.*, 166(3) (1990) 141.
- [76] G. Sposito, S.-H. Park and R. Sutton, *Clays and Clay Miner.*, 47 (1999) 192.
- [77] F.-R.C. Chang, N.T. Skipper and G. Sposito, *Langmuir*, 13 (1997) 2074.
- [78] R. Sutton and G. Sposito, *J. Colloid Interface Sci.*, 237 (2001) 174.
- [79] E.S. Boek, P.V. Coveney and N.T. Skipper, *J. Am. Chem. Soc.*, 117 (1995) 12608.
- [80] G. Sposito, *J. Colloid Interface Sci.*, 237 (2001) 174.
- [81] D.E. Smith, *Langmuir*, 14 (1998) 5959.
- [82] D.A. Young and D.E. Smith, *J. Phys. Chem. B*, 104 (2000) 9163.
- [83] A. Delville and S. Sokolowski, *J. Phys. Chem.*, 97 (1993) 6261.
- [84] A. Delville, *J. Phys. Chem.*, 99 (1995) 2033.
- [85] A. Delville, *J. Phys. Chem.*, 97 (1993) 9703.
- [86] A. Delville, *Langmuir*, 7 (1991) 547.
- [87] A. Delville, *Langmuir*, 8 (1992) 1796.
- [88] K.S. Smirnov and D. Bougeard, *J. Phys. Chem. B*, 103 (1999) 5266.
- [89] B.J. Teppen, K. Rasmussen, P.M. Bertsch, D.M. Miller and L. Schäfer, *J. Phys. Chem. B*, 101 (1997) 1579.
- [90] B.J. Teppen, C.-H. Yu, D.M. Miller and L. Schäfer, *J. Comput. Chem.*, 19 (1998) 144.
- [91] B.J. Teppen, C.-H. Yu, S.Q. Newton, D.M. Miller and L. Schäfer, *J. Phys. Chem. A*, 106 (2002) 5498.
- [92] J.O. Titiloye and N.T. Skipper, *Chem. Phys. Lett.*, 329 (2000) 23.

- [93] C.H. Bridgeman, A.D. Buckingham, N.T. Skipper and M.C. Payne, *Molec. Phys.*, 89(3) (1996) 879.
- [94] R. Wardle and G.W. Brindley, *Am. Mineral.*, 57 (1972) 732.
- [95] A. Chatterjee, T. Iwasaki, T. Ebina and A.A. Miyamoto, *Comput. Mat. Sci.*, 14 (1999) 119.
- [96] A. Chatterjee, T. Iwasaki and T. Ebina, *J. Phys. Chem. A*, 104 (2000) 8216.
- [97] A. Chatterjee, T. Iwasaki, T. Ebina and H. Hayashi, *Appl. Surface Sci.*, 121/122 (1997) 167.
- [98] T. Ebina, T. Iwasaki, Y. Onodera and A. Chatterjee, *Comput. Mat. Sci.*, 14 (1999) 254.
- [99] L.G. Gorb, E.V. Aksenenko, J.W. Adams, S.L. Larson, C.A. Weiss, D. Leszczynska and J. Leszczynski, *J. Molecul. Struct. (Theochem)* 425 (1998) 128.
- [100] J.D. Kubicki, G.A. Blake and S.E. Apitz, *Geoch. Et Cosmochim. Acta*, 60(24) (1996) 4897.
- [101] J.D. Kubicki, G.A. Blake and S.E. Apitz, *Geoch. Et Cosmochim. Acta*, 61(5) (1997) 1031.
- [102] J.D. Kubicki and D. Sykes, *Geoch. Et Cosmochim. Acta*, 59(23) (1995) 4791.
- [103] J.D. Kubicki, M.J. Itoh, L.M. Schroeter and S.E. Apitz, *Environ. Sci. Technol.*, 31 (1997) 1151.
- [104] A. Chatterjee, T. Iwasaki and T. Ebina, *J. Phys. Chem. A*, 106 (2002) 641.
- [105] A. Chatterjee, T. Iwasaki and T. Ebina, *J. Phys. Chem. A*, 104 (2000) 2098.
- [106] A. Chatterjee, T. Ebina and T. Iwasaki, *J. Phys. Chem. A*, 105 (2001) 10694.
- [107] D. Tunega, G. Haberhauer, M.H. Gerzabek and H. Lischka, *Langmuir*, 18 (2002) 139.
- [108] J.J. Pignatello, In: B.L. Sawhney, K. Brown (eds.), *Reactions and Movement of Organic Chemicals in Soil*, Soil Science Society of America, Special Publication SSSA, Madison WI, 1989, vol. 22, 45.
- [109] J.M. Adams and D.A. Jefferson, *Acta Crystallogr. B*, 32 (1976) 1180.
- [110] J.M. Adams, P.I. Reid, J.M. Thomas and M.J. Walters, *Clays and Clay Miner.*, 24 (1976) 267.
- [111] R.L. Ledoux and J.L. White, *J. Colloid Interface Sci.*, 21 (1966) 127.
- [112] J.M. Adams, *Clays and Clay Miner.*, 26 (1978) 291.
- [113] K. Nakamoto, M. Margoshes and R. Rundle, *J. Am. Chem. Soc.*, 77 (1955) 6480.
- [114] J.M. Adams, *Acta Crystallogr. B*, 35 (1979) 1084.
- [115] X. Xie and S. Hayashi, *J. Phys. Chem. B*, 103 (1999) 5949.
- [116] X. Xie and S. Hayashi, *J. Phys. Chem. B*, 103 (1999) 5956.
- [117] M. Zamama and M. Knidiri, *Spectrochim. Acta A*, 56 (2000) 1139.
- [118] M. Cruz, A. Laycock and J.L. White, *Perturbation of OH groups in Intercalated Donor-acceptor Complexes. I. Formamide, Methylformamide, and Dimethylformamide Kaolinite Complexes*, In *Proceedings of the International Clay Conference*, Tokyo, Israel University Press, Jerusalem, 1969, 775.
- [119] S. Olejnik, A.M. Posner and J.P. Quirk, *Clay Miner.*, 8 (1970) 421.
- [120] P.J.R. Uwins, I.D.R. Mackinnon, J.G. Thomson and A.J.E. Yago, *Clays and Clay Miner.*, 41 (1993) 707.
- [121] R.L. Frost, S.J. Van Der Gaast, M. Zbik, J.T. Kloprage and G.N. Paroz, *Appl. Clay Sci.*, 20 (2002) 177.
- [122] R.L. Frost, J. Kristof, E. Horvath and J.T. Kloprogge, *Spectrochim. Acta Part A: Molec. and Biomolec. Spectrosc.*, 56(6) (2000) 1191.
- [123] R.L. Frost, W. Forsling, A. Holmgren, J.T. Kloprogge and J. Kristof, *J. Raman. Spectrosc.*, 29 (1998) 1065.

- [124] R.L. Frost, J. Kristof, E. Horvath and J.T. Klopprogge, *Spectrochim. Acta Part A: Molec. and Biomolec. Spectrosc.*, 56(9) (2000) 1711.
- [125] R.L. Frost, T.H. Tran, L. Rintoul and J. Kristof, *Analyst*, 123 (1998) 611.
- [126] R.L. Frost, J. Kristof, G.N. Paroz, T.H. Tran and J.T. Klopprogge, *J. Colloid Interface Sci.*, 204 (1998) 227.
- [127] R.L. Frost, J. Kristof, E. Horvath and J.T. Klopprogge, *Langmuir*, 17 (2001) 3216.
- [128] J. Kristof, R.L. Frost, J.T. Klopprogge, E. Horvath and M.J. Gabor, *Therm. Anal. Calorim.*, 56 (1999) 885.
- [129] J. Kristof, E. Horvath, R.L. Frost and J.T. Klopprogge, *J. Therm. Anal.*, 63 (2000) 279.
- [130] S. Hayashi, *J. Phys. Chem.*, 99 (1995) 7120.
- [131] S. Hayashi, *Clays and Clay Miner.*, 45 (1997) 724.
- [132] W.N. Martens, R.L. Frost, J. Kristof and E. Horvath, *J. Phys. Chem. B*, 106 (2002) 4162.
- [133] M. Raupach, P.F. Barron and J.G. Thompson, *Clays and Clay Miner.*, 35 (1987) 208.
- [134] J.G. Thompson and C. Cuff, *Clays and Clay Miner.*, 33 (1985) 490.
- [135] J.G. Thompson, *Clays and Clay Miner.*, 33 (1985) 173.
- [136] S. Olejnik, L.A.G. Aylmore, A.M. Posner and J.P. Quirk, *J. Phys. Chem.*, 72 (1968) 241.
- [137] M.J. Duer, J. Rocha and J. Klinowski, *J. Am. Chem. Soc.*, 114 (1992) 6867.
- [138] R.L. Frost, J. Kristof, E. Horvath and J.T. Klopprogge, *J. Phys. Chem. B*, 103 (1999) 9654.
- [139] C.T. Johnston, G. Sposito, D.F. Bocian and R.P. Birge, *J. Phys. Chem.*, 88 (1984) 5959.
- [140] P. M. Costanzo, C.V. Clemency and R.F. Giese, *Clays and Clay Miner.*, 28 (1980) 155.
- [141] L. Heller - Kallai, E. Huard and R. Prost, *Clay Miner.*, 26 (1991) 245.
- [142] J.M. Adams and G. Walzl, *Clays and Clay Miner.*, 41 (1980) 130.
- [143] G.C. Pimentel and A.L. McClellan, *The Hydrogen Bond: Freeman, London*, 105, 224, 285 (1960).
- [144] R.L. Frost, J. Kristof, G.N. Paroz and J.T. Klopprogge, *J. Phys. Chem. B*, 102 (1998) 8519.
- [145] G. J. Churchman, *Clays and Clay Miner.*, 38 (1990) 591.
- [146] C. Breen and S. Lynch, *Clays and Clay Miner.*, 36 (1988) 19.
- [147] M. Lipsicas, R. Raythatha, R.F. Giese and P.M. Costanzo, *Clays and Clay Miner.*, 34 (1986) 635.
- [148] A. Michalkova, D. Tunega and L. Turi Nagy, *J. Mol. Struct. (Theochem)*, 581 (2002) 37.
- [149] A. Michalkova, D. Tunega and L. Turi Nagy, in preparation.
- [150] A. Michalkova, D. Tunega and L. Turi Nagy, in preparation.
- [151] G. Kreese and J. Furthmüller, *Phys. Rev. B*, 54 (1996) 11169.
- [152] S.B. Handerlein, K.W. Weissmahr and R.P. Schwarzenbach, *Environ. Sci. Technol.*, 30 (1996) 612.
- [153] S.B. Handerlein and R.P. Schwarzenbach, *Environ. Sci. Technol.*, 21 (1993) 316.
- [154] K.W. Weissmahr, S.B. Handerlein, R.P. Schwarzenbach, E. Hany and R. Nüsch, *Environ. Sci. Technol.*, 31 (1997) 240.
- [155] K.W. Weissmahr, S.B. Handerlein and R.P. Schwarzenbach, *Soil. Sci. Soc. Am. J.*, 62 (1998) 369.
- [156] K.W. Weissmahr, M. Hildenbrand, R.P. Schwarzenbach and S.B. Handerlein, *Environ. Sci. Technol.*, 33 (1999) 2593.

- [157] S.A. Boyd, G. Sheng, B.J. Teppen and C.T. Johnston, *Environ. Sci. Technol.*, 35 (2001) 4227.
- [158] C.T. Johnston, M.F. De Oliviera, B.J. Teppen, G. Sheng and S.A. Boyd, *Environ. Sci. Technol.*, 35 (2001) 4767.
- [159] G. Sposito, *The Surface Chemistry of Soils*, Oxford University Press, New York, 1984.
- [160] P. Fusi, G.G. Ristori and M. Franci, *Clays and Clay Miner.*, 30 (1982) 306.
- [161] S. Saltzman and S. Yariv, *Soil. Sci. Soc. Am. Proc.*, 39 (1975) 474.
- [162] S. Saltzman and S. Yariv, *Soil. Sci. Soc. Am. Proc.*, 40 (1976) 34.
- [163] S. Yariv, J.D. Russell and V.C. Farmer, *Israel J. Chem.*, 4 (1966) 201.
- [164] L. Margulies, H. Rozen and A. Banin, *Clays and Clay Miner.*, 36 (1988) 476.
- [165] M.M. Mortland and K.V. Raman, *Clays and Clay Miner.*, 16 (1968) 393.
- [166] M. Kowalska, H. Guler and D.L. Cocke, *Sci. Total Environ.*, 141 (1994) 223.
- [167] B.L. Sawhney, *Clays and Clay Miner.* 33 (1985) 123.
- [168] I. Ahmad, T.J. Dines, C.H. Rochester and J.A. Andreson, *J. Chem. Soc. Farady Trans.*, 92 (1996) 3225.
- [169] R.A. Nyquist and S.E. Settineri, *Appl. Spectrosc.*, 44 (1990) 1552.
- [170] C.P. Conduit, *J. Chem. Soc.*, (1959) 3273.
- [171] F. Borek, *Naturwissenschaften*, (1963) 471.
- [172] W. Baitinger, P.v.R. Schleyer, T.S.S. R. Murty and L. Robinson, *Tetrahedron*, 20 (1964) 1635.
- [173] J.H.S. Green and H.A. Lauwers, *Spectrochim. Acta A*, 27 (1971) 817.
- [174] T. Urbanski and U. Dabrowska, *Bull. Acad. Pol. Sci.*, 7 (1959) 235.
- [175] G. Varsanyi, E. Molnar-Paal, D. Kosa and G. Keresztury, *Acta Chem. Acad. Sci. Hung.*, 100 (1979) 481.
- [176] E.F. Emery, T. Junk, R.E. Ferrell Jr., R. De Hon and L. G. Butler, *Environ Sci. Technol.*, 35 (2001) 2973.
- [177] R. Takenawa, Y. Komori, S. Hayashi, J. Kawamata and K. Kuroda, *Chem. Mater.*, 13 (2001) 3741.
- [178] D.M. More and R.C. Reynolds Jr., *X-Ray Diffraction and the Identification and Analysis of Clay Minerals*, Oxford University Press, New York, 1989.
- [179] D.M. Townsend and T.E. Myers, Technical Report IRRP-96-1, U. S. Army Engineer Waterways Experiment Station, Vicksburg, MS, 1996.
- [180] J.C. Pennington and J.M. Brannon, *Thermochim. Acta*, 384 (2002) 163.
- [181] D.L. Kaplan and A.M. Kaplan, *Appl. and Environ. Microbiol.*, 44(3) (1982) 757.
- [182] D.M. Townsend, T.E. Myers and D.D. Adrian, Technical Report IRRP-95-4, U. S. Army Engineer Waterways Experiment Station, Vicksburg, MS, 1995.
- [183] S.D. Comfort, P.J. Shea, L.S. Hundal, Z. Li, B.L. Woodbury, J.L. Martin and W.L. Powere, *J. Environ. Quality*, 24 (1995) 1174.
- [184] H.M. Selim, S.K. Xue and I.K. Iskandar, *Soil Sci.*, 160 (1995) 328.
- [185] S.K. Xue, I.K. Iskandar and H.M. Selim, *Soil Sci.*, 160 (1995) 317.
- [186] C.B. Price, J.M. Brannon, S.L. Yost and C.A. Hayes, Technical Report IRRP-00-11, U. S. Army Engineer Waterways Experiment Station, Vicksburg, MS, 2000.
- [187] C. Achtnich, H. Lenke, U. Klaus, M. Spiteller and H.-J. Knackmuss, *Environ. Sci. Technol.*, 34(17) (2000) 3698.
- [188] J.C. Pennington and W.H. Patric, Jr., *J. Environ. Quality*, 19 (1990) 559.
- [189] L.S. Hundal, J. Singh, E.L. Bier, P.J. Shea, S.D. Comfort and W.L. Powers, *Environ. Pollution*, 97 (1997) 55.

- [190] C.G. Hejiman, C. Hollinger, M.A. Glaus, R.P. Schwarzenbach and J. Zeyer, *Appl. Environ. Microbiol.*, 59 (1993) 4350.
- [191] C.G. Hejiman, E. Grieder, C. Hollinger and R.P. Schwarzenbach, *Environ. Sci. Technol.*, 29 (1995) 775.
- [192] J. Klausen, S. Trober, S.B. Handerlein and R.P. Schwarzenbach, *Environ. Sci. Technol.*, 29 (1995) 3296.
- [193] J.M. Brannon, T.E. Myers, Technical Report IRRP-97-2, U. S. Army Engineer Waterways Experiment Station, Vicksburg, MS, 1997.
- [194] C.B. Price, J.M. Brannon, S.L. Yost and C.A. Hayes, Technical Report IRRP-01-19, U. S. Army Engineer Waterways Experiment Station, Vicksburg, MS, 2001.
- [195] C.B. Price, J.M. Brannon and S.L. Yost, Technical Report IRRP-98-2, U.S. Army Engineer Waterways Experiment Station, Vicksburg, MS, 1998.
- [196] T.E. Myers, J.M. Brannon, J.C. Pennington, D.M. Townsend, W.M. Davis, M.K. Ochman, C.A. Hayes and K.F. Myers, Technical Report IRRP-98-8, U. S. Army Engineer Waterways Experiment Station, Vicksburg, MS, 1998.
- [197] A. Pelmeshnikov and J. Leszczynski. *J. Phys. Chem. B*, 103 (1999) 6886.
- [198] L. Gorb, R. Lutchyn, Yu. Zub, D. Leszczynska and J. Leszczynski, *J. Phys. Chem.*, submitted.
- [199] W.A. Sokalski, S. Roszak and K. Pecul, *Chem. Phys. Lett.*, (1988) 153.
- [200] L. Gorb, J. Gu, D. Leszczynska and J. Leszczynski, *Phys. Chem. Chem. Phys.*, 2 (2000) 5007.
- [201] D.L. Bish, *Clays and Clay Miner.*, 41 (1991) 738.

Chapter 13

Chemistry and applications of dinitramides

Per Sjöberg

NEXPLO Bofors AB, 691 85 Karlskoga, Sweden

1. HISTORY

The story of ammonium dinitramide (ADN), $\text{NH}_4\text{N}(\text{NO}_2)_2$, is intriguing and parallels world history of the late 20th century. ADN was probably first synthesized in the Soviet Union during the cold war. Its synthesis was never published, doubtless because of the military strategic value it was considered to have. Presumably it was used as an oxidizer for the propulsion of intercontinental missiles. Unconfirmed rumors claim that the fumes from ADN propellants are not detectable by radar. This must obviously have been a serious threat for NATO's early alert strategy against an intercontinental missile attack. It is also likely that ADN was produced in the Soviet Union until the breakdown of the latter. The change in military priorities that followed might be the reason that ADN has not been produced in the new Russian Federation.

It is indisputable that a large research effort on ADN must have been conducted by the Soviets. Russian scientists have published many studies on the subject since 1991, after ADN was described for the first time in the open literature.

The existence and preparation of stable dinitramides was disclosed publicly in two patent applications filed by the US military contractor SRI [1,2]. They cover a series of dinitramide salts, including ADN. The anion, $\text{N}(\text{NO}_2)_2^-$, was named here for the first time as dinitramide, in contrast to the covalent alkyl compounds called dinitramines. The protonated form of the dinitramide anion was named dinitraminic acid, $\text{HN}(\text{NO}_2)_2$.

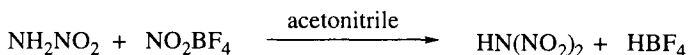
Thus it is notable that the dinitramide anion has likely been "first" synthesized twice, and was patented long after it was already being

used on an industrial scale. Despite a large ongoing research effort since ADN was resynthesized by SRI, there is today no published large-scale use. If it is true that ADN was successfully applied on a large scale by the Soviets, this means that today's research community has not yet reached the same level that existed 30 - 40 years ago.

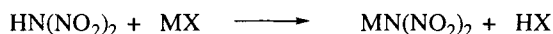
The lack of a cost-effective method for large-scale production inhibits the development of applications for dinitramides. The methods described in the patents are not suitable for industrial production due to expensive nitration agents. The method used in the Soviet Union has never been described openly. In 1997, the Swedish research establishment FOI published a patent application describing a method for using inexpensive mixed acid as a nitration agent for making dinitramides from a 'synthon' of ammonia. As a result, ammonium dinitramide (ADN) and a number of other salts are today commercially available on a semi-industrial scale from the Swedish explosives manufacturer NEXPLO Bofors AB. Yet dinitramide is not used on a large scale, but rather is studied for a number of different applications, such as solid and liquid propulsion, explosives, and gas generation in automotive safety devices. The potential importance of ADN is due to the fact that it is a stronger oxidant than the widely used ammonium perchlorate (AP) and does not contain chlorine.

2. SYNTHETIC METHODS

The synthetic methods described in SRI's 1991 patent applications [1,2] are based principally on the idea of nitrating nitramine to obtain the dinitramide. The nitration agents are various nitronium salts, such as NO_2BF_4 .



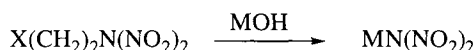
The dinitraminic acid is converted in a subsequent step by a cation exchange with a salt MX, where X could, for example, be a halide.



In principle, this route can also be described as nitration of ammonia, since nitramine can be obtained by nitration of ammonia with nitronium salts.

In the same patents is reported a method described as β -elimination of 1-(N,N-dinitramino)-2-trimethylsilylethane catalyzed by cesium fluoride. After recrystallization in ethyl acetate, the yield was 50% [3].

Russian researchers described a similar procedure, shown below, in which the dinitramide anion is used as a leaving group [4]. The dinitramide was synthesized with an elimination reaction from β -substituted alkyldinitramines, $XCH_2CH_2N(NO_2)_2$, and an alkali hydroxide. X is an electron-withdrawing group such as CN, NO_2 , $C(O)OR$, or $C(O)R$. M^+ is a metal cation, or ammonium to give ADN. With this method, dinitramides were synthesized as early as 1971 at the N.D. Zelinsky Institute of Organic Chemistry in the former Soviet Union [4].

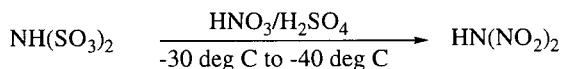


The SRI researchers later introduced an approach whereby ammonium nitrourethane can be nitrated with N_2O_5 or NO_2BF_4 to give dinitrourethane. In a subsequent step, the urethane is cleaved with ammonia resulting in ADN. This route has been used in the US in scaled-up syntheses.

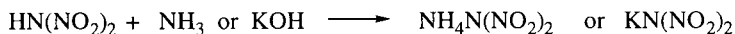
Nitrourea has also been shown to be a starting material [5]. Nitration with NO_2BF_4 in acetonitrile followed by neutralization with dry ammonia gave the dinitramide anion with a yield of 20.2%. Nitrourea is made by nitration of urea in mixed acid.

Despite the rather high yield for many of the methods described above, they are not suited for large bulk production of an oxidizer supposed to replace the low-cost bulk chemical AP. The costs of nitronium salts or dinitropentaoxide make them unsuitable for high-volume production. The procedures using β -elimination involve the same expensive reagents, since they are used in the making of the alkyldinitramines that are the starting materials.

Currently the most economical route to making dinitramides involves a mixture of nitric and sulfuric acids as the nitrating agent. The mixed acid is drastically less expensive than the nitration agents mentioned above. The substrate is potassium sulfamate, which, due to its basicity, is suitable for nitration in a strongly acidic solution. Since the dinitramide anion is thermally unstable in acidic environment at room temperature, the nitration is carried out at -30°C to -40°C .



The reaction mixture is then neutralized with potassium hydroxide to give a water solution of potassium dinitramide or with ammonia to give ADN. The overall yield is 30% - 40%.



After neutralization, the dinitramide is separated from the other anions, nitrate and sulfate, by quantitative liquid chromatography.

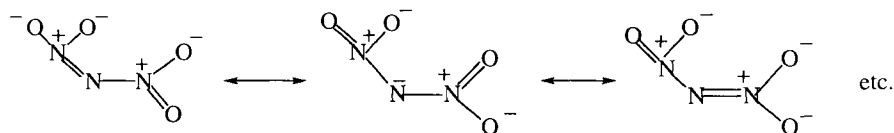
Since the starting materials are relatively inexpensive, this is currently the industrial method for making dinitramides. It was invented and patented by FOI, Sweden, in 1997 [6], and was then scaled up by NEXPLO Bofors, Sweden, to semi-production levels.

3. CHEMISTRY AND PROPERTIES

3.1 Reactivity

The dinitramide anion is chemically and mechanically stable in non-acidic water solutions and as salts. The non-metallic salts are often explosives that are capable of self-sustained burning and in some cases also detonation. The stability of most ionic dinitramides contrasts with the instability of covalently bonded dinitramines. Most alkyl dinitramines decompose at temperatures below 70°C and they are sensitive to shock and impact. The instability is attributed to the electron deficiency at the central nitrogen when substituted with two strongly electron-withdrawing nitro groups, as well as steric repulsion between these two negatively-charged groups.

This repulsion is diminished in the dinitramide ion since they are farther apart, due to sp^2 hybridization of the central nitrogen. An additional factor is the energetically favorable distribution of the net electronic charge throughout the dinitramide anion. This is formally pictured by the resonance structures:



The stability of the anion is reflected in the strength of the corresponding acid, dinitraminic acid. The pK_a is -5.6 , which means it is stronger than nitric acid and similar to sulfuric acid.

The stabilized valence structure in the dinitramide anion results in low reactivity toward electrophiles. Only under special conditions does the anion react as a nucleophile. For example, silver dinitramide is alkylated by alkyl halides in high yields to form the covalent dinitramine [7].

The electron affinity of the $N(NO_2)_2$ radical is unusually high, 5.0 eV. This agrees with the observation that anodic oxidation of dinitramide ions in acetonitrile occurs at a potential of 2.3-2.4 V [8], which is much higher than, for example, trinitromethanide ion (1.98 V) [9].

3.2 Physical properties

Listed below are some key properties of ADN. The crystals are yellowish and often very irregularly shaped. They are quite hygroscopic, of the same order of magnitude as ammonium nitrate (AN). Samples should therefore be kept under dry conditions. It is important that crystalline ADN does not undergo any phase transition, in contrast to AN.

Table 1.

Some properties of ammonium dinitramide.

Heat of formation	-148 kJ/mole
Heat of combustion	980 kJ/mole
Crytal density	1.81 g/ml
Melting point (DSC)	90.52 ⁰ C (onset), 93.59 ⁰ C (peak)

3.3 Chemical stability and compatibility

A large number of dinitramide salts have been reported in the literature. They are formed with metallic cations or with protonated organic nitrogen bases.

Most of the metal salts will probably have a limited practical value due to poor thermal stability, low melting points and high hygroscopicity. For example, the dinitramide salts of Li, Na, K, Rb, and Cs all suffer from significant gas losses already at 80°C.

So far, most interest has been focused on the dinitramide salts of nitrogen bases, particularly ADN. ADN starts to decompose slowly at 85°C. A vacuum stability test showed that 0.88 ml of gas per gram were evolved from a sample over a period of 40 hours. Despite this instability, it has been demonstrated that ADN-based formulations fulfill the military stability requirements at 80°C. However it is unlikely that ADN could be used in any military or commercial applications above its melting point. The rate of decomposition and its autocatalytic behavior conflict with safety considerations.

A peculiar feature of ADN is that the rate of decomposition increases suddenly by several orders of magnitude at about 60°C when the temperature is being lowered and then decreases again as the temperature continues to go down. This is contrary to an Arrhenius plot for a normal decomposition reaction. No explanation has been found for this behavior.

The decomposition of ADN can follow at least two different routes. One involves the formation, at 127°C, of ammonium nitrate and N₂O [10], followed by a second step, with onset above 200°C, in which the AN decomposes to NO₂ and water. Potassium dinitramide decomposes with an analogous initial step, forming KNO₃. A second route for ADN begins with dissociation of the salt into ammonia and dinitraminic acid, HN(NO₂)₂. This can be viewed as an acid/base equilibrium:



This is consistent with the observation that the relative thermal stabilities of the dinitramides parallel the pK_a values of the free bases. For example, the dinitramide of hydrazine (pK_a 7.4) is unstable compared to ADN (pK_a 10.5). The strongest organic bases are guanidine and its derivatives. Consequently the dinitramide anion forms stable salts with guanidine and guanyurea. The decomposition onsets for the salts are 212-215°C and 215-216°C, with no prior melting. The onset temperature for ADN is 127°C, with melting at 92°C. The energetics of a large number of possible ADN decomposition steps have been computed at the density functional level [11].

Compared to any of its salts, dinitraminic acid is extremely thermally unstable, and cannot be isolated at room temperature. The decay

in a water solution is acid catalyzed. In an 8 M solution of sulfuric acid, the loss is quite slow but at 10 M or above the decay is observed on a scale of minutes. At room temperature in a 'mixed acid' solution used for nitration, the dinitramide anion decomposes rapidly with evolution of N_2O and NO_2 gases. The temperature will very quickly reach the decomposition point for the nitric acid resulting in a violent evolution of NO_2 . This is the reason why the mixed acid nitration described above is performed at depressed temperatures. The decomposition products are N_2O , H_2O and HNO_3 . In a basic solution, the dinitramide anion is stable.

In water, $\text{N}(\text{NO}_2)_2^-$ undergoes photodegradation in daylight. The degradation products are nitrate (NO_3^-), nitrite (NO_2^-) and nitrous oxide (N_2O). The degradation occurs in the UV region since ADN does not absorb in the visible. The absorption is largest at 284 nm and the quantum yield for degradation is 0.10 MilliQ. In practice this means that the half-life of ADN in a water solution in sunlight is only approximately 6 minutes [12]. A practical implication therefore is that water solutions of dinitramides should always be kept in UV absorbing containers. Solid dinitramides do not undergo photodegradation to a significant degree. However, since they often are hygroscopic, the advice must be that powder should not be exposed to direct sunlight.

Reaction between ingredients in a propellant composition and ADN could not only reduce the shelf life but also be a safety problem since ADN decomposes autocatalytically. In cast-cured propellant compositions, isocyanates are often used as curing agents. Since isocyanates are reactive and strongly electrophilic, they interact exothermally with the dinitramide anion. A study shows that the reactivity varies for different isocyanates [13]. After curing, no interactions were detected, indicating that the reaction only occurs with the free isocyanate and not with the polyurethane that is formed in the curing process. It is therefore possible to use isocyanates if the curing reaction is not too slow and the isocyanate is not reactive toward ADN.

An aging study has been published for ADN formulated with various energetic binder systems: glycidyl azide polymer (GAP), poly(diethyleneglycol-4,8-dinitrate undeconate) (ORP-2) and polycaprolactone polymer (PCB), as well as the energetic softener butanetrioltrinitrate (BTTN) [14]. All compositions were aged at 71°C. The degradation was in all cases greater than for corresponding formulations based on HMX. However, all compositions met the shelf-life requirement set by weapon systems developers.

A different compatibility problem arises when ADN is mixed with KNO_3 . Aging studies show a drastic decrease in melting point. The reason is probably formation of eutectic solutions between the salts. This has also been observed in aging studies of GDN and KNO_3 but not when GDN is replaced by guanylurea dinitramide (GUDN).

The crystal structure of GUDN belongs to the orthorhombic space group $\text{Pna}2_1$, with a density of 1.7460 g/cm^3 . The packing of the ions is in an almost perfect layered structure. Within the layers, the ions are bonded in a two-dimensional network of hydrogen bonds. This is apparently strong enough to withstand the competition of hydrogen bonding in water solution, producing a low water solubility (5g/l at room temperature) in sharp contrast to other dinitramides [15]. Also the hygroscopicity is low compared to other dinitramide salts. Only 0.02% is gained in mass at a relative humidity of 75%. The low water solubility provides an efficient method for isolating GUDN from water solution by precipitation, by adding for example guanylurea sulfate to a solution of ADN. GDN is quite soluble in water but not as much as ADN. The guanidine salt is also rather hygroscopic and has, in contrast to GUDN, a point of deliquescence (97% relative humidity at 25°C).

3.4 Sensitivity

Sensitivities have been studied for a number of dinitramide salts. The impact sensitivity has been published for ADN by several different laboratories. Below are values reported from the Naval Air Warfare Center, China Lake (CL), and FOI. As can be seen, the impact sensitivity is somewhat greater than RDX. Neat ADN is classified as 1.1D according to the UN regulations for "Transport of Dangerous Goods," which is the same classification that applies for RDX.

Table 2.
Measured sensitivities.

Compound	Impact, h_{50}	Friction
ADN (CL)	8 – 12 cm, 2.5 kg	324 – 400 lbs (ABL)
ADN (CL)	11 – 12 cm, 2.5 kg	295 – 355 lbs (ABL)
ADN (FOI)	31 cm, 2 kg, BAM	> 35 kp
Prilled ADN (FOI)	59 cm, 2 kg, BAM	–
RDX (CL)	15 – 17 cm, 2.5 kg	500 – 600 lbs (ABL)
RDX (FOI)	38 cm, 2 kg, BAM	12 kp
HMX (CL)	20 cm, 2.5 kg	398 lbs

As for other explosives like RDX and HMX, the impact sensitivity depends not only upon the molecular structure but also crystal morphology and imperfections. There is no study that maps the relation between morphology and sensitivity for ADN. However, as can be seen above, the 2 kg impact sensitivity is decreased from 31 cm to 59 cm when ADN is prilled. On the other hand, another study shows the same sensitivity for prilled and neat ADN [16].

The sensitivity of GUDN differs radically from that of ADN. Exact numbers for the impact and friction sensitivities cannot be reported since the height for explosion is above the maximum height and mass of the fallhammer. The impact sensitivity is therefore above 49 J (RDX is about 4 J and ADN 3 J) and the friction above 350 J, which was also the result for ADN. The low sensitivity of GUDN has resulted in its being classified for transportation as 1.3C. GDN has a sensitivity of 7.4 J in the impact test, placing it between ADN and GUDN. It is known that the sensitivity of hydrazinium dinitramide is greater than ADN. Researchers with experience in its use warn colleagues in their publications. The trend for mechanical sensitivity is parallel to thermal stability. This suggests that the dissociation of the salt to the free base and dinitraminic acid also plays a role in the mechanism for transforming mechanical impact into an explosion. The salt from the stronger base has lower sensitivity. The extreme insensitivity for GUDN might also be a result of the layered crystal structure described above. The distance between the layers is the same as the van der Waals distance between the atoms in the different layers. The layers can therefore act as glide planes and thereby consume the impact energy and prevent bond rupture and subsequent ignition.

4. APPLICATIONS

4.1 Propulsion

ADN and compositions of ADN have been shown to be able to undergo self-sustained combustion with higher burn rates than the commonly used oxidizer AP. A basic study showed that the burn rate for compressed ADN was 7.4 mm/s at the sub-atmospheric pressure of 0.2 MPa and 54 mm/s at 6 MPa. Since ADN has a surplus of oxygen, its burn rate increases if a carbon source is added. The low-pressure burning is then expanded down to 0.02 MPa. The burn rate for a mixture of ADN and paraffin in the ratio 90:10 has been determined to be 50 mm/s at 7 MPa with a burn rate coefficient of 0.8 and a flame temperature of 2960 [17].

The burning mechanism is proposed to be similar to the mechanism for thermal decomposition. The low-pressure burning is dominated by the decomposition of ADN to AN and N_2O [18]. ADN is therefore viewed as a stronger oxidant than AP with the potential to give a higher specific impulse in propulsion. The replacement of AP by ADN in metal fuels gives an energy increase of 10-20% based on theoretical studies [19]. A computational comparison between ADN and the oxidizers AP, AN, CL-20 and hydrazine nitroformate (HNF) in an HTPB-IDP binder showed that only HNF had a higher specific impulse than ADN at 70% (volume) oxidizer. CL-20 outperformed ADN only at very high levels of oxidizer. At these levels, the viscosity and sensitivity would be problems [20]. In addition to its performance, the fact that ADN does not contain any halogens makes it even more interesting for tactical and environmental reasons.

Thiokol Corporation has a patent that covers the use of ADN in rocket compositions together with energetic binders and aluminum as fuel. The patent also covers other salts of dinitramides with nitrogen rich organic bases such as tetrazoles [21].

As mentioned earlier, ADN was probably used in rocket propulsion for strategic missiles in the former Soviet Union. Even though Russian researchers have published much scientific work on ADN since then, there have been no descriptions of the formulations that were used.

In Europe, ADN is studied as an environmentally-friendly alternative to AP in space programs. When AP-based rockets are used, they produce enormous volumes of hydrogen chloride, which is harmful due to its acidic and corrosive character. Also other chlorine derivatives are formed which are toxic and are likely to contribute to the destruction of the

earth's ozone layer. The alternative to AP has been AN, which does not contain any chlorine but suffers from phase instability at low temperatures. AN is also poor in performance compared to AP. This can be compensated for by adding a more energetic material such as HMX. Then the problem becomes increased sensitivity.

Since ADN can detonate, there is a safety issue with ADN-based formulations. Particularly in the US is this seen as a major obstacle to using ADN formulations. The US requirement is that only compositions falling in the category 1.3 according to the UN rules for transportation can be considered. So far no published ADN composition falls into this category. ADN compositions normally fail in the UN card gap test, which is one of the compulsory tests for group 1.3. Consequently the focus in US is on finding less sensitive formulations of ADN.

ADN is also of interest as an oxidant in tactical missiles. The higher performance is of course of great interest here also. It could, for example, be used for increasing the charge in the warhead. The other advantage is avoiding the plume of condensate that can be seen behind a missile propelled with an AP composition if the humidity is high enough. An invisible flight would significantly increase the safety of the platform from which the missile is launched. Since the condensation is caused by the hydrogen chloride originating from the chlorine in the AP, this is one of the guaranteed advantages in using the chlorine-free ADN.

Another future candidate for high-performing signature-free oxidants, besides ADN, is hydrazine nitroformate (HNF). The problem with HNF is its high friction sensitivity. One consequence is that it is not yet classified for commercial transportation according to UN rules.

4.2 Explosive compositions

It has been demonstrated that ADN detonates when ignited in a 25 mm steel tube, with an energy corresponding to 1 g of pentaerythritol tetranitrate (PETN). ADN is therefore classified as a high explosive [22]. It has been considered for use as an oxidizer and high explosive in underwater charges. Since it is an explosive as well as an oxidizer, there would be no need for RDX in the composite, as when AP is the oxidant. This would result in a better oxygen balance since ADN contributes more oxygen per unit mass than both AP and RDX. RDX actually consumes oxygen. Theoretically, more aluminum will burn per mass unit of charge, resulting in higher bubble energy. No experimental evidence has yet been

published. A problem might be that ADN is not as reactive toward aluminum as AP. If so, the effectiveness of ADN would be reduced.

Since ADN melts at 92°C, it would be theoretically possible to produce an ADN/aluminum composite by using melt-casting techniques similar to TNT-based composites. However there is a safety problem with this process, since ADN starts to decompose when melted, in contrast to the much more stable TNT.

The extremely insensitive GUDN could be of particular interest for insensitive munitions. The theoretically-calculated detonation pressure of GUDN places it between TNT and RDX (25.7 GPa) [23]. The low sensitivity combined with performance is unique and unmatched in the literature.

4.2.1 Phase-stabilizer in ammonium nitrate (AN)

It has been claimed that metal salts of dinitramides inhibit the low-temperature phase transition in AN that occurs at 32°C. This transition is a mayor obstacle to using AN as oxidant in propellants. At present, KNO_3 , CuO or NiO is used. In contrast to these substances, dinitramides increase the energy level of the stabilized AN. The use of dinitramides also results in a higher burn rate and lower pressure coefficient than non-stabilized AN or AN stabilized with the currently available stabilizers [24].

4.2.2 Liquid monopropellant

Since 1960, hydrazine has been the standard liquid monopropellant in space applications. Personnel safety and increased environmental awareness have become important issues in the context of propulsion system handling and operation. The cost of fueling a spacecraft with hydrazine has therefore increased significantly, along with the repeated lowering of the limit value of hydrazine exposure, which has been shown to be toxic, carcinogenic and volatile. Refueling in space has long been a target in the industry. The regulations will likely prohibit hydrazine from being used in such operations.

A new composition involving a solution of ADN in a mixture of glycerol and water has been presented as a new non-toxic monopropellant with a better specific impulse (I_{sp}) than hydrazine [25]. Below is a table of performance, I_{sp} at an expansion ratio of 50 and toxicity as LD_{50} orally, compared with hydrazine and hydroxylammonium nitrate (HAN).² HAN has over the past seven years emerged as a ‘Green

Propellant' candidate for space propulsion, instead of hydrazine. These figures suggest that ADN might be yet another solution, since the specific impulse is higher and toxicity lower.

Table 3.

Specific impulse and toxicity data for some monopropellant systems.

System	I_{sp} (ns/kg)	LD_{50} orally (mg/kg)
ADN/glycerol/water	2420	832 (pure ADN)
HAN/glycine/water	2001	325 (pure HAN)
Hydrazine	2325	59

4.2.3 Automotive safety

Guanylurea dinitramide (GUDN) mixed with oxidizers, e.g. potassium nitrate or copper nitrate, burns at a high rate with a low pressure coefficient, down to 0.2, and nearly without any temperature dependence in the range of -40°C to $+70^{\circ}\text{C}$. This, in combination with the fact that GUDN is thermally exceptionally stable, has made it interesting as a substance for gas-generating compositions in automotive safety devices. It has been shown that GUDN compositions do meet the tough long-term stability requirement set by the automotive industry, which is 107°C for 400 hours. Also the fact that GUDN, in sharp contrast to most other dinitramide salts, is only slightly soluble in water and not hygroscopic is an advantage in most practical applications, particularly when the product is supposed to last the service time of a new automobile.

5. IMPROVEMENT OF ADN

5.1 Stabilization of ADN

Thermal stability is an issue for ADN as an ingredient in military composites. The shelf life and the temperature at which it can be used depend on how well the low temperature degradation can be controlled. As described above, ADN is not as stable as, for example, nitramines or TNT. In these latter cases, the shelf life for the weapons systems does not really depend on the high explosives; their shelf lives are greater than the 'tactical lifetime' of the ordnance system. ADN more resembles nitrocellulose, which degrades slowly at low temperatures in an autocatalytic process. The degradation is therefore accelerating. One solution is to use a stabilizer

that chemically destroys the catalytic substance. Since the stabilizer is simultaneously being consumed, the degradation is inhibited for only a limited time. Without stabilizers, nitrocellulose could not have been used in ordnance as widely as it has been and still is.

Stabilizers that affect the degradation of ADN have been reported. Examples are hexamethylene tetramine, 2-nitrodiphenylamine and akardite II (methyldiphenylurea). They drastically decrease the rate of degradation, by a factor of 2 - 4 at 800°C [26]. MgO has the effect of increasing the time to autocatalytic decomposition in a melt at 98°C from 3 to 24 hours. Hexamine is used in commercially-available prilled ADN, in which it has been shown to reduce gas evolution after 40 hours at 80°C from 0.88 to 0.33 ml/g. Urea has also been shown to have this effect. All of the stabilizers described above are weak nitrogen bases except MgO. This agrees with the evidence that acids catalyze the degradation.

5.2 Handling properties

Neat ADN contains crystals shaped as needles or flakes. No method for re-crystallizing ADN to give more uniformly-shaped crystals has been reported. The ill-shaped crystals limit the amount of ADN in cast-cured compositions due to high viscosity. The only solution to this problem is to reshape the ADN crystals to be more regular. Since the melting point is not directly associated with decomposition, it is possible to use a method whereby ADN is melted.

A laboratory scale prilling process is simply melting ADN in an immiscible liquid. Stirring above the melting point causes shearing forces to produce droplets, which are quenched to hard spheres upon cooling of the mixture. This process is also an opportunity to dissolve stabilizers in the ADN while molten.

A problem with this process is the decomposition of ADN as the temperature is raised above the melting point. The problem is that the melting point at 92°C is only 40°C below the temperature of decomposition. At 110°C the decomposition becomes autocatalytic after 15 minutes, at 98°C after a few hours. This is not a problem on the laboratory scale, where the melting period can be reduced to a few minutes. On the industrial scale, where hundreds of kilos of ADN should be melted in a batch, the time is much longer. It is likely that most explosives producers would hesitate and most likely refrain from scaling up this process unless nothing is changed.

A continuous method for prilling ADN has been invented that might be a solution to the safety problem [27]. The ADN is fed continuously into a heating zone, where it is melted, and then into a non-solvent cooling fluid. This method would probably also increase the capacity and operational costs for prilling.

The liquid in which the droplets are quenched to prills could also serve as a moisture barrier for ADN. When the cooling liquid is filtered from the spheres after the prilling, there will still be a coating left on the surface of the prills, normally 3 - 5 weight percent. If this is a liquid that is water-repellent or hydrophobic, it will protect the ADN from water and thereby drastically reduce the hygroscopicity. This will eliminate the extra complexity associated with avoiding moisture in all steps of handling and storing. It is also common to use one of the liquid ingredients from the composition as cooling liquid and moisture barrier. An example is the widely-used softener dioctylphthalate. The advantage of this is of course that no new ingredient is added to the final composition.

REFERENCES

- [1] J.C. Bottaro, R.J. Schmitt, P.E. Penwell and S. Ross, Dinitramide Salts and Method of Making Same, US Patent No. 5,254,324 (1991).
- [2] J.C. Bottaro, R.J. Schmitt, and S. Ross, Method of Forming Dinitramide Salts, US Patent No. 5,198,204 (1991).
- [3] J.C. Bottaro, P.E. Penwell and R.J. Schmitt, J. Am. Chem. Soc., 119 (1997) 9405.
- [4] V.A. Tartakovsky and O.A. Luk'yanov., 25th International Annual Conference, Institute of Chemical Technology, Karlsruhe, Germany, 1994.
- [5] H. Hatano, T. Onda, S. Miyazakai and S. Suzuki, Europyro, 1995.
- [6] A. Langlet, H. Ostmark and N. Wingborg, Method of Preparing Dinitraminic Acid Salts Thereof, Int. App. No. PCT/SE96/00976.
- [7] O.A. Luk'yanov, N.I. Shlykova and V.A. Tartakovsky, Russ. Chem. Bull., 43 (1994) 10.
- [8] L. Ebersson, Acta Chem. Scand. B, 53 (1999).
- [9] L. Ebersson and F. Radner, J. Am. Chem. Soc., 113 (1991) 5825.
- [10] S. Lobbecke, H. H. Krause and A. Pfeil, Propell. Expl. Pyrotech., 22 (1997) 184.
- [11] P. Politzer, J. M. Seminario and M. C. Concha, J. Mol. Struct. (Theochem), 427 (1998) 123.
- [12] M. K. Beretvas, J. P. Hassett, S. E. Burns and T.M. Basford, Environ. Toxicol. Chem. 19 (2000) 2661.
- [13] H. Ostmark, N. Wingborg and A. Langlet, 16th International Symposium on Ballistics, San Francisco, CA, 1996.

- [14] M. L. Chan, A. Turner, L. Merwin, G. Ostrom, C. Mead and S. Wood, Log No. 4-015-OP-R, Naval Air Warfare Center, Weapons Division, China Lake, CA.
- [15] U. Bemm and H. Ostmark, Report No. FOA-R 00-01649-310 SE, FOI, 2000.
- [16] M. L. Chan, Naval Air Warfare Center, Weapons Division, China Lake, CA.
- [17] V. Weiser, N. Eisenreich, A. Bayer, M. Weindel and Klaus Menke., 28th International Annual Conference, Institute of Chemical Technology, Karlsruhe, Germany, 1997.
- [18] A. E. Fogelzang, V. P. Sinditskii, V. Y. Egorshhev, A. I. Levshenkov, V. V. Serushkin and V. I. Kolesov, 28th International Annual Conference, Institute of Chemical Technology, Karlsruhe, Germany, 1997.
- [19] Z. P. Pak, 29th Joint Propulsion Conference, AIAA/SAE/ASME/ASEE, Monterey, CA, 1993.
- [20] H. Ostmark, N. Wingborg and A. Langlet, 16th International Symposium on Ballistics, San Francisco, CA, 1996.
- [21] C. J. Hinshaw and R. B. Wardle, Int. Pub. No. PCT/US94/04270, 1994.
- [22] H. Ostmark, private communication, henric.oestmark@foi.se
- [23] T. K. Highsmith, C. J. Hinshaw and R. B. Wardle, Phase-Stabilized Ammonium Nitrate and Method of Making Same, US. Patent No. 5,292,387.
- [24] K. Anflo, T.A. Gronland and N. Wingborg, 36th Joint Propulsion Conference, AIAA/ASME/SAE/ASEE, Huntsville, AL, 2000.
- [25] S. Lobbecke, H. Krause and A. Pfeil, 28th International Annual Conference, Institute of Chemical Technology, Karlsruhe, Germany, 1997.
- [26] J. Guimont, Int. Appl. No. PCT/US97/10141, 1997.

Chapter 14

Polynitrogens as promising high-energy density materials: computational design

Ohyun Kwon^a and Michael L. McKee^b

^aDepartment of Chemistry, The University of Arizona,
Tucson, Arizona 85721, U.S.A.

^bDepartment of Chemistry, Auburn University,
Auburn, Alabama 36849, U.S.A.

1. Introduction

Since the discovery of gunpowder, explosives and propellants have been of practical importance for the advancement of human civilization. These explosives and propellants are primarily composed of energetic materials which generate high temperatures and pressures when they decompose to gaseous products [1,2]. The amount of released energy is highly dependent on the chemical structure of the material. Thus, the quest for more efficient explosives and rocket propellants has led to the investigation of new energetic chemical compounds. It has been suggested that high-energetic materials have the following optimal conditions. First, the decomposition of the energetic compound should be highly exothermic and unimolecular [2]. Second, the activation barriers should be at least 20 and preferably more than 30 kcal/mol in order to be kinetically stable with respect to unimolecular dissociation on the potential energy surface [3]. In other words, metastability is a crucial property of high-energetic materials [4]. This means that metastable molecules are local minima on the potential energy surface, while the dissociative products are the global minima. Such metastable species are often found to have somewhat long lifetimes, and may be trapped under certain experimental conditions. Usually, geometrically highly strained molecules such as cage compounds (i.e. cubanes) show large metastabilities on their potential energy surfaces [1].

Well-known energetic materials contain mainly nitrogen and oxygen atoms such as the nitrocarbons (-C-NO₂) or the nitroamine (-N-NO₂) group [1,2]. Typical explosives with nitroaryl groups are TNT (trinitrotoluene, C₇H₅O₆N₃) and TATB (triaminonitrobenzene, C₆H₆O₆N₆). RDX (C₃H₆O₆N₆) and HMX (C₄H₈O₈N₈), known as “hexogen” and “octogen”, respectively, are typical nitroamine explosives (Fig. 1). It is known that the materials with higher nitrogen concentrations (% by mass) produce a larger heat of explosion (ΔH_{exp}) [2]. Therefore, compounds containing only nitrogen (polynitrogens) have become attractive as promising high-energetic materials. The main advantage of pure polynitrogens as explosives or propellants is that these materials

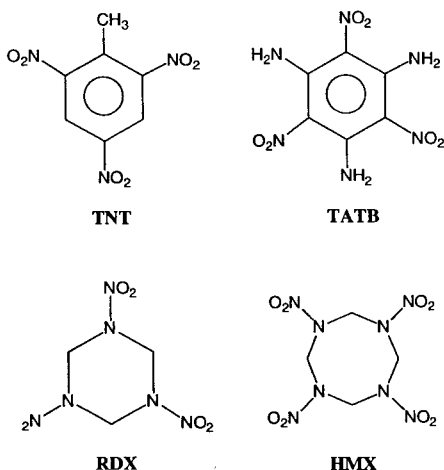


Fig. 1. Structures of TNT, TATB, RDX, and HMX.

decompose into pure N_2 molecules, which are environmentally safe [5]. Since its isolation in 1772 by Rutherford, Scheele, and Cavendish [6], N_2 gas has been known for its inertness, due to its $N\equiv N$ triple bond which has a bond dissociation energy of 225 kcal/mol [7]. The name of nitrogen originates from the Latin “*azote*” indicating the chemical inertness of N_2 [6]. In addition, polynitrogens are expected to be highly exothermic due to the large energy difference between the N-N single (~40 kcal/mol) and N=N double (100 kcal/mol) bonds in polynitrogens and the $N\equiv N$ triple (225 kcal/mol) bond in N_2 . Polynitrogens containing purely single and double bonds would easily dissociate into the much more stable N_2 molecules with large exothermic reaction energies [5].

The azide anion (N_3^-), first synthesized in 1890 by Curtius [6], is the first known polynitrogen. In contrast to N_2 , metal azides (i.e. $Pb(N_3)_2$ and NaN_3) and azide polymers (i.e. glycidyl azide polymer (GAP)) are quite reactive and explosive [2]. Before 1999, N_2 and N_3^- were the only known pure nitrogen species due to the great experimental difficulties in isolating new polynitrogens. Because the N-N single and N=N double bonds are so much weaker than the $N\equiv N$ triple bond, nitrogen does not readily form large molecules consisting of only single and double bonds. However, in 1999, Christie et al. reported a successful synthesis and characterization of the $[N_5^+AsF_6^-]$ salt, which contains the third pure nitrogen moiety, the N_5^+ cation [8]. Recently, the existence of neutral N_4 has also been identified experimentally [9-11]. It might be expected that N_4 should exist because phosphorus and arsenic, in the same periodic group as nitrogen, are stable as tetraatomic molecules [4,5,12].

At the same time, many theoretical calculations have been carried out over the last two decades to find new polynitrogens. Computational studies have been able to assist and encourage experimental work to find and identify unknown polynitrogens by providing information about molecular structures and kinetic stabilities on the potential energy surface with respect to N_2 . Many hypothetical structures of polynitrogens (from N_4 to N_{60}) have been predicted by quantum-mechanical calculations, which have led to the

successful isolation of some polynitrogen species. Prior to the synthesis of N_5^+ , computational results had already predicted that a five-atom polynitrogen with a positive charge should be detected by experiment [13]. In 2002, Bartlett and co-workers suggested the existence of the stable $[N_5^+N_5^-]$ salt from quantum-chemical calculations [14]. During the same year, Christe and coworkers reported the experimental detection of the N_5^- anion [15]. These facts clearly illustrate the successful use of computational modeling in the experimental characterization of newly synthesized polynitrogens.

This chapter will provide a review of known theoretical efforts for finding polynitrogen species and a reasonable computational strategy for designing new energetic materials. In addition, reaction energies of dissociations of some nitrogen-rich compounds are presented and discussed in terms of their exothermicities in comparison with their corresponding pure polynitrogens. This may give some insights for designing hypothetical energetic materials by computational techniques.

2. Known computational facts of polynitrogens

Geometries of minima for some polynitrogens are shown in Fig. 2. Recently,

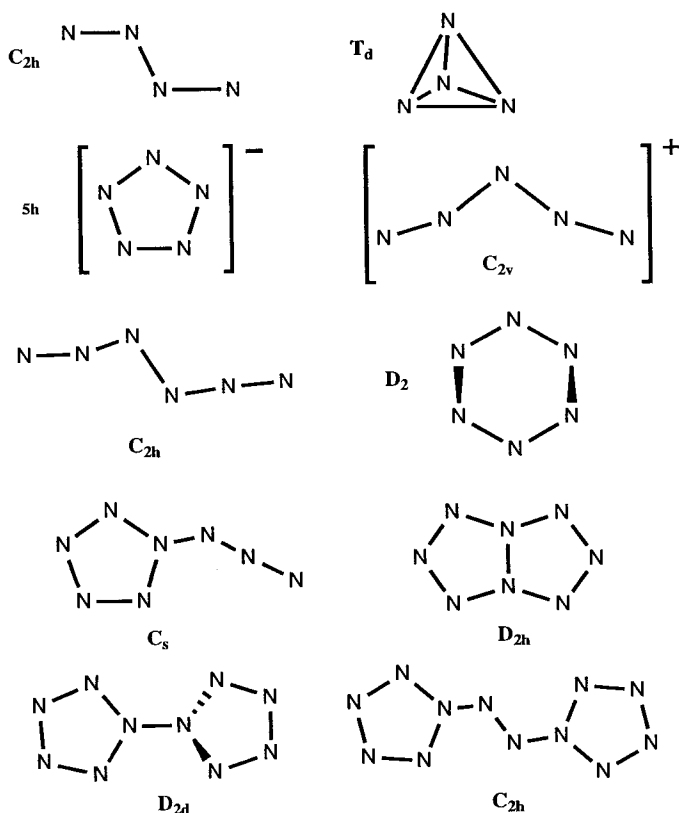


Fig. 2. Geometries of minima for some polynitrogens.

Bartlett's group has calculated the optimum geometries, IR spectra, and excitation energies of neutral, cationic, and anionic forms of polynitrogens up to N_{10} by using density functional theory (DFT) and coupled cluster (CC) methods [16]. This should provide useful information for finding new polynitrogen species as well as provide motivation for further calculations of larger systems.

In order to discover new polynitrogen molecules, the best starting point may be finding molecules of other elements or groups that are isovalent with the nitrogen atom. Since nitrogen is isovalent with P and As atoms as well as the CH group, any polynitrogen (N_n , $n \geq 4$) might be a possible synthetic target if their P_n and As_n , or $(CH)_n$ compounds are stable enough to survive on their potential energy surfaces [6]. For instance, P_4 and C_6H_6 are already known compounds; therefore the nitrogen counterparts, N_4 and N_6 may be feasible.

2.1. Computational methodology

Before reviewing polynitrogen compounds, we must briefly address computational methodology. Politzer and co-workers [17] have presented an overview of computational design and characterization of energetic materials which should be a good starting point for those who are interested in computational modeling of energetic materials.

Over the last decade, density functional theory (DFT) methods have become successful at reproducing molecular geometries and spectroscopic properties such as vibrational frequencies and NMR chemical shifts [18-20]. DFT often gives results of a quality comparable or even better than second-order Möller-Plesset (MP2) theory at a computational cost that is substantially less than that of *ab initio* electron-correlation methods. Recent DFT calculations of polynitrogens have been quite successful in predicting geometries, energetics, and vibrational frequencies. Gradient-corrected exchange-correlation functionals such as B3LYP and B3PW91 are the most popular among DFT methods [18-20].

It has been known that the qualitative shape of the potential energy surface is highly dependent on the level of theory and the size of basis set [18,20]. MP2 and DFT methods would be the best choice in order to obtain molecular geometries and characterize the nature of stationary points on the potential energy surface. Higher levels of theory such as CCSD(T) or QCISD(T) can be used for single-point energy calculations at the MP2- or DFT-optimized geometries. Appropriate basis sets for geometry optimizations should be at least triple-zeta quality basis sets with polarization and diffuse functions such as 6-311+G*. According to previous calculations of polynitrogens by Bartlett and co-workers, augmented correlation consistent basis sets such as aug-cc-PVDZ and aug-cc-PVTZ also give reliable geometries and energetics of polynitrogen molecules [14,16,21,22].

One should remember that the critical properties for effective high-energetic materials are large exothermicities and high dissociation barriers [2-4]. This fact emphasizes that accurate calculations of the potential energy surface of polynitrogens

will be necessary. Specifically, efficient explosives and propellants are characterized by their specific impulse, I_{sp} [2,23], which is expressed as Eq. (1) where ΔH_f is the enthalpy of formation (kcal/mol), and MW is molecular weight (g/mol). Thus, accurate calculation

$$I_{sp} = 265 \times (\Delta H_f / MW)^{1/2} \quad (1)$$

of ΔH_f of a molecule should provide a good indication as to its candidacy as an energetic material. Many possible polynitrogen structures such as N_4 and N_8 are highly symmetrical and their decomposition reactions into N_2 are symmetry-forbidden by the Woodward-Hoffmann rules [24]. As a consequence, many transition states tend to have biradical character, which indicates that there are significant contributions from more than one configuration. In order to describe the biradical character correctly, multiconfiguration methods [18,20] such as MCSCF [25] or CASPT2 [26] must be applied. MCSCF calculations provide a reasonable treatment of nondynamic electron correlation in the valence region (especially the HOMO and LUMO). In many cases, multiconfiguration second-order perturbation theory (CASPT2) with dynamic electron correlation may be combined with CASSCF calculations to obtain accurate potential energy surfaces. When using the CASSCF and CASPT2 procedures for polynitrogens, all $2p$ orbitals of nitrogen atoms should be included in an active space (if possible). For instance, N_4 has twelve $2p$ orbitals, hence an active space of 12-electrons in 12-orbitals (12e,12o) is recommended.

2.2. N_4

Previous theoretical studies have characterized the lowest-energy conformer of N_4 as an open-chain triplet C_{2h} structure [27-29]. On the other hand, the tetrahedral form of N_4 , which is the most stable singlet on the N_4 potential energy surface [4,27-41], is 183 kcal/mol higher in energy than $2N_2$ at the CCSD(T) level [31]. The energy of the open-chain triplet minimum was computed to be 13.4 kcal/mol lower than that of the tetrahedral singlet at the CCSD(T) level [29].

Tetrahedral N_4 is expected to dissociate into two N_2 molecules, but this reaction is forbidden by orbital symmetry. Dunn and Morokuma [33] characterized a transition state for the exothermic dissociation of tetrahedral N_4 into two N_2 and estimated the activation barrier to be 63 kcal/mol at the CASSCF(12e,12o) level, which indicates that N_4 is a metastable species with significant kinetic stability. The calculated potential energy surface of N_4 suggests that the low-lying triplet state might cross with the singlet surface (Fig. 3), which could reduce the activation energy barrier to about 30 kcal/mol [29,31,32].

Recent experimental studies supports the existence of tetrahedral N_4 in the nitrogen plasma as well as in liquid and solid nitrogen [9,10], whereas neutralization-reionization mass spectrometry study of N_4 suggests that observed species is the open-chain triplet structure [11].

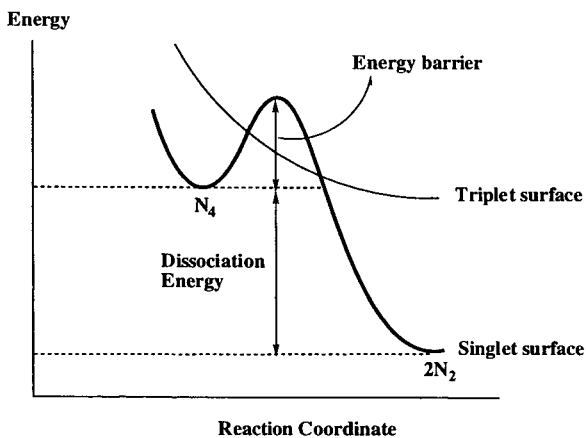


Fig. 3. Potential energy surface of N_4 .

2.3. N_5

N_5 can exist as either a linear or cyclic structure. Especially, the cyclic D_{5h} -symmetry N_5^- anion has attracted attention since it is isoelectronic with the cyclopentadienide anion ($C_5H_5^-$), and could replace the Cp ring in metallocenes. The N_5^- anion has been found in salts such as AgN_5 [5,6]. Quantum-mechanical calculations have found that metallocene analogues with a (η^5-N_5) ligand such as $Li(\eta^5-N_5)$ [42] and $Fe(\eta^5-N_5)_2$ [43,44] are energy minima on the potential energy surfaces. The calculated reaction energy for the dissociation of $Fe(\eta^5-N_5)_2$ into Fe and $5N_2$ is 227 kcal/mol, which suggests metal complexes with the η^5-N_5 ligand might be good candidates for energetic materials. Structures of the N_5^- ring-complex with metal elements were calculated at the DFT level [45]. It has been suggested that the bonding pattern of the N_5 ring is highly dependent on the metal elements (Fig. 4). Alkali (Na, K) and alkaline earth (Mg, Ca) metal complexes of N_5^- anion prefer bidendate-like complex as $M(\eta^2-N_5)_2$, whereas a unidendate-like complex is favored for $Zn(\eta^1-N_5)_2$. Quite recently, cyclic N_5^- anion has been detected by electrospray ionization mass spectrometry (ESI-MS) experiment [15].

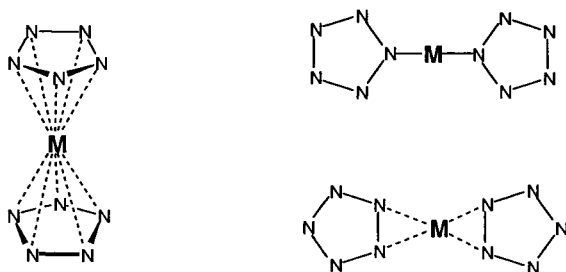


Fig. 4. Possible bonding between a metal element and N_5^- anion rings in $M(N_5)_2$ complexes.

On the other hand, the N_5^+ cation has been synthesized as the AsF_6^- salt in 1999 [8], and the crystal structure of $[N_5^+Sb_2^+F_{11}^-]$ was characterized in 2001 [46]. Bartlett and coworkers [14] suggested that the combination of the N_5^+ cation with the N_5^- anion should give a stable crystalline salt since calculated ionization potential (5.6 eV at the EOM-CCSD level) of N_5^- anion is large enough to stabilize N_5^+ cation (calculated electron affinity is 6.0 eV). In addition, they predicted that the $[N_5^+N_5^-]$ salt would be an efficient rocket fuel compared to hydrazine which is currently used as the propellant in spacecraft. Gagliardi et al. [47] also reported that the $[N_5^+N_5^-]$ salt is a local minimum in C_{2v} symmetry at the CASPT2 level, and that the ion pair is 24 kcal/mol higher in energy than the lowest-energy form of N_{10} , where two N_5 rings are linked to each other by a covalent bond.

Ab initio and DFT calculations by Nguyen and Ha [48] showed that the anion and cation of N_5 are kinetically stable with respect to dissociation into N_2 and N_3 species, whereas the N_5 radical is not a local minimum on the potential energy surface. The cyclic form of N_5^- is calculated to be more stable than the open-chain form and has a dissociation barrier of 28 kcal/mol to $N_2 + N_3^-$ in a reaction that is exothermic by 14 kcal/mol at the CCSD(T) level. On the other hand, the most stable N_5^+ conformer has the open-chain C_{2v} symmetry structure, which is in quite good agreement with an experimental characterization. The decomposition reaction of N_5^+ cation into $N_2 + N_3^+$ is calculated to have an activation energy barrier of 40 kcal/mol in a reaction endothermic by 27 kcal/mol at the CCSD(T) level. These results suggest that the N_5^- and N_5^+ ions are kinetically stable ions with a considerable energy barrier for fragmentation in the gas phase.

2.4. N_6

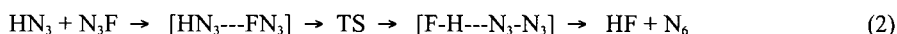
Previous theoretical calculations [22,35,48-55] have shown that the potential energy surface (PES) of N_6 isomers is highly dependent on the level of theory and basis sets. For instance, cyclic N_6 with D_{6h} symmetry, isoelectronic with benzene, was calculated to be a minimum at the HF level [49], but to become a higher-order saddle point at the MP2 level on the PES [35,49]. Higher-level calculations indicate that the lowest-energy form of cyclic N_6 is not the benzene-like D_{6h} structure but the twisted-boat geometry with D_{6h} symmetry [22,35,50]. This D_{6h} structure is probably not stable at room temperature because the dissociation frequency mode is only 73.6 cm^{-1} at the CCSD(T) level [22].

Some theoretical calculations suggested that introducing oxygen atoms into the ring plane could stabilize N_6 [23]. The N_6O_n ($n = 1, 2, 3$) compounds were studied theoretically, and N_6O_3 was found to be planar with D_{3h} symmetry. Its unimolecular energy barrier is estimated to be 62.4 kcal/mol at the CCSD(T) level. Another way to stabilize the N_6 ring is to form metal complexes such as $M(\eta_6-N_6)$, which can be considered as complexes of the M^{4+} cation and N_6^{4-} ligand [53]. DFT calculations show that $M(\eta_6-N_6)$ ($M = Ti, Zr, Hf, Th$) species with C_{6v} symmetry are 70-130 kcal/mol higher in energy than $M + 3N_2$ [53]. It has been suggested that planar N_6 stabilization arises from donor-acceptor bonding between the metal d and f orbitals and ring π orbitals.

The global minimum of N_6 has an open-chain diazide structure with C_{2h} symmetry

[22,35,51,52]. Gagliardi et al. explored the dissociation of N_6 into three N_2 molecules at the CASPT2 level and computed an energy barrier of 28.7 kcal/mol [51]. The potential energy surface of N_6 isomers has been also studied by using *ab initio* and DFT methods [54,55]. It is suggested that the prism-like D_{3h} structure (called prismane) has an activation barrier of 34.4 kcal/mol at the CCSD//DFT level, which is 137.2 kcal/mol higher in energy than the lowest energy minimum structure (open-chain C_{2h}) on the potential energy surface.

In order to investigate the possibility of synthesizing linear N_6 (still experimentally unknown), the following reaction scheme (Eq. 2) was proposed by Mezey



and co-workers [52]. They explored the potential energy surface of the above reaction sequence by DFT and CC methods and found that the reaction was exothermic with a reasonable energy barrier of 27.0 kcal/mol at the CCSD(T) level.

2.5. N_7

N_7 ions might apparently be the next polynitrogen species to be synthesized since only odd-numbered nitrogen clusters, such as N_3^- and N_5 ions, have been successfully synthesized so far. Among possible linear and cyclic isomers of N_7 ions, the open-chain N_7^- anion (C_2 symmetry) and N_7^+ cation (C_{2v} symmetry) are computed to be the lowest-energy forms on their potential energy surfaces [56,57]. Dissociation of these open-chain ions into fragments was explored with *ab initio* and DFT methods [57]. It was suggested that the N_7^- anion produces N_3^- anion and two N_2 molecules via a concerted process, whereas the N_7^+ cation decomposes into the kinetically stable linear N_5^+ cation and N_2 . Calculated barriers for decomposition of N_7^- anion and N_7^+ cation are 1.2 and 3.1 kcal/mol, respectively, at the G3(MP2) level which means they are not suitable as energetic materials.

Gagliardi and Pyykkö did MP2 and DFT calculations of ScN_7 and N_3MN_7 ($M = Ti, Zr, Hf, Th$), metal complexes with a planar N_7 ring, where $\eta^7-N_7^{3-}$ has 10π electrons, isoelectronic with the experimentally known $\eta^7-(C_7H_7)^{3-}$ ligand [58,59]. These metal complexes are predicted to be local minima, and dissociation barriers are computed to be 15-22 kcal/mol, which might be sufficiently high to allow isolation of these metal complexes with cyclic N_7 species. They also found that the isolated cyclic N_7^{3-} anion is computed to be a local minimum. These results suggest that formation of metal complexes could lead to the stabilization of anions of polynitrogens such as N_5^- , N_6^{4-} , and N_7^{3-} .

2.6. N_8

Like N_4 , cubic N_8 is expected to have a substantial dissociation barrier since the orbital correlation of N_8 with $4N_2$ shows a crossing of occupied and unoccupied orbitals [4]. Recent theoretical studies [3,60-63] have confirmed that the energy barrier for dissociation into N_2 molecules is predicted to be 10-22 kcal/mol depending on the level of theory, and the pathway is likely to be a stepwise dissociation reaction such as $N_8 \rightarrow N_2 +$

$N_6 \rightarrow 2N_2 + N_4$, etc. Another possible isomer of N_8 has a bicyclic D_{2h} structure consisting of two five-membered rings fused together [35]. This D_{2h} isomer would be very stable if synthesized because of the aromatic character with 10π electrons in the bicyclic rings.

Calculations have shown that the lowest-energy isomer of N_8 is azidopentazole (C_s symmetry), which is characterized as a five-membered ring with a three-atom nitrogen tail [3,35,63]. Three low-energy local minima including the bicyclic D_{2h} structure, are also located on the potential energy surface of N_8 and are about 200 kcal/mol lower in energy than cubic N_8 . Bartlett and co-workers [14] considered a possible N_8 ion pair but they concluded that the $[N_5^+ N_3^-]$ salt cannot exist as an ion pair because of the unbalance between EA (6.04 eV, EOM-CCSD level) of N_5^+ and IP (2.53 eV, EOM-CCSD level) of N_3^- .

Chung et al. calculated the dissociation reactions of azidopentazole and other openchain N_8 isomers into four N_2 molecules at the MP2 and CCSD(T) levels [3] and found that decomposition of azidopentazole favors breaking the five-membered ring first. They also found that the bicyclic D_{2h} structure fragments via isomerization to an open-chain structure. The energy barriers of dissociation or isomerization are estimated to be about 20 kcal/mol or less, which may not be enough for metastability. Li and Wang explored the potential energy surface for the formation and decomposition of N_8 ($N_5^+ + N_3^- \leftrightarrow N_8$) by using *ab initio* and DFT methods [62]. The calculated barriers of the reaction in forward and reverse directions were 2.0 and 23.4 kcal/mol, respectively at the QCISD//DFT level.

2.7. N_9 , N_{10} , N_{11} , and N_{12}

For N_9 , both neutral and cationic forms have open-chain C_{2v} structures [64]. DFT calculations have also shown that barrier of the reaction, $N_9 \rightarrow N_6 + N_3$, is predicted to be about 32 kcal/mol, whereas the barrier of the reaction, $N_9^+ \rightarrow N_7^+ + N_2$, is 2.1 kcal/mol. This suggests that neutral N_9 is kinetically more stable than the N_9^+ cation with respect to dissociation. Also, the relative kinetic stability of N_9 is completely opposite to other oddnumbered polynitrogens such as the N_5 and N_7 species, where ionic forms are kinetically more stable than the neutral forms.

N_{11} , another odd-numbered polynitrogen, is computed to have C_2 symmetry at the DFT level minimum, with two cyclic N_5 rings bonded to a single nitrogen atom [65]. The isomers containing a cyclic N_5 ring are more stable than structures with the four- or six-membered rings. The cyclic N_5 ring unit is also found in N_8 , and it can be inferred that the cyclic N_5 ring may be a stable structural unit for building larger polynitrogens. However, a possible anthracene-like structure of the N_{11}^+ cation (Fig 5) consisting of three fused aromatic five-membered rings was calculated at the DFT level [66] and found to be the least stable isomer of N_{11}^+ .

Strout and co-workers calculated possible dissociation pathways of open-chain N_9 and N_{11} . The lowest barrier was estimated to be 16.6 and 14.1 kcal/mol for N_9 ($N_9 \rightarrow N_7 + N_2$) and N_{11} ($N_{11} \rightarrow N_9 + N_2$), respectively, at the CCSD(T)//MP2 level [67]. Calculations of N_7 , N_9 , and N_{11} species suggest that the open-chain structures for these odd-numbered molecules will not be candidates for energetic materials since fragmentation barriers are too low.

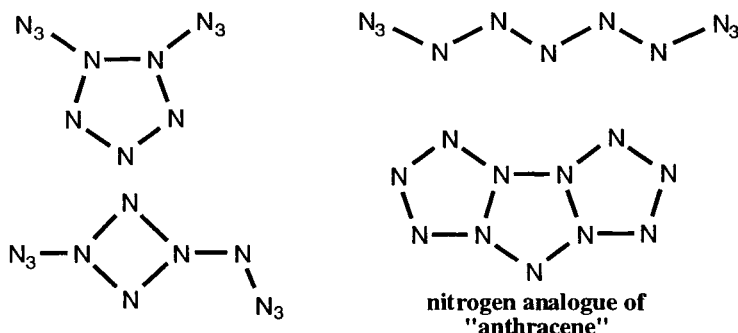


Fig. 5 Proposed N_{11}^+ structures. The anthracene analogue is the least stable of the four.

Schleyer and co-workers examined relative stabilities of possible N_{10} isomers at the MP2 and DFT levels [35]. Bispentazole (D_{2d} symmetry), where two cyclic N_5 rings are bonded to each other, is predicted to be the lowest-energy minimum, and the open-chain C_{2h} structure is located 18 kcal/mol higher in energy. Strout found the dissociation barrier of open-chain N_{10} into N_8 and N_2 at the CCSD(T) level to be 17-18 kcal/mol, which suggests acyclic N_{10} chain may not be feasible as an energetic material [68].

For N_{12} , the lowest-energy isomer has a planar geometry with two cyclic N_5 rings connected by a diazo ($-N=N-$) group, namely diazobispentazole (C_{2h} symmetry) [35]. Li and Zhao calculated the potential energy surface of N_{12} at the DFT level [69]. They found that the dissociation of diazobispentazole proceeds through N_5 ring-breaking with a barrier of only 4 kcal/mol. An open-chain N_{12} isomer (C_{2h} symmetry) is 18 kcal/mol higher in energy than diazobispentazole with a dissociation barrier of 15 kcal/mol to eliminate one N_2 molecule. Other N_{12} isomers also have low barrier for decomposition into fragments, which indicates N_{12} species are not kinetically stable enough to be energetic materials.

2.8. Larger polynitrogens

One can generate possible isomers of polynitrogens based on the cage, bowl, ring, and open-chain geometries. Until now, theoretical calculations of N_{14} through N_{60} have been reported [35,70-73]. Among them, N_{20} is the most likely polynitrogen to be synthesized since the hydrocarbon counterpart, dodecahedrane ($C_{20}H_{20}$), was predicted theoretically [74] and successfully isolated in experiment [75].

Ha et al. calculated possible isomers of N_{20} at the MP2 and DFT levels [72] and found that the cage structure (I_h symmetry) is about 200 kcal/mol higher in energy than the bowl (C_{5v} symmetry) and the ring (D_5) structures, whereas the most stable form of the carbon analogue, C_{20} , has the cage geometry. This is because the interaction of nitrogen lone pairs dominates the structural preference. The cage compound would maximize nitrogen lone-pair interactions, destabilizing this isomer relative to other C_{5v} and D_5 isomers.

Manaa has considered the fullerene-like N_{60} molecule, and proposed that it could be formed from six bispentazoles (N_{10}), or $[N_5^+ N_5^-]$ salts under extreme conditions [73]. AM1 and SCF levels of theory confirmed that N_{60} is a local minimum, and the reaction energy of $N_{60} \rightarrow 6N_{10}$ is estimated to be exothermic by 2430 kcal/mol at the SCF level, indicating N_{60} would be a super-high-energetic molecule if synthesized.

Calculations of polynitrogens larger than N_{12} have determined relative energetics and vibrational frequencies of possible isomers, but not activation barriers. Future work should explore the kinetic stabilities of these larger polynitrogens on their potential energy surfaces to validate their possible application as energetic materials.

3. Nitrogen-rich compounds, EN_n

Although pure polynitrogens usually have high exothermic reaction energies to form N_2 molecules, many suffer from kinetic instability as discussed in section 2. Nitrogen-rich compounds (EN_n where E = elements other than nitrogen) may be an alternative to improve kinetic stability while maintaining an energy release comparable to corresponding pure polynitrogens [76]. In section 2, several examples of nitrogen-rich compounds have been mentioned such as N_6O_n ($n = 1, 2, 3$) and metal complexes with η^5-N_5 , η^6-N_6 , and η^7-N_7 ligands.

Lee et al. [77] considered the E atom in EN_n as a catalyst, and pointed out that EN_n can dissociate into $E + N_n$ with a high activation barrier followed by low activation barriers for decomposition of N_n into $(n/2)N_2$. They also suggested that *p*-block elements such as Al and Ga would be expected to have strong covalency in the bonding with polynitrogens. In contrast, elements such as transition metals (Ti, Zr, Hf, Th), alkali (Na, K), and alkaline earth (Mg, Ca) metals are expected to form rather ionic complexes with polynitrogen species.

Compounds of azide ($-N=N^+=N^-$) such as NaN_3 and $Pb(N_3)_2$, which can be considered as nitrogen-rich compounds in the EN_n form, are known to be highly explosive [2]. In particular, nonmetal azides such as $B(N_3)_3$ and $Si(N_3)_4$ will probably produce large dissociation energies into N_2 molecules since the azide group acts as a pseudohalogen and is mainly covalently bonded to the nonmetals [78]. In this section, we will focus on the nitrogen-rich compounds of some nonmetal elements with respect to their thermal stabilities to N_2 molecules and will compare them with equivalent pure polynitrogens. In addition, we present dissociation energies of some nitrogen-rich compounds which have been computed by DFT. Hammerl and Klapötke studied nitrogen-rich CN_n compounds in both experiment and theory [79]. Their calculations show that the CN_9^- anion (See Fig. 6) decomposes into $CN_7^- + N_2$ with an activation barrier of 22.5 kcal/mol at the B3PW91 level, whereas the protonated form, CN_9H , has an activation barrier of 16.1 kcal/mol to formation of CN_7H and N_2 at the same level. These values can be compared with a previously estimated dissociation barrier (2.1 kcal/mol) of N_9^+ to form N_7^+ and N_2 [64], and suggests that the CN_9 anion has sufficient kinetic stability to be an energetic-material candidate when combined with an appropriate cation. This study clearly demonstrates that incorporation of a carbon atom enhances the stability of the N_9 unit by forming the CN_9^- anion.



Fig. 6. Molecular structure of CN_9^- anion and AlN_6 .

Since boron is known as a component of propellants, combining of boron and nitrogen atoms would be expected to give nitrogen-rich compounds with high exothermicities [80]. The dissociation reaction of $\text{B}(\text{N}_3)_3$ into $\text{BN} + 4\text{N}_2$ was calculated at the MP2 level to be about 81 kcal/mol, which is quite exothermic [81]. Klapötke and co-workers recently experimentally characterized the highly explosive $\text{B}(\text{N}_3)_3^{4-}$ anion in the form of a Li^+ salt and investigated the stabilization of $\text{B}(\text{N}_3)_3$ by forming adducts with pyridine ($\text{C}_5\text{H}_5\text{N}$) and pyrazine ($\text{C}_4\text{H}_4\text{N}_2$) [82]. Optimized structures of these adducts were computed to be minima at the DFT level.

Lee et al. investigated AlN_n ($n = 4-7$) as suitable candidates for energetic materials at *ab initio* and DFT levels [77]. Calculations predict that the dissociation reaction of AlN_6 (See Fig. 3) is 226 kcal/mol at the CCSD(T) level, which is more exothermic than the dissociation reaction of N_6 into 3N_2 (~ 155 kcal/mol) [51]. They suggested that AlN_n systems are better energetic materials than ScN_7 [58] since the calculated energy release per N_2 (48-75 kcal/mol) for AlN_n species is much larger than for ScN_7 (36 kcal/mol) [58]. This study clearly demonstrates that *p*-block elements are able to introduce various degrees of covalent/ionic bonding nature into nitrogen-rich compounds, which stabilize the corresponding pure polynitrogens.

Azide compounds of hypervalent main group elements such as Si and Ge are also highly explosive [83,84], but their structures and energetics have not been widely explored. Quite recently, the crystal structure of the $\text{Si}(\text{N}_3)_6^{2-}$ anion has been reported, which has 90% nitrogen content, enough to be a possible high-energetic material candidate [83,84]. It is noted that $\text{Si}(\text{N}_3)_6^{2-}$ ($\text{E} = \text{Ge}, \text{Pb}$) have been synthesized and are structurally known [83].

Thus, nitrogen-rich compounds of nonmetallic hypervalent elements seem to be potential candidates for energetic materials as revealed in the study of AlN_n species. Many candidates are likely to exist as azide compounds, $\text{E}(\text{N}_3)_n$. To evaluate possible energetic materials, dissociation reaction energies of some EN_n compounds ($\text{E} = \text{B}, \text{C}, \text{Si}, \text{Ge}$) (See Fig. 7) have been calculated at the B3LYP/6-31G* level. Two possible decomposition pathways have been considered. Table 1 shows reaction energies of decomposition of EN_n into E (ground state gaseous atom) + $(n/2)\text{N}_2$, and Table 2 presents reaction energies of N_2 elimination from EN_n . It is shown that dissociation reactions of CN_n compounds are more exothermic than those of BN_n . Nitrogen-rich compounds of boron might be more energetic in their anionic form rather than neutral form. Among tetraazide compounds of group 14 elements ($\text{C}, \text{Si}, \text{Ge}$), dissociation of GeN_{12} into 6N_2 gives the largest energy release. For the elimination of N_2 from EN_8 and EN_{10} , reaction energies have been computed to be almost two times more exothermic than those of corresponding N_8 and N_{10} . However, the N_2 elimination of BN_{12} and CN_{12} are hardly exothermic compared with that of N_{12} . It can be suggested that nitrogen-rich compounds of other main group elements such as gallium, phosphorus, and sulfur might become

potential energetic materials due to their ability to coordinate with possible polynitrogens such as N_3 or N_5 . In particular, since phosphorus is isovalent with nitrogen, pure polynitrogens (N_n) could be converted into P_mN_n ($m < n$) species, which would be another possible nitrogen-rich species. Recent calculations of P_2N_2 isomers show that the quasi-tetrahedral C_{2v} isomer turns out to be the most kinetically stable isomer with decomposition barrier of 32.8 kcal/mol into two $P \equiv N$ molecules as well as a barrier of 51.3 kcal/mol into N_2 and P_2 molecules at the CASPT2 level [85].

Table 1

Computed reaction energies (in kcal/mol) at the B3LYP/6-31G* level

$EN_n \rightarrow E + (n/2)N_2$	Reaction energy	$N_n \rightarrow (n/2)N_2$	Reaction energy
$BN_4 \rightarrow B + 2N_2$	-4.4	$N_4 \rightarrow 2N_2$	-171.3
$CN_4 \rightarrow C + 2N_2$	-14.5		
$BN_6 \rightarrow B + 3N_2$	45.5	$N_6 \rightarrow 3N_2$	-155.5
$CN_6 \rightarrow C + 3N_2$	29.5		
$BN_8 \rightarrow B + 4N_2$	-12.9	$N_8 \rightarrow 4N_2$	-187.0
$CN_8 \rightarrow C + 4N_2$	-26.7		
$BN_{10} \rightarrow B + 5N_2$	-80.2	$N_{10} \rightarrow 5N_2$	-224.9
$CN_{10} \rightarrow C + 5N_2$	-93.7		
$B(N_3)_4 \rightarrow B + 6N_2$	-81.6	$N_{12} \rightarrow 6N_2$	-289.5
$C(N_3)_4 \rightarrow C + 6N_2$	-96.0		
$Si(N_3)_4 \rightarrow Si + 6N_2$	-79.8		
$Ge(N_3)_4 \rightarrow Ge + 6N_2$	-125.5		

Table 2

Computed reaction energies (in kcal/mol) at the B3LYP/6-31G* level

$EN_n \rightarrow EN_{n-2} + N_2$	Reaction energy	$N_n \rightarrow N_{n-2} + N_2$	Reaction energy
$BN_6 \rightarrow BN_4 + N_2$	49.9	$N_6 \rightarrow N_4 + N_2$	15.9
$CN_6 \rightarrow CN_4 + N_2$	44.0		
$BN_8 \rightarrow BN_6 + N_2$	-58.4	$N_8 \rightarrow N_6 + N_2$	-31.5
$CN_8 \rightarrow CN_6 + N_2$	-56.2		
$BN_{10} \rightarrow BN_8 + N_2$	-67.3	$N_{10} \rightarrow N_8 + N_2$	-38.0
$CN_{10} \rightarrow CN_8 + N_2$	-67.0		
$B(N_3)_4 \rightarrow BN_{10} + N_2$	-1.4	$N_{12} \rightarrow N_{10} + N_2$	-64.5
$C(N_3)_4 \rightarrow CN_{10} + N_2$	-2.3		

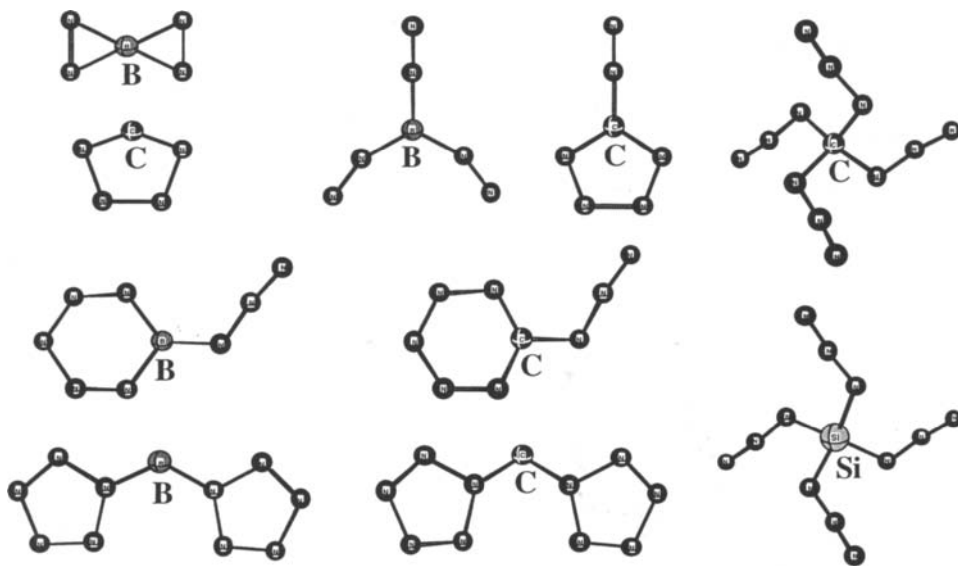


Fig. 7. Geometries of some EN_n species optimized at the B3LYP/6-31G(d) level.

Conclusions

The current role of theory in exploring polynitrogens as energetic material candidates has been reviewed. The exothermicity and kinetic stability, key properties in the characterization of energetic materials, can be estimated by theoretical methods for novel materials. Thus, theory can save time in the development cycle of high-energy materials by identifying promising candidates.

Polynitrogens are known to be strong candidates for energetic materials. Several have already made their real-world appearance with the aid of computational design. The prominent role of the N_3 ring in polynitrogens reported over the past couple of years suggests that it may be a building block for larger polynitrogens such as N_{60} . On the other hand, longer open-chain polynitrogens may not be suitable for energetic materials, since they have small barrier heights for elimination of one N_2 molecule. Another active research area is exploring the salt formed by the cation or anion of an energetic material or, better yet, the salt formed where both the cation and anion are an energetic material such as $[N^{5+}N^{5-}]$. In the future, attention will be focused on larger polynitrogens with cage-like or three-dimensional forms rather than acyclic ones.

Nitrogen-rich compounds may be the best alternative to pure polynitrogens as the former have enhanced kinetic stability while maintaining large dissociation reaction energies. For example, the kinetic stability of N_9 is increased by forming the CN_9^- anion, and AlN_6 decomposes into $Al + 3N_2$ with an energy release of 226 kcal/mol, which is much larger than the energy release (~155 kcal/mol) of N_6 into $3N_2$. Azide compounds of main-group elements are also of interest as potential candidates for energetic materials.

Calculated reaction energies of some EN_n compounds suggest that nitrogen-rich compounds of hypervalent main group elements might become potential energetic materials due to their ability to coordinate with possible polynitrogens such as N_3 or N_5 . Hypothetical $\text{P}(\text{N}_3)_3$ or $\text{S}(\text{N}_3)_6$ can be considered for future investigation of new energetic materials. E_mN_n ($m < n$) species could be in the region of nitrogen-rich energetic materials.

We hope that the present chapter will provide useful insights and understanding into the challenges of discovering energetic materials still hiding from the real world.

REFERENCES

- [1] G. A. Olah and D. R. Squire, *Chemistry of Energetic Materials*, Academic Press, Boston, 1991.
- [2] N. Kubota, *Propellants and Explosives: Thermochemical Aspects of Combustion*, Wiley-VCH, Weinheim, 2002.
- [3] G. Chung, M. W. Schmidt, and M. S. Gordon, *J. Phys. Chem. A*, 104 (2000) 647.
- [4] W. J. Lauderdale, J. F. Stanton, and R. J. Bartlett, *J. Phys. Chem.*, 96 (1992) 1173.
- [5] R. J. Bartlett, *Chemistry & Industry (London)*, 4 (2000) 140.
- [6] N. N. Greenwood and A. Earnshaw, *Chemistry of the Elements*, Butterworth-Heinemann, Boston, 1997.
- [7] J. E. Huheey, E. A. Keiter, and R. L. Keiter, *Inorganic Chemistry*, 4th Edition, HarperCollins College Publishers, New York, 1993.
- [8] K. O. Christe, W. W. Wilson, J. A. Sheehy, and J. A. Boatz, *Angew. Chem. Int. Ed.*, 38 (1999) 2004.
- [9] J. P. Zheng, J. Waluk, J. Spanget-Larsen, and D. M. Blake, *J. G. Radziszewski, Chem. Phys. Lett.*, 328 (2000) 227.
- [10] H. Östmark, O. Launila, S. Wallin, and R. Tryman, *J. Raman Spectrosc.*, 32 (2001) 195.
- [11] F. Cacace, G. de Petris, and A. Troiani, *Science*, 295 (2002) 480.
- [12] A. Hirsch, Z. Chen, and H. Jiao, *Angew. Chem. Int. Ed.*, 40 (2001) 2834.
- [13] P. Pyykkö and N. Runeberg, *J. Mol. Struct. (Theochem)*, 234 (1991) 279.
- [14] S. Fau, K. J. Wilson, and R. J. Bartlett, *J. Phys. Chem. A*, 106 (2002) 4639.
- [15] A. Vij, J. G. Pavlovich, W. W. Wilson, V. Vij, and K. O. Christe, *Angew. Chem. Int. Ed.*, 41 (2002) 3051.
- [16] R. J. Bartlett, S. Fau, M. Tobita, K. Wilson, and A. Perera. A survey of results for neutral and ionic polynitrogen compounds from N_2 to N_{10} is available from: <http://www.qtp.ufl.edu/~bartlett/polynitrogen.pdf>.
- [17] P. Politzer, J. S. Murray, J. M. Seminario, P. Lane, E. Grice, and M. C. Concha, *J. Mol. Struct. (Theochem)*, 573 (2001) 1.
- [18] F. Jensen, *Introduction to Computational Chemistry*, Wiley, New York, 1999.
- [19] W. Koch and M. C. Holthausen, *A Chemist's Guide to Density Functional Theory*, Wiley-VCH, Weinheim, 2000.
- [20] C. J. Cramer, *Essentials of Computational Chemistry: Theories and Models*, Wiley, New York, 2002.
- [21] S. Fau and R. J. Bartlett, *J. Phys. Chem. A*, 105 (2001) 4096.
- [22] M. Tobita and R. J. Bartlett, *J. Phys. Chem. A*, 105 (2001) 4107.
- [23] K. J. Wilson, S. A. Perera, R. J. Bartlett, and J. D. Watts, *J. Phys. Chem. A*, 105 (2001) 7693.
- [24] R. B. Woodward and R. Hoffmann, *The Conservation of Orbital Symmetry*, Verlag Chemie Academic Press, Weinheim, 1970.
- [25] B. O. Roos, P. R. Taylor, and P. E. M. Siegbahn, *Chem. Phys.*, 48 (1980) 157.
- [26] K. Andersson and B. O. Roos, *Int. J. Quantum Chem.*, 45 (1993) 591.
- [27] M. N. Glukhovtsev and P. v. R. Schleyer, *Int. J. Quantum Chem.*, 46 (1993) 119.
- [28] A. A. Korkin, A. Balkova, R. J. Bartlett, R. J. Boyd, and P. v. R. Schleyer, *J. Phys. Chem.*, 100 (1996) 5702.
- [29] M. Bittererová, T. Brinck, and H. Östmark, *J. Phys. Chem. A*, 104 (2000) 11999.
- [30] M. M. Francl and J. P. Chesick, *J. Phys. Chem.*, 94 (1990) 526.
- [31] T. J. Lee and J. E. Rice, *J. Chem. Phys.*, 94 (1991) 1215.

- [32] D. R. Yarkony, *J. Am. Chem. Soc.*, 114 (1992) 5406.
- [33] K. M. Dunn and K. Morokuma, *J. Chem. Phys.*, 102 (1995) 4904.
- [34] M. N. Glukhovtsev and S. Laiter, *J. Phys. Chem.*, 100 (1996) 1569.
- [35] M. N. Glukhovtsev, H. Jiao, and P. v. R. Schleyer, *Inorg. Chem.*, 35 (1996) 7124.
- [36] M. L. Leininger, T. J. Van Huis, and H. F. Schaefer III, *J. Phys. Chem. A*, 101 (1997) 4460.
- [37] F. M. Bickelhaupt, R. Hoffmann, and R. D. Levine, *J. Phys. Chem. A*, 101 (1997) 8255.
- [38] S. A. Perera and R. J. Bartlett, *Chem. Phys. Lett.*, 314 (1999) 381.
- [39] M. Bittererová, T. Brinck, and H. Östmark, *Chem. Phys. Lett.*, 340 (2001) 597.
- [40] T. J. Lee and C. E. Dateo, *Chem. Phys. Lett.*, 345 (2001) 295.
- [41] T. J. Lee and J. M. L. Martin, *Chem. Phys. Lett.*, 357 (2002) 319.
- [42] M. N. Glukhovtsev, P. v. R. Schleyer, and C. Maerker, *J. Phys. Chem.*, 97 (1993) 8200.
- [43] M. Lein, J. Frunzke, A. Timoshkin, and G. Frenking, *Chem. Eur. J.*, 7 (2001) 4155.
- [44] J. Frunzke, M. Lein, and G. Frenking, *Organometallics*, 21 (2002) 3351.
- [45] L. A. Burke, R. N. Butler, and J. C. Stephens, *J. Chem. Soc., Perkin Trans. 2*, (2001) 1679.
- [46] A. Vij, W. W. Wilson, V. Vij, F. S. Tham, J. A. Sheehy, and K. O. Christe, *J. Am. Chem. Soc.*, 123 (2001), 6308.
- [47] L. Gagliardi, G. Orlandi, S. Evangelisti, and B. O. Roos, *J. Chem. Phys.*, 114 (2001) 10733.
- [48] M. T. Nguyen and T.-K. Ha, *Chem. Phys. Lett.*, 335 (2001) 311.
- [49] R. Engelke, *J. Phys. Chem.*, 96 (1992) 10789.
- [50] T.-K. Ha and M. T. Nguyen, *Chem. Phys. Lett.*, 195 (1992) 179.
- [51] L. Gagliardi, S. Evangelisti, V. Barone, and B. O. Roos, *Chem. Phys. Lett.*, 320 (2000) 518.
- [52] L. J. Wang, P. Warburton, and P. G. Mezey, *J. Phys. Chem. A*, 106 (2002) 2748.
- [53] M. Straka, *Chem. Phys. Lett.*, 358 (2002) 531.
- [54] T. M. Klapötke, *J. Mol. Struct. (Theochem)* 499 (2000) 99.
- [55] Q. S. Li and Y. D. Liu, *J. Phys. Chem. A*, 106 (2002) 9538.
- [56] Y. D. Liu, J. F. Zhao, and Q. S. Li, *Theor. Chem. Acc.*, 107 (2002) 140.
- [57] Q. S. Li and J. F. Zhao, *J. Phys. Chem. A*, 106 (2002) 5928.
- [58] L. Gagliardi and P. Pykkö, *J. Am. Chem. Soc.*, 123 (2001) 9700.
- [59] L. Gagliardi and P. Pykkö, *J. Phys. Chem. A*, 106 (2002) 4690.
- [60] M. W. Schmidt, M. S. Gordon, and J. A. Boatz, *Int. J. Quantum. Chem.*, 76 (2000) 434.
- [61] L. Gagliardi, S. Evangelisti, A. Bernhardsson, R. Lindh, and B. O. Roos, *Int. J. Quantum Chem.*, 77 (2000) 311.
- [62] Q. S. Li and L. J. Wang, *J. Phys. Chem. A*, 105 (2001) 1979.
- [63] L. J. Wang, S. Li, and Q. S. Li, *J. Comput. Chem.*, 22 (2001) 1334.
- [64] Q. S. Li and L. J. Wang, *J. Phys. Chem. A*, 105 (2001) 1203.
- [65] Q. S. Li and Y. D. Liu, *Chem. Phys. Lett.*, 353 (2002) 204.
- [66] Y. D. Liu, P. G. Yiu, J. Guan, and Q. S. Lee, *J. Mol. Struct. (Theochem)*, 588 (2002) 37.
- [67] M. D. Thompson, T. M. Bledson, and D. L. Strout, *J. Phys. Chem. A*, 106 (2002) 6880.
- [68] D. L. Strout, *J. Phys. Chem. A*, 106 (2002) 816.
- [69] Q. S. Li and J. F. Zhao, *J. Phys. Chem. A*, 106 (2002) 5367.
- [70] J.-D. Gu, K.-X. Chen, H.-L. Jiang, J.-Z. Chen, R.-Y. Ji, Y. Ren, and A.-M. Tian, *J. Mol. Struct. (Theochem)*, 428 (1998) 183.
- [71] C. Chen and S.-F. Shyu, *Int. J. Quantum Chem.*, 73 (1999) 349.
- [72] T.-K. Ha, O. Suleimenov, and M. T. Nguyen, *Chem. Phys. Lett.*, 315 (1999) 327.
- [73] M. R. Manaa, *Chem. Phys. Lett.*, 331 (2000) 262.
- [74] J. M. Shulman, T. Venanzi, and R. L. Disch, *J. Am. Chem. Soc.*, 97 (1975) 5335.
- [75] L. A. Paquette, *Chem. Rev.*, 89 (1989) 1051.
- [76] L. J. Wang and P. G. Mezey, *J. Phys. Chem. A*, 106 (2002) 10391.
- [77] E. P. F. Lee, J. M. Dyke, and R. P. Claridge, *J. Phys. Chem. A*, 106 (2002) 8680.
- [78] I. C. Tornieporth-Oetting and T. M. Klapötke, *Angew. Chem. Int. Ed. Engl.*, 34 (1995) 511.
- [79] A. Hammerl and T. M. Klapötke, *Inorg. Chem.*, 41 (2002) 906.
- [80] P. Politzer, P. Lane, and M. C. Concha, *J. Phys. Chem.*, 103 (1999) 1419.
- [81] R. L. Mulinax, G. S. Okin, and R. D. Coombe, *J. Phys. Chem.*, 99 (1995) 6294.
- [82] W. Fraenk, T. Habereeder, A. Hammerl, T. M. Klapötke, B. Krumm, P. Mayer, H. Nöth, and M. Warchhold, *Inorg. Chem.*, 40 (2001) 1334.
- [83] A. C. Filippou, P. Portius, D. U. Neumann, and K.-D. Wehrstedt, *Angew. Chem. Int. Ed.*, 39 (2000) 4333.
- [84] A. C. Filippou, P. Portius, G. Schnakenburg, *J. Am. Chem. Soc.*, 124 (2002) 12396.
- [85] O. Kwon, P. M. Almond, and M. L. McKee, *J. Phys. Chem. A*, 106 (2002) 6864.

Chapter 15

Electronic structure calculations as a tool in the quest for experimental verification of N_4

Tore Brinck^a, Martina Bittererova^a and Henric Östmark^b

^aPhysical Chemistry, Royal Institute of Technology, SE-100 44 Stockholm, Sweden

^bDepartment of Energetic Materials, Swedish Defense Research Agency, SE-172 90, Sweden

1. INTRODUCTION

Polynitrogen compounds have received considerable attention in recent years as potential candidates for high energy density materials (HEDMs). The fact that most of these have a very high energy content is a consequence of the large bond energy of 228 kcal/mol of the triple bond in molecular nitrogen (N_2) compared to the bond energies of nitrogen-nitrogen single and double bonds, which typically amount to 39 and 100 kcal/mol, respectively. In addition to the favorable energetics of the polynitrogen compounds, they also have the added advantage that the energy releasing decomposition into N_2 leads to no deposition of harmful or environmentally benign substances.

Even though theoretical studies have identified a number of potentially metastable structures [1, 2], the experimentally observed nitrogen compounds are still few. The azide anion, N_3^- , was first synthesized in 1890 by Curtius [3]. Christie and coworkers have since 1999 reported the preparation and isolation of N_5^+ together with several different counter ions [4, 5]. A few other species, such as N_3 , N_3^+ , N_4^+ , and N_6^- , have been observed only as gaseous or matrix-isolated ions or radicals [6-12]. We recently reported the detection of cyclic N_5^- in a mass spectrometry experiment [13]. This observation has later been verified by Christie et. al. in a more elaborate study [14]. The experimental preparation and detection of an open-chain N_4 molecule was reported in 2002 by Cacace et al [15]. This species is expected to be unstable towards bimolecular decomposition and also too low in energy to be of any greater interest as a HEDM.

One of the most interesting candidates for a HEDM among the polynitrogen compounds is tetraazatetrahedrane [$N_4(T_d)$]. The energy release involved in the dissociation of this N_4 isomer into N_2 has been estimated to more than 180 kcal/mol [16]. Despite the incredibly high energy content, the

computed dissociation barrier is close to 60 kcal/mol, indicating that it is sufficiently stable for most potential applications [17]. However, all attempts of experimental preparation and detection of $N_4(T_d)$ have so far been unsuccessful. Radziszewski and coworkers reported to have made $N_4(T_d)$ in 2000 [18], but it was later shown that the reported isotope effect on the observed IR-band is not compatible with $N_4(T_d)$ [16]. Besides $N_4(T_d)$, a planar cyclic structure of D_{2h} symmetry, $N_4(D_{2h})$, has been identified as a potential target for synthesis. This isomer was for long considered to be too unstable to be of any greater interest. However, recent theoretical studies indicates that it may be sufficiently stable to be detected under certain conditions [19].

The history of N_4 clearly provides some hints to the challenges that faces theoretical chemistry in the development of new polynitrogen HEDMs. In 1975 Venanzi and Schulman made the first theoretical prediction of the stability of $N_4(T_d)$ [20]. While the reliability of the predicted potential energy surface of N_4 has gradually increased over the years, more than 25 years later there is still no positive experimental identification of a N_4 isomer with a closed structure. It is clear that the theorists need to increase their efforts to aid the experimental community not only in identifying targets for synthesis but also in analyzing potential synthetic routes and methods for detection of target molecules. In this chapter we will review the latest advances along these lines in the quest for experimental verification of a stable N_4 isomer.

2. ENERGETICS

2.1 N_4 singlet potential energy surface

Only two potentially stable minima on the singlet N_4 potential energy surface have been identified (see structures **1** and **3** in Fig. 1). A schematic depiction of the potential energy surface in the vicinity of these minima is presented in Fig. 2. The energy of $N_4(T_d)$ (**1**) relative two N_2 molecules has been estimated by means of electronic structure calculations in a large number of studies [16, 19-25]. Currently the best estimate of this value at 0 K is 182.2 kcal/mol, which was obtained using W2 theory [16]. This approach involves basis set limit extrapolation based on CCSD(T) calculation with basis set up to the size of aug-cc-pV5Z, and the uncertainty of the computed value is expected to be less than 0.5 kcal/mol [16]. For comparison, we note that MR-CISD(Q) calculations using a CAS(12/12) reference space and the cc-pVTZ basis set gave a value of 184.0 kcal/mol [19]. The dissociation of **1** proceeds via a transition state of C_s symmetry (**2TS**) that arises from an avoided crossing due to a change

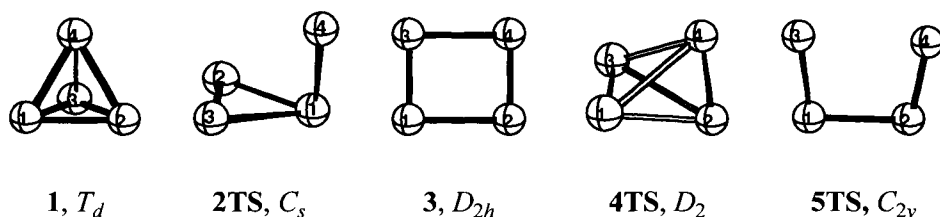


Fig. 1. Optimized geometries of stationary points on the N_4 singlet potential energy surface.

in electron configuration during the dissociation process [17]. The activation energy has been estimated in number of theoretical studies with values ranging from 52-75 kcal/mol [17, 21-24]. It should be noted that most of these have utilized single determinant based methods, which are not fully adequate for describing a multiconfigurational process, such as an avoided crossing. The most accurate values are probably those of Dunn and Morokuma who optimized the transition state at CAS(12,12)/DZP level and computed the activation barrier using this geometry to 64.5 and 62.4 kcal/mol at the CAS(12,12)/DZP and MR-CISD(Q)-CAS(4,4)/DZP levels, respectively [17]. However, in order to obtain an estimate of the activation barrier that is accurate to within a few kcal/mol, it would be necessary to perform MR-CI type calculations using a larger reference space and a bigger basis set including at least f -functions. Still, the computed values are all within a range that indicates the singlet surface dissociation barrier to be large enough to ensure the stability of **1**. Work by Yarkony has indicated that the effective barrier might be reduced to around 30 kcal/mol due to spin-orbit coupling to the triplet state [28]. We will return to discuss this observation in relation to new findings regarding the triplet potential energy surface in the next section of this chapter.

Another possible reaction channel for the decomposition of **1** involves the isomerization into $N_4(D_{2h})$ (**3**). In the D_2 symmetry group the electronic configurations of **1** and **3** differ in the occupation of the $5a$ and $4b_2$ orbitals [$(5a)^2(4b_2)^0$ in **1** and $(5a)^0(4b_2)^2$ in **3**]. In a recent study, we located the minimum crossing point (**4TS**) for these two configuration to be 70 kcal/mol above **1** at the CAS(8,8)/cc-pVTZ level [19]. Unfortunately, we were not able to locate a true transition state for the process. Korkin et al. also located the minimum crossing in D_2 symmetry, and computed the barrier to 70 kcal/mol at the MP2/6-31+G* level [24]. Thus, we can safely conclude that the

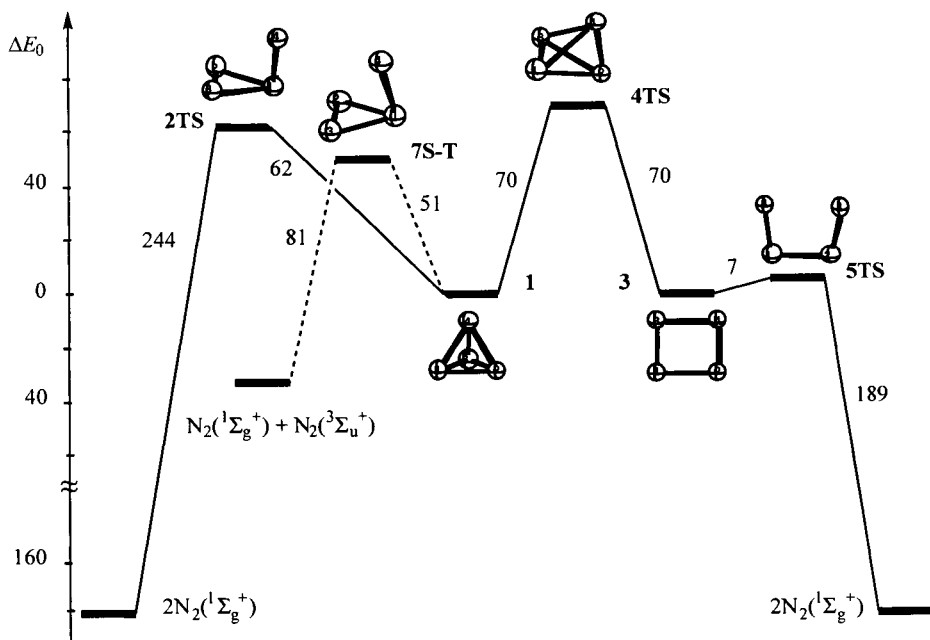


Fig. 2. Relative energies in kcal/mol at 0 K for stationary points on the N_4 singlet potential energy surface. The energies are best estimates based on CCSD(T), MR-CI and CAS-SCF calculations reported in Ref [17, 19, 26, 27]. Note that the spin-forbidden dissociation pathway that passes via the minimum crossing point **7S-T** is included. This pathway is discussed in the section (2.2) on the N_4 triplet potential energy surface. .

isomerization to **3** is not a viable pathway for decomposition of **1** under normal conditions.

Computations at the B3LYP/cc-pVTZ, MR-CISD(Q)/cc-pVTZ//CAS(12,12)/cc-pVTZ and CCSD(T)/cc-pVTZ levels all indicate that **3** is very similar but slightly higher in energy than **1** at 0 K; the computed energy differences are 0.1, 0.2 and 0.6 kcal/mol, respectively at the three levels [19]. On the basis of these results together with the very accurate prediction of the dissociation of **1** using W2 theory [16], we estimate the dissociation energy of **3** to -182.5 kcal/mol at 0 K.

We recently investigated the potential energy surface for dissociation of **3** at the CAS(12,12) level [19]. The dissociation process was found to proceed via a transition state of C_{2v} symmetry (**5TS**). Earlier studies had proposed a D_{2h} transition state [24, 29], however, it was shown that the D_{2h} structure is a second order saddle point rather than a transition state. Single point calculations at

different levels of theory were performed along the CAS(12,12) reaction path to estimate the activation barrier of dissociation. At our highest level MR-AQCC/cc-pVTZ//CAS(12,12)/cc-pVTZ, the zero-point corrected barrier amounts to 6.5 kcal/mol. The CCSD(T)/cc-pVTZ level gives a slightly higher value, 7.1 kcal/mol. These results indicate that **3** is more stable than previously believed and may be possible to synthesize and isolate at low temperatures.

2.2 N₄ triplet potential energy surface

Triplet state N₄ isomers are generally not considered as important target molecules for HEDMs, mainly because of their expected lower stabilities compared to their singlet state analogs. In particular, the open chain triplet N₄ isomers are generally unstable towards bimolecular decomposition due to localized unpaired electrons. However, an understanding of the N₄ triplet potential energy surface can still be of importance for the successful preparation and isolation of a stable singlet N₄ molecule. The very high energies of the singlet state N₄ isomers make them hard to synthesize from molecules in the ground state. One approach for introducing the necessary energy into the system would be the collision of ground state N₂ with an excited state N₂. The most promising candidates for this type of process are triplet excited states, since they generally have longer lifetimes than their singlet state analogs. The reaction

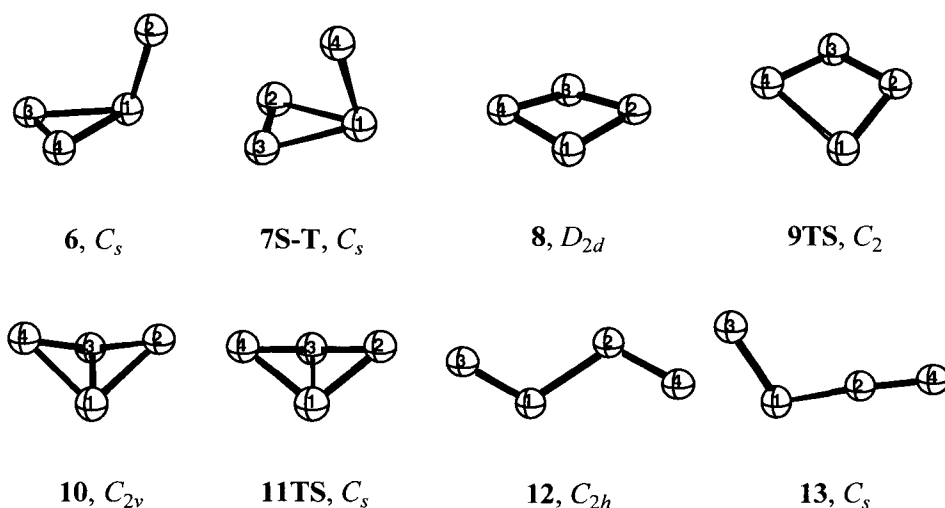


Fig. 3. Optimized geometries of stationary points on the N₄ triplet potential energy surface. Note that **6** is not a stationary point at higher levels of theory, and **7S-T** is the minimum crossing point between the ¹A' and the ³A'' surfaces.

between a singlet state N_2 and a triplet state N_2 will result in a product of triplet character. However, a triplet state N_4 molecule may lead to the generation of singlet state N_4 due to intersystem crossing, pending that its lifetime is sufficiently long. Consequently, an understanding of the triplet state potential energy surface is important for the exploration of new synthetic pathways. Intersystem crossing could also influence the stability of $N_4(T_d)$ (**1**). As already mentioned Lee and Rice and Yarkony have suggested that the effective dissociation barrier for **1** is likely to be reduced due to predissociative crossing between the singlet and triplet potential energy surfaces [22, 28].

Lee and Rice explored triplet potential energy surface in the tetrahedral region using Hartree-Fock and MP2 theory [22]. They found a stable minimum of C_s symmetry $^3A''$ (**6**), with a geometry similar to that of the transition state (**2TS**) for dissociation of **1**. Yarkony later showed that **6** is a minimum also at the CI-SD/DZP level [28]. However, we have demonstrated in a more recent study that this structure is not a minimum at higher levels of theory [30]. Optimizations using the B3LYP, CAS(12,12) and CCSD(T) methods together with polarized basis sets all lead to the dissociation of **6**. Considering that these results clearly show that the CI-SD method is not capable of correctly describing the triplet potential energy surface in the tetrahedral region, the reliability of the minimum crossing point between the singlet and triplet surfaces that Yarkony [28] determined using the same method can be questioned. In addition, a closer comparison between the minimum crossing point structure and the transition structure (**2TS**) of Dunn and Morokuma [17] indicates that the crossing would be post-dissociative, i.e. take place after passing the transition state, and thus not affect the reaction rate. In light of these findings, we decided to reoptimize the singlet-triplet crossing point at the state-averaged CAS(12,12)/DZP level [27]. The new structure **7S-T** is similar to that of Yarkony, but it is much less distorted from the geometry of **1**. In fact the geometry is intermittent between that of **1** and the dissociation transition state (**2TS**) of Dunn and Morokuma. This clearly indicates that starting from the minimum structure of **1** the singlet surface is likely to cross with the triplet surface before the point of the dissociation transition state is reached. Computations at the CAS(12,12)/cc-pVTZ//CAS(12,12)/DZP and CCSD(T)/cc-pVTZ//CAS(12,12)/DZP levels both indicate that the effective dissociation barrier of **1** due to this crossing is close to 51 kcal/mol [27, 31]. This shows that the stability of **1** is much higher than previously estimated based on the energy difference of 28 kcal/mol between the minimum crossing point and **1** obtained by Yarkony [28].

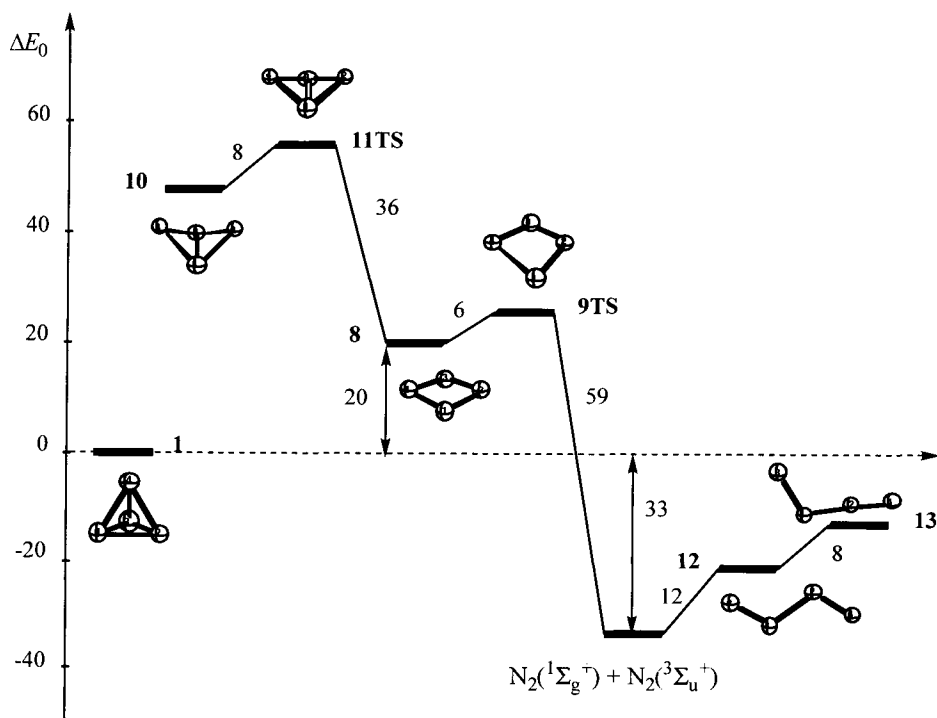


Fig. 2. Relative energies in kcal/mol at 0 K for stationary points on the N_4 triplet potential energy surface. The energies are best estimates based on CCSD(T), MR-CI and CAS-SCF calculations reported in Ref. [30].

According to our studies the lowest triplet state N_4 molecule with a closed structure is a 3A_1 minimum of D_{2d} symmetry (**8**) with two unpaired electrons in the $4e$ orbital[30]. This structure was confirmed by frequency calculations to be a true minimum at all investigate levels of theory, including the B3LYP/cc-pVTZ and CAS(12,12)/cc-pVTZ levels. Computations at the MR-CISD(Q)/DZP//CCSD(T)/DZP and CCSD(T)/DZP levels both gave a energy difference with respect to **1** of close to 16 kcal/mol. This indicates that the CCSD(T) single point computed value of 20.2 kcal/mol using the bigger cc-pVTZ basis should be highly accurate. Furthermore, the value is in excellent agreement with the CAS(12,12)/cc-pVTZ energy difference of 20.3 kcal/mol, while B3LYP/cc-pVTZ finds **8** to be only 8.7 kcal/mol higher in energy than **1**.

Computations using CAS(12,12) indicated that **8** dissociates via a 3B transition state of C_2 symmetry (**9TS**) [30]. The zero-point corrected activation barrier was shown to be 8.5 kcal/mol at the CAS(12,12)/cc-pVTZ level.

CCSD(T)/cc-pVTZ single point calculations at the CAS(12,12) geometries gave a barrier of only 1.9 kcal/mol. In this case CCSD(T) is expected to be less accurate due to the considerable multiconfigurational character of the wavefunction in the vicinity of the transition state. Highly accurate MR-AQCC calculations using the DZP basis set gave a barrier of 7.4 kcal/mol at 0 K. Our best estimate for the barrier is 6 kcal/mol, which is based on the MR-AQCC result and a basis set extrapolation using the CAS(12,12) and CCSD(T) calculations. This makes **8** sufficiently stable to be of interest as an intermediate in the synthesis of singlet state N₄. However, it should be noted **8** is structurally more similar to **3** than to **1**, and consequently **3** is the most likely isomer to be produced in an intersystem crossing process.

A second closed structured triplet state N₄ molecule (**10**, C_{2v} ³B₁) was also found to be a true minimum in the CAS(12,12) calculations [30]. However, this structure is more than 48 kcal/mol higher in energy than **1**. In addition, it has a near zero barrier towards dissociation. Thus, **10** cannot be considered a potential intermediate for synthesis of a stable N₄ molecule.

In addition to the triplet state N₄ isomers with closed structures, two open-chain isomers have been characterized by computational methods [24, 30, 32]. The first is a ³B_u minimum of C_{2h} symmetry (**12**) with one long central single bond and two shorter bonds in the ends of double bond character. The geometry of this species was optimized at the B3LYP/cc-pVTZ and CCSD(T)/DZP levels, and was confirmed to be a true minimum at the former level by frequency calculations [30]. However, our attempts to optimize the structure at the CAS(12,12)/cc-pVTZ level resulted in dissociation. It is not obvious whether the diverging results at different levels of theory are a consequence of the lack of dynamic correlation in the CAS-SCF treatment or the incapability of the single determinant methods to describe the dissociation process properly. In any case, it is clear that **12** would have a short lifetime under normal conditions. Korkin et al., have shown by QCISD(T)/6-311+G* calculations at the triplet geometry that the singlet state is 41.5 kcal/mol lower than the triplet state [24]. This defines **12** as an exciplex, and as such it is expected to dissociate rapidly due to intersystem crossing with the singlet potential energy surface. We note that at the CCSD(T)/cc-pVTZ//CCSD(T)/DZP level **12** is 21 kcal/mol lower in energy than **1** and 12 kcal/mol above the dissociation limit.

The second open-chain N₄ triplet is of C_s symmetry in the ³A'' state (**13**). This structure is 7.9 kcal/mol higher in energy at 0 K than **12** at the CCSD(T)/cc-pVTZ//CCSD(T)/DZP level. However, in contrast to **12**, **13** was found to be stable towards dissociation at the CAS(12,12) level. In addition, Korkin et al.

found **13** to be lower in energy at its equilibrium geometry than singlet state N_4 [24]. Thus, they concluded that **13** might be observed experimentally, as a long-lived intermediate, under certain conditions. It should be noted, however, that the natural bond orbital analysis indicates that the two unpaired electrons are localized to atom 3 (see Fig. 3), and consequently we expect that **13** will be highly unstable towards bimolecular decomposition [30].

The computational results for **12** and **13** are of interest in relation to the recent detection of an open chain N_4 [15]. This molecule was prepared from the N_4^+ cation and was detected to be a gaseous metastable species with a lifetime of at least 1 microsecond in an experiment based on neutralization-reionization mass spectrometry. On the basis of the geometry of N_4^+ and the fragmentation pattern of the $^{14}N_2^{15}N_2$ molecule, Cacace et al. concluded that the observed N_4 isomer is characterized by an open-chain geometry with two distinct, closely bound N_2 units joined by a longer weaker bond [15]. At first consideration, this would indicate that the detected species must be **12** and not **13**, since the latter has a central bond that is shorter than one of the end bonds; the bond lengths are 1.289 Å and 1.337 Å, respectively, at the CCSD(T)/DZP level [30]. However, from energy considerations one can easily realize that **13** is not likely to dissociate via a mechanism where one of the end bonds are broken, since the ground state dissociation products [$N(^4S) + N_3$] lie almost 50 kcal/mol higher in energy. Thus, **13** is more likely to dissociate into two N_2 molecules than $N + N_3$, and consequently **13** cannot be discarded from being the observed molecule based on the fragmentation pattern. On the contrary, **13** is a more likely candidate than **12**, based on the higher stability of the former.

3. SYNTHESIS

3.1 Excited state N_2 reactions

The high energies of $N_4(T_d)$ (**1**) and $N_4(D_{2h})$ (**3**) make them hard to synthesize from ground state molecules. Essentially two different types of approaches for synthesis of N_4 have been considered. The first utilizes excited state N_2 molecules to furnish the necessary energy, while in the second type the energy comes from unbound nitrogen atoms. Considering the first alternative, it should be noted that high concentrations of excited state N_2 molecules can experimentally be generated in liquid or solid nitrogen by laser irradiation, ion bombardment, r.f. excitation or in a hollow-cathode discharge. Two kinds of reactions are possible, either the combination of a ground state N_2 with an excited state N_2 ($N_2 + N_2^* \rightarrow N_4$), or a reaction between two excited state N_2

molecules ($\text{N}_2^* + \text{N}_2^* \rightarrow \text{N}_4$). In either case, a minimum of 11 eV of excitation energy has to be provided for production of **1**, since the reactants has to be higher in energy than the transition state for dissociation of **1**. The main advantage with the first kind of a reaction is that a collision between an excited state N_2 and a ground state N_2 is a more probable event than the collision between two excited state molecules. Unfortunately, the electronic structure of ground state N_2 is not optimal for formation of new N-N bonds.

One particular reaction that has been considered is the interaction between two N_2 in the lowest triplet state, $\text{N}_2(^3\Sigma_u^+)$. This state has a relatively long lifetime (1.9 s) and the excitation energy (6.2 eV) is sufficient to overcome the 11 eV limit. In addition, the excitation is of $\pi \rightarrow \pi^*$ character, which is suitable for the formation of new N-N bonds. In particular, the bond length and orbital occupancy of $\text{N}_2(^3\Sigma_u^+)$ are almost ideal for formation of **3**. However, the energy dissipation is likely to be a serious problem, since the deposited energy is more than 7.8 eV higher than the ground state energy of **3**.

In a recent theoretical study, Lee and Dateo argued that the most likely mechanism for formation of **1** involves the interaction of two N_2 molecules that possess N-N single bonds and where all of the other p -electrons are unpaired and accessible for formation of additional N-N single bonds [26]. This criteria discards the use of the low lying singlet and triplet states of N_2 , which all possess N-N multiple bonds. In addition, the higher lying singlet and triplet states generally have too short lifetimes to be of any greater interest. Lee and Dateo argue that the two lowest quintet states are good candidates for synthesis of **1**, since their equilibrium bond lengths are consistent with typical single bonds [26]. Furthermore, the $A' \ ^5\Sigma_g^+$ state is relatively long lived, since its radiative decay is a spin forbidden process that depend on spin-orbit coupling. One potential problem with using the quintet states are their high energies, which makes it harder to generate them at high concentrations under controlled conditions. In addition, a large amount of internal energy has to be dissipated upon the formation of **1**. The $A' \ ^5\Sigma_g^+ + A' \ ^5\Sigma_g^+$, $A' \ ^5\Sigma_g^+ + C''^5\Pi_u$, and $C''^5\Pi_u + C''^5\Pi_u$ asymptotes are 11.47, 13.29 and 15.11 eV, respectively, higher in energy than **1** [26, 33]. However, if the reaction leads to the formation of an excited state of **1** that subsequently relaxes to the ground state in a radiative process, the energy dissipation is likely to be less of a problem [26].

3.2 Nitrogen atom reactions

An alternative approach for making N_4 is to utilize the inherent energy in atomic nitrogen. The process of forming N_4 from two ground state nitrogen

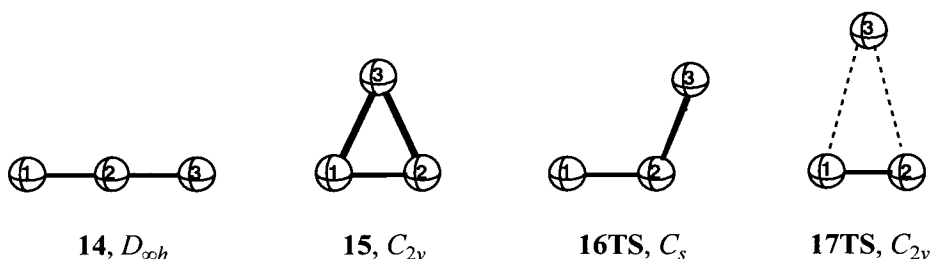


Fig. 4. Optimized geometries of stationary points on the N_3 doublet potential energy surface.

atoms, $N(^4S)$, and ground state N_2 is exothermic by 46 kcal/mol, and excited state nitrogen atoms can furnish even more energy. However, the formation of N_4 from three particles in a single-step mechanism is not a probable process. More likely is a two step mechanism, where N_3 is formed in the first step, and N_4 in the second step, i.e. $N + N_2 \rightarrow N_3$ followed by $N + N_3 \rightarrow N_4$.

The azide free radical, N_3 , has been studied extensively by computational and experimental methods. It has been shown that the ground state (**14**) is of $D_{\infty h}$ symmetry with an equilibrium bond length of 1.181 Å [34]. This geometry is not well suited for the formation of **1** in a reaction with atomic nitrogen, since this would involve a large geometrical rearrangement. In a recent study we analyzed the potential energy surfaces of the lowest lying triplet states in search for more suitable candidates for N_4 synthesis [35]. The initial probing of the potential energy surfaces, performed at the full valence CAS(15,12)/cc-pVTZ level, indicated that there should exist a stable N_3 isomer of C_{2v} symmetry in the 2B_1 state (**15**). A finding which is consistent with results of earlier MR-CISD calculations by Wasilewski using a smaller active space [36]. The **15** isomer was confirmed to be a true minimum also at the B3LYP/cc-pVTZ and CCSD(T)/cc-pVTZ levels of theory. It has one shorter bond (1.23 Å) of double bond character, and two single bonds that are of similar length (1.46-1.48 Å) as the bond in **1**. The energy at 0 K is higher than that of **14** by 29.9 and 30.8 kcal/mol at the CCSD(T)/cc-pVTZ and MR-CISD(Q)/cc-pVTZ//CAS(15,12/cc-pVTZ levels, respectively. The two isomers are connected by an isomerization transition state of C_s symmetry (**16TS**), which according to MRCI-SD(Q) calculations lies 31.5 kcal/mol higher in energy than **15** at 0 K. This barrier is sufficient to ensure that the isomerization is a very slow process under normal conditions. The dissociation into the spin-allowed products [$N(^2D) + N_2$] is an

5.2. Theoretical study

5.2.1. Interaction of 1,3,5-trinitrobenzene with nonhydrated surface of clay minerals

As we mention above the study of the interaction of nitroaromatic compounds with nonhydrated surface of clay minerals has been initiated by the hypothesis about the possibility for the adsorption of nitroaromatic compound on nonhydrated siloxane surface of clay minerals [152-158, 160-164]. This type of adsorption of 1,3,5-trinitrobenzene (TNB) on the siloxane surface of the mineral has been investigated theoretically by Pelmeshnikov et al. [197] and Gorb with co-workers [198]. Since most of results of these studies supplement each other let us to discuss them together.

The calculations of molecular models of siloxane sites of clay minerals with adsorbed TNB at the SCF, DFT (B3LYP) and MP2 levels of theory have been recently carried out [197]. A series of basis sets was used from the smallest 6-31G(d) up to the 6-311+G(d) set of atomic orbitals.

To investigate adsorption of TNB on the siloxane surface also the ONIOM technique has been applied [198] using bigger cluster models. The models of siloxane adsorption sites used in these studies are presented in Fig. 6. They have different sizes starting from the simplest one just having only silicon-oxygen hexagonal ring and up to the molecular system, which possesses the $\text{Al}_{22}\text{Si}_{13}\text{O}_{81}\text{H}_{44}$ stoichiometry. Depending on the size of the system, the adsorption complex of TNB on siloxane sites, the target cluster has been subdivided into the high level part calculated at the MP2/6-31G(d) or HF/6-31G(d) level of theory, the middle level part calculated at the HF/6-31G(d) level and the low level part calculated at the HF/3-21G or HF/STO-3G level of theory.

According to experimental data [153, 154] the NAC compounds adsorb on the nonhydrated siloxane surface coplanar to the plane of surface oxygens. Therefore, initially it has been shown that TNB molecule significantly interacts with the siloxane surface only in planar orientation with respect to the plane of basal oxygen atoms [197, 198]. Then only the coplanar orientation of TNB with respect to the siloxane surface was considered. Two views on the typical structure of such adsorption complexes are illustrated in Fig. 7.

are number of competing reactions, in particular formation of **14** in a near barrierless process, this reduces the probability of forming **15**. However, since the lifetime of $N(^2D)$ is very long (≈ 37 s) in a cryogenic nitrogen matrix, it can be expected that low concentrations of **15** will originate. Consequently we believe that **15** can be used as a precursor for synthesis of **1** according to the scheme.



Both steps are spin-allowed and exothermic reactions. A scan of the N_4 potential energy surface at the CAS(12,12)/cc-pVTZ level indicated that a perpendicular approach of $N(^2D)$ towards the molecular plane of **15** is most favorable for formation of **1**. This can also be rationalized from an analysis of the occupied orbitals in the two species. According to the computed dissociation pathway at the MRCI-SD(Q)/cc-pVTZ//CAS(15,12/cc-pVTZ level, **1** can be formed from **15** and $N(^2D)$ (Eq. 2) in a near barrierless process, as is expected for a radical recombination reaction. However, the scan of the potential energy surface shows that the reaction channel is rather narrow and that two N_2 molecules is likely to be formed in a competing process.

4. DETECTION

4.1 IR and Raman Spectroscopy

An important task for theory in the quest for experimental verification of N_4 is to provide spectral characteristics that allow its detection. The early computational studies focused on the use of infrared (IR) spectroscopy for the detection process. Unfortunately, due to the high symmetry of $N_4(T_d)$ (**1**), the IR spectrum has only one line of weak intensity [37]. Still, this single transition could be used for detection pending that isotopic labeling is employed. Lee and Martin has recently published a very accurate quartic force field of **1**, which has allowed the prediction of both absolute frequencies and isotopic shifts that can directly be used for assignment of experimental spectra (see Table 1.) [16]. The force field was computed at the CCSD(T)/cc-pVQZ level with additional corrections for core-correlation effects. The IR-spectrum of $N_4(D_{2h})$ (**3**) consists of two lines, which both have very low intensities [37]. To our knowledge, high level calculations of the vibrational frequencies have so far only been performed

Table 1.

Computed harmonic (ω) and fundamental (ν) frequencies, IR and Raman intensities and bond length for $N_4(T_d)$ (**1**)^a

Symmetry	Scaled B3LYP/6-311G* ^b	CCSD(T)/ aug-cc-pVTZ ^c	CCSD(T) Best estimate ^d	CCSD/aug-cc-pVDZ Intensities ^c	
	ω	ω	ν	IR	Raman
<i>E</i>	729	724	719	0	9.4
<i>A</i> ₁	939	936	936	11.7	30.4
<i>T</i> ₂	1321	1296	1288	0	45.6
<i>R</i> ₁₂ (Å)	1.446	1.461	1.452	1.443	

^a The units for frequencies, IR and Raman intensities are, cm⁻¹, km/mol and Å⁴/amu, respectively. ^b Ref. [37]. ^c Ref. [38]. ^d Ref. [16]

within the harmonic approximation. In an earlier study we estimated scaling factors for scaling of B3LYP/6-311G(d) harmonic frequencies to reproduce experimental frequencies in all-nitrogen compounds [37]. Scaled B3LYP frequencies together with CCSD(T)/cc-pVTZ harmonic frequencies are listed in Table 2. The latter are expected to compare well with experiment without scaling, considering the good agreement between harmonic frequencies computed at the CCSD(T)/aug-cc-pVTZ level [38] and Lee and Martin's accurate frequencies for **1** [16].

Raman spectroscopy provide complementary information to IR in that bands that are inactive in IR often are active in Raman, and vice versa. The Raman spectrum of **1** consists of three bands with relatively high intensity [37, 38], while the corresponding spectrum for **3** has two strong and one weaker line [37]. Thus, in contrast to IR, Raman provides a tool for fingerprinting of both molecules even without the use of isotopic labeling. In addition, the detection limit is expected to be lower in Raman than IR due to the very low intensities of the IR transitions. We have recently estimated the detection limit for **1** in liquid and solid nitrogen based on experimental measurements and computed Raman intensities for **1** and N₂. The following expression was used to compute the detection limit:

$$C_{\text{limit}} = \frac{2 N_{N_4} A_{N_2}}{S_{N_2} A_{N_4}} \quad (3)$$

where N_{N_4} is the noise in the N₄ region (600-1500cm⁻¹), S_{N_2} is the signal intensity for N₂ and A is the Raman activity. The derived expression is based on

Table 2.

Computed harmonic frequencies (ω), IR and Raman intensities and bond lengths for $N_4(D_{2h})$ (**3**)^a

Symmetry	Scaled B3LYP/6-311G* ^b	CAS(12,12)/ cc-pVTZ ^c	CCSD(T) cc-pVTZ ^c	B3LYP/6-311G* Intensities ^b	
	ω	ω	ω	IR	Raman
A_u	501	506	469	0	0
B_{2u}	532	536	523	1.5	0
A_g	951	886	923	0	23.0
B_{3g}	1017	1041	1026	0	7.3
B_{1u}	1395	1322	1322	0.087	0
A_g	1621	1528	1546	0	0.25
$R_{12}(\text{\AA})$	1.536	1.548	1.541		
$R_{13}(\text{\AA})$	1.250	1.272	1.267		

^a The units for frequencies, IR and Raman intensities are, cm^{-1} , km/mol and $\text{\AA}^4/\text{amu}$, respectively. ^b Ref. [37]. ^c Ref. [19].

the assumption that N_4 can be detected when the signal-to-noise ratio (S/N) is 2. The detection limit of **1** was estimated to be 34 ppm and 80 ppm in liquid and solid nitrogen, respectively, for a measurement time of 8 h using a laser power of 1000 mW in the investigated experimental set up.

4.2 LIF Spectroscopy

Laser-induced fluorescence (LIF) is a preferred method over IR and Raman for detection of compounds in low concentrations due to its higher sensitivity. However, it requires access to relatively low lying excited states with sizeable oscillator strengths and Franck-Condon factors with respect to the ground state.

In two recent publications we have tried to characterize the excited state properties of **1** and **3** in order to facilitate their detection by LIF-spectroscopy. Our main tool in this effort has been equation of motion coupled cluster theory (EOM-CC). The EOM-CCSD method, which is equivalent to linear response CCSD, has been shown to provide an accurate description of both valence and excited states even in systems where electron correlation effects play an important role [39]. Computed transition energies for excitations that are of mainly single substitution character are generally accurate to within 0.1 eV. We have found the EOM-CCSD method to perform particularly well in combination with the doubly-augmented cc-pVDZ (d-aug-cc-pVDZ) basis set. This basis seems to provide equally balanced descriptions of ground and excited states,

Table 3.

EOM-CCSD/d-aug-cc-pVDZ vertical excitation energies (ΔE_{vexc}) (in eV) and one photon oscillator strengths (f), and QR-CCSD/d-aug-cc-pVDZ two-photon transition probabilities (TPA) (in au) for $\text{N}_4(T_d)$ (**1**).

State	Character	$\Delta E_{\text{vexc}}^{\text{a}}$	f^{a}	TPA ^b
1^1T_1	valence	9.65	0	0
1^1A_2	valence	10.25	0	-
1^1T_2	valence	10.26	0.0336	0.761
1^1E	valence	10.28	0	15.818
2^1T_1	valence	10.30	0	0
2^1T_2	Rydberg	10.56	0.0005	0.083
3^1T_1	Rydberg	10.60	0	0
3^1T_2	Rydberg	10.65	0.1974	253.6
4^1T_1	Rydberg	10.67	0	0
1^1A_1	Rydberg	10.75	0	12.44

^a Ref. [19]. ^b Ref. [27]

including high lying Rydberg states. Our calculations predict that there are three optically accessible singlet states of T_2 symmetry at 10.26, 10.56 and 10.65 eV, respectively. The two lower transitions have relatively low intensities, while the third is stronger by about one order of magnitude. Still, this state is hard to reach using one-photon absorption, since the short excitation wavelength precludes the use of a high-power laser as the radiation source. We have therefore calculated the two-photon transition probabilities for excitation to the lowest lying states of **1** using quadratic response CCSD (QR-CCSD) theory [40]. The results presented in Table 3 clearly demonstrates that the selection rules for one- and two-photon transitions are different. However, it is found that the 3^1T_2 state is undoubtedly the most active for both one- and two-photon absorption. Since the ground state **1** is strongly bound, and since this transition is of Rydberg character, we believe the 3^1T_2 state to be bound. This fact together with the sizable two-photon transition probability is likely to make the 3^1T_2 state useful for LIF detection. However, the effective use of the corresponding transition in fingerprinting of **1** will require knowledge about the exact emission wavelength and the Franck-Condon factors for emission and absorption. Consequently, it will be necessary to characterize the excited state geometry and vibrational frequencies.

We have also computed the absorption energies for the lowest lying states of **3** [19]. There is a multitude of states below 10 eV, but the majority of the transitions are dipole-forbidden or have very low oscillator strengths. The most

interesting state for LIF spectroscopy is the first excited singlet state, which is of $^1B_{3u}$ character and lies at 1.57 eV. Although this state has a relatively low transition probability, the very low excitation energy makes it easy to pump using a high-power laser source. In addition, we have found that the optimized geometry is very similar to that of ground state **3**, indicating that the Franck-Condon factors for absorption and emission should be favorable [19].

SUMMARY

The dissociation energy for decomposition of $N_4(T_d)$ (**1**) into two N_2 molecules is 182 kcal/mol at 0 K according to the latest calculations. Despite this large energy difference the activation energy for the spin-allowed dissociation process is close to 60 kcal/mol. New calculations, presented in this chapter for the first time, indicate that the effective barrier due to intersystem crossing with the triplet state is close to 51 kcal/mol. This indicates that **1** is more stable than previously believed and would be an excellent high energy density material (HEDM) if synthesized. The other singlet state N_4 isomer, $N_4(D_{2h})$ (**3**), is very similar in energy to **1**. However, the dissociation barrier is only 7 kcal/mol at 0 K according to high level calculations. Thus, **3** is not a realistic candidate for a HEDM.

A number of triplet state N_4 isomers have been identified and characterized by high level ab initio calculations. These are expected to be too unstable to be of interest as HEDM. However, they might be of importance as intermediates in reactions where singlet state N_4 isomers are produced from excited and ground state N_2 molecules. An alternative approach for N_4 synthesis is to utilize the inherent energy in ground or excited state nitrogen atoms. We have demonstrated that **1** may be formed from nitrogen atoms in the 2D state and molecular nitrogen in a two step process. In the first step the reaction between $N(^2D)$ and N_2 results in the formation of a triangular N_3 isomer of C_{2v} symmetry. In the second step, **1** is formed from N and $N_3(C_{2v})$ in a near barrierless process. High concentrations of $N(^2D)$ can be generated in cryogenic nitrogen matrices, and thus this reaction could serve as a potential route for synthesis of **1**.

The **1** isomer is difficult to detect and identify by IR spectroscopy, since the IR spectrum only contains one weak line. In contrast, there are two transitions of intermediate strength in the Raman spectrum, and consequently Raman spectroscopy can be used for identification without the need of isotopic labeling. An alternative approach for detection is LIF spectroscopy. Excited state calculations, using linear and quadratic CCSD theory, indicates that the

3^1T_2 state, which lies 10.65 eV above the ground state, is accessible by two-photon laser excitation.

REFERENCES

- [1] M. N. Glukhovtsev, H. Jiao and P. v. R. Schleyer, *Inorg. Chem.*, 35 (1996) 7124, and references therein.
- [2] R. J. Bartlett, *Chem. Ind.*, (2000) 140.
- [3] T. Curtius, *Dtsch. Chem. Ges.*, 23 (1890) 3023.
- [4] K. O. Christe, W. W. Wilson, J. A. Sheehy and J. A. Boatz, *Angew. Chem. Int. Ed.*, 38 (1999) 2004.
- [5] A. Vij, W. W. Wilson, V. Vij, F. S. Tham, J. A. Sheehy and K. O. Christe, *J. Am. Chem. Soc.*, 123 (2001) 6308.
- [6] A. E. Douglas and W. J. Jones, *Can. J. Phys.*, 43 (1965) 2216.
- [7] J. M. Dyke, N. B. H. Jonathan, A. E. Lewis and A. Moris, *Mol. Phys.*, 47 (1982) 1231.
- [8] A. Friedman, A. M. Soliva, S. A. Nizkorodov, E. J. Bieske and J. P. Maier, *J. Phys. Chem.*, 98 (1994) 8896.
- [9] R. Tian, J. C. Facelli and J. Michl, *J. Phys. Chem.*, 92 (1988) 4073.
- [10] K. Hiraoka and G. Nakjima, *J. Chem. Phys.*, 88 (1988) 7709.
- [11] W. E. Thompson and M. E. Jacox, *J. Chem. Phys.*, 93 (1990) 1990.
- [12] M. S. Workentin, B. D. Wagner, F. Negri, M. Z. Zgierski, J. Lusztyk, W. Siebrand and W. D. D. M., *J. Phys. Chem.*, 99 (1995) 94.
- [13] A. Hahma, E. Holmberg, N. Hore, R. Tryman, H. Bergman and H. Östmark, presented at the 33rd International Conference of ICT(Ed.), Karlsruhe, 2002.
- [14] A. Vij, J. G. Pavlovich, W. W. Wilson, V. Vij and K. O. Christe, *Angew. Chem. Int. Ed.*, 41 (2002) 3051.
- [15] F. Cacace, G. de Petris and A. Troiani, *Science*, 295 (2002) 480.
- [16] T. M. Lee and J. M. L. Martin, *Chem. Phys. Lett.*, 357 (2002) 319.
- [17] K. M. Dunn and K. Morokuma, *J. Chem. Phys.*, 102 (1995) 4904.
- [18] J. P. Zheng, J. Waluk, J. Spanget-Larsen, D. M. Blake and J. G. Radziszewski, *Chem. Phys. Lett.*, 328 (2000) 227.
- [19] M. Bittererova, H. Östmark and T. Brinck, *Chem. Phys. Lett.*, 347 (2001) 220.
- [20] T. J. Venzani and J. M. Schulman, *Mol. Phys.*, 30 (1975) 281.
- [21] M. M. Francl and J. P. Chesick, *J. Phys. Chem.*, 94 (1990) 526.
- [22] T. J. Lee and J. E. Rice, *J. Chem. Phys.*, 94 (1991) 1215.
- [23] W. J. Lauderdale, J. F. Stanton and R. J. Bartlett, *J. Phys. Chem.*, 96 (1992) 1173.
- [24] A. A. Korkin, A. Balková, R. J. Bartlett, R. J. Boyd and P. v. R. Schleyer, *J. Phys. Chem.*, 100 (1996) 5702.
- [25] M. N. Glukhovtsev and S. Laiter, *J. Phys. Chem.*, 100 (1996) 1569.
- [26] T. J. Lee and C. E. Dateo, *Chem. Phys. Lett.*, 345 (2001) 295.
- [27] T. Brinck, M. Bittererova and H. Östmark, (2002) in preparation.
- [28] D. R. Yarkony, *J. Am. Chem. Soc.*, 114 (1992) 5406.

- [29] Å. Larsson, M. Larsson and H. Östmark, *J. Chem. Soc. Faraday Trans.*, 93 (1997) 2963.
- [30] M. Bittererova, T. Brinck and H. Östmark, *J. Phys. Chem. A*, 104 (2000) 11999.
- [31] It should be noted that this can be considered a lower bound to the barrier, since the single point calculations (no state-averaging) did not give identical energies for the singlet and triplet states, and for both methods we selected the lower energy to estimate the barrier. At the CAS(12,12)/cc-pVTZ//CAS(12,12)/DZP level the relative energies for the singlet and triplet state are 53.6 and 51.1 kcal/mol, respectively, and at the CCSD(T)/cc-pVTZ//CAS(12,12)/DZP level the corresponding energies are 50.8 and 56.4 kcal/mol, respectively. The state-averaged CAS(12,12)/DZP singlet and triplet energies of the minimum crossing point differed by less than $6 \cdot 10^{-3}$ kcal/mol.
- [32] M. N. Glukhovtsev and P. v. R. Schleyer, *Int. J. Quantum. Chem.*, 46 (1993) 119.
- [33] K. P. Huber and G. Herzberg, *Electronic Spectra of Polyatomic Molecules*, Van Nostrand Reinhold, New York, 1979.
- [34] C. R. Brazier, P. F. Bernath, J. B. Burkholder and C. J. Howard, *J. Chem. Phys.*, 89 (1988) 1762.
- [35] M. Bittererova, H. Östmark and T. Brinck, *J. Chem. Phys.*, 116 (2002) 9740.
- [36] J. Wasilewski, *J. Chem. Phys.*, 105 (1996) 10969.
- [37] H. Östmark, O. Launila, S. Wallin and R. Tryman, *J. Raman Spectrosc.*, 32 (2001) 195.
- [38] S. A. Perera and R. J. Bartlett, *Chem. Phys. Lett.*, 314 (1999) 381.
- [39] J. F. Stanton and R. J. Bartlett, *J. Chem. Phys.*, 98 (1993) 7029, and references therein.
- [40] C. Hättig, O. Christiansen, H. Koch and P. Jørgensen, *Chem. Phys. Lett.*, 269 (1997) 428.

This Page Intentionally Left Blank

Chapter 16

Changing the Properties of N_5^+ and N_5^- by Substitution

Stefan Fau and Rodney J. Bartlett

University of Florida, Quantum Theory Project, P.O. Box 118435, Gainesville,
FL 32611-8435, United States of America

The large vertical electron affinity of N_5^+ (6.1 eV) and its susceptibility to nucleophilic attack appear to be the largest obstacles towards use in practical high energy density materials. While the stability of an $N_5^+N_5^-$ salt was suggested, only salts with non-energetic cations like SbF_6^- have been reported. We explore CH, P, P_2 , CO, and O derivatives of N_5^+ and N_5^- in the search for cations with lower electron affinities and anions with larger ionization potentials. Geometries and enthalpies of formation are computed at the CCSD(T)-fc/6-31G** level. Vertical ionization potentials and electron affinities are determined by EOM-CCSD/POL1 single point calculations. NBO analysis of the electronic structure was performed at the B3LYP/aug-cc-pVDZ level. Only two cations, HCN_4^+ and $HNCN_3^+$, have significantly lowered vertical ionization potentials. Their geometries suggest that only the latter has a larger barrier towards unimolecular dissociation than N_5^+ . However, both cations are likely to transfer the proton to the anion. Cations of the $R-NCN_3^+$ type appear worthy of further investigation. Also, a mechanism for the oxidation of Br_2 by $N_5^+SbF_6^-$ is suggested.

1. INTRODUCTION

N_5^+ cations were detected by mass spectroscopy in 1995 and 1998 [1,2]. In the summer of 1999, the preparation of $N_5^+AsF_6^-$ was described [3]. $N_5^+SbF_6^-$ and $N_5^+Sb_2F_{11}^-$ followed in 2001 [4]. These reports received much attention since N_5^+ is only the third homoleptic nitrogen moiety isolated in macroscopic amounts. Its high heat of formation, ~350 kcal/mol [3], makes it a promising candidate for high energy density materials. However, there are difficulties: N_5^+ has a vertical electron affinity (vEA) of 6.0 eV [5], larger than the ionization potential (IP) of energetic anions like N_3^- (2.5 eV), dinitramide ($N(NO_2)_2^-$, >2.55 eV), NO_3^- (4.0

eV), and ClO_4^- (5.3 eV) [6]. This may explain the conspicuous absence of reports on N_5^+ salts of these anions.

Also, $\text{N}_5^+\text{SbF}_6^-$ has been shown to oxidize Br_2 (IP 10.5 eV) at 298K [4]. This is similar to the decomposition temperature of $\text{N}_5^+\text{AsF}_6^-$ (>293K) and lower than that of $\text{N}_5^+\text{SbF}_6^-$, 343K [3,4]. The mechanisms of the three processes are unknown. However, it is known that the N_5 radical dissociates without a barrier into $\text{N}_3 + \text{N}_2$ [5,7]. It is also known that the loss of N_3 from the N_5^+ -fragment in N_5^+N_5^- and " N_5^+N_3^- " is concurrent with the formation of a bond between the anion and the remaining " N_2^- "-fragment [5,8]. The barriers for these processes have been computed as 10-25 kcal/mol. Quasi-linear N_8 is known to lose N_2 with similar barriers [8,9]. One might speculate that both the oxidation of Br_2 and the decomposition of $\text{N}_5^+\text{AsF}_6^-$ and $\text{N}_5^+\text{SbF}_6^-$ involve simultaneous addition and dissociation reactions instead of electron transfer and subsequent dissociation of N_5 . This idea offers a solution to the apparent paradox of electron transfer from Br_2 (IP 10.5 eV) to N_5^+ (vertical EA 6.0 eV). Instead, focus is shifted to the unhampered ability of Br_2 to participate in a reaction with N_5^+ . In contrast, the reaction of AsF_6^- and SbF_6^- (IP >6.0 eV [6]) with N_5^+ probably involves transfer of F^- and consequently breaking of the strong As-F and Sb-F bonds. N_5F would then lose N_2 or N_3 as discussed above for N_8 . This idea is supported by the fact that $\text{N}_5^+\text{AsF}_6^-$ decomposes at lower temperatures than $\text{N}_5^+\text{SbF}_6^-$: AsF_6^- is less stable towards loss of F^- than SbF_6^- [10]. The observed oxidation power of $\text{N}_5^+\text{SbF}_6^-$ appears to be limited by the heat of reaction for $\text{N}_5^+ + \text{e}^- \rightarrow \text{N}_2 + \text{N}_3$, 10.4 eV.

We think that the biggest problem N_5^+ faces in practical high energy density materials is its large electron affinity: It reduces the number of possible anions for salt-formation and causes high reactivity with Lewis bases. A somewhat less electronegative cation should strike a better compromise between energy content and kinetic stability. The electronegativity of molecules and ions is partly determined by the electronegativity of the constituting atoms. Therefore, we explore ions derived from N_5^+ by substituting CH or P for the more electronegative N. Another variation is the replacement of two nitrogen atoms by C and O. At this point, it is useful to consider the charge-distribution in N_5^+ (Fig. 1). We see that the positive charge is distributed quite evenly over both the terminal and

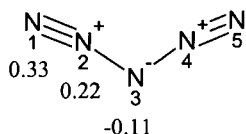


Fig. 1: NBO partial charges of N_5^+ (1) [8].

next-to-terminal atoms. From an electronegativity point of view, these are the best positions for carbon and phosphorus while oxygen would be best placed at the center. Of course, unusual numbers of bonds will most likely lead to high energy, low stability isomers. N-N single bonds without resonance stabilization are particularly unstable.

We have demonstrated that N_5^+ may form a salt with N_5^- [5] although side-reactions like the formation of covalently bound N_{10} or loss of N_2 from the anion may pose a problem. We found that the kinetic stability of N_5^+ is decreased when charge is diminished by charge transfer from the anion. Since the vertical ionization potential of N_5^- (5.6 eV [5,11]) is lower than the vertical electron affinity of N_5^+ , we also explore derivatives of N_5^- that may have a larger ionization potential and/or greater kinetic stability.

Additional knowledge is available from computational investigations. Geometries for N_5^+ were determined at many levels of theory from RHF/6-31G* over B3LYP/6-311+G(3df) to CCSD(T)-fc/cc-pVQZ [3,12-20]. Vibrational frequencies [3,5,8,12-14], NMR-shifts [3], and heats of formation [3,8,13,18] were published, too. The nature of bonding in N_5^+ was investigated in detail [8,18-21]. Other publications explore reactions that N_5^+ may undergo [5,7,8,14-17]. N_5^- has been the object of computational studies, too. Its heat of formation [5,7,18,22] and the barrier towards dissociation into N_3^- and N_2 have been determined [5,7,14,23,24]. Proton affinities in the gas-phase and in water have been studied [25-28]. Salts of N_5^- have been studied elsewhere [23,29-33].

2. COMPUTATIONAL METHODS

Most calculations were performed using ACES II [34]. Geometries were optimized at the MBPT(2)-fc/aug-cc-pVDZ [35] and CCSD(T)-fc/6-31G** [36] levels. Cartesian d-functions were used. Vibrational frequencies were calculated at the same levels of theory. Enthalpies for 298.15K and 1 bar were computed using STTHRM [37]. Vertical electron affinities and ionization potentials were determined by EA- and IP-EOM-CCSD calculations [38,39] using the POL1 basis set [40]. The IP-values are expected to be correct to approximately 0.3 eV [41]. EA-values are usually better [38]. NBO analyses were performed at the B3LYP/6-31G** level at the CCSD(T) geometries with Q-Chem 2.0 [42].

3. RESULTS

3.1. CHN_4^+

There are eight isomers of CHN_4^+ (**2-4**) that retain the electronic structure of N_5^+ (**1**). They vary in the position of the carbon atom and in which former lone-pair is protonated. Their geometries and Lewis structures are displayed in Fig. 2. A detailed description of these compounds is given elsewhere [11]. All isomers are minima. Relative enthalpies and Gibbs free energies are given in Table 1. They usually follow the expected trends: neighboring positive formal charges and σ -lone pairs at carbon are energetically unfavorable, and C-H bonds are preferred to N-H bonds. N-N single bonds have high energies. Their absence is the reason for the low energy of structure **4b**. From charge/electronegativity arguments alone, **4b** should be higher in energy than **2a** as in N_5^+ the terminal nitrogen carries a positive charge while the central atom is negatively charged.

The geometries of the isomers **2a**, **3a** and **4b** have been reoptimized at CCSD(T)-fc/6-31G*. They are given in Table 2. We see that the length of the $\text{N}\equiv\text{N}$ bonds of N_5^+ and the CHN_4^+ isomers are nearly identical. The $\text{C}\equiv\text{N}$ bonds are $\sim 0.04\text{\AA}$ longer, slightly more than expected from the difference in covalent radii (N: 0.74\AA , C: 0.77\AA). Except for the N2-N3 bond in **2a**, C-N and N-N bonds are shorter than expected, suggesting that **3a** and **4b** have higher kinetic stability than N_5^+ .

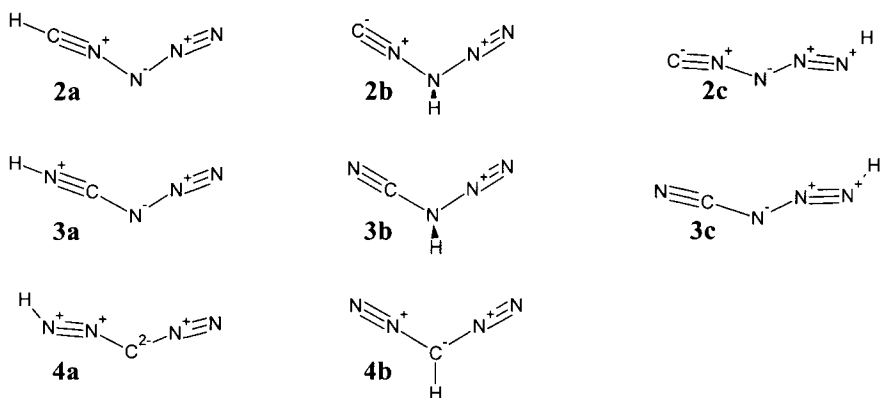


Fig. 2: Geometries and Lewis-structures of CHN_4^+ isomers. Non-hydrogen atoms are numbered from left to right.

Table 1

Symmetries, relative enthalpies and Gibbs free energies (298.15 K, 1 bar) in kcal/mol at MBPT(2)-fc/aug-cc-pVDZ [11].

		H _{rel}	G _{rel}			H _{rel}	G _{rel}			H _{rel}	G _{rel}
2a	C _S	37	37	2b	C _S	75	74	2c	C _S	104	104
3a	C ₁	0	0	3b	C ₁	29	28	3c	C _{2v}	49	50
4a	C _S	(46) ^a	(46) ^a	4b	C _S	1	1				

a) Probably ~7 kcal/mol too high because of bad frequencies.

Table 2

Symmetry, bond length in Å, and bond and dihedral angles in ° of N₅⁺ and the CHN₄⁺ isomers at CCSD(T)-fc/6-31G**.

		r ₁₂	r ₂₃	r ₃₄	r ₄₅	r _{XH}	a ₁₂₃	a ₂₃₄	a ₃₄₅	a _{XXH}
1	C _{2v}	1.131	1.337	1.337	1.131		165.9	108.1	165.9	
2a	C _S	1.159	1.346	1.320	1.134	1.077	166.0	108.7	166.5	177.7
3a	C ₁ ^a	1.164	1.314	1.302	1.132	1.009	169.2	115.8	168.0	170.9
4b	C _{2v}	1.134	1.347	1.347	1.134	1.077	176.7	115.9	176.7	122.1

a) d(H-1-2-3) = 112.9, d(1-2-3-4) = 168.5, d(2-3-4-5) = 180.0

Table 3

Vertical electron affinities of N₅⁺ and the CHN₄⁺ isomers in eV at EOM-CCSD/POL1//MBPT(2)-fc/aug-cc-pVDZ [11].

1	6.2	2a	5.0	2b	6.5	2c	8.4
		3a	4.9	3b	6.6	3c	8.2
		4a	7.2	4b	5.9		

The electron affinities of N₅⁺ and the CHN₄⁺ isomers are given in Table 3. Only **2a**, **3a**, and **4b** have lower electron affinities than N₅⁺. However, all three cations are susceptible to proton transfer to the anion required for salt-formation [11]. Therefore, replacement of the proton by a less mobile substituent will probably be necessary.

3.2. N₄P⁺ and N₃P₂⁺

While substituting nitrogen by phosphorus instead of CH avoids the problem of proton transfer, there are other difficulties: Phosphorus is heavier than CH, reducing the energy density. Also, multiple bonds between first- and second-row elements are usually less stable than those between first-row elements. The Lewis structures and geometries of the N₄P⁺ and N₃P₂⁺ isomers (**5-7** and **8-13**) are given in Fig. 3 and Table 4. All isomers are minima. The ions are covalently bound, except for **9**, which is a PNP⁺···N₂ complex. Cations **7** and **12** have N≡N triple bonds shorter than in N₅⁺ and longer-than-usual N-P single bonds,

Table 4

Symmetry, bond lengths in Å and bond angles in ° of $N_{5-x}P_x^+$ isomers at CCSD(T)-fc/6-31G*.

			r_{12}	r_{23}	r_{34}	r_{45}	a_{123}	a_{234}	a_{345}
N_5^+	1	C_{2V}	1.131	1.337	1.337	1.131	165.9	108.1	165.9
N_4P^+	5	C_S	1.507	1.324	1.320	1.135	168.0	110.8	167.1
	6	C_S	1.540	1.664	1.302	1.135	142.2	118.3	168.7
	7	C_{2V}	1.127	1.827	1.827	1.127	171.1	86.3	171.1
$N_3P_2^+$	8	C_S	1.942	1.676	1.292	1.137	141.2	117.8	169.3
	9	C_S	1.557	1.602	2.442	1.119	176.4	94.4	175.1
	10	C_S	1.517	1.289	1.657	1.539	169.8	124.6	142.0
	11	C_{2V}	1.516	1.304	1.304	1.516	169.4	114.3	169.4
	12	C_S	1.534	2.181	1.842	1.127	147.2	90.2	169.2
	13	$D_{\infty h}$	1.520	1.558	1.558	1.520	180.0	180.0	180.0

suggesting lower barriers to loss of N_2 . The other cations have the following bond lengths: $N \equiv N$ 1.14 Å, $N \equiv P$ 1.51-1.54 Å, $P \equiv P$ 1.94 Å, $N-N$ 1.29-1.34 Å, $N-P$ 1.56-1.68 Å, and $P-P$ 2.18 Å. Except for the linear cation **13**, the angle around the central atom is 110-125° for nitrogen and 86-94° for phosphorus. The angle around the next-to-terminal atom is 167-176° for nitrogen and 141-147° for phosphorus. The geometries of **11** and **13** have the shortest N-N and N-P bonds, suggesting larger barriers towards loss of N_2 or NP. Cations **6**, **8**, and **10** also have short N-N bonds.

The NPA partial charges are given in Table 5. As expected, the less electronegative phosphorus atoms carry positive charges that can be large. The charges of phosphorus atoms bound to nitrogen atoms are usually 0.5-1.2 e^- .

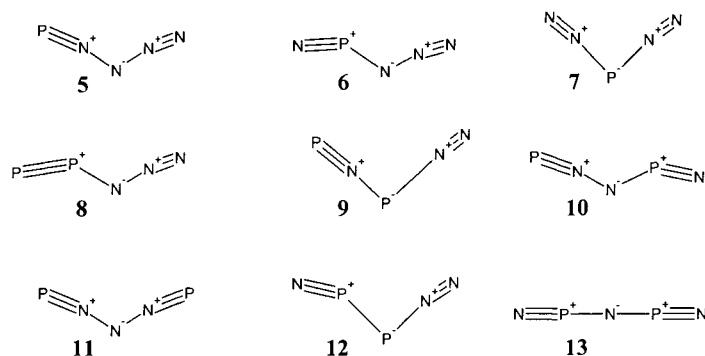


Fig. 3. Lewis structures of the N_4P^+ (**5-7**) and $N_3P_2^+$ isomers (**8-13**). Atoms are numbered from left to right.

Table 5

NPA charges for N_5^+ and the N_4P^+ and $N_3P_2^+$ isomers at B3LYP/6-31G*//CCSD(T)-fc/6-31G*.

	N_5^+	N_4P^+			$N_3P_2^+$					
	1	5	6	7	8	9	10	11	12	13
1	0.33	1.23	-0.45	0.31	0.45	1.12	1.16	1.10	-0.45	-0.55
2	0.22	-0.62	1.50	-0.22	0.66	-1.27	-0.57	-0.59	0.90	1.73
3	-0.11	-0.07	-0.56	0.81	-0.55	1.05	-0.52	-0.01	0.45	-1.36
4	0.22	0.19	0.21	-0.22	0.21	-0.09	1.44	-0.59	-0.21	1.73
5	0.33	0.26	0.30	0.31	0.24	0.19	-0.52	1.10	0.31	-0.55

Table 6

Vertical electron affinities of N_5^+ and the N_4P^+ and $N_3P_2^+$ isomers in eV at EOM-CCSD/POL1//CCSD(T)-fc/6-31G*.

N_5^+			1	6.1		
N_4P^+	5	6.4	6	8.8	7	6.2
$N_3P_2^+$	8	7.7	9	7.6	10	7.8
	11	5.9	12	7.7	13	8.0

Table 7

Enthalpies of formation for N_5^+ and the N_4P^+ and $N_3P_2^+$ isomers in kcal/mol at CCSD(T)-fc/6-31G*.

N_5^+			1	345		
N_4P^+	5	301	6	351	7	257
$N_3P_2^+$	8	293	9	221	10	310
	11	264	12	287	13	354

more positive than the charges of the replaced nitrogen atoms. Since the surrounding nitrogen atoms have correspondingly more negative charges, a substantial ionic contribution to bond energies can be expected. For both **11** and **13**, significant electron transfer is required to produce the expected dissociation products, NP and N_2P^+ .

The vertical electron affinities of N_5^+ and the phosphorus-substituted cations are given in Table 6. Most cations have electron affinities larger than 7.6 eV. Only the cations **5**, **7**, and **11** have electron affinities similar to that of N_5^+ . They are candidates for formation of salts with very electronegative anions like AsF_6^- , SbF_6^- , or N_5^- . The enthalpies of formation of the cations are given in Table 7. They vary between 221 kcal/mol for the $PNP^+ \cdots N_2$ complex **9** over 264 kcal/mol for the 1,5-diphospha cation **11** to 354 kcal/mol for the linear cation **13**.

In general, mono- and diphospha-substituted derivatives of N_5^+ are not suitable for the formation of salts as their electron affinities are too high. However, they promise to be more stable towards loss of N_2 or NP as their N-N single bonds are shorter than those in N_5^+ . Only the 1,5-diphospha cation **11** is worthy of further investigation because its geometry promises kinetic stability and its electron affinity is (slightly) lower than that of N_5^+ .

3.3. CN_3O^+

Since substitution of nitrogen by both CH and phosphorus often increased the vertical electron affinity, we want to investigate the effects of simultaneous substitution with more **and** less electronegative elements. As oxygen is divalent, it can only replace the central or terminal nitrogen atoms. Oxygen in the next-to-terminal position formally leads to nitrenes or carbenes. During optimization, these cations rearrange into cation-molecule complexes. The Lewis structures of the bound cations are given in Fig. 4. It should be noted that many of the cations are not very well described by single Lewis structures.

The geometries are given in Table 8. Since carbon, nitrogen, and oxygen have very similar covalent radii (0.77, 0.74, 0.73 Å) it is easy to compare bond lengths. We see that the $N \equiv N$ triple bonds tend to be shorter than in N_5^+ while $C \equiv N$ triple bonds tend to be longer than the difference in covalent radii suggests.

Table 8

Symmetry, bond lengths in Å and bond angles in ° of N_5^+ and the CN_3O^+ isomers at CCSD(T)-fc/6-31G*.

		r_{12}	r_{23}	r_{34}	r_{45}	a_{123}	a_{234}	a_{345}
1	C_{2v}	1.131	1.337	1.337	1.131	165.9	108.1	165.9
14	C_s	1.148	1.292	1.308	1.129	169.6	117.4	168.1
15	C_s	1.172	1.226	1.336	1.131	165.6	130.1	171.6
16	C_s	1.160	1.170	1.349	1.181	167.5	141.3	174.4
17	C_s	1.164	1.190	1.317	1.222	161.9	131.7	154.4
18	C_s	1.225	1.422	1.327	1.126	146.1	108.1	174.8
19	C_s	1.177	1.379	1.323	1.126	174.6	112.1	171.9

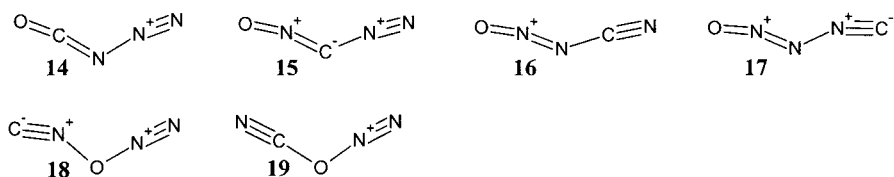


Fig. 4. Lewis structures of bound CN_3O^+ isomers. Atoms are numbered from left to right.

Table 9

NPA charges of N_5^+ and the CN_3O^+ isomers at B3LYP/6-31G*//CCSD(T)-fc/6-31G*.

atom	1	14	15	16	17	18	19
1	0.33	-0.22	-0.01	0.03	0.03	0.60	-0.09
2	0.22	0.97	0.32	0.63	0.59	-0.35	0.48
3	-0.11	-0.33	0.28	-0.01	0.18	-0.02	-0.18
4	0.22	0.23	0.03	0.35	-0.44	0.37	0.37
5	0.33	0.35	0.38	0.00	0.64	0.40	0.42

This is more pronounced for the isonitriles **17** and **18**. The N=O bonds in **15** to **17**, although formally double bonds, have lengths between those of the $\text{N}\equiv\text{N}$ and $\text{C}\equiv\text{N}$ triple bonds. The C=N and N=N bonds in **15** to **17** are only a little longer than the N=O double bonds and the difference in covalent radii suggest. However, the C=N double bond in **14** is 0.07\AA longer than that in **15**. This suggests that an $\text{O}\equiv\text{C}-\text{N}-\text{N}\equiv\text{N}$ resonance structure may be better suited to the geometry. The N-N and C-N single bonds in **14** to **17** appear stronger than the N-N bonds in N_5^+ . The N-N bonds are shorter and the C-N bonds are of similar length, despite the 0.03\AA increase in covalent radii. The C-O and N-O bonds in **18** and **19** are as expected from N_5^+ and the difference in covalent radii or longer.

Table 9 show that the charges at carbon are a little more positive and those at oxygen are usually more negative than the charges of the replaced nitrogen atoms. These differences are usually smaller than $\sim 0.3\text{ e}^-$. The azidylacylium cation **14** is a prominent exception. Generally, atoms of different type connected by the easily polarizable multiple bonds show larger charge variations due to their different electronegativities. The computed partial charges are too small to allow even qualitative estimates of ionic bonding.

Table 10

Vertical electron affinities of N_5^+ and the CN_3O^+ isomers in eV at EOM-CCSD/POL1//CCSD(T)-fc/6-31G*.

14	6.0	15	7.4	16	8.1	17	8.4
18	7.2	19	7.1			1	6.1

Table 11

Enthalpies of formation (298K, 1 bar) of N_5^+ and the CN_3O^+ isomers in kcal/mol at CCSD(T)-fc/6-31G*.

14	258	15	309	16	327	17	369
18	384	19	333			1	345

The vertical electron affinities and enthalpies of formation of the CN_3O^+ isomers are given in Table 10 and Table 11. Only the azidylacylium cation **14** is slightly less electronegative than N_5^+ . The other cations have vertical electron affinities between 7.1 and 8.4 eV, far too high for use with available energetic anions. The enthalpies of formation vary between 258 kcal/mol for **14** and 384 kcal/mol. It may be possible to isolate **14** since salts of both N_5^+ and $N(CO)_2^+$ have been prepared [3,43]. The dissociation of $N(CO)_2^+$ into $^3NCO^+$ and CO is endothermic by 108 kcal/mol [44] while the dissociation of N_5^+ into $^3N_3^+$ and N_2 is endothermic by only 10-15 kcal/mol [13,20]. Even including reaction barriers, the dissociation of the azidyl-group in **14** should be vastly preferred over loss of CO. However, the azidylacylium cation **14** should be more kinetically stable than N_5^+ (**1**) since the N-N bond in **14** is 0.03 Å shorter than in N_5^+ .

3.4. DERIVATIVES OF N_5^-

N_5^- has a vertical ionization potential of 5.6 eV [5,11]. N_5^- dissociates into N_3^- and N_2 with a barrier of ~27 kcal/mol [5,7]. Tetrazolate anion, the CH derivative, is experimentally well known and has a lower vertical ionization potential (4.5 eV [11]). However, since the previous chapters have shown that substitution by less electronegative elements can increase the electron affinity, we will consider P and CO derivatives. Substitution of O for N⁻ results in cyclic N_4O . N_4O , N_4P^- , and two possible CN_3O^- isomers are not yet known and we will investigate if they have better properties.

The Lewis structures and geometries are given in Fig. 5 and Table 12. N_5^- (**20**) is aromatic and all NN bonds have equal lengths. N_4O (**21**) has strongly alternating NN bond lengths and the p_π lone pair is only slightly delocalized (Table 13). N_4O is not aromatic. N_4P^- (**22**) is aromatic with a quite even distribution of p_π

electrons and very similar NN bond lengths. However, the NN bonds are longer than in N_5^- and suggest a reduced barrier to unimolecular dissociation. Neither of the CN_3O^- isomers is cyclic. One dissociates into a CO-N_3^- complex during optimization while the other one opens into **23**. **23** is the anion corresponding to the cation **16** and has slightly longer bond-lengths in the NCN group. The two

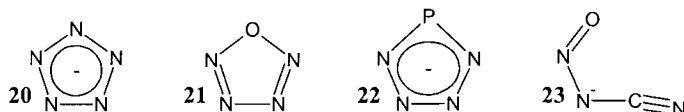


Fig. 5. Lewis structures of N_5^- , N_4O , N_4P^- , and CN_3O^- . Atoms are numbered counter-clockwise from the heaviest atom.

Table 12

Bond lengths in Å and bond angles in ° for N_5^- , N_4O , N_4P^- , and CN_3O^- at CCSD(T)-fc/6-31G*.

		r_{12}	r_{23}	r_{34}	r_{45}	a_{512}	a_{123}	a_{234}	a_{234}
20	D_{5h}	1.339				108.0			
21	C_{2v}	1.391	1.261	1.422		106.5	108.1	108.7	
22	C_{2v}	1.689	1.341	1.350		93.4	108.9	114.4	
23	C_s	1.268	1.338	1.369	1.184		117.7	114.7	170.2

Table 13

NPA charges and p_π occupation numbers for N_5^- , N_4O , N_4P^- , and CN_3O^- at B3LYP/6-31G**//CCSD(T)-fc/6-31G*.

	charge					p_π occupation				
	1	2	3	4	5	1	2	3	4	5
20	-0.20	-0.20	-0.20	-0.20	-0.20	1.20	1.20	1.20	1.20	1.20
21	-0.18	0.15	-0.06	-0.06	0.15	1.67	1.06	1.10	1.10	1.06
22	0.62	-0.66	-0.15	-0.15	-0.66	1.12	1.26	1.18	1.18	1.26
23	-0.52	0.14	-0.50	0.40	-0.52	1.47	0.98	1.42	0.92	1.20

Table 14

Enthalpy of formation in kcal/mol (CCSD(T)-fc/6-31G*) and vertical ionization potential in eV (EOM-CCSD/POL1//CCSD(T)-fc/6-31G*) for N_5^- , N_4O , N_4P^- and CN_3O^- .

	$\Delta_f H$	vIP		$\Delta_f H$	vIP		$\Delta_f H$	vIP		$\Delta_f H$	vIP
20	80	5.6	21	90	13.0	22	53	4.3	23	46	4.0

extra electrons appear as a lone pair at N2 and cause a significant increase in the NN and NO bond lengths as well as a large decrease in the NNO angle.

Table 14 shows the enthalpies of formation and vertical ionization potential of N_4O and the three anions. Only the neutral N_4O has a larger vertical ionization potential than N_5^- . Its enthalpy of formation is 10 kcal/mol larger than that of N_5^- . However, as indicated by the NN and NO single bonds, it is not very stable. The barrier ($\Delta_a H$) towards dissociation into N_2O and N_2 is only 2 kcal/mol.

4. SUMMARY AND CONCLUSIONS

The high heat of formation of the N_5^+ cation (~ 350 kcal/mol) makes it very attractive as a component of high energy density materials (HEDMs). However, its large vertical electron affinity (vEA) of 6.1 eV poses a problem: So far, the preparation of only $\text{N}_5^+\text{AsF}_6^-$, $\text{N}_5^+\text{SbF}_6^-$, and $\text{N}_5^+\text{Sb}_2\text{F}_{11}^-$ has been reported. The oxidation of Br_2 (IP 10.5 eV) by $\text{N}_5^+\text{SbF}_6^-$ shows that N_5^+ is also susceptible to nucleophilic attack by Lewis bases. Calculations on N_5^+N_5^- show that such a crystal may exist, but nucleophilic attack of the anion is a likely side-reaction. We think that less electronegative derivatives of N_5^+ may be less sensitive to both reduction and nucleophilic attack.

Investigation of CHN_4^+ isomers shows three isomers with lower vertical electron affinities than N_5^+ . The bond lengths of one of them, HNC-N_3^+ (**3a**), suggest higher kinetic stability towards loss of N_2 than in N_5^+ . However, all CHN_4^+ isomers are acidic enough to lose the proton to N_5^- or CHN_4^- . Therefore, the proton must be replaced by a less mobile monovalent substituent, e.g. CH_3 , halogens or pseudohalogens.

Substituting nitrogen by phosphorus avoids the problem of hydrogen transfer. On the other hand, the larger weight of phosphorus reduces the energy density. None of the N_4P^+ isomers has a lower vertical electron affinity (vEA) than N_5^+ . Of the N_3P_2^+ isomers, only the 1,5-diphospha cation **11** seems promising. Its vEA is slightly lower than that of N_5^+ and short N-N single bonds suggest an increased barrier to loss of NP.

All but one CN_3O^+ isomer have vertical electron affinities between 7.1 and 8.4 eV. The vEA of OC-N_3^+ (**14**) is only slightly lower than that of N_5^+ . The bonds to the central atom are shorter than in N_5^+ , suggesting increased kinetic stability towards unimolecular dissociation. It should be possible to isolate $\text{OCN}_3^+\text{SbF}_6^-$ since the corresponding N_5^+ and $\text{N}(\text{CO})_2^+$ salts exist.

Except for the neutral N_4O , none of the investigated N_5^- derivatives has an increased vertical ionization potential. N_4O dissociates into N_2O and N_2 with a

barrier of only 2 kcal/mol. The CN_3O^- isomers are not cyclic: One dissociates into a CO-N_3^- complex during optimization while the other transforms into an open-chain structure.

None of the investigated derivatives of N_5^+ and N_5^- are very promising. Most of them have increased vertical electron affinities or decreased vertical ionization potentials. Three cations (OCN_3^+ , PN_3P^+ , and $\text{HC(N}_2)_2^+$) have slightly reduced vEAs. The vEAs of HCN_4^+ and HNCN_3^+ are more than 1 eV lower than that of N_5^+ . We expect increased kinetic stability towards unimolecular dissociation for the latter. However, all CHN_4^+ isomers are susceptible to proton transfer towards the anion. Cations of the R-NC-N_3^+ type appear worthy of further investigation.

ACKNOWLEDGEMENTS

This work was supported by the U.S. Air Force Office of Scientific Research under grant no. F49620-01-1-0072.

REFERENCES

-
- [1] R. Huang, C. Liu, F. Huang, F. Lin, L. Zheng, *Huaxue Tongbao* 39 (1995) 61.
 - [2] T. Matsunaga, T. Ohana, T. Nakamura, K. Ishikawa, M. Iida, Y. Koga, S. Fujiwara, *Kayaku Gakkaishi* 59 (1998) 200.
 - [3] K.O. Christe, W.W. Wilson, J.A. Sheehy, J.A. Boatz, *Angew. Chem. Int. Ed.* 38 (1999) 2004.
 - [4] A. Vij, W.W. Wilson, V. Vij, F.S. Tham, J.A. Sheehy, K.O. Christe, *J. Am. Chem. Soc.* 123 (2001) 6308.
 - [5] S. Fau, K.J. Wilson, R.J. Bartlett, *J. Phys. Chem. A* 106 (2002) 4639.
 - [6] P.J. Linstrom and W.G. Mallard (eds.), NIST Chemistry WebBook, NIST Standard Reference Database Number 69, National Institute of Standards and Technology, Gaithersburg MD, 2003 (<http://webbook.nist.gov>).
 - [7] M.T. Nguyen, T.K. Ha, *Chem. Phys. Lett.* 335 (2001) 311.
 - [8] S. Fau, R.J. Bartlett, *J. Phys. Chem. A* 105 (2001) 4096.
 - [9] G. Chung, M.W. Schmidt, M.S. Gordon, *J. Phys. Chem. A* 104 (2000) 5647.
 - [10] K.O. Christe, D.A. Dixon, D. McLemore, W.W. Wilson, J.A. Sheehy, J.A. Boatz, *J. Fluorine Chem.* 101 (2000) 151.
 - [11] S. Fau, R.J. Bartlett, submitted to *J. Chem. Phys.*
 - [12] P. Pyykkö, N. Runeberg, *Theochem* 80 (1991) 279.
 - [13] M.T. Nguyen, T.K. Ha, *Chem. Phys. Lett.* 317 (2000) 135.
 - [14] L. Gagliardi, G. Orlandi, S. Evangelisti, B.O. Roos, *J. Chem. Phys.* 114 (2001) 10733.
 - [15] W.G. Xu, G.L. Li, L.J. Wang, S. Li, Q.S. Li, *Chem. Phys. Lett.* 314 (1999) 300.

-
- [16] L.J. Wang, Q.S. Li, P. Warburton, P.G. Mezey, *J. Phys. Chem. A* 106 (2002) 1872.
- [17] L.J. Wang, P.G. Mezey, *Chem. Phys. Lett.* 363 (2002) 87.
- [18] X. Wang, H.R. Hu, A. Tian, N.B. Wong, S.H. Chien, W.K. Li, *Chem. Phys. Lett.* 329 (2000) 483.
- [19] R. Ponec, J. Roithova, X. Girones, K. Jug, *THEOCHEM* 545 (2001) 255.
- [20] I.S.K. Kerkines, A. Papakondylis, A. Mavrides, *J. Phys. Chem. A* 106 (2002) 4435.
- [21] R.D. Harcourt, T.M. Klapötke, *Z. Naturforsch. B* 57 (2002) 983.
- [22] V.A. Ostrovskii, G.B. Erusalimskii, M.B. Shcherbina, *Zh. Org. Khim.* 29 (1993) 1297.
- [23] M.T. Nguyen, M.A. McGinn, A.F. Hegarty, J. Elguero, *Polyhedron* 4 (1985) 1721.
- [24] M.N. Glukhovtsev, P.v.R. Schleyer, C. Maerker, *J. Phys. Chem.* 97 (1993) 8200.
- [25] O. Mo, J.L.G. De Paz, M. Yanez, *J. Phys. Chem.* 90 (1986) 5597.
- [26] J. Catalan, M. Sanchez-cabezudo, J.L.G. De Paz, J. Elguero, *THEOCHEM* 43 (1988) 415.
- [27] V.G. Andrianov, M.A. Shokhen, A.V. Eremeev, *Khim. Geterotsykl. Soedin.* 4 (1989) 508.
- [28] V.A. Ostrovskii, G.B. Brusilimskii, M.B. Shcherbinin, *Zh. Org. Khim.* 31 (1995) 1422.
- [29] M. Alcamí, O. Mo, M. Yanez, *J. Phys. Chem.* 93 (1989) 3929.
- [30] M. Lein, J. Frunzke, A. Timoshkin, G. Frenking, *Chem.-Eur. J.* 7 (2001) 4155.
- [31] L.A. Burke, R.N. Butler, J.C. Stephens, *J. Chem. Soc. Perk. T. 2* 9 (2001) 1679.
- [32] L. Gagliardi, P. Pyykkö, *J. Phys. Chem. A* 106 (2002) 4690.
- [33] G. Frison, F. Mathey, A. Sevin, *J. Phys. Chem. A* 106 (2002) 5653.
- [34] ACES II is a program product of the Quantum Theory Project, University of Florida. Authors: J.F. Stanton, J. Gauss, J.D. Watts, M. Nooijen, N. Oliphant, S.A. Perera, P.G. Szalay, W.J. Lauderdale, S.A. Kucharski, S.R. Gwaltney, S. Beck, A. Balková, B.E. Bernholdt, K.K. Baeck, P. Rozyczko, C. Hober, R.J. Bartlett. Integral packages included are VMOL (J. Almlöf, P.R. Taylor); VPROPS (P.R. Taylor) ABACUS; (T. Helgaker, H.J.A. Jensen, P. Jørgensen, J. Olsen, P.R. Taylor).
- [35] T.H. Dunning Jr., *J. Chem. Phys.* 90, (1989) 1007. R.A. Kendall, T.H. Dunning Jr., R.J. Harrison, *J. Chem. Phys.* 96 (1992) 6769.
- [36] W.J. Hehre, R. Ditchfield, J.A. Pople, *J. Chem. Phys.* 56 (1972) 2257. P.C. Hariharan, J.A. Pople, *Theor. Chim. Acta* 28 (1973) 213. M.M. Francl, W.J. Pietro, W.J. Hehre, J.S. Binkley, M.S. Gordon, D.J. DeFrees, J.A. Pople, *J. Chem. Phys.* 77 (1982) 3654.
- [37] Thermodynamic data are calculated based on statistical thermodynamics. STTHRM uses the rigid rotor, harmonic oscillator and ideal gas approximations. Effects of nuclear spin on the rotational symmetry factor are ignored. Internal rotations are treated as vibrations. The electronic partition function is integer, based on multiplicity and spatial degeneracy. The program is available upon request from the RJB group.
- [38] M. Nooijen, R.J. Bartlett, *J. Chem. Phys.* 102 (1995) 3629 and references cited therein.
- [39] J.F. Stanton, J. Gauss, *J. Chem. Phys.* 101 (1994) 8938 and references cited therein.
- [40] A.J. Sadlej, *Collec. Czech. Chem. Commun.* 53 (1988) 1995. A.J. Sadlej, *Theor. Chim. Acta* 79 (1992) 123.
- [41] M. Nooijen, J.G. Snijders, *Int. J. Quantum Chem.* 48 (1993) 15. For ionization potentials, equation-of-motion coupled-cluster, coupled-cluster linear response theory,

and coupled-cluster Greens function are identical although derived from different points of view.

- [42] J. Kong, C.A. White, A.I. Krylov, C.D. Sherrill, R.D. Adamson, T.R. Furlani, M.S. Lee, A.M. Lee, S.R. Gwaltney, T.R. Adams, C. Ochsenfeld, A.T.B Gilbert, G.S Kedziora, V.A. Rassolov, D.R. Maurice, N. Nair, Y. Shao, N.A. Besley, P.E. Maslen, J.P. Dombroski, H. Daschel, W. Zhang, P.P. Korambath, J. Baker, E.F.C. Byrd, T. van Voorhis, M. Oumi, S. Hirata, C.P. Hsu, N. Ishikawa, J. Florian, A. Warshel, B.G. Johnson, P.M.W. Gill, M. Head-Gordon, J.A. Pople, *J. Comput. Chem.* 21 (2000) 1532.
- [43] I. Bernhardt, T. Drews, K. Seppelt, *Angew. Chem. int. Ed.* 38 (1999) 2232.
- [44] M.C. Carvalho, V.F. Juliano, C. Kascheres, M.N. Eberlin, *J. Chem. Soc., Perkin Trans. 2* 1997 (1997) 2347.

This Page Intentionally Left Blank

Index for Parts 1 and 2

A

additivity, atom and group volumes:
 1: 185-188
 ADN: see ammonium dinitramide
 aluminum combustion: 1: 259-261
 ammonium dinitramide (ADN):
 combustion: 1: 398,399 2: 374
 decomposition: 1: 29,30,33,
 394-396,398,399,401,402
 general: 1: 23,28,29,389-403
 simulations: 1: 164,165
 ammonium nitrate (AN):
 decomposition: 1: 30,32
 general: 1: 6,23,27,28,393,394,
 398-400
 simulations: 1: 164,165
 ammonium perchlorate (AP):
 combustion: 2: 290,297,374,375,
 379-437
 decomposition: 1: 29 2: 374,
 375,379-437
 general: 1: 23,28,29,342,390,
 398-400 2: 127,131,297,
 374-437
 potential energy surface:
 2: 375-377,379-437
 AN: see ammonium nitrate
 AP: see ammonium perchlorate

B

band gap: see band structure
 band structure:
 general: 1: 173,174,327-339
 2: 72-77,80,86,87,146

and initiation: 2: 72,73
 boron combustion: 1: 259-261
 burning rate, combustion:
 2: 250-258,273-285,
 299-347,360,363-368

C

Chapman-Jouguet pressure: see
 detonation pressure
 Chapman-Jouguet state: 1: 168,169
 2: 136,137,193,194,198,220,221
 CL-20 (HNIW):
 decomposition: 1: 19
 general: 1: 16,18,19,22,152,398
 2: 6,34,36
 simulation: 1: 153-159
 combustion:
 aluminum: 1: 259-261
 ammonium dinitramide (ADN):
 1: 398,399 2: 374
 ammonium perchlorate (AP):
 2: 290,374,375,379-437
 boron: 1: 259-261
 burning rate: 2: 250-258,
 273-285,299-347,360,363-368
 flame structure: 2: 226,228,239,
 249-258,273-285
 foam layer: 2: 299-347
 GAP: 2: 297-306,332-347
 HMX: 2: 267-272,285-288,290,
 297-306,317-319,332-340,344,
 356-369,374
 ignition: 2: 297-347
 nitrate esters: 2: 259-269,285,286

- RDX: **2**: 297-332,340-347,374
 reaction zone:
 condensed phase:
 2: 227-234,243-258,
 273-285,299-347,
 353-369
 gas phase: **2**: 227,228,
 234-258,273-285,299-347,
 356-369
 multi-phase: **1**: 126
 2: 299-347
 simulation: **2**: 227,249-288,
 297-347,351,356-369
 steady: **2**: 227,249-273,298-347,
 352,353,356-369
 surface: **2**: 227-290,299-347,
 351,353-369
 unsteady (quasi-steady):
 2: 273-288,352,353,362-369
 wave: **2**: 226
 compression effects: **1**: 147-150,155,
 169,170,173,174,307-316 **2**: 73,
 77-87,102,105,106,118,128,
 139-142,147-153
 crystal and molecular packing:
 1: 150-161,164,165,188-211,
 216-226,302,303
 crystal plastic deformation:
 2: 47,101-121,133
 crystal surface distortion: **2**: 101-121
 crystal volume, effective: **1**: 186-188
- D**
- DADNE: see FOX-7
 DATB:
 decomposition: **2**: 26
 general: **2**: 30,40,41
 decomposition:
 ammonium dinitramide (ADN):
 1: 29,30,33,394-396,398,399,
 401,402
 ammonium nitrate (AN): **1**: 32
 ammonium perchlorate (AP):
 1: 29 **2**: 374,375,379-437
 CL-20: **1**: 19
 DATB: **2**: 26
 difluoramines: **1**: 26,27
 dimethylnitramine (DMNA):
 1: 140-142
 EDNA: **2**: 45
 FOX-7 (DADNE): **1**: 56-60,
 91-106
 GAP: **2**: 297-306,332-347
 general: **1**: 13,30-34,62-83,131,
 132 **2**: 5-18,25-27,35-48,
 53-69,143,144,228-234,374,375
 table: **1**: 13
 hexanitrostilbene: **1**: 72,73
 HMX: **1**: 16-19,32,53-60,82,83,
 93,94,139,140 **2**: 7,45,87-97,
 297-306,317-319,332-340
 methylene nitramine: **1**: 144-146
 2: 53,64-69
 nitrate esters: **1**: 8-10
 2: 259-269,285,286
 nitro/*aci*-tautomerism: **1**: 61-83
 2: 35,36
 nitroguanidine (NQ): **1**: 25,56-60
 nitromethane (NM): **1**: 14,15,
 64-69,142-144
 NTO: **1**: 21,24,25,32-34,78-81
 PETN: **1**: 8-10,30
 picric acid (PA): **1**: 11-14,72,73
 polynitrogen systems: **1**: 409-413,
 422-433,441-452
 RDX: **1**: 16-19,30,32,51-60,
 81-83,131-139 **2**: 26,45,46,
 54,55,69,91,297-332,340-347,
 374

TACOT: **1:** 72
 TATB: **1:** 11-14,72,73 **2:** 7,
 10-12,26
 Tetryl: **1:** 11-14,72,73
 TNAZ: **1:** 20,21,32,33
 TNT: **1:** 11-14,30,32,33,72,73,
 75 **2:** 7,9,10,26,40,42
 1,3,5-trinitrobenzene (TNB):
2: 40
 defects, lattice: see lattice defects
 deflagration: **2:** 139,140
 deformation, crystal:
2: 47,101- 121,133
 deformation density: **1:** 215,
 225-230,241,242,246
 density: **1:** 150,161-163,185-188,393
 table: **1:** 22,23,27,29,209,210
 detonation:
 and initiation: **1:** 1,77,127,
 168-172,341 **2:** 1,5-12,
 25-27,35,36,40,45-48,53-72,
 119,120,125,135-181
 and initiation, simulation:
1: 146-150,171-173
2: 161-163,168-175,180,181,
 209,210
 detonation energy: see energy release
 detonation pressure: **1:** 27,93,185
2: 135-141,147
 table: **1:** 27
 detonation velocity: **1:** 22,23,93,185
2: 10,27-32,40,41,43,119,120,
 135-141,176
 table: **1:** 22,23 **2:** 28-32
 2,4-diamino-1,3,5-trinitrobenzene: see
 DATB
 difluoramines:
 decomposition: **1:** 26,27
 general: **1:** 26,27,199,208,209,
 260-270

dimethylnitramine (DMNA):
 decomposition: **1:** 140-142
 general: **1:** 262,282,283,289-292
 simulation: **1:** 140-142,163,164,
 289-292
 dinitramides: **1:** 23,28-30,33,164,165,
 228,229,240-243,389-403 **2:** 374
 dinitraminic acid: **1:** 262,389-397
 direction-dependence, initiation and
 shock propagation: **1:** 147,148
2: 77,81,131,141,149,167
 dissipation of energy: **2:** 7,8,11,12,
 103,109-121
 DMNA: see dimethylnitramine

E

EDNA:
 decomposition: **2:** 45
 general: **1:** 23 **2:** 33
 effective crystal volume: **1:** 186-188
 electronic deformation density:
1: 215,225-230,241,242,246
 electronic density: **1:** 215-243
2: 12
 electronic excitation: **1:** 169,173,174,
 327-339,435-437 **2:** 10,73,74,
 80,86,143-148
 electrostatic potential: **1:** 215,235,
 236,249,258,259 **2:** 12-18
 energy density: **1:** 236-241
2: 115-118
 energy dissipation: **2:** 7,8,11,12,103,
 109-121
 energy release: **1:** 1,2,6,58,59,62,
 166-173,247,260,261,265-270,405,
 406,415-417,422-424 **2:** 1,2,5,7,
 8,11,12,53-69,127,135,136,151,
 176-179,193,229,249,250,278-285,

301-347

table: **1**: 59,265-270,416**2**: 248,249

enthalpy of formation: see heat of formation

enthalpy of sublimation: see heat of sublimation

enthalpy of vaporization: see heat of vaporization

equations of state: **2**: 194-197, 200-210,221

ethylene dinitramine: see EDNA

explosives:

primary: **1**: 341 **2**: 127secondary: **1**: 341,342 **2**: 127**F**flame structure: **2**: 226,228,239, 249-258,273-285,353,360foam layer: **2**: 299-347force fields: **1**: 129,130,146-174, 194,197-199,281-292 **2**: 103, 108-112,167,195-207,213-215,378

FOX-7 (DADNE):

decomposition: **1**: 56-60,91-106general: **1**: 19,20,23,50,51,77,78, 92,158,159,266simulation: **1**: 54-60,158,159tautomerism: **1**: 102**G**

GAP:

combustion: **2**: 297-306,332-347decomposition: **2**: 297-306, 332-347general: **2**: 297**H**heat of formation: **1**: 247-271, 393,441,449,451table: **1**: 29,262-264,265-270, 447,449,451heat of sublimation: **1**: 149,152-159, 164,165,199-210,249,258-261, 271,306 **2**: 15table: **1**: 209,210,304heat of vaporization: **1**: 162,249, 258-261,271,294

heat release: see energy release

hexanitrostilbene:

decomposition: **1**: 72,73general: **1**: 22,72 **2**: 32

high-nitrogen systems: see polynitrogen systems

HMX:

combustion: **2**: 267-272,285-288, 290,297-306,317-319,332-340, 344,356-369,374compression effects: **1**: 307-316decomposition: **1**: 16-19,32, 53-60,82,83,93,94,139,140 **2**: 7,45,87-97,297-306,317-319,332-340elasticity: **1**: 316-320general: **1**: 16,22,23,26,27,50,51, 77,78,93,187,199,202,219,220, 225,227-230,235,236,279-323, 341-343,371,397 **2**: 6,8,34, 72,87,113,127,135,136,141, 144,147,151,160-163,174,175, 210,211,220,226,227,234,241, 242,257,297,351-353heat of sublimation: **1**: 306

potential energy surface:

1: 282-288pressure effects: **1**: 307-316,

320,321
 simulations: **1**: 54-60,153-159,
 163,164,292-320 **2**: 90-97
 tautomerism: **1**: 82,83
 thermal conductivity: **1**: 298-302
 thermal expansion coefficient:
1: 303-305
 HNIW: see CL-20
 HOMO, LUMO (also see band
 structure): **2**: 75-77,83-86,141
 hot spots:
 and defects: **1**: 147-149
2: 7,8,168-172
 general: **1**: 127,147-149,172,320
2: 7-12,71,102,109-121,
 137-142,153,163-165,168-172,
 177-179
 and initiation: **2**: 7,8,71,72,102,
 109-121,168-172
 and strain: **1**: 147 **2**: 7-9
 Hugoniot relation: **1**: 130,168,169
2: 125,128,133-137,170,197-211
 hydrazine: **1**: 398-401
 hydrogen bonding: **1**: 20,65-77,92,
 158,159,240-243 **2**: 11,142

I

ignition:
 combustion: **2**: 297-347
 simulation: **2**: 299-332,346,347
 initiation:
 and band structure: **2**: 72,73
 and detonation: **1**: 1,77,127,
 168-172,341 **2**: 1,5-12,
 25-27,35,36,40,45-48,53-72,
 119,120,125,135-181
 and detonation, simulation:
1: 146-150,171-173
2: 161-163,168-175,180, 181,

209,210
 direction dependence: **1**: 147,148
2: 77,81,131,141,149,167
 and hot spots: **2**: 7,8,71,72,102,
 109-121,168-172
 and lattice defects: **1**: 127,
 147-149 **2**: 7,8,38,71,72,
 108,109,138,140,153,163,
 168-172
 models: **1**: 146-150,166-173
2: 72,73
 and plastic deformation: **2**: 47,
 101-121
 stimuli: **1**: 1,128,341 **2**: 1,5,
 25-34,36-48,71,101-121
 intrinsic propellant stability:
2: 288-290

L

lattice defects:
 effects on initiation: **1**: 127,147-
 149,172 **2**: 7,8,38,71,72, 108,
 109,138,140,153,163,168-172
 formation: **1**: 147 **2**: 38
 and hot spots: **1**: 147-149
2: 7,8
 vacancies, voids: **1**: 172
2: 7,8,81-86
 lattice deformation: see deformation,
 crystal
 lattice energy: see heat of sublimation
 lattice structure:
 general: **1**: 150-161,164,165,
 188-211,216-226,302,303
 NTO: **1**: 217-219,222-225
 table: **1**: 218
 lattice vibrations: **1**: 128,148,149
2: 8,9,42,55-57,68,72,110,111,
 119,120,145-168,181,211

M

methylene nitramine:

decomposition: **1:** 144-146

2: 45,53,64-69

simulation: **1:** 145,146

molecular and crystal packing:

1: 150-161,164,165,188-211,216-

226,302,303

N

nanoenergetic materials: **2:** 126,

151-153,175-181

NC: see nitrate esters

NG: see nitrate esters

nitrate esters:

combustion: **2:** 259-269,285,286

decomposition: **1:** 8-10

2: 259-269,285,286

general: **1:** 6-10,22,342 **2:** 226,

227,234,240-242

simulations: **1:** 162,163

nitrocellulose (NC): see nitrate esters

nitroglycerine (NG): see nitrate esters

nitroguanidine (NQ):

decomposition: **1:** 25,56-60

general: **1:** 23,50,51,77,78,342

simulations: **1:** 54-60

nitromethane (NM):

decomposition: **1:** 14,15,64-69,

142-144

general: **1:** 22 **2:** 73-87,127,

139-141,154-157,167,174,220

potential energy surface: **2:** 73,74

tautomerism: **1:** 63-69

simulations: **1:** 143,144,160-162

nitronic acids: **1:** 61-83

NMR chemical shifts: **2:** 27-34,36-47

NQ: see nitroguanidine

NTO:

decomposition: **1:** 21,24,25,32-34,78-81

general: **1:** 23,77-79,217-219,

222-225,228,230-240,265

2: 14,16,142

lattice structure: **1:** 217-219,

222-225

table: **1:** 218

tautomerism: **1:** 78-81

O

octanitrocubane (ONC): **1:** 15,199,

209,210,261,268 **2:** 16

ONC: see octanitrocubane

P

PETN:

decomposition: **1:** 8-10,30

general: **1:** 9,22,23,77,78,327,

332-335,338,342,399

2: 73,127,139-141,167,209,21

simulations: **1:** 155-159,163

phonons: see lattice vibrations

picramide: **1:** 22,74,76,77 **2:** 30

picric acid:

decomposition: **1:** 11-14,72,73

general: **1:** 6,11,22,72,73,76,77,

342 **2:** 16,30

plastic crystal deformation: **2:** 47,

101-121,133

pollution:

general: **1:** 2,343-346,380 **2:** 2

interactions with soil: **1:** 344-380

simulations: **1:** 347,348,351-366,

371-380

polynitrogen systems:
 decomposition: **1:** 409-413,
 422-433,441-452
 general: **1:** 406-418,421-437,
 441-452
 potential energy surface:
1: 409-413,422-429
 potential energy:
 functions: **1:** 129,130,146-174,
 194,197-199,281-292 **2:** 103,
 108-112,167,195-207,213-215,
 378
 surface:
 ammonium perchlorate (AP):
2: 375-377,379-437
 FOX-7: **1:** 97,101
 general: **1:** 76 **2:** 53-69,
 143,144,149
 HMX: **1:** 282-288
 nitromethane: **2:** 73,74
 polynitrogen systems:
1: 409-413,422-429
 pressure effects: **1:** 155-161,173,
 174,307-316,320,321 **2:** 75,78,
 79,83,85-87,117-120,136,139,
 140,174,213-215,218,219,221,
 234-290,362-364
 primary explosives: **1:** 341 **2:** 127
 propellant intrinsic stability: **2:** 288-
 290
 propellant reaction zone: see
 combustion reaction zone
 pyrolysis equations: **2:** 233,234

R

RDX:
 combustion: **2:** 297-332,340-
 347,374

decomposition: **1:** 16-19,30,32,
 51-60,81-83,92-94,131-139
2: 26,45,46,54,55,69,297-332,
 341-348
 general: **1:** 6,16,20,22,23,50,77,
 78,92,93,131,187,327,328,332,
 333,336-338,341-343,371,
 396-400 **2:** 6-8,33,73,86,89,
 94,103-108,112-115,127,138,
 141,144,160,163,167,174,175,
 220,226,234,241,242,297
 simulations: **1:** 54-60,134-139,
 152-159
 tautomerism: **1:** 81-83
 reaction zone, propellant: see
 combustion reaction zone
 rigid molecule approximation:
1: 150-159

S

secondary explosives: **1:** 341,342
2: 127
 sensitivity:
 correlations: **1:** 58,59,247
2: 5-18,25,36-40,43,44,72,
 141,162,163
 factors determining: **1:** 397
2: 5-18,102,141,142,153,
 160-165,168-172
 and nitro, *aci*-nitro tautomerism:
1: 61-83
 table: **1:** 22,23,59,78,397
2: 28-34
 shock wave:
 direction-dependence: **1:** 147,148
2: 77,81,131,141,149,167
 general: **1:** 1 **2:** 1,71,125,
 128-137
 simulation: **1:** 128-131,168-172

- 2: 161-163,168-175,180,181,
197-211
- simulation:
- ammonium dinitramide (ADN):
 - 1: 164,165
 - ammonium nitrate (AN):
 - 1: 164,165
 - CL-20: 1: 153-159
 - combustion: 2: 227,249-288,
297-347,351,356-369
 - dimethylnitramine (DMNA):
 - 1: 140-142,163,164,289-292
 - force fields: 1: 129,130,146-174,
194,197-199,281-292 2: 103,
108-112,167,195-207,213-215,
378
 - FOX-7 (DADNE): 1: 54-60,158,
159
 - HMX: 1: 54-60,153-159,163,164,
292-320 2: 90-97
 - ignition: 2: 299-332,346,347
 - initiation and detonation:
 - 1: 146-150,171-173
 - 2: 161-163,168-175, 180, 181,
209,210
 - methodology: 1: 51,53,54,
128-131,347,348 2: 161-163
 - methylene nitramine: 1: 145,146
 - nitrate esters: 1: 162,163
 - nitroguanidine (NQ): 1: 54-60
 - nitromethane (NM): 1: 143,144,
160-162
 - PETN: 1: 155-159,163
 - pollution (interactions with soil):
 - 1: 347,348,351-366,371-380
 - RDX: 1: 54-60,134-139,152-159
 - shock wave: 1: 128-131,168-172
2: 161-163,168-175,180,181,
197-211
 - TNT: 1: 155
 - specific impulse: 1: 93,400,401,408
table: 1: 27,401
 - state equations: 2: 194-197,200-210,
221
 - surface distortion, crystal:
 - 2: 101-121
- T**
- TACOT:
- decomposition: 1: 72
 - general: 1: 22,72
- TATB:
- decomposition: 1: 11-14,72,73
2: 7,10-12,26
 - general: 1: 11,22,72-74
2: 10-12,30,72,127,141,142,
162,174,210,211
 - thermal conductivity: 2: 11
- tautomerism:
- general: 1: 61,62
 - nitro, *aci*-nitro: 1: 61-83
2: 35,36
 - and sensitivity: 1: 61-83
- 1,3,5,7-tetranitro-1,3,5,7-
tetraazacubane: 1: 261,268
- Tetryl:
- decomposition: 1: 11-14,72,73
general: 1: 11,22,72,342 2: 34
- thermal conductivity:
- HMX: 1: 298-302
 - TATB: 2: 11
- TNAZ:
- decomposition: 1: 20,21,32,33
general: 1: 16,20,21,265
2: 16,33
- TNB: see 1,3,5-trinitrobenzene
- TNT:
- decomposition: 1: 11-14,30,32,

- 33,72,73,75 2: 7,9,10,26,35,
40,42
 general: 1: 6,11,22,23,72-77,
341-343,370,371,400
 2: 16,29,141
 simulation: 1: 155
 toxicity: 1: 2,342,398-401 2: 2
 table: 1: 401
 2,4,6-triamino-1,3,5-trinitrobenzene:
 see TATB
 trigger linkage: 2: 8-14
 2,4,6-trinitroaniline: see picramide
 1,3,3-trinitroazetidine: see TNAZ
 1,3,5-trinitrobenzene (TNB):
 decomposition: 2: 40
 general: 1: 22,369,371-380
 2: 28
 2,4,6-trinitrophenol: see picric acid
 2,4,6-trinitroresorcinol: 1: 22
 2: 30,40,41
 2,4,6-trinitrotoluene: see TNT

V

- vibrational energy, molecular:
 1: 136,137,141,146,148, 149,172,
 249 2: 7-12,42,53-69,72,74,102,
 109-121,143-181
 vibrational excitation: see vibrational
 energy, molecular
 vibrons: see vibrational energy,
 molecular
 volume:
 additivity: 1: 185-188
 atom: 1: 185-188
 crystal (effective): 1: 186-188
 group: 1: 185-188

This Page Intentionally Left Blank